WILEY-VCH

Edited by Srabanti Ghosh

Conjugated Polymer Nanostructures for Energy Conversion and Storage Applications

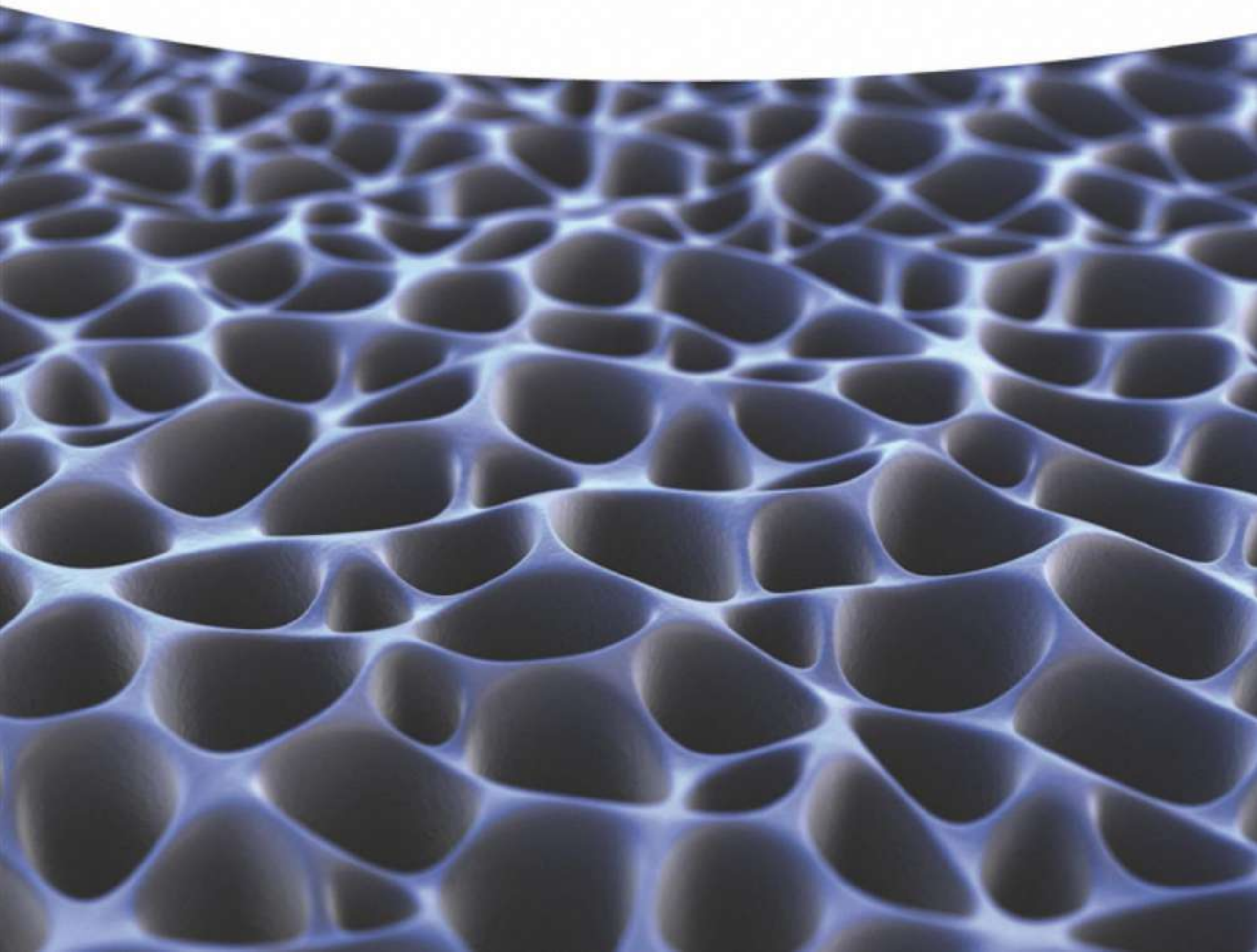

Conjugated Polymer Nanostructures for Energy Conversion and Storage Applications

Conjugated Polymer Nanostructures for Energy Conversion and Storage Applications

Edited by
Srabanti Ghosh

WILEY-VCH

Editor

Dr. Srabanti Ghosh
Central Glass & Ceramic Research Institute
Energy Materials and Devices Division
196, Raja S. C. Mullick Road
700 032 Kolkata
India

Cover Image: © enot-poloskun/Getty Images

Library of Congress Card No.:
applied for

British Library Cataloguing-in-Publication Data
A catalogue record for this book is available from the British Library.

Bibliographic information published by the Deutsche Nationalbibliothek
The Deutsche Nationalbibliothek lists this publication in the Deutsche Nationalbibliografie; detailed bibliographic data are available on the Internet at <http://dnb.d-nb.de>.

Print ISBN: 978-3-527-34557-1
ePDF ISBN: 978-3-527-82010-8
ePub ISBN: 978-3-527-82012-2
oBook ISBN: 978-3-527-82011-5

Typesetting SPi Global, Chennai, India
Printing and Binding

Printed on acid-free paper

10 9 8 7 6 5 4 3 2 1

Contents

Preface

Twenty years after the discovery of conjugated polymers, the concept of conjugated polymer in nano-dimension emerged in recent decades and continues to attract scientific community with the objective of tuning the intrinsic properties or integrated systems with multiple functionalities for the application in energy domain. Recognizing the importance of conjugated polymers with their unique nanostructures and beneficial characteristics of low cost, good environmental stability, high conductivity, high carrier mobility, good mechanical properties, and large specific surface area have drawn considerable attention for renewable energy conversion and storage applications. This book will give a comprehensive description of synthesis and characterization of conjugated polymer nanostructures and hybrid or composites materials for energy conversion applications such as water splitting or degradation of organic pollutants, photovoltaics, and solar cells and energy storage devices, such as supercapacitors, lithium ion battery electrodes. The main objective is to present the state of art of interesting conjugated polymer-based nanomaterials for energy conversion and energy storage technologies, including fundamentals, functionalities, and challenges. The book is divided into three parts, each devoted to fundamentals, fabrication, characterization, and applications of conjugated polymer nanostructures in energy conversion and storage.

The initial section includes one chapter on fundamental aspects of conjugated polymer nanostructures including conductivity mechanisms, electrical, and electrochemical properties of conjugated polymer and confers the factor that significantly affect these properties. Another three chapters in this part discuss the fabrication of conjugated polymer nanostructures through various methods. Chapter 2 focuses on recent advances of conventional chemical synthesis strategies for controlled conjugated polymer nanostructures via different template based as well as template-free techniques. Chapter 3 highlights template-free method for the fabrication of conjugated polymers, such as electrospinning, electrochemical polymerization, vapor phase polymerization, self-assembly, plasma polymerization, preferential growth, etc. Chapter 4 discusses the growth mechanism of conjugated polymers through pulse radiolysis studies and use of gamma-radiolysis as new methodology for synthesizing nanostructured conjugated polymers. Chapter 5 describes the characterization techniques of conjugated polymer nanostructure in three domains such as microscopy, spectroscopy, and electrochemical method, which display potential utility in applications, including photocatalysis, storage devices, photovoltaics, etc.

In Part II, conjugated polymer nanostructures for solar energy conversion and environmental protection consists of four chapters. Chapter 6 provides an overview of the use of conjugated polymer nanostructures as catalysts support in fuel cells application. In Chapter 7, highlights the photocatalytic activity of the polymer nanostructure and nanohybrid catalysts for pollutants removal and solar water splitting. The next chapter (Chapter 8) discusses progress in conjugated polymer nanocomposites for photocatalytic application and solar light harvesting. Chapter 9 focuses on the chemical and physical strategies for developing nanostructured conjugated polymer as active layer in solar cell and photovoltaic application.

In Part III, conjugated polymer nanostructures for energy storage contains three chapters. Chapter 10 addresses an overview of fabrication methods and designing concepts of conjugated polymer-based materials and their potential for supercapacitor and lithium ion battery and review on the latest trends in supercapacitor and lithium ion battery research through extensive analysis of the literature and by highlighting notable research examples. Advances in conjugated polymer-based nanocomposites as electrode materials with the charge-discharge efficiencies and capabilities, energy/power densities, and cycle life of these nanocomposites are reviewed and presented in Chapter 11. Finally, Chapter 12 provides a comparative overview of using conducting polymers nanowires with carbon nanotube and graphene-based nanocomposites for supercapacitors applications. In order to make each contribution complete in itself, there is some unavoidable overlap among the chapters.

I believe this book deliver a comprehensive understanding of conjugated polymer nanostructures fundamentals, challenges, and applications that may be a valuable guide for broad readership of university student, researchers, and engineers in various fields of material sciences, catalysis, environment, and energy to find the latest information.

Kolkata, 2020 *Srabanti Ghosh*

Acknowledgment

The success of this edited book is the result of sharing valuable knowledge and critical review of respective topics from each contributing author. I would like to thank all the contributors for their excellent chapters.

I would also like to express my sincere gratitude to the publisher WILEY-VCH and to the team of Dr. Daniela Bez, Mrs. Abisheka Santhoshini, and others involved in the successful production of this book.

Finally, lots of love and gratitude toward my husband Atanu and family members for their unconditional support and patience.

Part I

Design and Characterization of Conjugated Polymer Nanostructures

1

Fundamentals of Conjugated Polymer Nanostructures

Thanh-Hai Le[1] *and Hyeonseok Yoon*[1,2]

[1] *Chonnam National University, Graduate School, Department of Polymer Engineering, 77 Yongbong-ro, Gwangju 61186, South Korea*
[2] *Chonnam National University, School of Polymer Science and Engineering, 77 Yongbong-ro, Gwangju 61186, South Korea*

1.1 Introduction

Earlier research on the design and development of materials related to conjugated polymers has attracted renewed interest, which has contributed to the materials being accepted as robust alternatives to their inorganic counterparts, therefore leading to large and substantial practical research efforts. Since the time when polyacetylene was discovered in 1977 by Hideki Shirakawa, Alan Heeger, and Alan MacDiarmid, many kinds of conjugated polymers have been developed, such as polypyrrole (PPy), polyaniline (PANI), polythiophene (PT), poly(*p*-phenylene vinylene) (PPV), and their derivatives [1]. Conjugated polymers contain a carbon backbone, which holds interchanging single (σ) and double (π) bonds that allow electrons to be delocalized, and thus contribute towards various electronic, electrical, electrochemical, and optical characteristics. Owing to the π-conjugated system coupled with the inherent characteristics of polymers, conjugated polymers have competitive properties over those of their inorganic counterparts, such as mild synthetic conditions, chemical diversity, structural flexibility, tunable electrical/optical properties, anticorrosion, and lightweight [2, 3]. Note also that, by converting bulk conjugated polymers into nanostructures, the resulting nano-dimensionality features can lead to beneficial properties, such as quantized energy level, enlarged surface area, more efficient and rapid doping/dedoping, and enhanced crystallinity [4–7]. Conjugated polymers have been hybridized with other functional materials to overcome their limitations in terms of conductivity, stability, and solubility. These materials have been successfully utilized in a wide range of optoelectronic [8–12], energy conversion [13, 14], energy storage [15, 16], photocatalytic [4, 17], and biomedical applications [5, 18].

This chapter will present the fundamentals of conjugated polymer and their nanostructures, and focus on electronic, electrical, optical, and electrochemical properties. These properties depend on the dopants, doping level, and inherent

Conjugated Polymer Nanostructures for Energy Conversion and Storage Applications,
First Edition. Edited by Srabanti Ghosh.

properties of conjugated systems such as chain conformation, aggregation state, shape, and size of the nanomaterials. Better understanding of these properties and charge transport mechanisms will contribute to extending the use of conjugated polymers over a wide range of applications, from optoelectronic to medical applications, as well as in energy conversion/storage devices and systems.

1.2 Electronic and Electrical Properties

1.2.1 Conductive Mechanism

1.2.1.1 Inherent Molecular Structure

In general, energy band theory has been used to clarify the key differences between semiconductors, conductors, and insulators. The band gap is identified as being the energy difference between the lowest unoccupied molecular orbital (LUMO) of the conduction band and the highest occupied molecular orbital (HOMO) of the valence band in a material. In conductor materials, the conduction band overlaps the valence band, such that electrons are able to move freely and disseminate between the two bands. In contrast, semiconductor materials can conduct electricity under some excitation conditions because of their small band gap. When the band gap becomes too large for electrons to cross (no electricity is conducted), the material is known as an insulator. Energy band theory fails to explain why conjugated polymers, which are organic materials, can conduct electricity. The charge transport mechanisms of conjugated polymer at the molecular level have been investigated from both theoretical and experimental evidences by many research groups [19, 20]. The most commonly accepted mechanism based on the high electrical conductivity and simple chemical structure of polyacetylene is represented in Figure 1.1. In general, the existence of interchanging single and double bonds through the polymer backbone is an inherent property of conjugated polymers. These single and double bonds contain a localized σ-bond, which is known to allow formation of a strong chemical bond. Moreover, it is recognized that each double bond also holds a **delocalized π-bond**, which is however weaker compared with the σ-bond [21, 22]. Here, the overlap between p_z-orbitals in the chain of conjugated π-bonds allows the π-electrons to freely move across the carbon backbone. As a result, the conjugated π-bonds can

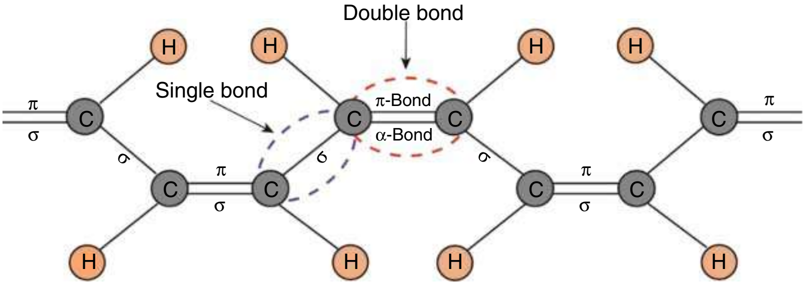

Figure 1.1 Scheme describing the conjugated π-system in *cis*-polyacetylene.

conduct electricity. However, it is believed that conjugated π-bonds cannot make conjugated polymers become high-conductivity materials owing to a distinct disorder in the polymer matrix. Structural and morphological disorders hinder delocalization of π-electrons, thus delaying charge transport along the polymer chain [23–25]. Consequently, the metallic charge conduction of a pristine conjugated polymer is fairly weak. A discovery by Hideki Shirakawa, Alan Heeger, and Alan MacDiarmid on electrically conductive polyacetylene modified the ways that physicists and chemists think about conductance in polymeric materials. The work involved using an external exciting factor called "doping," whereby a halogen dopant removes an electron from a delocalized π-bonding of polyacetylene and creates a hole. In turn, an electron of an adjacent double bond is delocalized and couples with the hole, which generates a new hole, therefore, allowing very high conductivities of up to 10^5 S/cm. Since this pioneering work was published, many theories have been proposed to explain the conductivity mechanism of conjugated polymers. Some formations of local excitations, such as polarons, bipolarons, and solitons, have been considered as charge carriers [20, 26, 27].

1.2.1.2 Doping and Band Structure Evolution

The conductivity of pristine conjugated polymers is in the range of 10^{-6}–10^{-10} S/cm, which is at the boundary between an insulator and a semiconductor (Figure 1.2). However, their conductivities can be tuned through the process of doping [28]. The structural and morphological disorder can be reduced when conjugated systems are doped. Doping induces the formation of charge carries such as solitons, polarons, and bipolarons, which reduce lattice distortion [29]. As a result, doping has contributed towards the creation of novel conjugated polymers, whereby the conductivity of the pristine system can be upgraded to semiconducting or even metallic levels. For example, polyacetylene doped with iodine achieved a high conductivity of approximately 10^4 S/cm, as reported by Tsukamoto et al. [30, 31], which is as high as the conductivity of lead at room temperature (4.8×10^4 S/cm). Through the achievement of high conductivity, conjugated polymers have gradually become more useful as candidate materials for various practical applications.

Doping in semiconductors is the process of introducing impurities into the crystal lattice of the material to modulate its conductivity. The number of valence electrons of the impurity, namely, the dopant, defines the type of doping and

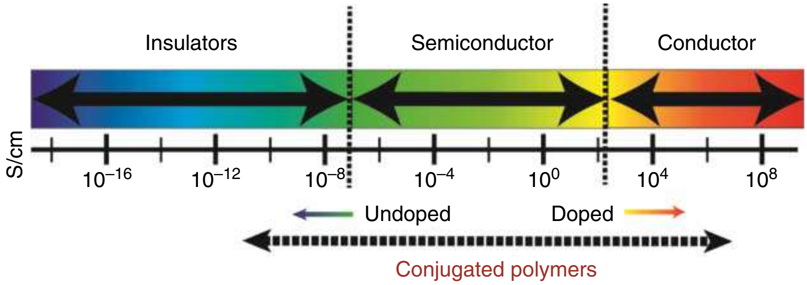

Figure 1.2 Conductivity range of conjugated polymers based on doped/undoped states.

conductivity of semiconductor materials. For example, a silicon atom has four electrons in its outer shell. When a phosphorus atom (five valence electrons) or boron atom (three valence electrons) replaces a silicon atom, it will form negative (a free electron, p-type doped) or positive sites (a hole, n-type doped), respectively, on the crystal lattice of silicon. These sites play the role of charge carriers, and increase the conductivity of the silicon crystal by up to $10^6\ \mathrm{S\,cm^{-1}}$. Because of the π-conjugated system, it is acknowledged that the doping mechanism of polymers is completely different from that of conventional semiconductors [28]. From the electron transfer aspect, the doping in conjugated polymers is a partial redox process, which generates delocalized charges on the polymer backbone [30]. The dopant plays the role of supplying additional electrons to the conjugated polymer or removing electrons from the polymer chain. Its mechanism is related to the process of adding electrons to the lowest available energy state of the conduction band (reduction) or removing electrons from the highest available energy state of the valence band (oxidation). The reduction or oxidation process is known to construct charge carriers, which are commonly described in various forms such as polarons, bipolarons, or solitons, in conjugated polymers. Typically, conjugated polymers exist in the form of non-degenerate or degenerate systems based on their ground state structure. The nondegenerate ground-state polymers have two different electronic structures with different energies, such as polyacetylene [32, 33], whereas degenerate ground-state polymers have identical electronic structures and energies, such as poly(tetraphenylquinodimethans) (PTPhQ), polyparaphenylene, polythiophene, PANI, and PPy [32, 34]. Both polarons and bipolarons have been detected as the charge carriers in non-degenerate systems, while solitons play the role of charge carriers in degenerate systems [19, 29, 34, 35]. Consequently, the flow/delocalization of charge carriers along the skeleton backbone allows the polymer to be conductive. The reduction and oxidation processes of conjugated polymers are related to the concept of p-type and n-type doping in organic semiconductors, respectively [11, 26]. From the perspective of physicists and chemists, n-type doping of conjugated polymers is known as the transfer of electrons from the HOMO of the dopant species to the LUMO of the polymer, which results in augmented electron density. On the other hand, in p-type doping, an electron from the HOMO of the polymer moves to the LUMO of the dopant species, therefore creating a hole within the polymer chain. Henceforth, the amount of incorporated dopant ions to the unit monomers of conjugated polymers is defined as the doping level. Controlling the doping level can tune the mobility and density of the charge carriers and thus the conductivity of conjugated polymers [36–38].

In general, a conjugated polymer is capable of sustaining/encountering p-type doping or n-type doping through an oxidation or reduction step to be conductive. The oxidation/reduction processes will lead to the formation of either negative or positive polarons/bipolarons, as presented in Figure 1.3. The positively charged forms provide p-type doping, while negatively charged forms provide n-type doping. The delocalization of these polarons/bipolarons along the polymer backbone leads to enhanced electronic conductivity. As has been reported, the negative polaron/bipolaron ratio in n-doping is not stable in comparison with the positive

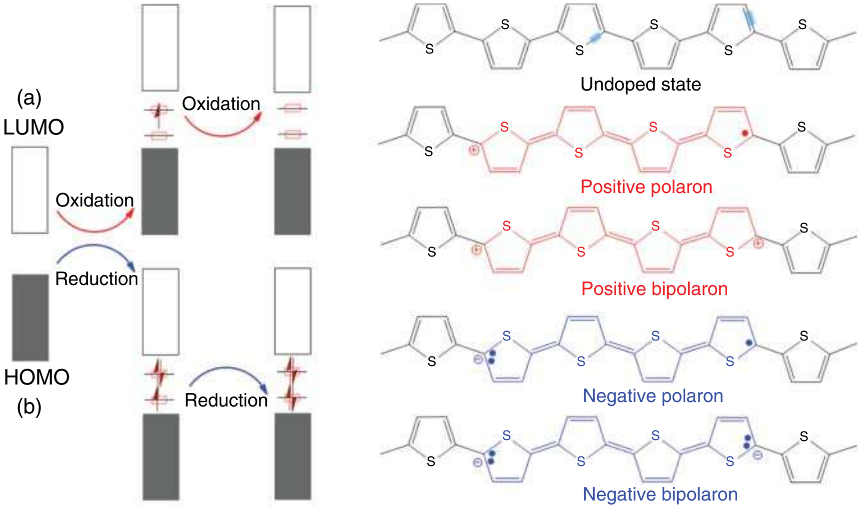

Figure 1.3 Electronic band and chemical structures of polythiophene (PT) with (a) p-type doping and (b) n-type doping. Source: Le et al. [26]. Licensed under CC BY 4.0.

forms, making the p-doping option more common in fundamental research as well as in practical applications. For example, p-doping of nondegenerate ground-state PPy has been reported as capable of creating different electronic energy band structures as the doping level increases. Pristine or undoped PPy has a wide band gap of approximately 3.16 eV and hence is considered to be an insulator (Figure 1.4a). Once oxidation starts occurring owing to halogen doping, π-electrons are removed from the HOMO of pristine PPy, which involves the transformation of a benzoid-like to a quinoid structure, forming radical cations, namely, positive polarons [20, 39]. This takes place along with the appearance of two new symmetric electronic states within the band gap, which reduces the band gap from 3.16 to 2.26 eV (Figure 1.4b). Upon increasing the oxidation level, a second electron is transferred from the HOMO of PPy to the LUMO of the dopant, forming a di-cation, which is a positive bipolaron (Figure 1.4c). In other words, PPy has higher quinoid features in the bipolarons as compared with polarons. Further oxidation of PPy will cause an overlap of neighboring bipolarons to form new contracted bipolaronic bands, as presented in Figure 1.4d. Thus, p-doping induces new electronic states or optical transitions in the energy band structure of PPy, which can be observed as longer wavelength absorptions.

In comparing degenerate with nondegenerate ground-state polymers, the degenerate ground-state polymer has a simpler model, known as a *trans*-polyacetylene. When polyacetylene encompasses an uneven number of carbon atoms in the polymer chain, the interchange of single and double bonds will produce a conjugated system with two similar electronic structures (A and B phases) and identical energies (Figure 1.5a). The neutral state of the polyacetylene contains an unpaired electron between the two structures, which is also known as a neutral soliton (Figure 1.5d). While delocalizing along the polymer backbone, if a neutral soliton meets another,

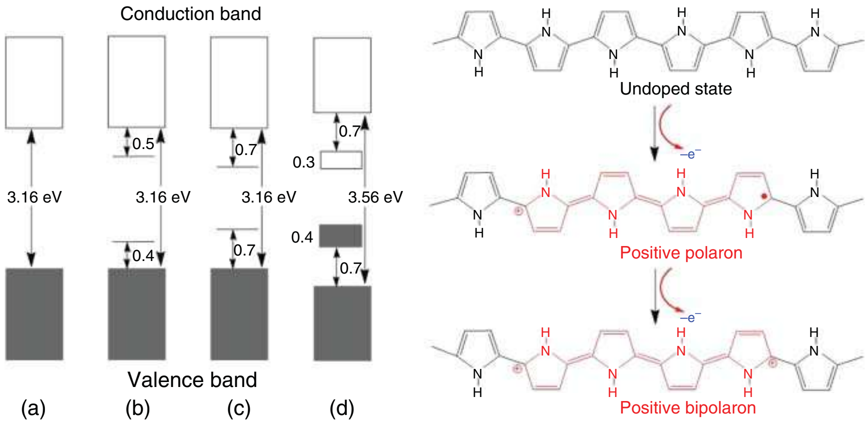

Figure 1.4 Electronic bands and chemical structures illustrating (a) undoped; (b) polaron; (c) bipolaron; and (d) fully doped states of polypyrrole (PPy). Source: Le et al. [26]. Licensed under CC BY 4.0.

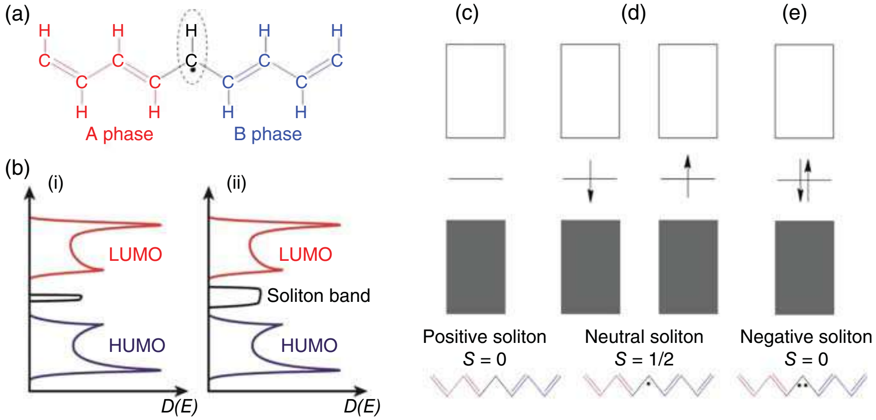

Figure 1.5 (a) Schematic illustration of the geometric structure of a neutral soliton on a trans-polyacetylene chain; (b) a soliton band with light doping (i) and heavy doping (ii); The band structure of trans-polyacetylene containing (c) a positively charged soliton, (d) a neutral soliton, and (e) a negatively charged soliton. Source: Le et al. [26]. Licensed under CC BY 4.0

they will combine and generate a double bond. When *trans*-polyacetylenes undergo an oxidation or reduction process by a dopant species, a neutral soliton can either receive or donate an electron, which results in the generation of positive or negative spin-less solitons ($S = 0$) (Figure 1.5c,e). In the transport along the polymer chain, the charged soliton can overlap with others, which leads to the formation of a soliton band-like structure [26, 40, 41]. This band can be expanded by increasing the oxidation/reduction level and lies between the HOMO and LUMO of *trans*-polyacetylene (Figure 1.5b). When the structure becomes a nondegenerate ground-state system such as *cis*-polyacetylene, the solitons become unstable in this polymer and tend to transform to polarons/bipolarons.

Overall, polarons, bipolarons, and solitons play the role of charge carriers and enable electrical conductivity in nondegenerate and degenerate ground-state conjugated polymers and their nanostructures [20]. There are major external factors that impact conjugated polymer conductivity, e.g. temperature, as well as the degree of doping and chain orientation. Additional factors will be discussed in Sections 1.3.2 and 1.3.3.

1.2.2 Charge Carrier Transport Models

In principle, the electrical properties of conjugated polymers have a strong dependence on the presence of disorder in the material, including main and end chains, external coupling, voids, entangled chains, and doping deficiencies/blemishes. Initially, it was difficult to understand disordered materials, so the issue was avoided, or the materials were forced into ordered systems. Since Anderson presented the basic concept of localization in 1958, localized electrons could be used to explain the charge transport properties observed in homogeneously disordered materials. It is known that within a perfect crystal with periodic potentials, the wave functions will form Bloch waves, which can delocalize in a mean free path (l) throughout the structure of materials (electrons tend to hop from site to site, which leads to generating a band). On the other hand, the degree of disorder can change the wave function. For example, within disordered systems, structural defects and impurities cause significant electronic wave function scattering, which can result in localization. If the material has strong disorder, the overlap of the wave function may decline rapidly and thus the system exhibits higher insulator behavior. The localized wave function (Ψ) can be expressed as

$$\Psi(r) \infty \exp\left(-\frac{r - r_0}{\xi}\right) \tag{1.1}$$

where r is the position and ξ is the localization length of the state of an atom. In later years, Mott recognized that electrons at the center of the band can be delocalized, whereas electrons at the band tail tend to localize owing to the contribution of electrons from localized orbitals in deep potential fluctuations [42, 43]. Here, the critical energy (E_c) was proposed in terms of the "mobility edge" to describe the transition point between the extended and localized states of electrons, which appeared as a band inside the band gap (Figure 1.6). The locations of the Fermi level (E_F) and E_c determine the conductivity in different materials. When the position of E_F is in the region of the localized states, the conductivity of the material vanishes, therefore exhibiting non-metallic behavior, despite there being a limited density of states at the Fermi level. Conversely, if E_F lies in the region of the extended states, as shown in Figure 1.6c, the material exhibits metallic behavior at low temperature and possesses a finite DC conductivity. Therefore, the mobility edge specifying the metal–insulator transitions and the DC conductivity can be found from the Drude or Boltzmann theory, where the DC conductivity (σ) of weak disordered materials is described by

$$\sigma = \frac{ne^2\tau}{m} \tag{1.2}$$

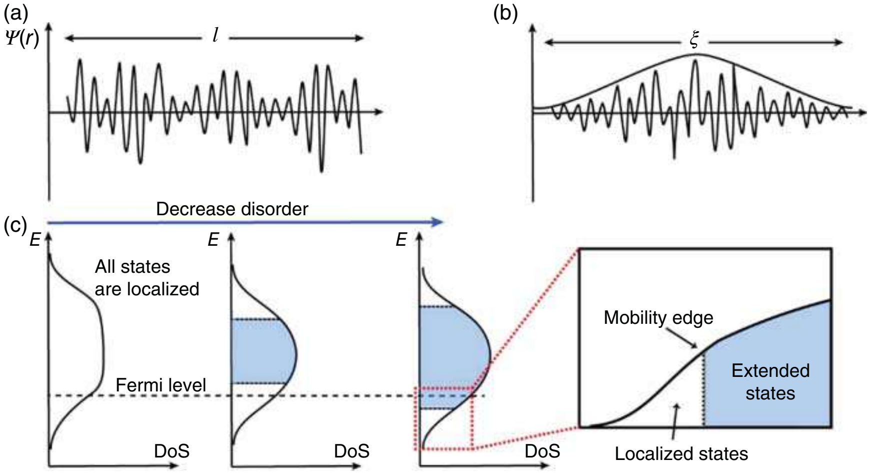

Figure 1.6 Anderson metal–insulator transition in single-band model. (a) Typical wave function of localization state with localization length, (b) extended block wave function with the mean free path, and (c) mobility edge in a disordered system.

where e is the electronic charge, $\tau = \frac{l}{v_F}$ is the relaxation time, and m and n are the effective mass and density of the carrier, respectively [43–46]. In weak disordered systems, the Fermi wavelength (k_F) is much shorter than the mean free path, and thus $k_F l \gg 1$ in this system.

$$k_F l = \frac{\left[h(3\pi^2)^{\frac{2}{3}}\right]}{e^2 \rho n^{1/3}} \tag{1.3}$$

In (1.3), ρ is the resistivity. The theory of Anderson localization does not fully describe the electrical properties/metallic state of highly doped conjugated polymers. Therefore, Epstein et al. [47] pointed out the delocalization of charges in conjugated polymers based on the study of an inhomogeneous disordered model, which is related to 3D metallic crystalline domains (such as rod-like [weakly metallic system], expanded "mesoscopic" coil-like, expanded coil-like, and weakly linked fibers) affected by a disordered quasi-1D medium [48, 49]. According to experimental data, the model agrees well with the frequency-dependent dielectric constant of doped PANI and PPy [47–49]. Moreover, the classic Mott's variable range hopping model can be used to explain the charge transport based on the hopping of states, charge carriers in disordered systems, or energy-limited tunneling between domains near the Fermi energy [50, 51]. For highly doped polymers, l is approximately 10 Å, charge-carrier density is of the order of 10^{21} cm^{-3}, and $k_F l \approx 1$–10 at room temperature. The metallic states of various conjugated polymers have been reported, and Table 1.1 summarizes these.

The concentration of the dopant, doping time, and distinction of the polymer that affect the conductivity of conjugated polymers implies a complicated internal mechanism. Many authors from the research community have made an effort to improve the conductivity of conjugated polymers by using different types of

Table 1.1 Maximum metallic states observed in doped conjugated polymers.

Conjugated polymer	Repeat unit	Chain orientation	Conductivity (S/cm)
Polyacetylene	C_2H_2	High	10^4–10^5
PPV	C_6H_4-C_2H_2	High	10^4
PPy	C_5H_2N	Low	400
PANI	C_6H_4-NH	Low	400
Poly(3-methylthiophene)	C_5H_2S-CH_3	Low	400
PEDOT	$C_7H_4O_2S$	Low	300

Source: Le et al. [26]. Licensed under CC BY 4.0.

dopants. According to their chemical nature, dopants can be classified into three groups, including inorganic (i.e. halogens, lithium, $MgCl_2$, $HClO_4$), organic (i.e. quaternary ammonium salts, acid acetic, hydroquinone-2), and large polymeric (i.e. polystyrene sulfonic acid, poly(2-acrylamido-2-methyl-propane sulfonic acid, polyvinyl phosphate) dopants). Table 1.2 shows the conductivities of conjugated polymers using various dopants, as reported in the literature to date. It is acknowledged that the chemical nature of the dopant species can affect both the structure and conductivity of conjugated polymers. Conjugated polymers can achieve very high conductivity with various small inorganic species as compared with organic and polymeric species. However, they have poor environmental stability owing to the high de-inserting, exchanging, and hydrophilic properties of small inorganic dopants. Large organic and polymeric dopants, in contrast, can improve the solubility, processability, and stability of conjugated polymers in various organic and aqueous phases by choosing the appropriate species. Because of their large chemical structure, large organic and polymeric molecules can limit the charge mobility in the polymer, affect the density of the polymer, and theretofore change the physical properties and surface topography of doped polymers. However, the strong adhesion of these dopants on conjugated polymers prevents the use of the polymer in many applications based on the insertion/de-insertion mechanism needed for supercapacitors, batteries, and electrochromic devices [52].

In general, the conductivity of conjugated polymers dramatically increases with an increase in the doping level. Tsukamoto et al. demonstrated the relationship between dopant ions and the electrical conductivity of conjugated polymers based on a study of I_2 doped stretched polyacetylene [30, 31]. In the initial observation, the gradually increasing conductivity of polyacetylene by I_2 doping implied the generation of highly ordered stacking structures, which are responsible for high conductivity rather than the primary structure of the polymer. After eight hours of doping, the conductivity saturated, which indicated the slow diffusion of the I_2 ions into the matrix of the polymer [30, 31]. In other words, the conductivity of conjugated polymers is proportional to the doping level and becomes saturated at high levels of dopant ions (fully doped level). Along with doping, de-doping is the process of reproducing the pristine conjugated polymer without degradation of the

Table 1.2 Typical examples of dopants for conjugated polymers and corresponding conductivities.

Conjugated polymer	Dopant	Chemical source	Doping method	Conductivity (S/cm)
Trans-polyacetylene	Na^+	$(C_{10}H_8)Na$	Solution doping	80
Poly(*p*-phenylene)	AsF_5	AsF_5	Vapor phase doping	1.5×10^4
Poly(*p*-phenylene vinylene)	CH_3SO_3H	CH_3SO_3H	Non-redox doping	10.7
	AsF_5	AsF_5	Vapor phase doping	57
Poly(3-vinylperylene)	ClO_4^-	$(C_4H_9)_4N(ClO_4)$	Electrochemical doping	10^{-5}
	AsF_6^-, PF_6^-, BF_4^-	$C_{16}H_{36}AsF_6N$, $(CH_3)_4N(PF_6)$, $(C_2H_5)_4N(BF_4)$	Electrochemical doping	30–100
	ClO_4^-	$LiClO_4$	Electrochemical doping	65
PPy	Cl^-	NaCl	Electrochemical doping	10
	Polystyrene sulfonate (PSS)/Cl^-	PSS/$FeCl_3$	Solution doping	4
	MeOH	MeOH	Vapor phase doping	0.74
	$C_{20}H_{37}O_4SO_3{}^-$	$C_{20}H_{37}O_4SO_3Na$	Solution doping	4.5
	$C_{10}H_{15}OSO_3{}^-$	$C_{10}H_{16}O_4S$	Solution doping	300
PANI	HCl	HCl	Non-redox doping	10
	I_2	I_2	Vapor phase doping	9.3
	$BF_4{}^-$	HBF_4	Solution doping	2.3×10^{-1}
PBTTT[a)]	FTS[b)]	$C_8H_4F_{13}SiCl_3$	Vapor phase doping	604 to 1.1×10^3
Poly(2-(3-thienyloxy) ethanesulfonate)	Na_2SO_3	Na_2SO_3	Solution doping	5
PT	Cl^-	$FeCl_3$	Vapor phase doping	10–25
PANI–PPy	ASPB	Anionic spherical polyelectrolyte brushes (ASPB)	Electrochemical doping	8.3

a) Poly(2,5-bis(3-tetradecylthiophen-2-yl)thieno[3,2-*b*]thiophene).

b) Tridecafluoro-(1,1,2,2-tetrahydrooctyl)-trichlorosila.

Source: Le et al. [26]. Licensed under CC BY 4.0.

polymeric structure. Doping/de-doping is a reversible process that is used in many modern applications.

As discussed previously, the electrical conductivity of conjugated polymers is strongly dependent on the doping level, and achieving maximum conductivity can be a technical challenge in the research community. Therefore, a number of doping methods have been evaluated and developed for conjugated polymers, including electrochemical doping, chemical doping, *in situ* doping, radiation-induced doping or photodoping, non-redox doping, and charge-injection doping, which are summarized in Table 1.3 [53–55]. Electrochemical and chemical doping techniques are popular in the literature because they involve simple procedures at low cost. Chemical doping can be performed directly by vapor-phase/gaseous or solution pathways. For vapor-phase doping, polymers generally are exposed to the gas phase of dopant compounds, such as bromine, iodine, chlorine, or AsF_5 in a closed system, in which the vapor pressure, temperature, and reaction time determine the final conductivity. Solution doping is accomplished by dipping the solid polymer in a soluble solvent containing dopant ions, such that the original form of the polymer is retained. Doping of conjugated polymers can be electrochemically performed during or after polymerization. By applying appropriate potentials between a conjugated polymer-coated working electrode and counter electrode, a redox reaction takes place at the interface of the material and electrolyte, and ions will diffuse to compensate for the losses at the nearby electrode. This doping method is easy and precisely controls the degree of doping, and is more readily reversible by monitoring the current passed when compared with chemical approaches. However, it is difficult to remove the doped polymer from the electrode and thus apply the process to large-scale fabrication of doped conjugated polymers for industrial applications. Overall, new discoveries in doping processing have led to achieving higher conductivity, in which both n-type and p-type dopants are used for improving the electrical conductivity of organic conjugated systems.

1.2.3 Temperature Dependence

Over the past four decades, there has been remarkable progress in the development of highly conjugated polymers. In highly doped cases, the conductivities of polymers can achieve very high levels comparable to those of their inorganic counterparts. A significant temperature dependence has been observed and investigated for a wide range of conjugated systems, such as polyacetylene, PANI, PPV, and PPy [56, 57]. Based on theoretical perspectives, the relationship between the temperature and conductivity or resistivity of doped conjugated polymers can be exploited in three regimes according to their reduced activation energy (W), as reported by Zabrodskii and Zinov'eva [58] using the following formula.

$$W(T) = -\frac{T[\mathrm{d}\ \ln\ \rho(T)]}{\mathrm{d}T} = \frac{\mathrm{d}(\ln\ \sigma)}{\mathrm{d}(\ln\ T)} \tag{1.4}$$

In the insulating regime, the charge transport mechanism is governed by a variable-range hopping mode near the Fermi level. Therefore, the conductivity (σ)

Table 1.3 Methods used for doping conjugated polymers.

Doping method	Controlled variables	Advantages	Disadvantages
Chemical doping	Vapor pressure, exposure time to dopant	Simple doping process by exposing the sample to a dopant vapor or immersion in a dopant solution	Performed as slowly as possible to avoid inhomogeneous doping. The doping levels obtained are not stable with respect to time Unexpected structural distortion may cause electrical conductivity decay Doping/de-doping shows low reversibility
Electrochemical doping	Amount of current passed	Doping level can be easily controlled by using an electrochemical cell with a controlled amount of current passed. Doping/de-doping is highly reversible and clean polymer can be retrieved Can be achieved with many dopant species	Unexpected structural distortion may cause electrical conductivity decay
Photo doping	Radiation energy of light beam	Charge carrier is formed without chemical compound (dopant). No distortion of the material structure	Electrical conductivity disappears rapidly when irradiation is discontinued owing to recombination of electrons and holes
Non-redox doping	Protonic acid strength	Number of electrons generally does not change	Depends on the degree of oxidation of conjugated polymers and degree of protonation of the material. Low conductivities are observed for some conjugated polymers
Charge-injection doping	Applying an appropriate potential on the polymer structure	Does not generate counter ions. Minimized distortion	Coulombic interaction between charge and dopant ions is very strong and can lead to changes in the energetics of the system

Source: Le et al. [26]. Licensed under CC BY 4.0.

follows Mott's law [59]:

$$\sigma = \sigma_0 \exp\left(\frac{T_0}{T}\right)^{1/(n+1)} \tag{1.5}$$

where σ_0 and T_0 are constants, and n is the dimensional conduction. Here, the resistivity is activated, and the activation energy has a negative temperature coefficient, which can be described by [60]

$$\log_{10} W(T) = A - x \log_{10} T \tag{1.6}$$

where $A = x\log_{10} T_0 + \log_{10} x$ [60]. Using Eq. (1.6), the slope x and the dimensionality of the sample can be observed.

At the critical boundary of the metallic-insulating regime, the activation energy is independent of temperature, and the slope in Eq. (1.6) becomes zero. The conductivity thus obeys a power law:

$$\sigma(T) = aT^{\beta} \tag{1.7}$$

Here, a is a microscopic length. Equation (1.7) is valid when β is in the range of 1/3 to 1. If β is higher than 1 or lower than 1/3, the system is dominated by insulating or metallic sites of the metallic–insulating transition, respectively. In the case of the metallic regime, $W(T)$ has a positive temperature coefficient and the conductivity at zero temperature is finite ($T \rightarrow 0$). Therefore, the conductivity in this regime is expressed by

$$\sigma = \sigma_0 + mT^{1/2} + BT^{p/2} \text{ (1.7)}, \qquad m = \alpha\left[\frac{4}{3} - \gamma\left(\frac{3F_\sigma}{2}\right)\right] \tag{1.8}$$

Here, σ_0 is the conductivity at zero-temperature, B is a constant of the localization effects, γF_σ is the interaction parameter, α is the diffusion coefficient parameter, and p is the value of the electron–phonon/electron–electron scattering rate calculated as $p = 3, 2$, and $3/2$ for inelastic electron–electron scattering, weakly disordered, and strongly disordered material, respectively. Localization and interaction induce conductivity via the "$mT^{1/2} + BT^{p/2}$" term [44, 46, 61]. In the case of disordered materials, charge transport at low temperatures is strongly affected by electron–electron interactions. Ahlskog et al. [60] have clearly reviewed the temperature dependence of conductivity in various regimes for conjugated polymers, which can be summarized in Table 1.4, for common, doped conjugated polymers.

It is acknowledged that the conductivity of conventional metals increases with a reduction in temperature, in contrast to the conductivity of doped conjugated polymers, in which conductivity increases with an increase in temperature. Some previous pioneering works have observed that the conductivity of doped conjugated polymers depends heavily on temperature at low doping levels but weakens at high doping levels [62, 63]. Therefore, the conductivity of doped conjugated polymers is strongly affected by the phonon-assisted hopping mechanism at localized states, which is affected by material imperfections or tunneling between metallic regions [30]. For instance, Roth et al. [63, 64] characterized the temperature dependence of the DC conductivity based on a study of iodine-doped polyacetylene by monitoring doping levels. They observed that there was a dramatic increase in

Table 1.4 σ (300 K) and $\rho_r = [\rho(1.3\text{ K})/\rho(300\text{ K})]$ values for several representative conjugated polymers in the metallic, critical, and insulating regimes.

Doped conjugated polymers	Metallic		Critical		Insulating	
	ρ_r	σ (S/cm)	ρ_r	σ (S/cm)	ρ_r	σ (S/cm)
Polyacetylene-I_2	<10	>5000	10–20	$3–5\times10^4$	>20	<3000
Polyacetylene-I_2	<5	$>5\times10^4$	9.8–165	$2–5\times10^4$	>400	$<2\times10^4$
Polyacetylene-$FeCl_3$	<2	$>2\times10^4$	2.6–11.4	$1–2\times10^4$	>27	$<10^4$
PPV-AsF_5	<5	300–2400	9.7–34	100–300	>50	<100
PPV-H_2SO_4	<2	$>4\times10^3–10^4$	4.7–27	1000–4000	>60	<1000
PPy	<2	300–400	2–10	200–300	>10	<200
PANI	<2	250–350	2–5	200–250	>10	<200

Source: Ahlskog et al. [60]. © 1997, IOP Publishing.

conductivity for low doping level samples as the temperature increased, whereas highly doped samples exhibited a small increase in conductivity. In another study, Aleshin et al. [65] investigated the temperature dependence of the DC conductivity of PF_6-doped poly(3,4-ethylenedioxythiophene) (PEDOT). The conductivity exhibited a very weak temperature dependence of $\rho_r = \left[\frac{\rho(1.4\text{ K})}{\rho(291\text{ K})}\right] = 1.5 - 2.8$, which suggests that the material lies on the metallic side of the metallic-insulating transition. It is recognized that the resistivity increases as the temperature drops to 10 K. At lower temperatures, there is a small decrease in resistivity, which is similar to conventional metal, owing to electron–electron interactions at low temperatures. Recently, camphor sulfonic acid-doped PANI was shown to exhibit metallic properties similar to conventional metals, with high conductivity in excess of 1000 S/cm at room temperature [66]. The resistivity weakened as the temperature decreased monotonically over a large range, from 300 to 5 K with $\rho_r = \left[\frac{\rho(5\text{ K})}{\rho(300\text{ K})}\right] \approx 0.4$. This discovery indicates that camphor sulfonic acid-doped PANI lies squarely on the metallic side of the metallic–insulator transition, in which the doped polymer exhibits conventional metallic behavior over a wide range of temperatures. Therefore, doped conjugated polymers can be used in many electronic applications as metallic materials.

1.3 Electrochemical Properties

1.3.1 Reversible Oxidation/Reduction Process and Charge Storage Behavior

Doping causes some basic changes (e.g. from benzoid to quinoid type) in the geometric structure of a polymer, which affects the generation of charge carriers. However, the initial structure can be rehabilitated by converting the polymer back to its undoped form through a de-doping process. In electrochemistry, doping/de-doping of conjugated polymers is reversible and corresponds to the oxidation/reduction process, which forms the basic concept of a charge/discharge cycle in polymer-based lithium-ion batteries and electrochemical capacitors. In general, p-type doping of conjugated polymers is the electrooxidation process in which electrons are removed from the polymer backbone and the lost electrons are balanced by the insertion of counter-anions from the electrolyte into the polymer skeleton. In contrast, n-type doping of conjugated polymers corresponds to the electro-reduction process, in which electrons are injected into the polymer matrix and counter-cations are added to readjust the overall electrical charge. For instance, electrooxidation and electro-reduction corresponding to the charge/discharge process of p-type and n-type doped PANI by sulfuric acid and lithium ions can be expressed as follows:

Electrooxidation (charging process): $\mathrm{PANI} + n\mathrm{SO}_4^{2-} \rightarrow \mathrm{PANI}^{2n+} : n\mathrm{SO}_4^{2-} + 2ne$
Electro-reduction (discharging process): $\mathrm{PANI}^{2n+} : n\mathrm{SO}_4^{2-} + 2ne \rightarrow \mathrm{PANI} + n\mathrm{SO}_4^{2-}$
Electrooxidation (charging process): $\mathrm{CP}^{n-}(\mathrm{Li}^+)_n + ne \rightarrow n\mathrm{CP} + n\mathrm{Li}^+$
Electro-reduction (discharging process): $n\mathrm{CP} + n\mathrm{Li}^+ \rightarrow \mathrm{CP}^{n-}(\mathrm{Li}^+)_n + ne$

The insertion/deinsertion of doping ions may cause a huge volume expansion, resulting in degrading the structure of bulk electrode materials. The use of conjugated polymers as the electrode material can provide free void volume in the electrode to prevent the so-called pulverization. Both pristine and doped conjugated polymers can be used as materials for anodes, cathodes, or both for energy storage devices. In general, cyclic voltammetry (CV) is a common technique used to characterize the redox reaction and investigate electron transfer kinetics during doping and de-doping of conjugated polymers. Under an applied potential and a constant scan rate, counter ions will be absorbed and de-absorbed on the polymer during the doping and de-doping processes through forward and backward scans, respectively. The oxidation step causes the polymer chain to become negatively charged, whereas the reduction step results in a positively charged form. The peak current density (A) of adsorbed species from the CV for the reversible system is then given by

$$i = n^2F^2A\Gamma v \left[\frac{\exp\theta}{RT(1+\exp\theta)^2}\right] \tag{1.9}$$

where n is the electron number, F is the Faraday constant (C/mol), v is the scan rate (V/s), Γ is the surface coverage of oxidized or reduced states (mol/cm^2), A is the active electrode area (cm^2), and $\theta = (nF/RT)(E - E)^{\circ}$. At the peak location, one-electron redox processes produce a symmetrical, cyclic voltammogram with $E - E^{\circ} = 0$ and $i_{\mathrm{R}} = -i_0$, and the current can be simplified as

$$i = \frac{n^2F^2A\Gamma v}{4RT} \tag{1.10}$$

It is noted here that the peak current density is proportional to the potential of the scan rate, which can only be applied to ultrathin film conjugated polymers and dopant ions with minor diffusion coefficients. For instance, Diaz et al. investigated the one-electron redox process through the electro-polymerization reaction of

BF_4-doped PPy thin film [67]. The cyclic voltammograms exhibit symmetrical redox peaks in the range of an applied potential of −0.4 and +0.3 V and scan rate from 10 to 100 mV/s. The current increase is proportional to an increase in the scan rate, and the cyclic voltammograms are not affected by diffusion due to stirring conditions. It is observed that after the polymer transferred from neutral to oxidized states, its color changed from yellow to black. Figure 1.7 indicates that the oxidation peaks exhibit a small negative potential shift and that the reduction peaks become more positive when the scan rate is increased [68]. The redox reactions may not take place completely owing to the limitation of the reaction time at high scan rates, and thus severe kinetic limitations may contribute to charge transfer at high scan rates. With increasing thickness polymer films or dopant ion size, the electrochemical process is affected by diffusion. Therefore, the symmetrical form of the voltammogram changes to an asymmetrical shape and the peak current density is then proportional to $v^{1/2}$.

In multi-electron redox processes, more than one pair of redox peaks can be observed in cyclic voltammograms, which are presented in Figure 1.8 for reversible p-doping of PANI. Two oxidation peaks appear at 0.72 and 0.31 V when the polymer undergoes a doping process at an applied scan rate of 50 mV/s. Two reduction peaks

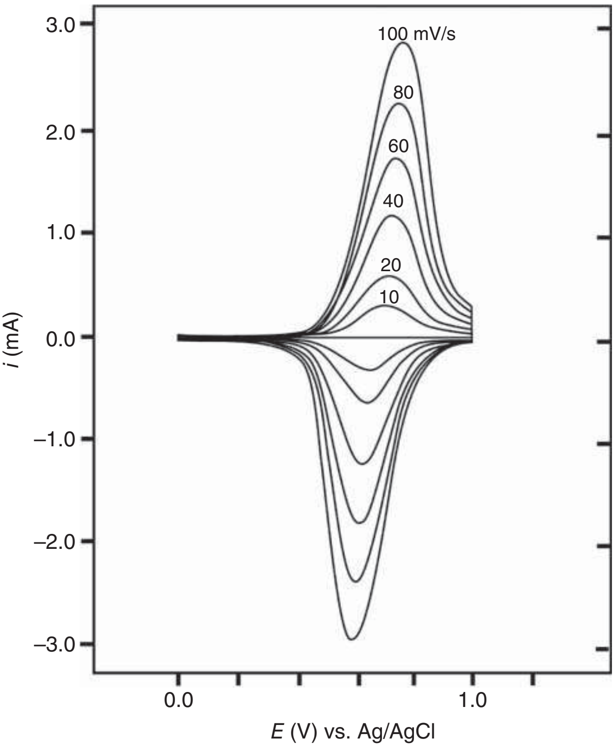

Figure 1.7 Cyclic voltammograms of a poly(*N*-phenyl-1-naphthylamine) film on Pt in 1 M $LiClO_4/CH_3CN$ solution at different scanning rates. Source: Guay et al. [68]. © 1990, American Chemical Society.

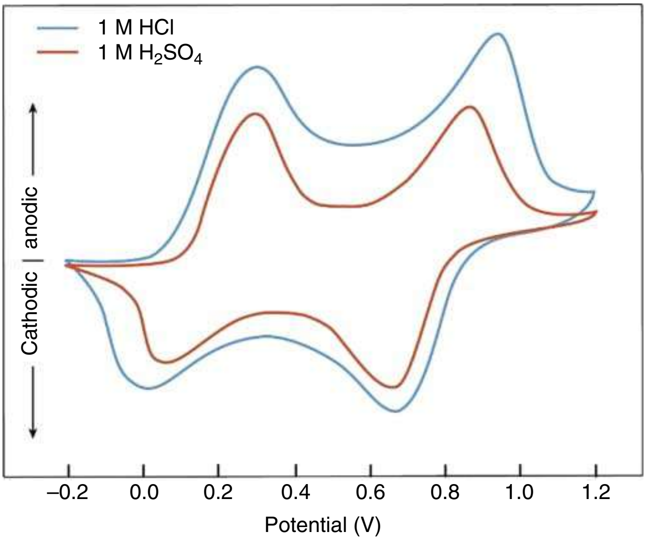

Figure 1.8 Cyclic voltammetry (CV) curves of a polyaniline (PANI) film doped with hydrochloric acid or sulfuric acid at the same potential scan rate of 50 mV/s. Source: Le et al. [26]. Licensed under CC BY 4.0.

are located at 0.48 and 0.09 V through the backward scan, which corresponds to de-doping of PANI. It is recognized that PANI exhibits different electrochemical behaviors when using different types of acid electrolytes, such as sulfuric and hydrochloric acid, which may result from disparities in the charges and sizes of counter-ions. Protons and anions are generated when dispersing hydrochloric and sulfuric acids into water, respectively. The main difference between the two acids is attributed to the disparities between SO_4^{2-} and Cl^- anions. The radius of (SO_4^{2-}) is 0.258 nm, which is higher than that of Cl^- (0.181 nm), where an increase of electrons in the shell is present, and thus the larger (SO_4^{2-}) ions may have less efficient diffusion into the polymer matrix than the smaller (Cl^-) ions under electrochemical doping. Alternatively, the type of dopant is also believed to affect the electrical conductivity of the doped polymer. Here, hydrochloric acid-doped PANI exhibits better electrical conductivity, which implies that the diffusion of dopant ions is a significant factor in the development of high conductivity of the conjugated polymer electrode based on electrochemistry.

As discussed previously, the redox reactions of conjugated polymers represent a reversible and stable process over a range of applied potentials. However, when scanning conjugated polymers at very high potentials, the structure of the electrode material is degraded, leading to loss of its electro-activity and a decrease in the potential window available for reversible reactions. This phenomenon has been observed in the early stages of development of conjugated polymers and is referred to as overoxidation [69]. Overoxidation is an irreversible reaction and its mechanism is not clearly understood. Beck and coworkers observed the overoxidation of PPy and polythiophene, and speculated that the contamination of strong nucleophiles such as OH^-, CN^-, and Br^- in an electrolyte solution may be added to the polymer matrix upon strong polarization, or radical cations may be added, therefore causing polymer destruction and irreversible oxidation with peak potentials ranging from 1.8 to 2.2 V [69–71]. The electrical conductivity of the doped polymer will be destroyed and the polymer will suddenly become an insulator again. Lewis et al. found that the overoxidation of PPy appeared at a potential as low as 0.65 V, and that the overoxidation potential highly depended on the pH of the supporting electrolyte [72]. In some cases, there was no overoxidation detected when the pH approached zero owing to the high stability of the polymer at this pH [72, 73]. Hence, an appropriate selection of electrolyte, solvent, and redox potential window is necessary to retain the high reversible redox reaction of conjugated polymers, which has led to proposals for many practical applications.

1.3.2 Swelling and De-swelling Behavior

The reversible redox reaction of conjugated polymers can be associated with high volumetric changes in the dimensions of conjugated polymers [74–76]. Swelling and de-swelling phenomena in conjugated polymers have been reported as their state switches from the oxidized to the reduced form, which provide the basis for a new generation of actuator applications. Therefore, many studies have been performed to evaluate the volume changes of conjugated polymers during the redox process, and different mechanisms have been proposed. Kertész et al. found that charge transfer correlates with the increase/decrease in the carbon length and the carbon angle of the polymer (change of geometry) when it receives or loses electrons during the doping/de-doping process [77]. This leads to a change in the intrinsic conformation of the polymer skeleton. On the other hand, it is acknowledged that the movement of counter-ions during the charge balancing process may affect the volume change of the polymer system owing to the occupation/displacement of ions in the polymer matrix. This may be associated with the spontaneous diffusion of solvent molecules into the region of higher concentration of dopant-ions/dopant-ion concentrations in order to equalize concentrations both inside and outside of the polymer matrix. In other words, the movement of the solvent may change the arrangement and concentration of ions in the polymer matrix and may lead to the formation of a semipermeable membrane and its corresponding osmotic pressure. This phenomenon has been reported as an osmotic expansion, which contributes to the total volume change of a conjugated polymer and underlies the primary concept for the development of polymer actuators (Figure 1.9).

In summary, the mechanism of swelling/de-swelling or actuation in conjugated polymers is attributed to a change in the intrinsic conformation of the polymer skeleton and osmotic expansion of the polymer phase due to ions and solvent [78]. The actuation of conjugated polymers can be monitored by a chemical or electrochemical process [79]. In principle, the typical mechanism of the electrochemical actuation in conjugated polymers is described in Figure 1.10. When the conjugated polymer undergoes the oxidation process, electrons are removed, which leads to the formation of positive-charge polarons. To compensate for the charge loss, small anions

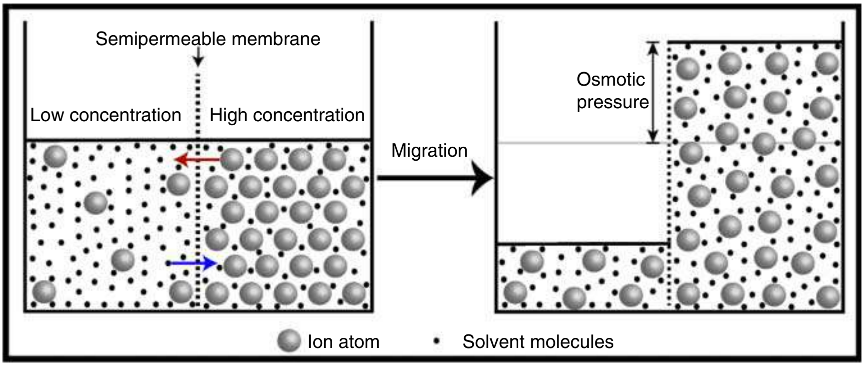

Figure 1.9 Effect of osmotic pressure when driving fluid flow across a membrane.

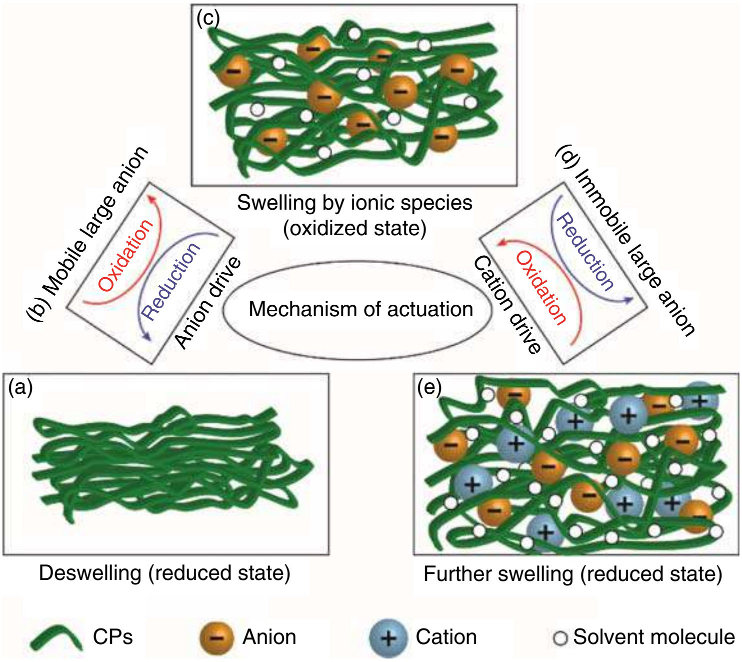

Figure 1.10 Mechanism of electrochemo-mechanical actuation in conjugated polymers. Source: Le et al. [26]. Licensed under CC BY 4.0.

then move into the polymer matrix and create ionic bonds with the polymer backbone, resulting in a small increase of the polymer volume. These anions can be dislodged from the polymer matrix when it is reduced to its initial state by applying a negative voltage (Figure 1.10a–c). In general, p-doping is associated with the anion-driven actuation and intrinsic polymer conformation change which cause swelling through oxidation and de-swelling through reduction [80].

However, full ejection can only be observed for small dopant-ions. When the dopant anion size is large enough, such as for dodecylbenzene sulfonic acid, poly(4-styrenesulfonate), and polyvinylsulfonate, the anions are immobilized and are permanently trapped inside the polymer matrix. Charge compensation during the reduction step then occurs through the affiliation of cations from the electrolyte and causes further expansion (Figure 1.10c–e). This phenomenon is coined in this paper as “cation-driven actuation.” At each step of incorporation of ions into the polymer matrix, the ions in motion cause a large, different concentration inside and outside of the polymer matrix. Hence, solvent molecules move in the polymer matrix to neutralize the anion or cation contraction, and the resulting osmotic expansion contributes to the total volume change of the polymer during actuation. This has been confirmed by several groups through observations of expansion reduction based on an increase of electrolytes using electrochemical quartz crystal microbalance and optical beam deflection studies [81–83]. Bay et al. investigated the effects of dopant ions and solvent molecules in an electrolyte solution on the expansion/contraction on dodecylbenzene sulfonate doped PPy [78]. The expansion was found to be reduced by 30% when the concentration of dopant ions in the electrolyte increased from 0.1 to 1.0 M. Similar results were also obtained by Aydemir et al. and Maw et al. [84, 85], suggesting that the movement of the solvent is associated with the concentration of ions in the polymer matrix and electrolyte solution during the redox reaction [75].

Consequently, conjugated polymer actuation is determined by the microstructures of the polymer and type/concentration of dopant and electrolyte. In addition to promoting the potential of those significant factors, it is necessary to develop more advanced actuating systems to achieve high-performance soft actuators based on conjugated polymer. To date, several notable systems have been introduced, such as out-of-plane actuators, linear actuators, and bilayer–trilayer actuators [79].

1.3.3 Electrochromism

It is acknowledged that the reversible doping/de-doping process of conjugated polymer is induced by oxidation/reduction processes. Such reversible redox processes cause a visible change of color in conjugated polymers and this phenomenon is known as electrochromism. This exceptional property of conjugated polymers has attracted global attention for various electrochromic applications such as smart windows, electrochromic displays, and rearview mirrors [86–88]. Both the energy gap and dopant are believed to mutually instigate the color conversion of conjugated polymers. The insertion/de-insertion of dopant ions via doping/de-doping induces the reorganization of the polymer’s electronic structure, which results in a reduced energy gap for possible π–π^* transitions. Furthermore, the formation of sub-bands by charge carriers such as polarons and bipolarons modulates the absorbance (new band gap) of the conjugated polymers, leading to the change in their color. Doped conjugated polymer thin films show strong absorption spectra in the visible region, whereas pristine or undoped conjugated polymer thin films are colorless and transparent owing to the high energy gap (>3.0 eV). In the case when un-doped conjugated polymers possess a lower band gap of approximately 2.0 eV, they can absorb visible spectra and exhibit various colors in this state. However, their absorption/emission in the doped state can shift to the near-infrared region because of the lower band gap of the doped polymer [86].

Conjugated polymers can display variations in color for different redox states. As a notable example, PANI exhibits color changes from transparent yellow to green, blue, and violet for various doped states (Figure 1.11). These electrochromic forms are caused by the protonation/deprotonation process or/and the insertion/de-insertion of dopant ions through p-doping of PANI using the CV technique in salt, acid, and organic solvents. In this case, heteroatoms such as nitrogen play a critical role as the injection sites for anions or protons in order to generate radical cations/doped forms [85, 86]. Their color change and protonation/redox states are clearly illustrated in Figure 1.11. Similarly, by the complexation of conjugated polymers, absorption spectra can be upgraded from the visible to the near-infrared and infrared regions [89]. The switching time of the color variations strongly depends on the migration velocities of protons/dopant ions throughout the polymer matrix. Hence, the electrochromic properties of conjugated polymers depend on the size (discuss in Section 1.4), the pH of the electrolyte solution, redox capability, temperature, and the chemical structure of the polymer. In order to extend the use of conjugated polymers to the next generation of electrochromic devices, the properties of conjugated polymers must be further improved to fulfill the standard requirements of the devices, such as long lifespan, high color contrast, and rapid color change switching.

1.4 Optical Properties

The optical properties of conjugated polymers have largely motivated their industrial applications in optoelectronics and photonics, including light-emitting diodes, solar cells, and field-effect transistors. In general, the optical properties of these materials reflect their geometry and electronic structure, and the materials mainly respond to light by the absorption and emission characteristics of either pristine or doped materials. These properties are strongly dependent on the size, morphology, doping state, and properties of conjugated systems. Therefore, understanding the photophysical properties and charge transport under light excitation should arouse great interest in the development of conjugated polymers for the next generation of optoelectronic, photocatalyst, and imaging and sensing applications. The evolution of the band gap structure and/or optical properties through the introduction of doping has already been discussed in Sections 1.3 and 1.4.3. In this section, the optical properties of conjugated polymers are mainly evaluated based on their inherent structure.

1.4.1 Band Gap of Conjugated Polymers

In general, the electronic band structure is a key parameter for understanding the mechanism of an organic conjugated system used for optoelectronic applications.

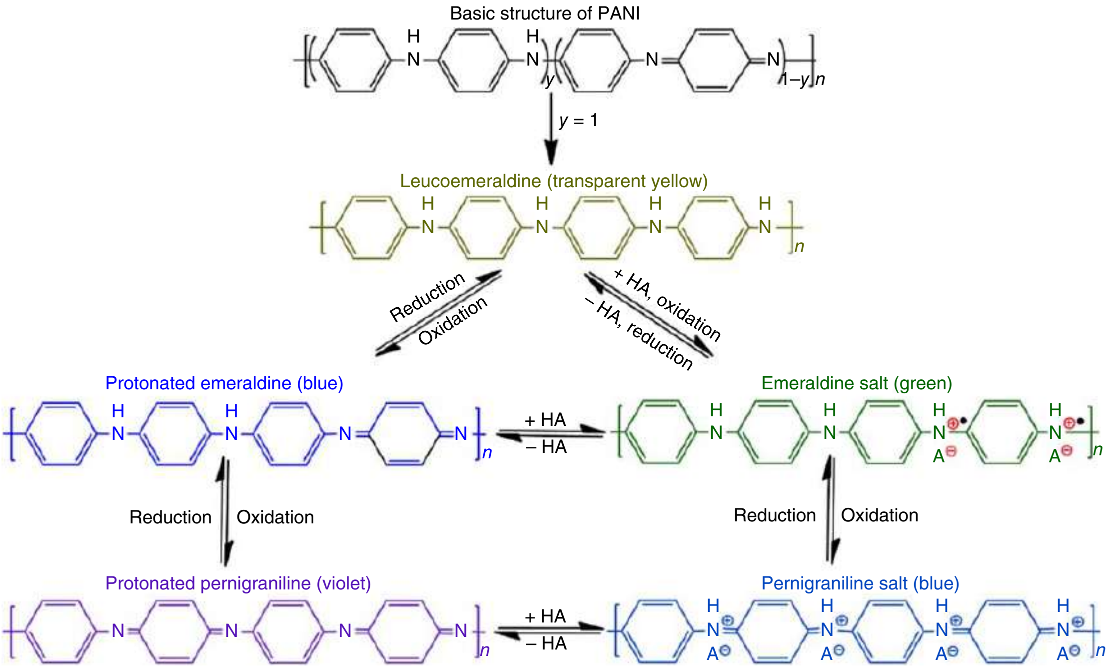

Figure 1.11 Different redox/protonation states and colors of PANI. Source: Le et al. [26]. Licensed under CC BY 4.0.

It is acknowledged that conjugated polymers exhibit similar **electronic band gap** properties as conventional semiconductors along with electron–electron and electron–hole coupling (i.e. a three-dimensional band structure) [90]. The origin of the band gap in conjugated polymers comes from the interchange of single and double bonds in their structure, where a π-electron from the ground state (HOMO) can absorb a photon and jump into the excited π^* state (LUMO), which leaves behind a positively charged hole. Electrons and holes are bonded to each other by Coulomb interaction, forming a neutral quasiparticle, namely, an exciton. The attraction between electron–hole results in the creation of an exciton band below the conduction band threshold [91]. The new excited state is coined the **optical band gap** (E_{opt}) and the exciton binding energy ($E_b = E_g - E_{\text{opt}}$) is in the range of 0.5–1.0 eV for various conjugated polymers (Figure 1.12) [91]. Finally, electrons and holes tend to recombine to form the initial form and yield an energy decay **through the radiative or non-radiative process**. Conjugated polymers in solid and liquid phases are characterized by weak intermolecular and strong intramolecular interactions, respectively. Thus, two different forms of excitons, i.e. intrachain and interchain (including both single and triplet excitons), have been identified in π-conjugations along sections of the polymer skeleton resulting from the delocalization of the π-electron system. Among them, interchain excitons are generated by the coupling of two nearby intrachains derived from two different polymer chains, or are derived by single-chain folding in polymer nanoparticles, films, or coiled configurations. This mechanism is responsible for electron delocalization between polymer chains, thus causing a reduction in the band gap of the solid-state material and nanoparticles, leading to a three-dimensional band structure (**interchain band gap**). As a result, both singlets and triplets are thus formed in the intrachain and interchain [92]. It is noted that conjugated polymers also exhibit a similar size dependence regarding optical properties as other nanostructured semiconductors, which refers to the extent of **π-conjugation or conjugation length in terms**

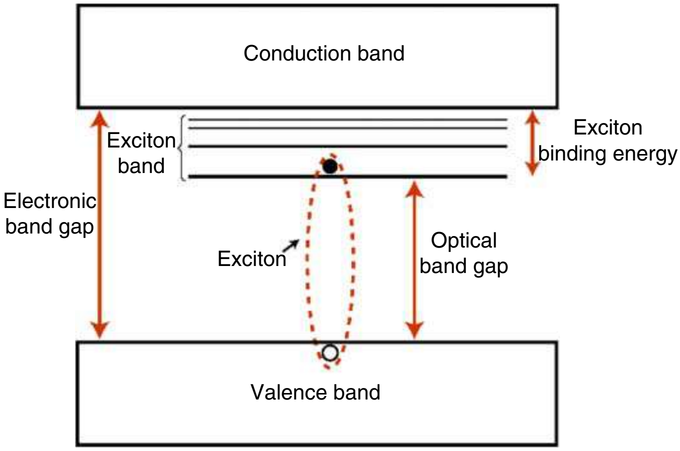

Figure 1.12 Electronic band gap structure and exciton levels formed in conjugated polymers.

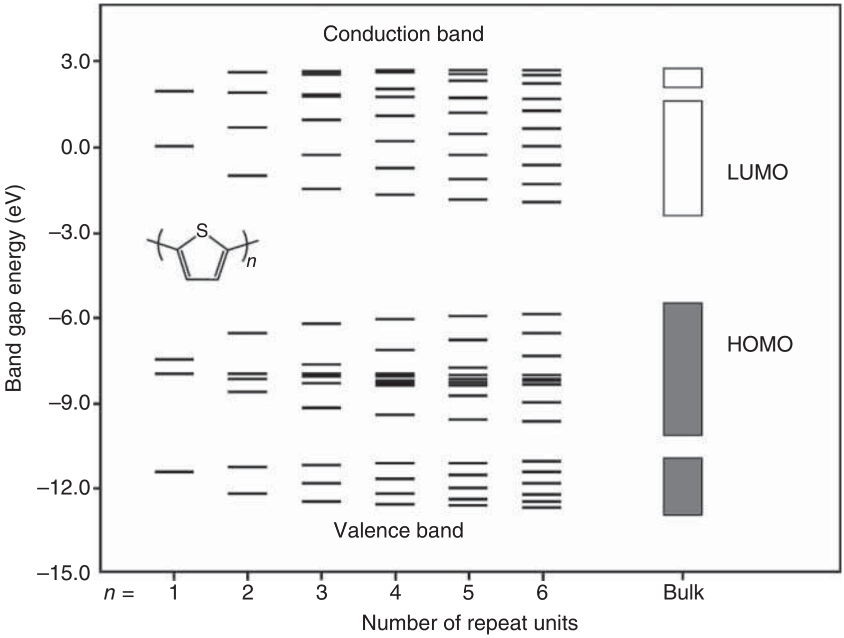

Figure 1.13 Band gap evolution of polythiophene as conjugation length increases. Source: Salzner et al. [93]. © 1998, Elsevier.

of bond length and length of a conjugation chain. The quantum size effects of conjugated polymers originate from the delocalization of π-electrons in the repeating units along the polymer chain. Representatively, Figure 1.13 shows the band gap evolution for polythiophene with increasing numbers of monomer units. When the monomers units increase, the number of π-electrons in the chain increases allows a greater number of atomic orbitals in the overlapping region. The total number of molecular orbitals from both bonding and antibonding is increased along with the width of the energy band. This causes a lower band gap between the conductance band and valence band in larger polymers or bulk materials, known as quantum confinement at the nanoscale. Therefore, the band gap of conjugated polymers (the HOMO–LUMO gap) increases with the decrease of the conjugation length. Another specificity of non-degenerate ground polymers, namely, **planarity** [94] arising from torsional strain, has been considered as an additional factor which limits the delocalization of π-electrons along the backbone, and is thus partially responsible for the larger band gap as the dihedral angle increases (reduced planarity) [95]. It is believed that the presence of heteroatoms in the aromatic system, electron withdrawing and electron donating substituents, and aromaticity determine the electronic and optical properties of conjugated polymers. **Different heteroatoms or substituent** groups contribute to the changes of the optical properties in conjugated polymers, defining the material's electron affinity. For example, heteroatoms have higher electron affinities and tend to decrease the delocalization of π-electrons along the polymer backbone, resulting in lowering of the band gap. Patra et al. confirmed the effect of heteroatoms (S and Se) based on density functional theory (DFT) and optical studies of polyselenophenes and polythiophenes. The presence of S or thieno-fused aromatic units leads to a decrease of 0.2 eV in the band gap compared with Se or seleno-fused units because sulfur has higher electron affinity than selenium (2.073 eV vs. 2.021 eV). With the larger electron affinity of 0.22 eV to S, NH^- induces a larger band gap of 3.1 eV in PPy vs. polythiophene (2.0 eV) [96]. **In the case of aromaticity**, the overlapping p_z-orbitals of π-electrons within these systems could offer different forms, such as aromatic and quinoid (resonance structures). Aromaticity causes π-electrons to be confined within the ring, and limits electron delocalization throughout the polymer backbone under the resonance effect, thus resulting in a larger band gap.

In summary, the single photo-excitation configuration of conjugated polymers causes the jump of an electron from the valance band to the conductance band, and the band gap of a π-conjugated system is the linear combination of the band gaps derived from **interchains** and **intrachains** affected by the following:

- Conjugation length,
- Planarity,
- Heteroatoms in the aromatic system and/or electron-withdrawing and electron-donating substituents, and
- Aromaticity/resonance structure.

Therefore, the band gap and optical properties of conjugated polymers are strongly affected by their chemical structure and morphological characteristics, such as the chain conformation, aggregation state, shape, and size of the polymers.

1.4.2 Absorption and Emission

In conjugated polymers, the chemical structure, conformational order, and overall nanostructure are known to have a significant effect on the electronic band structure, and thereby determine the absorption and emission spectra (or emission colors). Upon photoexcitation by a sufficiently excited photon, an electron is promoted from the HOMO (the π band) to the LUMO (the π^* band) to form an exciton. According to the orientation of spin, a singlet or triplet exciton can be defined. If the electrons in the excited state have the same spin state as in the ground state, they are considered singlet excitons. In contrast, if an excited state electron has the same spin orientation as another unpaired electron (or the opposite spin state as it had in the ground state), it is called a triplet exciton. Depending on the energy of photon excitation, the different excited states can be described by a Jablonski diagram (Figure 1.14a). The singlet ground states are denoted as $S_{0,}$ and the different singlet excited states are defined as S_1, S_2, and S_3, respectively. Similarly, triplet excited states are presented as T_1, T_2, and T_3, and each electronic level has a distinct vibrational energy. The excited state electrons can migrate from a high energy level to a lower energy level by internal conversion, crossing, and relaxation processes. Consequently, an electron can return to the ground state through radiative recombination or unwanted pathway – non-radiative recombination. Radiative recombination is

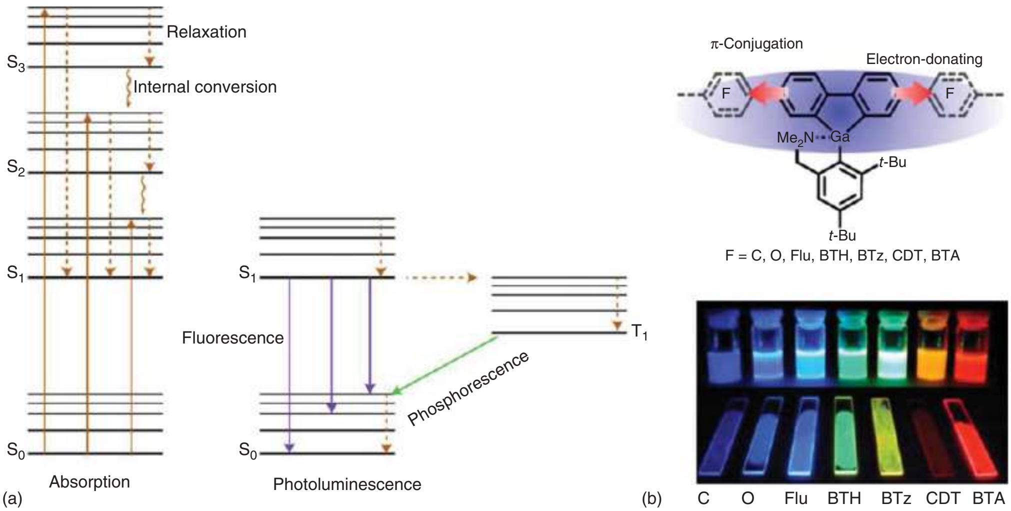

Figure 1.14 (a) Jablonski energy diagram demonstrates the energy levels of conjugated polymers for the quantum mechanical processes of absorption, fluorescence, and phosphorescence. (b) Chemical structure and photoluminescence images of poly-GafC, poly-GafO, poly-GafFlu, poly-GafBTH, poly-GafBTz, poly-GafCDT, and poly-GafBTA, under UV light (365 nm). Source: Based on Matsumoto et al. Reprinted with permission from [97]. Copyright 1990, American Chemical Society.

one of the most useful processes in conjugated polymers to generate **photoluminescence** with red-shift or longer wavelengths in comparison with absorbed light. The emitted light derived from the singlet excitons is referred to as **fluorescence**, while light derived from triplet excitons is referred to as **phosphorescence**, which normally occurs over longer time scales and at a lower intensity than fluorescence. The emission properties of conjugated polymers such as PPVs were discovered in the early 1990s and were attributed to the delocalization of π-electrons along the polymer backbone [98]. It was reported that PPVs could emit a light over a large region from green to yellow, which suggested that polymers can be used for the development of light-emitting diodes. It is now known that the chemical structure, chain conformation, and the size define color emission via the band gap of conjugated polymers.

Different chemical structures have been designed to tune the color from blue to red regions for different conjugated polymers, such as poly(9,9-dioctylfluorenyl-2,7-diyl), poly[(9,9-dioctyl-2,7-divinylene-fluorenylene)-alt-*co*-(2-methoxy-5-(2-ethylhexyloxy)-1,4-phenylene)], poly[(9,9-dioctylfluorenyl-2,7-diyl)-*co*-(1,4-benzo-(2,1′,3)-thiadiazole)], poly[2-methoxy-5-(2-ethylhexyloxy)-1,4-phenylenevinylene], poly(3-alkylthiophene), poly(*p*-phenylene), and poly(2,5-di(3=,7=-dimethyloctyl) phenylene-1,4-ethynylene). The photoluminescence quantum yield of conjugated polymers can range from 20% such as for polythiophene dots up to 80% in the case of polyparaphenylene and polyfluorene nanostructures [99–102]. The absorption and emission spectra depend on the molecule length of conjugated polymers. However, the absorption intensity and photoluminescence quantum yield are in inverse proportion to the length of the polymer chain. Hou et al. [103] observed that the photoluminescence quantum yield decreases for the larger conjugated polymer molecules, namely poly[2-methoxy-5-(2-ethylhexyloxy)-1,4-phenylenevinylene]. Simultaneous absorption and emission measurements on single molecules have proven that the quenching of photoluminescence occurs by an increase in the conformation defects, which trap electrons as the prolongation of the polymer chain increases (affect the polymer folding and packing during the nanostructure preparation process) [103, 104]. Matsumoto et al. [97] synthesized full visible colors of conjugated polymers using gallafluorene (Gaf)-containing various comonomers such as 2,5-didecylbenzene-1,4-diboronic acid bis-(pinacol) ester (**C**), 2,5-didecyloxybenzene-1,4-diboronic acid bis(pinacol)ester (**O**), 2,7-bis(4,4,5,5-tetramethyl-1,3,2-dioxaborolan-2-yl)-9,9-didodecylfluorene (**Flu**), 4,4′-didodecyl-2,2′-bithiophene-5,5′-diboronic acid bis(pinacol)ester (**BTH**), 4,7-bis(trimethylsilylethynyl)-2-(2-decyltetradecyl)-2*H*-benzo[*d*]-[1,2,3]triazole (**BTz),** 2,6-bis-(4,4,5,5-tetramethyl-1,3,2-dioxaborolan-2-yl)-4,4-dioctyl-4*H*-cyclopenta[2,1-*b*:3,4-*b*′]dithiophene (**CDT**), and 4,7-bis[3-hexyl-5-(trimethylstannyl)thiophen-2-yl]benzo[*c*]-[2,1,3]thiadiazole (**BTA**). The Gaf unit plays a role as an electron-donor in π-conjugated systems, where the electronic interaction between Gaf and various comonomers leads to different band gaps and results in the display of dark blue, blue, cyan, green, yellow, orange, or red colors (Figure 1.14b). Schütze et al. [105] prepared defect-free oligo(phenylene ethynylene)s rods with increased chain length up to 43 repeat units. It was found that the absorption and emission wavelengths red-shifted with increasing chain length and finally covered a blue region (400–460 nm). Therefore, most of the recent studies have focused on creating different emission colors based on different conjugated polymers and their derivatives along with monitoring chain conformation and chain alignment by controlling the size, aggregation, heteroatoms, and electron-withdrawing and electron-donating substituents.

Along with full visible color tuning, conjugated polymers, as well as their nanostructures, also exhibit high photoluminescence quantum yield, good thermal stability, good absorption, biocompatibility, non-toxicity, and high-functionalization sites, making them promising candidate materials for biology, biomedical, and optoelectronic applications [106]. The main drawback of conjugated polymers is their color instability, which can reduce the life-span of some devices such as light-emitting diodes (LEDs) [107]. Reducing the migration of excitons to defect sites significantly enhances color stability [108, 109]. Further research to understand the mechanism of quenching in conjugated polymers will enable higher performance of conjugated polymers for photoluminescence applications.

1.4.3 Coherent Exciton Diffusion and Energy Transfer

In conjugated polymers, two types of electronic energy transfer have been discovered: intrachain transfer and interchain transfer [110, 111]. The energy transfer occurs by excitons hopping along a conjugated polymer chain or two polymer chains [25]. However, the generated interchain and intrachain excitons in conjugated polymers are governed by electrostatically bound electron–hole pairs and structural defects that prevent the production of a high flow of current in certain cases. This is the result of the low dielectric constant of conjugated polymers, which is in the range of 3–4 [112]. Various electron donor–acceptor systems in terms of p–n heterojunctions have been developed to improve the dissociation of excitons and thus enable a higher energy transfer process, in which appropriate electron donor/acceptor material can aid in breaking the Coulomb attraction (dissociation), which can then allow excitons to diffuse to the interface and produce a photocurrent suitable for photovoltaic applications. Conjugated polymers can be used as electron donor or electron acceptor material according to the device requirements. The charge carriers can be formed by photo-excitation in photovoltaic cells or by charge-injection in organic light emitting diodes. The diffusion of excitons in conjugated polymers playing the role of electron donor–acceptor materials in the conversion process from singlet excitons of the photovoltaic cell is described in Figure 1.15.

The two materials have different ionization energies and electron affinities and thereby create an electrostatic force at the interface. Under the excitation of an appropriate light wavelength, the electrons of the polymer (the donor material) will move to the LUMO and leave holes in the HOMO, forming excitons in the small charged region. When excitons are generated at the interface of the two materials, the electrons will transfer to the higher electron affinitive material and the holes will move to the lower ionization potential material and generate photocurrent.

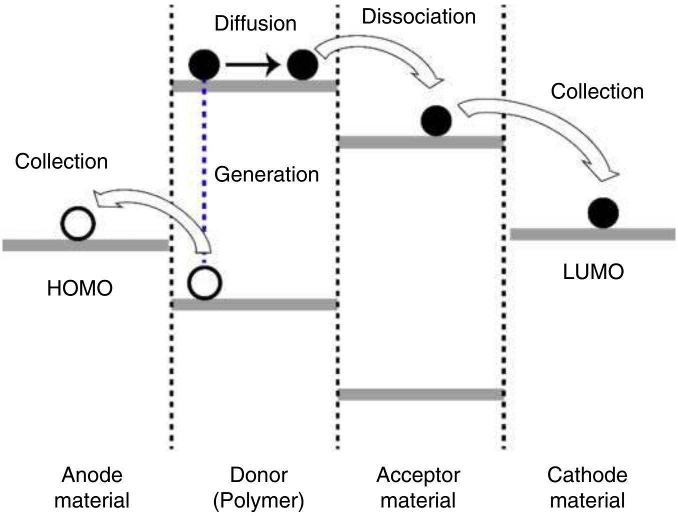

Figure 1.15 Exciton diffusion and energy transfer in conjugated polymers through charge annihilation.

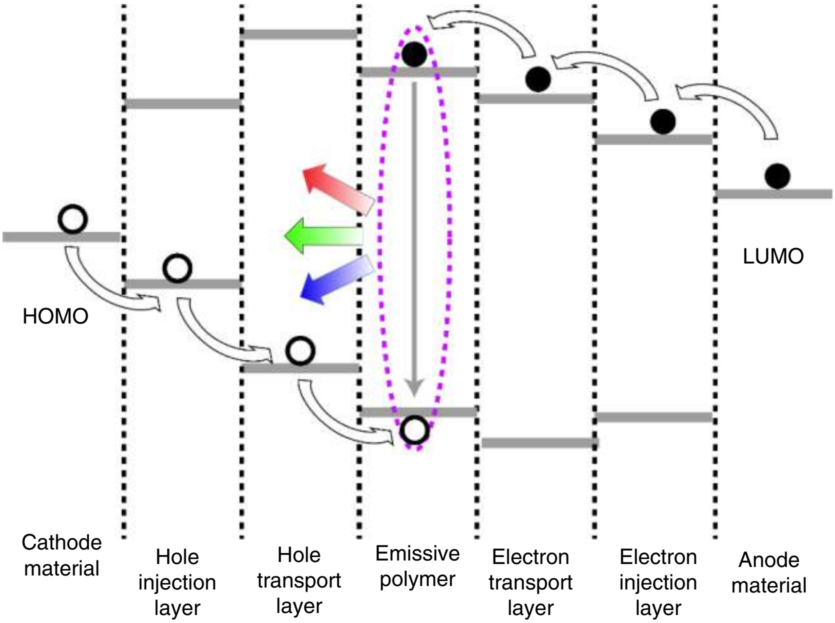

Figure 1.16 Exciton diffusion and energy transfer in conjugated polymer through electron–hole recombination.

Similarly, Figure 1.16 presents the typical energy transfer for hole injection and electron injection conjugated polymer materials in LEDs. Under an applied current between two electrodes, electrons and holes are injected from the anode and cathode electrodes, respectively, and then transfer to the emitting material. Consequently, this leads to the formation of singlet and triplet excitons in the conjugated polymer (emitting layer) and light is emitted through the recombination mechanism.

It is noted that excitons can be governed in the excited state of conjugated polymers with ratios of 25% and 75% for singlet and triplet states, respectively [113]. Harvesting the light/energy from single excitons leads to a low conversion efficiency owing to a 75% loss caused by the absence of triplet excitons. Therefore, many researchers have attempted to collect both singlet and triplet excitons to maximize efficiency [114, 115]. Many strategies have been introduced, including multiple processes such as **single-triplet energy transfer and singlet fission-triplet energy transfer for photovoltaics,** as well as thermally activated delayed fluorescence, hybridized local and charge-transfer excited state, and triplet-fusion delayed fluorescence, for organic light-emitting diodes (OLEDs) [116–118]. In general, the exciton diffusion length (L_D) of conjugated polymers defines the distance that excitons can diffuse over their lifetime in a presented material [119, 120]. It plays a significant role in many organic optoelectronic devices and can be defined as the root mean square of an exciton's displacement from its initial position (dL_i) during the exciton's lifetime (τ) as

$$L_\mathrm{D} = \sqrt{\frac{\sum dL_\mathrm{i}^2}{N}} = \sqrt{2ZD\tau} \tag{1.11}$$

where Z is the dimensional number, D is the diffusion coefficient, N is the number of excitons, and i represents an individual exciton. In one-dimensional structures, the factor 2 is usually omitted and the exciton diffusion length can be expressed as

$$L_\mathrm{D} = \sqrt{D\tau} \tag{1.12}$$

However, the lifetime of an exciton is ultrafast (<1 ns) and diffusion lengths are less than 20 nm in typical conjugated polymer films, which is less than the optical absorption pass length [121]. Finally, the thin film has less efficiency in absorbing light and only limited excitons are diffused to the interface of the planar heterojunction in photovoltaic devices (low L_D). The bulk heterojunction concept has been used to enhance the diffusion of excitons to the interface by increasing the surface interactions of donor and acceptor materials. In addition, improving the interfacial area between electron donor and acceptor material via nanostructured conjugated polymers (1D, 2D, and 3D) can offer higher quantum conversion efficiencies as compared with thick film or bulk conjugated polymers, as the larger effective area provides better surface interactions and prevents energy losses [122]. In contrast to photovoltaic cells, a larger L_D in OLEDs can cause low luminous efficiency because excitons decay through non-radiative pathways, including oxidation defects and electrodes [123, 124].

Understanding the mechanisms of energy transfer in conjugated polymers including the exciton diffusion pathway(s) and length(s) should improve the performance of conjugated polymers and their nanostructures based on current optoelectronic applications, and their low cost should make them attractive for the next generation of devices.

1.5 Unique Properties at the Nanoscale

First, it is important to note that conjugated polymer nanostructures (CPNs) can show higher conductivities compared to their bulk counterparts. Martin group demonstrated that the conductivity of conjugated polymer nanotubes grown in a template was much higher than that of their bulk counterparts [57]. The enhancement in conductivity was related to the high orientation of the polymer chains nearby the template walls and as a result elongated conjugation length. When the diameter of the nanotube became larger, the conductivity decreased because the portion of the more disordered core would increase. Similar examples showing the size effect of CPNs on the conductivity have been reported [58, 59]. Reducing the dimensions of conjugated polymers into a nanometer scale offers more opportunities to increase the chain orientation, crystallinity, and doping level of the polymer. The transport properties of CPNs are still a subject of great interest and play an important role in fundamental research and industrial application of conjugated polymers.

CPNs have higher surface area and smaller dimensions, enabling them to show more efficient and rapid electrochemical reactions. In addition, at the nanoscale, the morphology of conjugated polymers has a crucial effect on their electrochemical properties. Notably, a recent work by Park et al. demonstrated a correlation between the morphology and electrochemical performance of PANI nanostructures with different aspect ratios (Figure 1.17) [125]. Although all the PANI nanostructures had similar CV curve shapes, the integrated area of the CV curve clearly increased in the order of nanospheres < nanorods < nanofibers. Both anodic (I_{pa}) and cathodic (I_{pc}) peak current densities increased with increasing scan rate, indicating that the electrode kinetics were subject to a surface-controlled redox process. The anodic (E_{pa}) and cathodic (E_{pc}) peak potentials were plotted as a function of the logarithm of the scan rate (v) to calculate the electron transfer coefficient (α) and electron transfer rate constant (k_{s}) from Laviron's theory [126].

$$E_{\mathrm{pa}} = a + \left[\frac{2.303RT}{(1-\alpha)n_{\alpha}F}\right] \log v \tag{1.13}$$

$$E_{\mathrm{pc}} = b - \left[\frac{2.303RT}{\alpha n_{\alpha}F}\right] \log v \tag{1.14}$$

$$\log k_{\mathrm{s}} = \alpha \log(1-\alpha) + (1-\alpha)\log \alpha - \alpha(1-\alpha)\frac{nF\Delta E_{\mathrm{p}}}{2.3RT} - \log \frac{RT}{nFv} \tag{1.15}$$

The evaluated α and k_{s} values were found to be 3.6×10^{-1} to 3.7×10^{-1} s^{-1} and 4.3×10^{-1} s^{-1} for PANI nanofibers, with the latter value being higher than that of nanorods (3.1×10^{-1} s^{-1}) and nanospheres (2.6×10^{-1} s^{-1}), suggesting that the electron transfer capability of the PANI nanostructures strongly depended on their morphological characteristics.

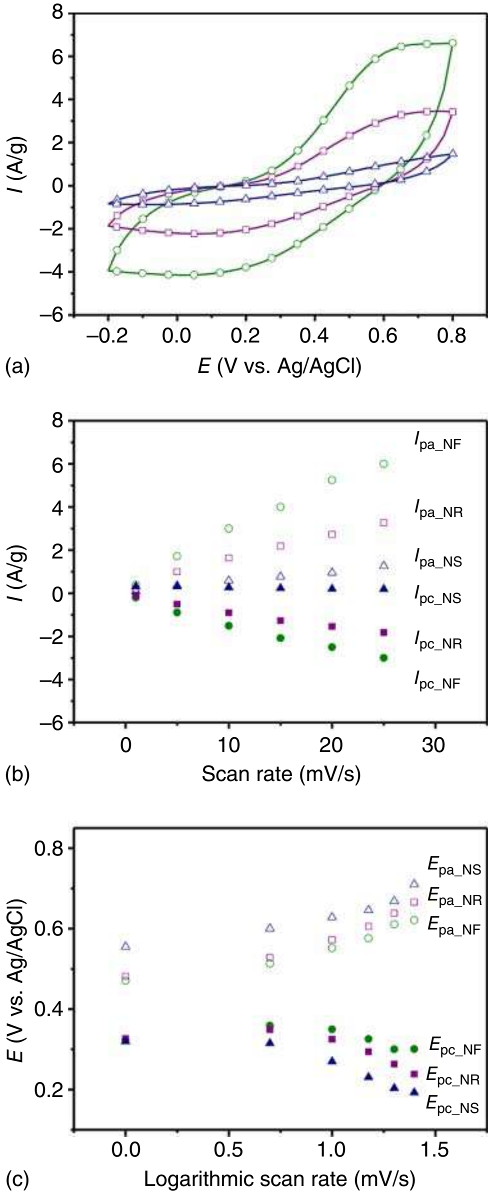

Figure 1.17 CV analysis of PANI nanostructures with three different shapes (nanospheres, NS; nanorods, NR; and nanofibers, NF) performed in a 1 M sulfuric acid dopant solution. (a) Cyclic voltammograms of electrodes consisting of PANI nanostructures at the same scan rate (25 mV/s); (b) plots of the peak current (the anodic peak current, I_{pa}; the cathodic peak current, I_{pc}) vs. the scan rate; and (c) plots of the peak potential (the anodic peak potential, E_{pa}; the cathodic peak potential, E_{pc}) vs. the log of the scan rate. Source: Park et al. [125]. © 2012, American Chemical Society.

1.6 Conclusion

The fundamentals of conjugated polymers as well as their nanostructures, including electrical, electronic, optical, and electrochemical properties, have become more important over the last three decades as the utility of conjugated polymers has been discovered. Deep understanding of these properties will provide opportunities for the development of various applications which directly utilize CPNs. Various theoretical charge transport models have been proposed for both pristine and doped conjugated polymers. However, there remain challenges to overcome because of several issues associated with polymeric conjugated systems, including structural defects, chain conformation, and interchain interactions. With the aid of novel spectroscopy and simulation methods, extended studies that can determine the correlations between/among doping reaction, color changes, swelling/de-swelling, and conductivity may provide the knowledge that can define the charge transport kinetics/mechanisms for a wide range of conjugated polymers. The conductivity of pristine conjugated polymers dominates the insulator–semiconductor transition and offers unique optical properties, such as absorption and photoluminescence. The electrical conductivity of conjugated polymers can be successfully enhanced by chemical, electrochemical, or photodoping, where both n-type and p-type dopings can be used to activate metallic behaviors in conjugated polymers. The formation of charge carriers (polarons, bipolarons, and solitons), their mobility, and the mobility of excitons in pristine and doped conjugated polymers are strongly affected by the dopant, doping state, and the inherent properties of conjugated systems such as chain conformation, aggregation state, and shape and size of the material. Possessing many advantages such as tunable absorption/emission spectra and conductivity, chemical structure diversity, as well as being environmentally friendly, may facilitate the use of conjugated polymers in many applications, such as in energy storage (fuel cells, batteries, and electrochemical capacitors), photocatalysts for dye removal and water splitting, and in photovoltaics. The major drawbacks of conjugated polymers are their low stability and lower conductivity as compared to metals, which limits their use in transistors and memory devices. Overcoming the current drawbacks in conjugated polymers will increase their potential as candidates for diverse novel applications.

References

1. Hall, N. (2003). Twenty-five years of conducting polymers. *Chem. Commun.* (1): 1–4.
2. Huang, W.-S., Humphrey, B.D., and MacDiarmid, A.G. (1986). Polyaniline, a novel conducting polymer. Morphology and chemistry of its oxidation and reduction in aqueous electrolytes. *J. Chem. Soc., Faraday Trans.* 1 (82): 2385–2400.
3. McCullough, R.D., Lowe, R.D., Jayaraman, M., and Anderson, D.L. (1993). Design, synthesis, and control of conducting polymer architectures: structurally homogeneous poly(3-alkylthiophenes). *J. Org. Chem.* 58: 904–912.
4. Ghosh, S., Remita, H., and Basu, R.N. (2018). Conducting polymers nanostructures as novel materials for efficient solar light harvesting. In: *Visible-Light-Active Photocatalysis: Nanostructured Catalyst Design, Mechanisms, and Applications* (ed. S. Ghosh), 227–252. Weinheim, Germany: Wiley-VCH Verlag GmbH & Co. KGaA.

5 Gangopadhyay, R. and De, A. (2000). Conducting polymer nanocomposites: a brief overview. *Chem. Mater.* 12: 608–622.

6 Tuncel, D. (2019). π-Conjugated nanostructured materials: preparation, properties and photonic applications. *Nanoscale Adv.* 1: 19–33.

7 Shi, Y., Peng, L., Ding, Y. et al. (2015). Nanostructured conductive polymers for advanced energy storage. *Chem. Soc. Rev.* 44: 6684–6696.

8 Gribkova, O.L., Omelchenko, O.D., Tameev, A.R. et al. (2016). The specific effect of graphene additives in polyaniline-based nanocomposite layers on performance characteristics of electroluminescent and photovoltaic devices. *High Energy Chem.* 50: 134–138.

9 Dimitrov, S.D., Schroeder, B.C., Nielsen, C.B. et al. (2016). Singlet exciton lifetimes in conjugated polymer films for organic solar cells. *Polymers* 8: 14.

10 Wang, Q., Jin, Z., Zhang, X. et al. (2017). Cellular architecture-based all-polymer flexible thin-film photodetectors with high performance and stability in harsh environment. *Adv. Mater. Technol.* 2: 1700185.

11 Philip, B., Xie, J., Abraham, J.K., and Varadan, V.K. (2004). A new synthetic route to enhance polyaniline assembly on carbon nanotubes in tubular composites. *Smart Mater. Struct.* 13: N105–N108.

12 Facchetti, A. (2011). Π-conjugated polymers for organic electronics and photovoltaic cell applications. *Chem. Mater.* 23: 733–758.

13 Ghosh, S., Teillout, A.-L., Floresyona, D. et al. (2015). Conducting polymer-supported palladium nanoplates for applications in direct alcohol oxidation. *Int. J. Hydrogen Energy* 40: 4951–4959.

14 Hou, W., Xiao, Y., Han, G., and Lin, J.-Y. (2019). The applications of polymers in solar cells: a review. *Polymers* 11: 143.

15 Bryan, A.M., Santino, L.M., Lu, Y. et al. (2016). Conducting polymers for pseudocapacitive energy storage. *Chem. Mater.* 28: 5989–5998.

16 Muench, S., Wild, A., Friebe, C. et al. (2016). Polymer-based organic batteries. *Chem. Rev.* 116: 9438–9484.

17 Ghosh, S., Remita, H., and Basu, R.N. (2018). Visible-light-induced reduction of Cr(VI) by PDPB-ZnO nanohybrids and its photo-electrochemical response. *Appl. Catal., B* 239: 362–372.

18 Braeken, Y., Cheruku, S., Ethirajan, A., and Maes, W. (2017). Conjugated polymer nanoparticles for bioimaging. *Materials (Basel)* 10: 1420.

19 Stafström, S. and Chao, K.A. (1984). Polaron-bipolaron – soliton doping in polyacetylene. *Phys. Rev. B: Condens. Matter* 30: 2098–2103.

20 Bredas, J.L. and Street, G.B. (1985). Polarons, bipolarons, and solitons in conducting polymers. *Acc. Chem. Res.* 18: 309–315.

21 Ravichandran, R., Sundarrajan, S., Venugopal, J.R. et al. (2010). Applications of conducting polymers and their issues in biomedical engineering. *J. R. Soc. Interface* 7: S559–S579.

22 Wise, D.L., Wnek, G.E., Trantolo, D.J. et al. (1998). *Electrical and Optical Polymer Systems: Fundamentals, Methods and Application*. Boca Raton, FL: CRC Press.

23 Roth, S. and Bleier, H. (1987). Solitons in polyacetylene. *Adv. Phys.* 36: 385–462.

24 Hertel, D., Bässler, H., Scherf, U., and Hörhold, H.H. (1999). Charge carrier transport in conjugated polymers. *J. Chem. Phys.* 110: 9214–9222.

25 Collini, E. and Scholes, G.D. (2009). Coherent intrachain energy migration in a conjugated polymer at room temperature. *Science* 323: 369–373.

26 Le, T.-H., Kim, Y., and Yoon, H. (2017). Electrical and electrochemical properties of conducting polymers. *Polymers* 9: 150.

27 Su, W.P., Schrieffer, J.R., and Heeger, A.J. (1979). Solitons in polyacetylene. *Phys. Rev. Lett.* 42: 1698–1701.

28 MacDiarmid, A.G., Mammone, R.J., Kaner, R.B. et al. (1985). The concept of “doping” of conducting polymers: the role of reduction potentials. *Philos. Trans. R. Soc. London, Ser. A* 314: 3–15.

29 Heeger, A.J., Kivelson, S., Schrieffer, J.R., and Su, W.P. (1988). Solitons in conducting polymers. *Rev. Mod. Phys.* 60: 781–850.

30 Tsukamoto, J. (1992). Recent advances in highly conductive polyacetylene. *Adv. Phys.* 41: 509–546.

31 Tsukamoto, J., Takahashi, A., and Kawasaki, K. (1990). Structure and electrical properties of polyacetylene yielding a conductivity of 10^5 S/cm. *Jpn. J. Appl. Phys.* 29: 125–130.

32 Brédas, J.L., Chance, R.R., and Silbey, R. (1982). Comparative theoretical study of the doping of conjugated polymers: polarons in polyacetylene and polyparaphenylene. *Phys. Rev. B: Condens. Matter* 26: 5843–5854.

33 Chiang, C.K., Fincher, C.R., Park, Y.W. et al. (1977). Electrical conductivity in doped polyacetylene. *Phys. Rev. Lett.* 39: 1098–1101.

34 Furukawa, Y. (1996). Electronic absorption and vibrational spectroscopies of conjugated conducting polymers. *J. Phys. Chem.* 100: 15644–15653.

35 Conwell, E.M. and Mizes, H.A. (1991). Metallic state of polymers with nondegenerate ground states. *Phys. Rev. B: Condens. Matter* 44: 937–942.

36 Zhang, Y., de Boer, B., and Blom, P.W.M. (2009). Controllable molecular doping and charge transport in solution-processed polymer semiconducting layers. *Adv. Funct. Mater.* 19: 1901–1905.

37 Zhang, Y. and Blom, P.W.M. (2011). Electron and hole transport in poly(fluorene-benzothiadiazole). *Appl. Phys. Lett.* 98: 143504.

38 Nollau, A., Pfeiffer, M., Fritz, T., and Leo, K. (2000). Controlled n-type doping of a molecular organic semiconductor: naphthalenetetracarboxylic dianhydride (NTCDA) doped with bis(ethylenedithio)-tetrathiafulvalene (BEDT-TTF). *J. Appl. Phys.* 87: 4340–4343.

39 Patil, A.O., Heeger, A.J., and Wudl, F. (1988). Optical properties of conducting polymers. *Chem. Rev.* 88: 183–200.

40 Abdelhamid, M.E., O’Mullane, A.P., and Snook, G.A. (2015). Storing energy in plastics: a review on conducting polymers & their role in electrochemical energy storage. *RSC Adv.* 5: 11611–11626.

41 Mishra, A.K. (2018). Conducting polymers: concepts and applications. *J. At. Mol. Condens. Nano Phys.* 5: 159–193.

42 Mott, N.F. and Davis, E. (1979). *Electronic Processes in Non-crystalline Materials.* New York, NY: Oxford University Press.

43 Lee, P.A. and Ramakrishnan, T.V. (1985). Disordered electronic systems. *Rev. Mod. Phys.* 57: 287–337.

44 Ahlskog, M. and Menon, R. (1998). The localization-interaction model applied to the direct-current conductivity of metallic conducting polymers. *J. Phys. Condens. Matter* 10: 7171–7181.

45 Anderson, P.W. (1958). Absence of diffusion in certain random lattices. *Phys. Rev.* 109: 1492–1505.

46 Saxena, V., Malhotra, B.D., and Menon, R. (2002). Charge transport and electrical properties of doped conjugated polymers. In: *Handbook of Polymers in Electronics* (ed. B.D. Malhotra), 3–65. Shrewsbury, Shropshire, UK: Rapra Technology Limited.

47 Epstein, A.J., Joo, J., Kohlman, R.S. et al. (1994). Inhomogeneous disorder and the modified Drude metallic state of conducting polymers. *Synth. Met.* 65: 149–157.

48 Kohlman, R.S., Zibold, A., Tanner, D.B. et al. (1997). Limits for metallic conductivity in conducting polymers. *Phys. Rev. Lett.* 78: 3915–3918.

49 Kohlman, R.S., Joo, J., Min, Y.G. et al. (1996). Crossover in electrical frequency response through an insulator–metal transition. *Phys. Rev. Lett.* 77: 2766–2769.

50 Joo, J., Long, S.M., Pouget, J.P. et al. (1998). Charge transport of the mesoscopic metallic state in partially crystalline polyanilines. *Phys. Rev. B: Condens. Matter* 57: 9567–9580.

51 Zuo, F., Angelopoulos, M., MacDiarmid, A.G., and Epstein, A.J. (1987). Transport studies of protonated emeraldine polymer: a granular polymeric metal system. *Phys. Rev. B: Condens. Matter* 36: 3475–3478.

52 Guimard, N.K., Gomez, N., and Schmidt, C.E. (2007). Conducting polymers in biomedical engineering. *Prog. Polym. Sci.* 32: 876–921.

53 Wang, P.-C. and MacDiarmid, A.G. (2008). Vapor phase secondary doping of polyaniline (emeraldine salt) thin films with *o*-chlorophenol investigated by UV–VIS–NIR: effects of primary dopants, substrate surfaces, and pre-treatments of organic vapors. *React. Funct. Polym.* 68: 201–207.

54 Kulszewicz-Bajer, I., Proń, A., Abramowicz, J. et al. (1999). Lewis acid doped polyaniline: preparation and spectroscopic characterization. *Chem. Mater.* 11: 552–556.

55 Chiang, C.K., Blubaugh, E.A., and Yap, W.T. (1984). Electrochemical studies on doping of polyacetylene. *Polymer* 25: 1112–1116.

56 Basescu, N., Liu, Z.X., Moses, D. et al. (1987). High electrical conductivity in doped polyacetylene. *Nature* 327: 403–405.

57 Menon, V.P., Lei, J., and Martin, C.R. (1996). Investigation of molecular and supermolecular structure in template-synthesized polypyrrole tubules and fibrils. *Chem. Mater.* 8: 2382–2390.

58 Zabrodskii, A.G. and Zinov'eva, K.N. (1983). Low-temperature conductivity and metal–insulator transition in compensate n-Ge. *J. Exp. Theor. Phys.* 59: 425.

59 Mott, N.F. (1969). Conduction in non-crystalline materials. *Philos. Mag.* 19: 835–852.

60 Ahlskog, M., Reghu, M., and Heeger, A.J. (1997). The temperature dependence of the conductivity in the critical regime of the metal–insulator transition in conducting polymers. *J. Phys. Condens. Matter* 9: 4145–4156.

61 Ahlskog, M., Reghu, M., Heeger, A.J. et al. (1996). Electronic transport in the metallic state of oriented poly(*p*-phenylenevinylene). *Phys. Rev. B: Condens. Matter* 53: 15529–15537.

62 Chiang, C.K., Park, Y.W., Heeger, A.J. et al. (1978). Conducting polymers: halogen doped polyacetylene. *J. Chem. Phys.* 69: 5098–5104.

63 Roth, S., Bleier, H., and Pukacki, W. (1989). Charge transport in conducting polymers. *Faraday Discuss. Chem. Soc.* 88: 223–233.

64 Roth, S. and Carroll, D. (2004). *One-Dimensional Metals: Conjugated Polymers, Organic Crystals, Carbon Nanotubes*. Weinheim, Germany: Wiley-VCH.

65 Aleshin, A., Kiebooms, R., Menon, R. et al. (1997). Metallic conductivity at low temperatures in poly(3,4-ethylenedioxythiophene) doped with PF_6. *Phys. Rev. B: Condens. Matter* 56: 3659–3663.

66 Lee, K., Cho, S., Heum Park, S. et al. (2006). Metallic transport in polyaniline. *Nature* 441: 65–68.

67 Diaz, A.F., Castillo, J.I., Logan, J.A., and Lee, W.-Y. (1981). Electrochemistry of conducting polypyrrole films. *J. Electroanal. Chem. Interfacial Electrochem.* 129: 115–132.

68 Guay, J., Paynter, R., and Dao, L.H. (1990). Synthesis and characterization of poly(diarylamines): a new class of electrochromic conducting polymers. *Macromolecules* 23: 3598–3605.

69 Bull, R.A., Fan, F.R.F., and Bard, A.J. (1982). Polymer films on electrodes: VII. Electrochemical behavior at polypyrrole-coated platinum and tantalum electrodes. *J. Electrochem. Soc.* 129: 1009–1015.

70 Barsch, U. and Beck, F. (1996). Anodic overoxidation of polythiophenes in wet acetonitrile electrolytes. *Electrochim. Acta* 41: 1761–1771.

71 Novák, P., Rasch, B., and Vielstich, W. (1991). Overoxidation of polypyrrole in propylene carbonate: an in situ FTIR study. *J. Electrochem. Soc.* 138: 3300–3304.

72 Lewis, T.W., Wallace, G.G., Kim, C.Y., and Kim, D.Y. (1997). Studies of the overoxidation of polypyrrole. *Synth. Met.* 84: 403–404.

73 Li, Y. and Qian, R. (2000). Electrochemical overoxidation of conducting polypyrrole nitrate film in aqueous solutions. *Electrochim. Acta* 45: 1727–1731.

74 Pei, Q. and Inganaes, O. (1992). Electrochemical applications of the bending beam method. 1. Mass transport and volume changes in polypyrrole during redox. *J. Phys. Chem.* 96: 10507–10514.

75 Lizarraga, L., Marı´ a Andrade, E., and Victor Molina, F. (2004). Swelling and volume changes of polyaniline upon redox switching. *J. Electroanal. Chem.* 561: 127–135.

76 Otero, T.F., Angulo, E., Rodríguez, J., and Santamaría, C. (1992). Electrochemomechanical properties from a bilayer: polypyrrole/non-conducting and flexible material – artificial muscle. *J. Electroanal. Chem.* 341: 369–375.

77 Kertész, M., Vonderviszt, F., and Pekker, S. (1982). Change of geometry of polyacetylene upon charge transfer. *Chem. Phys. Lett.* 90: 430–433.

78 Bay, L., Jacobsen, T., Skaarup, S., and West, K. (2001). Mechanism of actuation in conducting polymers: osmotic expansion. *J. Phys. Chem. B* 105: 8492–8497.

79 Kilmartin, P.A. and Travas-Sejdic, J. (2010). Nanostructural aspects of conducting-polymer actuators. In: *Nanostructured Conductive Polymers*, 599–630. New York, NY: Wiley.

80 Takashima, W., Pandey, S.S., Fuchiwaki, M., and Kaneto, K. (2002). Cyclic step-voltammetric analysis of cation-driven and anion-driven actuation in polypyrrole films. *Jpn. J. Appl. Phys.* 41: 7532–7536.

81 Naoi, K., Lien, M., and Smyrl, W.H. (1991). Quartz crystal microbalance study: ionic motion across conducting polymers. *J. Electrochem. Soc.* 138: 440–445.

82 Qiu, Y.-J. and Reynolds, J.R. (1991). Dopant anion controlled ion transport behavior of polypyrrole. *Polym. Eng. Sci.* 31: 417–421.

83 Matencio, T., De Paoli, M.A., Peres, R.C.D. et al. (1995). Ionic exchanges in dodecylbenzenesulfonate doped polypyrrole Part 1. Optical beam deflection studies. *Synth. Met.* 72: 59–64.

84 Maw, S., Smela, E., Yoshida, K., and Stein, R.B. (2005). Effects of monomer and electrolyte concentrations on actuation of PPy(DBS) bilayers. *Synth. Met.* 155: 18–26.

85 Aydemir, N., Kilmartin, P.A., Travas-Sejdic, J. et al. (2015). Electrolyte and solvent effects in PPy/DBS linear actuators. *Sens. Actuators, B* 216: 24–32.

86 Barnes, A., Despotakis, A., Wong, T.C.P. et al. (1998). Towards a ‘smart window’ for microwave applications. *Smart Mater. Struct.* 7: 752–758.

87 Pagès, H., Topart, P., and Lemordant, D. (2001). Wide band electrochromic displays based on thin conducting polymer films. *Electrochim. Acta* 46: 2137–2143.

88 Ji, L., Dai, Y., Yan, S. et al. (2016). A fast electrochromic polymer based on TEMPO substituted polytriphenylamine. *Sci. Rep.* 6: 30068.

89 Schwendeman, I., Hwang, J., Welsh, D.M. et al. (2001). Combined visible and infrared electrochromism using dual polymer devices. *Adv. Mater.* 13: 634–637.

90 Barford, W. (2013). Excitons in conjugated polymers: a tale of two particles. *J. Phys. Chem. A* 117: 2665–2671.

91 Scholes, G.D. and Rumbles, G. (2006). Excitons in nanoscale systems. *Nat. Mater.* 5: 683–696.

92 Cornil, J., Beljonne, D., Calbert, J.-P., and Brédas, J.-L. (2001). Interchain interactions in organic π-conjugated materials: impact on electronic structure, optical response, and charge transport. *Adv. Mater.* 13: 1053–1067.

93 Salzner, U., Lagowski, J.B., Pickup, P.G., and Poirier, R.A. (1998). Comparison of geometries and electronic structures of polyacetylene, polyborole, polycyclopentadiene, polypyrrole, polyfuran, polysilole, polyphosphole, polythiophene, polyselenophene and polytellurophene. *Synth. Met.* 96: 177–189.

94 Jenekhe, S.A. (1987). New electronically conducting polymers: effects of molecular structure on intrinsic electronic properties. In: *Conducting Polymers* (ed. L. Alcácer), 149. Dordrecht: Springer Netherlands.

95 Roncali, J. (2007). Molecular engineering of the band gap of π-conjugated systems: facing technological applications. *Macromol. Rapid Commun.* 28: 1761–1775.

96 Cade, P.E. (1967). The electron affinities of the diatomic hydrides CH, NH, SiH and PH. *Proc. Phys. Soc.* 91: 842–854.

97 Matsumoto, T., Tanaka, K., and Chujo, Y. (2015). Synthesis and characterization of gallafluorene-containing conjugated polymers: control of emission colors and electronic effects of gallafluorene units on π-conjugation system. *Macromolecules* 48: 1343–1351.

98 Burroughes, J.H., Bradley, D.D.C., Brown, A.R. et al. (1990). Light-emitting diodes based on conjugated polymers. *Nature* 347: 539–541.

99 Ariu, M., Lidzey, D.G., Sims, M. et al. (2002). The effect of morphology on the temperature-dependent photoluminescence quantum efficiency of the conjugated polymer poly(9,9-dioctylfluorene). *J. Phys. Condens. Matter* 14: 9975–9986.

100 Asada, K., Kobayashi, T., and Naito, H. (2006). Control of effective conjugation length in polyfluorene thin films. *Jpn. J. Appl. Phys.* 45: L247–L249.

101 Greenham, N.C., Samuel, I.D.W., Hayes, G.R. et al. (1995). Measurement of absolute photoluminescence quantum efficiencies in conjugated polymers. *Chem. Phys. Lett.* 241: 89–96.

102 Piris, J., Dykstra, T.E., Bakulin, A.A. et al. (2009). Photogeneration and ultrafast dynamics of excitons and charges in P3HT/PCBM blends. *J. Phys. Chem. C* 113: 14500–14506.

103 Hou, L., Adhikari, S., Tian, Y. et al. (2017). Absorption and quantum yield of single conjugated polymer poly[2-methoxy-5-(2-ethylhexyloxy)-1,4-phenylenevinylene] (MEH-PPV) molecules. *Nano Lett.* 17: 1575–1581.

104 Sun, K., Chen, H., Wang, L. et al. (2014). Size-dependent property and cell labeling of semiconducting polymer dots. *ACS Appl. Mater. Interfaces* 6: 10802–10812.

105 Schütze, F., Krumova, M., and Mecking, S. (2015). Size control of spherical and anisotropic fluorescent polymer nanoparticles via precise rigid molecules. *Macromolecules* 48: 3900–3906.

106 Botiz, I., Astilean, S., and Stingelin, N. (2016). Altering the emission properties of conjugated polymers. *Polym. Int.* 65: 157–163.

107 Schneider, J.A., Dadvand, A., Wen, W., and Perepichka, D.F. (2013). Tuning the electronic properties of poly(thienothiophene vinylene)s via alkylsulfanyl and alkylsulfonyl substituents. *Macromolecules* 46: 9231–9239.

108 Ramsdale, C.M., Barker, J.A., Arias, A.C. et al. (2002). The origin of the open-circuit voltage in polyfluorene-based photovoltaic devices. *J. Appl. Phys.* 92: 4266–4270.

109 Kietzke, T., Neher, D., Kumke, M. et al. (2004). A nanoparticle approach to control the phase separation in polyfluorene photovoltaic devices. *Macromolecules* 37: 4882–4890.

110 Beljonne, D., Pourtois, G., Silva, C. et al. (2002). Interchain vs. intrachain energy transfer in acceptor-capped conjugated polymers. *Proc. Natl. Acad. Sci. U.S.A.* 99: 10982–10987.

111 Yu, J., Hu, D., and Barbara, P.F. (2000). Unmasking electronic energy transfer of conjugated polymers by suppression of O_2 quenching. *Science* 289: 1327–1330.

112 Laquai, F., Park, Y.-S., Kim, J.-J., and Basché, T. (2009). Excitation energy transfer in organic materials: from fundamentals to optoelectronic devices. *Macromol. Rapid Commun.* 30: 1203–1231.

113 Yersin, H. (2004). Triplet emitters for OLED applications. Mechanisms of exciton trapping and control of emission properties. In: *Transition Metal and Rare Earth Compounds: Excited States, Transitions, Interactions III* (ed. H. Yersin), 1–26. Berlin, Heidelberg: Springer Berlin Heidelberg.

114 Zhang, Y., Wang, Y., Song, J. et al. (2018). Near-infrared emitting materials via harvesting triplet excitons: molecular design, properties, and application in organic light emitting diodes. *Adv. Opt. Mater.* 6: 1800466.

115 Chen, R., Tang, Y., Wan, Y. et al. (2017). Promoting singlet/triplet exciton transformation in organic optoelectronic molecules: role of excited state transition configuration. *Sci. Rep.* 7: 6225.

116 Li, D., Hu, Y., and Liao, L.-S. (2019). Triplet exciton harvesting by multi-process energy transfer in fluorescent organic light-emitting diodes. *J. Mater. Chem. C* 7: 977–985.

117 Tao, Y., Yuan, K., Chen, T. et al. (2014). Thermally activated delayed fluorescence materials towards the breakthrough of organoelectronics. *Adv. Mater.* 26: 7931–7958.

118 Tritsch, J.R., Chan, W.-L., Wu, X. et al. (2013). Harvesting singlet fission for solar energy conversion via triplet energy transfer. *Nat. Commun.* 4: 2679.

119 Pope, M. and Swenberg, C.E. (1999). *Electronic Processes in Organic Crystals and Polymers*, 2e. United Kingdom: Oxford University Press.

120 Lin, J.D.A., Mikhnenko, O.V., Chen, J. et al. (2014). Systematic study of exciton diffusion length in organic semiconductors by six experimental methods. *Mater. Horiz.* 1: 280–285.

121 Tamai, Y., Ohkita, H., Benten, H., and Ito, S. (2015). Exciton diffusion in conjugated polymers: from fundamental understanding to improvement in photovoltaic conversion efficiency. *J. Phys. Chem. Lett.* 6: 3417–3428.

122 Hedley, G.J., Ruseckas, A., and Samuel, I.D.W. (2017). Light harvesting for organic photovoltaics. *Chem. Rev.* 117: 796–837.

123 Antoniadis, H., Rothberg, L.J., Papadimitrakopoulos, F. et al. (1994). Enhanced carrier photogeneration by defects in conjugated polymers and its mechanism. *Phys. Rev. B: Condens. Matter* 50: 14911–14915.

124 Burin, A.L. and Ratner, M.A. (2000). Exciton migration and cathode quenching in organic light emitting diodes. *J. Phys. Chem. A* 104: 4704–4710.

125 Park, H.-W., Kim, T., Huh, J. et al. (2012). Anisotropic growth control of polyaniline nanostructures and their morphology-dependent electrochemical characteristics. *ACS Nano.* 6: 7624–7633.

126 Laviron, E. (1979). General expression of the linear potential sweep voltammogram in the case of diffusionless electrochemical systems. *J. Electroanal. Chem. Interfacial Electrochem.* 101: 19–28.

2

Chemical Synthesis of Conducting Polymers Nanostructures

Srabanti Ghosh[1] *and Dipanwita Majumdar*[2]

[1] *CSIR – Central Glass and Ceramic Research Institute, 196, Raja S.C. Mullick Road, Kolkata 700032, India*
[2] *Chandernagore College, Department of Chemistry, Chandannagar, Hooghly, West Bengal 712136, India*

2.1 Introduction

In last few decades, conjugated polymer has seen astonishing advances, leading to the synthesis of a wide variety of materials that demonstrated significant physicochemical properties, depending on their shape, size, structure, optoelectronic properties, etc., which has allowed expansion of their application possibilities in different fields of electronics, biomedical, energy, and environmental technologies [1, 2]. It is worth noting that conducting polymer nanostructures (CPNs) have shown improved catalytic performance at low dimensionality [3]. The possibility to tailor the physical characteristics and of modifying the surface chemistry during their synthesis makes CPNs suitable, not only as catalyst supports, but also as efficient catalysts, having several advantages of structural and functional versatility by molecular design, solution processability, light weight, and low processing cost [4, 5].

Hence, the nature of molecular precursors and the synthesis route play an important role in the CPNs material properties and characteristics that control and govern the catalysis and other applications. Up to now, various synthetic strategies have been developed for the controlled fabrication of CPNs with different diameters, thicknesses, and lengths. Various nanostructures of conjugated polymers, such as nanoparticles, nanowires/nanofibers, nanobelts/nanoribbons vesicles, hollow capsules, nanotubes, nanosheets, etc., can be prepared using particular oligomers, and the obtained CPNs possess superior electrical conductivity, large surface area, high carrier mobility, high electrochemical activity, etc. [6–8].

CPNs can be synthesized by different methods such as nanopore-template, gamma radiation, electrospinning, e-beam lithography, vapor-phase deposition, focused ion-beam etching, DNA scaffolding, etc. [9–13]. For controlled fabrication of CPNs, mainly, template-based synthesis and template-free synthesis are utilized. There are three kinds of template-based synthesis that have been followed, namely, hard-template method, soft-template method, and novel wire-template method. On the other hand, template-free strategy including self-assembly, electrospinning, and

Conjugated Polymer Nanostructures for Energy Conversion and Storage Applications,
First Edition. Edited by Srabanti Ghosh.

seeding approach, etc. has been used widely for the synthesis of nanostructured polymers [14–16]. In this chapter, we present an overview on the recent progress achieved in the fabrication of different CPNs. This chapter covers the common methods for the synthesis of CPNs such as the template-directed method and template-free synthesis including self-assembly technique, electrospinning, etc.

2.2 Template-Based Synthesis

Template-based synthesis is one of the most common strategies for fabricating CPNs with controlled shapes and tunable dimensions/sizes. Traditionally, conducting polymers have been synthesized via chemical or electrochemical oxidation of monomers, followed by the coupling of charged monomers to produce the polymer chains. In addition, using nanostructured matters as templates may provide the spatial confinement to promote growth of conducting polymers in nano dimensions. It is worth noting that CPNs with controllable morphology and size are obtained in presence of used templates or after removal of the templates.

2.2.1 Hard-Template Method

The hard template route has been considered to be a common technique using track-etch polycarbonate (PC) or polyester (PE) membranes, anodic aluminum oxide (AAO) membranes, etc. as templates for the synthesis of CPNs [17, 18]. In particular, porous membrane materials such as AAO, particle track-etched membranes (PTM) containing massive micro-/nanopores are commonly used where a monomer solution is loaded into their pores and further the polymerization of the monomer takes place within the channels through chemical and/or electrochemical reactions. The PC-PTM and the AAO membranes have been successfully used for the synthesis of conducting polymer (CP) with controllable nanorods, nanofibers, and nanotubes of conducting polymers such as polypyrrole (PPy), polyaniline (PANI), poly(3-hexylthiophene) (P3HT), polythiophene (PTh), poly(3-methylthiophene) (P3MT), etc. [19–24]. For example, Foulger and coworker [25] reported the synthesis of 1D poly(3,4-ethylenedioxythiophene) (PEDOT) nanostructures in the form of tubes, rods, thimbles, and belts using an AAO template (pore size $\sim$ 250 nm, thickness $\sim$ 60 μm) through a chemical oxidative polymerization method as shown in Figure 2.1. The use of an Al_2O_3 membrane with a pore diameter of 250 nm as a template resulted in a range of unique 1-D PEDOT nanotubes structures in the solution.

PANI nanowires with improved electrochemical properties were fabricated using electrochemical synthesis in an AAO template by Mallouk and coworker [26]. In another study, simultaneous growth of core MnO_2 and shell PEDOT by electrochemical deposition in AAO template was reported by Liu and Lee [27]. Figure 2.2 displays the growth of MnO_2/PEDOT coaxial nanowires through co-electrodeposition. They proposed that the PEDOT may have grown into the MnO_2 core layer and phase segregation of these two materials may have forced the MnO_2 to grow in the spaces left by the PEDOT shells as the cores.

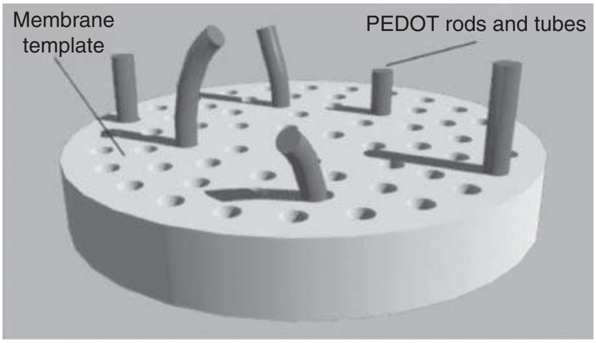

Figure 2.1 Schematic presentation of the synthesis of PEDOT nanostructures using Al_2O_3 membrane as a template. Source: Reproduced with permission from Ref. [25]. Copyright 2005, Royal Society of Chemistry.

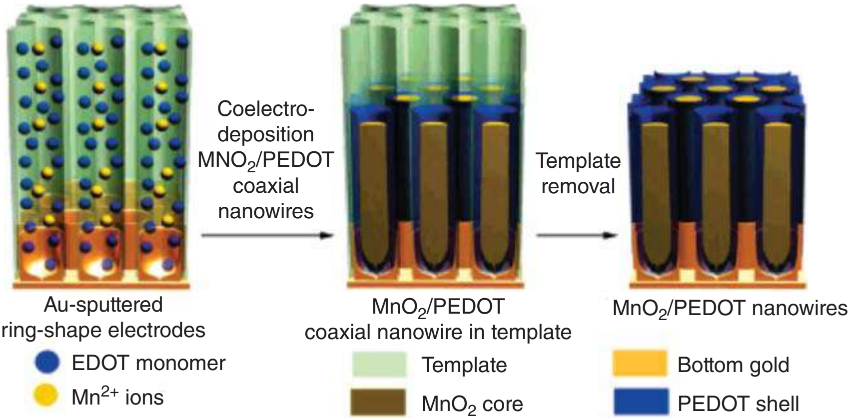

Figure 2.2 Schematic of synthesis of MnO_2/PEDOT coaxial nanowires. Source: Liu and Lee [27]. © 2008, American Chemical Society.

Lee and coworker reviewed the use of PC-PTM templates for the synthesis of hollow or solid CPNs with the controllable processes, mechanisms, and the factors determining their morphology, size and properties besides exploring the application prospects [28]. PPy tubules with different diameters (50 and 400 nm), synthesized by Orgzall et al. [29] using the pores of nuclepore polycarbonate membranes (doped with *para*-toluenesulfonate, PTS), can result in high conductivity of 30–50 S/cm. Further, Wu et al. [30] fabricated free-standing PPy nanotube-based films through self-degraded template methods. Besides the AAO and PC-PTM templates, other hard templates including zeolites, silica-based mesoporous molecular sieves, oxides, polyoxometalates and nanotubular TiO_2 porous membranes, etc. often have been used for CPNs synthesis [31–36]. For example, the nanowires or nanotubes arrays fabricated from mesoporous silica are interconnected by small pillars formed within the micro- or mesopores in the silica pore walls by Bein and coworker [37]. They prepared conducting filaments of PANI in the 3 nm wide hexagonal channel of the aluminosilicate mobil composition of matter no. 41 (MCM-41). Moreover, inorganic nanostructures, such as the V_2O_5 fibers or MnO_2 nanowires, are also used as reactive template and have potential for the synthesis of tunable sizes and shapes of CPNs [38, 39]. A simple *in situ* polymerization method was developed by Li et al. [40] to synthesize uniform one-dimensional V_2O_5@polyaniline core/shell nanobelts in the absence of any surfactant and additional initiator, which found usefulness in reversible lithium batteries. Another interesting report using one-dimensional methyl orange fibrils hard templates was proposed by Dai and Lu [41] to synthesize PPy, PANI, and PEDOT conducting polymer microtubules but effectively acted as soft templates.

Hard-template approach can also be used for the controlled synthesis of segmented polymer nanowires along their axis, for example, two-segmented Ni–PPy, Au–PANI, CdS–PPy and CdS–PTh nanowires, tri-segmented Ni–PPy–Pd, Au–PPy–Au, Ni–Au–PANI, Ni–PEDOT–Au, and tetra-segmented Au–PEDOT–PPy–Au nanowires, which demonstrated multifunctional properties including high conductivities, good charge-transport abilities, and excellent optoelectronic characteristics [42–46]. Although, controlled CPNs nanostructures with tunable size and morphology can be obtained by using hard template but often involvement of multistep process, removal of the template by either heating, or chemical treatment may affect the structure of polymer which make this process less suitable for the large-scale productions.

2.2.2 Soft-Template Method

The soft template has broad prospects for development in CPNs because of its advantages such as its good repeatability, simplicity of the process, and no requirement for the removal of template. Conceptually, the soft templating involves congregation of supramolecular entities such as self-assembled arrangements of structure-directing molecules like surfactants [3]. The soft template mediated different fabrication processes that have been used for the synthesis of CPNs including micro-/mini-emulsion polymerization, reversed-microemulsion, layer-by-layer self-assembly and block copolymer mediated, etc. [47, 48]. Various soft materials such as surfactants, liquid crystals (LCs), copolymers, and other amphiphilic molecules are used to form micelles or reversed micelles in solutions for guiding the *in situ* anisotropic growth of conducting polymers nanostructures [49]. It was shown that the morphology, diameter, and length of conjugated polymer are mainly dependent on the pre-assembled micelles depending on the types and concentrations of amphiphilic matters. Surfactant mediated soft templates are widely used to synthesize CPNs. For example, Jang et al. [50] synthesized monodispersed polypyrrole nanoparticles of diameter 5 nm in a microemulsion with alkyl-trimethylammonium bromide cationic surfactants. They proposed that the surfactants have alkyl lengths between C6 and C16 because alkyl chains shorter than C6 with weak hydrophobic interactions and are most suitable for microemulsion polymerization, while alkyl chains longer than C16 have too high a viscosity to form self-assembled nanostructures. Hence, the nature of the surfactants as well as their concentrations has a big impact on the morphology and size of the nanostructured

CP. Guo and coworkers [51, 52] used sodium dodecyl sulfate (an anionic surfactant) to control the morphology of PANI in the forms of granules, nanofibers, nanosheets, rectangular submicrotubes, and fanlike/flowerlike aggregates, which depend on the concentrations of sodium dodecyl sulfate (SDS) and HCl. Jang et al. [53] prepared PPy nanocapsules via a soluble polypyrrole core and a crosslinked polypyrrole shell by sequentially using initiators of two different oxidation potentials. It was shown that a linear PPy core soluble in alcohol was produced in the first stage using copper (II) chloride with a lower oxidation potential ($E°$ of +0.16 V), while an insoluble crosslinked polypyrrole shell was created in the later stage using iron (III) chloride with higher oxidation potential ($E°$ of +0.77 V) (Figure 2.3). Finally, PPy nanocapsules were obtained when excess methyl alcohol was added, which etched the linear polypyrrole core along with the surfactants, and the crosslinked polypyrrole shell was retained.

Yoon and coworker [54, 55] explored formation mechanism of conducting PPy nanotubes through chemical oxidation polymerization in sodium bis(2-ethylhexyl) sulfosuccinate (dioctyl sulfosuccinate sodium salt [AOT]) reverse (water-in-oil) emulsions. Figure 2.4a,b displays the field emission scanning electron microscopy (FE-SEM) and the transmission electron microscopy (TEM) images of prepared PPy nanotubes with diameter 94 ± 13 nm, and their length was more than 2 μm. The electron diffraction pattern (Figure 2.4b, inset) indicates amorphous nature of the PPy nanotubes with a diffusive ring. It is noted that PPy nanotube dimensions were affected by synthetic variables such as the weight ratio of aqueous $FeCl_3$ solution/AOT, type of apolar solvent, and reaction temperature. The weight ratio of aqueous $FeCl_3$ solution relative to AOT varied from 0.16 to 0.22 in composition of pyrrole/aqueous $FeCl_3$ solution, 20/80 by weight percent, as a result, the diameter of the PPy nanotubes increased with increasing weight ratio of aqueous $FeCl_3$ solution to AOT as shown in Figure 2.4c. They also proposed the relationship

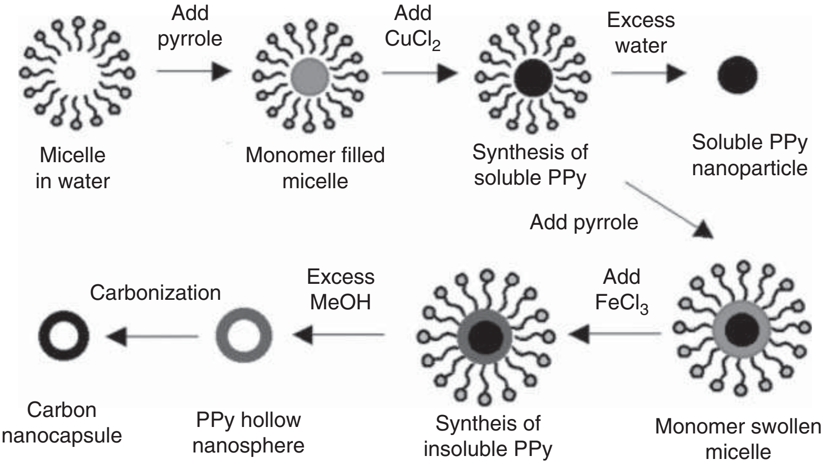

Figure 2.3 Schematic diagram of the microemulsion fabrication of polypyrrole hollow nanospheres. Source: Jang et al. [53]. © 2004, Royal Society of Chemistry.

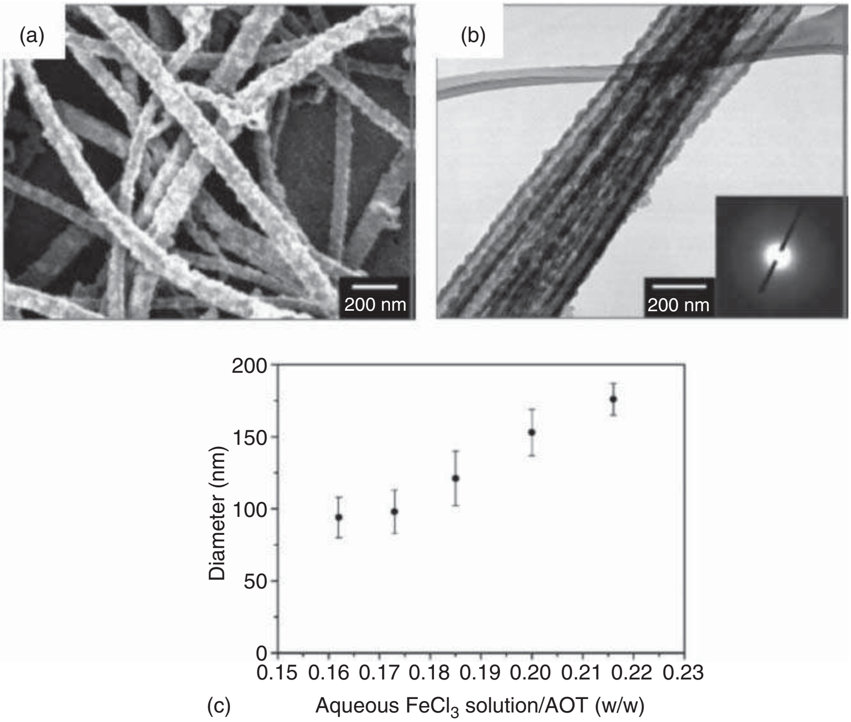

Figure 2.4 (a) FE-SEM and (b) TEM image of PPy nanotubes, inset: electron diffraction pattern of PPy nanotubes. (c) Diameter variation of PPy nanotubes as a function of the weight ratio of aqueous $FeCl_3$ solution to AOT. Source: (c) Jang and Yoon [54]. © 2005, American Chemical Society.

between the diameter and the conductivity of the nanotubes, a slight increment in conductivity was observed with decreasing diameter of PPy nanotubes.

Cationic surfactants such as cetyltrimethylammonium bromide (CTAB), dodecyltrimethylammonium bromide (DTAB) are also used to form lamellar mesostructures as soft templates for the oxidative polymerization of PPy, PANI, and PEDOT nanowires/ribbons in widths of 25–85 nm and in lengths exceeding several micrometers using ammonium peroxodisulfate (APS) an oxidant [56, 57]. Figure 2.5a shows a scanning electron microscopy (SEM) image of the PPy with a homogeneous nanoclip morphology having average diameter in the 50–70 nm range. Both PANI and PEDOT powder also possesses similar nanoclip morphology with diameters of ~100 nm for PANI and ~200 nm for PEDOT (Figure 2.5b,c), respectively. They proposed the formation mechanism based on lamellar micelles that are composed of a folded, twin-tailed complex of $(CTA)_2S_2O_8$ in 1 M aqueous HCl (Figure 2.5d,e). The positively charged monomers may preferably migrate to the interface between the micellar complex and aqueous HCl medium (Figure 2.5d,e), where the oxidation of the monomers will occur. The template will remain intact until all $S_2O_8^{2-}$ in solution is consumed; i.e. the template will eventually be broken by consumption of the $S_2O_8^{2-}$ ions, which bridge the cetrimonium ions.

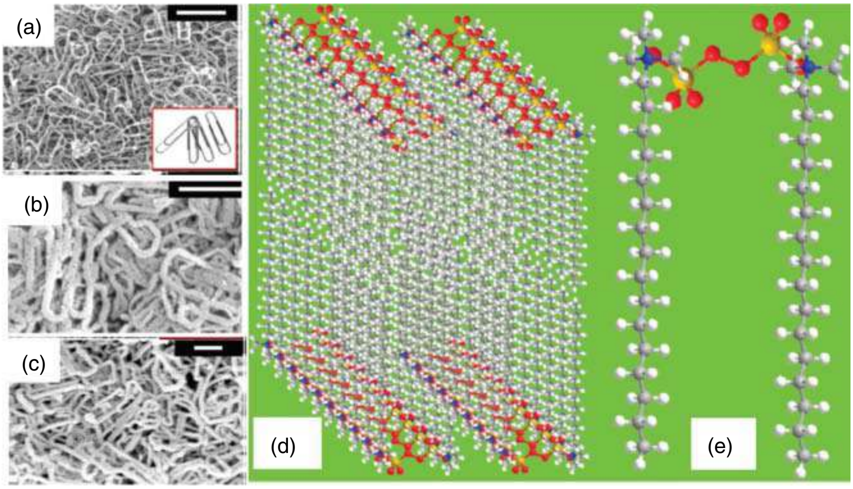

Figure 2.5 SEM images of (a) PPy·Cl nanoclips (scale bar, 1 μm; inset, digital picture of paper clips), (b) PANI·HCl nanoclips (scale bar, 1 μm), and (c) PEDOT·Cl nanoclips (scale bar, 1 μm). Schematic presentation of (d) lamellar structure of the $(CTA)_2S_2O_8$ complex micelle and (e) individual $(CTA)_2S_2O_8$ complex with protonated monomer. Source: (d, e) Liu et al. [56]. © 2010, American Chemical Society.

The results showed that the careful combination of experimental parameters, such as surfactants, oxidizing/doping agents, pH, temperature, and other structure-directing agents, provides enormous possibilities of fabricating nanostructures with desirable morphology. Zhang et al. used various anionic, cationic, or non-ionic surfactants with various oxidizing agents to prepare varied PPy nanostructures [58]. In addition, efforts have been devoted to obtain PANI nanowires with different morphologies doped with different acids (acetic acid, HCl, and *p*-toluene sulfonic acid), which were prepared by using CTAB as the soft template [59]. Wang and coworkers [60] developed a soft-template method based on AOT reversed micelles for the fabrication of the regular and well-dispersed PEDOT nanorods with widths of 40–60 nm and lengths of 370–460 nm using $Ce(SO_4)_2{\cdot}4H_2O$ as an oxidant. Moreover, *in situ* sacrificial oxidative template route has been developed by Li et al. [61] for the bulk synthesis of two-dimensional nanorings and flat hollow capsules of PANI nanostructures. A self-organized template, lyotropic liquid crystals (LC) with hexagonal phases, was also used for the synthesis of anisotropic conducting polymer nanostructrures [62]. For the first time, Hulvat and Stupp [63, 64] reported the fabrication of ordered PEDOT nanostructures into hexagonal LC by electropolymerization technique. Furthermore, Remita and coworkers [65], developed swollen hexagonal mesophases composed of oil-swollen tubes with tunable diameters, which can be used to effectively control the morphology and the size of the nanostructures. A series of CPNs such as poly-(diphenylbutadiyne) (PDPB), PEDOT, PPy, and P3HT with controlled size and morphology have been prepared using swollen hexagonal mesophases [66–69]. Ghosh et al. [70] developed a single step approach for the preparation of PEDOT nanostructures in the hydrophobic

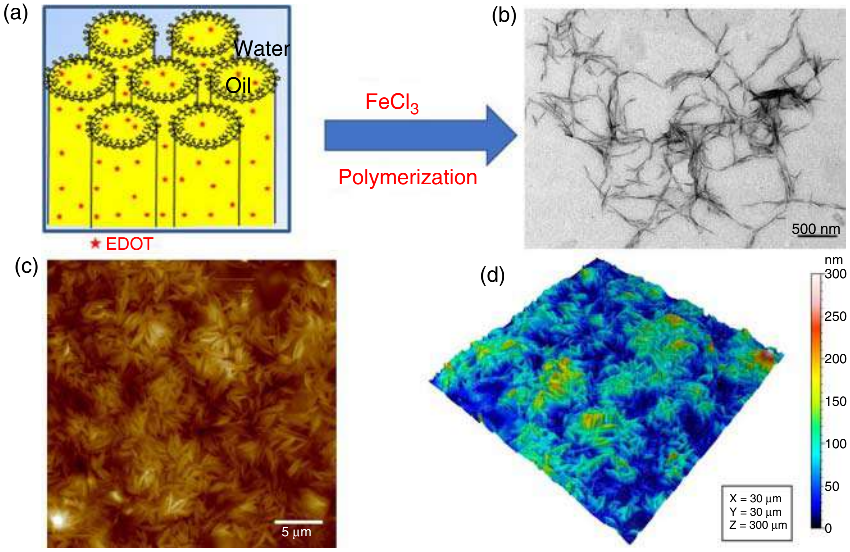

Figure 2.6 (a) Hexagonal mesophases doped with 3,4-ethylenedioxythiophene (EDOT) monomer. (b) Transmission electron micrograph (TEM) of PEDOT nanospindles synthesized in presence of 0.3 M NaCl. (c) Typical AFM topographic image of PEDOT nanospindles extracted from mesophases. (d) The corresponding 3D AFM image of PEDOT nanostructures. Source: Reproduced on permission from Ref. [70], copyright 2014, The Royal Society of Chemistry.

domains of cationic surfactant-based hexagonal mesophases (Figure 2.6). Hexagonal mesophases composed of oil-swollen surfactant-stabilized tubes arranged on a triangular lattice in salted water and doped with 3,4-ethylenedioxythiophene (EDOT) monomers in the oil phase were used as soft templates (Figure 2.6a). Polymer nanostructures are produced via chemical oxidative polymerization of EDOT monomers using $FeCl_3$ as an oxidizing agent. The PEDOT spindle nanostructures of 40 nm thick and several hundred nanometers long are obtained as shown in Figure 2.6b. Atomic force microscope (AFM) topographic image and the corresponding 3D AFM image showed well dispersed isolated PEDOT spindle nanostructures with a regular shape (Figure 2.6c,d).

Ghosh et al. [71] also reported the controlled synthesis of micrometers long nanofibers of conducting poly-(diphenylbutadiyne) (PDPB) were synthesized in the oil tubes of the hexagonal mesophases by photo-induced radical polymerization using a chemical initiator. The average diameter of the polymer nanofibers increases with the diameter of the oil cylinder of the soft template from 5 to 19 nm as shown in Figure 2.7. Thus, the diameter of the as prepared PDPB nanostructures can be varied by approximately fourfold by tuning the diameter of the confining oil tubes, which can be simply swelled by simultaneous variation of the ratio water/oil and salt concentration in the aqueous phase. The anisotropic shape of the templated polymer nanostructure presumably reflects the geometry of the hydrophobic domains of the hexagonal mesophases, which indicate direct template effect.

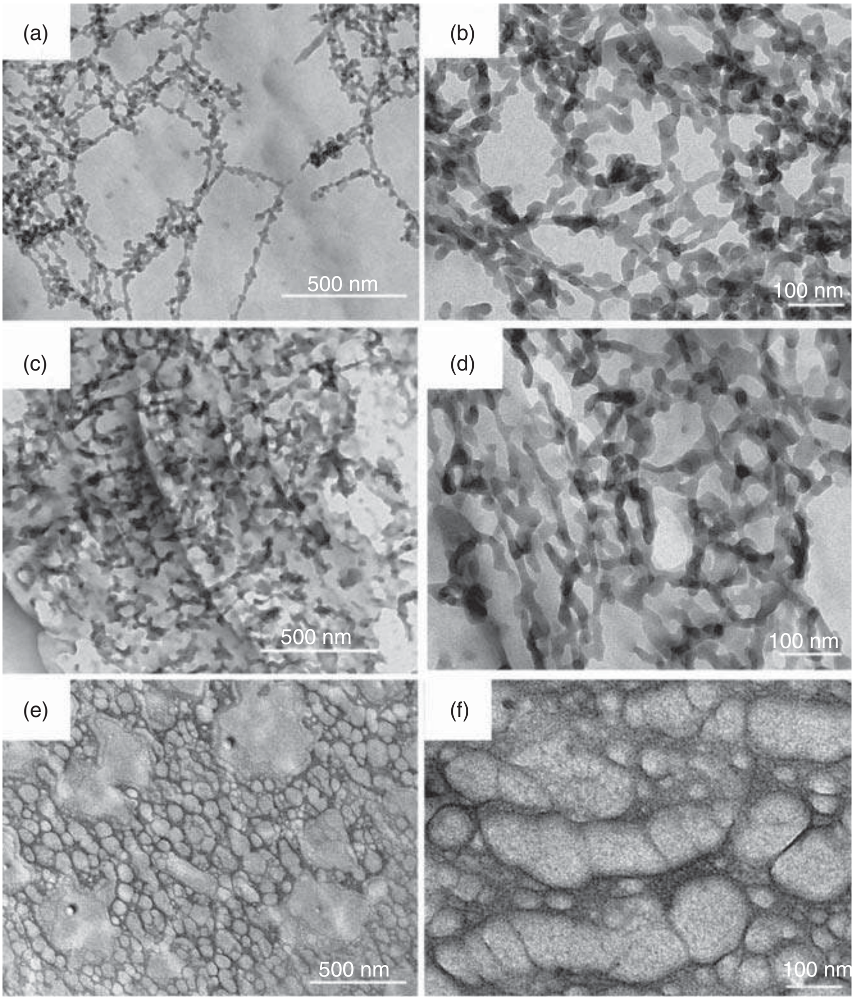

Figure 2.7 Transmission electron micrographs of PDPB nanostructures prepared by UV-irradiation in mesophases with (a, b) $\phi = 2.21$ and Cs = 0.3 M NaCl, (c, d) $\phi = 0.98$ and Cs = 0.1 M NaCl, and (e, f) $\phi = 0.72$ and Cs = 0 M NaCl. Source: Reproduced with permission from Ref. [70]. Copyright 2014, The Royal Society of Chemistry.

Moreover, the dimension and the morphology of the nano-objects grown in the liquid-crystalline phase strongly depend on composition ranging from columnar, lamellar, or cubic phases [72]. A chemical affinity template based on block copolymer is also used for the electropolymerization PPy and thiophene derivatives in order to form CPNs [73]. Bioactive aqueous gel matrices formed by peptide amphiphile may provide a reservoir for the uptake of hydrophobic monomer molecule and can be used for polymerization in the confined region [74]. Niu et al. [75] discovered that the rod-like tobacco mosaic virus (TMV) can be used as the template to profitably obtain 1D-conducting PANI, and polypyrrole nanowires via a hierarchical assembly process (Figure 2.8).

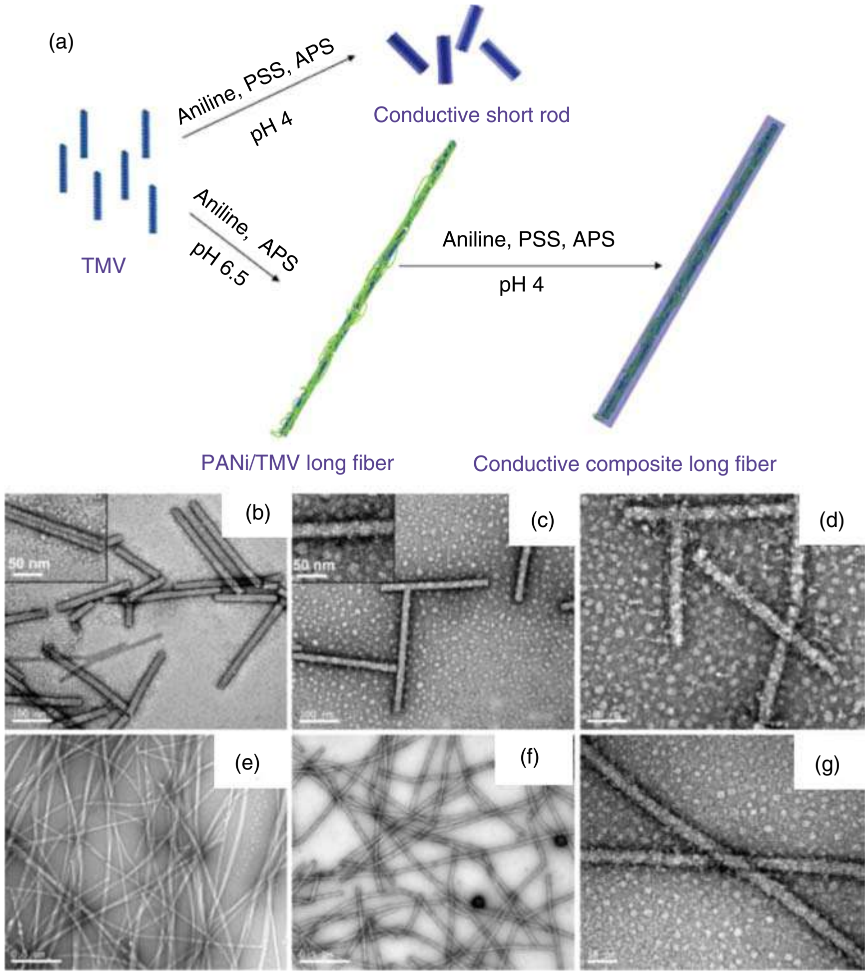

Figure 2.8 (a) Schematic presentation of synthesis of conductive polyaniline/TMV composite nanowires. (b) TEM images of wt-TMV (inset showing the outer and inner diameters of pristine TMV to be 18 nm and 4 nm respectively, the latter could be detected by negative staining), (c) PSS/PANI/TMV nanowire from the pH 5, (inset showing that the inside channel of the composite wire became less prominent even after negative staining) (d) PSS/PANI/TMV composite nanowire from the pH 4, (e) PANI/TMV long fiber (LF), (f) PSS/PANI/LF, and (g) an enlarged image of PSS/PANI/LF. Source: Reproduced with permission from Ref. [75]. Copyright 2007, the American Chemistry Society.

Conductive PANI/TMV composite nanowires can be prepared by incubation of TMV (tobacco mosaic virus), aniline, poly(styrenesulfonate) (PSS), and APS at room temperature (Figure 2.8a). Figure 2.8b shows the diameter of native TMV is around 18 nm and the 4 nm inner channel can be clearly observed in set of Figure 2.8b. Upon coating with PANI/PSS at pH 5.0, the diameter of composite nanowires was measured as 22 nm (Figure 2.8c). Similarly, the PSS/PANI/TMV nanowires formed at pH 4.0 showed an increased diameter of ~26 nm, while the length remained very similar to native TMV particles (Figure 2.8d). The formation of highly branched PANI at neutral reaction pH prevents lateral association of single PANI/TMV nanofibers (denoted as PANI/TMV/long 1D fibers [LFs]) due to the increase of steric repulsion (Figure 2.8e). When preformed PANI/TMV/LF was treated with PSS, aniline, and APS at pH 4.0 or 5.0 (Figure 2.8a), long 1D fibers (denoted as PSS/PANI/LF) were produced with increased diameters (Figure 2.8f,g). Meier et al. [76] disclosed a unique way to produce conducting PANI nanowires with a core–shell architecture using amyloid nanofibers template. The amyloid nanofibers exhibit hydrophobic pockets that may preassemble the aniline monomers and directs polymer morphology, primarily to suppress defects in the polymer chain, which are unfavorable to charge transport that can promote many potential applications including optics, sensing, and biomedical engineering. Nagarajan et al. [77] developed a novel approach with conjugated oligomers (terthiophene) as redox mediators and vastly expanded the types of substrates (thiophenes, pyrroles) that can be polymerized by enzymatic methods under milder pH conditions using soybean peroxidase.

DNA molecules also used as effective soft templates for the controlled fabrication of CP nanostructures. A series of polymer nanostructures such as polyindole nanowires, PPy nanowires, PANI nanowires, etc. has been reported using DNA molecule as template [12, 78, 79]. Biomolecule based templated synthesis of CPNs further extended with using living cells and a neural cell-templated conducting polymer coating for microelectrodes and a hybrid conducting polymer-live neural cell electrode was reported by Martin and coworkers [80]. Moreover, it is noted that ionic liquids have been used as a soft templates for the synthesis of PANI nanostructures [81]. Organic molecules also used as “soft templates” for the synthesis of high performance conjugated polymers nanotubes as well [82]. Sacrificial oxidative templates using $V_2O_5/H_2O_2/H_3PO_4$ mixture can serve as both oxidant and sacrificial template for polymerization of PANI nanorings [61].

Evidently, the soft-template method is a useful strategy for the synthesis, and control of conducting polymer nanostructures comparable with the hard-template method. The soft template method possesses several advantages of low cost and versatility, high yield, easy operation, ambient liquid conditions, etc., which is suitable for the large-scale production. The shortage of the soft template method arises from poor stability of the soft templates and the difficulty in a fine control over size and morphology of CPNs like hard template. In this context, the discontinuous morphology of CPNs as electrode materials limits their application in energy storage devices. In the presence of a soft template, polymerization rate became slower, yield CP nanostructures with lower aspect ratios and the stabilizer sterically restrict the directional fiber growth mechanism governing polymer chain growth in aqueous solution [83].

2.3 Template-Free Synthesis

It is feasible to obtain various controlled CPNs without using any external templates or structure-directing agents as well [84–87]. The process is based on the fact that the conjugated polymers show a general inclination to grow preferentially in one direction. Conjugated polymers usually grow linearly to form semi-rigid rod-like morphology [88, 89]. This anisotropy can be further transcribed into nano-sized bundles through carefully-controlled preparation parameters [90]. The preparation of CPNs without the aid of any template has always been a facile, uncomplicated, and cost-effective approach since this can successfully avoid the rigorous post-treatment procedures for template removal and product purification [91, 92]. Additionally, this also avoids unwanted deformation of the synthesized polymer structures that inadvertently get introduced during such purification processes. Moreover, these techniques yield scalable products as well as reproducible results. Strategies under "template-free synthesis" generally include self assembling process, electrospinning, conjugated hydrogel formation, and pH-controlled techniques that have been reported to obtain appreciable product yields that are briefly summarized in the following paragraphs.

2.3.1 Self Assembly via Interfacial Polymerization

Interfacial polymerization (IP) process involves oxidative coupling of monomers at low temperature with limited side reactions without the use of catalysts or phase transfer agents. It involves step polymerization of two reactive monomers or agents, respectively, dissolved in two immiscible phases and the reaction is carried out at the interface of the two immiscible systems. The fascinating fact is that the mass and charge diffusion through the interface controls the crystallinity and morphology of the growing conjugated polymer nanostructures [93–96]. It is well accomplished that various non-covalent interactions, Van der Waals forces such as dipole–dipole interactions, ion–dipole interactions, hydrophobic forces, π–π stacking, hydrogen bonding, etc. direct the building blocks to arrange spontaneously in thermodynamically favored anisotropic aggregates or oriented morphology under suitable conditions (self-assembly phenomenon). Various nanofibers/nanowires, hollow nanotubes of conducting PANI, PPy, PEDOT, etc. as well as their functionalized derivatives have been successfully obtained by *in situ* doping interfacial polymerization in the presence of various organic acid as dopants [93].

Considerable morphology control can be successfully attained by regulating the synthetic conditions such as various oxidants, dopants types, different molar ratios of monomer/dopant as well as monomer/oxidant, solvents, as well as polymerization reaction time and reaction temperature. Qin and coworkers [96] carried out three types of PANI nanostructures fabrication using interfacial polymerization by the application of different oxidants such as APS as a single oxidant, while APS/$FeCl_3$, APS/$K_2Cr_2O_7$ as mixed oxidants, respectively, as depicted from their SEM images in Figure 2.9a–c. The combination of mixed oxidants favored faster rate of interfacial polymerization with appreciable influence on the morphology/microstructure and accordingly improved the electrochemical properties of the resultant nanostructures were observed. Again, morphology of salicylic acid doped PANI could be modified from 1D-nanotubes to 3D-hollow spheres merely by changing the dopant to monomer ratio via self-assembly phenomena.

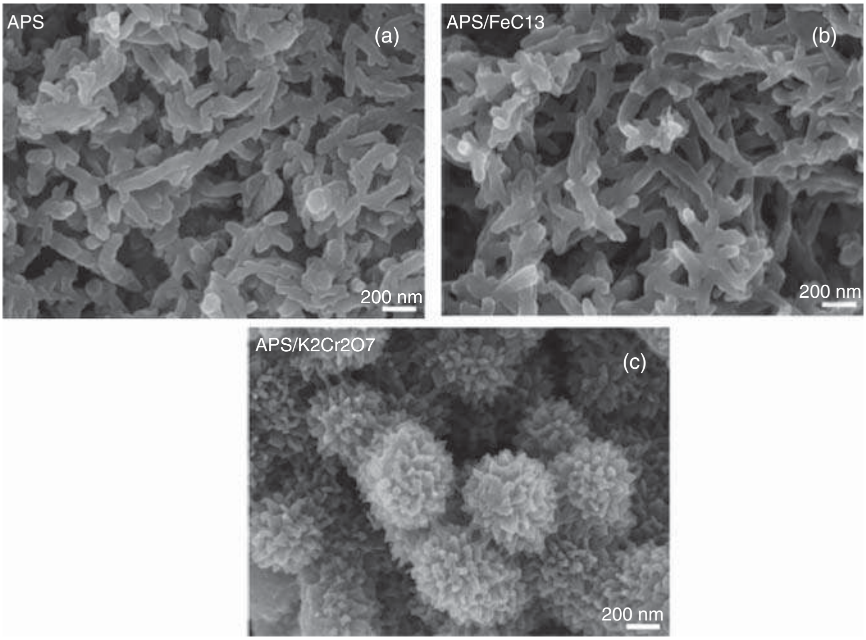

Figure 2.9 (a–c) SEM images for nanostructured PANIs prepared by interfacial polymerization by using ammonium peroxodisulfate (APS), APS/$FeCl_3$, and APS/$K_2Cr_2O_7$ as the oxidant respectively. Source: Reproduced with permission from Ref. [96]. Copyright 2015 Elsevier.

The resultant hollow micelles produced on varying the reactants ratio through the aid of hydrogen bonding acted as "molecular templates" for the formation of corresponding nanostructures [97]. PANI nanotubes and nanofibers of high crystallinity having diameter range of 80–170 nm were successfully obtained using "micelle soft-template" technique using dicarboxylic acids dopants with varying numbers (n) of $-CH_2-$ groups ($n = 0$–4). The larger diameters of the nanostructures were obtained with increasing the number of $-CH_2-$ groups in the dopant and accordingly the conductivity of the nanotubes also varied [98]. Further, free synthesis of PANI nanotubules in the presence of $C_{60}(OSO_3H)_6$ or 3,6-disulfonaphthylthiourea (PAMAM4.0-[naphthyl$(SO_3H)_2]_{24}$) as protonic acid dopants resulted in formation of PANI nanotubes having diameter in the order of hundreds of nanometers and several micrometers long. Here, water is assumed to play an important role in controlling the self-assembled morphology of aniline/PAMAM4.0[naphthyl-$(SO_3H)_2]_{24}$ and aniline/$C_{60}(OSO_3H)_6$ in the formation of tubular morphology and hence inducing high conducting properties of the resulting materials [99]. Self-assembly also played important role in obtaining sub-micron sized D-camphor-10-sulfonic acid doped PANI as well as *p*-toluenesulfonic acid doped-PPy nanotubes, nanotube-junctions, and dendritic structures. It was proposed that hollow spherical structures aggregated through self-assembly to form the tubular and dendrimeric morphology owing to several operating non-covalent interactions during stationary reaction condition [100].

Few years later, superhydrophobic, highly conducting PANI rambutan-like hollow spheres were reported using self-assembled process. Perfluorooctane sulfonic acid not only served as an effective dopant and molecular template, but also promoted superhydrophobicity due to the presence of hydrophobic alkyl substituents in the structure. It was proposed that such hollow morphology resulted from cooperative effect of self-assembly processes of the dopant as well as dopant/monomer salt micelles that function as the soft template of such PANI nanostructures [101]. Further systematic studies strengthened the previous proposition as many research group subsequently reported various nanostructures of conjugated polymers, namely, nanofibers, nanospheres, and nanotubes, simply by varying the reaction parameters to control the shapes and concentration of the micelles formed by dopant, dopant/monomer salt, or supermolecules that served as the "*in situ* soft template" through self-assembly process [91, 102].

It has also been observed that the morphology and diameter of the template-free conducting polymer micro/nanostructures are strongly affected by the structures of the monomer, dopant, and oxidant, as well as by the preparation conditions. The preparation conditions include the concentrations of dopant, oxidant, and monomer, and the molar ratio of the dopant and oxidant to monomer, as well as the reaction temperature, time, and stirring. Hollow microspheres of PANI, for instance, could be modified into corresponding nanotubes either by changing the polymerization reaction temperature or by altering the monomer to dopant molar ratio. This finding further promoted simplification of the template-free method by omitting addition of organic acids as the dopants. This modification was later referred to as a simplified template-free method (STFM). It was proposed that the aniline monomer in aqueous solution form micelles that act as soft template for forming hollow spheres initially. As the polymerization proceeds, these hollow spheres linearly aggregate and elongate to form tubular morphology. Interestingly, it was observed that the conductivity of the STFM-assisted PANI nanofibers was comparable with the nanotubes obtained via conventional template-free method [103]. In addition, it has been realized that the diameter generally decreases with decreasing redox potential of the oxidants employed for polymerization. An empirical equation, shown in the following text, was formulated accordingly in Eq. (2.1), where d is the average outer diameter of the nanofibers and $E^{\circ}{}_{\mathrm{ox}}$ is the standard redox potential of the oxidants, respectively.

$$\log d = 0.69 + 0.71E^{\circ}_{\mathrm{ox}} \tag{2.1}$$

Thus, it is accomplished so far that STFM is by far the simplest approach for fabricating CPNs as it not only saves on templates fabricating procedures but also avoids post-treatment and also simplifies the reagents requirement [91, 103–105]. Hence, we find that a diversity of different conducting polymers nanostructures such as nanotubes, nanowires, nanofibers, nanocapsules, etc. have been successfully prepared using template-free chemical approach [104, 105]. PANI nanotubes have can also be prepared by the template-free method using high pH polymerization technique PANI so-formed are believed to be formed via head-to-tail coupling of aniline monomers. Insightful investigations by Stejskal et al. [106] revealed that aniline polymerization at high pH aqueous medium initiates ortho-coupling of aniline monomers, which can subsequently be oxidized to “phenazine-like moieties.” The pH of the medium slowly drops as the reaction proceeds, as sulfuric acid is liberated from the reaction of APS. The so-formed phenazine units are supposed to assemble into clusters (to assemble as nanocrystallites) that guide the growth process of PANI nanotubes once the pH falls sufficiently. It is the nanometer-sized oligomer PANI crystallites that essentially serve as nucleation templates for the PANI nanotubes [107, 108].

In another approach, Huang et al. [109] employed aqueous/organic interfacial polymerization technique for obtaining high-class PANI nanofibers with diameters ranging in between 30 and 50 nm under ambient laboratory conditions. Haldorai et al. [110] described microwave-assisted aqueous/ionic liquid interfacial oxidative polymerization technique as a simple, economic, and reliable way for synthesis of high productive copolymer nanostructures such as poly(aniline-*co*-*p*-phenylenediamine) (poly(Ani-*co*-pPD)) nanorods in presence of acid dopants. Nuraje et al. [111, 112] also reported interfacial crystallization of PANI and PPy at the liquid/liquid interface that yielded single-crystalline, rice-like nanocrystals with average dimensions of 63 nm × 12 nm (for PANI) and 70 nm × 20 nm (for PPy), respectively. Few years later, Ma et al. [95] designed highly conducting well-aligned dodecatungstosilic acid ($H_4SiW_{12}O_{40}$) doped-PANI belts obtained via interfacial polymerization method. The interfacial polymerization technique has also been useful for polymerization of EDOT leading to PEDOT nanorods with high structural orderliness and conductivity [111]. Subsequently, detailed systematic reviews covering plausible formation mechanisms and dynamics, determining synthetic parameters that dictate various physicochemical properties of these self-assembled 1D CPNs, have been reported in the literature [102, 113, 114]. Again, helical hexaazatrinaphthylene nanowires were obtained from surface-assisted assembly at the solvent/substrate interface. Such helical structure was proposed to arise from the formation of ∼300 nm multilayered that self-assembled through interdigitation and intercalation of side chains that ultimately twisted into helix structure to minimize surface energy [115].

2.3.2 Post-synthetic Self-assembly Process

Nanowires of P3ATs were first reported to self-assemble from dilute solutions in poor solvents like cyclohexanone, *n*-decane at high temperatures around 50∼90 °C and allowed to cool slowly to room temperature that induced assembling of polymer chains into nanowires. It was also found that the nanowire diameter was ∼15 nm independent of the alkyl-side chain length, whereas the thickness (t) varied with the side-chain length as revealed by transmission electron microscopy (TEM) [116]. Amphiphilic rod coil block copolymers containing rod-like π-conjugated polymer block co-jointed with flexible coil block (e.g. polystyrene) in solution self-assembled into various ordered aggregates were also fabricated that exhibited as excellent fluorescent microtubes [117]. P3AT nanorods were prepared by solvent-induced aggregation by adding hexane (good solvent for alkyl side chains but poor solvent for polymer backbones) to P3AT/chloroform where the nanorods adopted helical conformation and the morphology could be controlled by varying the solvent composition or P3AT concentration [118]. Moreover, adjusting good/poor solvent ratio, nanowires and nanorings of various copolymers such as P3BT-*b*-P3HT were also reported [119]. Even molecular weight of the conjugated polymers controls the mechanism of self-assembly leading to nanostructure formation. As observed for P3HT in *p*-xylene with less than critical molecular weight (~10 kDa), increased polymer concentration (0.2–0.5 mg/ml) changes the 1D nanowhiskers into 2D nanoribbons, while higher than critical molecular weight chains only forms nanowire aggregates [120].

2.3.3 Wet Spinning Process

Among the different fiber spinning methods, wet or solution spinning process is the most primitive one. Initially, wet spinning was employed for producing synthetic fibers around late nineteenth century [121]. In wet spinning, the polymer is first dissolved in a suitable solvent and then directly squeezed into a liquid taken coagulation bath, leading to solidification/precipitation of the polymer fiber, as depicted in Figure 2.10a [121]. The liquid is such that it would be miscible with the spinning solvent but will not dissolve the polymer. PANI was the first conducting polymer that was wet-spun into a fiber by wet spinning [122]. Other conducting polymers including PPy and PEDOT: PSS were wet-spun subsequently for various applications [123–125]. Subsequently modified methods of wet spinning have come up to produce smarter materials for various applications. To

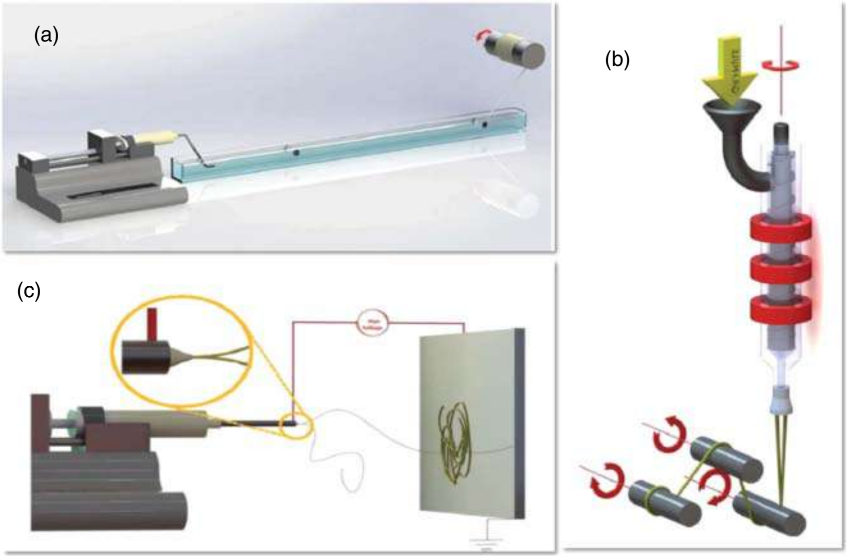

Figure 2.10 Schematic representation of (a) wet spinning, (b) melt spinning, and (c) electrospinning techniques. Source: Reproduced with permission from Ref. [121] Copyright 2016, The Royal Society of Chemistry.

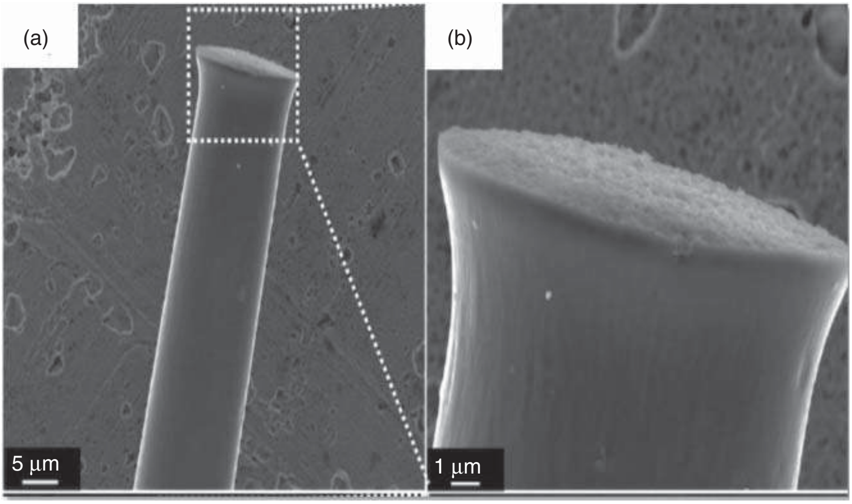

Figure 2.11 (a, b) SEM images of as-spun PEDOT/PSS fibers by hot-drawing-assisted wet-spinning method at different magnifications. Source: Reproduced with permission from Ref. [126] Copyright 2016, The Royal Society of Chemistry.

illustrate, poly(3,4-ethylenedioxythiophene)/poly(styrenesulfonate) (PEDOT/PSS) microfibers prepared by hot-drawing assisted wet-spinning process, morphology of which has been shown in Figure 2.11, when further treated with ethylene glycol as dopant showed improved mechanical and electrical performances to be potentially applied as fast responding wearable heaters and electromechanical actuators [126].

2.3.4 Melt Spinning

Majority of the commercially available synthetic polymer fibers are produced by melt-spinning technique. It is a very simple process in which dry polymer granules/chips are melted within the extruder (squeezer), which later on is used as the spinning dope as demonstrated in Figure 2.10b. The so-obtained polymer filament is then quenched and solidified in a fast fiber solidifying cooler. Thus, it avoids the need of solvents required for dissolution of polymers [121]. It is therefore a preferred method for those polymers that forms stable melt. However, few reports of the melt spinning of conducting polymers exist due to some major limitations of thermal instability. Besides, the technique has limited potential to produce extremely thin fibers. Kim et al. were the first to produce melt-spun PANI/PPy blend, used for textile sensors. However, the composite displayed poor electrical conductivity primarily due to inhomogeneity in composition (2.9×10^{-7} S/cm with 40 wt% PPy) [127].

2.3.5 Dry Spinning

Dry spinning is another class of spinning technology for obtaining fiber morphology of different polymers [121]. Compared to wet spinning, solidification is achieved more easily through evaporation of the solvent, which must be highly volatile, and without requiring a coagulation bath. Dry spinning is suitable for polymers which are susceptible to thermal degradation or those that cannot form viscous melt. It is also well suited for those purposes where specific surface characteristics of fibers are required. Polymers such as polyurethane, polyacrylonitrile, and fibers based on ophthalamide, polybenzimidazoles, polyamidoimides, and polyimides due to better physicomechanical fiber properties can be effectively drawn using this technique. However, as most conducting polymers have low solubility in common organic solvents, this process is in general, less suited for the fabrication of conjugated polymer nanofibers [121].

2.3.6 Electrospinning

Electrospinning has been among the easiest and widely explored efficient techniques employed to design continuous and aligned conducting polymer nanofibers as well as their composites under the influence of electric field [128]. The basic electrospinning set up (as depicted in Figure 2.10c) comprises of three major components: high-voltage power supply, spinneret, and a conductive collector [121]. A jet is generated when the repulsion forces of charged solution supersedes the solution surface tension under high electrostatic field. As the jet flows, the solvent evaporates or the melt solidifies with certain diameters ranging from nanometer to micrometer that get accumulated on the collector surface. Controlling the applied electric potential, solution viscosity, concentration/conductivity of solution, humidity of the environment, as well as separation between the nozzle and the collector, the morphology of the electrospun wires can be tuned more effectively compared with other spinning techniques discussed earlier [129]. Several conducting polymers nanofiber synthesis has been attempted with success by using electrospinning technique. For instance, highly uni-axially aligned nanofibers of poly[2-methoxy-5-((2-ethylhexyl)oxy)-*p*-phenylenevinylene] (MEH-PPV) or P3HT were obtained using electrospinning technique, exhibited strong polarized photoluminescence emission, opening new doors for new generation organic lasers, polarized light-sources and nanoscale sensors. High alignment of the nanofibers was obtained on U-shaped metallic device functioning similar to a traverse guide in a common wind-up system (Figure 2.12a), whereas the randomly oriented fibers resulted on collection on silicon wafers, showing important role of collectors in electrospinning synthesis process (Figure 2.12b) [130]. Even high conducting blends of electrospun PANI and poly(ethylene oxide) (PEO) and its analogues in chloroform, as well as coaxial PANI and poly(vinyl alcohol) (PVA) nanofibers in water, have been reported [131, 132]. PANI is found to exhibit poor processability by electrospinning owing to its poor solubility in common organic solvents. However, adding suitable more viscous, insulating polymer (such as PEO) increases the efficiency of nanofiber formation but at the expense of conductivity. The key factor to obtain fibers of good quality is to optimize the PEO content. Reducing PEO concentration leads to bead formation on the fibers surfaces attributed to capillary instability of the jet caused by surface tension factors. It is further observed that dimension of fibers can be varied by changing the mode of

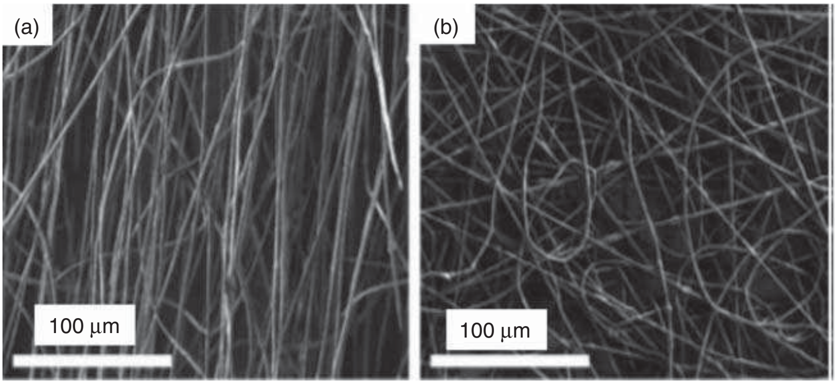

Figure 2.12 SEM micrographs of electrospun MEH-PPV/PEO nanofibers in 1 : 20 mass ratio: (a) aligned nanofibers collected on U-shaped metal device and (b) random nanofibers collected on silicon wafer collector of MEH-PPV/PEO. Source: Reproduced with permission from Ref. [130] Copyright 2011, The Royal Society of Chemistry.

its collection. The morphology of the electrospun nanofibers also depends on the usage mode of collection. A static collector promoted larger diameter than the rotating collector. The rotations promote stretching effect on the fibers that leads to a narrow distribution of the diameters [133]. Subsequently, Chronakis et al. and Choi group reported a method of fabricating electrospun PPY and PEDOT: PSS/polyvinylpyrrolidone (PVP) nanofibers respectively [134, 135]. Feng et al. [136] prepared electrospun PPy/PEO nanofibers with diameters in the range of about 70–300 nm with improved electrical conductivity. Liu et al. [137] also reported the fabrication of aligned PEDOT fibers and tubes based on electrospinning and oxidative chemical polymerization. Uniform diameter-based nanofibrous blends of a conducting polymer of poly[2,5-(2′-ethylhexyloxy)]-1,4-phenylenevinylene (electron donor) with methanofullerene (electron acceptor) were developed using electrospinning technique that facilitated ultrafast charge transfer, highly promising for the fabrication of nanostructured heterojunction photovoltaic cells.

The electrospinning process thus has emerged to be the solitary method that can lead to continuous long nanofibers of high aspect ratios and good surface quality to produce coaxial nanocables of conducting polymers and their composites for useful applications to nanoelectronics [138]. However, the method is not fruitful to obtain pure nanofibers or nanotubes of all types of conducting polymers without the assistance of flexible insulating polymer chains. Such problems primarily originate from low molecular weight polymer chains, high chain rigidity, and poor solubility of most conjugated polymers that limits their practical utility [49, 138].

2.3.7 Seeding Approach

Zhang et al. first proposed the single-step “seeding approach” strategy for the rapid bulk synthesis of various CP nanowires/fibers. In this method, the nature and morphology of the employed nanofibrillar seeds are very crucial for nanofiber

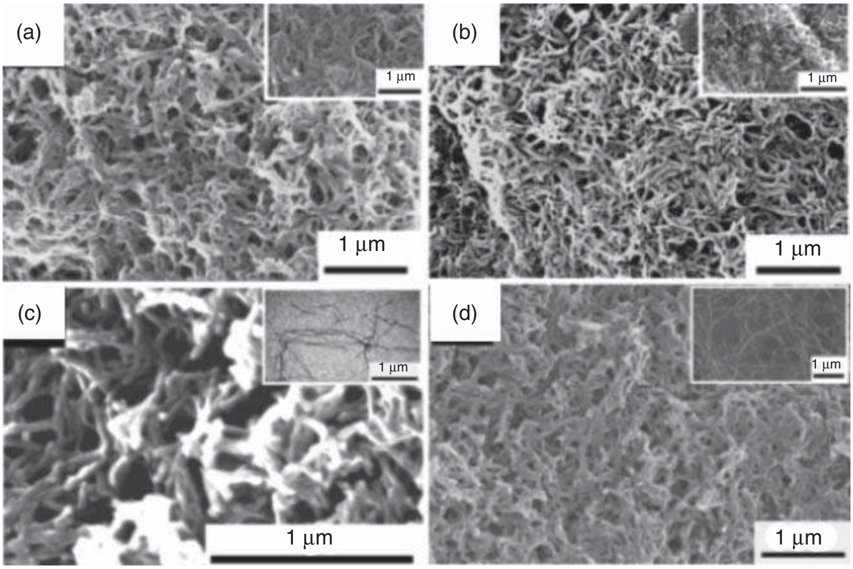

Figure 2.13 SEM images of HCl-doped PANI emeraldine nanofibers obtained using seeding approach (a) 1.5 mg of emeraldine-HCl salt, (b) 1.6 mg of HiPco single walled nanotube (SWNT), (c) 1.0 mg of hexapeptide $AcPHF_6$, and (d) 4 mg of V_2O_5 nanofibers, respectively. The inset images in each case show the SEM images of respective pristine materials used as seeding agents in the synthesis of HCl-doped PANI emeraldine nanofibers. Source: Reproduce on permission from Ref: [139] copyright 2004, The American Chemical Society.

synthesis, which may be of various types such as organic, inorganic, and biological systems, namely, (i) PANI nanofibers, (ii) bundles of single-walled carbon nanotubes (SWCNT), (iii) nanofibrous peptides, and (iv) V_2O_5 nanofibers. The resulting nanofibers have been depicted in Figure 2.13 [139, 140]. The method offers precise control on the morphology in bulk and hence on the properties, such as nanofibers of PANI with diameter 20–60 nm show electrical conductivity of 2–10 S/cm; PPy nanofibers with diameter of 60–90 nm possess ~50 S/cm electrical conductivity, and PEDOT nanofibers with diameter 100–180 nm display ~16 S/cm bulk electrical conductivity respectively [38, 140]. These nanostructures have been designed using one-step reaction without the aid of organic dopants, surfactants, and/or bulk quantities of insoluble templates. A typical monomer solution, when subjected to a chemical oxidative polymerization of the monomers, is seeded with very minute quantity of nanofiber seeds (usually <1%), dramatically morphological change from conjugated polymer nanoparticles to almost exclusively nanofibers results. For instance, as the reaction was seeded with PANI particulates, nanofibers resulted while on seeding with PPy nanospheres, however, nanospheres (~170 nm diameter) of emeraldine, HCl precipitate was mostly formed [140]. The general shape of the seed seems to control the overall morphology of the precipitate (fibers vs. particles), although no significant impact on the length, diameter, etc. was established. Bulk synthesis of PPy nanofibers of average diameter ~80–100 nm using V_2O_5 nanofiber seeding agent and ferrous chloride ($FeCl_2$) and H_2O_2 as oxidants was also reported adopting a green approach lately [141]. Thus, the seeding approach promotes single-step bulk synthesis of 1D-conducting polymer nanofibers/tubes/wires rapidly and more effectively than template-based techniques.

Thus, the aforementioned discussion highlights that template-free approach has great potential for preparing diversified micro- or nanostructures as per application requirement. The template-free route is becoming more popular and attractive owing to its simplicity, cost-effectiveness, and flexibility for thin-film device fabrication. The procedure successfully addresses many problems faced during solid template approach due to the limitations imposed by the pore structure of the template used. Nonetheless, the concerned formation mechanisms are quite complicated and not clearly understood till date. Moreover, the template-free method limits precise control over the morphology and properties, which still need to be addressed.

2.3.8 Whisker Method of Polymer Synthesis

The whisker method was first demonstrated by Ihn et al. [116, 142] with poly(3-alkylthiophene)s to readily crystallize in the form of "ribbon-shaped whiskers" from dilute polymer solutions taken in relatively poor solvents. Such whiskers formation depended on the solvent nature, temperature, and alkyl side-chain length of the monomer. The polymer chains obtained by this technique were found to arrange and align with their backbones at right angles to the whisker direction. Typically, it was observed that for alkyl side-chain lengths of 3–12 carbon atoms of thiophene-derivative, the resultant whiskers' widths were found to be around 15 nm and tens of microns long with large aspect ratios. Figure 2.14a displays the topography of the P3HT monolayer nanowhiskers obtained on dipping Si wafer in the chloroform solution of P3HT. The inset shows the magnified view of the P3HT nanowhiskers. Thickness of the so-formed whiskers generally found to be approximately two to three times the $a/2$ lattice dimension of unit cell of the polymer. Further, the macromolecules within the whiskers are so aligned that the

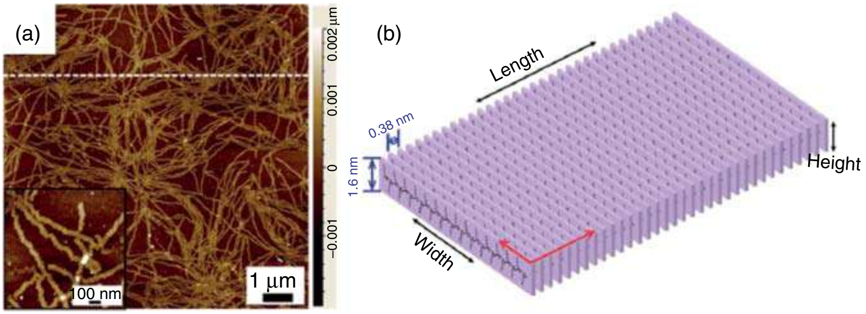

Figure 2.14 (a) AFM image of monolayer of poly(3-hexylthiophene) nanowhiskers on Si-wafer substrate (inset showing magnified view of the same) and (b) schematic representation of the polymer arrangement within the whiskers. Source: Reproduced with permission from Ref. [142] Copyright 2013, The Royal Society of Chemistry.

polymer backbones remain perpendicular to the whisker length, as schematically represented in Figure 2.14b [142].

2.3.9 Mixed-Solvent Technique

The mixed solvents technique was commonly employed to obtain conjugated polymer nanowires for photovoltaic applications [118, 143–147]. This method drives the formation of polymer nanowires by using the combination of good and bad solvents. Polymers are usually dissolved in a good solvent and then bad solvent is gradually added to it in small proportions. Mixed solvent triggers unfavorable interactions between the polymer chains as the bad solvent introduces aggregation and self-assembly of the polymer chains. Hence, the quantity of bad solvent in the mixture determines the extent of crystallization in the resultant polymers. Very recently this technique has been very useful for the synthesis of conducting polymer hydrogels (CPHs) [148].

2.3.10 Reprecipitation Technique

Kasai group [149] first developed the technique for the synthesis of organic nanomaterials where the particle formation was regulated by nucleation and growth, or through spinodal phase separation that involves rapid mixing of a mixture of liquids or solid phases. The dimensions of polymer nanoparticles are controlled by the water temperature and the polymer solution concentration. Kurokawa et al. [150] employed this process to synthesize poly(thiophene) nanoparticles. In the experiment, the polymer dissolved in tetrahydrofuran (THF) solvent was injected into vigorously stirred de-ionized water by using a microsyringe to obtain the desired nanoparticles. Szymanski et al. [151, 152] used analogous reprecipitation technique to prepare highly fluorescent conjugated polymer nanoparticles like MEH-PPV for biosensor applications. Figure 2.15 illustrates the transmission electron micrograph of the as-prepared assembled MEH-PPV polymer nanoparticles that were subjected to near-field scanning optical microscopy (NSOM), (an ultraresolution microscopy technique that combines the nanoscale resolution of scanning probe microscopy with the chemical specificity of optical spectroscopy) to measure their size distribution as well as observe fluorescence/absorbance of these individual nanoparticles.

Yabu et al. [153] employed modified reprecipitation method to develop regular-sized polymer nanoparticles. Here, small amount of poor solvent such as water was slowly dropped into a polymer solution such as polystyrene dissolved in tetrahydrofuran (THF) solvent. As the good solvent (THF) was evaporated, fine nanoparticles of the polymer were separated out.

2.4 Conducting Polymer Hydrogels

Hydrogels, by definition, are generally three-dimensional (3D) microstructured polymeric networks with high level of hydration and their electrical conductivity

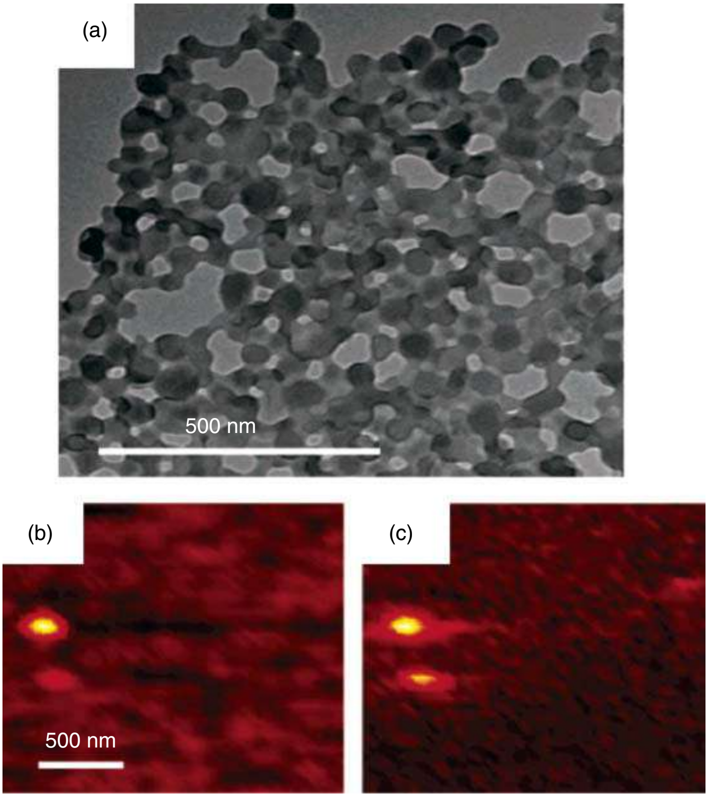

Figure 2.15 (a) TEM image of a dense island of polymer MEH-PPV nanoparticles. (b, c) Correlation scanning force and fluorescence near-field scanning optical microscopy (NSOM) image of a sparse nanoparticle film. Source: Reproduced with permission from Ref. [151] Copyright 2005, American Chemical Society.

can be enhanced by incorporating various conducting materials within them [148, 153–157]. Furthermore, these materials possess softness, plasticity and mechanical integrity, porosity, and high surface area. Numerous reviews describing synthesis, properties, and potential applications are available in the literature [158]. CPHs have emerged as a novel class of unique materials that synergize the merits of electrically conducting polymers and mechanically strong, insulating polymer hydrogels. Their hierarchical porous crosslinked 3D structure imparts high mechanical stability, unique chemical and physical behavior, along with outstanding electrochemical properties that open up potentiality in electrochemical applications, including robust-long live energy storage devices, lithium-ion battery (LIB) electrodes, electrochemical capacitors (ECs), biofuel cells, printable electronic devices, and biosensors. Various CPHs have been prepared till date, some of which has been depicted in Figure 2.16. These materials show unique novel properties, such as shape memory elasticity, fast functionalization with various guest objects, and fast removal of organic pollutants from aqueous solutions and widely employed in biomedical as well as in energy storage applications [158, 159].

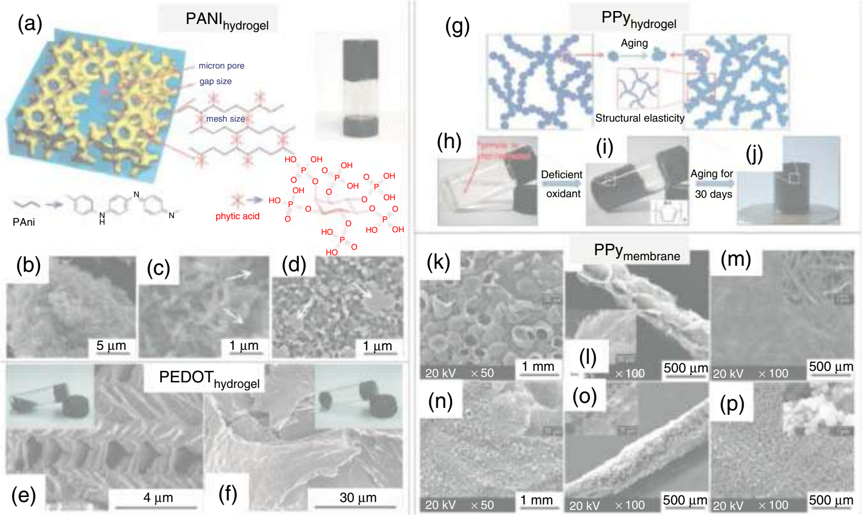

Figure 2.16 (a) Schematic representation of chemical structure and molecular architecture description of phytic acid-gelated and doped PANI hydrogel. (Inset) A photograph of PANI hydrogel within glass vial [159]. (b–d) Scanning electron microscopic (SEM) and transmission electron microscopic (TEM) images of PANI hydrogel [160]. The white arrows in (c) and (d) indicate the micron-sized pores present in the PANI hydrogel samples. (e, f) SEM pictures of PEDOT hydrogel morphology synthesized using different oxidants [161]. The inset photos in (e, f) indicate the nature of the products-S obtained from corresponding oxidants. (g) Schematic demonstration of PPy hydrogel synthesis via chemical oxidation. (h, i) Photographs of PPy hydrogel synthesis inside glass vials and as-formed PPy hydrogel (j) [148]. (k–p) SEM images of PPy membrane obtained via template-mediated polymerization [162]. The insets in each case show the cross-sectional view at high magnifications of the samples. Source: Reprinted with permission from Refs [148, 158, 160–162]. Copyright 2012 PNAS, USA Group; 2011 Royal Society of Chemistry and 2017, American Chemical Society.

One of the popular methods involves preparation of hydrogel containing a supporting polymer that forms a matrix for the synthesis of the conducting polymer. The synthesis starts with the formation of a hydrogel matrix, in which the monomer solution is then distracted. The resultant matrix is then suspended in an oxidant solution, which on diffusion (interfacial polymerization) yields the CPH. PANI hydrogels have been obtained employing phytic acid as gelator–cum-dopant to form a gel network [160–162]. A large variety of derivatives of PANI, PPy, and PEDOT have been obtained by this process and employed in various technological fields [163, 164]. Besides, amphiphilic functionalized-thiophene hydrogel with unusual two-dimensional building blocks has been prepared using single-step process via combination of oxidative coupling polymerization and non-covalent crosslinking strategy in the recent past [165]. Again, PPy nanotube hydrogel with controlled morphology has been synthesized lately, by oxidative polymerization in the presence of dye molecules as templates; exhibited exceptionally high electrochemical activity [166]. Another similarly interesting conducting polymer based material is aerogel. Aerogels are a novel class of highly porous nanomaterials that have unique physicochemical properties such as ultra-low density, large specific area, disordered open pores, elaborate 3D networks, etc. [167, 168]. An aerogel is obtained when the liquid phase of a gel is replaced by a gas in such a way that its solid network is retained, with only a slight or no shrinkage in the gel. Zhang et al. [169] reported a sequence of conjugated polymer aerogels based on PEDOT/PSS. But the non-conducting PSS significantly decreases the conductivity of these aerogels. However, recently developed aerogels based on emulsion template by the aid of supercritical drying or freeze drying have considerably enhanced the adsorption capacity and enhanced electrochemical capacitance of the resultant composite aerogel [170].

CPHs are first growing techniques owing to tunability in filler configuration, size, specific surface area, density, hydrophilic group numbers, etc., which are in designing and fabricating of these systems [171]. These hydrogels with enhanced effective surface area, reduced interfacial tension, and increased wettability along with unique morphology and functionalities are finding wide range of applications in the field of nanoelectronics and energy storage utilities [172, 173]. In spite of the tunability of some physicochemical properties in hybrid porous hydrogels, the main limitations of these materials are their non-homogeneity and random composition due to poor compatibility of the constituents. In the recent years, biological molecules incorporation into CPHs increases their mechanical flexibility and electrical conductivity besides biocompatibility and electrochemical capacity. Well-designed 3D-CPHs are, thus, fast developing potential candidates for next-generation drug delivery systems, tissue engineering, biosensing and energy storage /harvesting devices [158].

2.5 Nanolithography

Nanolithography technique deals with the research and application of fabrication of nanometer-scale structures, such as nanopatterning. Thus, the technique facilitates simultaneous synthesis as well as positioning/orienting of the conducting polymer nanowires. Various nanolithographic fabrication techniques are available in the literature in details that focus on various nano-patterning techniques/procedures suitable for device fabrication and their engineering applications [174].

2.5.1 Dip-Pen Nanolithography (DPN)

Dip-pen nanolithography (DPN) is one of the well-known nanolithography techniques in which an AFM tip like a “pen” is engaged to create patterns directly on a range of substrates with variety of inks as demonstrated schematically in Figure 2.17 [10].

Here, ink-coated AFM tip is brought into contact with a suitable substrate as a result of which the molecules diffuse out from the AFM tip to the surface through

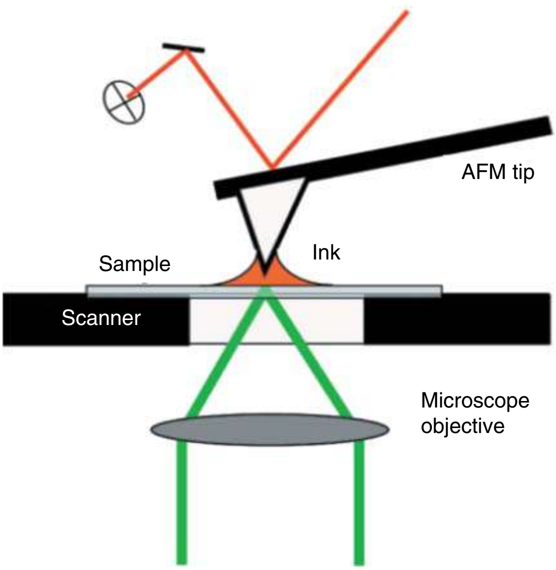

Figure 2.17 Operating principle of Dip-pen nanolithography (DPN). Source: Noyet al. [10], © 2002, American Chemical Society.

or over a water meniscus and assemble along the tip pathway to form a stable nanostructure [10]. Day-by-day the progressing DPN technology is becoming extraordinarily useful tool to study the fundamental consequences of miniaturization [175]. Lim and Mirkin [176, 177] synthesized conducting polymer nanowires through DPN technique using self-doped sulfonated-PANI and doped polypyrrole as “ink” on a positively charged surface using 2% (trimethoxysilyl)propyldiethylenetriamine (DETA). As these doped conducting polymers are negatively charged, an electrostatic interaction made it feasible to sketch conducting polymer nanowires using DPN. Moreover, the width of the polymer pattern is controllable owing to its linear dependence on the root of contact time. Maynor et al. [178] reported PEDOT line patterning on anodic silicon surface coupled with oxidation. As time progressed, it was realized that the structures produced by DPN cannot be passed down directly as electronic devices components as they have been made on insulting substrates. Moreover, the DPN generated pristine conducting polymers cannot be easily doped to enhance their conductivity. As a result, Dravid and his group attempted acid promoted polymerization technique for DPN patterning of conducting polymers. The reactive liquid precursors after patterning polymerize to generate solid products by controlling the ink composition to optimal to execute typical DPN. They reported that conducting polymers formed by pyrrole and THF satisfy the patterning criteria and can be patterned successfully. Figure 2.18 shows the SEM image of the as-formed PPy patterns clearly indicate that the polymer chains are well-aligned [179]. The as-prepared conducting polymers also undergo simultaneous doped by the acid added as catalyst to the liquid mixture. Thus, upon solidification, the doped conducting polymers are found to exhibit high conductivity as well as crystallinity.

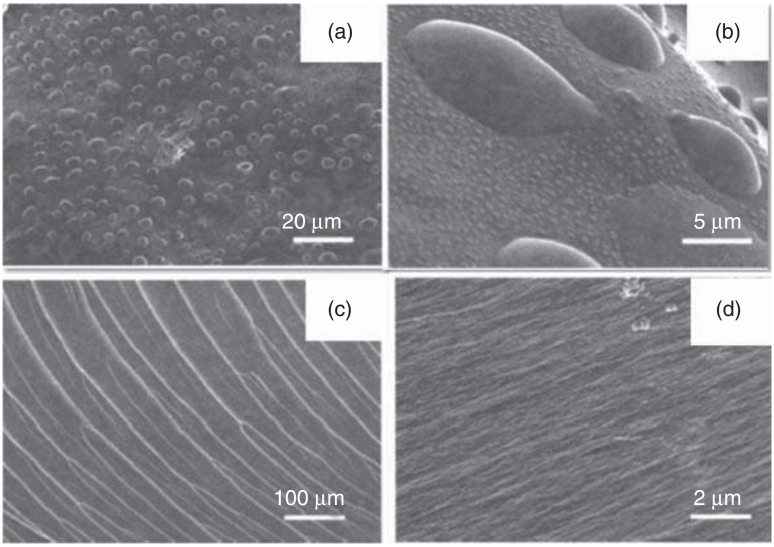

Figure 2.18 SEM images taken from the surface and cross section of the conducting polymer at different magnifications (a) the hierarchal polymer dots in low magnification, (b) indicate large numbers of nano- dots around micro-dots structures indicated in (a), (c) cross-sectional view of the sample indicating linear morphology with bifurcated structures and (d) is the magnified image of a portion of image (c). Source: Reproduced on permission from Ref. [179], Copyright 2004, The American Institute of Physics.

2.5.2 Nanoimprint Lithography

Nanoimprint lithography (NIL) technique employs a nanostructured mold that can be transferred into a polymer by imprinting the mold onto the polymer [180]. The nanostructures fabrication on the mold is chiefly carried out by e-beam lithography. This process takes time and is indeed very expensive. However, once these molds get designed and prepared, they can be used repeatedly. The advantage of NIL technique is that it can be used for very small areas as well as for vast area based roll-to-roll processing and large imprintings. NIL has been mostly employed to produce desired nanomorphologies for organic solar cell applications [181]. Ramanathan and Yun groups [182, 183] independently reported techniques for fabricating array of “individually addressable” conducting polymer nanowires using electron-beam lithography. Kim et al. [184] designed nanopatterns of polythiophene derivatives on flexible plastic substrate using NIL from which photovoltaic devices were fabricated subsequently after spin-coating phenyl-C61-butyric acid methyl ester (PCBM) and evaporating Al. The measured short-circuit current of the resultant nanoimprinted devices got increased with the interfacial area of the structures. The power conversion efficiency was also considerably enhanced with the interfacial area, successfully obtained after adopting this technique. Again, high density as well as periodic patterns of P3HT nanopillars was reported by Aryal group using this sophisticated procedure [185]. Further, well-arranged and high density nanopillars of poly(methyl methacrylate) (PMMA) and P3HT were fabricated by this technique using nanoporous silicon mold. At first, large-scale preparation of nanoporous silicon mold using anodic alumina template was carried out using plasma etching technique. The mold was designed to have dimensions of 50–80 nm width and 100–900 nm deep. The pore depth and profile were regulated by the plasma etching conditions such as Cl_2:Ar ratio, time, pressure, bias power, etc. The obtained NIL-imprinted P3HT nanopillars were subsequently employed for fabricating organic solar cell devices [185]. Conducting-polymer fabrication methods based on NIL are quite attractive because it is possible to synthesize conducting polymers in a desired position and successfully avoid the tedious and problematic post-synthesis positioning task.

NIL has gained considerable interest due to its cost effectiveness and high throughput achieved based on the mechanical deformation of the resist polymer by heating above the glass transition temperature (T_g) or by UV crosslinking. However, NIL can only be applied to the polymers that have T_g or possess UV-crosslinkable functionalities. Furthermore, in NIL, a high resolution stamp is required for creating a high resolution pattern, which leads to costly and time-consuming fabrication process. Subsequently, a novel approach to control the lateral dimensions CPNs was employed by using an isotropic plasma etching (IPE) based on NIL. This modification improved the resolution of the printed pattern independent of the thickness of the conducting polymer layer, and the etching of the conducting polymer could successfully be avoided [186]. In the recent past, keeping in view of improving pattern resolution, versatility, and reproducibility of the technique, a cost-effective, straightforward innovation for direct patterning of conductive polymers such as polypyrrole film was used that enabled well-oriented structures with desired dimensions on solid substrates that can be easily assembled into functional devices by employing electrohydrodynamic lithography (EHL). Figure 2.19a represents schematically the mode of operation of EHL patterning [187]. Thin liquefied polymer with viscosity η confined-film develops characteristic undulations at height along axis-$z = h_o$ on applying a constant voltage, U in-between the electrodes or across the capacitor gap (d). The contact potentials on each interface generate electric field, E_f that drives the flow. The dielectric constant (ε_o) of the film and the gap ε_g mediate the electrical forces from the applied voltage, which is again balanced by surface tension, γ leading to characteristic spacing (λ), arising out of instability with viscosity, leading to undulations to rise in pillar-like heights as depicted in Figure 2.19b. The spacing λ given by the following equation,

$$\lambda = \frac{2\sqrt{2}\pi/[\gamma(d-h_o)^3/\varepsilon_o]}{U} \tag{2.2}$$

Thus, the varied force field channelizes "the instability" toward the protruding line structures to form columnar-bridges between the two electrodes, followed by a thickening of the well-oriented nanopillars resulting in a positive replica of the master pattern of the upper electrode as shown in Figure 2.19c [187]. The different CP based line and columnar patterns obtained by EHL technique have been studied using optical microscopy and AFM and their images are shown in Figure 2.19d–f and the corresponding dimensions of those patterns have been

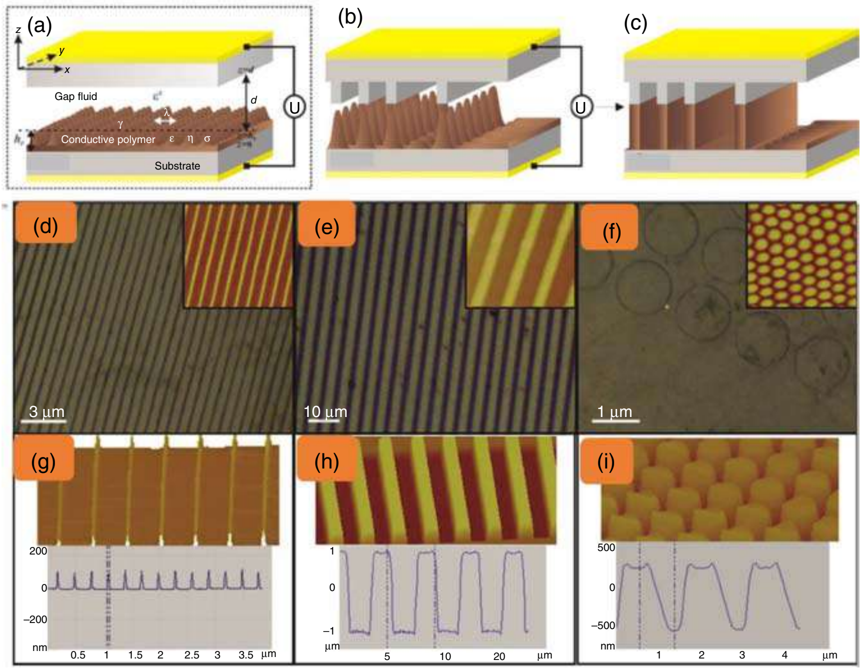

Figure 2.19 (a–c) Schematic representation of electrically driven patterning setup and mode of operation. (d–i) Replication of line and columnar patterns obtained using EHL. AFM images inset, three-dimensional AFM micrographs with cross section analysis and optical microscopic images with height showing fabricated PPy structures: (d) and (g) nanolines of 120 nm wide and 100 nm height; followed by (e) and (h) structures with a pitch of 0.5 μm, 2.5 μm wide and 2.0 μm height microlines and ultimately submicrometer pillars with diameter 1.2 μm and height 700 nm as shown in (f) and (i) respectively. Source: Reproduced on permission from ref [187], copyright 2016, American Chemical Society.

presented with cross section analysis, as indicated in Figure 2.19g–i respectively. Such innovative techniques pave the way for accessing scale sizes below submicron range and opens up new possibilities of fine tailoring the dimensions of the devices for nano-optoelectronic applications [187].

2.6 Conclusion and Future Prospects

Conjugated polymer nanostructures have seen extraordinary advances in last few decades, leading to the synthesis of a wide variety of morphology that present different properties, depending on their structure, shape, size, etc., which have allowed broadening their application possibilities in different fields of electronics, biomedical, energy, chemical, and environmental technologies. Several issues related to the formation mechanisms and the advantages as well as limitations have been explored. The latest advancements in the two modes of synthesis – with template and template-free strategies of CPNs – have been systematically discussed.

Novel methods have come up with the ability to assemble π-conjugated molecular building units including small molecules, oligomers, and even polymers into well-oriented crystalline 1D to 3D nanostructures, thus opening new opportunities for discovering smart materials with tunable electronic, optoelectronic, photonic, and outstanding mechanical properties. Special attention on the synthesis of hollow PANI nanostructures such as nanocapsules, nanospheres, nanotubes, etc. due to their hollow/void structure, high surface area, high conductivity, as well as tunable chemical and physical properties and appreciable environmental stability has been paid as they have been found to be highly promising candidates for development of nano-electronic devices, sensors, supercapacitors, energy storage devices, and other applications. Besides, different nanolithographic fabrication techniques have also been highlighted that focus on diversified nano-patterning procedures highly suitable for miniature device fabrication and engineering applications.

Although various synthesizing methods have been established, aimed at creating different types of conjugated polymer nanostructures with controllable morphologies and sizes, there are several challenges that must be addressed. The precision in controlling the composition, morphology and dimensions, crystal structure, etc. and hence the property of these organic semiconductor nanostructures is still unsatisfactory and a better control on synthetic procedure is highly desirable to assist systematic studies to uncurtain the restrictions on elementary properties such as charge carrying, exciton and photon transport behavior, and mechanical potency. Even though many studies on optoelectronic and electrochemical behavior have been performed, in comparison, very little knowledge on tuning the mechanical properties of these conducting polymer nanomaterials is known, which again is indispensable for most practical applications. Furthermore, few fundamental questions, especially related to the unexpected and drastic way the nanoscale conducting polymers differ from those in the bulk phases, are still to be well-addressed. Even issues related to scalable synthesis of these materials needs to be solved. Hence, simple, green, cost-effective synthetic methodologies concentrating on large-scale manufacturing of these nanomaterials with appropriate morphology still remain to be a perpetual concern to the scientific community for the purpose of designing genuine organic based nanoelectronic devices.

References

1 Swager, T.M. (2017). 50th anniversary perspective: conducting/semiconducting conjugated polymers. A personal perspective on the past and the future. *Macromolecules* 50: 4867–4886.

2 Moliton, A. and Hiorns, R.C. (2004). Review of electronic and optical properties of semiconducting π-conjugated polymers: applications in optoelectronics. *Polym. Int.* 53: 1397–1412.

3 Ghosh, S., Thandavarayan, M., and Basu, R.N. (2016). Nanostructured conducting polymers for energy applications: towards a sustainable platform. *Nanoscale* 8: 6921–6947.

4 Morin, P.-O., Bura, T., and Lecler, M. (2016). Realizing the full potential of conjugated polymers: innovation in polymer synthesis. *Mater. Horiz.* 3: 11–20.

5 Evans, D. (2018). A bird's eye view of the synthesis and practical application of conducting polymers. *Polym. Int.* 67: 351–355.

6 Shi, Y., Peng, L., Ding, Y. et al. (2015). Nanostructured conductive polymers for advanced energy storage. *Chem. Soc. Rev.* 44: 6684–6696.

7 Pecher, J. and Mecking, S. (2010). Nanoparticles of conjugated polymers. *Chem. Rev.* 110: 6260–6279.

8 Ghosh, S., Ramos, L., and Remita, H. (2018). Swollen hexagonal liquid crystals as smart nanoreactors: implementation in materials chemistry for energy applications. *Nanoscale* 10: 5793–5819.

9 Tuncel, D. (2019). π-Conjugated nanostructured materials: preparation, properties and photonic applications. *Nanoscale Adv.* 1: 19–33.

10 Noy, A., Miller, A.E., Klare, J.E. et al. (2002). Fabrication of luminescent nanostructures and polymer nanowires using dip-pen nanolithography. *Nano Lett.* 2: 109–112.

11 Lim, J.H. and Mirkin, C.A. (2002). Electrostatically driven dip-pen nanolithography of conducting polymers. *Adv. Mater.* 14: 1474–1477.

12 Ma, Y., Zhang, J., Zhang, G., and He, H. (2004). Polyaniline nanowires on Si surfaces fabricated with DNA templates. *J. Am. Chem. Soc.* 126: 7097–7101.

13 Bilger, D., Homayounfar, S.Z., and Andrew, T.L. (2019). A critical review of reactive vapor deposition for conjugated polymer synthesis. *J. Mater. Chem. C* 7: 7159–7174.

14 Jiang, L., Wang, X., and Chi, L. (2011). Nanoscaled surface patterning of conducting polymers. *Small* 7: 1309–1329.

15 Pan, L., Qiu, H., Dou, C. et al. (2010). Conducting polymer nanostructures: template synthesis and applications in energy storage. *Int. J. Mol. Sci.* 11: 2636–2657.

16 Martin, C.R. (1995). Template synthesis of electronically conductive polymer nanostructures. *Acc. Chem. Res.* 28: 61–68.

17 Martin, C.R. (1994). Nanomaterials: a membrane-based synthetic approach. *Science* 266: 1961–1966.

18 Lee, W. and Park, S.J. (2014). Porous anodic aluminum oxide: anodization and templated synthesis of functional nanostructures. *Chem. Rev.* 114: 7487–7556.

19 Vito, S.D. and Martin, C.R. (1998). Toward colloidal dispersions of template-synthesized polypyrrole nanotubules. *Chem. Mater.* 10: 1738–1741.

20 Rahman, A. and Sanyal, M.K. (2007). Novel switching transition of resistance observed in conducting polymer nanowires. *Adv. Mater.* 19: 3956–3960.

21 Long, Y.-Z., Li, M.-M., Gu, C. et al. (2011). Recent advances in synthesis, physical properties and applications of conducting polymer nanotubes and nanofibers. *Prog. Polym. Sc.* 36: 1415–1442.

22 O'Brien, G.A., Quinn, A.J., Iacopino, D. et al. (2006). Polythiophene mesowires: synthesis by template wetting and local electrical characterisation of single wires. *J. Mater. Chem.* 16: 3237–3241.

23 Fu, M., Zhu, Y., Tan, R., and Shi, G. (2001). Aligned polythiophene micro- and nanotubules. *Adv. Mater.* 13: 1874–1877.

24 Park, D.H., Kim, H.S., Jeong, M.-Y. et al. (2008). Significantly enhanced photoluminescence of doped polymer metal hybrid nanotubes. *Adv. Funct. Mater.* 18: 2526–2534.

25 Han, M.G. and Foulger, S.H. (2005). 1-dimensional structures of poly(3,4-ethylenedioxythiophene) (PEDOT): a chemical route to tubes, rods, thimbles, and belts. *Chem. Commun.* 24: 3092–3094.

26 Cao, Y. and Mallouk, T.E. (2008). Morphology of template-grown polyaniline nanowires and its effect on the electrochemical capacitance of nanowire arrays. *Chem. Mater.* 20: 5260–5265.

27 Liu, R. and Lee, S.B. (2008). MnO_2/poly(3,4-ethylenedioxythiophene) coaxial nanowires by one-step co-electrodeposition for electrochemical energy storage. *J. Am. Chem. Soc.* 130: 2942–2943.

28 Cho, S.I. and Lee, S.B. (2008). Fast electrochemistry of conductive polymer nanotubes: synthesis, mechanism, and application. *Acc. Chem. Res.* 41: 699–707.

29 Orgzall, I., Lorenz, B., Ting, S.T. et al. (1996). Thermopower and high-pressure electrical conductivity measurements of template synthesized polypyrrole. *Phys. Rev. B* 54: 16654–16658.

30 Wu, J., Sun, Y., Pei, W.-B. et al. (2014). Polypyrrole nanotube film for flexible thermoelectric application. *Synth. Met.* 196: 173–177.

31 Treuba, M., Montero, A.L., and Rieumont, J. (2004). Pyrrole nanoscaled electropolymerization: effect of the proton. *Electrochim. Acta* 49: 4341–4349.

32 Cho, M.S., Choi, H.J., and Ahn, W.S. (2004). Enhanced electrorheology of conducting polyaniline confined in MCM-41 channels. *Langmuir* 20: 202–207.

33 Zhang, Z., Sui, J., Zhang, L. et al. (2005). Synthesis of polyaniline with a hollow, octahedral morphology by using a cuprous oxide template. *Adv. Mater.* 17: 2854–2857.

34 Kulesza, P.J., Chojak, M., Miecznikowski, K. et al. (2002). Polyoxometallates as inorganic templates for monolayers and multilayers of ultrathin polyaniline. *Electrochem. Commun.* 4: 510–515.

35 Kowalski, D. and Schmuki, P. (2010). Polypyrrole self-organized nanopore arrays formed by controlled electropolymerization in TiO_2 nanotube template. *Chem. Commun.* 46: 8585–8587.

36 Xie, K., Li, J., Lai, Y. et al. (2011). Polyaniline nanowire array encapsulated in titania nanotubes as a superior electrode for supercapacitors. *Nanoscale* 3: 2202–2207.

37 Wu, C.G. and Bein, T. (1994). Conducting polyaniline filaments in a mesoporous channel host. *Science* 264: 1757–1759.

38 Zhang, X., MacDiarmid, A.G., and Manohar, S.K. (2005). Chemical synthesis of PEDOT nanofibers. *Chem. Commun.* (42): 5328–5330.

39 Pan, L.J., Pu, L., Shi, Y. et al. (2007). Synthesis of polyaniline nanotubes with a reactive template of manganese oxide. *Adv. Mater.* 19: 461–464.

40 Li, G.C.C., Zhang, C.Q.Q., Peng, H.R.R., and Chen, K.Z.Z. (2009). One-dimensional V_2O_5@polyaniline core/shell nanobelts synthesized by an in situ polymerization method. *Macromol. Rapid Commun.* 30: 1841–1845.

41 Dai, T.Y. and Lu, Y. (2007). Water-soluble methyl orange fibrils as versatile templates for the fabrication of conducting polymer microtubules. *Macromol. Rapid Commun.* 28: 629–633.

42 Lahav, M., Weiss, E.A., Xu, Q., and Whitesides, G.M. (2006). Core−shell and segmented polymer−metal composite nanostructures. *Nano Lett.* 6: 2166–2171.

43 Callegari, V.V. and Demoustier-Champagne, S.S. (2010). Interfacing conjugated polymers with magnetic nanowires. *ACS Appl. Mater. Interfaces* 2: 1369–1376.

44 Jackowska, K., Biegański, A.T.T., and Tagowska, M. (2008). Hard template synthesis of conducting polymers: a route to achieve nanostructures. *J. Solid State Electrochem.* 12: 437–443.

45 Hernández, R.M.M., Richter, L.L., Semancik, S.S. et al. (2004). Template fabrication of protein-functionalized gold−polypyrrole−gold segmented nanowires. *Chem. Mater.* 16: 3431–3438.

46 Callegari, V.V., Gence, L.L., Melinte, S.S., and Demoustier-Champagne, S.S. (2009). Electrochemically template-grown multi-segmented gold-conducting polymer nanowires with tunable electronic behavior. *Chem. Mater.* 21: 4241–4247.

47 Jang, J., Bae, J., and Park, E. (2006). Selective fabrication of poly(3,4-ethylenedioxy thiophene) nanocapsules and mesocellular foams using surfactant-mediated interfacial polymerization. *Adv. Mater.* 18: 354–358.

48 Yoon, H., Choi, M., Lee, K.J., and Jang, J. (2008). Versatile strategies for fabricating polymer nanomaterials with controlled size and morphology. *Macromol. Res.* 16: 85–102.

49 Yin, Z. and Zheng, Q. (2012). Controlled synthesis and energy applications of one-dimensional conducting polymer nanostructures: an overview. *Adv. Energy Mater.* 2: 179–218.

50 Jang, J., Oh, J.H., and Stucky, G.D. (2002). Fabrication of ultrafine conducting polymer and graphite nanoparticles. *Angew. Chem. Int. Ed.* 41: 4016–4019.

51 Zhou, C.Q., Han, J., and Guo, R. (2009). Synthesis of polyaniline hierarchical structures in a dilute SDS/HCl solution: nanostructure-covered rectangular tubes. *Macromolecules* 42: 1252–1257.

52 Zhou, C.Q., Han, J., and Guo, R. (2008). Dilute anionic surfactant solution route to polyaniline rectangular sub-microtubes as a novel nanostructure. *J. Phys. Chem. B* 112: 5014–5019.

53 Jang, J., Li, X.L., and Oh, J.H. (2004). Facile fabrication of polymer and carbon nanocapsules using polypyrrole core/shell nanomaterials. *Chem. Commun.* 7: 794–795.

54 Jang, J. and Yoon, H. (2005). Formation mechanism of conducting polypyrrole nanotubes in reverse micelle systems. *Langmuir* 21: 11484–11489.

55 Jang, J. and Yoon, H. (2003). Facile fabrication of polypyrrole nanotubes using reverse microemulsion polymerization. *Chem. Commun.* 6: 720–721.

56 Liu, Z., Zhang, X.Y., Poyraz, S. et al. (2010). Oxidative template for conducting polymer nanoclips. *J. Am. Chem. Soc.* 132: 13158–13159.

57 Zhang, X.Y., Lee, J.S., Lee, G.S. et al. (2006). Chemical synthesis of PEDOT nanotubes. *Macromolecules* 39: 470–472.

58 Zhang, X.Y.Y., Lee, J.S.S., Zhang, X.Y.Y. et al. (2006). Controllable synthesis of conducting polypyrrole nanostructures. *J. Phys. Chem. B* 110: 1158–1165.

59 Wu, J., Sun, Y., Xu, W., and Zhang, Q. (2014). Investigating thermoelectric properties of doped polyaniline nanowires. *Synth. Met.* 189: 177–182.

60 Mao, H., Liu, X., Chao, D. et al. (2010). Preparation of unique PEDOT nanorods with a couple of cuspate tips by reverse interfacial polymerization and their electrocatalytic application to detect nitrite. *J. Mater. Chem.* 20: 10277–10284.

61 Li, G., Li, Y., Li, Y. et al. (2011). Polyaniline nanorings and flat hollow capsules synthesized by in situ sacrificial oxidative templates. *Macromolecules* 44: 9319–9323.

62 Forney, B.S., Baguenard, C., and Guymon, C.A. (2013). Effects of controlling polymer nanostructure using photopolymerization within lyotropic liquid crystalline templates. *Chem. Mater.* 25: 2950–2960.

63 Hulvat, J.F. and Stupp, S.I. (2003). Liquid-crystal templating of conducting polymers. *Angew. Chem. Int. Ed.* 42: 778–781.

64 Hulvat, J.F.F. and Stupp, S.I. (2004). Anisotropic properties of conducting polymers prepared by liquid crystal templating. *Adv. Mater.* 16: 589–592.

65 Surendran, G.G., Tokumoto, M.S.S., dos Santos, E.P.P. et al. (2005). Highly swollen liquid crystals as new reactors for the synthesis of nanomaterials. *Chem. Mater.* 17: 1505–1514.

66 Ghosh, S., Natalie, K.A., Ramos, L. et al. (2015). Conducting polymer nanostructures for photocatalysis under visible light. *Nat. Mater.* 14: 505–511.

67 Ghosh, S., Natalie, K.A., Remita, S. et al. (2015). Fabrication of a visible-light response polymer nanostructure with superior photocatalytic activity. *Sci. Rep.* 5: 18002 (1–9).

68 Yuan, X., Floresyona, D., Aubert, P.-H. et al. (2018). Photocatalytic degradation of organic pollutant with polypyrrole nanostructures under UV and visible light. *Appl. Catal., B* 242: 284–292.

69 Floresyona, D., Goubard, F., Aubert, P.-H. et al. (2017). Highly active poly(3-hexylthiophene) nanostructures for photocatalysis under solar light. *Appl. Catal., B* 209: 23–32.

70 Ghosh, S., Remita, H., Ramos, L. et al. (2014). PEDOT nanostructures synthesized in hexagonal mesophases. *New J. Chem.* 38: 1106–1115.

71 Ghosh, S., Ramos, L., Dazzi, A. et al. (2015). Size tunable synthesis of one-dimensional conducting polymer nanostructures in hexagonal mesophases. *New J. Chem.* 39: 8311–8320.

72 Sadanandhan, K., Devaki, S.J., Narayanan, R.K., and Cheriyathuchenaaramvalli, M. (2015). Electrochemically patterned transducer with anisotropic PEDOT through liquid crystalline template polymerization. *ACS Appl. Mater. Interfaces* 7: 18028–18037.

73 Komiyama, H., Komura, M., Akimoto, Y. et al. (2015). Longitudinal and lateral integration of conducting polymer nanowire arrays via block-copolymer-templated electropolymerization. *Chem. Mater.* 27: 4972–4982.

74 Hsu, L., Cvetanovich, G.L., and Stupp, S.I. (2008). Peptide amphiphile nanofibers with conjugated polydiacetylene backbones in their core. *J. Am. Chem. Soc.* 130: 3892–3899.

75 Niu, Z., Liu, J., Lee, L.A. et al. (2007). Biological templated synthesis of water-soluble conductive polymeric nanowires. *Nano Lett.* 7: 3729–3733.

76 Meier, C., Lifincev, I., and Welland, M.E. (2015). Conducting core–shell nanowires by amyloid nanofiber templated polymerization. *Biomacromolecules* 16: 558–563.

77 Nagarajan, S., Kumar, J., Bruno, F. et al. (2008). Biocatalytically synthesized poly(3,4-ethylenedioxythiophene). *Macromolecules* 41: 3049–3052.

78 Hassanien, R., A-Hinai, M., Al-Said, S.A.F. et al. (2010). Preparation and characterization of conductive and photoluminescent DNA-templated polyindole nanowires. *ACS Nano* 4: 2149–2159.

79 Madsen, M. and Gothelf, K.V. (2019). Chemistries for DNA nanotechnology. *Chem. Rev.* 119: 6384–6458.

80 Richardson-Burns, S., Hendricks, J.L., Povlich, L.K. et al. (2007). Polymerization of the conducting polymer poly(3,4-ethylenedioxythiophene) (PEDOT) around living neural cells. *Biomaterials* 28: 1539–1552.

81 Pahovnik, D., Žagar, E., Kogej, K. et al. (2013). Polyaniline nanostructures prepared in acidic aqueous solutions of ionic liquids acting as soft templates. *Eur. Polym. J.* 49: 1381–1390.

82 Yin, H. and Yang, J. (2011). Synthesis of high-performance one-dimensional polyaniline nanostructures using dodecylbenzene sulfonic acid as soft template. *Mater. Lett.* 65: 850–853.

83 Park, H.W., Kim, T., Huh, J. et al. (2012). Anisotropic growth control of polyaniline nanostructures and their morphology-dependent electrochemical characteristics. *ACS Nano* 6: 7624–7633.

84 Lu, C.-F., Liao, S.-F., Wang, K.-H. et al. (2019). Rapid template-free synthesis of nanostructured conducting polymer films by tuning their morphology using hyperbranched polymer additives. *Nanoscale* 11: 20977–20986.

85 Diaz-Orellana, K.P. and Roberts, M.E. (2015). Scalable, template-free synthesis of conducting polymer microtubes. *RSC Adv.* 5: 25504–25512.

86 Wan, M., Liu, J., Qiu, H. et al. (2001). Template-free synthesized microtubules of conducting polymers. *Synth. Met.* 119: 71–72.

87 Romero-García, J., Ledezma-Pérez, A., Martínez-Cartagena, M. et al. (2019). Chapter 12: Radical addition polymerization: enzymatic template-free synthesis of conjugated polymers and their nanostructure fabrication. In: *Methods in Enzymology*, vol. 627 (eds. N. Bruns and K. Loos), 321–337. Academic Press.

88 Li, Y. and Shi, J. (2014). Hollow-structured mesoporous materials: chemical synthesis, functionalization and applications. *Adv. Mater.* 26: 3176–3205.

89 Sanchez-Ballester, N.M.M., Rydzek, G.G., Pakdel, A.A. et al. (2016). Nanostructured polymeric yolk–shellcapsules: a versatile tool for hierarchical nanocatalyst design. *J. Mater. Chem. A* 4: 9850–9857.

90 Tran, H.D.D., Li, D.D., and Kaner, R.B.B. (2009). One-dimensional conducting polymer nanostructures: bulk synthesis and applications. *Adv. Mater.* 21: 1487–1499.

91 Wan, M. (2008). A template-free method towards conducting polymer nanostructures. *Adv. Mater.* 20: 2926–2932.

92 Zhao, Q., Jamal, R., Zhang, L. et al. (2014). The structure and properties of PEDOT synthesized by template-free solution method. *Nanoscale Res. Lett.* 9: 557.

93 Dallas, P. and Georgakilas, V. (2015). Interfacial polymerization of conductive polymers: generation of polymeric nanostructures in a 2-D space. *Adv. Colloid Interface Sci.* 224: 46–61.

94 Yuan, C., Zhang, L., Hou, L. et al. (2014). Green interfacial synthesis of two-dimensional poly(2,5-dimethoxyaniline) nanosheets as a promising electrode for high performance electrochemical capacitors. *RSC Adv.* 4: 24773–24776.

95 Ma, H., Luo, Y., Yang, S. et al. (2011). Synthesis of aligned polyaniline belts by interfacial control approach. *J. Phys. Chem. C* 115: 12048–12053.

96 Zeng, F., Qin, Z., Liang, B. et al. (2015). Polyaniline nanostructures tuning with oxidants in interfacial polymerization system. *Prog. Nat. Sc.: Mater. Int.* 25: 512–519.

97 Zhang, L. and Wan, M. (2003). Self-assembly of polyaniline—from nanotubes to hollow microspheres. *Adv. Funct. Mater.* 13: 815–820.

98 Zhang, Z., Wan, M., and Wei, Y. (2006). Highly crystalline polyaniline nanostructures doped with dicarboxylic acids. *Adv. Funct. Mater.* 16: 1100–1104.

99 Qiu, H., Wan, M., Matthews, B., and Dai, L. (2001). Conducting polyaniline nanotubes by template-free polymerization. *Macromolecules* 34: 675–677.

100 Wei, Z., Zhang, L., Yu, M. et al. (2003). Self-assembling sub-micrometer-sized tube junctions and dendrites of conducting polymers. *Adv. Mater.* 15: 1382–1385.

101 Zhu, Y., Hu, D., Wan, M.X. et al. (2007). Conducting and superhydrophobic rambutan-like hollow spheres of polyaniline. *Adv. Mater.* 19: 2092–2096.

102 Kim, N.-J., Kwon, J.-H., and Kim, M. (2013). Highly oriented self-assembly of conducting polymer chains: extended-chain crystallization during long-range polymerization. *J. Phys. Chem. C* 117: 15402–15408.

103 Ding, H.J., Wan, M.X., and Wei, Y. (2007). Controlling the diameter of polyaniline nanofibers by adjusting the oxidant redox potential. *Adv. Mater.* 19: 465–469.

104 Zhang, L.J., Long, Y.Z., Chen, Z.J., and Wan, M.X. (2004). The effect of hydrogen bonding on self-assembled polyaniline nanostructures. *Adv. Funct. Mater.* 14: 693–698.

105 Ding, H.J., Shen, J.Y., Wan, M.X., and Chen, Z.J. (2008). Formation mechanism of polyaniline nanotubes by a simplified template-free method. *Macromol. Chem. Phys.* 209: 864–871.

106 Stejskal, J., Sapurina, I., Trchova, M., and Konyushenko, E.N. (2008). Oxidation of aniline: polyaniline granules, nanotubes, and Oligoaniline microspheres. *Macromolecules* 41: 3530–3536.

107 Janosevic, A., Ciric-Marjanovic, G., Marjanovic, B. et al. (2008). Synthesis and characterization of conducting polyaniline 5-sulfosalicylate nanotubes. *Nanotechnology* 19: 135606.

108 Trchova, M., Sedenkova, I., Konyushenko, E.N. et al. (2006). Evolution of polyaniline nanotubes: the oxidation of aniline in water. *J. Phys. Chem. B* 110: 9461–9468.

109 Huang, J., Virji, S., Weiller, B.H., and Kaner, R.B. (2003). Polyaniline nanofibers: facile synthesis and chemical sensors. *J. Am. Chem. Soc.* 125: 314–315.

110 Haldorai, Y., Zong, T., and Shim, J.-J. (2011). Microwave-assisted facile and rapid synthesis of self-assembled conducting copolymer nanorods via aqueous/ionic liquid interfacial polymerization. *Mater. Chem. Phys.* 127: 385–390.

111 Nuraje, N., Su, K., Yang, N.-I., and Matsui, H. (2008). Liquid/liquid interfacial polymerization to grow single crystalline nanoneedles of various conducting polymers. *ACS Nano* 2: 502–506.

112 Su, K., Nuraje, N., Zhang, L. et al. (2007). Fast conductance switching in single-crystal organic nanoneedles prepared from an interfacial polymerization-crystallization of 3,4-ethylenedioxythiophene. *Adv. Mater.* 19: 669–672.

113 Wan, M. (2009). Some issues related to polyaniline micro-/nanostructures. *Macromol. Rapid Commun.* 30: 963–975.

114 Xia, L., Wei, Z., and Wan, M. (2010). Conducting polymer nanostructures and their application in biosensors. *J. Colloid Interface Sci.* 341: 1–11.

115 Gao, B.X., Li, J.J., Li, M.Y. et al. (2009). Hierarchical self-assembled nanostructures from the organic n-type semiconductor hexaazatrinaphthylene. *ChemPhysChem* 10: 3197–3200.

116 Ihn, K.J., Moulton, J., and Smith, P. (1993). Whiskers of poly(3-alkylthiophene)s. *J. Polym. Sci., Part B: Polym. Phys.* 31: 735–742.

117 Jenekhe, S.A. and Chen, X.L. (2000). Supramolecular photophysics of self-assembled block copolymers containing luminescent conjugated polymers. *J. Phys. Chem. B* 104: 6332–6335.

118 Kiriy, N., Jahne, E., Adler, H.-J. et al. (2003). One-dimensional aggregation of regioregular polyalkylthiophenes. *Nano Lett.* 3: 707–712.

119 He, M., Zhao, L., Wang, J. et al. (2010). Self-assembly of all-conjugated poly(3-alkylthiophene) diblock copolymer nanostructures from mixed selective solvents. *ACS Nano* 4: 3241–3247.

120 Liu, J., Arif, M., Zou, J. et al. (2009). Controlling poly(3-hexylthiophene) crystal dimension: nanowhiskers and nanoribbons. *Macromolecules* 42: 9390–9393.

121 Mirabedini, A., Foroughi, J., and Wallace, G.G. (2016). Developments in conducting polymer fibres: from established spinning methods toward advanced applications. *RSC Adv.* 6: 44687–44716.

122 Pomfret, S.J., Adams, P.N., Comfort, N.P., and Monkman, A.P. (2000). Electrical and mechanical properties of polyaniline fibres produced by a one-step wet spinning. *Polym. J.* 41: 2265–2269.

123 Foroughi, J., Spinks, G.M., Wallace, G.G., and Whitten, P.G. (2008). Production of polypyrrolefibres by wet spinning. *Synth. Met.* 158: 104–107.

124 Foroughi, J., Spinks, G.M., and Wallace, G.G. (2009). Effect of synthesis conditions on the properties of wet spun polypyrrolefibres. *Synth. Met.* 159: 1837–1843.

125 Jalili, R., Razal, J.M., Innis, P.C., and Wallace, G.G. (2011). One-step wet-spinning process of poly(3,4-ethylenedioxythiophene): poly(styrenesulfonate) fibers and the origin of higher electrical conductivity. *Adv. Funct. Mater.* 21: 3363–3370.

126 Zhou, J., Mulle, M., Zhang, Y. et al. (2016). High-ampacity conductive polymer microfibers as fast response wearable heaters and electromechanical actuators. *J. Mater. Chem. C* 4: 1238–1249.

127 Kim, B., Koncar, V., Devaux, E. et al. (2004). Electrical and morphological properties of PP and PET conductive polymer fibers. *Synth. Met.* 146: 167–174.

128 Huang, Z.M., Zhang, Y.Z., Kotakiand, M., and Ramakrishna, S. (2003). A review on polymer nanofibers by electrospinning and their applications in nanocomposites. *Compos. Sci. Technol.* 63: 2223–2253.

129 Li, D. and Xia, Y. (2004). Electrospinning of nanofibers: reinventing the wheel? *Adv. Mater.* 16: 1151–1170.

130 Yin, K., Zhang, L., Lai, C. et al. (2011). Photoluminescence anisotropy of uni-axially aligned electrospun conjugated polymer nanofibers of MEH-PPV and P3HT. *J. Mater. Chem.* 21: 444–448.

131 Liu, H., Kameoka, J., Czaplewski, D.A., and Craighead, H.G. (2004). Polymeric nanowire chemical sensor. *Nano Lett.* 4: 671–675.

132 Wei, M., Lee, J., Kang, B., and Mead, J. (2005). Preparation of core-sheath nanofibers from conducting polymer blends. *Macromol. Rapid Commun.* 26: 1127–1132.

133 Frontera, P., Busacca, C., Trocino, S. et al. (2013). Electrospinning of polyaniline: effect of different raw sources. *J. Nanosci. Nanotechnol.* 13: 4744–4751.

134 Chronakis, I.S., Grapenson, S., and Jakob, A. (2006). Conductive polypyrrole nanofibers via electrospinning: electrical and morphological properties. *Polymer* 47: 1597–1603.

135 Choi, J.J., Lee, J.J., Choi, J. et al. (2010). Electrospun PEDOT:PSS/PVP nanofibers as the chemiresistor in chemical vapour sensing. *Synth. Met.* 160: 1415–1421.

136 Feng, Z.Q., Wu, J., Cho, W. et al. (2013). Highly aligned poly(3,4-ethylene dioxythiophene) (PEDOT) nano- and microscale fibers and tubes. *Polymer* 54: 702–708.

137 Liu, H.A., Zepeda, D., Ferraris, J.P., and Balkus, K.J. (2009). Electrospinning of poly(alkoxyphenylenevinylene) and methanofullerene nanofiber blends. *ACS Appl. Mater. Interfaces* 1: 1958–1965.

138 Wang, W., Li, W., and Zhang, R. (2010). The preparation of conducting polymer micro- and nanofibers by electrospinning. *J. Polym. Mater.* 27: 293–302.

139 Zhang, X., Goux, W.J., and Manohar, S.K. (2004). Synthesis of polyaniline nanofibers by “nanofiber seeding”. *J. Am. Chem. Soc.* 126: 4502–4503.

140 Zhang, X. and Manohar, S.K. (2004). Bulk synthesis of polypyrrole nanofibers by a seeding approach. *J. Am. Chem. Soc.* 126: 12714–12715.

141 Liu, Z., Liu, Y., Poyraz, S., and Zhang, X. (2011). Green-nano approach to nanostructured polypyrrole. *Chem. Commun.* 47: 4421–4423.

142 Guo, Y., Jiang, L., Ma, X. et al. (2013). Poly(3-hexylthiophene) monolayer nanowhiskers. *Polym. Chem.* 4: 4308–4311.

143 Moule, A.J. and Meerholz, K. (2008). Controlling morphology in polymer–fullerene mixtures. *Adv. Mater.* 20: 240–245.

144 Li, L.G., Lu, G.H., and Yang, X.N. (2008). Improving performance of polymer photovoltaic devices using an annealing-free approach via construction of ordered aggregates in solution. *J. Mater. Chem.* 18: 1984–1990.

145 Zhao, Y., Shao, S.Y., Xie, Z.Y. et al. (2009). Effect of poly(3-hexylthiophene) nanofibrils on charge separation and transport in polymer bulk heterojunction photovoltaic cells. *J. Phys. Chem. C* 113: 17235–17239.

146 Kim, J.H., Park, J.H., Lee, J.H. et al. (2010). Bulk heterojunction solar cells based on preformed polythiophene nanowiresvia solubility-induced crystallization. *J. Mater. Chem.* 20: 7398–7405.

147 Sun, S.Y., Salim, T., Wong, L.H. et al. (2011). A new insight into controlling poly(3-hexylthiophene) nanofiber growth through a mixed-solvent approach for organic photovoltaics applications. *J. Mater. Chem.* 21: 377–386.

148 Lu, Y., He, W., Cao, T. et al. (2014). Elastic, conductive, polymeric hydrogels and sponges. *Sci. Rep.* 4: 5792.

149 Kasai, H., Nalwa, H.S., Oikawa, H. et al. (1992). A novel preparation method of organic microcrystals. *Jpn. J. Appl. Phys.* 31: L1132–L1134.

150 Kurokawa, N., Yoshikawa, H., Hirota, N. et al. (2004). Size-dependent spectroscopic properties and thermochromic behavior in poly(substituted thiophene) nanoparticles. *ChemPhysChem* 5: 1609–1615.

151 Szymanski, C., Wu, C., Hooper, J. et al. (2005). Single molecule nanoparticles of the conjugated polymer MEH-PPV, preparation and characterization by near-field scanning optical microscopy. *J. Phys. Chem. B* 109: 8543–8546.

152 Wu, C.F., Szymanski, C., and McNeill, J. (2006). Preparation and encapsulation of highly fluorescent conjugated polymer nanoparticles. *Langmuir* 22: 2956–2960.

153 Yabu, H., Higuchi, T., and Shimomura, M. (2005). Unique phase-separation structures of block-copolymer nanoparticles. *Adv. Mater.* 17: 2062–2065.

154 Sidorenko, A., Krupenkin, T., Taylor, A. et al. (2007). Reversible switching of hydrogel-actuated nanostructures into complex micropatterns. *Science* 315: 487–490.

155 Green, R.A., Baek, S., Poole-Warren, L.A., and Martens, P.J. (2010). Conducting polymer-hydrogels for medical electrode applications. *Sci. Technol. Adv. Mater.* 11: 014107 (1–13).

156 Mano, N.N., Yoo, J.E.E., Tarver, J.J. et al. (2007). An electron-conducting cross-linked polyaniline-based redox hydrogel, formed in one step at pH 7.2, wires glucose oxidase. *J. Am. Chem. Soc.* 129: 7006–7007.

157 Dai, T. and Jia, Y. (2011). Supramolecular hydrogels of polyaniline-poly(styrene sulfonate) prepared in concentrated solutions. *Polymer* 52: 2550–2558.

158 Tomczykowa, M. and Plonska-Brzezinska, M.E. (2019). Conducting polymers, hydrogels and their composites: preparation, properties and bio-applications. *Polymers* 11: 350.

159 Pan, L., Yu, G., Zhai, D. et al. (2012). Hierarchical nanostructured conducting polymer hydrogel with high electrochemical activity. *Proc. Natl. Acad. Sci. U.S.A.* 109: 9287–9292.

160 Tomczykowa, M. and Plonska-Brzezinska, M.E. (2019). Conducting polymers, hydrogels and their composites: preparation, properties and bioapplications. *Polymers* 11: 350.

161 Du, R., Xu, Y., Luo, Y. et al. (2011). Synthesis of conducting polymer hydrogels with 2D building blocks and their potential-dependent gel-sol transitions. *Chem. Commun. (Cambridge)* 47: 6287–6289.

162 Mao, J., Li, C., Park, H.J. et al. (2017). Conductive polymer waving in liquid nitrogen. *ACS Nano* 11: 10409–10416.

163 Karbarz, M., Gniadek, M., Donten, M., and Stojek, Z. (2011). Intra-channel modification of environmentally sensitive poly(N-isopropylacrylamide) hydrogel with polyaniline using interphase synthesis. *Electrochem. Commun.* 13: 714–718.

164 Tao, Y., Zhao, J.X., and Wu, C.X. (2005). Polyacrylamide hydrogels with trapped sulfonated polyaniline. *Eur. Polym. J.* 41: 1342–1349.

165 Du, R., Xu, Y., Luo, Y. et al. (2011). Synthesis of conducting polymer hydrogels with 2D building blocks and their potential-dependent gel–sol transitions. *Chem. Commun.* 47: 6287–6289.

166 Wei, D., Lin, X., Li, L. et al. (2013). Controlled growth of polypyrrole hydrogels. *Soft Matter* 9: 2832–2836.

167 Kim, K.H., Vural, M., and Islam, M.F. (2011). Single-walled carbon nanotube aerogel-based elastic conductors. *Adv. Mater.* 23: 2865–2869.

168 Biener, J., Stadermann, M., Suss, M. et al. (2011). Advanced carbon aerogels for energy applications. *Energy Environ. Sci.* 4: 656–667.

169 Zhang, X.T., Chang, D.W., Liu, J.R., and Luo, Y.J. (2010). Conducting polymer aerogels from supercritical CO_2 drying PEDOT-PSS hydrogels. *J. Mater. Chem.* 20: 5080–5085.

170 Zhang, X.T., Li, C.Y., and Luo, Y.J. (2011). Aligned/unaligned conducting polymer cryogels with three-dimensional macroporous architectures from ice-segregation-induced self-assembly of PEDOT-PSS. *Langmuir* 27: 1915–1923.

171 Nguyen, D. and Yoon, H. (2016). Recent advances in nanostructured conducting polymers: from synthesis to practical applications. *Polymers* 8: 118 (1–38).

172 Lin, P., Yan, F., and Chan, H.L.W. (2009). Improvement of the tunable wettability property of poly(3-alkylthiophene) films. *Langmuir* 25: 7465–7470.

173 Xie, X.N., Lim, S.X., Wang, Y. et al. (2010). A Nanosegregant approach to superwettable and water-attracting surfaces. *Macromol. Chem. Phys.* 211: 2187–2192.

174 Salaita, K., Wang, Y., and Mirkin, C.A. (2007). Applications of dip-pen nanolithography. *Nat. Nanotechnol.* 2: 145–155.

175 Ginger, D.S., Zhang, H., and Mirkin, C.A. (2004). The evolution of dip-pen nanolithography. *Angew. Chem. Int. Ed.* 43: 30–45.

176 Ivanisevic, A. and Mirkin, C.A. (2001). “Dip-pen” nanolithography on semiconductor surfaces. *J. Am. Chem. Soc.* 123: 7887–7889.

177 Lim, J.-H. and Mirkin, C.A. (2002). Electrostatically driven dip-pen nanolithography ofconducting polymers. *Adv. Mater.* 14: 1474–1477.

178 Maynor, B.W., Filocamo, S.F., Grinstaff, M.W., and Liu, J. (2002). Direct-writing of polymernanostructures: poly(thiophene) nanowires on semiconducting and insulatingsurfaces. *J. Am. Chem. Soc.* 124: 522–523.

179 Su, M., Aslam, M., Fu, L. et al. (2004). Dip-pen nanopatterning of photosensitive conducting polymer using a monomer ink. *Appl. Phys. Lett.* 84: 4200–4202.

180 Cheyns, D., Vasseur, K., Rolin, C. et al. (2008). Nanoimprinted semiconducting polymer films with 50 nm features and their application to organic heterojunction solar cells. *Nanotechnology* 19: 424016.

181 Battaglia, C., Escarré, J., Söderström, K. et al. (2011). Nanoimprint lithography for high-efficiency thin-film silicon solar cells. *Nano Lett.* 11: 661–665.

182 Ramanathan, K., Bangar, M.A., Yun, M. et al. (2005). Bioaffinity sensing using biologically functionalized conducting-polymer nanowire. *J. Am. Chem. Soc.* 127: 496–497.

183 Yun, M., Myung, N.V., Vasquez, R.P. et al. (2004). Electrochemically grown wires for individually addressable sensor arrays. *Nano Lett.* 4: 419–422.

184 Kim, M.S., Kim, J.S., Cho, J.C. et al. (2007). Flexible conjugated polymer photovoltaic cells with controlled heterojunctions fabricated using nanoimprint lithography. *Appl. Phys. Lett.* 90: 123113.

185 Aryal, M.M., Buyukserin, F.F., Mielczarek, K.K. et al. (2008). Imprinted large-scale high density polymer nanopillars for organic solar cells. *J. Vac. Sci. Technol., B* 26: 2562–2566.

186 Huang, C., Dong, B., Lu, N. et al. (2009). A strategy for patterning conducting polymers using nanoimprint lithography and isotropic plasma etching. *Small* 5: 583–586.

187 Rickard, J.J.S., Farrer, I., and Oppenheimer, P.G. (2016). Tunable nanopatterning of conductive polymers via electrohydrodynamic lithography. *ACS Nano* 10: 3865–3870.

3

Template-Free Synthesis of Nanostructured Conjugated Polymer Films

Gabriela Ramos Chagas, Thierry Darmanin, and Frédéric Guittard

Université Côte d'Azur, NICE Lab, IMREDD, 61-63 Avenue Simone Veil, 06200 Nice, France

3.1 Introduction

Since the discovery of the first conducting polymer by the electrosynthesis of acetylene doped with iodine vapor in 1977 by Shirakawa, MacDiarmid, and Heeger, [1] conducting polymers have received a great attention due to their special properties. The importance of this discovery was highlighted in 2000 by awarding the Nobel Prize in chemistry to the authors of this achievement [2]. Since there, the field of organic conducting polymers has attracted the interest of many academic and industrial researchers who are searching of new synthesis or manufacturing methods and potential applications [3, 4]. Nowadays, the main three families of aromatic molecules that are subject of study for various researchers are polypyrrole (PPy), polyaniline (PANI), and polythiophene; however, many other molecules have been discovered every day. Scheme 3.1 shows some examples of conducting polymers.

Since the method is one of the most important parameters in the final properties for structuration, various approaches are widely employed to fabricate conducting polymers nanostructures, such as hard template methods (using metal oxide or mesoporous templates), soft template methods (micellar polymerization, emulsion, layer-by-layer deposition), and template-free methods (electropolymerization, electrospinning, plasma polymerization, self-assembly) [5, 6]. Even though the hard-template route is the most used approach to obtain conducting polymer nanostructures, this presents many disadvantages as the post-removal template step and the limited size and morphology available templates. Therefore, the soft template and template-free methods have gained more space due to their versatility compared with hard template methods. The template-free route is a simple, cheap, and scalable method to produce conducting polymers nanostructures in a reproducible and uniform way.

This chapter reviews the template-free synthesis of conducting polymers nanostructures including electrospinning, electrochemical polymerization, plasma polymerization, and vapor phase polymerization. We will discuss the main aspects of each method, advantages and disadvantages, materials, and applications.

Conjugated Polymer Nanostructures for Energy Conversion and Storage Applications,
First Edition. Edited by Srabanti Ghosh.

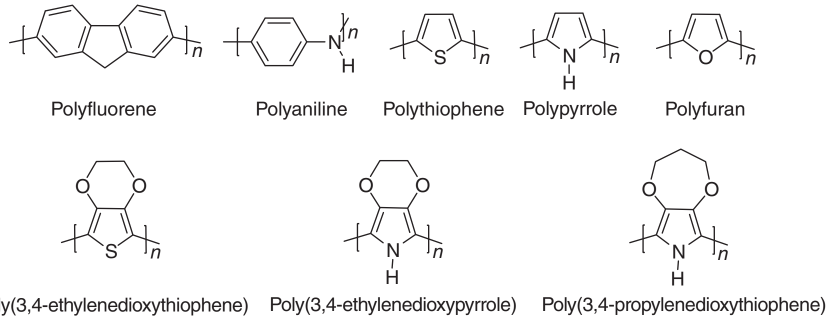

Scheme 3.1 Examples of conducting polymers.

3.2 Template-Free Synthesis

Template-free method is a simple, versatile, and powerful approach to synthesize conducting polymers nanostructures [5]. Contrary to the hard-template method, the template-free route does not require a membrane as a template or a post-treatment to template removal. Indeed, template-free method is a cost-effective technique, which produces uniform conducting polymers nanostructures in a scalable and reproducible path. As a versatile method, various conducting polymer nanostructures can be formed, such as tubes, spheres, rods, wires, fibers, and so on.

Nevertheless, the controllability of morphology and size of nanostructures obtained is quite poor mainly if compared with that of the hard-template method. However, these properties are directly affected by the structure of the monomer, dopant, method, solvent, temperature, pH, etc., so the morphology and the size of nanostructures can be easily addressed to the desired final properties.

Thereby, with some preliminary experiments and literature, it is easy to find a facile and efficient route to form conducting polymer nanostructures with a controllable morphology and particles size, which inspires the researches to find new methods and approaches in this field.

Up to now, several techniques can be used to fabricate conducting polymers nanostructures, such as electrospinning, plasma polymerization, chemical and electrochemical polymerization, self-assembly, and so on. In the sequence of this chapter, some of these methods will be further discussed.

3.2.1 Electrochemical Polymerization

A famous engineering route toward to design nano- and microstructured conducting polymers with a wide range of wettability is the electrochemical polymerization or electropolymerization [7]. This technique is classified as a “bottom–up” approach and presents many advantages toward the other techniques. Nevertheless, the electropolymerization do not only provide films with controllable surface morphology and wettability as well is considerably simpler, faster, and more cost-effective technique when compared with the conventional chemical polymerization [8].

Indeed, this technique does not require high voltages or the use of catalyst/initiators to polymerize.

The electrochemical polymerization consists in a fast process that guarantees the polymerization, deposition, and structuration of the film in only one step. The principle of this method is the oxidation of the monomer in an electrochemical cell to induce the polymerization and the deposition of the film on the working electrode. The monomer, dissolved in an appropriate solvent and electrolyte, is oxidized at the surface of an electrode by application of an anodic potential. The polymerization involves several subsequent steps and many researchers reported different mechanisms, as described by Sabouraud et al. for the PPy [9]. A general and representative mechanism of the electropolymerization is displayed in Scheme 3.2.

The electropolymerization starts with the generation of a radical cation by the oxidation of the monomer. The coupling of two radical cations or one radical and a monomer and the successive elimination of two protons results in the formation of a dimer. In the sequence, the oxidation of the dimer and the sequential coupling with additional synthons (monomer, oligomer) propagates the polymeric chain growth. The termination step occurs when there is no more monomer on the media, when the polymer precipitates/deposits or due parallel reactions that cause the “death” of the active polymerization sites [4, 9].

Many are the parameters that affect the electropolymerization, such as the monomer structure and concentration, the solvent, the electrolyte, the voltage, the temperature, the deposition time, or the method [10–12]. Wolfs et al. [13] reported the use of many supporting electrolytes and solvents in the electropolymerization of poly(3,4-ethylenedioxythiophene) (PEDOT) films. Structured surfaces with various shapes were obtained with high polar solvents while the less polar solvents gave smoother surfaces (Figure 3.1). In opposition, when the supporting electrolyte was changed, no significant variation on the morphology was observed on the formed fibers structures. Similarly, Poverenov et al. [14] found a very significant solvent

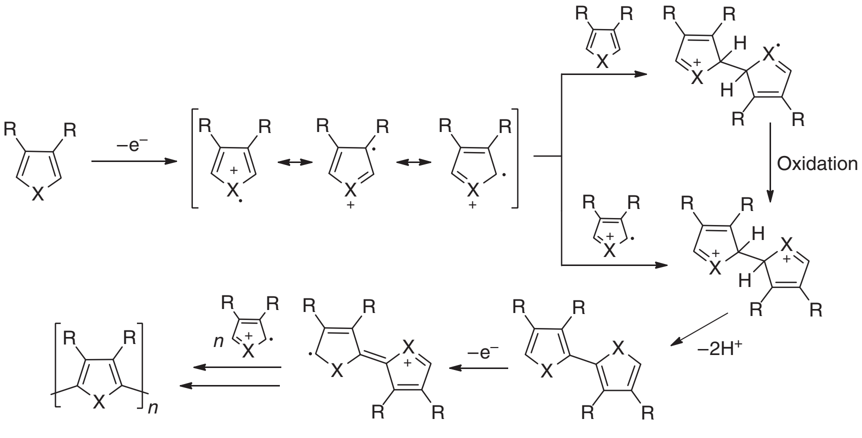

Scheme 3.2 General mechanism of electropolymerization.

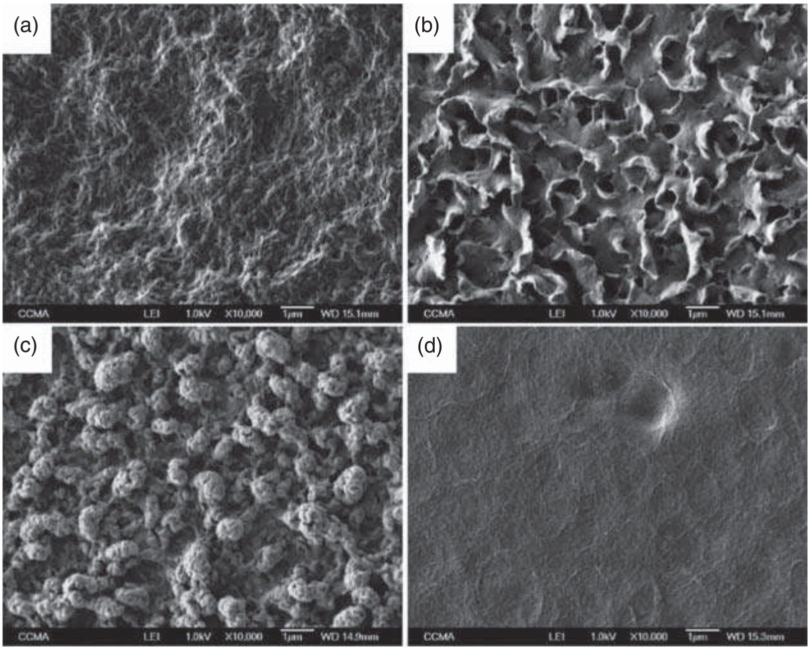

Figure 3.1 Scanning electron microscopy (SEM) images of PEDOT derivative obtained by electropolymerization in different solvents: (a) propylene carbonate, (b) benzonitrile, (c) nitrobenzene, and (d) dichloromethane. Constant potential method at 200 mC/cm^2, Bu_4NPF_6 as electrolyte. Source: Wolfs et al. [13].

effect but a small electrolyte effect for PEDOT films prepared by electropolymerization because the main parameters seem to be the solubility of the oligomers produced in the first instance of electropolymerization. The morphology has found to be directly related to the electrochromic properties, which showed differences for using acetonitrile and propylene carbonate as solvent, such as the transparency, coloration efficacy, and contrast. The choice of the solvent can even influence in the nucleation and growth mechanisms of the conducting polymers, as reported by Schrebler and co-authors [15] for the polythiophene.

Indeed, not only the progressive grows of the polymer but also its properties will strongly depend on the method chosen. For example, Bellanger et al. [16] have pointed out that the choice of the electrochemical method had influence in the surface oleophobicity for nanostructured poly(3,4-ethylenedioxypyrrole) (PEDOP) derivatives. The electrochemical polymerization at constant potential had led to an oleophobic surfaces with $\theta_{\text{hexadecane}} = 110°$ due to the presence of nanoporosities on the film. However, $\theta_{\text{hexadecane}} = 140°$ had been found when the method was changed for galvanostatic and pulse deposition. Both methods are efficient to produce nanoporous surfaces that increase the oleophobicity of the films. Using these same methods, Ocón et al. [17] had shown films of poly-3-methylthiophene grown as a homogeneous coating on indium tin oxide (ITO) and graphite substrates for pulse deposition, while a heterogeneous structure was observed for galvanostatic method.

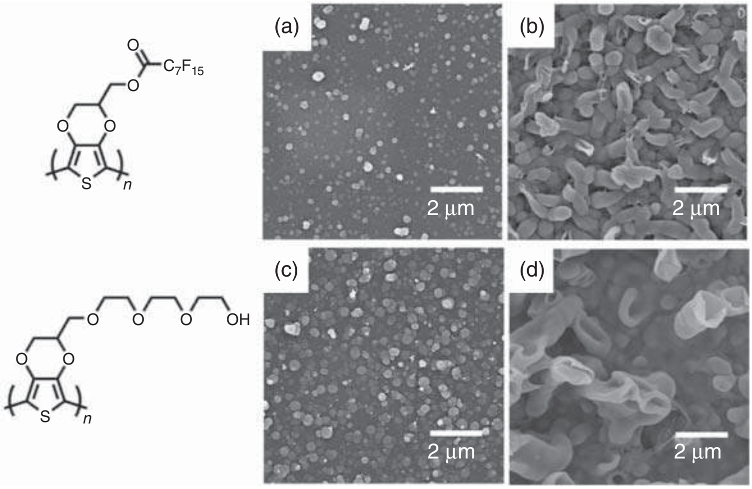

Figure 3.2 SEM images of electrodeposited PEDOT derivatives by applying a constant voltage of 1.4 V (vs. Ag/Ag$^+$) at (a, c) 25 °C for 30 seconds and (b, d) 0 °C for 90 seconds. Source: Adapted with permission from [18]. Copyright 2012, American Chemical Society.

Even though the monomer oxidation potential is independent of the pH and temperature, they influence on the behavior of the polymerization. Luo et al. [18] observed an effect of temperature on the formation of the structures for thiophene derivatives. They observed a formation of nanodots structures on the surface when the electropolymerization was carried out at 25 °C, but tubular structures when the temperature decreases to 0 °C (Figure 3.2). Bazzaoui and co-authors [19] had shown the influence of the pH on the adherence of the PPy film formed. When the electropolymerization was carried at acid and neutral pH, homogeneous and adherent films were formed by potentiostatic mode while for the PPy coatings produced in basic pH non-adherent films were obtained.

In order to control the formation of surface nanostructures, the core responsible for the polymerization (such as pyrrole, thiophene, 3, 4-ethylenedioxythiophene (EDOT), etc.) is probably the most important parameter because each molecule leads to different polymerization capacity and solubility, which can highly influence the morphology. PEDOT derivatives were electropolymerized in similar conditions (tetrabutylammonium electrolyte in anhydrous acetonitrile) generating various morphologies: fibers [20], spheres [21], and cauliflower-like structures [22]. The side group grafted on EDOT moiety influences prior the solubility of the polymer in the moment of the deposition step. Various morphologies were also reported for PEDOP and 3,4-propylenedioxypyrrole (ProDOP) electropolymerized films by differing the side group [23–25]. Using indole derivatives, the position of the main substituent showed to govern the surface morphology of electropolymerized films [26]. The authors described that for the substituents on 4-position on indole moiety, smooth surfaces were formed. However, for 5-position and 6-position of the fluorinated substituent on indole moiety, it predominates the formation of fibers and spheres, respectively. Here, the polymerization of indole is more favorable in certain positions, and the location of the substituent may influence the polymerization and the way in which the monomers are linked to one another forming different structures. The authors demonstrated that fiber structures can be obtained by interfacial polymerization because the polymerization is directional, while spheres are obtained when the polymerization is equal in all directions. Indeed, for 4-position in indole moiety, the polymerization should not be favorable to form any structure on the surface. Similarly, Zang et al. [27] reported the importance of the experimental conditions in directing the formation of structures. The authors fabricated an electrochemically synthesized superhydrophilic PPy in an aqueous solution by using phosphate buffer solution (PBS) in the absence of templates, surfactants, and structure-directing molecules. In this work, the presence of the hydrogen bonding between phosphate and pyrrole (Py) oligomers is essential to producing the 1D nanofiber structure, and the electrostatic interactions between ion dopant and Py oligomers lead to an irregular nanostructure (Figure 3.3).

In order to produce porous structures such as nanotubes, nanocups, or hollow spheres without templates, the electropolymerization approach is an excellent choice. In this process, gas bubbles acting as soft template should be produced directly during electropolymerization. The first report of porous structures formation such as nanotubes or nanocapsules by electropolymerization was shown by Shi and co-authors in 2003 [28–30]. The authors fabricated such interesting structures by the electropolymerization of pyrrole in aqueous solution in different sulfonic acids. By doing the deposition by cyclic voltammetry, they observed the formation H_2 bubbles from H^+ ($2H^+ + 2e^- \rightarrow H_2$) going from sulfonic acids, during the back scans. Tubular structures and cups of very large porosity were reported as function of the potential range or the scan rate. The sulfonate function acts as surfactant for the stabilization of gas bubbles. Also using pyrrole as the monomer, Parakhonskiy et al. [31, 32] formed hollow microcontainers by electropolymerization. Margaritondo and co-authors [33] investigated the microcontainer shape in electropolymerization of pyrrole on H_2 bubbles using real-time microradiography. They observed the existence of a deformation force at the three-phase boundary changing from spherical to elliptical and then to cylindrical. In a relatively similar approach, the group of Debiemme-Chouvy [34–37] observed the formation of PPy nanowires without strong acid and in the presence of anions of weak acid such as monohydrogenophosphate and non-acidic anions (perchlorate). Here, in potentiostatic conditions (constant potential of 0.78 V vs. saturated calomel electrode [SCE]), the authors observed the release of O_2 bubbles from H_2O ($2H_2O \rightarrow O_2 + 4H^+ + 4e^-$) (Figure 3.4).

However, because most of the monomers being not soluble in water and the electropolymerization in water needing high monomer concentration, a new strategy has been recently reported. The templateless electropolymerization process was found to be possible in organic solvent such as dichloromethane without any surfactant or acid if only trace water is present in solution. The role of the monomer is fundamental because it must act as a surfactant for the stabilization of gas bubbles. Exceptional results such as vertically aligned nanotubes with strong water adhesion were obtained with 3,4-phenylenedioxythiophene (PheDOT),

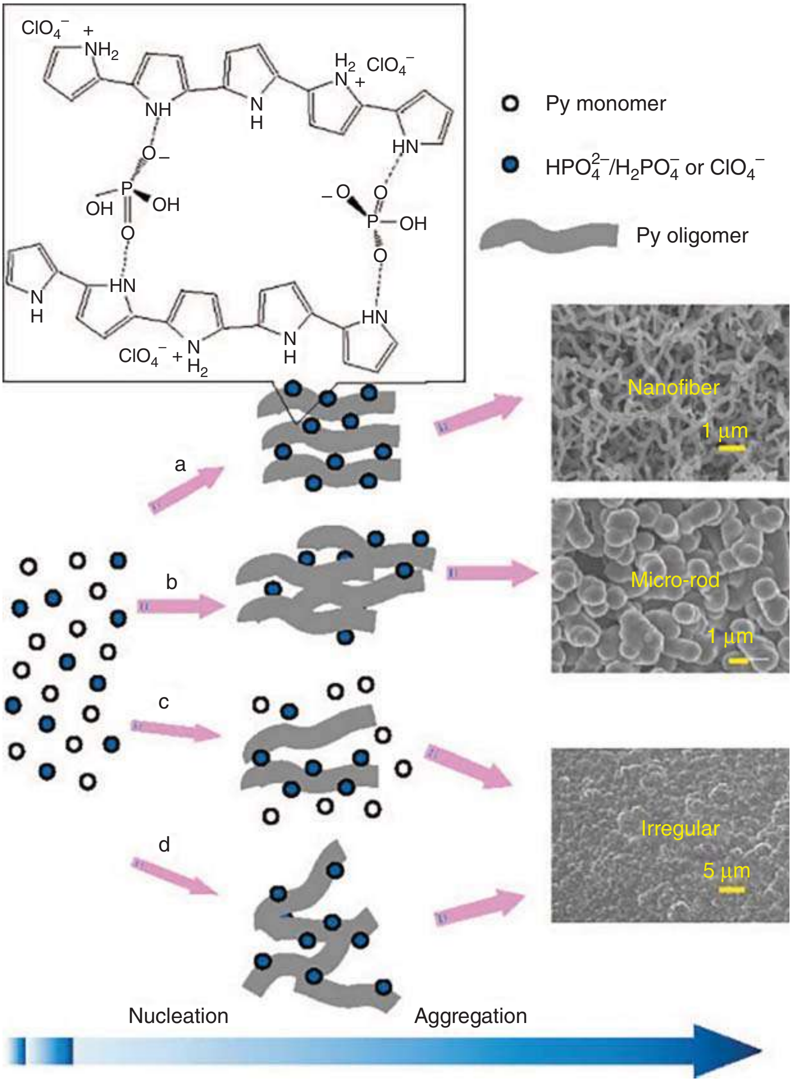

Figure 3.3 Schematic representation and SEM images of the favored structures formed by the different experimental conditions proposed by Zhang and co-authors: (a) nanofibers were formed when the hydrogen bonds favor the self-alignment; (b) microrods when the random aggregation process is comparable to the self-alignment process, (c, d) irregular shaped forms when the random aggregation process dominates. Source: Adapted with permission from [27]. Copyright 2004, American Chemical Society.

3,4-naphthalenedioxythiophene (NaphDOT), or thienothiophene derivatives, as shown in Table 3.1.

When various thienothiophene monomers were used, varying by their monomer core and side group chain, the authors observed the formation of structures from nanorods to nanofibers, nanotubes, and nanospheres and a mechanism

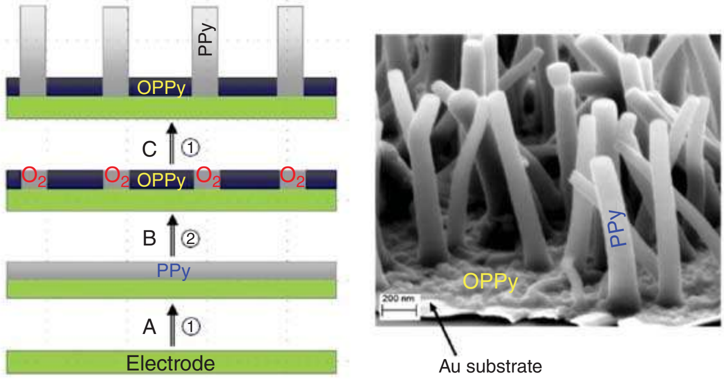

(a) (b)

Figure 3.4 (a) Schematic representation of PPy nanowire electroprocess where: in step A an electrochemical deposition of an ultrathin film of PPy, in step B is represented the generation of OH^- which overoxidize polypyrrole (OPPy) and of O_2 nanobubbles, which protect PPy against the action of OH^-, and in step C is showed the growth of the PPy nanowires. (b) SEM image of PPy deposited at 0.75 V/SCE in 0.15 M Py, 0.2 M K_2HPO_4, 10^{-3} M $LiClO_4$ on Au/mica substrate. Source: Adapted with permission from [36]. Copyright 2015, Elsevier.

was proposed [39, 41–45]. Unidimensional structures (1D-structures), like fiber or tubes, were formed by the presence of monomers with extended aromatic system due to the π–π stacking interactions, which are very strong attractive forces that decrease the possibility to other forces matches them. In other cases, for non-extended aromatic system, such as hydrocarbon chains as side group, the π–π stacking forces are weakened and probably comparable with other hydrophobic interactions, resulting in a three-dimensional (3D) growth (structures), such as spheres or rods [41]. Indeed, the porosity and size of the nanotubes showed to be dependent on the electrolyte and electrochemical method. The formation of nanotubes is due to the stabilization by the polymer of gas bubbles produced *in situ* during electropolymerization using no surfactant nor template, and it was demonstrated that the water content plays an important role even if it is not the unique parameter [42]. The process to obtain nanotubes without hard templates is extremely rare in the literature and basically all the studies use deposited metals, scarcely conducting polymers.

Although there are several works reporting how each parameter could affect the electropolymerization, the singularities of each system (specially the monomer) require a deep investigation in order to have a comprehensive evaluation concerning the influence of parameters on the process (solvent, electrochemical method, electrolyte, and solvent). In the last few years, pyrene moiety has been called the attention of researches for their combined fluorescent and superhydrophobic properties. A fabrication of fluorescent superhydrophobic coating was presented by Xu et al. [46] by the electropolymerization of polypyrene coating followed by a chemical vapor deposition of tetraethoxysilane (TEOS) and

Table 3.1 Examples of porous structures reported in the literature by templateless electropolymerization in organic solvent (dichloromethane).

Monomer	Surface topography	References
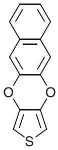	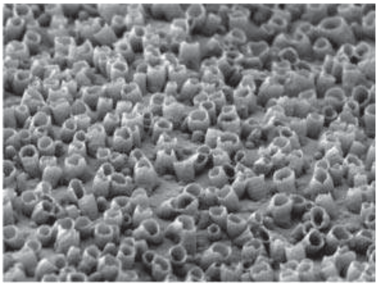	[38]
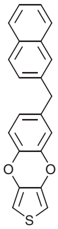	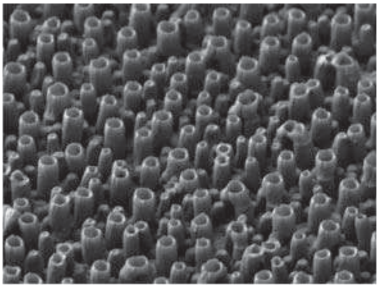	[39]
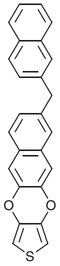	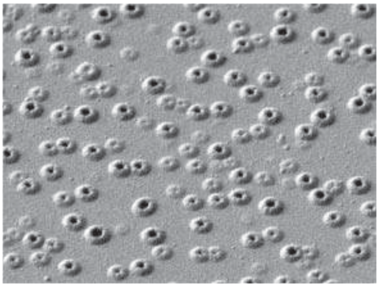	[40]
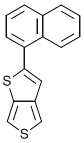	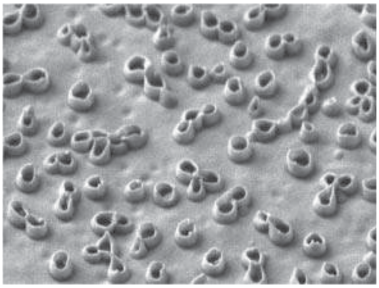	[41]

1H,1H,2H,2H-perfluorooctyltriethoxysilane (POTS). The hybrid polypyrene/silica coating exhibits strong blue-green fluorescence emission derived from the excimer forms and microstructured surfaces achieving $\theta_{\text{water}} = 163°$ and $\alpha = 4°$. Polypyrene surfaces were also fabricated via electropolymerization technique using acetonitrile and tetrabutylammonium perchlorate as solvent and electrolyte, respectively. The combination of micro- and nanostructures generates surfaces with superhydrophobic and parahydrophobic behavior where the water adhesive behavior was dependent on the pyrene derivative [47, 48] and the conditions used for the electrochemical polymerization [49], such as electrolyte, solvent, method, etc. Besides the superhydrophobicity, these polypyrene surfaces also showed a fluorescent behavior emitting on the green region, independent of the side chain or conditions used to fabricate these nanostructures, increasing the range of application of these films (Figure 3.5) [47–50].

Indeed, electropolymerized polypyrene surfaces were also used to put in evidence a new physical phenomenon of superpropulsion where an elastic object can be propelled by a catapult-like system with an efficient gain in kinetic energy [51]. The same surfaces were also used to validate the so-called Ejection Test Method (ETM) using a new apparatus system for better characterize the water adhesion behavior of liquid droplets on rigid [52] and elastic [53] substrates. For that, nanostructured superhydrophobic and parahydrophobic polypyrene films were fabricated in one-step method by electrochemical polymerization. The substrates were placed on a catapult-like apparatus that, when loaded with an initial amplitude A, the plate is subject to a sudden and large acceleration, ejecting the water droplet from the substrate with an ejection velocity of plate V_{p}. The ejection time t_{e}, the velocity of the plate V_{p}, and the maximum acceleration a_{max} were noted and can be used to characterize quantitatively the differences on the water adhesion behavior among the substrates. Figure 3.6 resumes the ETM work and shows the procedure used.

Due to the new developments on the smart materials area, many works reported the fabrication of stimulus-sensitive surfaces produced by electropolymerization. Various monomers were used to generate surfaces with wetting switchability by the pH, voltage, ion exchange, etc. [54–56]. These surfaces were basically composed by copolymers where one monomer provide the property (superhydrophobicity, anti-fouling, structuration, etc.) and the other a sensitive group to the desired stimulus.

Many authors had already reported that the surface structure is the key parameter to reduce bacterial adhesion. The polypyrene films also have shown a potential application to serve as coatings with reduced bacterial adhesion and to prevent biofilm formation [50, 57]. Studying fluorinated and nonfluorinated surfaces, it was shown that is not totally necessary to use superhydrophobic surfaces to get anti-bacterial properties, but instead these properties rely on a combination between the wettability and the topography of the film. A reduction of 30–70% in the bacterial adhesion for hydrophobic polypyrenes and 60–90% for superhydrophobic polypyrene was obtained for *Staphylococcus aureus* and *Pseudomonas aeruginosa* strains. After a long exposure to bacterial strains, all the polypyrene surfaces demonstrated a high efficiency against biofilm formation and reduced by 90–99% the bacteria coverage. Whereas the polypyrene films have different hydrophobicity, it seems that roughness and nanostructures are more important parameters to avoid bacteria adhesion [50]. These results demonstrate the capability of these surfaces to be used as coatings to prevent bacterial interactions. Bruzaud et al. [58] revealed that the bacterial adherence requires the control of surface topography using a

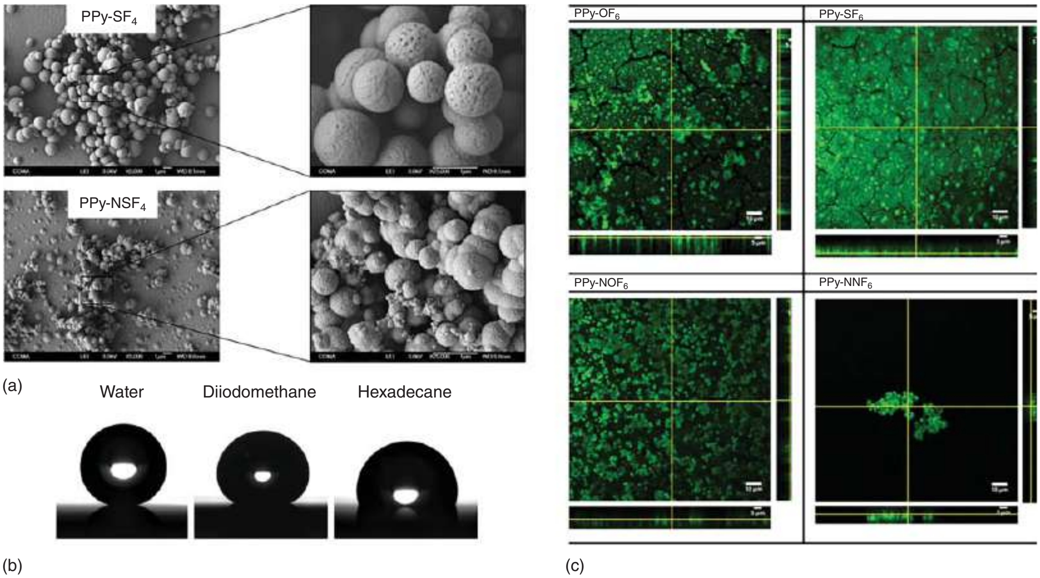

Figure 3.5 (a) SEM images, (b) wettability, and (c) fluorescence of nanostructured polypyrene films produced by electrochemical polymerization. Source: Ramos Chagas et al. [47].

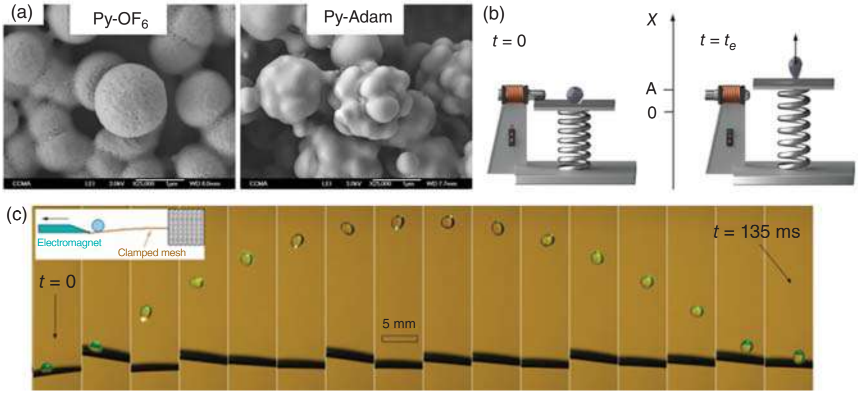

Figure 3.6 (a) SEM images of nanostructured polymer surface. Source: Raufaste et al. [51]. (b) Schematic representation of a catapult-like system proposed by Raufaste and co-authors for the ETM to better characterize the water adhesion of surfaces with different adhesive behaviors. Source: Ramos Chagas et al. [52]. © 2018, American Chemical Society. (c) Time sequence pictures of the ejection process. Source: Ramos Chagas et al. [53].

superhydrophobic PEDOT functionalized with a fluorinated chain. They showed that this property is highly associated with the water adhesion and the structures: surfaces with low water adhesion and limited crevice features provided the greatest anti-bacterial properties. Anti-bacterial coating based on electrodeposited pyrrole on Nitinol alloys were fabricated by Saugo et al. [59, 60]. Gallium, zinc, cobalt, and silver species were immobilized in hollow rectangular-sectioned microtubes of PPy to evaluate the anti-bacterial activity. The best results for the various coatings against *Escherichia coli* were obtained with gallium species that also exhibited a good corrosion protection performance. Indeed, several works reported the fabrication of anti-corrosion coatings using electropolymerized PPy and PANI films [61–64].

3.2.2 Electrospinning

Electrospinning is one of the most efficient techniques to produce sub-micron or nanoscale polymer fibers under a high electrical field. Although several techniques can fabricate fiber mats, such as self-assembly or template method, electrospinning approach has shown many advantages face to standard techniques: (i) facile, simple, and cost-effective method to produce nanofibers, (ii) high capacity of production and scale-up, (iii) large surface area, (iv) easy topography control, (v) tunable fiber diameter, (vi) suitable porosity, (vii) do not require a template neither a post-treatment for template removal, (viii) absence of heating during the process, (ix) fast solvent evaporation, etc. [65]. The electrospinning nanofibers can be affected by the monomer used, solution concentration, solvent, temperature, humidity, as well as by the process parameters, as applied voltage, spinning distance, feed rate, and needle diameter, for example [66, 67].

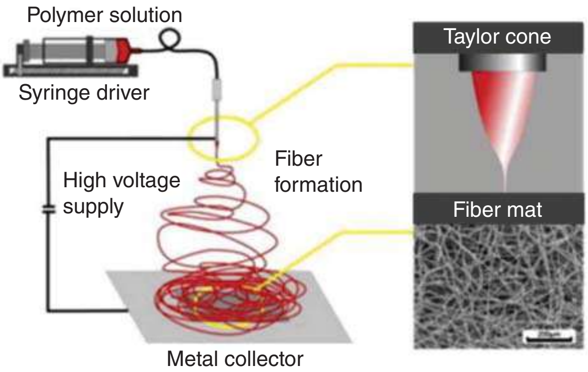

Figure 3.7 Schematic illustration of the basic setup for electrospinning. Source: Nieuwland et al. [71].

However, conducting polymers need to be highly soluble and the solution must have a certain viscosity, conductivity, and surface tension. Even being a powerful method to fabricate nanofibers of conducting polymers, the researchers can find a difficulty in solubility of conducting polymers on organic solvents. The method is performed by applying an electrical field to draw a polymer droplet into a fine fiber followed by deposition onto a grounded collector. The polymer solution is extruded to form a droplet at the needle tip by a syringe pump. When the polymer liquid is exposed to the electric field, the fibers start to be formed into a structure known as a Taylor cone. Then, the electrostatic forces overcome the surface tension of the liquid leading the jet of polymer solution being ejected from the tip of Taylor cone and traveling directed toward the collector with opposite charges. During this path, the excess electrical charges cause the elongation of jet and a rapid evaporation of solvent takes place leading to the deposition of polymers nanofibers on the grounded collector as randomly oriented [67–70]. A schematic representation of electrospinning system is illustrated in Figure 3.7.

PANI is one of the most studied conductive polymers because of its easy synthesis, high conductivity, and interesting redox catalytic properties. Several works reported the use of electrospun PANI fibers for application in energy store, conversion, supercapacitors, and counter electrodes. Peng et al. reported a directly deposit of conductive 10-camphorsulfonic acid (CSA)-doped PANI blended with polylactic acid (PLA) composite films (PANI.CSA–PLA) on rigid and flexible substrates by electrospinning method [72]. The three-dimensional porous fibrous PANI.CSA–PLA films can be obtained in a short time at room temperature and the results indicate good electrocatalytic performance for I_3^-/I^- electrolyte and a reasonably good photoelectrical conversion efficiency, achieving 82% performance level of the sputtered Pt electrode. These porous fibers are potentially applicable as counter electrodes for efficient DSSC (dye-sensitized solar cells) (Figure 3.8).

The electrospinning of PANI and poly(vinylidene fluoride-*co*-hexafluoropropylene) (PVdF-HFP) affords composite membrane electrolytes, which exhibit a higher power conversion efficiency of 7.20% than the value for the PVdF-HFP

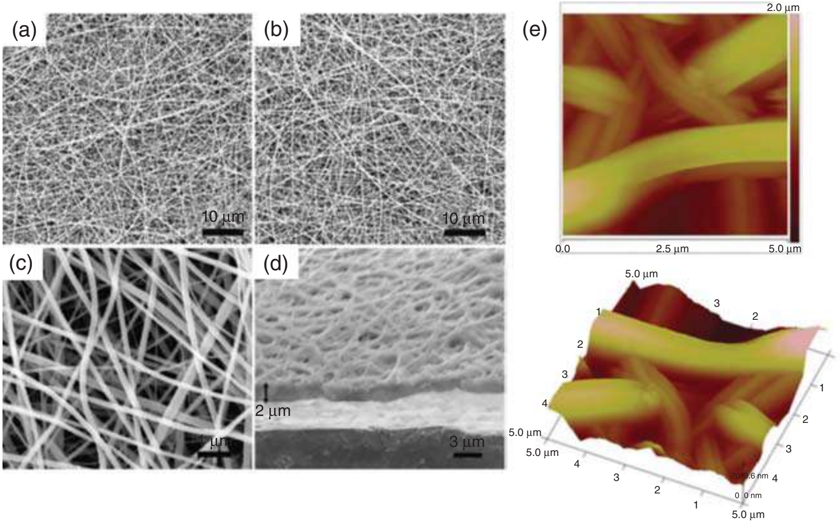

Figure 3.8 SEM images of the PANI-PLA and PANI.CSA–PLA film at the (a–c) top views and (d) cross sectional view. (e) 2D and 3D atomic force microscopy (AFM) images of the PANI.CSA–PLA composite film. Source: Adapted with permission from [72]. Copyright 2012, Royal Society of Chemistry.

membrane of 6.42% [73]. The incorporation of PANI in the composite membrane electrolytes reduced the charge transfer resistance, which accelerates the I_3^-/I^- redox reaction enhancing the power conversion efficiency of the DSSC. Binder-free supercapacitor electrodes based on PANI/PEO nanofibers were fabricated via a single step electrospinning process with an enhanced conductivity and stability of the electrodes by the addition of a small concentration of carbon nanotubes (CNTs) [74]. Specific capacitance retentions of 70% and 81.4% were observed for PANI/PEO and PANI/PEO/CNT based electrodes, respectively, after 1000 cycles. Nevertheless, electrospun PANI fibers have been also applied in several other applications, such as nanogenerators [75], medical treatments [76], and so on.

The fabrication of nanofibers of PEDOT by electrospinning method was first reported in 2008, however, up to now it was not reported the electrospinning of pure PEDOT. The combination of PEDOT and poly(styrenesulfonate) (PSS) has been attracted the researches because of their promising sensing behaviors to diverse vapors and gases. Choi et al. [77] described the synthesis of electrospun PEDOT:PSS/PVP (polyvinylpyrrolidone) nanofibers with an average diameter of 200 nm, electrical conductivity of 2.3×10^{-4} S/cm, and good reproducibility in organic vapor sensing (ethanol, methanol, tetrahydrofuran, and acetone). Two years later, the authors showed the first study of the aromatic volatile organic compounds (VOCs) sensor using electrospun PEDOT:PSS/CNTs/polymer composite nanofibers [78]. The responses of these nanofibers to the aromatic VOCs were explored by monitoring the change in the electrical resistance of the electrospun nanofibers when being exposed to benzene, toluene, and *o*-xylene at room temperature. A high response to the aromatic VOCs at room temperature was found

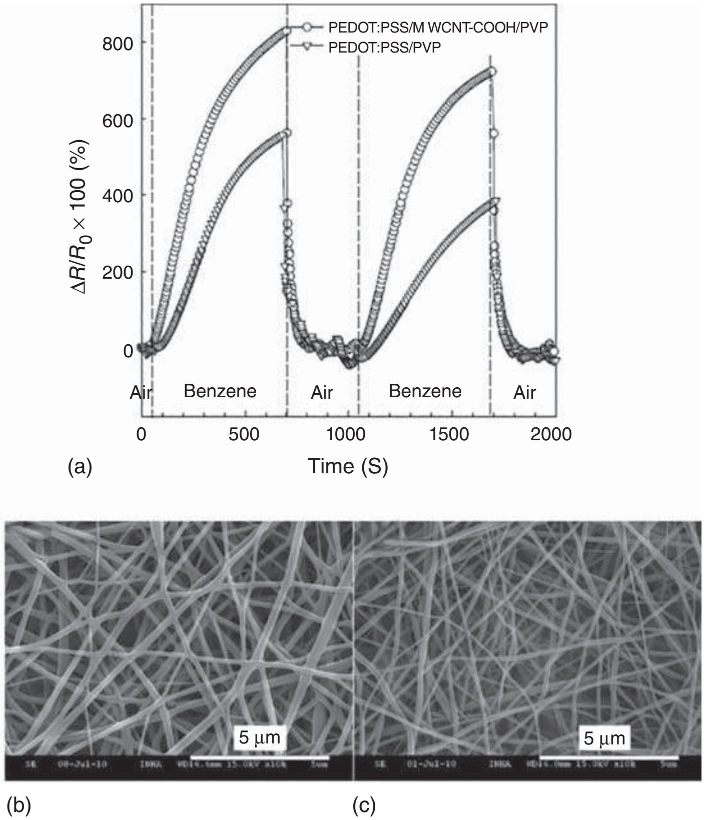

Figure 3.9 (a) Response upon cyclic exposure to benzene vapor at room temperature and (b, c) SEM images of electrospun PEDOT:PSS/carbon nanotubes/polymer composite nanofibers and PEDOT:PSS/PVP nanofibers, respectively. Source: Adapted with permission from [78]. Copyright 2012, Elsevier.

for the electrospun nanofibers especially with benzene, which was based on the possible swelling of the electrospun nanofibers, the molar volume, and the ppm concentration of the aromatic VOCs (Figure 3.9).

In other hand, electrospun PEDOT:PSS/PVP fibers were also fabricated by electrospinning and used as a quartz crystal microbalance (QCM) sensor for detecting CO gas (5–50 ppm) by Zhang et al. [79]. Indeed, the size effect of nanofibers makes the PEDOT:PSS/PVP more comprehensive as organic vapor/gas sensor, but also on solar cells and electronic devices. Schrote and Frey [80] proposed the fabrication of a highly sensitive sensor for radiation detection using conducting nanofibers of PEDOT:PSS/PVA (polyvinyl alcohol) by electrospinning. The nanofibers, with diameters ranging from 100 to 300 nm, exhibit a much faster change in conductivity after exposed in X-ray irradiation than fibers exposed to γ irradiation. The decrease in of the molecular ordering of PEDOT chains demonstrates a breakdown in the intrachain interactions leading to the favoring of polaron formation, which is a very known mechanism for change in conductivity. A blend of plasma-modified chitosan and PEDOT was reported by Kiristi et al. [81] to obtain conducting nanofibers using PVA as a supporting polymer by electrospinning method. The electrospun plasma-modified chitosan (PMCh)/PVA/PEDOT blend showed an average fiber diameter of 170–200 nm and good activity against Gram positive bacteria, suggesting the blend for biomedical applications. Zhao et al. [82] reported the process of fabrication of PEDOT:PSS by using a very small amount of very high molecular weight poly(ethylene oxide) (PEO) that provides stability in electrospinning process without interfering the percolation path. They obtained nanofibers with 297–432 nm of diameter and high conductivity of 35.5 S/cm. Zarrin et al. [83] reported the fabrication of conductive PEDOT nanofibers through electrospinning assisted by poly(acrylic acid) (PAA). The homogeneous film, with an amorphous structure and fibers with 300 nm of diameter, showed an electrical conductivity of 0.16 S/cm for a proportion of 50 : 50 of PEDOT:PAA. Marega and Saini [84] studied the effect of introduce the conducting polymer PPy into a blend with PEO. They observed the conductivity increases from 0.03 to 8.9 and 13.1 S/cm $\times (10^{-6})$ in the fibers containing 30% and 50% of Py monomer. This improvement was correlated with the morphology of the electrospun nanofibers, which may have oriented conductive Py molecules along the longitudinal direction of fibers, increasing their charge-carrier mobility.

Bounioux et al. [85] demonstrated that tuning of the rheology of native solutions of poly(3-octyl thiophene) (P3OT) via the use of a solvent mixture and optimization of the concentration of the polymer solution facilitates electrospinning of well-shaped microfibers in a single step of the polymer and CNTs hybrids. In addition, they showed that P3OT-CNT dispersions may be used for a single step electrospinning of well-shaped functional fibers simplifying the process as compared with previously reported. The high degree of crystallinity of P3OT-CNT hybrids as compared with the native polymer fibers suggesting that the hybrid fibers should exhibit improved charge carrier mobility and light absorption at a broad spectral range and thus may be valuable components for photoactive materials and smart textiles applications. Pierini et al. [86] highlighted that the mechanical and electrical properties of electrospun P3HT (poly(3-hexylthiophene))/PEO/GO (graphite oxide) can be modulated by filling the fibers with well-dispersed and oriented GO nanosheets and by modifying the GO reduction level. Their results show that the crystallinity and the P3HT chains orientation as well as the mechanical properties of the nanofibers could be tuned by adding GO into the fibers.

3.2.3 Vapor Phase Polymerization

A convenient route to produce thin films using both soluble and insoluble conducting polymers is the vapor phase polymerization. This technique offers a fast and facile production of pure, uniform, and highly conducting polymer thin films on a wide range of substrate materials and polymers, such as PPy, PANI, PEDOT, etc. The technique involves heating the monomer under either atmospheric or reduced pressure conditions, which, in turn, forms a vapor. The monomer vapor then undergoes condensation onto a substrate containing an oxidant layer where polymerization is

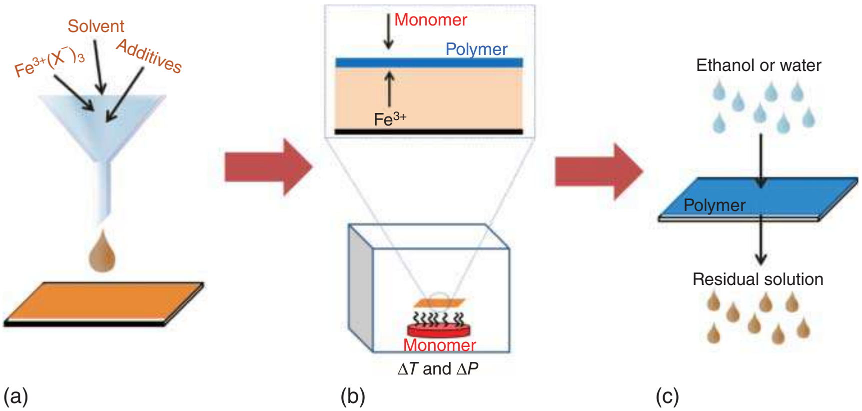

Figure 3.10 Illustration of the steps of vapor phase polymerization method: (a) deposition of the oxidant solution onto the substrate, (b) exposure of this substrate to the condensed vapor of the desired monomer for polymerization at controlled conditions of temperature and pressure, and (c) washing step to remove the excess of oxidant and monomer from the polymer film. Source: Brooke et al. [87]. Copyright 2017, Elsevier.

initiated resulting in film formation (Figure 3.10). The vapor phase polymerization overcomes problems associated with performance and processability due to insolubility of the conducting polymers. For this reason, the technique has gained strong interest among the researchers for producing high-conductivity and/or high optically transparent conducting polymers by a simpler, faster, and tunable process way.

The polymerization of conducting polymer by vapor phase has been primarily conducted using iron salts as oxidants, mainly $FeCl_3$ and $Fe(Tos)_3$ [88–94]. Brooke et al. [95, 96] synthesized by vapor phase polymerization EDOT and pyrrole polymers using $FeCl_3$ and $Fe(Tos)_3$ as oxidant and different chambers parameters. The electrical conductivity of 4500 S/cm and optical transparency of the optimized PEDOT:OTf rivaled that of commercially transparent metal oxides with an acceptable electrochemical stability, thus suggesting their use as a transparent electrode in optoelectronic devices. Jia et al. [97, 98] reported the use of different additives to improve the thermoelectric properties of PEDOT films. The vapor phase polymerized PEDOT films mixed with ethylene glycol as solvent and 1-butyl-3-menthylinidazolium tetrafluoroborate as additive displayed the high power factor of $45.3\,\mu W/(m\,K^2)$, which is 122% higher than that prepared without any additive or post-treatment solvent, along with enhanced electrical conductivity. Indeed, the authors obtained a highly conductive PEDOT film when, after the vapor phase polymerization, a H_2SO_4 post-treatment was applied. In order to enhance the thermopower of the PEDOT, a novel strategy using polyethylenimine as an effective reducing agent was also employed. It was demonstrated that the thermopower of well-ordered crystallites in PEDOT films significantly increases more than five times, from 11 to $59\,\mu V/K$ by using the reducing agent in dimethylformamide solution.

PEDOT based composites were polymerized by vapor phase polymerization by Jones and co-authors [99–101] for applications as supercapacitors and electronic

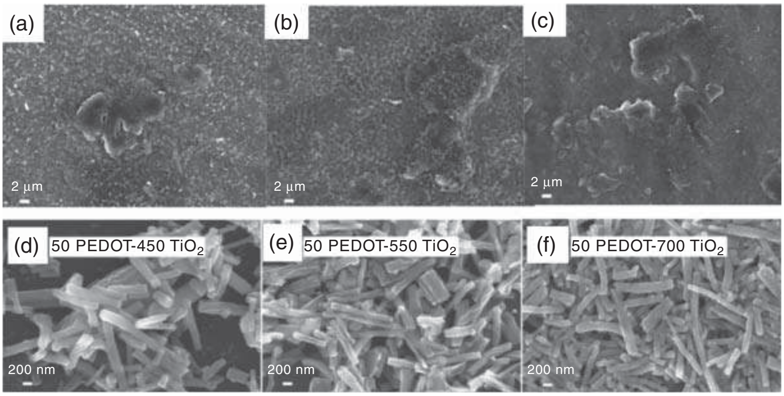

Figure 3.11 SEM images of vapor phase polymerized PEDOT on carbon coated aluminum foil prepared under different temperatures: (a) 60 °C, (b) 80 °C, and (c) 110 °C, and when TiO_2 was used as substrate by different preparation methods for calcination: (d) 450 °C, (e) 550 °C, and (f) 700 °C in air for four hours. Source: Adapted with permission from [99] and [100]. Copyright 2017, Elsevier.

devices (Figure 3.11). Using a highly conductive commercial carbon coated aluminum foil as substrate, the PEDOT based composite can be used as electrode materials directly without adding current collector. By this simple and efficient process, PEDOT based composites exhibit specific capacitance up to 134 F/g with the polymerization temperature of 110 °C. In other hand, when TiO_2 fibers were prepared as substrates for the PEDOT vapor phase polymerization process, the highest specific capacitance was 88 F/g at 50 °C. Indeed, flexible and transparent PEDOT films with an electrical conductivity >1000 S/cm were produced by vapor phase polymerization. The choice of cationic oxidant initiator and anionic dopant has a significant effect on film morphology, optical absorption, and conductivity.

A new one-step protocol for synthesizing nanostructured PEDOT and its metal-oxide composites is proposed by a hydrolysis-assisted vapor phase polymerization strategy by Wang et al. [93]. Here, the control of the hydrolysis of an inorganic salt with simultaneous polymerization of a conducting polymer drives the growth of hybrid nanostructures from 1D nanofibers to 2D nanoflowers and nanostructures from monolithic to core–shell. The structure–property relationship is discussed based on the capacitance of PEDOT with different morphologies: 1D fibrillar structure shows a higher capacitance compared to 2D nanoflowers because this morphology enhances electrolyte diffusion kinetics that facilitates PEDOT doping and dedoping. The same group reported the polymerization by vapor phase of pyrrole for potential application as energy store and supercapacitors forming different structures (Figure 3.12) [102, 103]. Microtubular structures were obtained by a novel condensing vapor phase polymerization strategy deposit on porous substrates such as hard carbon fiber paper or glass fiber filter paper with a capacitance of 342 F/g. Water vapor condensation and polymerization occur simultaneously water droplets act as structure-directing templates for the formation of PPy microtubes. In contrast, nanofibrillar structures resembling nanobrushes

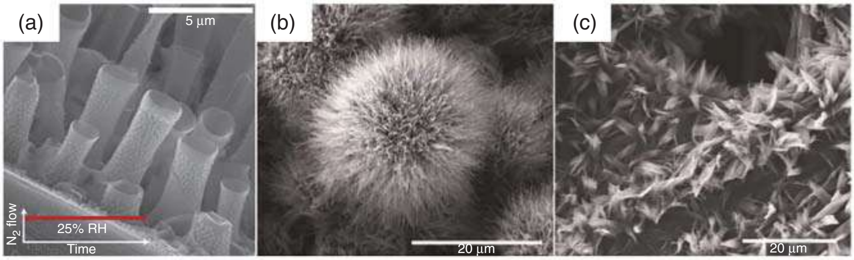

Figure 3.12 SEM images of the vapor phase polymerized PPy generating structures as (a) microtubes and (b, c) nanobrushes. Source: Adapted with permission from [102] and [103]. Copyright 2017, American Chemical Society and 2017, Royal Society of Chemistry.

of PPy were deposited by the same technique at low temperatures (50 °C). With a capacitance of 144.7 F/g and high reversibility in 1 M $LiClO_4$, these nanobrushes increase the electrolyte accessible surface area as well as ease swelling effects induced by oxidation and solvated counter ions, being well addressed for storing electrochemical energy.

Ala et al. [104] fabricated electrically conductive textiles via vapor phase polymerization of PEDOT film on cotton, cotton/polyethylene terephthalate (PET), cotton/Lycra, and PET fabrics. Conducting polymers were also deposited in a cotton towel and corduroy fabric as described by Cheng et al. [105]. Patel et al. [106] demonstrating the effect of two processing methods on the thermoelectric properties of thin films of poly(2,5-bis(3-tetradecylthiophen-2-yl)thieno[3,2-*b*]thiophene) (PBTTT). They observed that thin films doped by vapor phase polymerization yield α values that are a factor of 2 higher than the films produced by immersion in a solvent containing 4-ethylbenzenesulfonic acid at comparable high value of σ. The vapor phase polymerized PBTTT films yield a high conductivity and a large power factor of $\sim$100 $\mu W/(m\,K^2)$.

3.2.4 Plasma Polymerization

As well as vapor phase polymerization, plasma polymerization is an attractive dry deposition technique because it can quickly deposit strongly adherent films without requiring the use of solvents and additives from different monomers precursors. The properties of the deposited film can be easily controlled using the plasma parameters, such as power, gas flow, and pressure. In addition, plasma polymerization processes are faster compared with the traditional techniques that demand multistep processes. The advantage of this technique is that the film is formed from reactions in the gas phase, which propagates and deposits on the surface. Hereafter, the monomer reacts to produce the polymer without introducing any chemical oxidant compound and the oxidation is promoted by the impact of the free electrons that travel along the electric field in which the monomer molecules collide.

Polyfuran spherical particles were synthesized by plasma polymerization with average diameter increasing linearly from 172 to 456 nm with 2.91 nm/W growth rate and a hydrophilic behavior (contact angle from 52° to 92°) [107, 108]. The conductivity of polyfuran particles is very low, from 10^{-9} to 10^{-11} S/cm, in the region of non-conductor materials, maybe because of a high contact resistance among particles, which rule the transference of charges, but the activation energy is located in the interval of organic semiconductors. PPy films deposited by plasma polymerization were carried out under different radio frequency power and pyrrole flow rates [109, 110]. The authors verified that lower radio frequency power, such as 10 W, can improve the electrical conduction. However, a noticeable enhancement in conduction is achieved by the I_2 doping which reduces the electrical resistance of the film to almost half of other un-doped pyrrole films. Plasma polymerized PPy doped with I_2 was used to coat polycaprolactone scaffolds to improve cellular adhesion and fibroblast proliferation [111]. In this work, the authors described the characterization of the nanofibers (diameter between 290 and 530 nm) and the results show that the scaffolds modified with plasma polymerized pyrrole provide a suitable environment for fibroblast adhesion, growth, and viability.

Nanostructured plasma polymerized PANI were described by Park et al. [112–114]. The preparation of nanofibers and nanoparticles were done by an intense plasma cloud type atmospheric pressure plasma jets device with a single bundle of three glass tubes. With a molecular weight of 533 kDa and a polydispersity index of 1.9, the nanosized particles were successfully synthesized on the glass, plastic, and interdigitated gas sensor electrode substrates using novel atmospheric pressure plasma jets (APPJs) at room temperature [113]. Indeed, the authors also studied the effect of I_2 doping on PANI films. When increasing the I_2 doping time, a decrease in the width and thickness of the PANI nanofibers is observed while the roughness and grain size of the PANI films increased (Figure 3.13).

Hussain et al. [115] synthesized PANI/CNT composites to be tested for supercapacitor applications in 0.2 M Na_2SO_4 electrolyte solution. An improved capacitance was obtained when the polymer layer was applied by plasma polymerization from 12 to 1225 F/g at a scan rate of 5 mV/s. Composites of multi-walled CNTs with P3HT and PPy were synthesized by plasma polymerization [116]. The obtained composites were used as counter electrodes in DSSC that exhibited power conversion efficiencies of 1.24% and 0.80% and a short circuit current densities of 5.61 and 4.19 mA/cm^2 for the P3HT/multi-walled carbon nanotubes (MWCNTs) and PPy/MWCNT-based cells, respectively.

A biosensor based on the plasma polymerized PANI/tin oxide/reduced graphene oxide nanocomposite was fabricated by Wu et al. [117] to detect glucose. This method takes advantage of both the high-affinity adsorption of glucose oxidase and the relatively good electrochemical activity of the nanocomposite. The fabricated biosensor exhibited a high detection limit of 0.047 ng/ml, good reproducibility, and real application. Antonio-Carmona et al. [118] described the copolymerization of pyrrole and aniline on the surface of polyurethane (PU) foams by the plasma polymerization method using different parameters. Homogeneous sheet and spherical nanostructures of PPy-*co*-PANI coating PU can be obtained through this polymer-

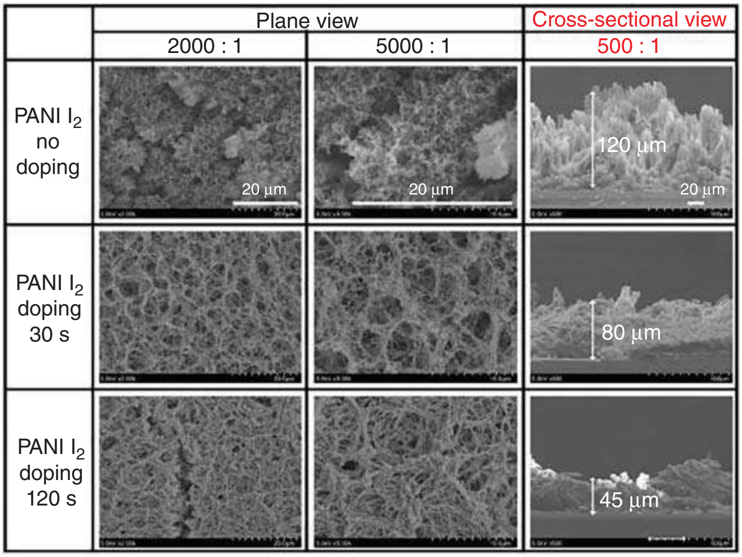

Figure 3.13 SEM images of plasma polymerized PANI films grown on glass substrates after 30 minutes deposition without I_2, with 30 seconds I_2 doping and with 120 seconds of I_2 doping following deposition. Plane images in left and middle; cross-sectional images in right. Source: Adapted with permission from [112]. Copyright 2017, Molecular Diversity Preservation International.

ization method to use as supports for microorganism immobilization and tested in municipal wastewater treatment in anaerobic batch and continuous packed-bed reactors. The composite with the best chemical oxygen demand (COD) removal efficiency during the batch wastewater treatment at 48 hours was that obtained at 50 W and 30 minutes, which was associated to the polymers morphology deposited onto the PU foam surface. It was observed that in the continuous wastewater treatment at 54 hours of hydraulic retention time, 76% of COD removal can be achieved.

3.3 Conclusions

In this book chapter, most of the reviewed articles dedicated to the synthesis of conducted polymers using a templateless fashion are described presenting the advantages and disadvantages of this approach. In the literature, a wide range of template-free techniques have been developed to synthesize conducting polymers such as electropolymerization, electrospinning, plasma polymerization, vapor phase polymerization, and so on. Such approaches offer a powerful and a cost-effective way to generate uniform and structured conducting polymer-based materials in a scalable and reproducible process for numerous and practical applications.

References

1 Shirakawa, H., Louis, E., MacDiarmid, A.G. et al. (1977). Synthesis of electrically conducting organic polymers: halogen derivatives of polyacetylene, $(CH)_x$. *J. Chem. Soc. Chem. Commun.* 16: 578–580.

2 The Nobel Prize. (2000). The Nobel Prize in Chemistry 2000. https://www.nobelprize.org/nobel_prizes/chemistry/laureates/2000/ (accessed 14 August 2020) (n.d.).

3 Jang, J. (2006). Conducting polymer nanomaterials and their applications. *Adv. Polym. Sci.* 199: 189–259. https://doi.org/10.1007/12_075.

4 Li, C., Bai, H., and Shi, G. (2009). Conducting polymer nanomaterials: electrosynthesis and applications. *Chem. Soc. Rev.* 38: 2397–2409. https://doi.org/10.1039/b816681c.

5 Ghosh, S., Maiyalagan, T., and Basu, R.N. (2016). Nanostructured conducting polymers for energy applications: towards a sustainable platform. *Nanoscale* 8: 6921–6947. https://doi.org/10.1039/c5nr08803h.

6 Xia, L., Wei, Z., and Wan, M. (2010). Conducting polymer nanostructures and their application in biosensors. *J. Colloid Interface Sci.* 341: 1–11. https://doi.org/10.1016/j.jcis.2009.09.029.

7 Darmanin, T. and Guittard, F. (2014). Wettability of conducting polymers: from superhydrophilicity to superoleophobicity. *Prog. Polym. Sci.* 39: 656–682. https://doi.org/10.1016/j.progpolymsci.2013.10.003.

8 Darmanin, T., De Givenchy, E.T., Amigoni, S., and Guittard, F. (2013). Superhydrophobic surfaces by electrochemical processes. *Adv. Mater.* 25: 1378–1394. https://doi.org/10.1002/adma.201204300.

9 Sabouraud, G., Sadki, S., and Brodie, N. (2000). The mechanisms of pyrrole electropolymerization. *Chem. Soc. Rev.* 29: 283–293. https://doi.org/10.1039/a807124a.

10 Bellanger, H., Darmanin, T., de Givenchy, E.T., and Guittard, F. (2013). Influence of long alkyl spacers in the elaboration of superoleophobic surfaces with short fluorinated chains. *RSC Adv.* 3: 5556. https://doi.org/10.1039/c3ra40302e.

11 Karami, H., Asadi, M.G., and Mansoori, M. (2012). Pulse electropolymerization and the characterization of polyaniline nanofibers. *Electrochim. Acta* 61: 154–164. https://doi.org/10.1016/j.electacta.2011.11.097.

12 Çaglar, A., Cengiz, U., Yildirim, M., and Kaya, İ. (2015). Effect of deposition charges on the wettability performance of electrochromic polymers. *Appl. Surf. Sci.* 331: 262–270. https://doi.org/10.1016/j.apsusc.2015.01.103.

13 Wolfs, M., Darmanin, T., and Guittard, F. (2011). Versatile superhydrophobic surfaces from a bioinspired approach. *Macromolecules* 44: 9286–9294.

14 Poverenov, E., Li, M., Bitler, A., and Bendikov, M. (2010). Major effect of electropolymerization solvent on morphology and electrochromic properties of PEDOT films. *Chem. Mater.* 22: 4019–4025. https://doi.org/10.1021/cm100561d.

15 Valle, M.A., Cury, P., and Schrebler, R. (2002). Solvent effect on the nucleation and growth mechanisms of poly(thiophene). *Electrochim. Acta* 48: 397–405.

16 Bellanger, H., Darmanin, T., Taffin de Givenchy, E., and Guittard, F. (2013). Influence of intrinsic oleophobicity and surface structuration on the superoleophobic properties of PEDOP films bearing two fluorinated tails. *J. Mater. Chem. A* 1: 2896. https://doi.org/10.1039/c2ta00517d.

17 Ocón, P., Herrasti, P., and Rojas, S. (2001). Galvanostatic and pulse potential synthesis of poly-3-methylthiophene. Polymer as catalytic support. *Polymer (Guildf)* 42: 2439–2448. https://doi.org/10.1016/S0032-3861(00)00577-2.

18 Luo, S.-C., Sekine, J., Zhu, B. et al. (2012). Polydioxythiophene nanodots, nanowires, nano-networks, and tubular structures: the effect of functional groups and temperature in template-free electropolymerization. *ACS Nano* 6: 3018–3026.

19 Martins, J.I., Bazzaoui, M., Reis, T.C. et al. (2009). The effect of pH on the pyrrole electropolymerization on iron in malate aqueous solutions. *Prog. Org. Coatings* 65: 62–70. doi:https://doi.org/10.1016/j.porgcoat.2008.09.011.

20 Godeau, G., N'Na, J., Darmanin, T., and Guittard, F. (2015). Azidomethyl-EDOT as a platform for tunable surfaces with nanostructures and superhydrophobic properties. *J. Phys. Chem. B* 119: 6873–6877. https://doi.org/10.1021/acs.jpcb.5b03462.

21 Darmanin, T. and Guittard, F. (2015). Highly polar linkers (urea, carbamate, thiocarbamate) for superoleophobic/superhydrophobic or oleophobic/hydrophilic properties. *Adv. Mater. Interfaces* 2: 1500081/1–1500081/7. https://doi.org/10.1002/admi.201500081.

22 Godeau, G., Guittard, F., and Darmanin, T. (2016). Nucleoside surfaces as a platform for the control of surface hydrophobicity. *RSC Adv.* 6: 62471–62477. https://doi.org/10.1039/C6RA10149F.

23 Mortier, C., Darmanin, T., and Guittard, F. (2017). Direct electrodeposition of superhydrophobic and highly oleophobic poly(3,4-ethylenedioxypyrrole) (PEDOP) and poly(3,4-propylenedioxypyrrole) (PProDOP) nanofibers. *ChemNanoMat* 3: 885–894. https://doi.org/10.1002/cnma.201700236.

24 Mortier, C., Darmanin, T., and Guittard, F. (2015). A bioinspired approach to produce parahydrophobic properties using PEDOP conducting polymers with branched alkyl chains. *Pure Appl. Chem.* 87: 805–814. https://doi.org/10.1515/pac-2015-0104.

25 Mortier, C., Darmanin, T., and Guittard, F. (2018). Major influence of the hydrophobic chain length in the formation of poly(3,4-propylenedioxypyrrole) (PProDOP) nanofibers with special wetting properties. *Mater. Today Chem.* 7: 65–75. https://doi.org/10.1016/j.mtchem.2018.01.003.

26 Chagas, G.R., Darmanin, T., and Guittard, F. (2015). Nanostructured superhydrophobic films synthesized by electrodeposition of fluorinated polyindoles. *Beilstein J. Nanotechnol.* 6: 2078–2087. https://doi.org/10.3762/bjnano.6.212.

27 Zang, J., Li, C.M., Bao, S.J. et al. (2008). Template-free electrochemical synthesis of superhydrophilic polypyrrole nanofiber network. *Macromolecules* 41: 7053–7057. https://doi.org/10.1021/ma801345k.

28 Qu, L., Shi, G., Chen, F., and Zhang, J. (2003). Electrochemical growth of polypyrrole microcontainers. *Macromolecules* 36: 1063–1067.

29 Yuan, J., Qu, L., Zhang, D., and Shi, G. (2004). Linear arrangements of polypyrrole microcontainers. *Chem. Commun.* 8: 994–995.

30 Qu, L., Shi, G., Yuan, J. et al. (2004). Preparation of polypyrrole microstructures by direct electrochemical oxidation of pyrrole in an aqueous solution of camphorsulfonic acid. *J. Electroanal. Chem.* 561: 149–156. https://doi.org/10.1016/j.jelechem.2003.07.028.

31 Parakhonskiy, B. and Shchukin, D. (2015). Polypyrrole microcontainers: electrochemical synthesis and characterization. *Langmuir* 31: 9214–9218. https://doi.org/10.1021/acs.langmuir.5b01931.

32 Parakhonskiy, B., Andreeva, D., Helmuth, M., and Shchukin, D.G. (2009). Hollow polypyrrole containers with regulated uptake/release properties. *Langmuir* 25: 4780–4786. https://doi.org/10.1021/la804002x.

33 Kim, J.T., Seol, S.K., Je, J.H. et al. (2009). The microcontainer shape in electropolymerization on bubbles. *Appl. Phys. Lett.* 94: 34103.

34 Debiemme-Chouvy, C. (2009). Template-free one-step electrochemical formation of polypyrrole nanowire array. *Electrochem. Commun.* 11: 298–301. https://doi.org/10.1016/j.elecom.2008.11.030.

35 Fakhry, A., Pillier, F., and Debiemme-Chouvy, C. (2014). Templateless electrogeneration of polypyrrole nanostructures: impact of the anionic composition and pH of the monomer solution. *J. Mater. Chem. A* 2: 9859–9865. https://doi.org/10.1039/c4ta01360c.

36 Fakhry, A., Cachet, H., and Debiemme-Chouvy, C. (2015). Mechanism of formation of templateless electrogenerated polypyrrole nanostructures. *Electrochim. Acta* 179: 297–303. https://doi.org/10.1016/j.electacta.2015.03.025.

37 Debiemme-Chouvy, C., Fakhry, A., and Pillier, F. (2018). Electrosynthesis of polypyrrole nano/micro structures using an electrogenerated oriented polypyrrole nanowire array as framework. *Electrochim. Acta* 268: 66–72. https://doi.org/10.1016/j.electacta.2018.02.092.

38 Szczepanski, C.R., M'Jid, I., Darmanin, T. et al. (2016). A template-free approach to nanotube-decorated polymer surfaces using 3,4-phenylenedioxythiophene (PhEDOT) monomers. *J. Mater. Chem. A* 4: 17308–17323. https://doi.org/10.1039/C6TA07639D.

39 Darmanin, T. and Guittard, F. (2016). A one-step electrodeposition of homogeneous and vertically aligned nanotubes with parahydrophobic properties (high water adhesion). *J. Mater. Chem. A* 4: 3197–3203. https://doi.org/10.1039/C5TA09253A.

40 Gbilimou, A., Darmanin, T., Godeau, G., and Guittard, F. (2018). A templateless electropolymerization approach to nanorings using substituted 3,4-naphthalenedioxythiophene (NaPhDOT) monomers. *ChemNanoMat* 4: 140–147. https://doi.org/10.1002/cnma.201700269.

41 Ramos Chagas, G., Darmanin, T., Godeau, G., and Guittard, F. (2018). Nanocups and hollow microspheres formed by a one-step and templateless electropolymerization of thieno[3,4-*b*]thiophene derivatives as a function of the substituent. *Electrochim. Acta* 269: 462–478. https://doi.org/10.1016/j.electacta.2018.03.036.

42 Ramos Chagas, G., Darmanin, T., and Guittard, F. (2016). One-step and templateless electropolymerization process using thienothiophene derivatives to develop arrays of nanotubes and tree-like structures with high water adhesion. *ACS Appl. Mater. Interfaces* 8: 22732–22743. https://doi.org/10.1021/acsami.6b08536.

43 Ramos Chagas, G., Akbari, R., Godeau, G. et al. (2017). Electrodeposited poly(thieno[3,2-*b*]thiophene) films for the templateless formation of porous structures by galvanostatic and pulse deposition. *ChemPlusChem* 82: 1351–1358. https://doi.org/10.1002/cplu.201700389.

44 Darmanin, T., Laugier, J.P., Orange, F., and Guittard, F. (2016). Influence of the monomer structure and electrochemical parameters on the formation of nanotubes with parahydrophobic properties (high water adhesion) by a templateless electropolymerization process. *J. Colloid Interface Sci.* 466: 413–424. https://doi.org/10.1016/j.jcis.2015.12.029.

45 Darmanin, T. and Guittard, F. (2017). The major influence of the substrate nature on the formation of nanotubes with high water adhesion using a templateless electropolymerization process. *Synth. Met.* 224: 99–108. https://doi.org/10.1016/j.synthmet.2016.12.018.

46 Xu, L., Tong, F., Lu, X. et al. (2015). Multifunctional polypyrene/silica hybrid coatings with stable excimer fluorescence and robust superhydrophobicity derived from electrodeposited polypyrene films. *J. Mater. Chem. C* 3: 2086–2092. https://doi.org/10.1039/C4TC02653E.

47 Ramos Chagas, G., Morán Cruz, G., Méallet-Renault, R. et al. (2019). Superhydrophobic and fluorescent properties of fluorinated polypyrene surfaces using various polar linkers prepared via electropolymerization. *React. Funct. Polym.* 135: 65–76. https://doi.org/10.1016/j.reactfunctpolym.2018.12.001.

48 Ramos Chagas, G., Xie, X., Darmanin, T. et al. (2016). Electrodeposition of polypyrenes with tunable hydrophobicity, water adhesion, and fluorescence properties. *J. Phys. Chem. C* 120: 7077–7087. https://doi.org/10.1021/acs.jpcc.5b11586.

49 Ramos Chagas, G., Darmanin, T., Godeau, G. et al. (2017). Superhydrophobic properties of electrodeposited fluorinated polypyrenes. *J. Fluorine Chem.* 193: 73–81. https://doi.org/10.1016/j.jfluchem.2016.11.019.

50 Ramos Chagas, G., Morán Cruz, G., Giraudon-Colas, G. et al. (2018). Anti-bacterial and fluorescent properties of hydrophobic electrodeposited non-fluorinated polypyrenes. *Appl. Surf. Sci.* 452: 352–363. https://doi.org/10.1016/j.apsusc.2018.04.268.

51 Raufaste, C., Ramos Chagas, G., Darmanin, T. et al. (2017). Superpropulsion of droplets and soft elastic solids. *Phys. Rev. Lett.* 119: 108001. https://doi.org/10.1103/PhysRevLett.119.108001.

52 Ramos Chagas, G., Celestini, F., Raufaste, C. et al. (2018). Experimental characterization of droplet adhesion: the ejection test method (ETM) applied to surfaces with various hydrophobicity. *J. Phys. Chem. A* 122: 8693–8700. https://doi.org/10.1021/acs.jpca.8b08037.

53 Ramos Chagas, G., Fradin, C., Celestini, F. et al. (2019). Dynamic wetting properties of mesh substrates with tunable water adhesion. *ChemPhysChem* 20 https://doi.org/10.1002/cphc.201900443.

54 Ramos Chagas, G., Kiryanenko, D., Godeau, G. et al. (2017). pH-driven wetting switchability of electrodeposited superhydrophobic copolymers of pyrene bearing acid functions and fluorinated chains. *ChemPhysChem* 18: 3429–3436.

55 Darmanin, T. and Guittard, F. (2013). pH- and voltage-switchable superhydrophobic surfaces by electro-copolymerization of EDOT derivatives containing carboxylic acids and long alkyl chains. *ChemPhysChem* 14: 2529–2533. https://doi.org/10.1002/cphc.201300283.

56 Taleb, S., Darmanin, T., and Guittard, F. (2014). Elaboration of voltage and ion exchange stimuli-responsive conducting polymers with selective switchable liquid-repellency. *ACS Appl. Mater. Interfaces* 6: 7953–7960. https://doi.org/10.1021/am501279h.

57 Morán, G., Ramos Chagas, G., Hugelier, S. et al. (2018). Superhydrophobic polypyrene films to prevent *Staphylococcus aureus* and *Pseudomonas aeruginosa* biofilm adhesion on surfaces: high efficiency deciphered by fluorescence microscopy. *Photochem. Photobiol. Sci.* 17: 1023–1035. https://doi.org/10.1039/c8pp00043c.

58 Bruzaud, J., Tarrade, J., Celia, E. et al. (2017). The design of superhydrophobic stainless steel surfaces by controlling nanostructures: a key parameter to reduce the implantation of pathogenic bacteria. *Mater. Sci. Eng., C* 73: 40–47. https://doi.org/10.1016/j.msec.2016.11.115.

59 Saugo, M., Brugnoni, L.I., Flamini, D.O., and Saidman, S.B. (2018). Immobilization of antibacterial metallic cations (Ga^{3+}, Zn^{2+} and Co^{2+}) in a polypyrrole coating formed on Nitinol. *Mater. Sci. Eng., C* 86: 62–69. https://doi.org/10.1016/j.msec.2018.01.009.

60 Saugo, M., Flamini, D.O., Brugnoni, L.I., and Saidman, S.B. (2015). Silver deposition on polypyrrole films electrosynthesised onto Nitinol alloy. Corrosion protection and antibacterial activity. *Mater. Sci. Eng., C* 56: 95–103. https://doi.org/10.1016/j.msec.2015.06.014.

61 Flamini, D.O., Valle, M.I., Sandoval, M.J. et al. (2018). Electrodeposition study of polypyrrole-heparin and polypyrrole-salicylate coatings on Nitinol. *Mater. Chem. Phys.* 209: 76–85. https://doi.org/10.1016/j.matchemphys.2018.01.065.

62 Jiang, L., Syed, J.A., Lu, H., and Meng, X. (2019). In-situ electrodeposition of conductive polypyrrole-graphene oxide composite coating for corrosion protection of 304SS bipolar plates. *J. Alloys Compd.* 770: 35–47. https://doi.org/10.1016/j.jallcom.2018.07.277.

63 Jiang, L., Syed, J.A., Gao, Y. et al. (2017). Electropolymerization of camphorsulfonic acid doped conductive polypyrrole anti-corrosive coating for 304SS bipolar plates. *Appl. Surf. Sci.* 426: 87–98. https://doi.org/10.1016/j.apsusc.2017.07.077.

64 Ren, Y.J., Chen, J., Zeng, C.L. et al. (2016). Electrochemical corrosion characteristics of conducting polypyrrole/polyaniline coatings in simulated environments of a proton exchange membrane fuel cell. *Int. J. Hydrogen Energy* 41: 8542–8549. https://doi.org/10.1016/j.ijhydene.2016.03.184.

65 Wen, P., Zong, M.-H., Linhardt, R.J. et al. (2017). Electrospinning: a novel nano-encapsulation approach for bioactive compounds. *Trends Food Sci. Technol.* 70: 56–68. https://doi.org/10.1016/j.tifs.2017.10.009.

66 Mendes, A.C., Stephansen, K., and Chronakis, I.S. (2017). Electrospinning of food proteins and polysaccharides. *Food Hydrocolloids* 68: 53–68. https://doi.org/10.1016/j.foodhyd.2016.10.022.

67 Ghorani, B. and Tucker, N. (2015). Fundamentals of electrospinning as a novel delivery vehicle for bioactive compounds in food nanotechnology. *Food Hydrocolloids* 51: 227–240. https://doi.org/10.1016/j.foodhyd.2015.05.024.

68 Reneker, D.H., Yarin, A.L., Fong, H., and Koombhongse, S. (2000). Bending instability of electrically charged liquid jets of polymer solutions in electrospinning. *J. Appl. Phys.* 87: 4531–4547.

69 Yarin, A.L., Koombhongse, S., and Reneker, D.H. (2001). Bending instability in electrospinning of nanofibers. *J. Appl. Phys.* 89: 3018–3026.

70 Soares, R.M.D., Siqueira, N.M., Prabhakaram, M.P., and Ramakrishna, S. (2018). Electrospinning and electrospray of bio-based and natural polymers for biomaterials development. *Mater. Sci. Eng., C* 92: 969–982. https://doi.org/10.1016/j.msec.2018.08.004.

71 Nieuwland, M., Geerdink, P., Brier, P. et al. (2013). Food-grade electrospinning of proteins. *Innovative Food Sci. Emerg. Technol.* 20: 269–275. https://doi.org/10.1016/j.ifset.2013.09.004.

72 Peng, S., Zhu, P., Wu, Y. et al. (2012). Electrospun conductive polyaniline–polylactic acid composite nanofibers as counter electrodes for rigid and flexible dye-sensitized solar cells. *RSC Adv.* 2: 652–657. https://doi.org/10.1039/c1ra00618e.

73 Elayappan, V., Murugadoss, V., Angaiah, S. et al. (2015). Development of a conjugated polyaniline incorporated electrospun poly(vinylidene fluoride-*co*-hexafluoropropylene) composite membrane electrolyte for high performance dye-sensitized solar cells. *J. Appl. Polym. Sci.* 42777: 1–8. https://doi.org/10.1002/app.42777.

74 Simotwo, S.K., DelRe, C., and Kalra, V. (2016). Supercapacitor electrodes based on high-purity electrospun polyaniline and polyaniline–carbon nanotube nanofibers. *ACS Appl. Mater. Interfaces* 8: 21261–21269.

75 Khalifa, M., Mahendran, A., and Anandhan, S. (2019). Durable, efficient, and flexible piezoelectric nanogenerator from electrospun PANi/HNT/PVDF blend nanocomposite. *Polym. Compos.* 40: 1663–1675. https://doi.org/10.1002/pc.24916.

76 Chen, Y., Li, C., Hou, Z. et al. (2015). Polyaniline electrospinning composite fibers for orthotopic photothermal treatment of tumors in vivo. *New J. Chem.* 39: 4987–4993. https://doi.org/10.1039/c5nj00327j.

77 Choi, J., Lee, J., Choi, J. et al. (2010). Electrospun PEDOT:PSS/PVP nanofibers as the chemiresistor in chemical vapour sensing. *Synth. Met.* 160: 1415–1421. https://doi.org/10.1016/j.synthmet.2010.04.021.

78 Choi, J., Park, D.W., and Shim, S.E. (2012). Electrospun PEDOT:PSS/carbon nanotubes/PVP nanofibers as chemiresistors for aromatic volatile organic compounds. *Synth. Met.* 162: 1513–1518. https://doi.org/10.1016/j.synthmet.2012.06.028.

79 Zhang, H.-D., Yan, X., Zhang, Z.-H. et al. (2016). Electrospun PEDOT:PSS/PVP nanofibers for CO gas sensing with quartz crystal microbalance technique. *Int. J. Polym. Sci.* 2016: 1–6.

80 Schrote, K. and Frey, M.W. (2013). Effect of irradiation on poly(3,4-ethylenedioxythiophene): poly(styrenesulfonate) nanofiber conductivity. *Polymer (Guildf)* 54: 737–742. https://doi.org/10.1016/j.polymer.2012.11.062.

81 Kiristi, M., Oksuz, A.U., Oksuz, L., and Ulusoy, S. (2013). Electrospun chitosan/PEDOT nanofibers. *Mater. Sci. Eng., C* 33: 3845–3850. https://doi.org/10.1016/j.msec.2013.05.018.

82 Zhao, W., Yalcin, B., and Cakmak, M. (2015). Dynamic assembly of electrically conductive PEDOT:PSS nanofibers in electrospinning process studied by high speed video. *Synth. Met.* 203: 107–116. https://doi.org/10.1016/j.synthmet.2015.02.018.

83 Zarrin, N., Tavanai, H., Abdolmaleki, A., and Bazarganipour, M. (2018). An investigation on the fabrication of conductive polyethylene dioxythiophene (PEDOT) nanofibers through electrospinning. *Synth. Met.* 244: 143–149. https://doi.org/10.1016/j.synthmet.2018.07.013.

84 Marega, C. and Saini, R. (2018). Preparation and characterization of conductive polymer blends of polypyrrole and poly(ethylene oxide). *J. Nanosci. Nanotechnol.* 18: 1283–1289. https://doi.org/10.1166/jnn.2018.15248.

85 Bounioux, C., Avrahami, R., Vasilyev, G. et al. (2016). Single-step electrospinning of multi walled carbon nanotubes – poly(3-octylthiophene) hybrid nano-fibers. *Polymer (Guildf)* 86: 15–21. https://doi.org/10.1016/j.polymer.2016.01.034.

86 Pierini, F., Lanzi, M., Nakielski, P. et al. (2016). Electrospun poly(3-hexylthiophene)/poly(ethylene oxide)/graphene oxide composite nanofibers: effects of graphene oxide reduction. *Polym. Adv. Technol.* 27: 1465–1475. https://doi.org/10.1002/pat.3816.

87 Brooke, R., Cottis, P., Talemi, P. et al. (2017). Recent advances in the synthesis of conducting polymers from the vapour phase. *Prog. Mater Sci.* 86: 127–146. https://doi.org/10.1016/j.pmatsci.2017.01.004.

88 Koshiba, Y., Hirai, M., Horike, S. et al. (2018). In situ monitoring of vapor-phase polymerization and characterization of poly(3,4-ethylenedioxythiophene) thin films. *Sensors Mater.* 30: 2873–2879.

89 Amdad Ali, M., Wu, K.-H., McEwan, J., and Lee, J. (2018). Translated structural morphology of conductive polymer nanofilms synthesized by vapor phase polymerization. *Synth. Met.* 244: 113–119. https://doi.org/10.1016/j.synthmet.2018.07.007.

90 Robinson, M.T., Simons, C.E., Cliffel, D.E., and Jennings, G.K. (2017). Photocatalytic photosystem I/PEDOT composite films prepared by vapor-phase polymerization. *Nanoscale* 9: 6158–6166. https://doi.org/10.1039/c7nr01158j.

91 Bansal, M., Sharma, M., Bullen, C., and Svirskis, D. (2018). Free standing PEDOT films prepared by vapour phase polymerisation as electrically tuneable barriers to drug permeability. *Mater. Sci. Eng., C* 84: 248–253. https://doi.org/10.1016/j.msec.2017.12.002.

92 Sharma, A., Andersson, G., Rivnay, J. et al. (2018). Insights into the oxidant/polymer interfacial growth of vapor phase polymerized PEDOT thin films. *Adv. Mater. Interfaces* 5: 1800594. https://doi.org/10.1002/admi.201800594.

93 Wang, H., Diao, Y., Rubin, M. et al. (2018). Metal oxide-assisted PEDOT nanostructures via hydrolysis-assisted vapor-phase polymerization for energy storage. *ACS Appl. Nano Mater.* 1: 1219–1227. https://doi.org/10.1021/acsanm.7b00382.

94 Zuber, K., Shere, H., Rehmen, J. et al. (2018). Influence of postsynthesis heat treatment on vapor-phase-polymerized conductive polymers. *ACS Omega* 3: 12679–12687. https://doi.org/10.1021/acsomega.8b02191.

95 Brooke, R., Franco-Gonzalez, J.F., Wijeratne, K. et al. (2018). Vapor phase synthesized poly(3,4-ethylenedioxy-thiophene)-trifluoromethanesulfonate as a transparent conductor material. *J. Mater. Chem. A* 6: 21304–21312. https://doi.org/10.1039/c8ta04744h.

96 Brooke, R., Fabretto, M., Vucaj, N. et al. (2015). Effect of oxidant on the performance of conductive polymer films prepared by vacuum vapor phase polymerization for smart window applications. *Smart Mater. Struct.* 24: 35016. https://doi.org/10.1088/0964-1726/24/3/035016.

97 Jia, Y., Liu, C., Liu, J. et al. (2019). Efficient enhancement of the thermoelectric performance of vapor phase polymerized poly(3,4-ethylenedioxythiophene) films with poly(ethyleneimine). *J. Polym. Sci., Part B: Polym. Phys.* 57: 257–265. https://doi.org/10.1002/polb.24778.

98 Jia, Y., Li, X., Jiang, F. et al. (2017). Effects of additives and post-treatment on the thermoelectric performance of vapor-phase polymerized PEDOT films. *J. Polym. Sci., Part B: Polym. Phys.* 55: 1738–1744. https://doi.org/10.1002/polb.24422.

99 Tong, L., Liu, J., Boyer, S.M. et al. (2017). Vapor-phase polymerized poly(3,4-ethylenedioxythiophene) (PEDOT)/TiO_2 composite fibers as electrode materials for supercapacitors. *Electrochim. Acta* 224: 133–141. https://doi.org/10.1016/j.electacta.2016.12.004.

100 Tong, L., Skorenko, K.H., Faucett, A.C. et al. (2015). Vapor-phase polymerization of poly(3,4-ethylenedioxythiophene) (PEDOT) on commercial carbon coated aluminum foil as enhanced electrodes for supercapacitors. *J. Power Sources* 297: 195–201. https://doi.org/10.1016/j.jpowsour.2015.06.128.

101 Skorenko, K.H., Faucett, A.C., Liu, J. et al. (2015). Vapor phase polymerization and mechanical testing of highly electrically conductive poly(3,4-ethylenedioxythiophene) for flexible devices. *Synth. Met.* 209: 297–303. https://doi.org/10.1016/j.synthmet.2015.07.033.

102 Santino, L.M., Acharya, S., and D'Arcy, J.M. (2017). Low-temperature vapour phase polymerized polypyrrole nanobrushes for supercapacitors. *J. Mater. Chem. A* 5: 11772–11780. https://doi.org/10.1039/c7ta00369b.

103 Santino, L.M., Hwang, E., Diao, Y. et al. (2017). Condensing vapor phase polymerization (CVPP) of electrochemically capacitive and stable polypyrrole microtubes. *ACS Appl. Mater. Interfaces* 9: 41496–41504. https://doi.org/10.1021/acsami.7b13874.

104 Ala, O., Hu, B., Li, D. et al. (2017). Conductive textiles via vapor phase polymerization of 3,4-ethylene dioxythiophene. *ACS Appl. Mater. Interfaces* 9: 29038–29046. https://doi.org/10.1021/acsami.7b06771.

105 Cheng, N., Zhang, L., Kim, J.J., and Andrew, T.L. (2017). Vapor phase organic chemistry to deposit conjugated polymer films on arbitrary substrates. *J. Mater. Chem. C* 5: 5787–5796. https://doi.org/10.1039/c7tc00293a.

106 Patel, S.N., Glaudell, A.M., Kiefer, D., and Chabinyc, M.L. (2016). Increasing the thermoelectric power factor of a semiconducting polymer by doping from the vapor phase. *ACS Macro Lett.* 5: 268–272. https://doi.org/10.1021/acsmacrolett.5b00887.

107 Zuniga, R., Cruz, G.J., Olayo, M.G. et al. (2015). Synthesis and superficial characterization of plasma polyfuran thin films. *Polym. Bull.* 72: 839–850. https://doi.org/10.1007/s00289-015-1309-4.

108 Olayo, M.G., Zuniga, R., Gonzalez-Salgado, F. et al. (2017). Structure and morphology of plasma polyfuran particles. *Polym. Bull.* 74: 571–581. https://doi.org/10.1007/s00289-016-1730-3.

109 Li, C., Hsieh, J.H., and Lee, Y.T. (2017). Fabrication and structural characterization of plasma polymerized polypyrrole thin film. *Surf. Coat. Technol.* 320: 206–212. https://doi.org/10.1016/j.surfcoat.2017.01.049.

110 Li, C., Hsieh, J.H., and Lee, Y.T. (2017). Effects of radio frequency power on the microstructures and properties of plasma polymerized polypyrrole thin films. *Vaccum* 140: 132–138. https://doi.org/10.1016/j.vacuum.2016.09.009.

111 Cruz, Y., Muñoz, E., Gomez-Pachón, E.Y. et al. (2019). Electrospun PCL-protein scaffolds coated by pyrrole plasma polymerization. *J. Biomater. Sci., Polym. Ed.* 30: 832–845. https://doi.org/10.1080/09205063.2019.1603338.

112 Park, C.-S., Jung, E.Y., Kim, D.H. et al. (2017). Atmospheric pressure plasma polymerization synthesis and characterization of polyaniline films doped with and without iodine. *Materials (Basel)* 10: 1272. https://doi.org/10.3390/ma10111272.

113 Park, C.-S., Kim, D.H., Shin, B.J., and Tae, H.-S. (2016). Synthesis and characterization of nanofibrous polyaniline thin film prepared by novel atmospheric pressure plasma polymerization technique. *Materials (Basel)* 9: 39. https://doi.org/10.3390/ma9010039.

114 Park, C.-S., Kim, D.H., Shin, B.J. et al. (2016). Conductive polymer synthesis with single-crystallinity via a novel plasma polymerization technique for gas sensor applications. *Materials (Basel)* 9: 812. https://doi.org/10.3390/ma9100812.

115 Hussain, S., Kovacevic, E., Amade, R. et al. (2018). Plasma synthesis of polyaniline enrobed carbon nanotubes for electrochemical applications. *Electrochim. Acta* 268: 218–225. https://doi.org/10.1016/j.electacta.2018.02.112.

116 Cogal, S., Ela, S.E., Cogal, G.C. et al. (2018). Plasma-enhanced modification of multiwalled carbon nanotube with conducting polymers for dye sensitized solar cells. *Polym. Compos.* 39: 668–674. https://doi.org/10.1002/pc.23983.

117 Wu, S., Su, F., Dong, X. et al. (2017). Development of glucose biosensors based on plasma polymerization-assisted nanocomposites of polyaniline, tin oxide, and three-dimensional reduced graphene oxide. *Appl. Surf. Sci.* 401: 262–270. https://doi.org/10.1016/j.apsusc.2017.01.024.

118 Antonio-Carmona, Y., Martínez-Amador, S., Ovando-Medina, V. et al. (2019). Plasma polymerization of pyrrole and aniline on polyurethane foams for microorganism immobilization and wastewater treatment. *Desalin. Water Treat.* 155: 15–23. https://doi.org/10.5004/dwt.2019.24001.

4

Use of High Energy Radiation for Synthesis and Kinetic Study of Conjugated Polymers

Teseer Bahry[1], *Zhenpeng Cui*[1], *and Samy Remita*[1,2]

[1] *Université Paris-Saclay, Institut de Chimie Physique, ICP, UMR 8000, CNRS, Bâtiment 349, Campus d'Orsay,*
15 avenue Jean Perrin, Orsay Cedex 91405, France
[2] *Conservatoire National des Arts et Métiers, CNAM, EPN 7, Département Chimie Vivant Santé, 292 Rue*
Saint-Martin, 75141, Paris Cedex 03, France

4.1 Recent Advancements Toward Facile Preparation of Processable CPs

Intrinsically conducting polymers (CPs) are extraordinary class of material that combines the electrical properties of metals and semiconductors with a polymer's ability to flex and/or stretch [1]. Generally, the synthesis of CPs is feasible and easy. However, CPs have some limitations that restrict their applications due to the poor processability that is attributed to the rigidity and interchain interactions of the polymer chains [2]. Moreover, these polymers are highly branched and crosslinked due to polaron/bipolaron charge interactions. CPs are therefore poorly soluble in common industrial solvents. Thus, the key hurdle to uptake these polymers in commercial products is lack of existing facile synthetic methods of producing useful quantities as well as simple approaches for processing bulk polymer into useful forms [1].

Nowadays, the scientific community is tremendously endeavoring to develop and upgrade new synthesis methodologies for CPs [3, 4]. The common methods to synthesize CPs are chemical oxidation or electrochemical polymerization [5–7]. Based on these conventional methods, numerous studies were carried out to optimize the properties of CPs, to control structure and to functionalize CPs [8]. Research reports showed that nanostructured conducting polymers in the form of nanofibers and nanosponges are characterized by significantly improved capacitance values as compared with their non-nanostructured counterparts [9]. For this purpose, reverse microemulsion polymerization [10, 11] and CPs composite with carbon nanotubes (CNTs) [12, 13] have been employed to fabricate polymers nanotubes [14], wires [15], nano-rods [16], fibers [17], etc. Furthermore, polymer-metal oxide nanocomposites were used to enhance their thermal, mechanical, and chemical properties [18]. Even though these previously mentioned methods are well understood and controlled, still remain many obstacles to overcome such as chemical contamination, purification steps, and processability. In literature, there are several

Conjugated Polymer Nanostructures for Energy Conversion and Storage Applications,
First Edition. Edited by Srabanti Ghosh.

approaches that have been adopted towards production of processable forms of CPs as follows [1, 19]:

i) Removal of interchain charge interactions by reducing CPs to their non-conducting state making them soluble in some solvents such as dimethylformamide (DMF) and dimethyl sulfoxide (DMSO)
ii) Resorting to use of substitute polymers by flexible and long alkyl chains rendering them soluble in common solvent (chloroform, toluene, etc.)
iii) Preparation of water-soluble CPs using a template-guided enzymatic approach
iv) Preparation of aqueous colloidal dispersions of CPs in the presence of a water-soluble polyelectrolyte such as polystyrene sulfonic acid
v) Vapor phase polymerization method to produce thin films of both soluble and insoluble CPs, and nanocomposites thereof
vi) Self-doping approach for increasing the solubility of CPs in aqueous solutions by using ionizable functional groups.

For the sake of simplifying the preparation of nanostructured CPs with the view to obtain processable polymers, finding an alternative synthesis and processing approaches would be immensely helpful. In this respect, radiolysis synthesis is already known as an interesting method for the synthesis of non-conducting polymers [20]. However, radiation induced polymerization via the interaction of high energetic rays with the matter is narrowly used to prepare CPs [21]. The preparation of CPs using gamma irradiation was predominantly accompanied by the addition of chemical oxidants. As reported in the literature, ionizing radiation affects polymer morphology and leads to tailoring their nanostructure. Indeed, Karim et al. synthesized polypyrrole (PPy) using γ-radiation induced oxidative polymerization with ammonium peroxydisulfate (APS) as chemical oxidant [22]. Moreover, they also prepared buckyball shaped conducting polythiophene by gamma induced polymerization method in presence of $FeCl_3$ as an oxidizing agent [23]. However, in order to produce CPs, radiation induced polymerization was used alone for the first time, in the absence of any external oxidizing species, only few years ago. This radiation methodology based on either γ-rays or accelerated electrons and dedicated to the synthesis of nanostructured CPs was recently developed by Remita's team [21]. Hence, we concisely preview in this chapter all the potential approaches to proceed with CPs nanostructures production by radiolytic methodology.

4.2 Preface to Radiation Induced Oxidative Polymerization of CPs Nanostructures in Aqueous Solutions

It is well known that γ-rays and X-rays radiolysis are very often used at ambient temperature and pressure in order to initiate, in the absence of external chemical initiators, oxidation, or reduction reactions through the control of the initiator radicals, which depend on the nature of the irradiated medium (atmosphere, solvent, potential solute) [24–27]. The principle is that upon irradiation the deoxygenated aqueous solutions at neutral pH generate the following various radiolytic species [28–30]:

$$H_2O \rightsquigarrow e_{aq}^{\ -}, HO^{\cdot}, H^{\cdot}, H_3O^{+}, H_2O_2, H_2 \tag{4.1}$$

The radiolytic products of water radiolysis are varied between oxidizing species and reducing ones. In the presence of air, $H^{\cdot}$ atoms and solvated electrons $e_{aq}^{\ -}$ are scavenged by molecular oxygen O_2 to produce respectively perhydroxyl radicals ($HO_2^{\cdot}$) and superoxyde radicals ($O_2^{\cdot-}$), which are the two acido-basic forms of the couple $HO_2^{\cdot}/O_2^{\cdot-}$ ($pK_a\,(HO_2^{\cdot}/O_2^{\cdot-}) = 4.8$ at 298 K) [29, 31]. As a consequence, when irradiating aerated aqueous solutions at neutral pH, only two short-lived transient species are formed, namely, hydroxyl radicals ($HO^{\cdot}$) and $O_2^{\cdot-}$ with radiolytic yields of 2.8×10^{-7} mol/J and 3.4×10^{-7} mol/J, respectively [32]. The standard redox potential of $HO^{\cdot}$ (at pH = 7) is quite high and amounts to $E°'(HO^{\cdot}/H_2O) = 2.2\,V_{SHE}$ [29]. On the contrary, $O_2^{\cdot-}$ is almost a poor oxidizing species with relatively low redox potential that amounts to $E°'(HO_2^{\cdot}/H_2O_2) = 0.9\,V_{SHE}$ [29]. Hence, $HO^{\cdot}$ radicals are strong oxidizing species and should evidently enable oxidation induced polymerization of some interesting organic monomers, such as 3,4-ethylenedioxythiophene (EDOT), which has oxidation potential that amounts to 1.4 V vs. Ag/AgCl [33].

Now, if aqueous solutions are degassed with nitrous oxide (N_2O), $e_{aq}^{\ -}$ are quantitatively and immediately converted into $HO^{\cdot}$. As a consequence, when irradiating N_2O-saturated aqueous solutions at neutral pH, only two short-lived transient species are formed: $HO^{\cdot}$ and $H^{\cdot}$ (hydrogen atoms). In these conditions, due to the poor reactivity and to the low yield of formation of hydrogen atoms, $HO^{\cdot}$ radicals can be considered as the only oxidizing species, and their radiolytic yield of formation ($G(HO^{\cdot}) = 5.6 \times 10^{-7}$ mol/J) is higher than that obtained under aerated conditions ($G_{HO^{\cdot}} = 2.8 \times 10^{-7}$ mol/J).

EDOT molecules are soluble in water and present some specific chemical properties, which make them interesting building blocks for the synthesis of functional π-conjugated systems such as PEDOT [21, 34]. In fact, due to their strong electron donor effect, the ether groups at the β and β′ positions of thiophene rings, which confer a high reactivity to the free α and α′ positions, prevent the formation of parasite α–β′ linkages during polymerization. These interesting properties of EDOT enabled Remita and co-workers [21] to successfully synthesize PEDOT polymers by using γ-irradiation. Starting from an aqueous solution of EDOT monomers, it was possible to synthesize polymers under soft conditions: at air and at room temperature without introduction of any external chemical initiators [21]. In addition, the synthesis was feasible under various conditions (O_2 or N_2O saturated aqueous solutions) [21, 35]. In comparison with the usual electrochemical methods, this new γ-rays-based radiolytic way presents some advantages concerning the easy preparation of the samples, where no supporting electrolyte is needed, and the ability to work under atmospheric conditions without purging solutions with an inert gas. In contrast to the electrochemical approach, which leads to the direct deposition of CPs onto conducting substrates, the described radiolysis method leads to the formation of CPs dispersed in water enabling their further deposition over conducting or even non-conducting surfaces [21].

Radiation induced polymerization of CPs is a promising method towards producing processable CPs nanostructures and noticeably exhibits several advantages over other conventional methods. As it appears, radiation-based method does not require special equipment, can be performed under various conditions, and is free from metal contaminations. Moreover, this method could lead to formation of suspended nanostructured CPs in aqueous solutions as well as directly onto substrates. Using radiolysis should also lead to chemical processes, which can be switched on and off upon exposure or removal of ionizing radiation instead of using initiator or stopper molecules.

4.2.1 Studying Kinetic Mechanism of $HO^{\cdot -}$Induced EDOT Polymerization in Aqueous Solution

Understanding the mechanism of oxidative polymerization of conducting polymers and studying the reaction mechanism between the generated radicals from radiolysis process and the studied monomers is a pivotal point to advance the development of this original synthetic method. For this purpose, time resolved absorption spectroscopy coupled with pulsed radiolysis was used in order, first, to study EDOT oxidation mechanism and, second, to definitely identify the nature of PEDOT growth process. In this context, the reaction between hydroxyl radicals and EDOT monomers was mainly followed with the aim to identify the different transient species involved in the first steps of $HO^{\cdot -}$induced PEDOT polymerization. Spectrokinetic analysis of experimental data and molecular simulations of absorption spectra were used to confirm the rate constants values and to identify the transient and stable species involved in the mechanism. The experimental setup (available at ICP, Orsay, Paris-Saclay University) includes a picosecond laser-triggered electron accelerator ELYSE [36, 37] coupled with a time-resolved absorption spectroscopic detection system. A mixed simulation method was used, using the Monte-Carlo (MC) sampling of the molecular geometries, the density functional theory (DFT) calculation of the electron structures, and the polarized continuum modeling (PCM) of the solvent (Figure 4.1). An N_2O-purged stock EDOT aqueous solution of 200 ml was used, which circulated in the 10 × 10 mm fused silica irradiation cell at a flow rate of 100 ml/min by means of a peristaltic pump. Since the electron pulses were applied at a frequency of 5 Hz, the solution was renewed between each pulse and it was possible to apply up to 400 pulses for each kinetic measurement [31, 38].

In acidic and neutral aqueous solutions under N_2O, $HO^{\cdot}$-induced oxidation of EDOT was found to imply the oxidation of EDOT into a transient species, $EDOT^{\cdot +}$ radical cation and possibly into $(EDOT\text{-}HO)^{\cdot}$ adduct, which dimerizes and deprotonates leading to a stable product, namely, $EDOT_2$ dimer. In alkaline medium, this mechanism is mostly different since $HO^{\cdot}$ deprotonates into its alkaline form, $O^{\cdot -}$, the oxide radical, which adds onto EDOT monomer. This addition leads to the formation of an open cycle, which prevents any dimerization of EDOT and consequently any polymerization of PEDOT. Hence, in acidic and neutral aqueous solutions, after one pulse irradiation (40 Gy), no other products than $EDOT_2$ dimers were observed,

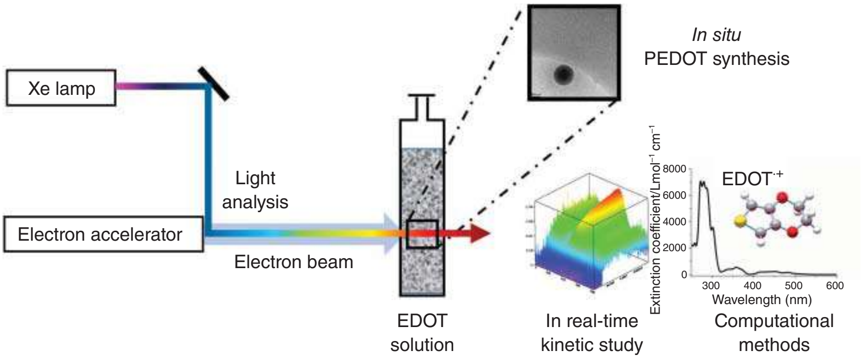

Figure 4.1 The picosecond laser-triggered electron accelerator ELYSE at University Paris-Saclay (Orsay) coupled with a time-resolved absorption spectroscopic detection system. The figure shows the involvement in the work of the in real-time kinetic study of the growth mechanism, of the molecular simulations of the absorption spectra of the transient species involved in the growth mechanism as well as the experimental characterizations of the obtained PEDOT polymers as observed on the Cryo-TEM image [31]. Source: Adapted with permission from Copyright 2015, American Chemical Society.

demonstrating that no polymerization takes place in these experimental conditions. The interesting results obtained by pulse radiolysis proved without any ambiguity that PEDOT polymerization is not a chain reaction. On the contrary, it has been demonstrated to proceed through a step-by-step mechanism made up of the following recurrent steps: (i) oxidation/activation, (ii) growth/chain length increase, and (iii) deprotonation [31].

In fact, the amount of hydroxyl radicals generated by one pulse during the pulsed radiolysis study was not enough to ensure polymerization. It only enabled the incomplete transformation of EDOT monomers into dimers. According to a step-by-step mechanism, the quantitative polymerization of EDOT into PEDOT requires a very much higher concentration in hydroxyl radicals, which should reach at least twice that of EDOT. Nevertheless, in pulse radiolysis experiments, the dose per pulse could not be significantly increased. Then, in order to check whether EDOT polymerization effectively proceeds through a step-by-step oxidation process and with the aim to synthesize conducting PEDOT polymers by using an electron beam, aqueous solutions containing 10 mM in EDOT were irradiated in a closed cell under N_2O atmosphere with a series of consecutive electron pulses of 40 Gy (delivered at a frequency of 10 Hz).

Taking into account a step-by-step polymerization process, 10 mM in hydroxyl radicals are needed for the quantitative dimerization of 10 mM in EDOT into 5 mM in $EDOT_2$, then an additional amount of 5 mM in $HO^{\cdot}$ is needed for the quantitative transformation of $EDOT_2$ into 2.5 mM in $EDOT_4$ and so on. This means that at least 20 mM in hydroxyl radicals are necessary to ensure the quantitative polymerization of EDOT monomers into PEDOT polymers. The use of two $HO^{\cdot}$ radicals for one EDOT molecule is understandable since each EDOT monomer is bound to two EDOT neighbors inside the same polymer chain, which means that it must be twice oxidized. Thus, the theoretical irradiation dose (D_{max}), which should lead to the total oxidation of EDOT into PEDOT by $HO^{\cdot}$ radicals, can be determined as follows:

$$D_{\max}\,(\mathrm{Gy}) = \frac{2[\mathrm{EDOT}]_0\,(\mathrm{mol/l})}{\mathrm{G_{ox}}\,(\mathrm{mol/J})\,d\,\left(\mathrm{kg/l}\right)} \tag{4.2}$$

where $D_{\max}$ is the irradiation dose (in Grays, 1 Gy corresponding to 1 J/kg), where $[\mathrm{EDOT}]_0$ is the initial concentration of EDOT monomers, G_{ox} is the yield of EDOT oxidation which is equal to the radiolytic yield of $HO^{\cdot}$ production (5.6×10^{-7} mol/J under N_2O atmosphere), and d is the solution density ($d \sim 1$ kg/l for diluted aqueous solutions).

According to Eq. (4.2), 36 kGy were necessary for the total polymerization of 10 mM in EDOT. Knowing that each pulse corresponded to a dose of 40 Gy, complete polymerization was requiring more than about 1000 successive pulses. In order to quantitatively polymerize EDOT, the colorless and limpid aqueous solution of 10 mM in EDOT was irradiated at a dose of 180 kGy, which corresponds to the accumulation of 4500 pulses of 40 Gy/pulse. After this irradiation, the solution became turbid. Its UV–Vis absorption spectrum is displayed in Figure 4.2a [31]. No noticeable absorption band was present in the spectrum. Nevertheless, a continuous scattering appeared due to the presence of a brown-yellow suspension in the bulk of the irradiated solution (inset of Figure 4.2a). This spectrum and the turbidity of the solution were in good agreement with results previously obtained by steady-state radiolysis suggesting that polymerization effectively took place [21].

The ATR-FTIR spectrum of the polymer powder is presented in the upper part of Figure 4.2b in the wave number region 1600–600 $\mathrm{cm^{-1}}$ together with the spectrum of pure non irradiated EDOT (bottom of Figure 4.2b) [31]. The two spectra were found in good agreement with those reported for PEDOT and EDOT when polymerized by γ-rays. The IR spectrum of the polymer powder displays vibrations at 1485, 1441, and 1365 $\mathrm{cm^{-1}}$ which are attributed to C=C and C–C stretching modes in the thiophene ring. The vibrations observed at 1288, 1240, 1171, and 1059 $\mathrm{cm^{-1}}$ are assigned to the stretching modes of the ethylenedioxy groups (C–C and C–O–R–O–C). The vibration modes of C—S bond, which are present in the thiophene ring, can be observed at 941 and 901 $\mathrm{cm^{-1}}$. Note that the intense C–H stretching band at 754 $\mathrm{cm^{-1}}$, observed in the spectrum of EDOT, is clearly absent in the ATR-FTIR spectrum of polymers. This definitely demonstrates, without any ambiguity, that EDOT polymerization has quantitatively taken place thanks to α,α′-coupling reactions and that the resulting solid powder obtained after lyophilization is effectively composed of PEDOT polymers. This demonstrates that such as γ-irradiation, electron beam irradiation enables the radiosynthesis of PEDOT polymers. [33] While one electron pulse lead to the formation of $\mathrm{EDOT_2}$ dimers as stable products, the use of a series of successive pulses is necessary to generate enough hydroxyl radicals to form PEDOT polymers. Here it is evidenced that electron irradiation can successfully be used as an alternative way for the synthesis of PEDOT polymers and also that PEDOT growth effectively proceeds through a step by step oxidation process as expected.

Aqueous solutions containing 10 mM in EDOT and irradiated by the electron beam at 180 kGy were observed by Cryo-transmission electron microscopy just

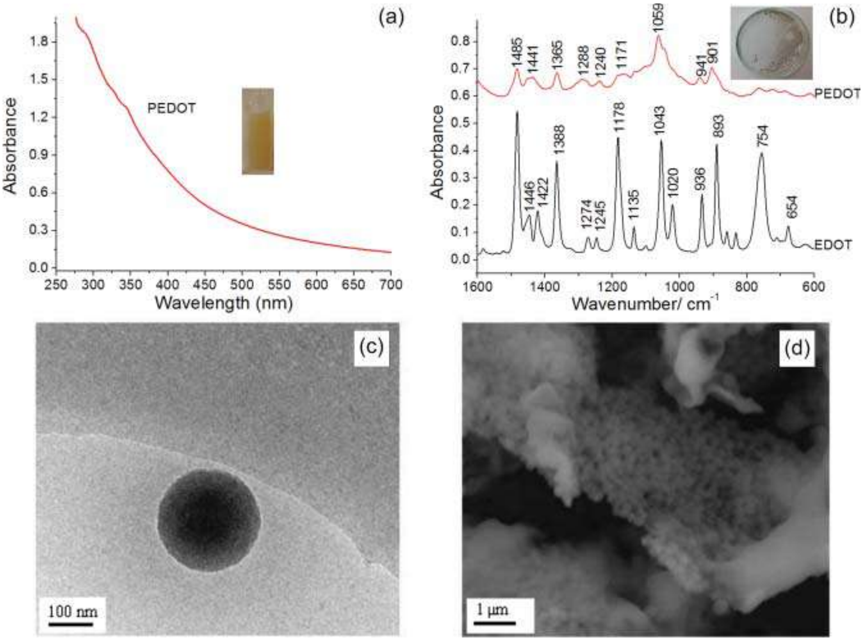

Figure 4.2 (a) Absorption spectrum of a N_2O-saturated aqueous solution of EDOT (10 mM) irradiated by an electron beam at a dose of 180 kGy (4500 pulses, 40 Gy/pulse). The reference was water, and path length was 1 mm; (inset) photography of a cell containing PEDOT aqueous suspension radiosynthesized by an electron beam. (b) ATR-FTIR spectra of pure EDOT (bottom spectrum) and PEDOT polymers radiosynthesized at 180 kGy (top spectrum); (inset) photo of a cup containing the lyophilized radiosynthesized PEDOT powder. (c) Cryo-TEM image of radiosynthesized PEDOT in aqueous solution. A PEDOT nanoparticle of around 250 nm is observed. (d) SEM image of lyophilized radiosynthesized PEDOT powder. Aggregates of spherical PEDOT nanoparticles are observed [31]. Source: Adapted with permission from Copyright 2015, American Chemical Society.

after irradiation in order to investigate the structure and morphology of PEDOT polymers in aqueous solution. Representative images show the presence of low density globular structures forming spherical nanoparticles with a diameter ranging between 200 and 250 nm (Figure 4.2c) [31]. This result was in agreement with polymer size and shape found after γ-rays induced PEDOT synthesis. Since no other low-density objects were observed during Cryo-TEM experiments, these spherical nanoparticles were supposed to be made up of PEDOT polymer nanostructures. Each observed nanoparticle should be composed of interdigitated polymer chains. Since no α-β′ linkages could occur during polymerization, radiosynthesized PEDOT nanostructures should be composed of linear chain polymers, which are no branched nor networked. Thus, the globular structure observed on Figure 4.2c should correspond to a self-assembly of independent amorphous PEDOT chain polymers. The presence of ethylenedioxy groups (H-bond acceptors) should explain not only the hydrosolubility of PEDOT polymers but also the as-observed packing and nanostructuration of the spherical supramolecular PEDOT self-assemblies.

In order to characterize the morphology of the polymers after a deposition procedure, the 180 kGy-irradiated sample was lyophilized and the black powder obtained was deposited then characterized by scanning Electron Microscopy (SEM) microscopy. The images indicated the presence of very close packed polymeric particles (Figure 4.2d) [31]. Once more PEDOT polymers appear as spherical nanoparticles. These structures should come from the globular nanostructures already observed in aqueous solution by Cryo-TEM. The particles observed by SEM were almost monodisperse in size with a mean diameter of 220 nm, which is close to that observed by Cryo-TEM in aqueous solution. This proves that neither phase transition nor deposition procedure affects the size and shape of radiosynthesized PEDOT nanoparticles. This would imply the existence of very strong hydrogen–bond interactions into each polymer nanoparticle. Therefore, the synthesis of nanostructured PEDOT polymers is successful, thanks to the electrons beam irradiation of EDOT aqueous solution. The radiosynthesized PEDOT polymers form monodisperse nanoparticles the morphology of which is kept after deposition onto substrate.

Further investigation based on pulsed electron beam irradiation was proceeded to oxidize EDOT monomers and to induce polymers growth by using sulfate radicals, $SO_4^{\cdot-}$, instead of hydroxyl radicals, $HO^{\cdot}$ [38]. The purpose of this study was to check the influence of the nature of the oxidizing species and of the presence of an inorganic compound (namely, $K_2S_2O_8$) onto the morphology of radiosynthesized polymers. The results demonstrated the versatility of the radiolytic methodology based on pulse electron beam irradiation, and highlighted, without any ambiguity, the efficiency of alternative oxidizing radicals, such as sulfate radicals for the preparation of nanostructured conducting polymers. The success of PEDOT polymers synthesis by using accumulated electron pulses definitely demonstrates that conducting polymers growth proceeds through a step-by-step oxidation mechanism and not according to a chain reaction.

4.2.2 Gamma-Radiation Induced Oxidative Polymerization of EDOT in Aerated Aqueous Solutions at Neutral pH

The incipient form of this method was initially instituted by γ-radiolysis of aerated aqueous solutions of 3,4-ethylenedioxythiophene (EDOT) [21]. The concept is that the radiolysis of aerated aqueous solutions provides the medium with several oxidizing species namely $HO^{\cdot}$ and $O_2^{\cdot-}$. These generated oxidizing species could insure the oxidation of EDOT monomers. Accordingly, the irradiation conditions were studied in details to get the product in optimal form. Within this framework, to approach the synthesis of PEDOT by γ-radiolysis, the yield of oxidation was needed to be determined. As elucidated in related studies [21, 31], by knowing the extinction coefficients of EDOT in aqueous solution that were calculated from UV–Vis absorption spectra, one can deduce the initial radiolytic yield of EDOT consumption from the variation of EDOT concentration as a function of the irradiation dose. The extrapolated value of the radiolytic yield of EDOT consumption under air was found equal to the radiolytic yield of production of $HO^{\cdot}$ that amounts to $G_{-\mathrm{EDOT}\,0} = G_{\mathrm{HO}^\cdot} = 2.8 \times 10^{-7}$ mol/J [21]. Note that this value was found almost constant whatever the initial concentration of EDOT. This finding demonstrates that EDOT amount was sufficient to scavenge all the hydroxyl radicals produced by gamma-radiolysis and highlights the fact that only hydroxyl radicals react with EDOT. As mentioned earlier, $\mathrm{HO}^\cdot$ is a strong oxidizing species since its apparent standard redox potential at pH = 7 amounts to $E^{\circ\prime}_{\mathrm{SHE}}$ $(\mathrm{HO}^\cdot/\mathrm{H_2O}) = 2.2\,\mathrm{V_{SHE}}$ [29] enabling oxidation of EDOT. Contrariwise, the formed $\mathrm{O_2}^{\cdot-}$ radicals possess very low redox potential $[E^{\circ\prime}_{\mathrm{SHE}}\ (\mathrm{O_2}^{\cdot-}/\mathrm{H_2O_2}) = 0.9\,\mathrm{V_{SHE}}]$ [29], making them being considered as poor oxidizing species. As a consequence, the relatively low apparent redox potential of $\mathrm{O_2}^{\cdot-}$ does not allow the reaction with EDOT the oxidation potential of which amounts to 1.4 V $\mathrm{Ag/AgNO_3}$ [33]. Whatever EDOT concentration ranging from 1 to 10 mM, the results showed that EDOT disappearance parallels the formation of species that absorb at both 290 and 350 nm. These absorption maxima could be attributed to dimers and oligomers of EDOT, which could be formed according to the step by step oxidation process highlighted by pulse radiolysis:

$$\mathrm{EDOT} + \mathrm{HO}^\cdot \rightarrow (\mathrm{EDOT} - \mathrm{HO})^\cdot \text{ or } \mathrm{EDOT}^{\cdot+} + \mathrm{HO}^- \tag{4.3}$$

$$2\,(\mathrm{EDOT} - \mathrm{HO})^\cdot \text{ or } 2\,\mathrm{EDOT}^{\cdot+} \rightarrow \text{dimers then oligomers} \tag{4.4}$$

These absorption bands are in good agreement with the absorption spectra of dimers experimentally and theoretically found by the previously described pulsed radiolysis studies. [31] Auxochromic substitution (by the ethylenedioxy group) in EDOT dimers can explain the shift in their absorption maxima as compared with those of bithiophene molecules, which are known to absorb at 246 and 301 nm [39].

The yield of EDOT oxidation, $G_{-\mathrm{EDOT}\,0}$, was found decreasing with the dose and became much lower than $G_{\mathrm{HO}^\cdot}$ at high doses. This is because of the competitive reactions of hydroxyl radicals with EDOT dimers and oligomers, which take place in the medium and which become more and more preponderant as the amount of EDOT decreases. Indeed, the oxidation potential of the dimers and the oligomers is lower than that of the monomers enabling their oxidation by hydroxyl radicals. So the process of oxidative coupling of the units continues as the polymer grows [40].

On the other hand, the yield of EDOT consumption was found independent of the initial EDOT concentration. This definitely demonstrates that the process attributed to PEDOT radio-induced synthesis does not proceed through a chain reaction. In particular, $\mathrm{EDOT}^{\cdot+}$ radical cation does not react with EDOT monomer. This is consistent with the pulsed radiolysis results previously described: PEDOT radio-induced synthesis could only proceed through a recurrent $\mathrm{HO}^\cdot$ oxidation process: $\mathrm{HO}^\cdot$ reacts with EDOT monomers, then with dimers, and then with oligomers. The quantitative synthesis of PEDOT polymers throughout such a step-by-step mechanism necessarily implies the use of two $\mathrm{HO}^\cdot$ radicals for the oxidation of one EDOT molecule (in α and α' positions). Thus, the theoretical irradiation dose ($D_{\max}$) that should lead to the total oxidation of EDOT into PEDOT can be calculated from Eq. (4.2). For instance, 7.2 and 72 kGy are necessary for the total polymerization of respectively 1 and 10 mM in EDOT dissolved in aerated aqueous solution.

In the respect of PEDOT characterizations, the ATR-FTIR observations evidenced their successful formation [21]. Moreover, the obtained spectra were in very good agreement with those previously reported for PEDOT in literature [41–43] and for PEDOT synthesized by accelerated electrons as highlighted before [31]. The PEDOT nature of the radiosynthesized polymers, which compose the solid phase, was also proved thanks to the determination of its melting point. Indeed, a temperature of 145 °C was measured, which is very close to the reported PEDOT melting point value (146 °C) [44]. This result also proves the absence of impurities in the radiosynthesized products. The morphological features were also observed directly in the aqueous solution by Cryo-TEM and after deposition onto substrate by AFM [21]. The microscopic observations revealed formation of globular self-assembled structures made up of PEDOT polymeric chains. The mean diameter of the observed nanoparticles was 200 nm. The dimensions of the nano-objects observed by Cryo-TEM closely match those of AFM. As at will be demonstrated in the next paragraph, the presence of substituted hydroxyl groups along the polymer chains explains the packing and the nanostructuration of the observed spherical supramolecular PEDOT self-assemblies besides their hydrosolubility and the solvation of PEDOT polymers.

In order to enhance the yield of oxidation and in order to check whether other oxidizing species can enable the oxidative polymerization in aqueous solutions, the radiolysis methodology took further advances by varying the experimental conditions (atmosphere and additive). For this purpose, the radiolytic methodology was extended to the synthesis of PEDOT polymers in N_2O-saturated aqueous solutions in the presence and in the absence of sodium azide. The oxidative polymerization was induced through two different oxidizing species: $HO^{\cdot}$ (hydroxyl) and $N_3^{\cdot}$ (azide) radicals, as will be discussed in the following text.

4.2.3 Effect of Oxidizing Species on Gamma-Radiation-Induced Synthesis of PEDOT

The original radiolytic methodology based on γ-rays was extended to the synthesis of PEDOT polymers in N_2O-saturated aqueous solutions of EDOT at neutral pH. In these conditions and depending on the presence of sodium azide salt, two different oxidizing species are formed, namely, hydroxyl radicals ($HO^{\cdot}$) and azide radicals ($N_3^{\cdot}$) [35]. Since the redox potentials of these two oxidative radicals (which are higher than that of EDOT monomers) and their well-known oxidation mechanisms are quite different, one can expect the formation of two kinds of PEDOT polymers with tuned characteristics. Under N_2O in the absence of NaN_3 as already explained, e_{aq}^- are quantitatively and immediately converted into $HO^{\cdot}$ which can be considered as the only oxidizing species with a radiolytic yield of formation [$G(HO^{\cdot}) = 5.6 \times 10^{-7}$ mol/J]. Under these conditions $H^{\cdot}$ atoms are present in the medium with a radiolytic yield $G_{H^{\cdot}} = 0.6 \times 10^{-7}$ mol/J. Nevertheless, due to their relatively small amount and unknown reactivity, the presence of $H^{\cdot}$ atoms is often neglected [45]. Now, in aqueous solutions containing sodium azide (NaN_3 at 10 mM for 1 mM in EDOT or 100 mM for 10 mM in EDOT, dissociated into Na^+ and N_3^- ions) and saturated by nitrous oxide, $HO^{\cdot}$ radicals are very quickly scavenged by

N_3^- ions leading to the quantitative formation of $N_3^{\cdot}$. In the presence of NaN_3, the concentration of EDOT monomers being always ten times lower than that of N_3^- ions, the direct oxidation of EDOT by $HO^{\cdot}$ can be neglected. Thus, when irradiating N_2O-saturated aqueous solutions at neutral pH in the presence of NaN_3, the radiolytic yield of formation of $N_3^{\cdot}$ amounts to 5.6×10^{-7} mol/J.

Once again, according to a step by step mechanism, in the absence of NaN_3, the total irradiation dose (D_{max}) that should enable the quantitative synthesis of PEDOT in N_2O-saturated aqueous solutions is twice the dose necessary for the total oxidation of EDOT monomers and can be calculated as previously explained according to Eq. (4.2), but by using $G(HO^{\cdot})$ instead of $G_{HO^{\cdot}}$. In a N_2O-saturated aqueous solution containing 10 mM in EDOT, the dose that is necessary for the total oxidation of EDOT amounts to 18 kGy, and the dose D_{max} that is necessary for the complete synthesis of PEDOT amounts to 36 kGy.

In the absence of sodium azide salt, N_2O-saturated aqueous solutions containing 10 mM in EDOT were irradiated at increasing doses up to 70 kGy. This latter dose was high enough to ensure the total polymerization of EDOT. Figure 4.3a displays the evolution of the UV–Vis absorption spectrum of this solution as a function of the dose. The spectra show at low irradiation doses, up to about 20 kGy (the dose that produces 10 mM hydroxyl radicals), two absorption bands that appear at 290 and 350 nm (Figure 4.3a), which demonstrates the formation of dimers as highlighted by pulse radiolysis study [31]. Above 20 kGy, no absorption band is observed around 250 nm. This clearly indicates that EDOT has completely disappeared. If the dose is higher than the total irradiation dose, as observed in the case of 70 kGy irradiation dose in Figure 4.3a, the absorption bands of the dimers disappear and an intense absorption band appears at around 370 nm together with a continuous scattering, the intensity of which increases with the irradiation dose. This has been ascribed to the lengthening of EDOT oligomers. In fact, at doses higher than 36 kGy, the appearance of a continuous scattering component, in the extinction spectrum of the irradiated solutions, was explained to result from the formation of a brown-yellow suspension in the bulk solution. This suspension became denser and the solution appeared more turbid as the irradiation dose was increasing.

After the deposition of this suspension onto ITO substrate, the resulting film displayed an intense absorption band at 550 nm. According to the performed ATR-FTIR analysis, this indicates that the suspension was made up of polymers, denoted PEDOT-OH, formed at high doses, thanks to the recurrent step-by-step $HO^{\cdot}$ oxidation process. After irradiation at high doses (from 36 to 70 kGy), very slow precipitation of the suspension was observed. This precipitation corresponds to a sedimentation process of the PEDOT-OH polymers of relatively high molecular weights. Note that this precipitation cannot be assigned to the hydrophobia of the radiosynthesized polymers. Indeed, after adding either cyclohexane or dichloromethane to the aqueous suspensions (v/v) and after stirring and decantation, the polymer particles always remain in the aqueous phase, whereas the organic phase systematically appears colorless, as illustrated in the case of dichloromethane (Figure 4.3a, insert). This result definitely proves the hydrophilic properties of PEDOT-OH polymers.

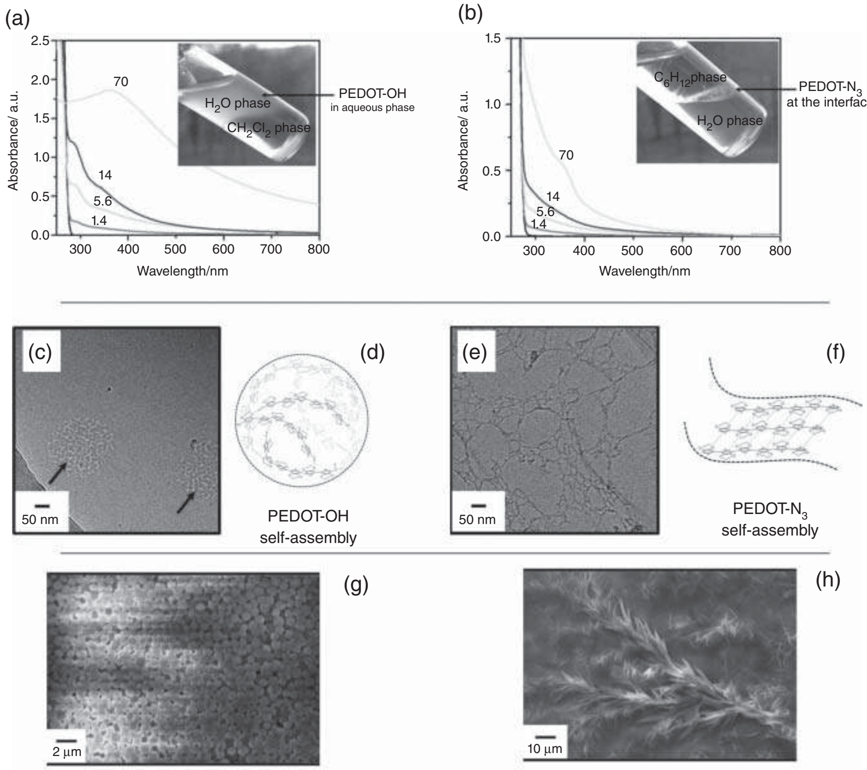

Figure 4.3 Absorption spectra of a N_2O-saturated aqueous solution containing 10 mm EDOT irradiated in the absence of NaN_3 (a) and in presence of NaN_3 (b) with increasing doses: 0, 1.4, 5.6, 14, and 70 kGy. The optical path length was 0.1 cm. The reference was water. Inset (a) Image of an aqueous solution irradiated at 70 kGy after the addition of dichloromethane as a denser organic phase (v/v): PEDOT-OH suspension remains in the upper aqueous phase. Inset (b) Image of an aqueous solution irradiated at 70 kGy after the addition of cyclohexane as a less dense organic phase (v/v): PEDOT-N_3 polymers remains at the interface between the two liquid phases. Cryo-TEM images of aqueous samples containing 10 mM in EDOT irradiated at 36 kGy under N_2O atmosphere: (c) in the absence of NaN_3 (PEDOT-OH) and (e) in the presence of NaN_3 (PEDOT-N_3). (d) A schematic representation of a single spherical polymer nanoparticle that highlights H-bond interactions between the chains. (f) A schematic representation of a single nanostructure highlighting π-stacking interactions between the chains. SEM images of PEDOT polymers after deposition onto gold substrates. Polymers were obtained after irradiation at 70 kGy: (g) in the absence of NaN_3 (PEDOT-OH) and (h) in the presence of NaN_3 (PEDOT-N_3). Source: Lattach et al. [35].

When considering γ-radiolysis under N_2O this time in the presence of NaN_3, $HO^{\cdot}$ radicals are scavenged by N_3^- leading to $N_3^{\cdot}$ radicals, which can then be considered as the only oxidizing species able to react with EDOT. However, $N_3^{\cdot}$ radicals are known as an alternative oxidizing system more selective than $HO^{\cdot}$: it is a soft one-electron oxidant $E^{\circ\prime}(N_3^{\cdot}/N_3^-) = 1.33\,V_{SHE}$ at pH = 7. All in all, by analogy with the case of hydroxyl radicals, in the presence of NaN_3, the total irradiation dose (D_{max}), which should enable the quantitative synthesis of PEDOT in N_2O-saturated aqueous solutions, is twice the dose necessary for the total oxidation of EDOT monomers and can be calculated according to Eq. (4.2), but by using $G(N_3^{\cdot})$ instead of $G(HO^{\cdot})$ or $G_{HO^{\cdot}}$. In an N_2O-saturated aqueous solution containing 10 mM in EDOT in the presence of azide salt, the dose that enables the total oxidation of EDOT amounts to 18 kGy and the dose D_{max}, which is necessary for the complete production of PEDOT is then about 36 kGy.

Accordingly, in the presence of sodium azide salt, N_2O-saturated aqueous solutions containing EDOT (10 mM) were irradiated at increasing doses up to 70 kGy. The evolution of the UV–Vis absorption spectrum of this solution as a function of the dose is displayed (Figure 4.3b). At low irradiation doses, up to about 20 kGy (the dose that produces 10 mM in azide radicals), two shoulders appear and grow up at 290 and 350 nm demonstrating once again the formation of dimers. When the dose becomes higher than the total irradiation dose, as observed in the case of 70 kGy-irradiation on Figure 4.3b, the absorption bands of dimers disappear and a more intense absorption band grows up around 370 nm. Again, this should result from the lengthening of EDOT oligomers. Moreover, a brown-colored suspension was observable within the bulk, which quickly deposits at the bottom of the solution. Note that the fast precipitation process, observed in this case, explains the absence of any scattering component in the extinction spectra of Figure 4.3b.

After the deposition of this suspension onto ITO substrate, the resulting film displayed a broad absorption between 500 and 600 nm, indicating that the suspension was made of polymers, noted PEDOT-N_3, formed at high doses, thanks to the $N_3^{\cdot}$-induced oxidation process. After irradiations at high doses (from 36 to 70 kGy), a precipitate was systematically observed. This precipitation is not only due to a sedimentation process of the PEDOT-N_3 polymers of relatively high molecular weight. It also results from the poor hydrophilic properties of these systems. Indeed, after adding either cyclohexane or dichloromethane solvents to the aqueous suspensions (v/v) and after stirring and decantation, the polymer particles always remain at the organic solvent–water interface as illustrated in the case of cyclohexane (insert of Figure 4.3b). This result proves the amphiphilic properties of PEDOT-N_3 polymers. Note that at the interface, these polymers appear as clustered fibers.

One can note that, for the same initial concentration in EDOT (10 mM), the spectral evolution in the presence of NaN_3 (Figure 4.3b) is similar to that observed in the absence of this salt (Figure 4.3a). However, when comparing both evolutions, one can note that for a given irradiation dose, the maximal absorption is always lower in the presence of NaN_3. Even if hydroxyl radicals and azide radicals oxidize EDOT and induce polymerization through the formation of EDOT dimers, it seems that the two implied mechanisms are somewhat different. Maybe the kinetic growth of dimers, oligomers, and polymers is slower in the case of $N_3^{\cdot}$. This would induce a lower polymerization yield and lower values of the maximal absorbance. However, such an interpretation is not in agreement with the observed dose effect. On another hand, the products of EDOT oxidation could be chemically and structurally different depending on $N_3^{\cdot}$ or $HO^{\cdot}$ nature of the oxidizing radicals. This could explain the different spectral properties of the products obtained either in the presence or in the absence of azide salt. In addition, the poor hydrophilic properties of the products formed in the presence of NaN_3 lead to their deposition at the bottom of the solution and their adsorption onto the walls of the samples.

The assertion of the successful formation of PEDOT-OH and PEDOT-N_3 was realized by ATR-FTIR and melting point measurements. The obtained results were in good agreement with those previously reported about PEDOT in literature. The melting point of both PEDOT-OH and PEDOT-N_3 was found at a temperature of 145 °C, which is very close to the PEDOT melting point value (146 °C) already reported. This result demonstrates once again the high purity of the radiosynthesized products and thus the efficiency of the radiolytic procedure. Also, the recorded ATR-FTIR spectra demonstrate without any ambiguity that $N_3^{\cdot}$ and $HO^{\cdot}$-induced EDOT polymerizations both take place thanks to α-α'coupling reactions and that the resulting solid powders obtained after centrifugation are effectively composed of PEDOT polymers. The wavenumber region 2000–700 cm^{-1} of the spectra of PEDOT-OH and PEDOT-N_3 shows remarkably comparable spectral features. However, significant differences were observed above 2000 cm^{-1}. Indeed, the spectrum of PEDOT-OH was found to exhibit a very large band between 3200 and 3600 cm^{-1} which was attributed to the presence of hydroxyl groups all along the polymers. The spectrum of PEDOT-N_3 was in turn characterized by an absorption in two different infrared regions: between 2110 and 2065 cm^{-1} and between 3565 and 3525 cm^{-1}. These characteristic peaks were attributed to the presence of azide anions in the solid phase. The noticeable differences between these two kinds of polymers were explained by the difference that exists between the well-known oxidizing behaviors of $HO^{\cdot}$ and $N_3^{\cdot}$. The $HO^{\cdot}$ radical either adds onto aromatic molecules to afford radical adducts or abstract electrons leading to radical cations, whereas $N_3^{\cdot}$ azide radicals only form radical cations through electron abstraction. The presence of hydroxyl groups in PEDOT-OH (coming from $HO^{\cdot}$-adducts) explains the existence of strong intermolecular interactions between the functionalized polymers through hydrogen bonds. It also confers to PEDOT-OH polymers hydrophilic properties, which explain their poor solubility into organic solvents as previously discussed. Contrarily to PEDOT-OH, PEDOT-N_3 polymers, which result from $N_3^{\cdot}$-induced EDOT oxidation, should not contain alcohol functionalities. This was proven by the absence of a large O–H band in the ATR-FTIR spectrum of PEDOT-N_3. The absence of such a polar group in the PEDOT-N_3 polymer impacts its solubility in water and explains its poor hydrophilic properties.

From what was observed in the spectral findings (UV–Vis and ART-FTIR), no doubt that the difference between oxidizing behaviors of $HO^{\cdot}$ and $N_3^{\cdot}$ influences the nanostructures morphology of PEDOT-OH and PEDOT-N_3. The captured Cryo-TEM images clearly show these differences in nanostructures (Figure 4.3c and Figure 4.3e) [35]. $HO^{\cdot}$ induces the polymerization of EDOT leading to spherical nanoparticles with a diameter comprised between 100 and 300 nm. These observations are consistent with previous results concerning hydroxyl-induced radiosynthesis of PEDOT under air atmosphere. PEDOT-OH globular nanostructures should correspond to self-assemblies of independent amorphous PEDOT-OH chain polymers as schematically represented (Figure 4.3d). The presence of hydroxyl groups, which has previously been demonstrated, should explain not only the hydrosolubility of PEDOT-OH polymers but also the as-observed packing and nanostructuration of the spherical supramolecular PEDOT-OH self-assemblies. Note that ethylenedioxy groups (H-bond acceptors) present all along the polymer chains could also be involved in hydrogen bonds with the hydroxyl groups.

Differently, $N_3^{\cdot}$ induces the polymerization of EDOT leading to different PEDOT nanostructures quite different from those obtained in the case of PEDOT-OH. Instead of a compact spheroidal morphology, which was found in the case of PEDOT-OH (Figure 4.3c), the obtained Cryo-TEM images clearly display nano-objects forming fibrillar or lamellar (plate-like) nanostructures, more or less folded, with a maximal fiber thickness of 10 nm and a length that can reach several microns (Figure 4.3e) [35]. Due to the thickness of the fibers, each of them should correspond to a self-assembly of linear PEDOT-N_3 polymer chains as schematically represented in Figure 4.3f. Since hydroxyl groups are not present in PEDOT-N_3 polymers, the packing of these polymers cannot result from H-bonds. This self-assembling should come from π-stacking interactions between conjugated polymers, which maintain the polymer chains parallel to each other and which can maybe confer to the polymers a lamellar structure. On another hand, this self-assembling could explain the macroscopic observation of PEDOT-N_3 polymers as clustered fibers at the interface between water and organic solvent. Also, the fact that PEDOT-N_3 polymers can either interact by van der Waals interactions (π-stacking interactions) or by hydrogen bonds, thanks to the presence of ethylenedioxy groups, could explain the amphiphilic properties of these polymers.

The observed nanostructures of PEDOT-OH and PEDOT-N_3 by SEM after a deposition procedure, as might be expected, were found consistent with what had been observed by cryo-TEM in aqueous solutions. SEM images of PEDOT-OH indicate the presence of very close-packed spheroidal polymeric particles (Figure 4.3g). The particles observed by SEM after deposition are polydisperse in size with a diameter comprised between 200 nm and 1 μm. Differently, the SEM images of PEDOT-N_3 highlighted the presence of close-packed lamellar (plate-like) structures characterized by a maximal thickness of about 1 μm (Figure 4.3h).

As demonstrated earlier, changing oxidizing species ($HO^{\cdot}$ or $N_3^{\cdot}$) leads to different UV–Vis absorption properties of radiosynthesized CPs, different hydrophilicities and different morphologies. This has been confirmed thanks to the use of an alternative strong oxidizing species, namely, $SO_4^{\cdot -}$, which was used to oxidize and polymerize EDOT monomers dissolved in aqueous solutions in the presence of an inorganic salt, the potassium persulfate ($K_2S_2O_8$). [38] This study once again showed the versatility of the radiolytic methodology based on gamma-rays and pulsed electron beam irradiation, and highlighted, without any ambiguity, the efficiency of alternative oxidizing radicals for the preparation of nanostructured conducting polymers.

4.2.4 Extension of the Radiolytic Procedure to the Synthesis of Polypyrrole (PPy) Nanostructures

To demonstrate the versatility of the radiolytic method in water under N_2O, the radiolytic procedure based on $HO^{\cdot}$-induced polymerization was extended to the successful synthesis of another representative CP, namely, PPy starting from Py monomers [46]. Similar properties, in terms of nanostructuration and hydrophilicity, were obtained in case of PPy when comparing to PEDOT-OH. In solution and after deposition, PPy nanostructures show as highlighted by Cryo-TEM, SEM, and AFM chaplet like spherical nanoparticles with diameters comprised between 80 and 200 nm. The merit of the work is that radiosynthesized PPy nanostructures are characterized by a very good thermal stability and an electrical conductivity that is five times higher than that of chemically synthesized PPy.

As previously described, the versatility of radiation-based methodology for the synthesis of CPs nanostructures was largely demonstrated in neutral aqueous media. Differently, in alkaline medium, in particular under N_2O, $HO^\cdot$ radical deprotonates into its alkaline form, which adds onto EDOT monomer, leading to an open cycle and preventing any dimerization of EDOT and consequently any polymerization of PEDOT as demonstrated by pulsed radiolysis [31]. In order to check the effect of pH on radiation induced CPs growth, works were conducted in acidic aqueous media.

4.2.5 Effect of pH on the Polymerization of EDOT Monomers

It has been shown in literature that low pHs prevent conducting polymers from overoxidation [47] and improve their electrical conductivity by doping effect [48] and structural optimization [49]. Gamma-irradiation was then used to radiolytically prepare conducting organic materials in acidic aqueous media and then to study their properties. In this framework, the endeavor was to polymerize EDOT monomers in very acidic aqueous solutions under N_2O (at $pH = 0$ in presence of $HClO_4$ or HCl), by exploiting the oxidizing species produced by γ-radiolysis in these acidic conditions ($HO^\cdot$ or $Cl_2^{\cdot-}$ respectively) [50].

In case of using $HClO_4$ to adjust the pH of the aqueous solution under N_2O, knowing that perchlorate ions (ClO_4^-) remain unreactive upon radiolysis, two reactive species should be considered: $HO^\cdot$ and $H^\cdot$ with the following radiolytic yield $G(HO^\cdot) = 2.8 \times 10^{-7}$ mol/J and $G(H^\cdot) = 3.4 \times 10^{-7}$ mol/J. $HO^\cdot$ is known as a very oxidizing species that enables in particular oxidation-induced polymerization of EDOT monomers in neutral aqueous solutions. Differently, $H^\cdot$ is generally known as less reactive and its reactions are often neglected in neutral media due to its low G value at $pH = 7$ [31]. Nevertheless, $H^\cdot$ becomes predominant at $pH = 0$ and thus its reactivity onto EDOT monomers cannot be omitted as demonstrated in some cases in literature [39]. Interestingly, when hydrochloride acid (HCl) is used (instead of $HClO_4$) in order to adjust the pH, $HO^\cdot$ radicals are quantitatively transformed into dichloride radical anions, $Cl_2^{\cdot-}$ [51]. Therefore, the main species produced by γ-radiolysis of very acidic aqueous solutions containing HCl under N_2O are $Cl_2^{\cdot-}$ (instead of $HO^\cdot$) and $H^\cdot$ [45]. While the total radiolytic yield of production of $H^\cdot$ atoms remains the same as that found in the case of $HClO_4$, the radiolytic yield of $Cl_2^{\cdot-}$ amounts to $G\left(Cl_2^{\cdot-}\right) = 2.8 \times 10^{-7}$ mol/J. Such as $HO^\cdot$, $Cl_2^{\cdot-}$ is a strong oxidizing species with a very high standard redox potential: $E^\circ\ (Cl_2^{\cdot-}/Cl^-) = 2.1\ V_{SHE}$ [52]. As in the case of hydroxyl radicals, the oxidation of EDOT monomers and their polymerization into PEDOT should then be possible thanks to $Cl_2^{\cdot-}$ [50].

Thus, under N_2O at pH 0, in presence of $HClO_4$ or with HCl, $HO^{\cdot}$, or $Cl_2^{\cdot -}$ should quantitatively oxidize EDOT. Effectively, in both cases, the effective yield of oxidation of EDOT monomers was found equal to 2.8×10^{-7} mol/J, proving by the same way that hydrogen atoms are not involved in EDOT polymerization. With such an oxidation yield, the dose needed for quantitative polymerization of 10 mM in EDOT amounts to 72 kGy at pH = 0 according to Eq. (4.2).

Acidic aqueous solution containing 10 mM in EDOT and 1 M in $HClO_4$ and acidic aqueous solution containing 10 mM in EDOT and 1 M in HCl were then both irradiated at 72 kGy under N_2O atmosphere. Also, for comparison purpose a neutral aqueous solution containing 10 mM in EDOT in the absence of acids was irradiated under N_2O at the same dose. The photographs of the three solutions obtained after irradiation (insert of Figure 4.4) as well as their UV–Vis absorption spectra are displayed on Figure 4.4. After a 72 kGy-irradiation, the solution prepared in neutral medium appears yellow (photography c in insert of Figure 4.4) and its absorption spectrum (spectrum c of Figure 4.4) displays an intense absorption band at around 350 nm in total agreement with the previous works conducted in neutral aqueous media [21, 35, 53]. This band was shown to be characteristic of PEDOT oligomers produced in the neutral medium by water radiolysis. Differently, after irradiation at 72 kGy, the solutions prepared at pH 0 in the presence of HCl (photography a in insert of Figure 4.4) or in the presence of $HClO_4$ (photography b) both appear as dark blue suspensions, which is the typical color of PEDOT polymers when obtained in their oxidized state [54, 55]. Remarkably, when considering the absorption spectra of the two acidic solutions irradiated at 72 kGy in presence of HCl (spectrum a of Figure 4.4) or $HClO_4$ (spectrum b), two shoulders are observed in both cases at 350 and 450 nm, which can be attributed to the presence, in very acidic medium, of PEDOT polymers prepared upon irradiation. As a matter of fact, PEDOT polymers are known to usually display, in solution, characteristic peaks in this wavelength region, which are assigned to π–π^* transitions in the polymer backbones. In addition to these shoulders, a large absorption band was observed in both cases at around 700 nm in the case of HCl (spectrum a) and in the case of $HClO_4$ (spectrum b). This large band can be considered as polaron or bipolaron bands, which are both characteristic of PEDOT polymers when obtained in their oxidized state (p-type doping) [56].

The *in situ* doping process of PEDOT polymers radiosynthesized in very acidic aqueous solutions was definitely confirmed by both ATR-FTIR spectroscopy and Energy-Dispersive X-ray (EDX) analysis: first EDX enabled the detection of an additional chemical element, namely, chlorine atom, not present in the organic monomers but found homogeneously dispersed in the deposited solid sample; second, ATR-FTIR spectrum of PEDOT polymers radiosynthesized in very acidic aqueous solutions highlighted the presence of a less common infrared band located at 1640 cm^{-1} [12, 57]. This band had already been observed in earlier works in the case of PEDOT polymers synthesized by conventional methods and doped with chloride ions. This peak originates from the quinoidal structure of thiophene ring. The presence of this band together with the results obtained by EDX highlights the doping of PEDOT synthesized in very acidic media either by Cl^- or ClO_4^- anions coming from HCl or $HClO_4$ dissociation. This point is in full agreement with the

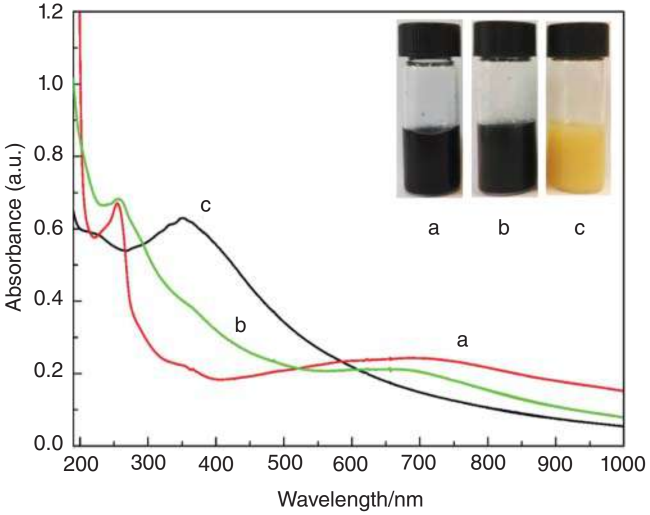

Figure 4.4 UV–Vis absorption spectra of PEDOT polymers synthesized after 72 kGy irradiation of aqueous solutions containing 10 mM in EDOT under N_2O atmosphere (a) in presence of HCl (1 M) at pH = 0, (b) in presence of $HClO_4$ (1 M) at pH = 0, and (c) in the absence of acids at neutral pH. All the spectra were recorded after 10 times dilution. The optical path length was 0.2 cm. The reference was water. Insert: photographs of the corresponding aqueous solutions. Source: Cui et al. [50].

results obtained by UV–Vis absorption spectroscopy (absorption band at 700 nm) and with the colors of the irradiated solutions.

Contrarily to PEDOT oligomers produced in neutral aqueous media, PEDOT polymers synthesized under the same atmosphere (N_2O) at pH = 0 were found doped. The doping of radiosynthesized PEDOT polymers should result from the presence in the medium of considerable amounts (1 M) of hydrochloric acid or perchloric acid. PEDOT polymers produced in presence of either HCl or $HClO_4$ seem to be in the same oxidized state since the doping bands are located at approximately the same wavelength. In terms of morphology, the observations made by SEM and AFM microscopies showed that PEDOT polymers self-assemble into polydisperse globular nanoparticles (size comprised between 200 and 500 nm) [50]. Since PEDOT morphology in very acidic medium is comparable with that of PEDOT nanostructures obtained in pure neutral aqueous media (in the absence of any additive such as NaN_3 or $K_2S_2O_8$), one can conclude that neither the acidity of the medium (presence of HCl or $HClO_4$ at 1 M) nor the reactivity of $Cl_2^{\cdot -}$ radicals affect the final morphology of PEDOT radiosynthesized polymers.

4.3 Radiation-Induced Synthesis of CPs Nanostructures by Reduction-Polymerization Route

Usually CPs are synthesized by oxidation of monomers as previously shown. Nevertheless, there are some works in literature concerning the synthesis of CPs by reduction of monomers by the way of conventional methods [58]. Radiation-based methodology was moreover used in order to radiolytically produce PEDOT nanostructures, thanks to a reduction-polymerization route. In particular, γ-rays were used to produce solvated electrons (e_{aq}^{-}) in an aqueous solution containing EDOT monomers under N_2 atmosphere. Contrarily to the common approach based on the use of oxidizing radicals, such as hydroxyl radicals ($HO^{\cdot}$), azide radicals ($N_3^{\cdot}$), sulfate radicals ($SO_4^{\cdot -}$), or dichloride radical anions, $Cl_2^{\cdot -}$, hydrated electrons produced by water radiolysis are known as very reducing species and were used to reduce EDOT and then to initiate the reduction–polymerization of PEDOT polymers through coupling reactions.

Evidently in order to quantitatively reduce EDOT and then to synthesize PEDOT, hydroxyl radicals produced under N_2 atmosphere must be scavenged. This is possible, under N_2 atmosphere, in the presence of isopropanol, $(CH_3)_2CHOH$ (at a relatively high concentration, 0.2 mol/l, for example). In these conditions $HO^{\cdot}$ (as well as $H^{\cdot}$ atoms) are quantitatively converted into $(CH_3)_2C^{\cdot}OH$ isopropanol radicals [59, 60], which are not able to oxidize EDOT. In fact, they are almost reducing species, the redox potential of which amounts to $-1.8\ V_{SHE}$ at $pH = 7$. As a consequence, when irradiating N_2-saturated aqueous solutions in the presence of isopropanol, in addition to hydrated electrons ($Ge_{aq^-} = 2.8 \times 10^{-7}$ mol/J), only an additional reducing short-lived transient species is quantitatively formed, namely, isopropanol radicals, the radiolytic yield of which being $G\left(\left(CH_3\right)_2C^{\cdot}OH\right) = G_{HO^{\cdot}} = 3.4 \times 10^{-7}$ mol/J.

The radiolytic study demonstrated that, under N_2 in presence of isopropanol, the yield of EDOT reduction is equal to Ge_{aq^-}. [61] This means that isopropanol radicals don't reduce EDOT and that only hydrated electrons react onto EDOT molecules. Consequently, the dose that is necessary for the total reduction of 10 mM in EDOT amounts to 36 kGy, while, assuming once again a step-by-step growth mechanism, the dose D_{max} that is necessary for the complete synthesis of PEDOT amounts to 72 kGy according to Eq. (4.2). Indeed, from a kinetic point of view, the dose effect study showed that similarly to hydroxyl radicals that lead to PEDOT by the way of oxidation of monomers ($PEDOT_{ox}$), the process initiated by hydrated electrons that leads to $PEDOT_{red}$ does not proceed through a chain reaction. In fact, the quantitative synthesis of $PEDOT_{red}$ polymers throughout a reduction-polymerization route proceeds through a step-by-step mechanism and therefore the use of two hydrated electrons per EDOT molecule is needed.

In terms of optical properties, the recorded UV–Vis absorption spectrum of the aqueous solution irradiated at 72 kGy under N_2 in the presence of isopropanol and containing $PEDOT_{red}$ did not show any change or shift when comparing with the spectrum previously obtained for $PEDOT_{ox}$ synthesized at the same irradiation dose in water under N_2O. When it comes to ATR-FTIR, the spectra of $PEDOT_{red}$ and $PEDOT_{ox}$ appeared relatively slightly displaced. Nevertheless, the findings proved, without any ambiguity, that PEDOT polymers were obtained by radiolysis either by reduction-polymerization or by oxidation polymerization [61].

Figure 4.5 displays the resulted morphological structures of $PEDOT_{red}$ synthesized, thanks to e_{aq}^{-} in aqueous solution under N_2 atmosphere, as obtained

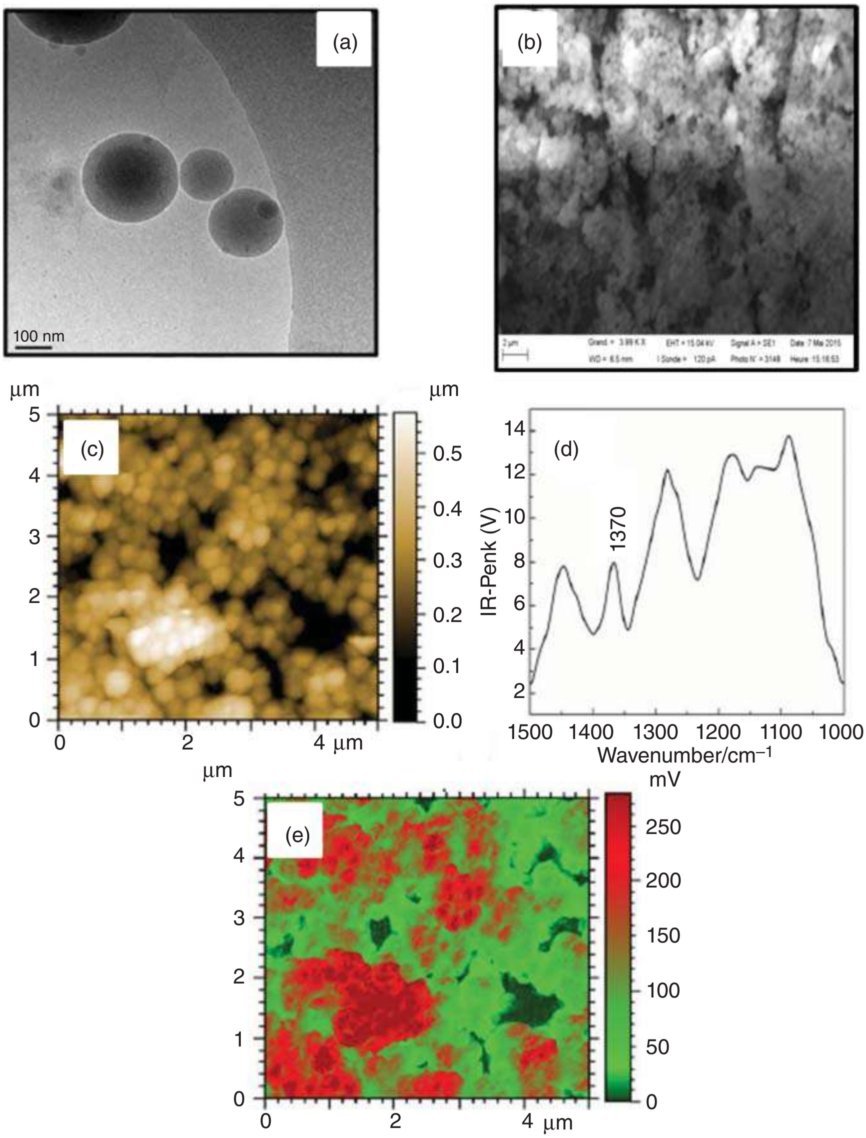

Figure 4.5 Microscopic and AFM-IR characterizations of aqueous samples containing 10 mM in EDOT irradiated at 72 kGy under N_2 in the presence of isopropanol. (a) Cryo-TEM image of $PEDOT_{red}$ polymers exhibiting spherical nano-objects with diameters comprised between 100 and 500 nm, (b) SEM image of $PEDOT_{red}$ polymers after lyophilization and deposition onto carbon tape adhered to aluminum mounts, (c) AFM topographic image of $PEDOT_{red}$ polymers in contact mode after lyophilization and deposition onto ZnSe prism, (d) AFM-IR spectrum of $PEDOT_{red}$ polymers, and (e) AFM-IR chemical mapping of $PEDOT_{red}$ polymers with the IR source tuned to the C—C band at 1370 cm^{-1}. Source: Cui et al. [61].

by cryo-TEM, SEM, and AFM-IR. Representative cryo-TEM image shows the presence of low-density globular nanostructures forming polydisperse spherical nanoparticles with a diameter comprised between 100 and 500 nm as observed on Figure 4.5a. The displayed SEM image in Figure 4.5b depicts very close-packed spheroidal polymeric nanoparticles. These SEM observations agree well with the morphology of $\mathrm{PEDOT_{red}}$ particles observed in aqueous solution by cryo-TEM (Figure 4.5a) without any significant change in the mean size and in the shape. Then, the packing of the particles and their flattening onto the substrate when deposited and dried do not seem to affect the nanostructuration of $\mathrm{PEDOT_{red}}$ polymers. All these observations are consistent with the reported characterizations of $\mathrm{PEDOT_{ox}}$ polymers synthesized under N_2O by oxidation-polymerization route induced either by γ-rays or by accelerated electrons.

In order to further prove that the spherical nanoparticles observed by cryo-TEM and SEM were effectively made up of PEDOT polymer chains, $\mathrm{PEDOT_{red}}$ polymers were imaged and characterized by AFM-IR (Figure 4.5c–e). According to the topological image of $\mathrm{PEDOT_{red}}$ recorded in contact mode (Figure 4.5c), the bottom dark areas having no thickness correspond to the substrate. The topography of $\mathrm{PEDOT_{red}}$ displayed as the bright areas corresponds to the thicker regions made up of close-packed spherical nanoparticles (100–300 nm in diameter). This AFM observation agrees well with the morphology of $\mathrm{PEDOT_{red}}$ globular nanoparticles observed by Cryo-TEM and SEM (Figure 4.5a,b). In order to confirm that these nanostructures are made up of PEDOT polymers, the sample was observed by AFM-IR in the range of 1000–1500 $\mathrm{cm^{-1}}$ (Figure 4.5d). The obtained spectrum displays a peak at 1370 $\mathrm{cm^{-1}}$, which corresponds to the C–C stretching band of PEDOT as observed in typical ATR-FTIR spectra. This definitely demonstrates that the nanoparticles observed in Figure 4.5a–c contain close-packed PEDOT polymer chains. Since the AFM-IR technique also enables the chemical mapping of the sample, this wavenumber 1370 $\mathrm{cm^{-1}}$ was chosen for AFM-IR chemical mapping of the sample. The chemical map was scanned and the absorption strength was recorded (Figure 4.5e). In this figure, the red areas indicate a stronger absorption at the characteristic wavenumber, which is caused by a thicker layer of $\mathrm{PEDOT_{red}}$ (∼300 nm). When comparing the topography (Figure 4.5c) and the chemical mapping (Figure 4.5e), one can observe that the stronger absorbing areas fit very well with the thicker regions, which implies that the spherical nanoparticles are mainly composed by PEDOT polymer chains. In conclusion, radiation chemistry in reducing conditions leads to the reduction of EDOT monomers and to the growth of PEDOT polymers, which self-assemble into spherical nanostructures (nanoparticles of few hundred nanometers in diameter), those observed by cryo-TEM, SEM, and AFM (Figure 4.5).

4.4 Radiation-Induced Synthesis of CPs/Metal Nanocomposites

As described in previous chapters, CPs were successfully synthesized through either radiation-induced reduction or oxidation polymerization routes. In the same way, synthesis of nanocomposites made of CPs and metal nanoparticles was attempted by the way of radiation chemistry. In literature, PEDOT/Ag nanocomposites had already been successfully synthesized by means of both chemical and electrochemical methods [62–64] and had also been shown to possess various potential applications [34, 65, 66]. According to these conventional synthetic methodologies, two-step method or one-pot method is usually applied to synthesize CPs nanocomposites [67, 68]. These latter usually show core–shell structures, the composition of which fundamentally depends on the preparation procedure [69, 70].

In fact the use of radiation-induced synthesis of shape controlled silver nanoparticles in aqueous solution was already conducted by Remita and coworkers [71, 72] on one hand, and the radiolytic preparation of nanostructured conducting PEDOT polymers was also realized as previously highlighted on the other hand [21, 35]. Thus, these two approaches represented good omens for the successful synthesis of PEDOT/Ag composites by radiolysis. Starting from an aqueous solution containing metal ions and EDOT monomers, the use of radiation chemistry for the *in situ* production of hydrated electrons as reducing species or hydroxyl radicals as oxidizing radicals was then conducted in order to synthesize CPs/metal nanocomposites [53].

It was shown that based on γ-radiolysis, PEDOT/Ag nanocomposites can simply be prepared by both two-step and one pot method. According to the two-step method, PEDOT polymers were first synthesized by either oxidation ($PEDOT_{ox}$) or reduction ($PEDOT_{red}$) of EDOT monomers and then, PEDOT/Ag nanocomposites were prepared by the further reduction of silver ions into metal nanoparticles. Differently, according to the one pot method, EDOT polymerization and metal ions reduction were achieved in parallel, in one step. As lastly previewed in reduction-polymerization route, γ-induced synthesis of $PEDOT_{red}$ proceeds in N_2-saturated aqueous solutions and in the presence of isopropanol. Under these conditions, two short-lived reactive transient species are formed, namely, e_{aq}^- and $(CH_3)_2C^{\cdot}OH$ radicals, with corresponding radiolytic yields (G-values), which amount to 2.8×10^{-7} mol/J and 3.4×10^{-7} mol/J. [73] Note that isopropanol radical is a reducing species with a redox potential of $-1.8\ V_{SHE}$ at pH = 7, which can quantitatively act as a reducing species towards Ag^+ but which cannot reduce EDOT monomers. [74] Consequently, EDOT is reduced with a radiolytic yield $G_{red}(EDOT) = 2.8 \times 10^{-7}$ mol/J, while Ag^+ ions are reduced by both e_{aq}^- and $(CH_3)_2C{\cdot}OH$, with a radiolytic yield: $G\left(\left(CH_3\right)_2C^{\cdot}OH\right) + Ge_{aq}^- = G_{red}\left(Ag^+\right) = 6.2 \times 10^{-7}$ mol/J. [75]

The ratio between EDOT (10 mM) and Ag was changed in case of one pot method, from 10 : 1 to 10 : 20, by varying the amount of $AgClO_4$ salt (from 1 to 20 mM). Whatever the ratio of EDOT to Ag, the aqueous solutions were always added with isopropanol (0.2 M), degassed with N_2 and irradiated at 72 kGy, which enables in all cases the total reduction of both EDOT and Ag^+ and production of $(PEDOT/Ag)_{red}$. Regarding two steps method, PEDOT polymers were first synthesized either by reduction (10 mM in EDOT in N_2-saturated aqueous solutions and in the presence of isopropanol, 0.2 M) or by oxidation of EDOT molecules (10 mM in EDOT in N_2O-saturated aqueous solutions) as highlighted before [35], and then silver nanoparticles were obtained by reduction of silver ions (10 mM in $AgClO_4$

in N_2-saturated aqueous solutions and in the presence of isopropanol, 0.2 M). The formed CPs nanocomposites from these two step methods were so-called $PEDOT_{red}/Ag_{red}$ and $PEDOT_{ox}/Ag_{red}$. At each step, a dose of 36 kGy was delivered to enable the quantitative synthesis of PEDOT/Ag nanocomposites [53].

UV–Vis absorption spectrophotometry, ATR-FTIR spectroscopy (spectra not shown), and EDX spectroscopy (Figure 4.6) [53] showed that no matter what was the opted procedure, all the prepared nanocomposites were made of PEDOT polymer nanostructures and silver nanoparticles. More interestingly, they all were found to be doped with perchlorate anions [73]. Nevertheless, the morphologies of PEDOT/Ag nanocomposites were almost different and depend on the preparation procedure. As can be seen from the presented cryo-TEM images in Figure 4.6a,b, the observations made on ($PEDOT_{ox}/Ag_{red}$) and ($PEDOT_{red}/Ag_{red}$) in aqueous solution appear similar. In both cases, representative images show the presence of low-density globular structures forming polydisperse spherical nanoparticles with a diameter comprised between 100 and 500 nm. This result was in very good agreement with the observations already made in the case of PEDOT synthesized alone (in the absence of silver) by radiolysis, either by EDOT oxidation or by EDOT reduction. Thus, these low-density globular objects were identified as self-assembled PEDOT polymers. As can be seen in Figure 4.6a,b, smaller nanoparticles (from few nm to 50 nm), which appear very more contrasted (darker), are systematically found adsorbed onto the bigger globular PEDOT nanoparticles. The relatively high

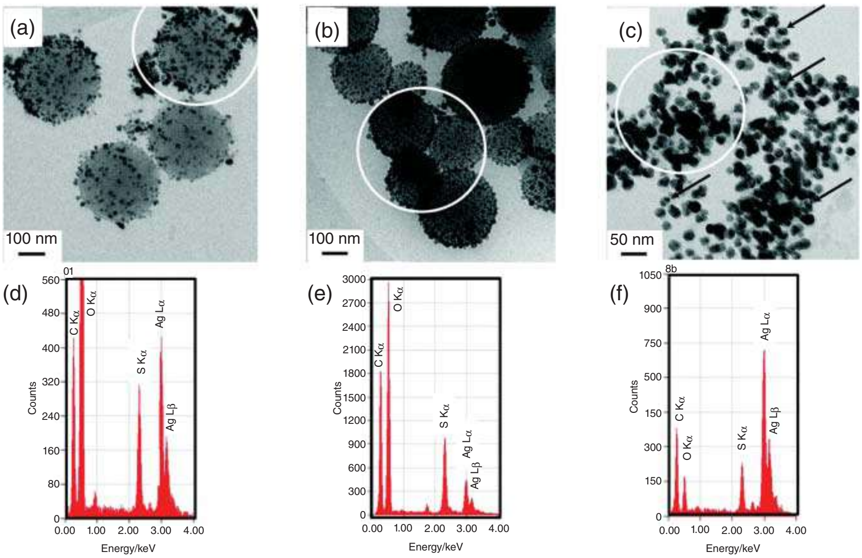

Figure 4.6 Cryo-TEM images of (a) sample containing ($PEDOT_{ox}/Ag_{red}$) synthesized according to two step method, (b) sample containing ($PEDOT_{red}/Ag_{red}$) also synthesized according to two step method and (c) sample containing $(PEDOT/Ag)_{red}$ prepared according to the one-pot method. Energy-dispersive X-ray (EDX) spectra (d), (e), and (f) corresponding to the elemental analysis of the circled areas of the cryo-TEM images [53]. [53] Source: Reproduced by permission of The Royal Society of Chemistry (RSC) on behalf of the Centre National de la Recherche Scientifique (CNRS) and the RSC.

contrast of these small particles suggests their metal nature. Since no other objects were observed during Cryo-TEM experiments, these small spherical nanoparticles were attributed to silver nanoparticles.

When it comes to $(\mathrm{PEDOT/Ag})_{\mathrm{red}}$ formed by one pot method, the structure and morphology shown in Figure 4.6c appear as granular mixtures. This observation was totally different from those made in case of $(\mathrm{PEDOT_{ox}/Ag_{red}})$ and $(\mathrm{PEDOT_{red}/Ag_{red}})$. Indeed, Figure 4.6c shows the presence of low-density globular nanostructures forming polydisperse spheroidal nanoparticles with a diameter between 10 and 50 nm. These organic particles, made of PEDOT polymers and obtained via the one-pot method, are ten times smaller than the PEDOT nanoparticles obtained via the two-step method. On the other hand, as can also be observed in Figure 4.6c, smaller nanoparticles, which appear much more contrasted (darker), are found to be embedded into the core of the bigger globular PEDOT nanoparticles. Some of these dark nanoparticles are indicated in the figure by arrows. The relatively high contrast of these smaller particles suggests once again that they are made of silver.

During Cryo-TEM observations, *in situ* EDX spectroscopy was used to check the chemical composition of radiosynthesized materials in order to prove the presence of sulfur atoms (which are only present in PEDOT polymers, one sulfur atom per EDOT molecule) and of silver atoms (which would be the signature of silver nanoparticles). The aim was also to check the molar ratio between both atoms in radiosynthesized PEDOT/Ag composites. EDX spectra (Figure 4.6, spectra d–f), which correspond respectively to the elemental analysis of the surrounded areas of cryo-TEM images (**a**, **b**, and **c**) of Figure 4.6, highlight the presence, in all samples, of S (Kα 2.31 keV) and Ag (Lα 2.98 keV and Lβ 3.15 keV). The detection of both sulfur and silver elements definitely demonstrated the concomitant presence, in all the analyzed areas of images **a**, **b**, and **c** of Figure 4.6, of both PEDOT polymers and silver nanoparticles. Also, a quantitative analysis performed in the surrounded areas of Figure 4.6 proved as scheduled the stoichiometric ratio (50% S and 50% Ag) between sulfur and silver in the radiosynthesized composites.

As demonstrated by cryo-TEM microscopy and EDX spectroscopy, composites prepared by two-step method are made of large spherical PEDOT nanoparticles at the surface of which smaller silver nanoparticles adsorb. Due to the two-step method used to produce $(\mathrm{PEDOT_{ox}/Ag_{red}})$ and $(\mathrm{PEDOT_{red}/Ag_{red}})$, PEDOT polymers are first synthesized, in the absence of inorganic ions, and self-assemble, thanks to Van der Waals interactions into globular organic nanoparticles. Silver nanoparticles are formed only during the second step. This explains their presence outside PEDOT nanoparticles. By contrast, in the one-pot method, silver ion reduction takes place in parallel with EDOT reduction. Then, since silver reduction is faster than that of EDOT [53], metal nanoparticles can form prior to the existence of PEDOT nanoparticles. Thus, as shown in Figure 4.6, image **c**, all silver nanoparticles are found surrounded by an organic shell. This could mean that EDOT reduction and polymerization occur in the vicinity of silver nanoparticles. Such a growth mechanism could be explained by the strong interaction, which exists between silver ions (or even atoms) and sulfur atoms of the EDOT monomers. Or maybe, PEDOT polymers are formed far from the silver nanoparticles, in the bulk of the aqueous solution, and then diffuse and adsorb at their surface, due to weak van der Waals interactions, enabling the thermodynamic stabilization of silver particles and avoiding their aggregation and sedimentation. This effect of polymers on silver nanoparticles had already been reported in the literature [76].

SEM was also used as a corroboratory tool to check the morphology of PEDOT/Ag nanocomposites [53]. In case of ($PEDOT_{ox}/Ag_{red}$) and ($PEDOT_{red}/Ag_{red}$), the composite nanoparticles observed using SEM after deposition were found polydisperse in size with a diameter comprised between 100 and 500 nm. These SEM observations agree well with the size and the shape of the ($PEDOT_{ox}/Ag_{red}$) and ($PEDOT_{red}/Ag_{red}$) particles previously observed in aqueous solution using cryo-TEM observations (Figure 4.6, images a and b). In contrast to these observations, no spherical nanoparticles were observed in case of $(PEDOT/Ag)_{red}$, which may be due to the fact that their relatively small size avoids their observation during SEM microscopy. In fact, SEM characterization showed that $(PEDOT/Ag)_{red}$ composites had become a compact hybrid after deposition. Also, when varying the EDOT/Ag ratio, from 10 : 5 to 10 : 20, as the proportion of silver increases, the $(PEDOT/Ag)_{red}$ composites become denser and form more compact blocks.

4.5 Toward Radiation-Induced Synthesis of CPs Nanostructures in Organic Solvents

All previous radiolytic studies were conducted in aqueous solutions with the aim to produce CPs nanostructures or CPs composites. Different strategies were adopted: oxidation and reduction routes, changing the atmosphere, varying the oxidizing species, and adjusting the pH. Nevertheless, the following question remains: what about changing the solvent? This is important for instance in order to enhance the processability and to synthesize CPs starting from hydrophobic monomers such as 3-hexylthiphene (3HT). The extension of original radiolytic methodology to the use of organic solvents is indeed a need since radiation-induced polymerization in aqueous solution cannot always be used. In fact, there are several obstructions that have been faced with γ-radiolysis of aqueous solutions, such as the poor processability, low solubility, and even sometimes the insolubility of some of concerned monomers, namely, 3-alkylthiophenes.

Indeed, the use of organic solvent to synthesize CPs was investigated by Koizumi and coworkers. [77] who studied the mechanism of oxidative polymerization of conducting polymers in several organic solvents by γ-irradiation. The study was performed on 3-octylthiophene (3OT) and the oxidative polymerization was initiated by γ-radiolysis of chloroform, hexane, and neat monomer solution. The polymerization was successfully induced in chloroform. The study showed that the products contain large amounts of small oligomers, and the yield of polymers with high molecular weight was found low. Furthermore, high irradiation dose and removal of the oligomers was shown to be necessary to obtain usable polymers for any potential applications.

A similar radiolytic approach was conducted in dichloromethane (DCM). Indeed, DCM is a very good solvent for many organic compounds and its gamma radiolysis is relatively well known under different conditions [78]. Moreover, DCM was already used to carry out electrochemical or radiolytical one-electron oxidation of solutes [78, 79], and it has been proved that irradiated DCM is a good oxidizing system [80]. Indeed, γ-irradiation of DCM solvent yields several oxidizing species that could enable first the oxidation of dissolved organic monomers and then their polymerization into CPs. With these in mind, strategy based on radiation chemistry was extended to the preparation of conducting polymers into organic solvents. In particular, starting from EDOT monomers dissolved in DCM solvent, the synthesis by γ-rays of PEDOT polymers was elaborated and optimized [81].

It is well established that γ-irradiation of deoxygenated solutions of DCM (under N_2 for instance) leads, within short nanosecond time scale, to the formation of solvated electrons in addition to neutral radicals and solvent radical cations which quickly lead to dichloromethyl ($CHCl_2^{\cdot}$) and chloromethyl ($CH_2Cl^{\cdot}$) radicals [79, 82]:

$$CH_2Cl_2 \rightarrow^{\rightarrow} \left[e^- + Cl^{\cdot} + CH_2Cl_2^{\cdot+}\right] \rightarrow^{\rightarrow} CHCl_2^{\cdot} + CH_2Cl^{\cdot} + HCl \tag{4.5}$$

All the generated radicals are well known as strong oxidizing agents toward organic materials. Some investigations highlighted the possibility of oxidation of aromatic hydrocarbons by neutral dichloromethyl and chloromethyl ($CHCl_2^{\cdot}$ and $CH_2Cl^{\cdot}$) radicals in spite of their relatively low redox potentials [80, 83], suggesting the idea that all these radicals should enable the oxidation of EDOT monomers and then their polymerization into PEDOT polymers, the yield of EDOT oxidation being equivalent to the yield of production of the oxidizing species coming from DCM radiolysis (G_{ox}). Once again, taking into account the step by step mechanism involved during CPs growth, the theoretical irradiation dose (D_{max}) that should lead to the total oxidation of EDOT into PEDOT can be expressed as a function of G_{ox} through Eq. (4.2) [31, 35], in which this time the density, d, is that of DCM solvent ($d = 1.35$ kg/l).

In this context, in order to check the dose effect and to evaluate the required irradiation dose for quantitative PEDOT preparation and then to determine the effective yield of EDOT oxidation, DCM solutions containing 10 mM in EDOT under N_2 atmosphere were irradiated at increasing doses up to 70 kGy. The UV–Vis absorption spectrum of the solution before irradiation is shown in insert of Figure 4.7. As observed, EDOT exhibits two absorption maxima at 242 nm and 259 nm, which are features of the π–π* electronic transitions in the thiophene rings within the DCM solvent. As demonstrated in previous works [31, 35], the study of the variation in EDOT concentration as a function of the irradiation dose should enable the determination of the radiolytic yield of EDOT oxidation (G_{ox}). However, stable and transient products (dimers of 1,1-dichloroethane, 1,2-dichloroethane, 1,1,2-trichloroethane and 1,1,2,2-tetrachloroethane) [84] were detected in irradiated solution of DCM and were found to absorb in the same wavelength region avoiding any direct calculation of G_{ox}. Nevertheless, as it will be shown, following the evolution of the intensity of PEDOT UV–Vis absorption spectrum as a function of the absorbed dose allowed first

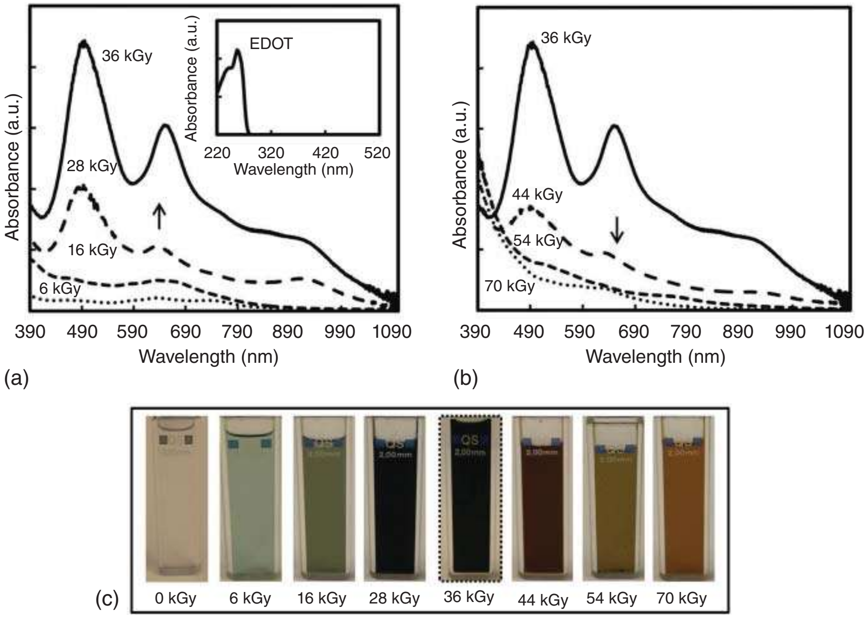

Figure 4.7 UV–Vis absorption spectra of DCM solution containing 10 mM in EDOT and irradiated under N_2 atmosphere at increasing doses from: (a) 0 to 36 kGy and (b) from 36 to 70 kGy. The reference was DCM. Insert of (a) UV–Vis absorption spectrum of the solution before irradiation (c) Photographs of DCM solution before and after irradiation at increasing doses [81]. [81] Source: Reproduced by permission of The Royal Society of Chemistry (RSC) on behalf of the Centre National de la Recherche Scientifique (CNRS) and the RSC.

the estimation of the radiation dose needed to achieve quantitative polymerization of EDOT monomers ($D_{\max}$) and second the calculation of G_{ox} according to Eq. (4.2).

In order to follow the progressive formation of PEDOT polymers, the DCM solution containing 10 mM in EDOT was irradiated under N_2 at increasing doses up to 70 kGy (Figure 4.7) and its absorption spectrum was recorded as a function of the irradiation dose. Up to irradiation dose of 36 kGy, progressively and remarkably, two peaks were being protruded at 490 and 650 nm (Figure 4.7a). These peaks were attributed to formation of PEDOT polymers and ascribed to the π–π^* transitions along the polymer chains. [85, 86] Whereas the observed peaks at approximately 800–1000 nm were attributed to polaron and/or bipolaron bands, which are characteristic of oxidized state of PEDOT [57, 87]: the considerable amount of hydrochloride acid produced from γ-radiolysis of DCM yields to different doping states of PEDOT polymers. As a consequence, the doped PEDOTs with chloride ions show an absorption peak at approximately 900 nm corresponding to the charge carrier band of the charged polymers [57]. In agreement, the corresponding ATR-FTIR spectra also showed the presence, whatever the irradiation dose, of a less common infrared band located at 1640 cm^{-1}. This band had already been observed in earlier studies in the case of PEDOT polymers doped with chloride ions [12, 57].

Proceeding, the solutions with irradiation doses higher than 36 kGy leads to gradual decrease in the absorption of PEDOT polymers at both 490 and 650 nm

(Figure 4.7b). DCM solution containing 10 mM in EDOT appears colorless before irradiation (Figure 4.7c). Distinctly, the irradiated solutions that are shown in Figure 4.7c got colored with sky blue right after gamma irradiation. This color parallelly darkens with proceeding the irradiation with higher doses up to 36 kGy. Dark blue and black precipitants were observed in irradiated solutions at doses of 28–36 kGy. However, when exceeding the dose of 36 kGy and continuing the irradiation up to 70 kGy, the solution gradated towards brown, then yellow, and finally orange, while the black precipitant appeared to be glue. These color fluctuations above 36 kGy and the spectral variations upon using overdose were ascribed to the overoxidation of PEDOT polymers, which evidently leads to degradation and breaking down of the polymer chains.

This overoxidation and degradation of PEDOT polymers irradiated above 36 kGy in DCM under N_2 atmosphere was demonstrated by ATR-FTIR spectroscopy and SEC chromatography. Indeed, the IR spectra showed the presence, in the case of an irradiation dose above 36 kGy, of a broadband from 1650 to 1730 cm^{-1}, which is the sign of an overoxidation state [88]. In particular, this band could be attributed to the formation of a carbonyl group. While, SEC analysis showed that more and more oligomers of lower molecular weight are formed at doses above 36 kGy, indicating

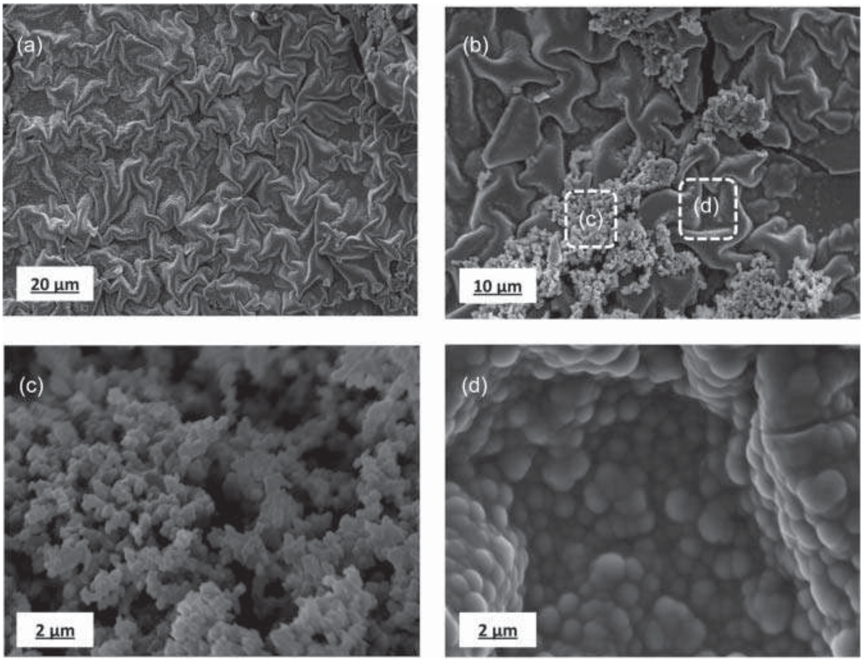

Figure 4.8 SEM images of dried PEDOT polymer powder after deposition onto carbon tape adhered to aluminum mounts and gold coating: (a) and (b). Images (c) and (d) are close view of SEM image (b). The powder was obtained after solvent evaporation. PEDOT polymers were synthesized by γ-radiolysis at 36 kGy of a DCM solution containing 10 mM in EDOT under N_2 atmosphere [81]. [81] Source: Reproduced by permission of The Royal Society of Chemistry (RSC) on behalf of the Centre National de la Recherche Scientifique (CNRS) and the RSC.

the occurrence of damage and breaking down of the polymer chains. Subsequently, these findings suggest that the radiation dose needed for quantitative polymerization of 10 mM in EDOT monomers (D_{max}) in DCM solvent under N_2 atmosphere amounts to 36 kGy and that, according to Eq. (4.2), the yield of EDOT oxidation (G_{ox}) amounts to 4.12×10^{-7} mol/J in these experimental conditions.

Morphology of PEDOT polymers synthesized under N_2 atmosphere in a DCM solution was checked by SEM microscopy after solvent evaporation. SEM images recorded after deposition of dried PEDOT polymers powder onto carbon tape adhered to aluminum mounts and gold coating are displayed on Figure 4.8. As can be seen in Figure 4.8a, SEM image displays a comprehensive view of creased film of PEDOT. Figure 4.8b shows closer view of this film in which globular clusters are observed. These globular particles can be clearly seen in Figure 4.8c. In a close view of the film creases in Figure 4.8d, it is possible to see that PEDOT film is composed of aggregated globules and packed spheroid particles with average size of 0.5 to 2 μm. These results are in good agreement with previous observations reported in the literature in the case of PEDOT polymers doped with chloride ions as prepared by electrochemical method [12]. To further confirm that PEDOT polymers radiosynthesized in DCM solvent are doped with chloride ions, *in situ* energy dispersive X-ray (EDX) analysis was performed on the PEDOT sample synthesized at 36 kGy during SEM experiments (but without gold coating). These experiments undoubtedly confirmed the presence of chlorine atoms within the sample.

4.6 The Electrical and Physical Properties of Radiosynthesized CPs

The importance of radiation induced polymerization is to achieve effective and simple synthesis of processable and usable forms of conducting polymers either in solution or after deposition. The radiation-based methodology is certainly one of the most appropriate techniques for promising production of CPs. As previewed, the methodology is versatile and reliable. In addition, as it will be presented, the properties of radiosynthesized CPs were in most cases evaluated and found comparable with those of conducting materials that were obtained by conventional methods in terms of physical and electrical properties.

One of the most important properties that characterize the polymers is generally their molecular weight. Indeed, the presence of long polymer chains, or more precisely having high π–π^* conjugation, gives CPs their remarkable electrical properties. Thus, size exclusion chromatography (SEC) analysis was used in order to characterize the molecular weight and the chain length of the radiosynthesized conducting polymers. Another important property of CPs is their electrochemical behavior. This behavior was highlighted in case of different CPs synthesized by radiation methodology by using cyclic voltammetry analysis and optical band gap ($E_{gap.op}$) calculations. The CV analysis enabled the determination of oxidation and reduction potentials of radiosynthesized polymers and thus the estimation of the energy level of the highest occupied molecular orbital (HOMO) from the ionization potential, the energy level of the lowest unoccupied molecular orbital (LUMO) from the electronic affinity, as well as the electronic band gap ($E_{\mathrm{gap.el}}$). In addition, the electrical conductivity of the radiosynthesized CPs and CPs nanocomposites, as measured by four-point probe technique, was also checked and compared with the electrical conductivities reported in literature for CPs synthesized by conventional methods. Besides, the physical properties of the radiosynthesized CPs and CPs nanocomposites were evaluated by using thermogravimetric analysis (TGA).

4.6.1 CPs Chain Lengths

The weight average molecular weight (Mw) and the molar mass at the maximum peak (Mp) of some processable radiosynthesized CPs were estimated from SEC with a polystyrene calibration. The SEC data obtained for these radiosynthesized conducting polymers (dissolved in THF at a concentration of 3 mg/ml) are displayed in Table 4.1. Mw and Mp were found to be 2630 and 1297 g/mol (around 18 and 9 monomer units, respectively) for PEDOT nanostructures synthesized in water under N_2O atmosphere, thanks to hydroxyl radicals oxidation (PEDOT-OH or $\mathrm{PEDOT_{ox}}$), 4145 and 2484 g/mol (around 29 and 17 monomer units respectively) for PEDOT synthesized in water under N_2 atmosphere, thanks to solvated electrons reduction ($\mathrm{PEDOT_{red}}$), 1423 and 1128 g/mol (around 10 and 8 monomer units) for PEDOT synthesized in very acidic aqueous medium ($\mathrm{PEDOT_{pH\,0}}$) [50] and finally 1308 and 1015 g/mol (around 9 and 7 units) for PEDOT synthesized in DCM solvent ($\mathrm{PEDOT_{DCM}}$) [81].

SEC data showed that all the detected polymers have reasonable molecular weights. Between all radiosynthesized CPs, $\mathrm{PEDOT_{red}}$ polymers are clearly characterized by the longer polymer chains (up to 29 monomer units). Nevertheless, the

Table 4.1 Summary of some optical and electronic band gaps reported in case of radiosynthesized CPs together with their molecular weights as deduced from SEC chromatography.

Radiosynthesized conducting polymers	Optical band gap $E_{\mathrm{gap.op}}$ (eV)	Electronic band gap $E_{\mathrm{gap.el}}$ (ev)	SEC data	
			Molar mass Mp (g/mol)	Molecular weight Mw (g/mol)
PPy [46]	1.90	—	—	—
PEDOT-OH ($\mathrm{PEDOT_{ox}}$) [35]	2.00	—	1297 (~9 units)	2630 (~18 units)
PEDOT-N_3 [35]	2.30	—	—	—
$\mathrm{PEDOT_{red}}$ [61]	1.90	—	2484 (~17 units)	4145 (~29 units)
$\mathrm{PEDOT_{pH\,0}}$ [50]	1.14	1.04	1128 (~8 units)	1423 (~10 units)
$\mathrm{PEDOT_{DCM}}$ [81]	1.65	1.61	1015 (7 units)	1308 (~9 units)

solubility of all radiosynthesized CPs was found poor in THF solvent. This clearly means that in all cases the longer radiosynthesized polymers were not detected by SEC and that the molar masses reported in Table 4.1 don't correspond to the maximal ones.

4.6.2 Optical and Electronic Band Gaps of CPs

The electronic ($E_{\text{gap.el}}$) and optical ($E_{\text{gap.op}}$) band gaps reported in case of radiosynthesized PEDOT polymers (PEDOT-OH, PEDOT-N_3 synthesized, thanks to azide radical oxidation, PEDOT$_{\text{red}}$, PEDOT$_{\text{pH 0}}$, and PEDOT$_{\text{DCM}}$) and radiation induced PPy polymers are shown in Table 4.1. Note that cyclic voltammetry measurements were carried out only in case of PEDOT$_{\text{pH 0}}$ and PEDOT$_{\text{DCM}}$ thanks to their better processability. These electrochemical experiments enabled to calculate the electronic energy band gaps ($E_{\text{gap.el}}$) of PEDOT$_{\text{pH 0}}$ and PEDOT$_{\text{DCM}}$ that amount, respectively, to 1.04 eV [50] and 1.61 eV [81]. Besides, the UV–Vis absorption spectra of PEDOT$_{\text{pH 0}}$ and PEDOT$_{\text{DCM}}$ (see Figure 4.4 spectrum a and Figure 4.7 spectrum a) enabled the determination of the optical energy band gaps ($E_{\text{gap.op}}$) of these two CPs which amount to 1.14 eV [50] and 1.65 eV [81], respectively. In case of the other radiosynthesized CPs, the optical energy band gaps were calculated from the UV–Vis absorption spectra obtained in previous works [35, 46, 61] and amount to 1.90 eV for PPy, 2.00 eV for PEDOT-OH, 2.30 eV for PEDOT-N_3, and 1.90 eV for PEDOT$_{\text{red}}$.

As seen from Table 4.1, PEDOT polymers obtained by reduction-polymerization route (PEDOT$_{\text{red}}$) present lower optical band gap than those of PEDOT polymers obtained by oxidation polymerization route (PPy, PEDOT-OH, and PEDOT-N_3). This difference is evidently originated from the fact the PEDOT$_{\text{red}}$ polymers are characterized by a higher molecular weight (see Table 4.1). Interestingly, despite their relatively low molecular weight, the polymers radiosynthesized in very acidic medium (PEDOT$_{\text{pH 0}}$) are characterized by the lowest optical and electrical band gaps in comparison with the other radiosynthesized CPs. This could be explained by the important *in situ* doping of PEDOT$_{\text{pH 0}}$ polymers by Cl^- ions [50]. In the same manner, the doping of PEDOT$_{\text{DCM}}$ polymers that are characterized by a low molecular weight should explain the small optical and electronic band gaps values obtained. A more likely reason of these findings is also the poor solubility of the prepared polymers, which prevents the detection by SEC of polymers with higher molecular weight.

4.6.3 Electrical Conductivities of CPs

The electrical conductivities reported in case of radiosynthesized CPs (PEDOT-OH, PEDOT synthesized by accelerated electrons, PEDOT$_{\text{red}}$, PEDOT$_{\text{pH 0}}$, PEDOT$_{\text{DCM}}$, PPy polymers, and PEDOT composites (PEDOT$_{\text{ox}}$/Ag$_{\text{red}}$, PEDOT$_{\text{red}}$/Ag$_{\text{red}}$, and (PEDOT/Ag)$_{\text{red}}$) are shown in Table 4.2. The electrical conductivities measured using the four-point probe technique after doping process were found interestingly remarkable for all radiosynthesized materials. For instance, the electrical conductivity of PPy polymers radiosynthesized in N_2O-saturated aqueous solutions was found

Table 4.2 Electrical conductivities of radiosynthesized CPs nanostructures and CPs nanocomposites as measured by using the four-point probe technique.

Radiosynthesized conducting polymers	**Electrical conductivity (S/cm)**
Radiosynthesized PPy	57×10^{-3} [46]
PEDOT-OH ($PEDOT_{ox}$)	9.8×10^{-3} [61]
PEDOT by accelerated electrons	0.9×10^{-3} [31]
$PEDOT_{red}$	3.4×10^{-3} [61]
$PEDOT_{pH\,0}$	3.3×10^{-3} [50]
$PEDOT_{DCM}$	2.6×10^{-3} [81]
$PEDOT_{ox}/Ag_{red}$	3.2×10^{-3} [53]
$PEDOT_{red}/Ag_{red}$	5.6×10^{-3} [53]
$(PEDOT/Ag)_{red}$	3.6×10^{-3} [53]

equal to 57×10^{-3} S/cm. This value is nearly five times higher than that of chemically synthesized PPy (12×10^{-3} S/cm) [46]. The measured electrical conductivities of $PEDOT_{ox}$ and $PEDOT_{red}$ were 9.8×10^{-3} S/cm and 3.4×10^{-3} S/cm respectively [61]. The value found in the case of $PEDOT_{red}$ is somewhat lower than that of $PEDOT_{ox}$. Note that PEDOT polymers synthesized through accelerated electrons also possess a remarkable electrical conductivity (0.9×10^{-3} S/cm). Furthermore, the electrical conductivity of PEDOT/Ag nanocomposites, which were radiolytically prepared according to two-step method or one-pot method, are all in the same order of magnitude (about 10^{-3} S/cm) and remain not far from the values found for $PEDOT_{ox}$ and $PEDOT_{red}$ [53]. The conductivity of PEDOT polymers synthesized in very acidic aqueous medium ($PEDOT_{pH\,0}$) was found to be 3.3×10^{-3} S/cm, and that of PEDOT polymers prepared in organic solvent ($PEDOT_{DCM}$) was found equal to 2.6 10^{-3} S/cm. These latter values have the same order of magnitude as the conductivities of PEDOT synthesized by radiolysis in neutral aqueous solutions and remain close to the conductivities reported in literature for PEDOT polymers produced by conventional methods [56, 89, 90]. The obtained electrical conductivity findings prove that the radiosynthesized materials are certainly semiconductors and no doubt about their implementation in practical applications.

4.6.4 Thermal Properties of CPs

The thermal properties of radiosynthesized CPs nanostructures and CPs nanocomposites were analyzed by TGA. TGA analysis of $PEDOT_{red}$ and $PEDOT_{ox}$ polymers and their degradation processes were found quite similar. In case of PEDOT/Ag composites, TGA revealed that all composites were characterized by the same thermal stability, which remains higher, over a wide range of temperatures, than that of pure PEDOT polymers synthesized in aqueous solutions by both radiolytic routes (oxidation and reduction). Also, the TGA analysis showed that the thermal stability can be enhanced by increasing the amount of silver into the composites. Besides, TGA analysis revealed that PEDOT polymers radiosynthesized in DCM solvent under N_2 atmosphere were characterized by the same good thermal stability as that of PEDOT polymers synthesized by γ-radiolysis in aqueous media. In case of PPy, a comparative study was carried out between chemically synthesized PPy by using $K_2S_2O_8$ as oxidant and radiosynthesized conducting PPy in aqueous solutions under N_2O. TGA analysis showed that both PPy polymers possess comparable good thermal stability [46]. Moreover, the TGA analysis was found in very good agreement with TGA data already reported in the literature concerning PPy polymers [91].

4.7 Comparative Studies Between Radiolytic Methodology and Conventional Methods

Different kinds of CPs were successfully synthesized by radiolysis under different experimental conditions either in aqueous solution or in organic solvent. While in most of related studies, the physicochemical properties of radiosynthesized CPs were found intrinsically good, in some studies these properties were also compared with those of CPs synthesized by conventional chemical or electrochemical methods.

Optical and electrical properties of PEDOT polymers synthesized by radiolysis in aerated aqueous solutions (containing 100 mM $LiClO_4$) were compared after deposition onto ITO substrate with those of PEDOT polymers electrosynthesized onto ITO electrode in the same environmental conditions [21]. Both polymers, doped with perchlorate ions, showed comparable UV–visible spectral features and capacitive current behavior as highlighted by cyclic voltammetry analysis [21]. Note that the UV–visible absorption spectrum of the PEDOT film obtained after deposition of radiosynthesized CPs displayed, in agreement with electrosynthesized PEDOT layers, an intense absorption band at 550 nm in addition to a shoulder at around 750 nm. This result was in agreement with the fact that polymer films, which are characterized by longer conjugation lengths in the solid state absorb at higher wavelengths than polymers in solution [92]. This result was also in agreement with absorption spectra of solid films of doped polythiophenes, which are characterized by absorption maxima in the region 480–520 nm [92]. The similarity in the absorption spectra and cyclic voltammograms of both radiosynthesized and electrosynthesized PEDOT polymers definitely highlight the successful synthesis of doped PEDOT polymers by the way of radiation chemistry [21].

Optical properties of PEDOT polymers synthesized in aqueous solution at very low temperature by the way of electron beam irradiation (by using sulfate radicals, $SO_4^{\cdot -}$, as oxidizing species) were also found very close to those of PEDOT polymers chemically synthesized in water at different temperatures (by using $K_2S_2O_8$ as oxidizing agent) [38].

Structural, optical, electrical, and thermal properties of PPy polymers synthesized by gamma-radiolysis in aqueous solutions under N_2O atmosphere were finally compared with those of PPy polymers chemically synthesized in the bulk by using $K_2S_2O_8$ as oxidant [46]. As highlighted in this study, both PPy polymers were characterized by comparable optical and thermal properties. Nevertheless, as previously mentioned, radiosynthesized PPy polymers were characterized by an electrical conductivity, which was found five times higher than that of chemically synthesized PPy [46].

4.8 Summary

Monomers oxidation induced polymerization, by using oxidizing species, is the conventional way to obtain conducting polymers. The most common approaches that are used to synthesize CPs are either chemical polymerization through adding oxidizing reagents or electro-polymerization by applying a potential across a solution containing the monomers. Even though these two methods are well understood and their mechanism is relatively well known, there still remain some problems such as chemical contamination, purification steps, and sometimes need to use a catalyst. On the other hand, conducting polymers have some limitations that restrict their applications due to difficult processability, low solubility in common solvents, and poor thermal stability.

Current research aims to develop new synthesis strategies and new conducting polymers with tuned morphologies and optimized properties. Apart from traditional methods of polymers synthesis, ionizing radiation induced polymerization by γ-rays or accelerated electrons has recently been developed. This new alternative methodology based on radiation chemistry was developed in order to polymerize different kinds of conducting polymers in aqueous solutions, in the absence of any external chemical initiators, thanks to the oxidation (and alternatively the reduction) of dissolved organic monomers by oxidizing (or reducing) radicals *in situ* produced in the medium during water radiolysis. Interestingly, by the use of pulse radiolysis, the growth of CPs was shown to proceed through a recurrent step-by-step oxidation process.

With radiolytic method, nanostructured PEDOT materials were obtained in water by EDOT oxidation using hydroxyl radicals ($HO^{\cdot}$), azide radicals ($N_3^{\cdot}$), sulfate radicals ($SO_4^{\cdot-}$), dichloride radical anions ($Cl_2^{\cdot-}$), and even by EDOT reduction, thanks to the use of hydrated electron (e_{aq}^-) generated by water radiolysis. Interestingly, chemical, morphological, optical, electrical, and thermal properties of PEDOT polymers were found dependent on the nature of the initiating radiolytic species. The versatility of the radiolytic method was demonstrated since PEDOT polymers were successfully produced in water under different atmospheres (air, O_2, N_2O, N_2), in presence of solutes which potentially act as doping agents, in very acidic aqueous medium and also in an organic solvent, such as DCM. Interestingly, CPs synthesized by radiolysis in acidic aqueous medium or in DCM are *in situ* produced in a doped state. The radiolytic procedure was also extended to the synthesis of other kinds of conducting materials since PPy polymer nanostructures as well as PEDOT/Ag nanocomposites were successfully prepared.

All the radiosynthesized CPs nanostructures were characterized by remarkable optical and electrical properties. Interestingly their performance was found comparable with other conducting polymers synthesized by chemical or electrochemical methods. From now on, radiolytic methodology fully appears as a promising alternative method for the preparation, not only in water but also in organic solvents, of conducting polymers with enhanced properties. The considerable electrical conductivity of some radiosynthesized polymers and, above all, their *in situ* doping and their low band gap foreshadow further advances in the field of conducting polymers synthesis and applications.

Finally, radiation induced synthesis of conducting polymers could interestingly be considered in soft or hard templates and even in complex matrices since high energy radiations are characterized by a strong penetrating power and are known to lead to very homogeneous processes. This evidently gives a glimpse of future promising applications

References

1 Freund, M.S. and Deore, B.A. (2007). *Self-Doped Conducting Polymers*. Wiley.

2 Ruiz, J., Gonzalo, B., Dios, J.R. et al. (2013). Improving the processability of conductive polymers: the case of polyaniline. *Adv. Polym. Tech.* 32 (S1): 180–188.

3 Heeger, A.J. (2001). Semiconducting and metallic polymers: the fourth generation of polymeric materials. *J. Phys. Chem. B* 105 (36): 8475–8491.

4 MacDiarmid, A.G. (2001). “Synthetic Metals”: a novel role for organic polymers (Nobel Lecture). *Angew. Chem.* 40 (14): 2581–2590.

5 Gospodinova, N. and Terlemezyan, L. (1998). Conducting polymers prepared by oxidative polymerization: polyaniline. *Prog. Polym. Sci.* 23 (8): 1443–1484.

6 Paradee, N. and Sirivat, A. (2014). Synthesis of poly(3,4-ethylenedioxythiophene) nanoparticles via chemical oxidation polymerization. *Polym. Int.* 63 (1): 106–113.

7 Zhang, X. and Manohar, S.K. (2004). Bulk synthesis of polypyrrole nanofibers by a seeding approach. *J. Am. Chem. Soc.* 126 (40): 12714–12715.

8 Roncali, J. (1992). Conjugated poly(thiophenes) – synthesis, functionalization, and applications. *Chem. Rev.* 92 (4): 711–738.

9 Tebyetekerwa, M., Yang, S., Peng, S. et al. (2017). Unveiling polyindole: free-standing As-electrospun polyindole nanofibers and polyindole/carbon nanotubes composites as enhanced electrodes for flexible all-solid-state supercapacitors. *Electrochim. Acta* 247: 400–409.

10 Zhang, X.T., Zhang, J., Song, W.H., and Liu, Z.F. (2006). Controllable synthesis of conducting polypyrrole nanostructures. *J. Phys. Chem. B* 110 (3): 1158–1165.

11 Siju, C.R., Narasimha Rao, K., Ganesan, R. et al. (2011). Synthesis of poly(3,4 ethylenedioxythiophene) nano structure using reverse microemulsion polymerization. *Phys. Status Solidi* 8 (9): 2739–2741.

12 Zhou, H., Han, G., Chang, Y. et al. (2015). Highly stable multi-wall carbon nanotubes@poly(3,4-ethylenedioxythiophene)/poly(styrene sulfonate) core–shell

composites with three-dimensional porous nano-network for electrochemical capacitors. *J. Power Sources* 274: 229–236.

13 Gupta, B., Mehta, M., Melvin, A. et al. (2014). Poly (3,4-ethylenedioxythiophene) (PEDOT) and poly (3,4-ethylenedioxythiophene)-few walled carbon nanotube (PEDOT-FWCNT) nanocomposite based thin films for Schottky diode application. *Mater. Chem. Phys.* 147 (3): 867–877.

14 Zhang, X., Lee, J.-S., Lee, G.S. et al. (2006). Chemical synthesis of PEDOT nanotubes. *Macromolecules* 39 (2): 470–472.

15 Choi, W., An, T., and Lim, G. (2009). Fabrication of conducting polymer nanowire sensor array. In: *2009 IEEE Sensors*, 1153–1151. IEEE.

16 Jang, J. and Yoon, H. (2005). Formation mechanism of conducting polypyrrole nanotubes in reverse Micelle systems. *Langmuir* 21 (24): 11484–11489.

17 Huang, J. (2006). Syntheses and applications of conducting polymer polyaniline nanofibers. *Pure Appl. Chem.* 78 (1): 15.

18 Aydın, M., Durmus, Z., Kavas, H. et al. (2011). Synthesis and characterization of poly(3-thiophene acetic acid)/Fe_3O_4 nanocomposite. *Polyhedron* 30 (6): 1120–1126.

19 Brooke, R., Cottis, P., Talemi, P. et al. (2017). Recent advances in the synthesis of conducting polymers from the vapour phase. *Prog. Mater Sci.* 86: 127–146.

20 Chapiro, A. (1979). Radiation induced polymerization. *Radiat. Phys. Chem.* 14 (1): 101–116.

21 Lattach, Y., Deniset-Besseau, A., Guigner, J.-M., and Remita, S. (2013). Radiation chemistry as an alternative way for the synthesis of PEDOT conducting polymers under “soft” conditions. *Radiat. Phys. Chem.* 82: 44–53.

22 Karim, M.R., Lee, C.J., and Lee, M.S. (2007). Synthesis of conducting polypyrrole by radiolysis polymerization method. *Polym. Adv. Technol.* 18 (11): 916–920.

23 Karim, M., Jae Lee, C., Jin Kim, H. et al. (2007). Preparation of buckyball-shaped conducting polythiophene by the gamma radiation-induced polymerization method. *Macromol. Symp.* 249–250: 234–240.

24 Remita, S. (2001). Radiation induced lipid peroxidation: factors which determine the oxidizability of lipids. *Can. J. Physiol. Pharmacol.* 79: 144–153.

25 Remita, S., Fontaine, P., Lacaze, E. et al. (2007). X-ray radiolysis induced formation of silver nano-particles: A SAXS and UV–visible absorption spectroscopy study. *Nucl. Instrum. Methods Phys. Res.* 263 (2): 436–440.

26 Varmenot, N., Remita, S., Abedinzadeh, Z. et al. (2001). Oxidation processes of *N,S*-diacetyl-L-cysteine ethyl ester: influence of S-acetylation. *J. Phys. Chem. A* 105 (28): 6867–6875.

27 Attia, J., Remita, S., Jonic, S. et al. (2007). Radiation-induced synthesis and cryo-TEM characterization of silver nanoshells on linoleate spherical micelles. *Langmuir* 23 (19): 9523–9526.

28 Spinks, J.W.T.W. and Woods, R.J. (1990). *An Introduction to Radiation Chemistry*, vol. 3. John-Wiley and Sons, Inc.

29 Ferradini, C. and Jay-Gerin, J.-P. (1999). La radiolyse de l’eau et des solutions aqueuses: historique et actualité. *Can. J. Chem.* 77 (9): 1542–1575.

30 Ferradini, C. and Jay-Gerin, J.-P. (2000). The effect of pH on water radiolysis: a still open question – a minireview. *Res. Chem. Intermed.* 26 (6): 549–565.

31 Coletta, C., Cui, Z., Archirel, P. et al. (2015). Electron-induced growth mechanism of conducting polymers: a coupled experimental and computational investigation. *J. Phys. Chem. B* 119 (16): 5282–5298.

32 Buxton, G.V., Greenstock, C.L., Helman, W.P., and Ross, A.B. (1988). Critical Review of rate constants for reactions of hydrated electrons, hydrogen atoms and hydroxyl radicals (·OH/·O− in aqueous solution). *J. Phys. Chem. Ref. Data* 17 (2): 513–886.

33 Lattach, Y., Garnier, F., and Remita, S. (2012). Influence of chemical and structural properties of functionalized polythiophene-based layers on electrochemical sensing of atrazine. *ChemPhysChem* 13 (1): 281–290.

34 Roncali, J., Blanchard, P., and Frère, P. (2005). 3,4-Ethylenedioxythiophene (EDOT) as a versatile building block for advanced functional π-conjugated systems. *J. Mater. Chem.* 15 (16): 1589–1610.

35 Lattach, Y., Coletta, C., Ghosh, S., and Remita, S. (2014). Radiation-induced synthesis of nanostructured conjugated polymers in aqueous solution: fundamental effect of oxidizing species. *ChemPhysChem* 15 (1): 208–218.

36 Belloni, J., Monard, H., Gobert, F. et al. (2005). ELYSE – a picosecond electron accelerator for pulse radiolysis research. *Nucl. Instrum. Methods Phys. Res., Sect. A* 539 (3): 527–539.

37 Marignier, J.L., de Waele, V., Monard, H. et al. (2006). Time-resolved spectroscopy at the picosecond laser-triggered electron accelerator ELYSE. *Radiat. Phys. Chem.* 75 (9): 1024–1033.

38 Coletta, C., Cui, Z., Dazzi, A. et al. (2016). A pulsed electron beam synthesis of PEDOT conducting polymers by using sulfate radicals as oxidizing species. *Radiat. Phys. Chem.* 126: 21–31.

39 Saunders, B.B., Kaufman, P.C., and Matheson, M.S. (1978). Reactions of thiophene with radiolytically produced radicals. 1. The hydroxyl radical. *J. Phys. Chem.* 82 (2): 142–150.

40 Bhattacharya, A., Amitabha, D., and Mandal, P.C. (1998). Carbonate radical induced polymerisation of pyrrole: a steady state and flash photolysis study. *J. Radioanal. Nucl. Chem.* 230 (1): 91–95.

41 Randriamahazaka, H., Noël, V., and Chevrot, C. (1999). Nucleation and growth of poly(3,4-ethylenedioxythiophene) in acetonitrile on platinum under potentiostatic conditions. *J. Electroanal. Chem.* 472 (2): 103–111.

42 Kvarnström, C., Neugebauer, H., Blomquist, S. et al. (1999). In situ spectroelectrochemical characterization of poly(3,4-ethylenedioxythiophene). *Electrochim. Acta* 44 (16): 2739–2750.

43 Bazzaoui, E.A., Aeiyach, S., and Lacaze, P.C. (1996). Electropolymerization of bithiophene on Pt and Fe electrodes in an aqueous sodium dodecylsulfate (SDS) micellar medium. *Synth. Met.* 83 (2): 159–165.

44 Irwin, M.D., Roberson, D.A., Olivas, R.I. et al. (2011). Conductive polymer-coated threads as electrical interconnects in e-textiles. *Fibers Polym.* 12 (7): 904.

45 Elliot, A.J., Geertsen, S., and Buxton, G.V. (1988). Oxidation of thiocyanate and iodide ions by hydrogen atoms in acid solutions. *J. Chem. Soc., Faraday Trans. 1 F* 84 (4): 1101–1112.

46 Cui, Z., Coletta, C., Dazzi, A. et al. (2014). Radiolytic method as a novel approach for the synthesis of nanostructured conducting polypyrrole. *Langmuir* 30 (46): 14086–14094.

47 Tehrani, P., Kanciurzewska, A., Crispin, X. et al. (2007). The effect of pH on the electrochemical over-oxidation in PEDOT:PSS films. *Solid State Ionics* 177 (39): 3521–3527.

48 Ouyang, J. (2013). Solution-processed PEDOT:PSS films with conductivities as indium tin oxide through a treatment with mild and weak organic acids. *ACS Appl. Mater. Interfaces* 5 (24): 13082–13088.

49 Yun, D.J., Jeong, Y.J., Ra, H. et al. (2016). Effective way to enhance the electrode performance of multiwall carbon nanotube and poly(3,4-ethylenedioxythiophene): poly(styrene sulfonate) composite using HCl–methanol treatment. *J. Phys. Chem. C* 120 (20): 10919–10926.

50 Cui, Z., Bahry, T., Dazzi, A. et al. (2019). Conducting polymers synthesized by γ-radiolysis in very acidic aqueous medium. *Radiat. Phys. Chem.* 159: 47–56.

51 Jayson, G.G., Parsons, B.J., and Swallow, A.J. (1973). Some simple, highly reactive, inorganic chlorine derivatives in aqueous solution. Their formation using pulses of radiation and their role in the mechanism of the Fricke dosimeter. *J. Chem. Soc., Faraday Trans. 1 F* 69: 1597–1607.

52 Schwarz, H.A. and Dodson, R.W. (1984). Equilibrium between hydroxyl radicals and thallium(I I) and the oxidation potential of OH (aq). *J. Phys. Chem.* 88 (16): 3643–3647.

53 Cui, Z., Coletta, C., Bahry, T. et al. (2017). A novel radiation chemistry-based methodology for the synthesis of PEDOT/Ag nanocomposites. *Mater. Chem. Front.* 1 (5): 879–892.

54 Heuer, H.W., Wehrmann, R., and Kirchmeyer, S. (2002). Electrochromic window based on conducting poly(3,4-ethylenedioxythiophene)-poly(styrene sulfonate). *Adv. Funct. Mater.* 12 (2): 89–94.

55 Pei, Q.B., Zuccarello, G., Ahlskogt, M., and Ingan, O. (1994). Electrochromic and highly stable poly(3,4-ethylenedioxythiophene) switches between opaque blue–black and transparent sky blue. *Polymer* 35 (7): 1347–1351.

56 Rumbau, V., Pomposo, J.A., Eleta, A. et al. (2007). First enzymatic synthesis of water-soluble conducting poly(3,4-ethylenedioxythiophene). *Biomacromolecules* 8 (2): 315–317.

57 Jang, J., Chang, M., and Yoon, H. (2005). Chemical sensors based on highly conductive poly(3,4-ethylenedioxythiophene) nanorods. *J. Adv. Mater.* 17 (13): 1616–1620.

58 Kitada, K. and Ozaki, S. (1995). Reductive polymerization of halothiophene. *Polym. J.* 27 (12): 1161–1166.

59 Song, L., Wang, M., Cong, Y. et al. (2007). The mechanism of 60Co γ-ray radiation induced interfacial redox reaction in inverse emulsion and its application in the synthesis of polymer microcapsules. *Polymer* 48 (1): 150–157.

60 Belloni, J., Mostafavi, M., Remita, H. et al. (1998). Radiation-induced synthesis of mono- and multi-metallic clusters and nanocolloids. *New J. Chem.* 22 (11): 1239–1255.

61 Cui, Z., Coletta, C., Rebois, R. et al. (2016). Radiation-induced reduction–polymerization route for the synthesis of PEDOT conducting polymers. *Radiat. Phys. Chem.* 119: 157–166.

62 Gangopadhyay, R. and De, A. (2000). Conducting polymer nanocomposites: a brief overview. *Chem. Mater.* 12 (3): 608–622.

63 Xu, P., Han, X., Zhang, B. et al. (2014). Multifunctional polymer–metal nanocomposites via direct chemical reduction by conjugated polymers. *Chem. Soc. Rev.* 43 (5): 1349–1360.

64 Armel, V., Winther-Jensen, O., Kerr, R. et al. (2012). Designed electrodeposition of nanoparticles inside conducting polymers. *J. Mater. Chem.* 22 (37): 19767–19773.

65 Groenendaal, L., Jonas, F., Freitag, D. et al. (2000). Poly(3,4-ethylenedioxythiophene) and its derivatives: past, present, and future. *Adv. Mater.* 12 (7): 481–494.

66 Jung, H.-R. and Lee, W.-J. (2011). Ag/poly(3,4-ethylenedioxythiophene) nanocomposites as anode materials for lithium ion battery. *Solid State Ionics* 187 (1): 50–57.

67 Mo, Z., Zuo, D., Chen, H. et al. (2007). Synthesis of graphite nanosheets/AgCl/polypyrrole composites via two-step inverse microemulsion method. *Eur. Polym. J.* 43 (2): 300–306.

68 Pillalamarri, S.K., Blum, F.D., Tokuhiro, A.T., and Bertino, M.F. (2005). One-pot synthesis of polyaniline–metal nanocomposites. *Chem. Mater.* 17 (24): 5941–5944.

69 Fujii, S., Aichi, A., Akamatsu, K. et al. (2007). One-step synthesis of polypyrrole-coated silver nanocomposite particles and their application as a coloured particulate emulsifier. *J. Mater. Chem.* 17 (36): 3777–3779.

70 Feng, X., Huang, H., Ye, Q. et al. (2007). Ag/polypyrrole core–shell nanostructures: interface polymerization, characterization, and modification by gold nanoparticles. *J. Phys. Chem. C* 111 (24): 8463–8468.

71 Remita, S., Mostafavi, M., and Delcourt, M.O. (1994). Stabilization, growth and reactivity of silver aggregates produced by radiolysis in the presence of edta. *New J. Chem.* 18: 581–588.

72 Mostafavi, M., Remita, S., Delcourt, M., and Belloni, J. (1996). Ligand effects on solvated metal cluster properties. *J. Chim. Phys. Phys.- Chim. Biol.* 93 (10): 1828–1842.

73 Remita, S. (1995). Effect of ligands on thermadynamics, kinetics and spectral properties of metalic aggregates synthesized by radiloysis. Doctoral thesis. University of Paris-Sud.

74 Mostafavi, M., Dey, G.R., François, L., and Belloni, J. (2002). Transient and stable silver clusters induced by radiolysis in methanol. *J. Phys. Chem. A* 106 (43): 10184–10194.

75 Remita, S., Fontaine, P., Rochas, C. et al. (2005). Radiation induced synthesis of silver nanoshells formed onto organic micelles. *Eur. Phys. J. D* 34 (1–3): 231–233.

76 Remita, S., Orts, J.M., Feliu, J.M. et al. (1994). STM identification of silver oligomer clusters prepared by radiolysis in aqueous-solution. *Chem. Phys. Lett.* 218 (1–2): 115–121.

77 Ishigaki, A. and Koizumi, H. (2012). Radiation-induced polymerization of 3-octylthiophene. *Radiat. Phys. Chem.* 81 (7): 803–806.

78 Emmi, S.S., Poggi, G., D'Angelantonio, M. et al. (2003). The solvatochromic effect on some oligothiophene radical cations: a pulse radiolysis and semiempirical investigation. *Radiat. Phys. Chem.* 67 (3): 251–256.

79 Alfassi, Z.B., Mosseri, S., and Neta, P. (1989). Reactivities of chlorine atoms and peroxyl radicals formed in the radiolysis of dichloromethane. *J. Phys. Chem.* 93 (4): 1380–1385.

80 Emmi, S.S., Beggiato, G., and Casalbore-Miceli, G. (1989). Transient species in the pulse radiolysis of methylene chloride and the self-reaction of chloromethyl radicals. *Int. J. Radiat. Appl. Instrum. Part C* 33 (1): 29–37.

81 Bahry, T., Cui, Z., Deniset-Besseau, A. et al. (2018). An alternative radiolytic route for synthesizing conducting polymers in an organic solvent. *New J. Chem.* 42 (11): 8704–8716.

82 Emmi, S.S., D'Angelantonio, M., Beggiato, G. et al. (1999). The generation and spectral characterization of oligothiophenes radical cations. A pulse radiolysis investigation11This paper was presented at the 10th International Meeting on Radiation Processing, 11–16 May 1997, Anaheim, California, U.S.A. *Radiat. Phys. Chem.* 54 (3): 263–270.

83 Ushida, K., Yoshida, Y., Kozawa, T. et al. (1999). Evidence of oxidation of aromatic hydrocarbons by chloromethyl radicals: reinvestigation of intersolute hole transfer using pulse radiolysis. *J. Phys. Chem. A* 103 (24): 4680–4689.

84 Truszkowski, S. and Szymański, W. (1994). Stable products and radicals in the radiolysis of dichloromethane and 1,1,-dichloroethane gamma-irradiated in an oxygen-free atmosphere. *J. Radioanal. Nucl. Chem.* 177 (2): 415–423.

85 Nie, T., Zhang, K., Xu, J. et al. (2014). A facile one-pot strategy for the electrochemical synthesis of poly(3,4-ethylenedioxythiophene)/Zirconia nanocomposite as an effective sensing platform for vitamins B2, B6 and C. *J. Electroanal. Chem.* 717-718: 1–9.

86 Hohnholz, D., MacDiarmid, A.G., Sarno, D.M., and Jones, J.W.E. (2001). Uniform thin films of poly-3,4-ethylenedioxythiophene (PEDOT) prepared by in-situ deposition. *ChemComm.* 23: 2444–2445.

87 Kim, T., Kim, J., Kim, Y. et al. (2009). Preparation and characterization of poly(3,4-ethylenedioxythiophene) (PEDOT) using partially sulfonated poly(styrene-butadiene-styrene) triblock copolymer as a polyelectrolyte. *Curr. Appl Phys.* 9 (1): 120–125.

88 Hui, Y., Bian, C., Wang, J. et al. (2017). Comparison of two types of overoxidized PEDOT films and their application in sensor fabrication. *Sensors* 17 (3): 628.

89 Van de Ruit, K., Cohen, R.I., Bollen, D. et al. (2013). Quasi-one dimensional in-plane conductivity in filamentary films of PEDOT:PSS. *Adv. Funct. Mater.* 23 (46): 5778–5786.

90 Jones, B.H., Cheng, K.-Y., Holmes, R.J., and Lodge, T.P. (2012). Nanoporous poly(3,4-ethylenedioxythiophene) derived from polymeric bicontinuous microemulsion templates. *Macromolecules* 45 (1): 599–601.

91 Hazarika, J. and Kumar, A. (2013). Controllable synthesis and characterization of polypyrrole nanoparticles in sodium dodecylsulphate (SDS) micellar solutions. *Synth. Met.* 175: 155–162.

92 Tour, J.M. and Wu, R. (1992). Synthesis and UV-visible properties of soluble α-thiophene oligomers. Monomer to octamer. *Macromolecules* 25 (7): 1901–1907.

5

Conjugated Polymer Nanostructures: Characterization

Samim Sardar[1] *and Srabanti Ghosh*[2]

[1] Linköping University, Department of Science and Technology, Laboratory of Organic Electronics,
Bredgatan 33, SE-601 74 Norrköping, Sweden
[2] CSIR-Central Glass and Ceramic Research Institute, Energy Materials and Devices Division,
196, Raja S.C. Mullick Road, Kolkata 700032, India

5.1 Introduction

Conjugated polymers are consisting of alternating single and double carbon–carbon bonds along the polymeric chains and widely investigated in various applications. The distinct conduction mechanism of these polymers generates the unique properties in a variety of conducting polymers (e.g. polyacetylene, polyaniline (PANI), polypyrrole (PPy), poly(*p*-phenylene-vinylene) (PPV), poly(3,4-ethylene dioxythiophene) (PEDOT), poly(3-hexylthiophene-2,5-diyl) (P3HT), and other polythiophene derivatives, etc.), which have recently received special attention in the areas of nanoscience and nanotechnology [1–4]. In particular, the conjugated polymer chain exhibits reversible chemical, electrochemical, and physical properties that can be controlled by a doping/de-doping process, which makes these polymers very attractive as functional materials for various applications [2]. Conjugated polymer nanostructures (CPNs) compared with their "bulk counterparts" display several advantageous properties, such as large surface areas, fascinating optoelectronic properties, mechanical flexibility, and shortened pathways for charge/mass/ion transport, mainly attributed to the particular packing and assembly of the polymer backbones at the nanoscale, which may have potential utility in photocatalysis and electrocatalysis, molecular sensing, photovoltaics, energy storage devices, etc. [5–9]. Various CPNs with controlled shape, composition such as nanoparticles (NPs), nanowires, nanofibers, and nanotubes, etc. have been reported that stimulating a lot of research efforts to develop novel methods for the fabrication of high-performance devices based on these nanostructured polymers possess several advantageous over inorganic materials in terms of cost and flexibility [10–12].

In last two decades, a rise in the interdisciplinary research on conjugated polymers has led to major advancement in the fundamental understanding of their electronic, photonic, and optoelectronic properties while enabling their applications in information, energy, and other technologies [3, 12, 13]. The exploration of diverse

Conjugated Polymer Nanostructures for Energy Conversion and Storage Applications,
First Edition. Edited by Srabanti Ghosh.

interesting properties of conjugated polymers has directed to various device applications such as efficient solar light absorption and good charge transport in thin films facilitate the development of large area, low-cost, photovoltaic devices [14–17]. Notably, high-mobility charge transport of conjugated polymers has enabled the development of thin-film transistors for printable and flexible electronics [18–23]. Additionally, the efficient exciton luminescence of CPNs is enabling the development of organic light-emitting diodes (OLEDs) for large-area full-color displays and solid-state lighting [24–27]. The major advancement in the science and applications of these materials has been made possible by the spectacular advances in the molecular design and synthesis of such electronic and optoelectronic materials, including π-conjugated small molecules, oligomers, and polymers [28–30]. It is worth noting that CPNs have fundamentally different electronic and optical properties compared with inorganic semiconductor nanostructures [9, 31]. The quantum size effect is much stronger in case of inorganic nanostructures when the size is comparable or smaller than the Bohr radius. However, in the case of CPNs, exciton sizes are tunable by both the chemical changes of the π-conjugated molecular structures and their intermolecular interactions as the extended π-conjugation systems has much smaller radius of the Frenkel excitons associated with it [32–36]. In general, CPNs are formed by self-assembly of the as designed molecular building blocks through weaker intermolecular interactions such as hydrogen bond, π–π stacking, and hydrophobic interactions, which lead to the molecular ordering in soft materials [31]. In order to shed light on the superior electrochemical or optoelectronics properties of conjugated polymer at nanoscale, it is important to measure carrier mobility, carrier concentration, composition through X-ray photoelectron spectra (XPS), and chemical structures using Fourier transform infrared (FTIR) spectra. Furthermore, it is necessary to follow spatial deposition of polymer nanostructure between electrodes or other functional interfaces with high spatial control for utilization of such light-emitting CPNs into photonic and electronic devices. It is essential to control the CPNs morphology, which can be followed through microscopy characterization for further exploitation in catalysis, photonic, or sensing applications. It was shown that following the unique features of conjugated polymers for emitting, and sensing UV–visible light, charge transfer (CT) through advanced spectroscopic techniques may be useful for diverse application of CPNs particularly in the field of energy conversion and storage. Understanding the fundamentals underlying the behavior of CPNs is required to envisage new applications and to design, fabricate, and control novel nanodevices.

This chapter provides an overview of recent progress in the characterization of CPNs, and particularly illustrates the general characterization techniques to understand the morphology, optical, and electrochemical properties through various advanced characterization tools. By controlling the dimensions of each constituent in the nanohybrids, the electronic energy levels of the hybrids can be engineered, which makes conducting polymers to be very useful for applications in energy domain. Hence, the characterization of CPNs and its hybrids is very important to obtain better insight into the design and application of well-defined nanohybrids in both the energy and environmental fields.

5.2 Morphological Characterization

The morphology of CPNs depends on the synthesis techniques. Conventionally, the simplest way to synthesize conjugated polymers is via chemical or electrochemical oxidation of monomers, and then polymer chain grows by the coupling of the charged monomers. During the polymerization process, the morphology can be controlled with the help of templates. Although there have been many reports of template-free synthesis, in order to produce morphology and size tunable nanostructures, template-based synthesis is the most preferred approach [37, 38]. For morphological characterization of CPNs, electron microscopy and scattering techniques are commonly used. A wide variety of complimentary methods is available, including transmission electron microscopy (TEM), cryo-TEM, scanning tunneling microscopy (STM), scanning electron microscopy (SEM), and atomic force microscopy (AFM). These techniques provide vital information to understand the relationship between the polymer nanostructures and their properties, which eventually helps in improving device efficiency.

5.2.1 Transmission Electron Microscopy (TEM)

TEM is a useful tool for studying the morphology and formation of CPNs. A beam of electrons is used to examine the structures of molecules and materials at the atomic scale. As the beam passes through a very thin sample, it interacts with the material, which projects an image of the sample onto the detector. The wavelength of electrons is much shorter than that of light, thus it can reveal much finer detail than even super-resolution light microscopy. In the first part, the characterization of different polymer nanostructures by TEM and high resolution TEM (HR-TEM) after synthesis is discussed using polypyrrole (PPy) as an example.

Jang et al. [39] prepared PPy hollow nanospheres by generating a soluble polypyrrole core and a crosslinked PPy shell by sequentially using initiators of different oxidation potentials as shown in Figure 5.1. The overall experimental procedure is illustrated in Figure 5.1a. A linear PPy core soluble in alcohol was produced in the first stage using copper(II) chloride with a lower oxidation potential (E° of +0.16 V), while an insoluble cross-linked PPy shell was created in the later stage using iron(III) chloride with higher oxidation potential (E° of +0.77 V). TEM image of soluble PPy nanoparticles used as the templating core is shown in Figure 5.1b. PPy hollow nanospheres were obtained by etching the soluble PPy core with methyl alcohol as shown in Figure 5.1c. The average wall thickness of PPy hollow nanospheres was 5 nm. Jang et al. [40] have fabricated PPy nanotubes by reverse microemulsion polymerization in an apolar solvent (Figure 5.1d). One-dimensional conjugated polymers are excellent candidates to be used as molecular wire materials because of their anisotropic structures and metal-like conductivity. Figure 5.1e showed the TEM image of hollow structures as nanotubes with the wall thickness of the PPy tubes c. 22 nm. Ultrahigh density arrays of PPy nanorods are also fabricated by Lee et al. [41], directly on the indium-tin oxide coated glass by an electropolymerization within a porous diblock copolymer template. Figure 5.1f

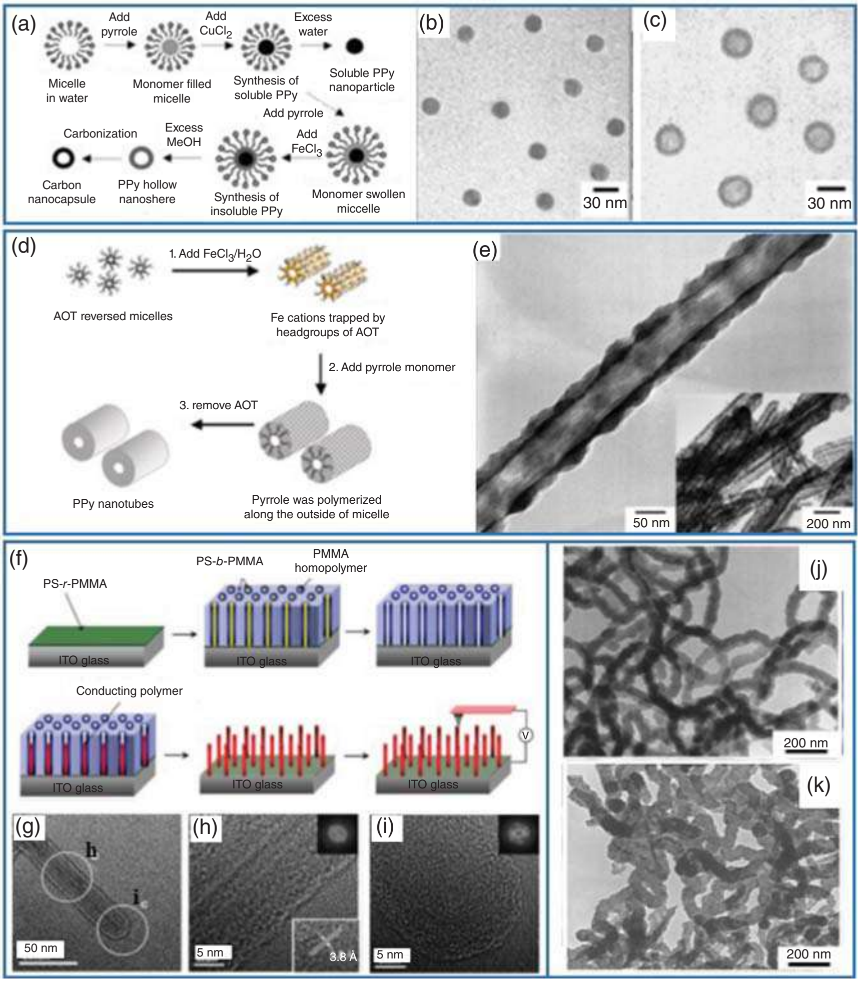

Figure 5.1 (a) Schematic representation of the synthesis of PPy nanoparticles and hollow nanospheres. TEM images of (b) PPy nanoparticles, and (c) PPy hollow nanospheres. Source: (b–c) Reproduced with permission from The Royal Society of Chemistry [39]. (d) Schematic representation of PPy nanotube fabrication process using reverse microemulsion polymerization. (e) TEM image of PPy nanotubes. Source: Reproduced with permission from The Royal Society of Chemistry [40]. (f) Schematic diagram of ultrahigh density array of PPy nanorods fabrication with block copolymer nanoporous templates. (g–i) High resolution TEM images of PPy nanorods. Source: Reproduced with permission from American Chemical Society [41]. (j) TEM images of PPy nanowires. (k) PPy nanowires after two hours annealing at 800 °C. Source: Reproduced with permission from The Royal Society of Chemistry [42].

showed a schematic diagram of the process used to fabricate ultrahigh density arrays of PPy nanorods. HR-TEM demonstrated that the main chains of PPy are aligned along the nanorod direction as shown in Figure 5.1g–i. A single nanorod has been observed, and the orientation of the PPy nanorod is maintained along the length of the nanorods, and the growth direction, as evidenced by the appearance of only two spots in the electron diffraction pattern (inset of Figure 5.1h). A high alignment of polymer chains confirmed by the HR-TEM led to an enhanced conductivity along the nanorod axes. Figure 5.1j,k showed TEM images of PPy nanowires and the annealed sample at 800 °C for two hours. The PPy nanowires have a diameter of about 80 nm and length up to a micron. Thus, TEM and HR-TEM are very useful in finding out the morphology of the synthesized nanostructures. TEM is also useful for real time monitoring of the synthesis of CPNs. Liu et al. [43] have reported direct imaging of the *in situ* electrochemical deposition of PEDOT using TEM with an electrochemical liquid flow cell. The PEDOT clusters formation during deposition was directly imaged and details of the deposition process were observed. PEDOT deposition began preferentially at the edge of the glassy carbon anodes and then oligomers were observed to form near the electrode surface. As the reaction continued, both the nucleation of new domains and the growth of pre-existing PEDOT deposits were detected, leading to systematic increase in film thickness and roughness. This study provides better understanding of the nucleation and growth mechanisms of CPN. In another report, Kim et al. [44] have introduced a simple and facile one-pot strategy, where the poly(3-hexylthiophene) (P3HT) chains are self-assembled into 1D P3HT nanowires (NWs) with simultaneous formation of thin film through the solvent evaporation of floated P3HT solution on water substrate. The formation mechanism has been elucidated through systematic TEM study. At first, P3HT in a toluene solution was dropped onto the surface of deionized (DI) water in glass vial. A thin film composed of P3HT NWs was formed on the surface of water after evaporation of the organic solvent. Figure 5.2a–c showed the TEM images taken at different stages of the solvent evaporation revealing the unique self-assembly mechanism behind the formation of P3HT NWs from the incorporation of P3HT nanoparticles (NPs). This method can lead to save wasted polymer during spin-coating process for thin-film fabrication because very small amount of polymer is needed (3–15 μl of 1 mg/ml solution).

The authors have extended this method to develop hybrid organic–inorganic thin film composed of P3HT and CdSe/ZnS quantum dots (QDs) as shown in Figure 5.2d. The morphology of P3HT/QD thin films with increasing concentration of QDs is shown in Figure 5.2e–g. A well-defined thin film of P3HT/QDs hybrid NWs is shown in Figure 5.2f. A large number of QDs hinder the self-assembly of P3HT during the solvent evaporation process, which leads to the shorter P3HT NWs.

5.2.1.1 Cryo-TEM

Traditional TEM use high-vacuum conditions and intense electron beams, which make difficulties in case of organic materials as the water that surrounds the organic molecules evaporates, and the high-energy electrons burn and destroy the molecules. In order to overcome these problems, cryo-TEM uses frozen samples, moderate electron beams, and sophisticated image processing. Cui et al. [45] have observed the morphology of PPy synthesized by the radiolytic method (γ-PPy), which reveals the presence of low-density globular structures forming polydisperse spherical nanoparticles of diameter between 80 and 200 nm. These particles systematically appeared self-assembled into nano chaplets due to the

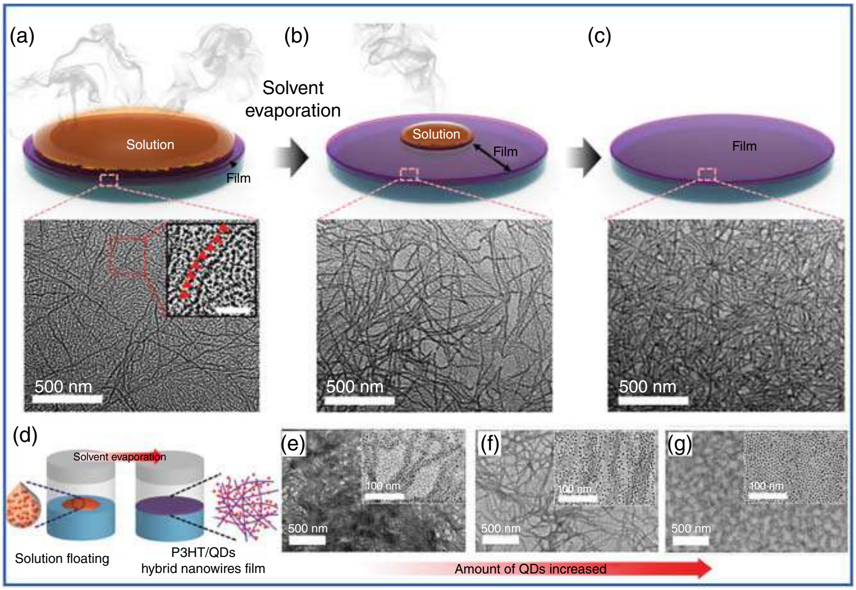

Figure 5.2 (a–c) TEM images at each evaporation stage of the formation of the P3HT thin film through solvent evaporation. The inset of (a) is a magnified image indicating wormlike particles before the growth of P3HT NWs (inset scale bar: 100 nm). (d) Schematic representation of one-pot fabrication of a thin film of hybrid P3HT NWs/QDs with simultaneous inducement of self-assembly and film fabrication of conjugated P3HT polymers with CdSe/ZnS QDs. (e–g) TEM images of a thin film consist of hybrid P3HT NWs/QDs with increasing amount of QDs. Source: Reproduced with permission from Wiley-VCH [44].

self-assembly of independent amorphous PPy polymer chains, which interact all together by hydrogen bonds [46, 47]. In another work, to check the morphology of the PEDOT polymers synthesized under an N_2 atmosphere in a dichloromethane solution through gamma irradiation, cryo-TEM microscopy was also used [48]. Lattach et al. [49] have synthesized PEDOT polymers through the radiolysis of N_2O-saturated aqueous solutions of 3,4-ethylenedioxythiophene by using two different oxidizing species; HO· (hydroxyl) and N_3· (azide) radicals. Cryo-TEM images revealed that HO· radicals lead to PEDOT-OH globular nanostructures with hydrophilic properties, whereas N_3· radicals enable the formation of amphiphilic PEDOT-N_3 fibrillar nanostructures. In another work, poly(3-hexylthiophene) (P3HT) assemblies in vitrified organic solvents were visualized at nanometer scale resolution by cryo-TEM [50]. The dispersions of P3HT 1 wt% were vitrified and visualized with cryo-TEM (Figure 5.3a,b). In the toluene dispersion, nanowires with a width of 20–30 nm, and >100 nm in length is observed. The inset (cryo-) low-dose electron diffraction (LDED) pattern shows a clearly visible ring (powder pattern) at $d = 0.38$ nm ($q = 16.5\ \text{nm}^{-1}$) that corresponds to the $\pi - \pi$ stacking of the thiophene chains.

In the oDCB dispersion, similar nanowires were formed, but they were much less abundant and the inset (cryo-)LDED pattern only showed a very diffuse diffraction

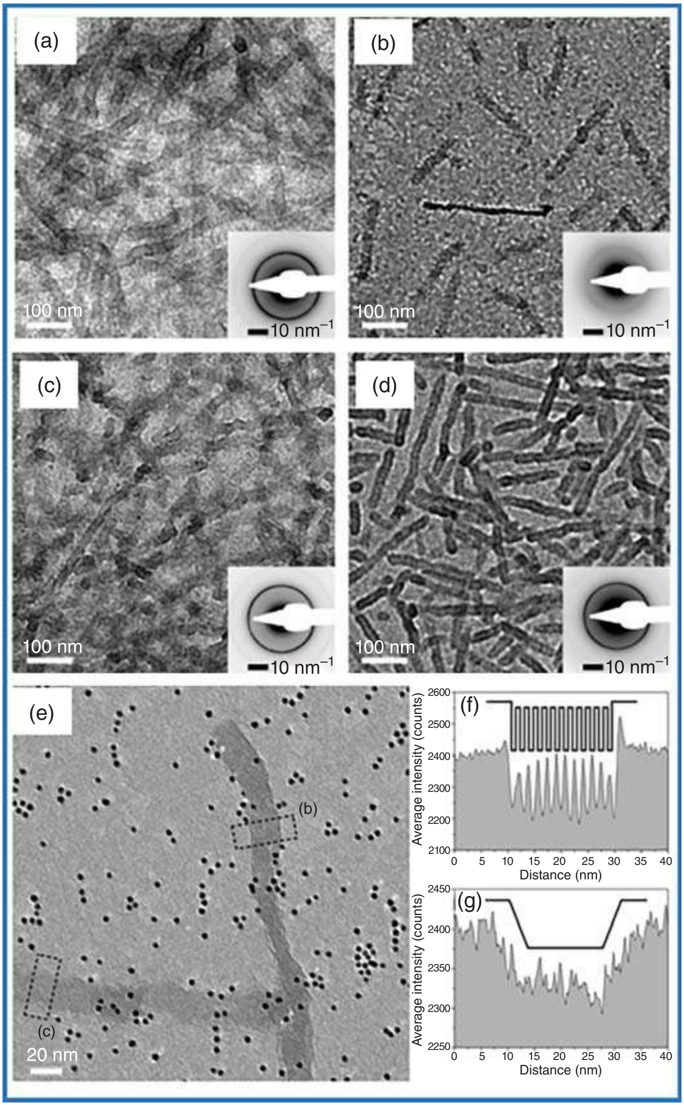

Figure 5.3 Cryo-TEM images of vitrified solutions of 1 wt% P3HT (a) in toluene and (b) in oDCB after aged for >7 days. These solutions were dropcasted and blotted on a carbon support film of a TEM grid in (c) toluene and (d) oDCB; insets show the (cryo-) LDED patterns corresponding to the samples. (e) Cryo-TEM image of two P3HT nanowires having different orientations, vitrified in oDCB. Au markers modified with 3–5 nm thiol surface are present for the purpose of electron tomography. The averaged line profile from box (f) reveals sharp interfaces and the 1.7 nm lamellar stacking, whereas the profile for box (g) reveals diffuse interfaces. Source: Reproduced with permission from American Chemical Society [50].

ring at $d = 0.38$ nm, indicating less ordering in the solution. The dried samples of the toluene and oDCB dispersions illustrated a rather similar dense packing of P3HT nanowires as shown in Figure 5.3c,d. Thus, it can be concluded that in toluene and oDCB dispersions, the same nanowires are formed. However, the oDCB dispersion contains less ordered aggregates resulting in a lower diffraction strength of the π–π stacking band in the LDED pattern, as compared with the toluene dispersion. Apart from observing mesoscopic features such as wire length, orientation, and diameter distribution, or overall crystallinity, in order to investigate the local 3D morphology of the P3HT nanowires in solution, 3–5 nm Au fiducial markers were added to the oDCB dispersion to aid in the alignment of the electron tomography (ET) data set. The tilt-series is displayed showing two intersecting P3HT nanowires and many 3–5 nm Au markers as shown in Figure 5.3e. For the vertical wire, the lamellar stacking can be clearly seen along its length and a line profile across the lamellar stacks showed a periodically varying contrast as shown in Figure 5.3f. Analyzing the periodicity, there are 12 lamellae bridging with a distance of $\sim$20 nm, which corresponds to the 1.7 nm stacking distance between the lamellae. An average intensity profile of the wire with lamellae perpendicular to the electron beam direction is shown in Figure 5.3g. This average intensity profile revealed diffuse edges in contrast with intensity profile of the vertical wire with well-defined edges and periodicity. The structural information in solutions/dispersions is important to understand the formation during all the processing steps necessary for realizing an organic electronic device. It is difficult to get structural information by X-ray diffraction (XRD) from dispersions in halogenated solvents, as the halogen atoms are much stronger scatters than the carbon-based polymers.

In this situation, Cryo-ET provides a useful platform for studying the internal structure of polymer nanoparticles as it enables complete 3D analysis of the nanospheres volume. McKenzie et al. [51] have investigated the dispersions of copolymers by 2D cryo-TEM, with in total 40 cryo-electron tomograms (3D cryo-TEM) and computer-aided visualizations (segmentations), from which a partial phase diagram is constructed as shown in Figure 5.4a–f. The analysis demonstrates that (i) inverse micellar structures form at high molecular weight (MW) and low PEO content (MW > 25 kDa; $f = 0.07$); (ii) vesicular structures form at high MW and intermediate PEO contents (MW > 19 kDa; $0.25 \leq f \geq 0.31$); (iii) and (iv) at lower MW and intermediate PEO content ($f = 0.22$–0.34) multi-lamellar morphologies coexist with bicontinuous polymer nanospheres (BPNs); (v) BPNs form from polymers with relatively low MW and low PEO content (MW ≤ 17 kDa, $f \leq 0.25$); (vi) at the highest PEO contents ($f = 0.47$) spherical micelles are formed. The authors have investigated the internal morphology of complex polymeric nanospheres through 3D analysis using cryo-ET and demonstrated that control of the internal structure can be readily achieved by changing the overall MW and relative hydrophilic content of the composite polymer.

5.2.1.2 Scanning Transmission Electron Microscopy (STEM)

Polymers are mainly consisting of carbon and other light elements, which are relatively weak electron scatterers and therefore give low scattering contrast.

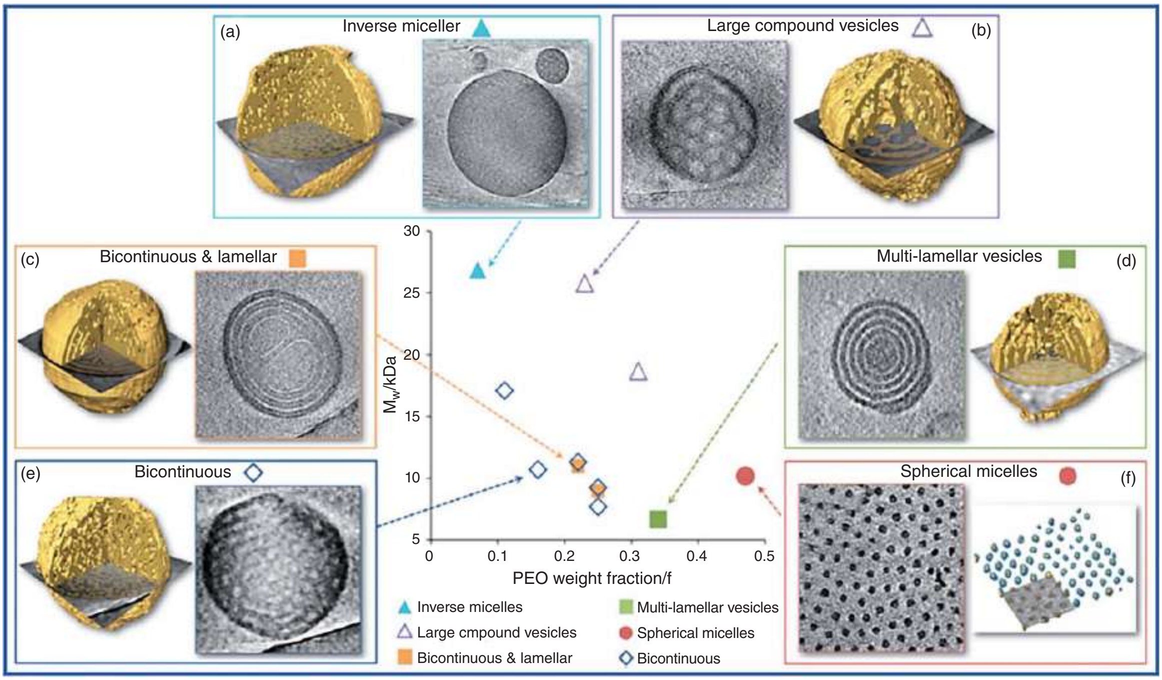

Figure 5.4 (a–f) Self-assembly behavior of poly(ethylene oxide)-b-poly(octadecyl methacrylate) (PEO-*b*-PODMA) block copolymers with corresponding slices are presented in a partial phase diagram through the 3D reconstructions, and computer-aided visualizations from the reconstructed tomograms (segmentations in yellow) that show the different morphologies. Source: Reproduced with permission from Wiley-VCH [51].

In conventional transmission electron microscopy (CTEM), using an objective aperture, staining, and/or low acceleration voltages may help in enhancing the scattering contrast, whereas phase contrast is enhanced via defocusing. However, these may lead to the structural organization of the specimen, introduce artefacts, and make the image difficult to interpret. In scanning transmission electron microscopy (STEM), imaging contrast appears mainly because of atomic number Z variations of the elements in the sample under investigation [52]. Because polymers mainly consist of carbon and other light elements, the total scattering elastic cross-section varies roughly as $Z^{3/2}$. Thus, STEM for polymers is mainly performed on filled or stained systems, where the contrast is created by the Z-variations between the filler or staining agent and the polymer matrix, or in case of polymeric multiphase systems, in which, an element with higher Z in the polymer chains substantially contributes to the contrast formation. In STEM, a focused electron beam is scanned across the specimen and typically forms a probe in the range of a few nanometers or less in size. Various detectors positioned below the specimen as shown schematically in Figure 5.5a collect the transmitted electrons [52].

For collection of electrons scattered with intermediate angle, an annular dark field (ADF) detector is used, whereas a high-angle annular dark field (HAADF) detector is applied to collect the scattered electron with the largest scattering angles. Electrons with large scattering angle originate from Rutherford scattering (screened by the atoms' electronic cloud) and have the apparent advantage that contrast formation is based on elastically scattered electrons and is incoherent (Figure 5.5b). Figure 5.5c,d represents images of the morphology of a photoactive layer acquired for defocus conditions by bright field (BF) CTEM at two different acceleration voltages, at 300 kV and at 80 kV, respectively. The image acquired at high acceleration voltage has only weak contrast between the 1-(3-methoxycarbonyl)propyl-1-phenyl-[6,6]-methanofullerene (PCBM) domains (dark areas) and the surrounding poly[2-methoxy-5-(3′,7′-dimethyloctyloxy)-1,4-phenylenevinylene (MDMO-PPV) matrix (Figure 5.5c). With decrease in the acceleration voltage (80 kV), the contrast between the PCBM and MDMO-PPV matrix polymer has increased as shown in Figure 5.5d. However, the interfaces between the PCBM domains and the matrix are fuzzy, which makes it difficult to identify the edges of the PCBM domains. HAADF-STEM images acquired on the same specimen but with two different camera lengths and collection angle-ranges at the HAADF detector are shown in Figure 5.5e,f. Applying a longer camera length (i.e. lower collection angles) under similar imaging conditions, the contrast between the PCBM domains and the MDMO-PPV matrix substantially increases. Figure 5.5g represents the contrast optimized HAADF-STEM image showing the interconnected network of the PCBM domains. Until now, we have discussed few spatially resolved techniques such as TEM, STEM, and cryo-TEM to map the polymer structure and determined the location of crystalline regions in polymers. However, electronic properties of polymers are directly affected by the nanoscale orientation of semicrystalline polymers. Panova et al. [54] have introduced an STEM technique (Figure 5.6a) to obtain spatially resolved maps of crystalline domain orientations over a field of view on the order of 1 μm with a spatial resolution

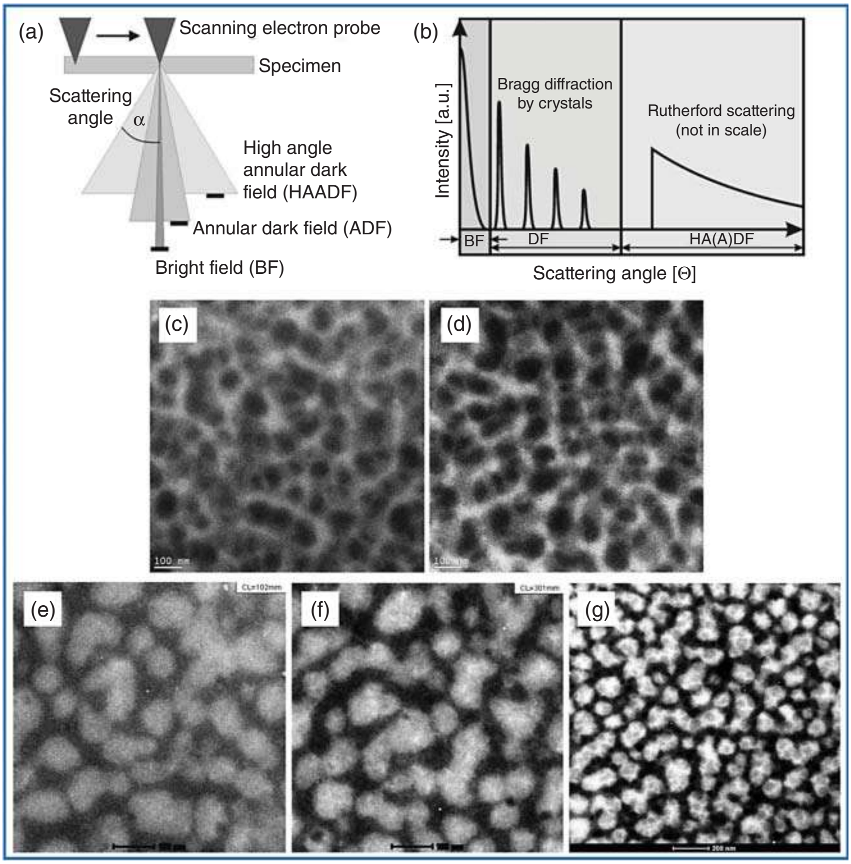

Figure 5.5 STEM. (a) Schematic representation of the scanning probe, the scattering angles and the respective detectors collecting the scattered electrons. (b) Qualitative representation of bright field and dark field scattering ranges (for same scattering angle ranges, the same grey scales are used for better visualization). BF CTEM images of the PCBM/MDMO-PPV photoactive layer acquired at (c) 300 kV and (d) 80 kV acceleration voltage; and HAADF-STEM images of the same sample acquired with camera lengths of (e) 100 mm and (f) 300 mm, that is collection angles ranging between 73 and 290 mrad; 24 and 120 mrad, respectively. (g) Contrast optimized HAADF-STEM image showing the interconnected network of the PCBM domains. Source: Reproduced with permission from American Chemical Society [53].

of 20 nm. The P3HT/polystyrene (PS) samples captured at an accelerating voltage of 200 kV are shown in Figure 5.6b–d. Figure 5.6b shows the ADF STEM image where large (~200 nm) oval disks were observed. It is noted that at higher magnification they were shown to exhibit rough internal features (Figure 5.6c). Energy-dispersive spectroscopy (EDS) confirmed that these structures were mostly P3HT (Figure 5.6d). A virtual dark field image with an aperture that includes the whole field of view of the detector is shown in Figure 5.6e, which contains signal from both the diffracting and amorphous regions and provides a measure of the relative thickness of the sample.

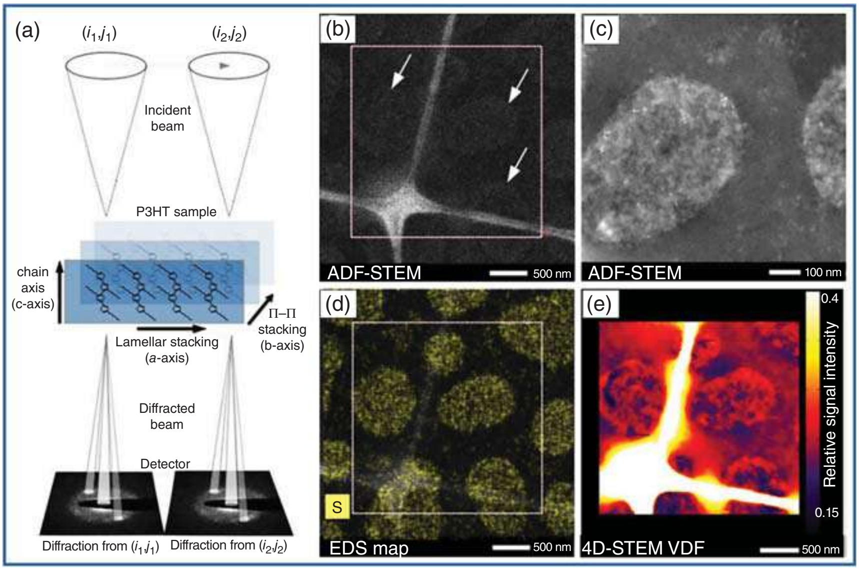

Figure 5.6 (a) Convergent beam rasters the beam across the sample (i, j) and captures a full diffraction pattern (K_x, K_y) for each probe location. Raw and minimally processed images of P3HT/PS (200 kV); (b) ADF-STEM image having oval clusters of P3HT is shown by white arrows. (c) Image at higher magnification to display the structure within. (d) An EDS map confirms the composition of the aggregates to be mostly P3HT, cumulative sulfur signal is shown in yellow. (e) A preliminary virtual dark field image can be reconstructed using the entirety of the field of view from the 4D-STEM dataset gathered over the square region delineated by white dashed lines in (b) and (d). The normalized relative cumulative signal intensity for each probe position is indicated by the color. Source: Reproduced with permission from Elsevier Ltd. [54].

These maps may prove useful for determining pathways for electronic charge transport in P3HT-containing materials. This is a general technique and can be applied to any semicrystalline polymer sample.

5.2.1.3 Scanning Tunneling Microscopy (STM)

Scanning probe techniques such as STM makes it possible to locally probe polymers on the nanometer scale. Using STM under ultra-high vacuum (UHV) conditions, there have been several reports such as imaging conjugated polymer chains on surfaces [55], observation of polymer – molecule nanojunctions [56], manipulation of single polymer chains [57], and conductance measurement of individual polymer chains as a function of their length [58]. Jethwa et al. [59] have used STM to image PPV-tertbutyldiphenylsilyl (TBDPS) polymers (poly(*p*-phenylene vinylene), which is functionalized with triethylene glycol side-chains, and are terminated by TBDPS protecting groups as shown in Figure 5.7a.

The image at the monomeric scale provides structural details for the individual monomers, such as side-chain conformations and information on regioisomerism within the polymer backbone, and provides insights into the synthetic route used to prepare the polymer [59]. Figure 5.7b represents a high-resolution STM image

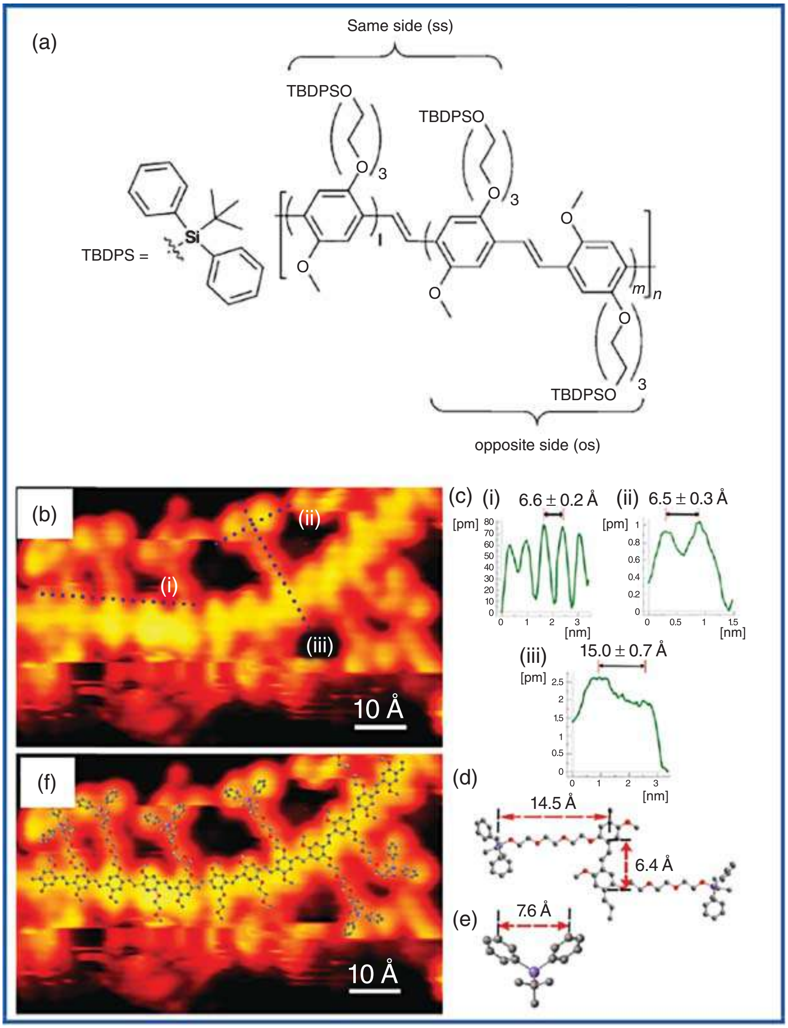

Figure 5.7 **STM.** (a) Chemical structure of PPV as functionalized with triethylene glycol side-chains terminated with TBDPS protecting groups (PPV-TBDPS). The relative positions of the side-chains on the PPV backbone are represented as SS (same side) and OS (opposite side). (b) High resolution image of PPV-TBDPS shows detail of backbone and side-chain conformations; $V_t = -1.3$ V, $I_t = 0.49$ nA, 84×58 nm^2. (c) (i–iii) Line profiles taken along blue dashed lines shown in (a). ChemBio3D Ultra molecular models (not energetically minimized) relating to distances in relevant line-profiles of (d) PPV-TBDPS ($n = 2$) and (e) TBDPS protecting group. (f) Molecular model overlay of PPV-TBDPS revealing the inferred conformations of the side-chains. (g) STM image of PPV backbone red and white arrows indicate symmetry reversal of electron density about the PPV backbone; $V_t = -2.2$ V, $I_t = 0.51$ nA, 6×6 nm^2. (h) Schematic representation showing the reversal of electron density either due to (i) regioisomerism (ii) rotation of the PPV backbone of a single type of regioisomer. Source: Reproduced with permission from The Royal Society of Chemistry [59].

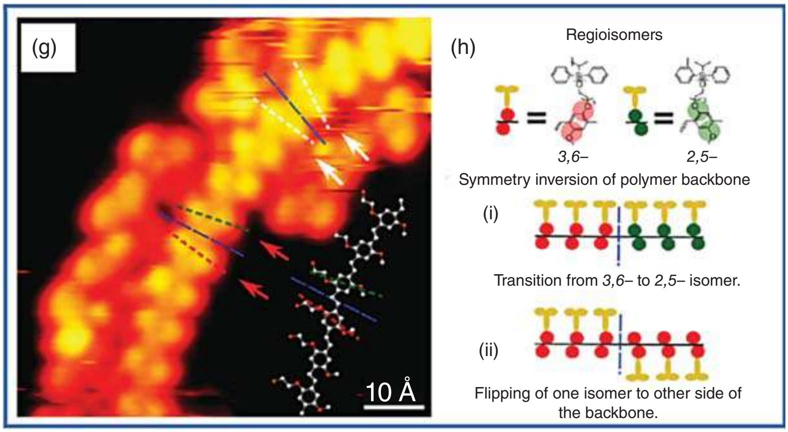

Figure 5.7 (*Continued*)

of the PPV-TBDPS polymer adsorbed on Au(111). The PPV backbone and the conformations of the TBDPS side-chains are clearly observed. Figure 5.7c showed the line profiles taken across the PPV backbone, the TBDPS groups and along the fully extended triethylene glycol chain. A comparison with the molecular model depicted in Figure 5.7d,e shows that the dimensions match favorably. In order to clarify, a 2D model of PPV-TBDPS is overlaid on top of the STM image as shown in Figure 5.7f. The presence of different regioisomers within the polymer backbone is a common structural defect associated with the polymers. The para methoxy- and TBDPS groups of PPV-TBDPS can be located at either the 3, 6-, or the 2,5-positions of the phenyl ring, creating two regioisomers as illustrated in Figure 5.7h. An alternative imaging mode is shown in Figure 5.7g where the two different regioisomers present in PPV are clearly distinguishable. This study demonstrates that it is possible to characterize complex polymers at the individual molecule level by using UHV-STM.

5.2.2 Field Emission Scanning Electron Microscopy (FESEM)

Materials science is the study of structure–property relationships via different techniques and the morphology is a key factor to performance of materials. Many microscopy techniques have been employed over the last few decades; the most ubiquitous is the scanning electron microscope (SEM). Typically, polymers have low conductivity and therefore are subject to charge build-up and electron beam damage. One way to mitigate both of these issues is to use low voltage SEM. However, low beam voltage operation normally results in low-resolution images. In order to improve resolution and contrast in the SEM, increasing the source brightness and decreasing the initial probe size by using a field emission filament is a good solution. Hu et al. [60] have tuned the thermoelectric performance of a conducting polymer by nanostructure evolution. The morphology of synthesized PEDOT was directly observed by using field emission scanning electron microscopy (FESEM) technique. The FESEM images of the bulk PEDOT powder as well as the PEDOT nanostructures are shown in Figure 5.8a–e. The nanostructured PEDOT samples revealed various morphologies including (Figure 5.8b) globular nanoparticles, (Figure 5.8c) nanorods or ellipsoidal nanoparticles, (Figure 5.8d) nanotubes, and (Figure 5.8e) nanofibers. The electrical conductivity, Seebeck coefficient, and power factor follow the sequence of bulk PEDOT $<$ globular nanoparticle $<$ nanorod or ellipsoidal nanoparticle $<$ nanotube $<$ nanofiber. In another work, Huang et al. [61] have demonstrated a template-free approach to fabricate a large area of length-controllable and well-oriented PPy nanowire arrays using a facial electrochemical polymerization strategy. Nanowire arrays with different length were prepared by changing the polymerization time as shown in Figure 5.8f–h. The relationship of the nanowire length and the polymerization time is shown in Figure 5.8i. The compact PPy film, PPy nanowire networks, and nanowire arrays were precisely synthesized by tuning the composition of the solution and electrochemical methods as shown in Figure 5.8j–l. When using PPy nanowire networks serving as the super capacitor electrode, counter-ions penetrate into the polymer and access the internal part through the pores of interstitial regions within the polymer. Thus, the specific capacitance is increased significantly since it is more accessible for the counter-ions as shown in Figure 5.8m–o. The advanced nanostructures could dramatically improve the device performance, which is demonstrated here by taking the example of PEDOT nanostructures and PPy nanowires. In order to characterize the nanostructures, FESEM is an essential tool to visualize the morphology of polymer nanostructure.

5.2.3 Atomic Force Microscopy (AFM)

AFM is another powerful characterization tool in the field of polymer science, capable of revealing surface structures with superior spatial resolution. It has been widely used to investigate surface morphology, phase segregation, roughness, packing of the polymer chains, conformation, mapping the distribution of electric charges, etc. of conducting polymers [63]. Taranekar et al. [64] have investigated the formation of unique nanoscale morphologies due to phase-segregation of polysiloxane domains and cross-linked PPy from the AFM images. Mazzio et al. [65] have studied the role of very small changes in P3HT regioregularity (RR) on the physical and electronic properties of P3HT nanowires based on 96–99% RR in P3HT with similar molecular weights and low dispersities and used AFM for the structural characterization. Massonnet et al. [66] have showed the AFM phase contrast images of the surface of PEDOT:OTf and PEDOT:PSS as shown in Figure 5.9a,b, respectively. The images reveal that PEDOT:OTf has a granular structure with large homogeneous domains, whereas PEDOT:PSS presents a poorly structured surface, where hard and soft domains are highly entangled. The presence of excess poly(4-styrenesulfonate) (PSS) makes the PEDOT:PSS amorphous and results in the embedding of PEDOT:PSS grains in a PSS rich matrix. The observed granular structure of PEDOT:OTf arises due to dense stacking of PEDOT chains having less sterically hindered OTf ions. In another report by Kobayashi et al. [68], single NPs of poly[2-methoxy-5-(2-ethylhexyloxy)-1,4 phenylenevinylene] (MEH-PPV) have been

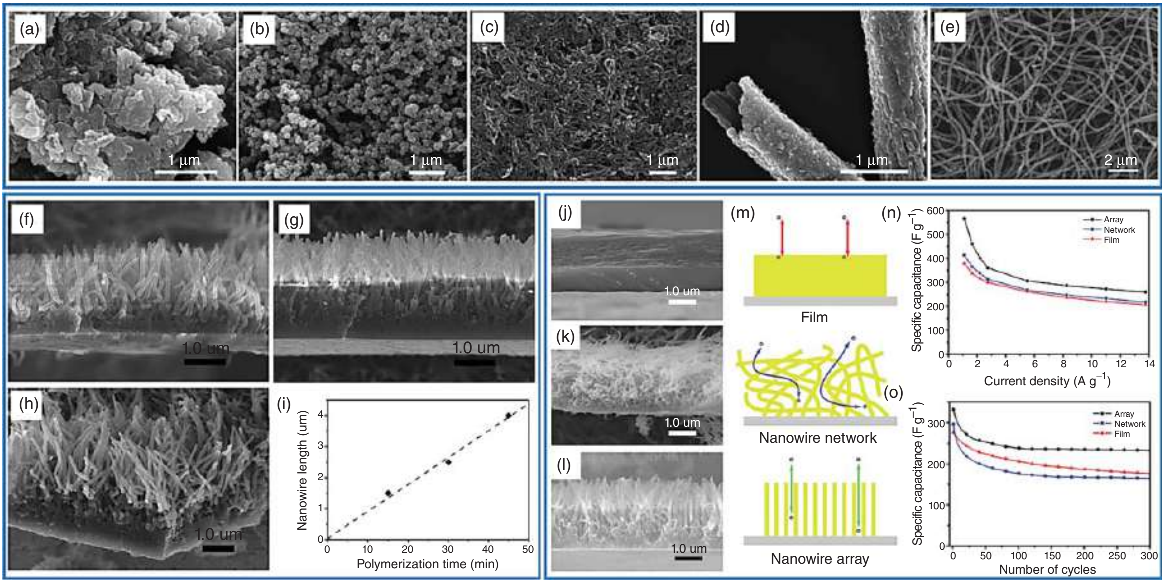

Figure 5.8 FESEM. FESEM images of (a) bulk PEDOT power and PEDOT nanostructures of (b) globular nanoparticles, (c) nanorods or ellipsoidal nanoparticles, (d) nanotubes, and (e) nanofibers. Source: Reproduced with permission. From The Royal Society of Chemistry [60]. Side view of PPy NW arrays having different length: (f) 1.5 mm; (g) 2.5 mm; and (h) 4.0 mm. (i) The plot of PPy NW length vs. polymerization time, reveals that the wire length depends linearly on the polymerization time. Source: Reproduced with permission from The Royal Society of Chemistry.[61]. FESEM images of (j) PPy film, (k) PPy nanowire network, and (l) PPy nanowire arrays. (m) Scheme of ion transport pathways, (n) specific capacitances, and (o) Capacitance as a function of the cycle number of PPy for different morphologies. Source: Reproduced with permission from Wiley-VCH [62].

characterized using simultaneous AFM and fluorescence micro spectroscopy. To apply local pressure on individual CP NPs, the tip of the AFM probe is used and the fluorescence microscope has simultaneously monitored changes in the fluorescence spectral shifts and emission intensities. Ghosh and co-workers [67] have also been able to directly observe the polymer regions via AFM topography imaging and then rapidly acquired high-resolution local chemical spectra at selected regions on the sample by AFM with tunable pulsed laser as an infrared (IR) source (AFMIR) (Figure 5.9c–f and g–i). When the sample absorbs the IR laser pulse, it gets warm via the photothermal effect, which results in a rapid thermal expansion of the absorbing region of the sample. Consequently, the thermal expansion pulse impacts

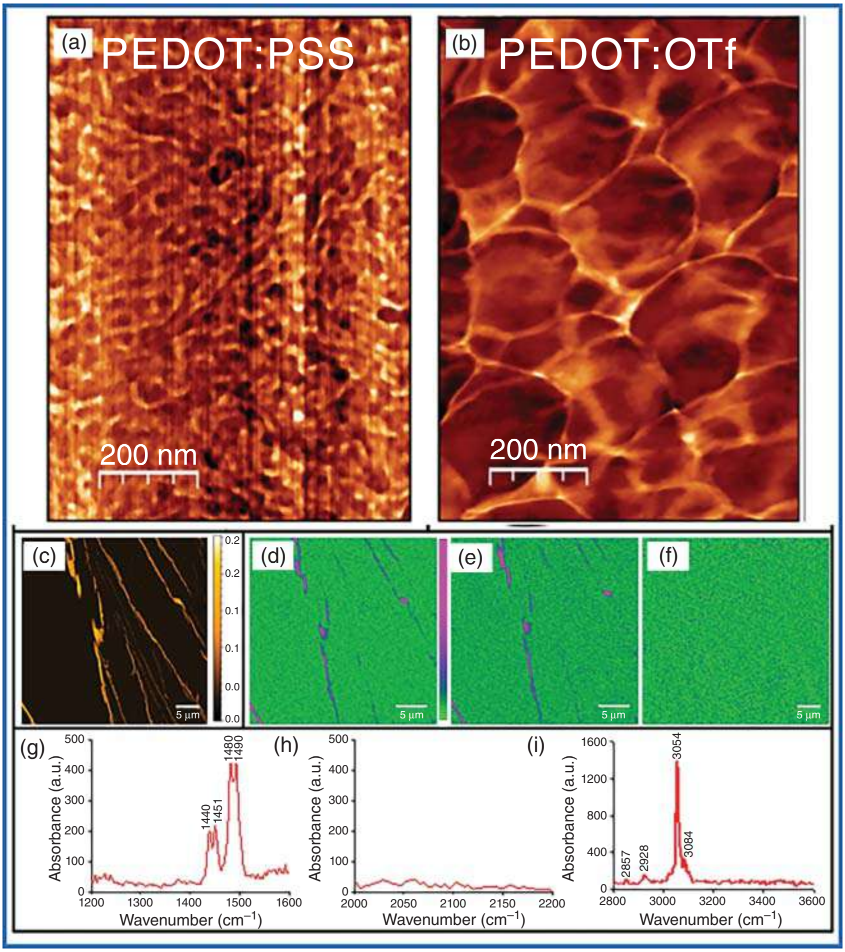

Figure 5.9 AFM. AFM phase images of (a) PEDOT:PSS and (b) PEDOT:OTf. Reproduced with permission from The Royal Society of Chemistry [66]. (c) Topographic image of PDPB nanofibers using conventional AFM. AFMIR mappings of the photo-induced PDPB polymer nanostructures at different fixed wavenumbers: 1490 cm^{-1} (d), 2146 cm^{-1} (e), and 3054 cm^{-1} (f). (g–i) nanoIR spectra recorded at three different spectral regions of the PDPB polymer. Source: Reproduced with permission from The Royal Society of Chemistry [67].

the tip of the AFM cantilever to oscillate. The local infrared absorption spectra are recorded as the amplitude of oscillations is proportional to the absorption and make chemical maps by scanning the surface at a given wavelength. As shown in Figure 5.9c,d, the surface topography of the poly(diphenylbutadiyne) (PDPB) nanostructures showed well dispersed fibers formed during deposition on the ZnSe substrates. The IR absorption signal measured by the cantilever when the laser is set at 1494 cm^{-1}. The brighter purple colors indicate regions of stronger IR absorption at this particular wave number and the absorption intensity differentiate the polymer domains, which are distinct from the low-intensity background (green color).

The spectral region of the triple bond stretching at 2300–2000 cm^{-1} was thoroughly analyzed and the disappearance of the monomer band at 2146 cm^{-1} after irradiation infer that the polymerization is complete (Figure 5.9e). When the wavenumber is fixed at 3054 cm^{-1}, a strong signal is measured that originates from the benzene ring in the PDPB polymer (Figure 5.9f). The combination of nanoscale probe from an AFM with tunable IR source provides simultaneous measurements of nanoscale morphology and the chemical composition mapping (Figure 5.9g–i), which confirms the presence of PDPB polymer nanostructures onto the substrate. Advanced AFM modes including conductive AFM (c-AFM), photoconductive AFM (pc-AFM), and scanning Kelvin probe force microscopy (KPFM) have been used to gain an understanding of the structure–performance relationship of polymer blends [69], which are discussed in Section 5.3.1.

5.3 Surface Characterization

5.3.1 Scanning Kelvin Probe Microscopy (SKPM) and Kelvin Probe Force Microscopy (KPFM)

Scanning Kelvin probe microscopy (SKPM) measures contact potential difference (CPD) between the tip and the sample with resolution in the nanometer range. The CPD can be converted to the work function of the sample when the measurement is performed under thermoequilibrium state. In SKPM, the AFM system operates in non-contact mode, and a conductive tip oscillates at the first resonant frequency of the cantilever over the sample surface as it is scanned laterally. Hallam et al. [70] have used SKPM with resolution-enhancing carbon nanotube tips to study charge transport on a 100 nm scale in a chain-extended, semicrystalline conjugated polymer. The network of polymer ribbons can be clearly resolved in AFM topography as shown in Figure 5.10a. Figure 5.10b represents the surface potential map taken immediately after the gate bias stress has well-defined regions in which the surface potential is more positive. According to the chosen color scale, these appear white, which are directly correlated with the ribbon morphology of the film. However, the ribbon topography before the stress exhibited smooth and uncorrelated potential landscape as shown in Figure 5.10c,d.

Thus, the periodic surface potential contrast seen in Figure 5.10b is only appears after the bias stress, and related directly to the trapping of charges. Charge trapping

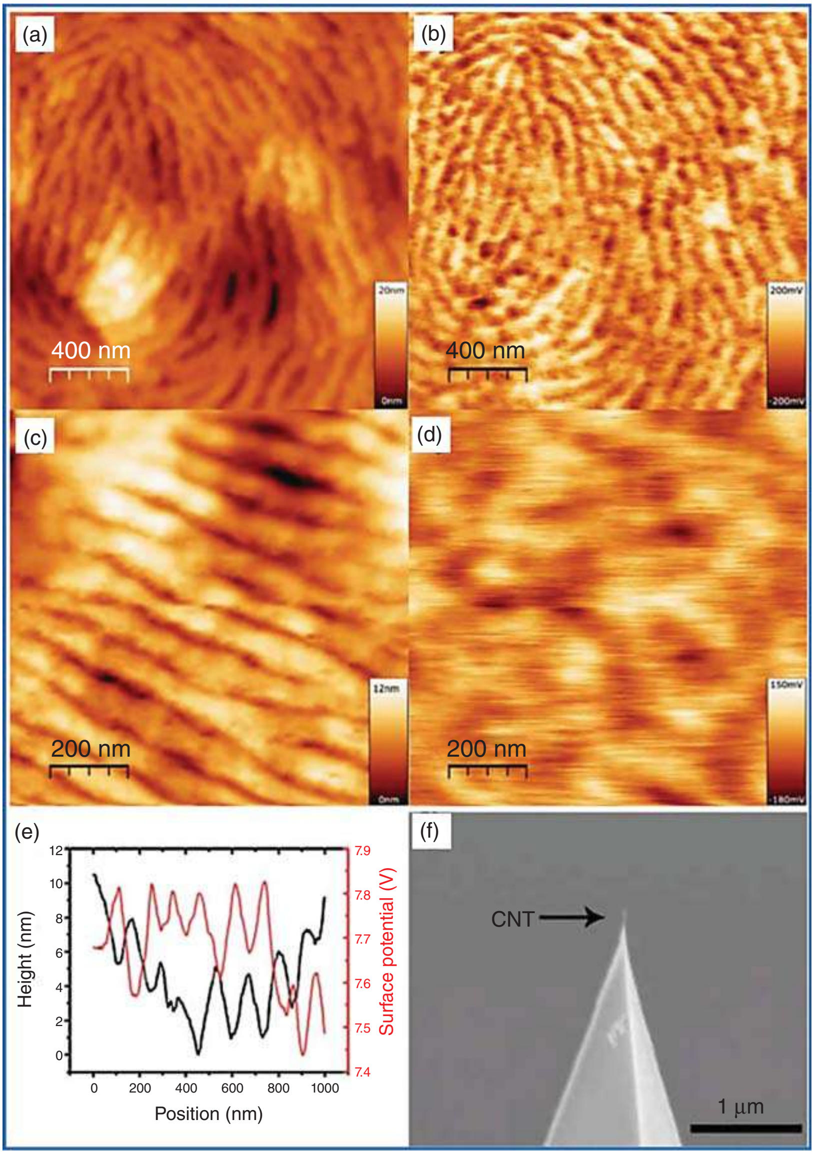

Figure 5.10 (a) AFM topography of an 80 nm thick "ribbon phase" pBTTT film. (b) Corresponding surface potential image after one hour stress at $V_g = -80$ V; (c), (d) Topography and surface potential of an unstressed pBTTT device. (e) Topography (black) and potential (red) line scans of a stressed device; (f) SEM image of a metal-coated AFM cantilever with a single-walled carbon nanotube (CNT) attached. Source: Reproduced with permission from American Physical Society [70].

occurs in well-defined sites preferentially instead of homogeneously throughout the film. Through analysis of single-line cross-sections as shown in Figure 5.10e, it is observed that the positive peaks in the surface potential coincide with the troughs in the ribbon topography and the regions of more negative potential coincide with the peaks in the topography. The topography peaks were assigned to the ordered polymer ribbons and the troughs to the disordered grain boundaries [71]. This can be attributed to the preferential charge trapping in the disordered grain boundary regions between the crystalline pBTTT ribbons. This study unambiguously showed that the disordered grain-boundary regions constitute preferential charge trapping sites and consequently lead to significant lateral nonuniformity on a 100 nm length scale of the induced carrier concentration under accumulation conditions. SKPM provides useful insight in understanding the charge transport properties of high-mobility, semicrystalline polymers. Gu et al. [72] have demonstrated photo-induced force microscopy (PiFM) technique for imaging organic solar cell bulk heterojunctions with nanoscale chemical specificity. This technique combines an AFM tip with a tunable infrared laser to induce a dipole for chemical imaging. Coupling the nanometer resolution of AFM with the chemical specificity of a tuned IR laser, authors have successfully shown the spatially map the donor and acceptor domains in a model all-polymer bulk heterojunction with resolution approaching 10 nm. Liscio et al. [69, 73] have studied the self-assembly of regioregular poly (3-hexylthiophene) (P3HT) fibers deposited on flat surfaces from $CHCl_3$ solutions using AFM and KPFM. In order to study these quasi-one dimensional objects, the effective area has been defined, which represents the area of sample surface interacting with the KPFM probe and it plays a crucial role in the estimation of the surface potential (SP) of nanofibers having a cross-section comparable with the apical diameter of the tip, i.e. 20 nm. The authors proposed a model, which provides a quantitative insight into nano-systems smaller than 20 nm through the estimation of the effective area. Figure 5.11a–f showed the topographic AFM and corresponding KPFM images of P3HT deposited on highly oriented pyrolytic graphite (HOPG), muscovite mica, and silica. The different solvent wettability of the substrates results in different lamellar packings. The correlation plots between the measured surface potential (SPs) and the corresponding fiber sizes for all three substrates are shown in Figure 5.11g.

The decrease in the P3HT SP with the width of the architecture is a purely geometrical artefact due to the convolution effects. The proposed model allowed the separation of P3HT and substrate contributions, reproducing the measured monotonic trend of the HOPG SP (red line in Figure 5.11h). After deconvolution, the bundles and substrate SPs are independent of the sizes (blue dots for HOPG). This model represents a useful tool to study the surface potential characteristics of nanowires with a high degree of precision paving the way towards their use as building blocks for the fabrication of electronic nanodevices with improved performance.

5.3.2 X-Ray Photoelectron Spectroscopy (XPS)

X-ray photoelectron spectroscopy (XPS) is a powerful technique useful for analyzing the surface chemistry of a material in order to elucidate the electronic structure,

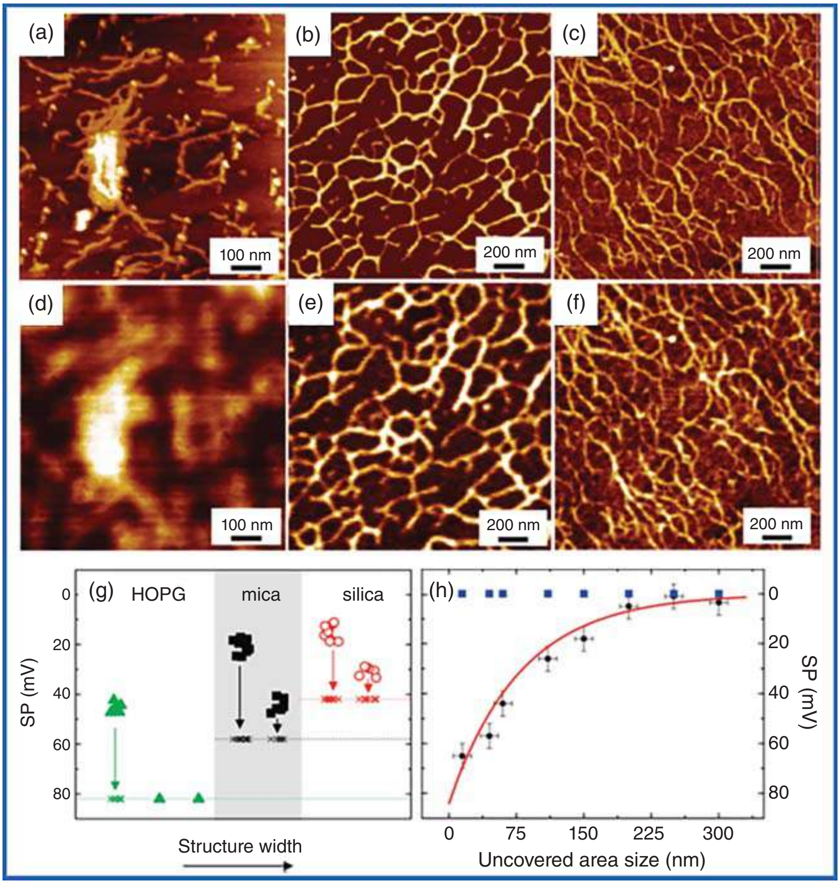

Figure 5.11 AFM and KPFM. AFM topography and corresponding KPFM images of P3HT fibers deposited on (a, d) HOPG, (b, e) mica, and (c, f) silica. Z-ranges were (a) 9 nm, (b) 6 nm, (c) 6 nm, (d) 120 mV, (e) 60 mV, and (f) 50 mV. (g) Measured SP values corresponding to the different P3HT structures on HOPG (2), mica (9), and silica (O) with different widths. The variation of the measured SPs of the nano-objects is calculated by using the convolution procedure, and the asymptotic SP values are displayed (dashed line) for each substrate. (h) Dependence of measured (9) and simulated(s) SP on the size of the uncovered HOPG surface area. Blue dots indicate the asymptotic SP values. Source: Reproduced with permission from Wiley-VCH [73].

elemental composition, and oxidation states of elements in a material. In order to alter or improve the performance and behavior of a material, surface modification have been used in a wide variety of applications. Thus, characterization of polymer surface modification is necessary to develop new polymeric materials. Guselnikova et al. [74] demonstrated a method for covalent modification of PEDOT:PSS using arenediazonium tosylate and characterized the surface using XPS. In another work, Massonnet et al. [66] have analyzed the layers of PEDOT:OTf, PEDOT:OTf doped with TfOH and PEDOT:OTf doped with H_2SO_4 (called PEDOT:Sulf) by XPS. The overview XPS spectra are presented in Figure 5.12a–c. The intensity of F (1s) signal

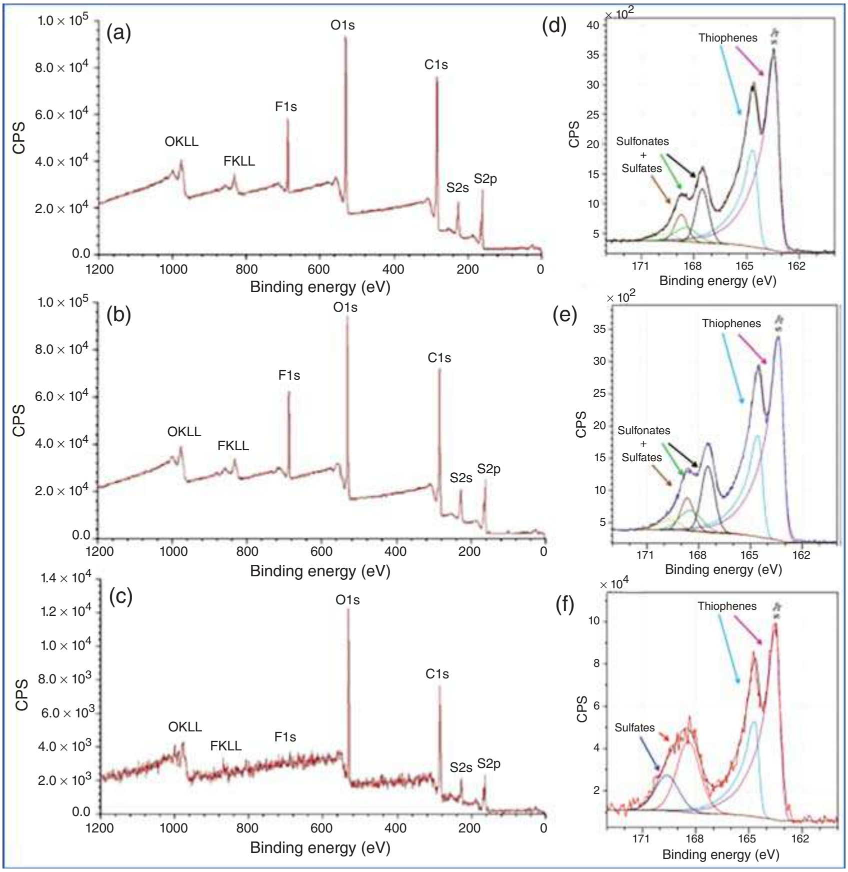

Figure 5.12 Overview XPS Spectra of (a) PEDOT: OTf; (b) PEDOT: OTf doped with TfOH; (c) PEDOT: Sulf. XPS S (2p) signals from (d) PEDOT: OTf in the pristine state, (e) PEDOT: OTf treated with TfOH, and (f) PEDOT: Sulf. Source: Massonnet et al. [66]. © 2015, Royal Society of Chemistry.

(688.5 eV), related to fluorinated species is slightly increased when PEDOT:OTf is doped with TfOH, supporting the hypothesis that new counter ions are inserted in the polymer. Upon doping with H_2SO_4, the F (1s) signal disappears, thus showing that OTf ions are withdrawn from the layer. As shown in Figure 5.12d–f for PEDOT:OTf, PEDOT:OTf doped with TfOH, and PEDOT:Sulf, respectively, signal clearly reveals peaks of the S (2p) from the thiophene units (163–167 eV), $SO_3^\bullet$ and $HSO_4^\bullet$ (167–171 eV). The observation clearly suggests that OTf ions have been replaced by $HSO_4^\bullet$ upon doping.

XPS is also useful in elucidating the surface composition and oxidation states of the as- prepared polymer nanohybrids. Ghosh et al. [75] have demonstrated a facile method to develop Pd nanoparticle (NP)-based multimetallic alloys incorporated on PPy nanofibers by *in situ* nucleation and growth of NPs using colloidal radiolytic technique and characterized the nanohybrids using XPS technique. In another work, XPS is utilized to confirm the nanohybrids formation based on PEDOT nanofibers and gold nanoparticles (Au NPs) [76].

5.4 Electrochemical Characterization

There has been a surge of interest to study the electrochemical phenomena of conjugated polymer for their application in electrochemical devices and other energy conversion applications [77–80]. A significant co-relation between the understanding of the electrochemical mechanisms and the development of advanced catalytic nanostructured materials has been established [81, 82]. The electrochemical activity is generally measured by cyclic voltammetry (CV) or linear sweep voltammetry (LSV). Particularly, CV is a very useful electrochemical technique to study the redox processes in a conjugated polymer. During redox processes, reduction makes negatively charged polymer chains, whereas oxidation results in positively charged polymer chains. Ions move in to the polymer matrix during doping while de-doping drive out the ions from matrix. The doping/de-doping process certainly affects the electrochemical properties of the conducting polymers. Not only that, the change of morphology of the polymers at the nanoscale also alters the electrochemical behavior significantly. Park et al. [83] have investigated the oxidation/protonation levels of three different PANI nanostructures, specifically nanospheres, nanorods, and nanofibers. A typical CV curve of PANI is shown in Figure 5.13a, which has two sets of distinct redox activity as indicated by the two pairs of anodic and cathodic current peaks corresponding to the electron transfer from/to PANI (leucoemeraldine/emeraldine salt) and deprotonation/protonation (emeraldine salt/pernigraniline) [84]. Figure 5.13b shows the CV analysis of three different PANI samples in 1 M H_2SO_4 electrolyte. The observed broad redox peaks result from the overlap of the two-redox processes. As depicted in Figure 5.13c, both anodic and cathodic peak currents increased linearly with scan rate, which can be attributed to the electrode kinetics that are subject to a surface-controlled redox process. The anodic (E_{pa}) and cathodic (E_{pc}) peak potentials are plotted as a function of the logarithm of the scan rate as shown in Figure 5.13d.

The electron transfer coefficient (α) and the electron transfer rate constant (k_s) are calculated by using Laviron theory [85]. The electron transfer coefficient values are found to be around $3.6–3.7 \times 10^{-1}$. The k_s value of PANI nanofibers (4.3×10^{-1} s^{-1}) is found to be higher than the k_s values of PANI nanorods (3.1×10^{-1} s^{-1}) and PANI nanospheres (2.6×10^{-1} s^{-1}). This can be attributed to the superior electron transfer capability of PANI nanofibers. Thus, the electrochemical properties of the electrodes are strongly affected by intrinsic charge-transport ability of the individual nanostructures. The conductivity of CPs can be improved successfully by electrochemical doping, both n-type and p-type, to induce an insulator-to-metal transition in the CPs. CPs offer many advantages in applications as in electrochemical capacitors, actuators, and sensors. Other voltammetry techniques also employed such as differential pulse voltammetry (DPV) and square wave voltammetry (SWV) techniques, where the current is measured before and after each potential step change (staircase

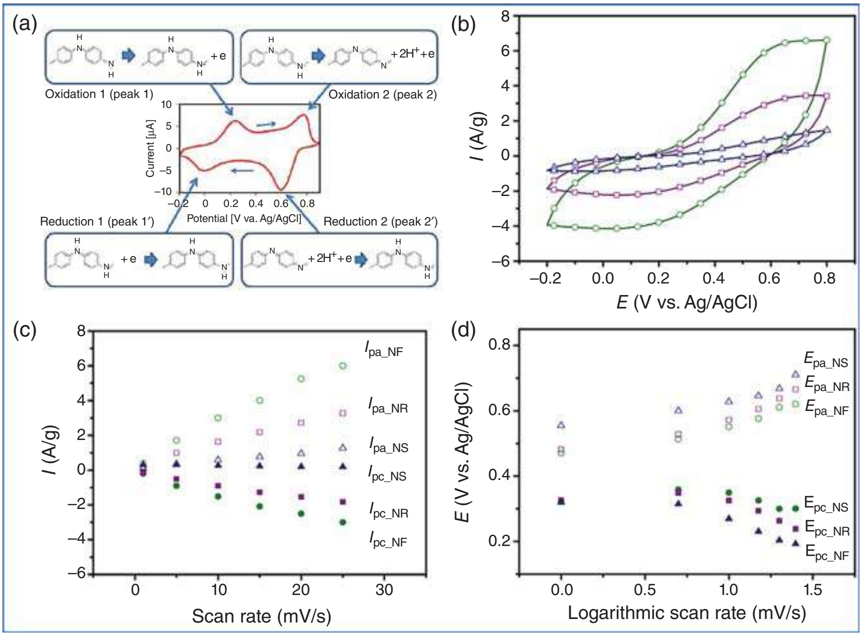

Figure 5.13 CV. (a) A typical cyclic voltammogram of PANI in HCl (pH 1) reveals two sets of redox couples. Reproduced with permission from MDPI. Source: Song and Choi [84]. © 2013, MDPI. CV curves of PANI nanostructures performed in a 1 M sulfuric acid solution: (b) at the same scan rate (25 mV/s) (c) plots of the peak current (the anodic peak current, I_{pa}; the cathodic peak current, I_{pc}) vs. the scan rate, and (d) plots of the peak potential (the anodic peak potential, E_{pa}; the cathodic peak potential, E_{pc}) vs. the logarithm of the scan rate. Source: Park et al. [83]. © 2012, American Chemical Society.

voltammetry) to resolve anodic or cathodic signals. Interestingly, electrochemical measurements have also been used for evaluation of the position of energy levels and the band gap of the conducting polymer nanostructures [9, 86]. For example, CV measurements have been used to calculate the experimental highest occupied molecular orbitals (HOMO) and lowest unoccupied molecular orbitals (LUMO) energy levels from the ionization potential and the electronic affinity, respectively, and determine the band gap of PEDOT nanospindles [87]. Figure 5.14 presents that the main *p*-doping (oxidation) and *n*-doping (reduction) are irreversible processes, and the values of the peak potentials vs. Ag/AgCl are +0.139 V (oxidation) and −1.552 V (reduction) for PEDOT nanospindles. This suggests the onset of oxidation and reduction processes occurring at lower potentials and polymer have a much lower energy gap of around 1.69 eV. The energetic levels of PEDOT nanospindles are determined by using the formula as follows:

$$E_{\mathrm{HOMO}}\ (\mathrm{eV}) \sim \text{ionization potential} = -4.8 - \mathrm{e}\ \left(E_{\mathrm{ox\_onset}} - 0.63\right) \tag{5.1}$$

$$E_{\mathrm{LUMO}}\ (\mathrm{eV}) \sim \text{electronic affinity} = -4.8 - \mathrm{e}\ \left(E_{\mathrm{red\_onset}} - 0.63\right) \tag{5.2}$$

Figure 5.14 CV of PEDOT nanospindles performed at 20 mV/s in acetonitrile, 0.1 M tetrabutylammonium perchlorate. Ferrocenium/ferrocene (F_c/F_c^+) redox potential is used to calibrate the pseudo reference electrode (0.63 V vs. Ag in the present study). Source: Ghosh et al. [87]. Licensed Under CC BY 4.0.

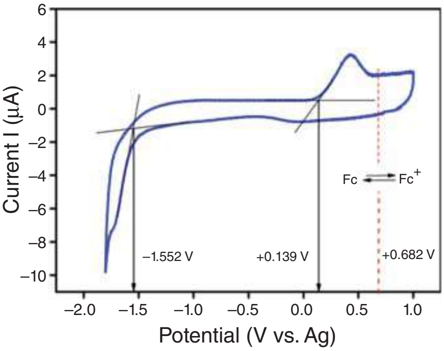

Electrochemical impedance spectroscopy (EIS) is a dynamic technique where a small potential sinusoidal perturbation is applied to the system and the amplitude and phase shift of the resulting current response are measured and useful to understand the electrochemical characteristics, including the double-layer capacitance, diffusion impedance, and determination of the rate of charge transfer. A Nyquist plot based on a mathematical approach generally consists of semicircle induced by the processes at polymer–solution interfaces, which is related to the electronic resistance within the electrode materials. Further, the results can be interpreted as an equivalent circuit (EC) mode and self-made fitting programs can normally be used to construct a quantitative fitting by using the correct electrical circuit [31].

Figure 5.15a shows the EIS Nyquist plots of PDPB nanofibers and PDPB-ZnO nanohybrids where the semicircle portion corresponds to the charge transfer process, with the diameter of the semicircle equivalent to the charge transfer resistance (R_{ct}) [88]. While the linear portion reflects the diffusion limited processes at the electrode interface. The charge transfer resistance (R_{ct}) of PDPB nanofibers (107.7 Ω) significantly lowered after formation of hybrid with ZnO (21.5 Ω, PDPB-ZnO), which indicates facile charge transfer at the polymer-semiconductor interface. Randles EC model for EIS fitted for the polymer based nanohybrids as shown in Figure 5.15. The total electrode impedance corresponds to the electron transfer resistance (R_{ct}) in series with the parallel connection of the double layer capacitance (C_{dl}) and Warburg impedance (Z_{w}). EIS can be repeated under different operating voltages to obtained Mott–Schottky plots through staircase potentio electrochemical impedance spectroscopy (SPEIS) investigation. Further, the energy band structure including band gaps, conduction band (CB) and valence band (VB) positions, and flat band potential can be determine using Mott–Schottky (M–S) analysis ($1/C^2$ vs. electrode potential).

$$\frac{1}{C^2} = \frac{2}{q\varepsilon\varepsilon_0 N_d}\left(V_{\mathrm{app}} - V_{\mathrm{FB}} - \frac{kT}{q}\right) \tag{5.3}$$

where ε is the dielectric constant of the semiconductor, ε_0 is the permittivity of the vacuum, N_d is the donor density, V_{app} is the applied potential, V_{FB} is the flat band potential, and kT/q is the temperature-dependent term. The intercept of linear plot at $1/C^2 = 0$ gives the flat band potential. Although, Mott–Schottky plot has a frequency–dependent slope, the extension of the linear part of the curve intersects the voltage axis at a point known as Schottky barrier or flat–band voltage. PDPB

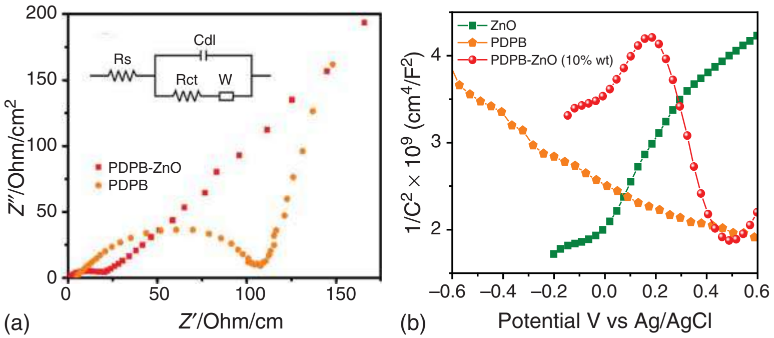

Figure 5.15 (a) The electrochemical impedance spectroscopy of PDPB nanofibers and PDPB-ZnO nanohybrids in 0.1 M Na_2SO_4 aqueous solution. Inset: Randles equivalent circuit model. (b) Mott–Schottky plots for pure ZnO, PDPB, and PDPB-ZnO nanohybrids in the presence of 0.1 M Na_2SO_4 electrolytes (pH 7) using an AC frequency of 1000 Hz. Source: Ghosh et al. [88]. © 2016, Elsevier.

nanofibers show positive slope to indicate the p-type semiconductor characteristics as shown in Figure 5.12b. The flat band potential was obtained from the extrapolation of the linear fit of the Mott–Schottky plot and found to be 1.61 V (vs. Ag/AgCl). Additionally, the co-existence of positive and negative slopes with two flat band potential values (−0.88 V and 0.68 V vs. Ag/AgCl) have been observed for PDPB-ZnO suggests the formation of p–n junction within the nanohybrids. An increase in the N_d value of PDPB-ZnO NHs (8.5×10^{19} cm^{-3}) compared with ZnO (2.5×10^{19} cm^{-3}) and PDPB nanofibers (8.5×10^{19} cm^{-3}) suggests improved charge transfer due to the formation of heterojunction in nanohybrid.

Moreover, the linear-sweep-voltammetry (LSV) has been used to investigate the photoelectrochemical performance of conjugated polymer using a three-electrode photoelectrochemical cell in 0.1 M Na_2SO_4 solution both under dark condition and under light illumination [76]. The current density in the dark remained at a very low level from −0.4 to 0.8 V (vs. Ag/AgCl), but a prompt photocurrent increase appeared after illumination with visible light in gold nanoparticle deposited polymer PEDOT nanofibers as shown in Figure 5.16a. The photocurrent density value of the Au/PEDOT electrode is significantly higher than that of the bare PEDOT electrode. This observation was confirmed with the on–off response under visible irradiation (λ = 400 nm), which demonstrated that Au/PEDOT nanohybrids showed a 13-fold increase in the photocurrent (90 $\mu A/cm^2$) due to the plasmonic enhancement contributed from Au nanoparticles (Figure 5.16b). This suggests that the electron transfer induced charge transfer, which enhances the charge separation at metal-polymer interface. The stability of the electrode can be followed by chronoamperometric measurement under continuous illumination (Figure 5.16c). The photocurrent density of Au/PEDOT nanohybrids drops about 5% after 240 minutes and then decreased slowly in which total loss is ~8%. Such high efficiency and good stability indicates that plasmonic nanoparticles modified CPNs represent a new generation electrode material for photoelectrochemical water splitting.

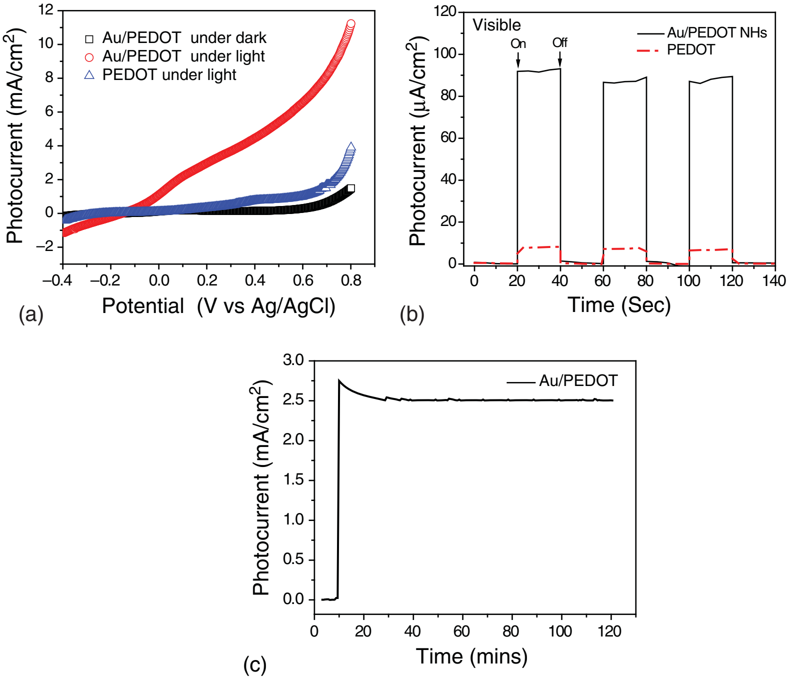

Figure 5.16 (a) LSV scans for Au/PEDOT nanohybrids and PEDOT nanofibers performed in 0.1 M Na_2SO_4 solution both under dark and under visible light illumination with output intensity 100 mW/cm^2. The scan rate was set at 20 mV/s. (b) Photocurrent response of PEDOT nanofibers and Au/PEDOT nanohybrids at zero bias voltage under 100 W/cm^2 incident power irradiation using Visible light source. (c) Chronoamperometry curves for Au/PEDOT nanohybrids at 0.23 V vs. Ag/AgCl under visible light illumination. Source: Ghosh et al. [76]. © 2018, Elsevier.

5.5 Spectroscopic Characterization

5.5.1 UV–Vis and Photoluminescence Spectroscopy

Conducting polymers contain π-conjugated backbone composed of linked unsaturated units resulting in extended π orbitals along the polymer chain, thus enabling charge transport and optical absorption. However, the property and electronic energy schemes of conducting polymers depend on its molecular structures and the extent of conjugation/interaction between molecular units. Lin et al. [89] have investigated the size-dependent optical properties of poly[(9,9-dioctylfluorenyl-2,7-diyl)-co-(1,4-benzo-{2,10,3}-thiadiazole)] (PFBT) NPs with sizes from 50 nm to 200 nm. The spectroscopic characteristics of the PFBT CPNs with various diameters are shown in Figure 5.17. The absorption spectrum of original PFBT and obtained CPNs with different sizes are shown in Figure 5.17a. With the increase in particle size, the absorption peak wavelengths of the nanoparticles red shifted from 378 to 399 nm. Some polymer chain segments are in good packing in certain regions of CPNs, which lead to longer chain length and

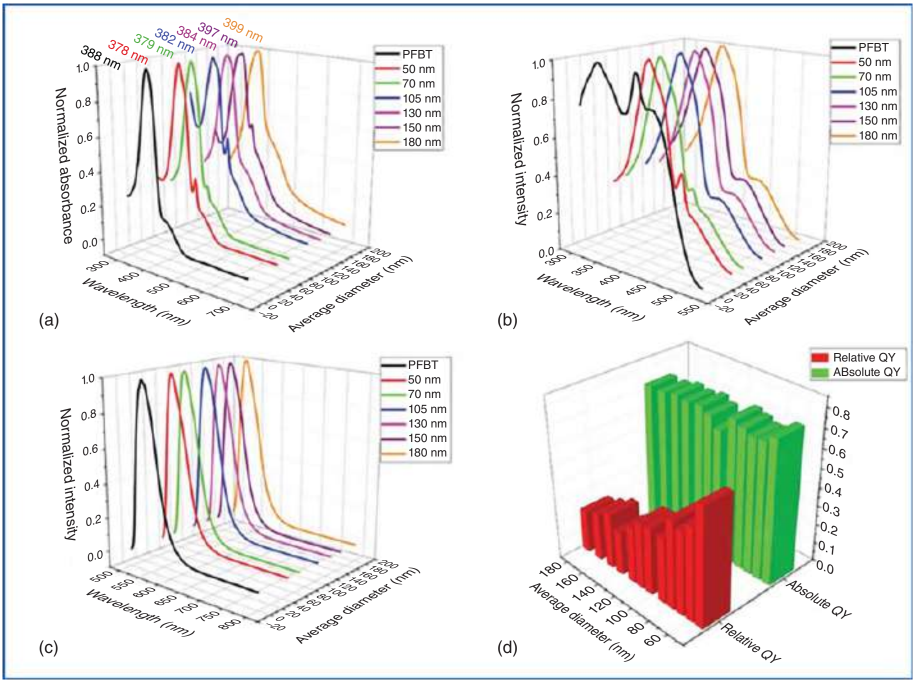

Figure 5.17 Optical properties. (a) Absorption spectra, (b) excitation spectra, (c) emission spectra, and (d) relative and absolute quantum yield of PFBT NPs having different diameters. Source: Lin et al. [89]. Licensed under CC BY 3.0.

stronger interchain electron interaction and eventually have lower energy in these regions (so called red sites [90]). However, those with shorter conjugated chain lengths are higher in energy and are called blue sites. Moreover, every chromophore could absorb photons and form excitons, but excitons in blue sites would quickly transfer to red sites.

Thus, the emission of CPNs mainly originates from singlet excitons in red sites, while the absorption derives from wider spread blue sites. So, the spectra properties should closely relate to the inner chain conformation of CPNs. As demonstrated in Figure 5.17b, compared with PFBT dissolved in tetrahydrofuran (THF), the peak wavelengths of CPNs in excitation spectrum are red shifted from 339 to 370 nm. They proposed that the red shift in absorption spectra as the diameter of CPNs increases mainly originates from light scattering of nanoparticles. However, it indicates clearly that CPNs with different sizes have similar inner chain structure and length. The fluorescence spectra of CPNs are blue shifted compared with PFBT dissolved in THF as shown in Figure 5.17c. After nanoparticle formation, the PS chains replaced THF to surround the PFBT chains. The lower polarity of PS chains might be the origin of the slight blue shift in the fluorescence spectra. Another important parameter reflecting the fluorescence property of CPNs is quantum yield (QY). Here, the relative QY was obtained by referring to rhodamine 6G ($QY = 0.95$). The relative and absolute QYs of CPNs with various sizes are depicted in Figure 5.17d. The absolute QY did not change much with increase in size and were approximately 0.7. Thus, the efficiency of electrons transferring from blue sites to red sites is almost the same with the change of size. On the other hand, the relative QY of CPNs had a declining trend when its diameter increased. The proportion of scattering in the total absorbance increases significantly with the increase in diameter, leading to a gradual decline in the calculated relative QY. Recently, Sardar et al. [91] developed an efficient light harvesting heterostructure based on PDPB nanofibers and ZnO nanoparticles (NPs) via a solution phase synthetic route and thoroughly characterized the optical properties. Figure 5.18a showed the UV–visible absorption spectra of pure PDPB, PDPB-ZnO, and ZnO nanostructures. The PDPB nanofibers show a broad absorption in the visible range, whereas bare ZnO NPs demonstrate an absorption peak at 365 nm, corresponding to the band-gap excitation (E_g of 3.39 eV). The PDPB-ZnO spectrum demonstrated the characteristics of both PDPB and ZnO, and it displayed enhanced absorption intensity in the visible range. As shown in Figure 5.18c, photoluminescence (PL) spectra of PDPB exhibited a strong dependency on the excitation wavelength. The emission peak is red shifted from 410 to 650 nm with change in excitation wavelengths from 350 to 600 nm. This can be attributed to the presence of multiple emitting states in the polymer nanofibers which are associated with the wide extend of conjugation in the different segments having various oligomeric and polymeric chains. The energy gaps (E_g) for PDPB oligomers and polymeric chains decrease as the length of the polymer chains increases (E_g of 3.99 eV for monomer whereas E_g of 1.96 eV for octamer), facilitating the greater charge delocalization [9].

The emission at 650 nm for the excitation wavelengths above 510 nm is due to the conjugated polymer chain, which acts as molecular wire. In contrast, the emission

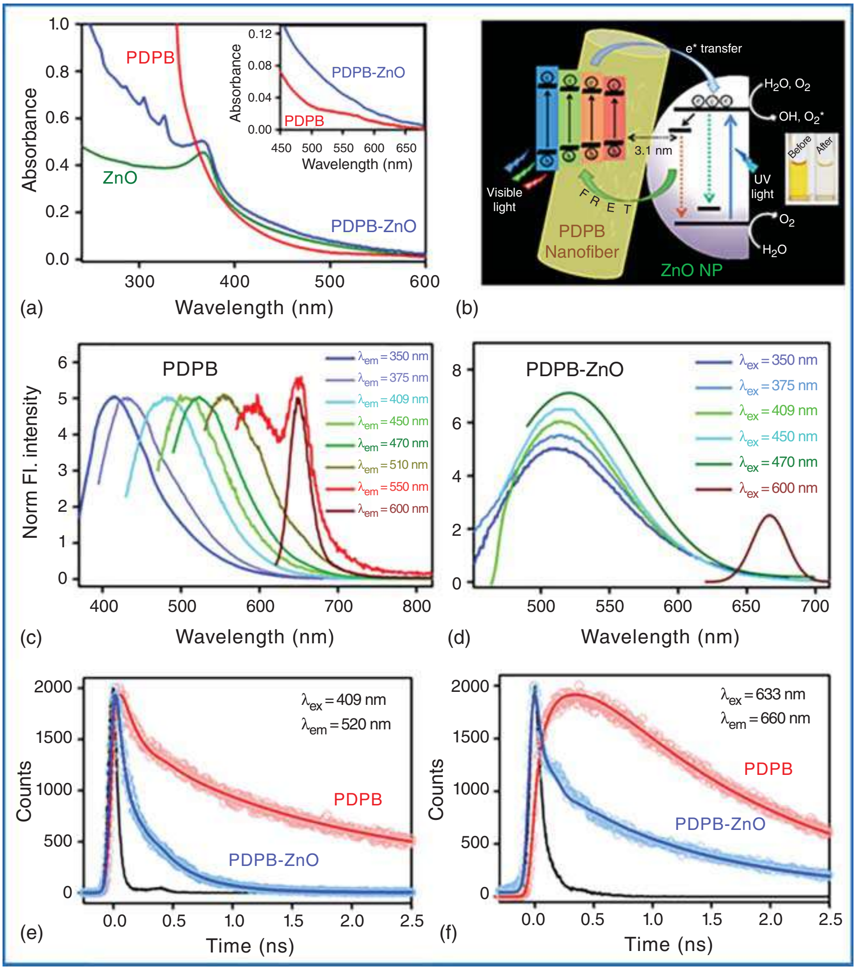

Figure 5.18 (a) UV–Vis absorption spectra of ZnO, PDPB-ZnO, and PDPB. (b) Diagram showing the interfacial carrier dynamics at the heterojunction showing the photocatalytic degradation of MO in aqueous solution. Emission spectra of (c) PDPB and (d) PDPB-ZnO at different excitation wavelengths. Fluorescence lifetime of PDPB and PDPB-ZnO at (e) 520 nm (excitation at 409 nm) and (f) 660 nm (excitation at 633 nm). Source: Sardar et al. [91]. Licensed under CC BY 4.0.

spectrum of the PDPB-ZnO light harvesting nanohybrids (LHNH) is independent on the excitation wavelength from 350 to 470 nm and originated from the oligomeric units of the polymer, as shown in Figure 5.18d. However, the emission spectrum of LHNH illustrates peak at 665 nm upon excitation at 600 nm, which can be attributed to polymer chains. The emission property of PDPB-ZnO LHNH can be attributed to the instant transfer of excited electron form the polymer nanostructures to the ZnO NPs and eventually deexcite through defect centers located at the near surface that arise from oxygen vacancies [92]. The picosecond resolved fluorescence decay of PDPB-ZnO LHNH (excitation with 409 nm laser, and monitored at a wavelength of 520 nm) shows significant shorter lifetime of 30 ps (74%) as compared with that of PDPB; 140 ps (45%), which can be correlated to the electron transfer process from PDPB oligomers to the ZnO NPs as shown in Figure 5.18e. The charge separation from polymeric chain of PDPB to ZnO NPs is also monitored from time resolved spectroscopy, as shown in Figure 5.18f. In summary, this study unravels the interfacial carrier dynamics, which is the key for efficient light harvesting by detailed steady state and ultrafast spectroscopic studies, suggesting the co-sensitization of ZnO NPs by multiple states of polymer nanofibers originated from oligomeric and polymer chain unit.

Femtosecond spectroscopy including pump–probe spectroscopy and fluorescence up conversion spectroscopy is very useful tools in understanding the behavior of excitons in terms of their migration and dissociation to form charge carriers [93]. In femtosecond pump–probe spectroscopy, the pump pulse excites the system under investigation, and the effect of the pump-induced excitation is detected by probe pulse. The change in optical density (ΔOD) is measured as a function of time by modulating the pump pulse and optically delaying the probe pulse relative to the pump pulse. Kandada et al. [94] have investigated the correlation between molecular scale morphology and charge generation across hybrid photovoltaic interfaces formed by metal oxides (ZnO and TiO_2) and a prototypical electron donor polymer, P3HT. The study has demonstrated that the local disorder of the polymer chains on the surface of the metal–oxide film provides better electron injection efficiencies than the crystalline phases, though the latter are essential for energy and charge transport. In recent times, more elaborate experimental configurations utilizing three optical pulses, such as pump–push–probe [95, 96] and pump–dump–probe [97, 98], have been employed, which revealed new insight into femtosecond torsional relaxation and detrapping of bound charge pairs of conjugated polymers. Grancini et al. [99] have investigated the dynamics of long-lived photo excited species in poly[2,6-(4,4-bis-(2-ethylhexyl)-4H-cyclopenta[2,1-b;3,4-b′]dithiophene)-alt-4,7-(2,1,3-benzothiadiazole)] (PCPDTBT):PCBM blend using quasi steady state photo-induced absorption optical spectroscopy, time-resolved electron spin resonance spectroscopy, and theoretical modeling. It has demonstrated that the polymer triplet state (T), populated through the interfacial CT state recombination, coexists with charge carriers and has no role in the degradation process caused by air exposure. Instead, the long-lived emissive interfacial CT state is responsible for the blend degradation in air by mediating direct electron transfer to contaminants, leading to the formation of reactive and harmful species, such as the superoxide. This study demonstrates that robust photovoltaic blends require an educated design of the interface energetics not only for charge separation but also for stability. Bargigia et al. [100] have investigated the excited-state dynamics of P3HT NPs in different media relevant to biology using absorption and transient absorption (TA) spectra taken under different pH conditions and showed that the charge-transfer states generated by the polarization of loosely bound polymer chains can act as precursor states for long-living polarons.

5.5.2 Fourier Transform Infrared Spectroscopy

Fourier transform-infrared spectroscopy (FTIR) is a reliable and cost-effective analytical tool for identification and assessment of the quality of polymers. FTIR combined with other techniques provides significant complementary data regarding molecular structure of the polymers. Hu et al. [60] have investigated the thermoelectric performance of conducting polymer nanostructures. As shown in Figure 5.19, the three bands at 1518, 1350, and 1205 cm^{-1} of the bulk PEDOT, which can be ascribed to the $C_\alpha = C_\beta$ asymmetric stretching mode of the thiophene ring, C—C and C=C stretching vibrations of the quinoidal structure of thiophene ring and the doping agents, respectively. The band shift to low wavenumbers is observed in the sequence of bulk PEDOT > globular nanoparticle > nanorod or ellipsoidal nanoparticle > nanotube > nanofibers. Additionally, the increased interchain and intrachain interactions due to the increase in doping, revealed by the band shift of 1205 cm^{-1}, which can be attributed to the conformation transition from the coiled benzoid to extended linear quinoid structure.

The bands at 1185 and 890 cm^{-1} attributed to the =C—H in-plane and out-of-plane deformation vibrations of pure 3, 4-ethylene dioxythiophene (EDOT) are not observed in the spectrum of PEDOT nanospindles synthesized in mesophases reported by Ghosh et al. [101] indicating that all EDOT monomer molecules have disappeared and successful polymerization. Ghosh et al. [102] interpreted the FTIR spectrum of PPy having the characteristic bands attributable to the C–C asymmetric stretching vibration at 1461 cm^{-1}, the stretching vibrations of C–N and C–C in the pyrrole ring observed at 1302 and 1547 cm^{-1}, respectively, which confirms effective polymerization. Moreover, the peak at 1674 cm^{-1} associated with carbonyl C=O group, which may originated due to chemical polymerization and over oxidation of PPy.

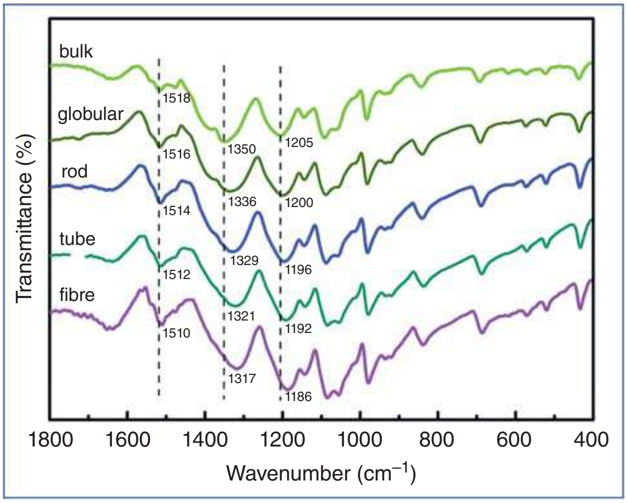

Figure 5.19 FTIR spectra of bulk PEDOT and different PEDOT nanostructures. Source: Hu et al. [60]. © 2015, Royal Society of Chemistry.

5.5.3 Nuclear Magnetic Resonance Spectroscopy

Nuclear magnetic resonance spectroscopy (NMR) is a very useful tool in detail structural characterization of polymers. Due to the wide range of structural and dynamic features of synthetic as well as natural polymers, different NMR methods have been reported in the literature. Wu et al. [103] have reported a complete mechanistic study on the nucleation of polymeric nanoparticles covering the generation of the clusters and the forthcoming aggregation to the nuclei by *in situ* ^{1}H NMR experiments using PANI as an example. This work utilizes the solvent in solvation shell as the sensitive probe to explore the transient process in nucleation, demonstrating its efficiency in achieving information such as the stepwise procedures, the nuclei sizes, and the growth kinetics. Figure 5.20a showed the *in situ* monitored 1H NMR spectra for 0.086 M aniline in 0.10 M sodium dodecyl sulfate (SDS). A continuous downfield shift is observed for water (HOD) peak, which can be attributed to the acceptance of the protons released during the formation of aniline oligomers. The result demonstrated that tetramers are the actual nucleation agents in this process and the co-operation of the tetramer deprotonation and the fusion of the protective SDS micelles facilitates the steady nucleation. The signal evolution from HOD unravels a wealth of information on the tetramer aggregation, which is the key step in the nucleation. The spectra for the polymerization of 0.086 M aniline in 0.005 M SDS is shown in Figure 5.20b. The initial pronounced spectral changes of the reaction environment occur in the SDS part rather than in the HOD. Figure 5.20c showed the nucleation mechanism of PANI in SDS spherical micelles. The study indicates that the assembly profile of the templates can be modified in the reaction, and the morphology of the polymer is determined by the template structure in the nucleation.

Gu et al. [104] used diffusion-ordered NMR spectroscopy (DOSY) as a complementary method for characterizing the size and size distribution of conjugated polymers P3HT-equivalent molecular weight (MWs) and MW distributions. Parenti et al. [105] employed both ^{1}H NMR and routine 2D NMR spectra in order to investigate the aggregation behavior of polythiophene conjugated polymers and also proposed to use solid-state NMR for poorly solvatochromic conjugated polymers which are prone to form π-stacked aggregates.

5.6 Other Techniques

There are many other techniques, which provide useful information in polymer characterization in addition to what we have discussed until now in this chapter. In this section, we will discuss few of them with a particular interesting example. Zhang et al. [106] have synthesized highly crystalline PANI nanotubes and nanofibers c. 80–170 nm in diameter by a “micelle soft-template” method in the presence of dicarboxylic acids dopants with different numbers (n) of $-CH_2-$ groups ($n = 0$–4). Here, XRD analysis has been employed to investigate the effect of dopant structure on the crystallinity of the PANI nanostructures. As shown in Figure 5.21a, the characteristic peaks centered at $2\theta = 18°$ and $25°$ are observed in all PANI nanostructures and

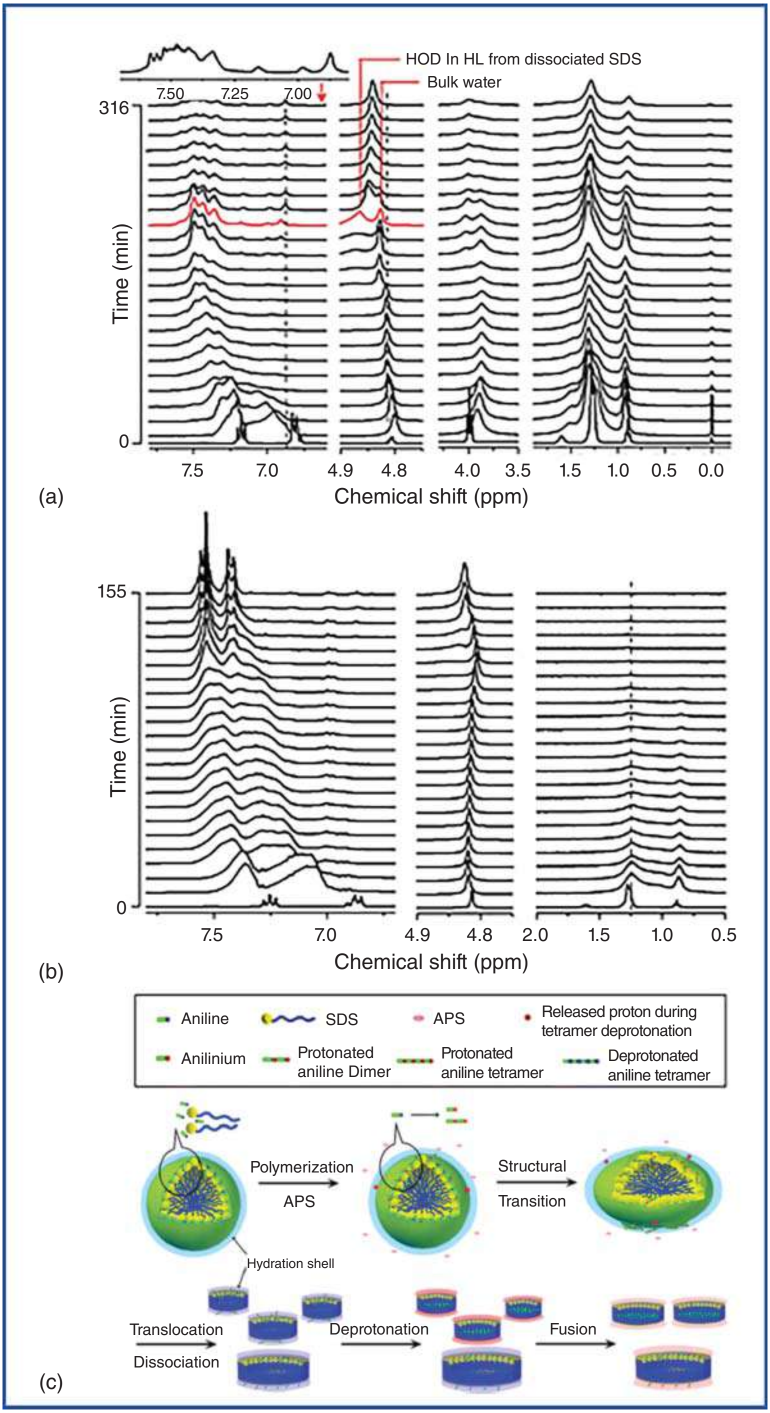

Figure 5.20 (a) ^{1}H NMR spectra performed *in situ* monitoring the temporal changes in the nucleation of polyaniline in 0.10 M SDS at 298.3 K. (b) ^{1}H NMR spectra of the polymerization of 0.086 M aniline in 0.005 M of SDS as a function of time. (c) Schematic representation of the nucleation of polyaniline in SDS micelles. Source: Wu et al. [103]. © 2013, American Chemical Society.

can be attributed to the periodicity perpendicular and parallel to the polymer chain, respectively. The interchain distance perpendicular to the polymer-chain direction is increased by 0.04 nm when the dopant was changed from oxalic acid ($n = 0$) to adipic acid ($n = 4$), while the interchain distance parallel to the polymer chain direction remained constant, as shown in Figure 5.21b. This study demonstrates that a big dopant leads to a large interchain distance.

Thermogravimetric analysis (TGA) is another interesting tool to measure weight changes in polymers as a function of temperature and time, which can be caused by decomposition and oxidation reactions as well as physical processes such as sublimation, vaporization, and desorption. As shown in Figure 5.22, the loading of polymer

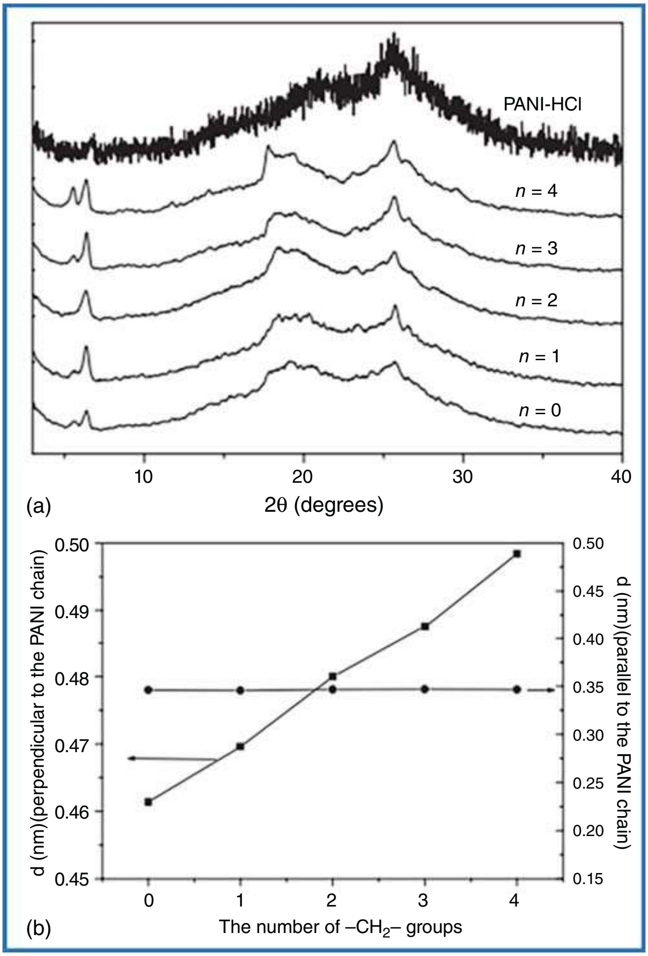

Figure 5.21 (a) XRD patterns of PANI nanostructures doped with different dicarboxylic acids having different numbers (n) of $-CH_2-$ groups ($n = 0-4$). (b) The effect of the number of $-CH_2-$ groups in the dopant on the interchain distances perpendicular and parallel to the PANI chain direction in the resulting PANI nanostructures. Source: Zhang et al. [106]. © 2006, John Wiley and Sons.

as well as the thermal stability of the PDPB-ZnO can be evaluated by TGA. The TGA graph of PDPB nanofibers showed onset of decomposition at about 185 °C until a major decomposition happens around 250 °C, which can be attributed to large-scale thermal degradation of polymeric chains. In contrast to polymer, pure ZnO NPs are very stable in the range of 30–600 °C. The thermal decomposition of PDPB nanofibers in PDPB-ZnO LHNH occurs at about 175 °C, which is slightly lower than that of pure PDPB (185 °C) may be associated with the interaction of interchains in PDPB macromolecule with ZnO NPs. The PDPB-ZnO LHNH exhibits a PDPB mass of as low as 4% determined from TGA curves (inset). The loading of metal nanoparticle on polymer surface can be determined by thermal gravimetric analysis. Notably, the thermal stability of the nanohybrids has been improved in comparison to bare polymer structure. The metal loading on PPy nanofibers can be also determined by TGA using high residual mass of PPy (~15–51%), which is consistent with calculated by inductively coupled plasma atomic-emission spectroscopic data [75].

Analysis of the vertical structure of polymer films is usually performed by using either environmental scanning electron microscopy (ESEM) on a cleaved sample or XPS, but they both lack spatial resolution in the horizontal direction. Nanotomography provides high spatial resolution in all three directions. However, this technique cannot give an indication on the chemical composition, unless a specific topography feature can be associated with a specific chemical structure. Linde et al. [107] have reported on a new approach for measuring the chemical composition of the 20 nm at the top or bottom of a polymer film based on a variation of the surface enhanced Raman scattering effect with laser illumination through a thin gold layer (~4 nm). Figure 5.23a,b shows three Raman spectra taken on bare quartz (dotted line), on overnight annealed (in a vacuum oven at 120 °C) polymer film on 4 nm gold layer (dashed line), and on as evaporated 4 nm gold layer (solid line) for poly[(9,9-dioctylfluorenyl-2,7-diyl)-alt-co-(1,4-benzo{2,1′,3}thiadiazole)] (F8BT) and poly[(9,9-dioctylfluorenyl-2,7-diyl)-co-(*N*,*N*′-diphenyl)-*N*,*N*′-di(*p*-butylphenyl)-1,4-diaminobenzene)] (PFB) films, respectively. The Raman spectra or both homopolymers taken over the gold (with and without annealing) are enhanced in respect to the one taken on the bare quartz. The authors have also observed that the dominant contribution to the Raman peak around 1609 cm^{-1}

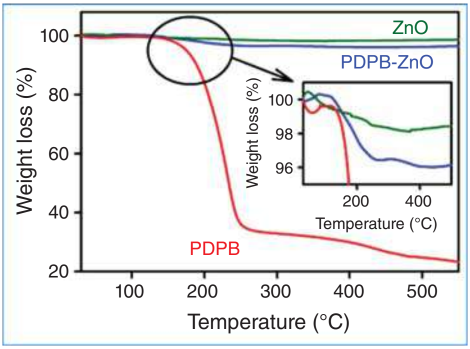

Figure 5.22 Thermogravimetric analysis profile of ZnO, PDPB-ZnO, and PDPB. Source: Sardar et al. [91]. Licensed under CC BY 4.0.

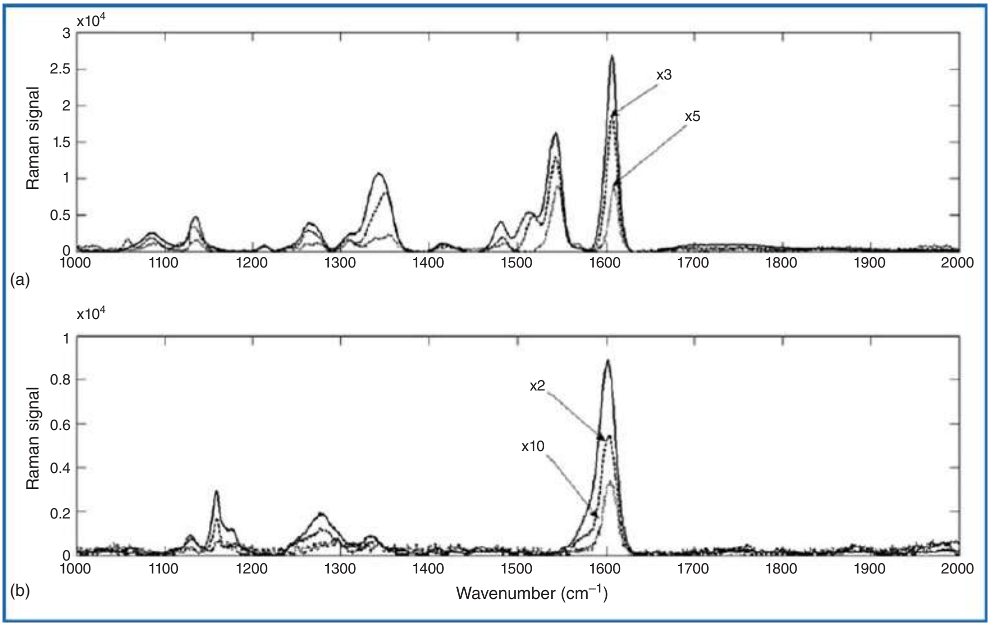

Figure 5.23 Raman spectra of F8BT (a) and PFB (b) under 660 nm laser. The dotted line is taken on the bare quartz, the dashed line is taken on 4 nm of gold annealed overnight, and the solid line is taken on 4 nm gold without annealing. Source: Linde et al. [107]. © 2012, American Chemical Society.

arises due to the surface-enhanced Raman scattering (SERS) enhancement of the PFB signal even when the thickness of the PFB layer was only 25 nm.

5.7 Conclusion

In this chapter, we described the characterization of CPNs, particularly illustrates the general characterization techniques to understand the morphology, optical, and electrochemical properties through various advanced characterization tools. Several state-of-the-art techniques have been highlighted such as TEM, cryo-TEM, STM, SEM, and AFM in order to understand the relationship between the polymer nanostructures and their properties, which eventually helps in improving device efficiency. SKPM and XPS were discussed to characterize the polymer surface modification. Recently, conducting polymers have found tremendous attention in the field of energy storage and catalysis, which necessitates the detail electrochemical characterization of the materials. The optical characterization using UV–Vis absorption, fluorescence (steady state and time resolved), and femtosecond spectroscopy were also discussed in detail by taking several examples. This chapter provides an overall view of different characterization techniques to get a deep insight into the mechanism of formation of polymer nanostructures and their fundamental properties for efficient device applications.

References

1. Li, C., Bai, H., and Shi, G. (2009). Conducting polymer nanomaterials: electrosynthesis and applications. *Chem. Soc. Rev.* 38: 2397–2409.
2. MacDiarmid, A.G. (2001). “Synthetic Metals”: a novel role for organic polymers (nobel lecture). *Angew. Chem. Int. Ed. Engl.* 40: 2581–2590.
3. Heeger, A.J. (2010). Semiconducting polymers: the third generation. *Chem. Soc. Rev.* 39: 2354–2371.
4. Heeger, A.J. (2001). Semiconducting and metallic polymers: the fourth generation of polymeric materials. *J. Phys. Chem. B* 105: 8475–8491.
5. Lu, X., Zhang, W., Wang, C. et al. (2011). One-dimensional conducting polymer nanocomposites: synthesis, properties and applications. *Prog. Polym. Sci.* 36: 671–712.
6. Long, Y.-Z., Li, M.-M., Gu, C. et al. (2011). Recent advances in synthesis, physical properties and applications of conducting polymer nanotubes and nanofibers. *Prog. Polym. Sci.* 36: 1415–1442.
7. Aleshin, A.N. (2006). Polymer nanofibers and nanotubes: charge transport and device applications. *Adv. Mater.* 18: 17–27.
8. Jang, J. (2006). Conducting polymer nanomaterials and their applications. In: *Emissive Materials Nanomaterials* (eds. A. Abe, K. Dušek and S. Kobayashi), 189–260. Berlin, Heidelberg: Springer Berlin Heidelberg.

9 Ghosh, S., Kouamé, N.A., Ramos, L. et al. (2015). Conducting polymer nanostructures for photocatalysis under visible light. *Nat. Mater.* 14: 505.

10 Shi, Y., Peng, L., Ding, Y. et al. (2015). Nanostructured conductive polymers for advanced energy storage. *Chem. Soc. Rev.* 44: 6684–6696.

11 Pecher, J. and Mecking, S. (2010). Nanoparticles of conjugated polymers. *Chem. Rev.* 110: 6260–6279.

12 Kim, F.S., Ren, G., and Jenekhe, S.A. (2011). One-dimensional nanostructures of π-conjugated molecular systems: assembly, properties, and applications from photovoltaics, sensors, and nanophotonics to nanoelectronics. *Chem. Mater.* 23: 682–732.

13 Shirakawa, H. (2001). The discovery of polyacetylene film: the dawning of an era of conducting polymers (nobel lecture). *Angew. Chem. Int. Ed.* 40: 2574–2580.

14 Coakley, K.M. and McGehee, M.D. (2004). Conjugated polymer photovoltaic cells. *Chem. Mater.* 16: 4533–4542.

15 Günes, S., Neugebauer, H., and Sariciftci, N.S. (2007). Conjugated polymer-based organic solar cells. *Chem. Rev.* 107: 1324–1338.

16 Chen, J.-T. and Hsu, C.-S. (2011). Conjugated polymer nanostructures for organic solar cell applications. *Polym. Chem.* 2: 2707–2722.

17 Xia, D., Li, C., and Li, W. (2019). Crystalline conjugated polymers for organic solar cells: from donor, acceptor to single-component. *Chem. Rec.* 19: 962–972.

18 Allard, S., Forster, M., Souharce, B. et al. (2008). Organic semiconductors for solution-processable field-effect transistors (OFETs). *Angew. Chem. Int. Ed.* 47: 4070–4098.

19 Coropceanu, V., Cornil, J., da Silva Filho, D.A. et al. (2007). Charge transport in organic semiconductors. *Chem. Rev.* 107: 926–952.

20 Kim, N.-K., Jang, S.-Y., Pace, G. et al. (2015). High-performance organic field-effect transistors with directionally aligned conjugated polymer film deposited from pre-aggregated solution. *Chem. Mater.* 27: 8345–8353.

21 Yang, J., Zhao, Z., Wang, S. et al. (2018). Insight into high-performance conjugated polymers for organic field-effect transistors. *Chem* 4: 2748–2785.

22 Li, M., Mangalore, D.K., Zhao, J. et al. (2018). Integrated circuits based on conjugated polymer monolayer. *Nat. Commun.* 9: 451.

23 Choi, S., Jeong, J.W., Jo, G. et al. (2019). Conjugated polymer/paraffin blends for organic field-effect transistors with high environmental stability. *Nanoscale* 11: 10004–10016.

24 Friend, R.H., Gymer, R.W., Holmes, A.B. et al. (1999). Electroluminescence in conjugated polymers. *Nature* 397: 121–128.

25 Grimsdale, A.C., Leok Chan, K., Martin, R.E. et al. (2009). Synthesis of light-emitting conjugated polymers for applications in electroluminescent devices. *Chem. Rev.* 109: 897–1091.

26 Reineke, S., Lindner, F., Schwartz, G. et al. (2009). White organic light-emitting diodes with fluorescent tube efficiency. *Nature* 459: 234.

27 Yang, Y., Wang, S., Zhu, Y. et al. (2018). Thermally activated delayed fluorescence conjugated polymers with backbone-donor/pendant-acceptor architecture for nondoped OLEDs with high external quantum efficiency and low roll-off. *Adv. Funct. Mater.* 28: 1706916.

28 Osaka, I. and McCullough, R.D. (2008). Advances in molecular design and synthesis of regioregular polythiophenes. *Acc. Chem. Res.* 41: 1202–1214.

29 Anthony, J.E. (2008). The larger acenes: versatile organic semiconductors. *Angew. Chem. Int. Ed.* 47: 452–483.

30 Tuncel, D. (2019). π-Conjugated nanostructured materials: preparation, properties and photonic applications. *Nanoscale Adv.* 1: 19–33.

31 Ghosh, S., Maiyalagan, T., and Basu, R.N. (2016). Nanostructured conducting polymers for energy applications: towards a sustainable platform. *Nanoscale* 8: 6921–6947.

32 Fu, H.-B. and Yao, J.-N. (2001). Size effects on the optical properties of organic nanoparticles. *J. Am. Chem. Soc.* 123: 1434–1439.

33 Xiao, D., Xi, L., Yang, W. et al. (2003). Size-tunable emission from 1,3-diphenyl-5-(2-anthryl)-2-pyrazoline nanoparticles. *J. Am. Chem. Soc.* 125: 6740–6745.

34 Xiao, D., Yang, W., Yao, J. et al. (2004). Size-dependent exciton chirality in (*R*)-(+)-1,1′-bi-2-naphthol dimethyl ether nanoparticles. *J. Am. Chem. Soc.* 126: 15439–15444.

35 Hu, D., Yu, J., Padmanaban, G. et al. (2002). Spatial confinement of exciton transfer and the role of conformational order in organic nanoparticles. *Nano Lett.* 2: 1121–1124.

36 Wang, F., Han, M.-Y., Mya, K.Y. et al. (2005). Aggregation-driven growth of size-tunable organic nanoparticles using electronically altered conjugated polymers. *J. Am. Chem. Soc.* 127: 10350–10355.

37 Martin, C.R. (1995). Template synthesis of electronically conductive polymer nanostructures. *Acc. Chem. Res.* 28: 61–68.

38 Cho, S.I. and Lee, S.B. (2008). Fast electrochemistry of conductive polymer nanotubes: synthesis, mechanism, and application. *Acc. Chem. Res.* 41: 699–707.

39 Jang, J., Li, X.L., and Oh, J.H. (2004). Facile fabrication of polymer and carbon nanocapsules using polypyrrole core/shell nanomaterials. *Chem. Commun.* (7): 794–795.

40 Jang, J. and Yoon, H. (2003). Facile fabrication of polypyrrole nanotubes using reverse microemulsion polymerization. *Chem. Commun.* (6): 720–721.

41 Lee, J.I., Cho, S.H., Park, S.-M. et al. (2008). Highly aligned ultrahigh density arrays of conducting polymer nanorods using block copolymer templates. *Nano Lett.* 8: 2315–2320.

42 Ma, Y., Jiang, S., Jian, G. et al. (2009). CNx nanofibers converted from polypyrrole nanowires as platinum support for methanol oxidation. *Energy Environ. Sci.* 2: 224–229.

43 Liu, J., Wei, B., Sloppy, J.D. et al. (2015). Direct imaging of the electrochemical deposition of poly(3,4-ethylenedioxythiophene) by transmission electron microscopy. *ACS Macro Lett.* 4: 897–900.

44 Kim, Y.-J., Jung, H.-T., Ahn, C.W., and Jeon, H.-J. (2017). Simultaneously induced self-assembly of poly(3-hexylthiophene) (P3HT) nanowires and thin-film fabrication via solution-floating method on a water substrate. *Adv. Mater. Interfaces* 4: 1700342.

45 Cui, Z., Coletta, C., Dazzi, A. et al. (2014). Radiolytic method as a novel approach for the synthesis of nanostructured conducting polypyrrole. *Langmuir* 30: 14086–14094.

46 Talarico, A.M., Szerb, E.I., Mastropietro, T.F. et al. (2012). Tuning solid state luminescent properties in a hydrogen bonding-directed supramolecular assembly of bis-cyclometalated iridium(iii) ethylenediamine complexes. *Dalton Trans.* 41: 4919–4926.

47 Zang, J., Bao, S.-J., Li, C.M. et al. (2008). Well-aligned cone-shaped nanostructure of polypyrrole/RuO_2 and its electrochemical supercapacitor. *J. Phys. Chem. C* 112: 14843–14847.

48 Bahry, T., Cui, Z., Deniset-Besseau, A. et al. (2018). An alternative radiolytic route for synthesizing conducting polymers in an organic solvent. *New J. Chem.* 42: 8704–8716.

49 Lattach, Y., Coletta, C., Ghosh, S., and Remita, S. (2014). Radiation-induced synthesis of nanostructured conjugated polymers in aqueous solution: fundamental effect of oxidizing species. *ChemPhysChem* 15: 208–218.

50 Wirix, M.J.M., Bomans, P.H.H., Friedrich, H. et al. (2014). Three-dimensional structure of P3HT assemblies in organic solvents revealed by cryo-TEM. *Nano Lett.* 14: 2033–2038.

51 McKenzie, B.E., Friedrich, H., Wirix, M.J.M. et al. (2015). Controlling internal pore sizes in bicontinuous polymeric nanospheres. *Angew. Chem. Int. Ed.* 54: 2457–2461.

52 Nellist, P.D. and Pennycook, S.J. (1999). Incoherent imaging using dynamically scattered coherent electrons. *Ultramicroscopy* 78: 111–124.

53 Loos, J., Sourty, E., Lu, K. et al. (2009). Imaging polymer systems with high-angle annular dark field scanning transmission electron microscopy (HAADF–STEM). *Macromolecules* 42: 2581–2586.

54 Panova, O., Chen, X.C., Bustillo, K.C. et al. (2016). Orientation mapping of semicrystalline polymers using scanning electron nanobeam diffraction. *Micron* 88: 30–36.

55 Scifo, L., Dubois, M., Brun, M., and euml; Rannou, P.; Latil, S.; Rubio, A.; Grévin, B. (2006). Probing the electronic properties of self-organized poly(3-dodecylthiophene) monolayers by two-dimensional scanning tunneling spectroscopy imaging at the single chain scale. *Nano Lett.* 6: 1711–1718.

56 Nakaya, M., Okawa, Y., Joachim, C. et al. (2014). Nanojunction between fullerene and one-dimensional conductive polymer on solid surfaces. *ACS Nano* 8: 12259–12264.

57 Kawai, S., Koch, M., Gnecco, E. et al. (2014). Quantifying the atomic-level mechanics of single long physisorbed molecular chains. *Proc. Natl. Acad. Sci. U.S.A.* 111: 3968–3972.

58 Lafferentz, L., Ample, F., Yu, H. et al. (2009). Conductance of a single conjugated polymer as a continuous function of its length. *Science* 323: 1193–1197.

59 Jethwa, S.J., Madsen, M., Knudsen, J.B. et al. (2017). Revealing the structural detail of individual polymers using a combination of electrospray deposition and UHV-STM. *Chem. Commun.* 53: 1168–1171.

60 Hu, X., Chen, G., Wang, X., and Wang, H. (2015). Tuning thermoelectric performance by nanostructure evolution of a conducting polymer. *J. Mater. Chem. A* 3: 20896–20902.

61 Huang, J., Wang, K., and Wei, Z. (2010). Conducting polymer nanowire arrays with enhanced electrochemical performance. *J. Mater. Chem.* 20: 1117–1121.

62 Wang, K., Wu, H., Meng, Y., and Wei, Z. (2014). Conducting polymer nanowire arrays for high performance supercapacitors. *Small* 10: 14–31.

63 Wang, D. and Russell, T.P. (2018). Advances in atomic force microscopy for probing polymer structure and properties. *Macromolecules* 51: 3–24.

64 Taranekar, P., Fan, X., and Advincula, R. (2002). Distinct surface morphologies of electropolymerized polymethylsiloxane network polypyrrole and comonomer films. *Langmuir* 18: 7943–7952.

65 Mazzio, K.A., Rice, A.H., Durban, M.M., and Luscombe, C.K. (2015). Effect of regioregularity on charge transport and structural and excitonic coherence in poly(3-hexylthiophene) nanowires. *J. Phys. Chem. C* 119: 14911–14918.

66 Massonnet, N., Carella, A., de Geyer, A. et al. (2015). Metallic behaviour of acid doped highly conductive polymers. *Chem. Sci.* 6: 412–417.

67 Ghosh, S., Ramos, L., Remita, S. et al. (2015). Conducting polymer nanofibers with controlled diameters synthesized in hexagonal mesophases. *New J. Chem.* 39: 8311–8320.

68 Kobayashi, H., Hirata, S., and Vacha, M. (2013). Mechanical manipulation of photophysical properties of single conjugated polymer nanoparticles. *J. Phys. Chem. Lett.* 4: 2591–2596.

69 Liscio, A., Palermo, V., and Samorì, P. (2010). Nanoscale quantitative measurement of the potential of charged nanostructures by electrostatic and Kelvin probe force microscopy: unraveling electronic processes in complex materials. *Acc. Chem. Res.* 43: 541–550.

70 Hallam, T., Lee, M., Zhao, N. et al. (2009). Local charge trapping in conjugated polymers resolved by scanning Kelvin probe microscopy. *Phys. Rev. Lett.* 103: 256803.

71 DeLongchamp, D.M., Kline, R.J., Jung, Y. et al. (2009). Controlling the orientation of terraced nanoscale “Ribbons” of a poly(thiophene) semiconductor. *ACS Nano* 3: 780–787.

72 Gu, K.L., Zhou, Y., Morrison, W.A. et al. (2018). Nanoscale domain imaging of all-polymer organic solar cells by photo-induced force microscopy. *ACS Nano* 12: 1473–1481.

73 Liscio, A., Palermo, V., and Samorı, P. (2008). Probing local surface potential of quasi-one-dimensional systems: a KPFM study of P3HT nanofibers. *Adv. Funct. Mater.* 18: 907–914.

74 Guselnikova, O.A., Postnikov, P.S., Fitl, P. et al. (2017). Tuning of PEDOT:PSS properties through covalent surface modification. *J. Polym. Sci., Part B: Polym. Phys.* 55: 378–387.

75 Ghosh, S., Bera, S., Bysakh, S., and Basu, R.N. (2017). Highly active multimetallic palladium nanoalloys embedded in conducting polymer as anode catalyst for electrooxidation of ethanol. *ACS Appl. Mater. Interfaces* 9: 33775–33790.

76 Ghosh, S., Mallik, A.K., and Basu, R.N. (2018). Enhanced photocatalytic activity and photoresponse of poly(3,4-ethylenedioxythiophene) nanofibers decorated with gold nanoparticle under visible light. *Sol. Energy* 159: 548–560.

77 Janáky, C. and Rajeshwar, K. (2015). The role of (photo)electrochemistry in the rational design of hybrid conducting polymer/semiconductor assemblies: from fundamental concepts to practical applications. *Prog. Polym. Sci.* 43: 96–135.

78 Yang, J., Liu, Y., Liu, S. et al. (2017). Conducting polymer composites: material synthesis and applications in electrochemical capacitive energy storage. *Mater. Chem. Front.* 1: 251–268.

79 Ghosh, S. and Basu, R.N. (2019). Polymer-based nanocomposites for direct alcohol fuel cells. In: *Nanomaterials for Alcohol Fuel Cells*, vol. 49 (eds. T. Inamuddin, A. Rangreez, F. Sen and A.M. Asiri), 271–292. Millersville: Materials Research Forum LLc.

80 Le, T.-H., Kim, Y., and Yoon, H. (2017). Electrical and electrochemical properties of conducting polymers. *Polymers* 9: 150.

81 Ghosh, S. and Basu, R.N. (2016). Electrochemistry of nanostructured materials: implementation in electrocatalysis for energy conversion applications. *J. Indian Inst. Sci.* 96: 293–313.

82 Ghosh, S., Ramos, L., and Remita, H. (2018). Swollen hexagonal liquid crystals as smart nanoreactors: implementation in materials chemistry for energy applications. *Nanoscale* 10: 5793–5819.

83 Park, H.-W., Kim, T., Huh, J. et al. (2012). Anisotropic growth control of polyaniline nanostructures and their morphology-dependent electrochemical characteristics. *ACS Nano* 6: 7624–7633.

84 Song, E. and Choi, J.-W. (2013). Conducting polyaniline nanowire and its applications in chemiresistive sensing. *Nanomaterials* 3: 498–523.

85 Laviron, E. (1979). General expression of the linear potential sweep voltammogram in the case of diffusionless electrochemical systems. *J. Electroanal. Chem.* 101: 19–28.

86 Yuan, X., Floresyona, D., Aubert, P.-H. et al. (2019). Photocatalytic degradation of organic pollutant with polypyrrole nanostructures under UV and visible light. *Appl. Catal., B* 242: 284–292.

87 Ghosh, S., Kouame, N.A., Remita, S. et al. (2015). Visible-light active conducting polymer nanostructures with superior photocatalytic activity. *Sci. Rep.* 5: 18002.

88 Ghosh, S., Remita, H., and Basu, R.N. (2018). Visible-light-induced reduction of Cr(VI) by PDPB-ZnO nanohybrids and its photo-electrochemical response. *Appl. Catal. B* 239: 362–372.

89 Lin, Y., Dong, C., Cao, F. et al. (2017). Size-dependent optical properties of conjugated polymer nanoparticles. *RSC Adv.* 7: 55957–55965.

90 Grey, J.K., Kim, D.Y., Norris, B.C. et al. (2006). Size-dependent spectroscopic properties of conjugated polymer nanoparticles. *J. Phys. Chem. B* 110: 25568–25572.

91 Sardar, S., Kar, P., Remita, H. et al. (2015). Enhanced charge separation and FRET at heterojunctions between semiconductor nanoparticles and conducting polymer nanofibers for efficient solar light harvesting. *Sci. Rep.* 5: 17313.

92 van Dijken, A., Meulenkamp, E.A., Vanmaekelbergh, D., and Meijerink, A. (2000). The kinetics of the radiative and nonradiative processes in nanocrystalline ZnO particles upon photoexcitation. *J. Phys. Chem. B* 104: 1715–1723.

93 Kee, T.W. (2014). Femtosecond pump–push–probe and pump–dump–probe spectroscopy of conjugated polymers: new insight and opportunities. *J. Phys. Chem. Lett.* 5: 3231–3240.

94 Kandada, A.R.S., Guarnera, S., Tassone, F. et al. (2014). Charge generation at polymer/metal oxide interface: from molecular scale dynamics to mesoscopic effects. *Adv. Funct. Mater.* 24: 3094–3099.

95 Bakulin, A.A., Rao, A., Pavelyev, V.G. et al. (2012). The role of driving energy and delocalized states for charge separation in organic semiconductors. *Science* 335: 1340.

96 Clark, J., Nelson, T., Tretiak, S. et al. (2012). Femtosecond torsional relaxation. *Nat. Phys.* 8: 225–231.

97 Busby, E., Carroll, E.C., Chinn, E.M. et al. (2011). Excited-state self-trapping and ground-state relaxation dynamics in poly(3-hexylthiophene) resolved with broadband pump–dump–probe spectroscopy. *J. Phys. Chem. Lett.* 2: 2764–2769.

98 Gaab, K.M. and Bardeen, C.J. (2004). Anomalous exciton diffusion in the conjugated polymer MEH−PPV measured using a three-pulse pump−dump−probe anisotropy experiment. *J. Phys. Chem. A* 108: 10801–10806.

99 Grancini, G., De Bastiani, M., Martino, N. et al. (2014). The critical role of interfacial dynamics in the stability of organic photovoltaic devices. *Phys. Chem. Chem. Phys.* 16: 8294–8300.

100 Bargigia, I., Zucchetti, E., Kandada, A.R.S. et al. (2019). The photophysics of polythiophene nanoparticles for biological applications. *ChemBioChem* 20: 532–536.

101 Ghosh, S., Remita, H., Ramos, L. et al. (2014). PEDOT nanostructures synthesized in hexagonal mesophases. *New J. Chem.* 38: 1106–1115.

102 Ghosh, S., Bhandary, N., Basu, S., and Basu, R.N. (2017). Synergistic effects of polypyrrole nanofibers and Pd nanoparticles for improved electrocatalytic performance of Pd/PPy nanocomposites for ethanol oxidation. *Electrocatalysis* 8: 329–339.

103 Wu, X., Liu, K., Lu, L. et al. (2013). In situ monitoring of the nucleation of polyaniline nanoparticles from sodium dodecyl sulfate Micelles: a nuclear magnetic resonance study. *J. Phys. Chem. C* 117: 9477–9484.

104 Gu, K., Onorato, J., Xiao, S.S. et al. (2018). Determination of the molecular weight of conjugated polymers with diffusion-ordered NMR spectroscopy. *Chem. Mater.* 30: 570–576.

105 Parenti, F., Tassinari, F., Libertini, E. et al. (2017). Π-Stacking signature in NMR solution spectra of thiophene-based conjugated polymers. *ACS Omega* 2: 5775–5784.

106 Zhang, Z., Wan, M., and Wei, Y. (2006). Highly crystalline polyaniline nanostructures doped with dicarboxylic acids. *Adv. Funct. Mater.* 16: 1100–1104.

107 Linde, S., Carella, A., and Shikler, R. (2012). New approach for analyzing the vertical structure of polymer thin films based on surface-enhanced Raman scattering. *Macromolecules* 45: 1476–1482.

Part II

Conjugated Polymer Nanostructures for Solar Energy Conversion and Environmental Protection

6

Conjugated Polymer Nanostructures for Catalysts Support in Fuel Cells Application

Srabanti Ghosh and Rajendra N. Basu

CSIR-Central Glass & Ceramic Research Institute, Energy Materials and Devices Division, 196, Raja S.C. Mullick Road, Kolkata, 700032, India

6.1 Introduction

Fuel cells have attracted great attention in order to achieve a future sustainable energy system which operating with hydrogen or hydrogen-rich fuels having low CO_2 emissions and potential application in the portable electronics and automobile industries [1, 2]. In this context, the electrochemical oxidation of small organic molecules such as ethanol, methanol, formic acid, glucose, etc. has been studied extensively in low-temperature fuel cells [3–6]. Compared with proton exchange membrane fuel cells (PEMFCs), the direct alcohol fuel cells (DAFCs) are most well studied system due to ease of using liquid fuels with higher energy density, portability, and simplicity [7, 8]. The primary components of a fuel cell are an ion conducting electrolyte, a cathode, and an anode, as shown in Figure 6.1.

For example, a fuel such as hydrogen is brought into the anode compartment and an oxidant, typically oxygen, into the cathode compartment. There is an overall chemical driving force for the oxygen and the hydrogen to react to produce water. Direct ethanol or methanol fuel cells (DEFCs or DMFCs) directly convert the chemical energy stored in liquid ethanol or methanol into electricity and electro oxidation of liquid fuel such as ethanol or methanol at anode is primarily driven by catalysts. The oxidation of methanol generates formic acid (HCOOH), formaldehyde (HCHO), formate ($HCOO^-$), and CO, along with the final oxidation product, carbon dioxide (CO_2). The complete oxidation of methanol (CH_3OH) in alkaline or acid media is a six electron oxidation process forming CO_2 (Eqs. (6.1) and (6.2)):

$$CH_3OH + 6\,OH^- \rightarrow CO_2 + 5\,H_2O + 6\,e^- \tag{6.1}$$

$$CH_3OH + H_2O \rightarrow CO_2 + 6H^+ + 6e^- \tag{6.2}$$

Ethanol oxidation reaction (EOR) generates various one carbon intermediates such as CO and carbohydrate (CH_x), as well as acetaldehyde (CH_3CHO) and acetic acid (CH_3COOH) via direct or indirect oxidation. In alkaline condition, oxidation of

Conjugated Polymer Nanostructures for Energy Conversion and Storage Applications,
First Edition. Edited by Srabanti Ghosh.

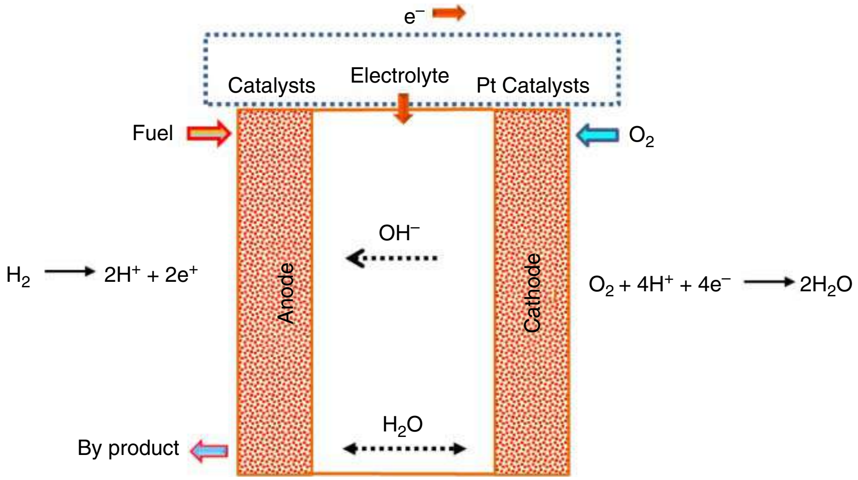

Figure 6.1 Schematic of a conventional fuel cell employing a proton conducting electrolyte. Electro-oxidation of H_2 occurs at the anode, creating protons that migrate across the electrolyte and participate in the electro-reduction of O_2 at the cathode.

ethanol (CH_3CH_2OH) generates 12 e^- (Eqs. (6.3) and (6.4)):

$$CH_3CH_2OH + 12\,OH^- \rightarrow 2\,CO_2 + 9\,H_2O + 12\,e^- \text{ (at anode)} \tag{6.3}$$

$$3\,O_2 + 6\,H_2O + 12\,e^- \rightarrow 12\,OH^- \text{ (at cathode)} \tag{6.4}$$

Although, Pt-based catalysts have been investigated extensively as efficient electrocatalysts for alcohol fuel cells; however, Pd is more abundant and less expensive and could promote alcohol oxidation more efficiently in alkaline media with high catalytic activity and anti-CO-poisoning [9–11]. A lot of efforts have been made to prepare efficient catalysts for alcohol electrooxidation through alloying approach via decreasing Pt loadings [12, 13], use of oxide-modified [14–16], or conducting carbon-modified [17, 18]. Notably, the fabrication of high-efficiency catalysts for cathodic oxygen reduction reaction (ORR) is critical for large-scale applications of PEMFCs [19–21]. Moreover, desirable characteristics of fuel cell electrodes include not only high activity toward the electrochemical reaction, but also chemical stability under reducing (anode) or oxidizing (cathode) atmospheres, resistance to poisoning by impurities in the fuel, and structural stability over long periods of operation. Additionally, the catalysts supporting material must be electronically and ionically conducting and electrochemically active and have high surface areas. Carbon materials, especially Vulcan XC-72 carbon black, are widely used catalyst support in fuel cells but low resistance to corrosion at high potentials, micropores leading to limited accessible surface, impermeability to gases and liquids, and low proton conductivity limit the catalyst performance, which reduced fuel cell performance and durability [19, 20]. Recently, nanostructured conductive polymers (CPNs) have aroused considerable research interest owing to their unique properties over their bulk counterparts, such as large surface areas, high conductivity, and shortened pathways for charge/mass transport, which make them promising candidates for broad applications in energy conversion and storage, fuel cell, and super capacitor [22–25]. In this context, a series of conducting polymer (CP) such as polypyrrole (PPy), polyaniline (PANI), poly-3-methyl thiophene (PMT), poly(3,4-ethylenedioxythiophene) (PEDOT), poly(*o*-phenylenediamine) (POPD), etc. (as shown in Figure 6.2) have been tested as catalysts support for the electrocatalytic reactions [26–29]. Various approach have been followed to deposit the nanostructured electrocatalysts on conducting polymer surface via direct mixing or *in situ* synthesis [30–32]. In recent years, tremendous research effort has been also focused on modified polymer nanostructures to support electrocatalysts for various catalytic reaction because of their strong interaction, high stability, and rich electrochemical properties [33, 34]. Hence, conjugated polymers have been effectively integrated with carbon nanotubes and graphene nanosheets for fuel cell applications, which showed superior electrocatalytic performance owing to their synergistic effects of both components.

This chapter presents the representative applications of nanostructured conductive polymers as active electrode materials or catalysts support for electrocatalysis and fuel cell applications. In this chapter, simple pathways to tailor polymer nanostructures as well as modified polymer architectures for improving electrocatalytic performances for both anode and cathode electrocatalysts were summarized. These results provide fundamental insight into electrocatalysts support but also offer an important guideline for design of advanced electrode materials for fuel cell application.

6.2 Conducting Polymer Nanostructures for Electrocatalysts Support

Recently, conjugated polymer nanostructures emerging as a new class of redox active materials with π-conjugated skeletons, superior optoelectronic properties, high surface areas, and great flexibility in the molecular design of conjugated skeletons [23, 24]. Thus, the complementary utilization of these properties makes CPNs as promising supporting materials for the preparation of advanced electrocatalysts with the following advantages, such as the intrinsic robust conjugated structure confers good stability to the nanoparticles against aggregation through strong interaction between nanofibers with metal content and increase the dispersion of metal catalysts, which may facilitate the transportation of electroactive species and fast kinetics further lower the catalysts loading. The enhanced electrocatalytic activity may be associated with the facile charge transfer at conductive polymer interfaces and efficient diffusion paths for the electroactive species and high electronic conductivity. The CPNs can be fabricated from zero to three dimensions and tunable sizes from several to hundreds of nanometers using facile techniques and providing unlimited possibilities in the design of functionalized nanostructured carbon materials as support, which strongly influences the overall catalytic efficiency of metal catalysts. These are the unique feature for CPNs, as compared with other carbon

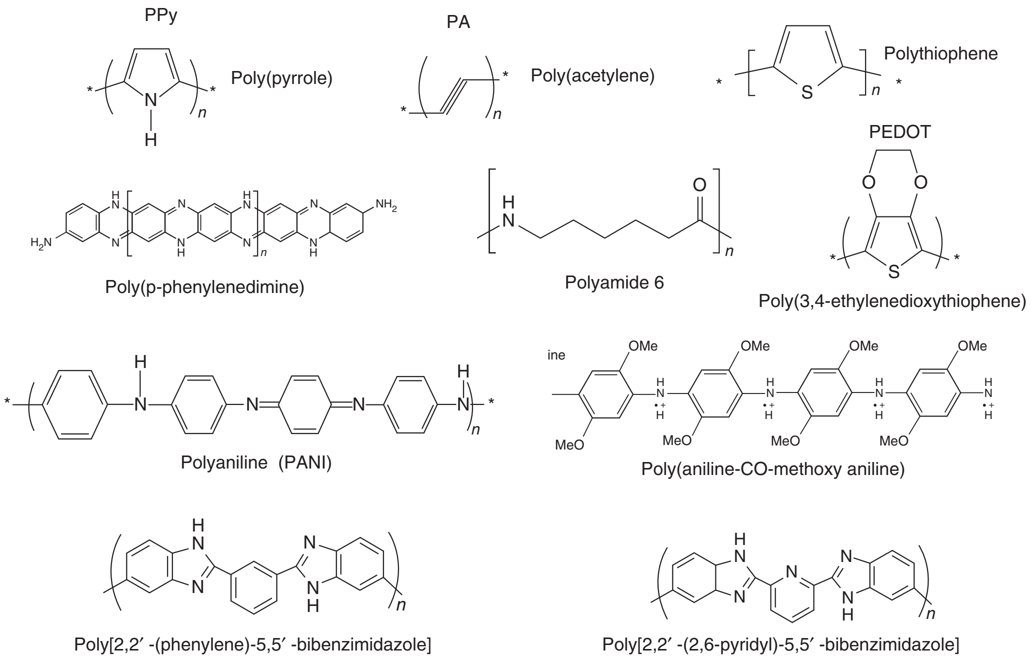

Figure 6.2 Chemical structures of commonly used conducting polymer as catalysts support.

support. Particular attention has been paid to control over polymer nanostructures and incorporation of metal catalysts within the framework [30]. The most commonly used method that includes *in situ* methods through polymerization in the presence of nanoparticles (NPs) or synthesis of polymer network with nanostructures and direct mixing via *ex situ* where the polymer is dissolved in an appropriate solvent, then catalyst is added to the polymer solution under vigorous stirring or polymer modified with other carbon or oxides materials then metal catalysts deposited [30, 35–37]. Each of these methodologies has its strengths and limitations.

6.2.1 Metal Catalysts Deposited on Conducting Polymer Nanostructures

Incorporation of noble metal nanoparticles with conducting polymer (CP) greatly expands the impact of electrochemical and catalytic applications with excellent high electrical conductivity, large surface area, short path lengths for the ions transport, and superior electrochemical activity of CP with varied functionalities of metallic nanoparticles at the molecular (nanoscale) level [36, 37]. A series of Pt NPs based electrocatalysts supported on a CP such as mono- and multilayers of platinum nanoparticles deposited PEDOT as nanostructures [26], platinum microparticles into PANI films [28], PPy containing catalysts [38], PANI nanotubules supported platinum catalyst NPs [39], and PANI hollow tubes loaded with tiny platinum NPs [40] have been employed for electrocatalytic oxidation of methanol and ethanol. For example, Salavagione et al. [41] reported the synthesis of Pt nanoparticles on polyaniline for methanol oxidation reaction (MOR). Similarly, Jiang and Lin [42] explored the use of 3D matrix of the novel nanocomposite on a glassy carbon electrode (GCE), which is consisted of nanorods of poly(*N*-acetylaniline) as electrocatalyst supports and embedded with platinum nanoclusters for the electrochemical oxidation of methanol under acidic medium. Kim et al. [43] developed a new approach using ice-template to the synthesis of two-dimensional polyaniline nanosheets deposited with high areal density Pt nanocrystals of 2.7 nm as shown in Figure 6.3a,b). The composite catalyst thus obtained has a large electrochemically active area of 94.57 m^2/g and showed good electrocatalytic performance for methanol oxidation, both in activity and stability, and excellent carbon monoxide tolerance, suggesting it has potential application in fuel cells (Figure 6.3c).

Notably, conducting polymer with one-dimensional (1D) nanostructures has been extensively tested as electrocatalyst supports. 1D nanostructures have (i) high surface area-to-volume ratio, (ii) high electronic conductivity, (iii) abundant surface defects, and (iv) unique quantum effects, which endow CPNs with a high percentage of active atoms exposed on their surface and an improved catalysts support. For example, Viswanathan and coworkers [44] electrodeposited platinum by the galvanostatic square wave method on PPy nanotubule electrode, which showed high catalytic activity for methanol oxidation. In addition, Pt incorporated on POPD nanotube through electrodeposition demonstrated 13 times higher catalytic activity than that of conventionally synthesized POPD electrode with

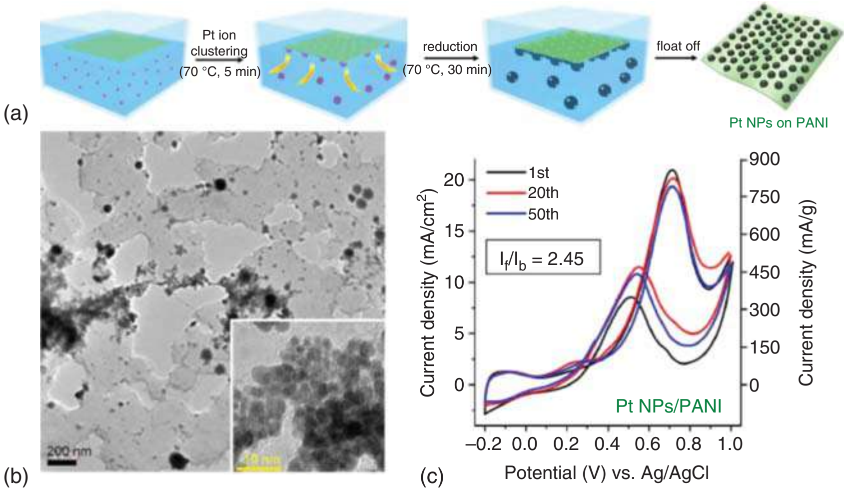

Figure 6.3 (a) Schematic illustration of the synthesis of Pt NPs supported on PANI nanosheets at the air–water interface. (b) TEM image of Pt NPs supported by a PANI nanosheet. (c) Typical CV profiles of Pt NPs supported by a PANI nanosheet in an aqueous solution containing 0.1 M $HClO_4$ and 1 M methanol at a scan rate of 50 mV/s. Source: Adapted with permission from [43]. Copyright 2017, American Chemical Society.

the same metal loading [45]. It has been proposed that the nanotubular morphology of POPD electrode may provide effective dispersion of Pt NPs, which facilitates the easier access of methanol to the catalytic sites, thus leading to an increased activity and a higher stability. Theses 1D polymer nanostructures have been obtained using rack-etch polycarbonate, polyester membranes, and anodic aluminum oxide membranes as solid templates; however, these approaches require multistep process and the removal of the template may causes deformation in polymer structure. Chen et al. [46] proposed a strategy of using template free PANI nanofibers (PANI NFs) diameter about 60 nm, which was synthesized by interfacial polymerization and uniform smaller Pt NPs of diameter around 1.8 nm was then deposited onto PANI NFs. The obtained electrocatalysts showed a higher electrochemical active surface area and higher methanol oxidation reaction catalytic activity than the Pt/C for DMFCs. Similarly, Wang and coworkers [47] developed PANI nanofiber-supported supra-high density Pt NPs or Pt/Pd hybrid NPs for constructing different electrochemical devices with high performance for methanol oxidation. Sun et al. [48] design of a new class of core–shell superstructure consisting of Pt nanocube assemblies (NCAMs) as the active core and polyaniline as the protective and conductive shell as a highly efficient MOR electrocatalyst. Moreover, another kind of carbon nitride (CN_x) nanofiber has been prepared by the calcination of polypyrrole nanowires at very high temperature and Pt/CN_x composite illustrated good electrocatalytic activity for methanol oxidation [49]. Ghosh et al. [50] showed the synergistic effects of PPy nanofibers and Pd nanoparticles for highly improved electrocatalytic performance of Pd/PPy nanocomposites for ethanol oxidation. Pd/PPy nanocomposites showed superior electrocatalytic activity

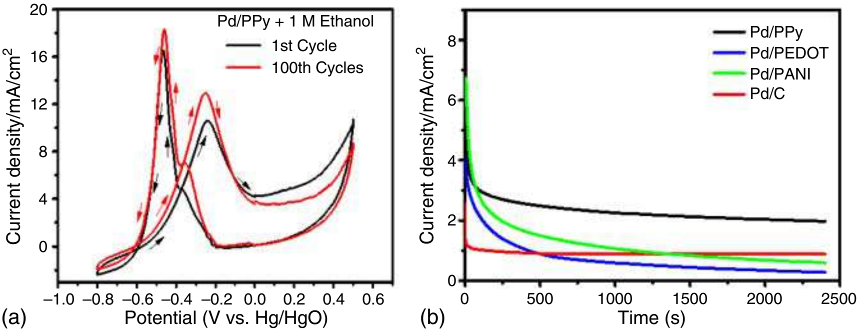

Figure 6.4 (a) Cyclic voltammograms of the first (black solid line curve) and the 100th (red solid line curve) cyclic runs for the electrocatalytic oxidation of 1 M ethanol in 1 KOH using Pd/PPy electrode. (b) Chronoamperometric curves for the ethanol electrooxidation at −0.30 V vs. Hg/HgO on a glassy carbon electrode modified with Pd/PPy (black curve), Pd/PEDOT (blue curve), Pd/PANI (green curve), and Pd/C (red curve) in a solution of 1 M KOH and 1 M EtOH under a constant potential of 0.3 V. Source: Ghosh et al. [50]. © 2017, Springer Nature.

and the mass activity of 7.5 and 78 times higher than that of commercial Pd/C and bulk Pd/PPy composites as improved by the presence of polymer nanofibers (Figure 6.4a). Comparative study on using different polymer such as PPy, PEDOT, and PANI as support showed superior electrocatalytic activity for EOR indicates the maximum stable peak current density (forward peak current) obtained for Pd/PPy (12.9 mA/cm^2), than other electrode materials Pd/PEDOT (4.05 mA/cm^2), and Pd/PANI (7.05 mA/cm^2). It is noted that the specific catalytic activities of the catalysts follow the order Pd/PPy > Pd/PANI > Pd/PEDOT, which consistent with the relative order of electrochemically active surface areas (ECSAs) as calculated, i.e. $\mathrm{ECSA_{Pd/PPy}}$ (104 m^2/g) > $\mathrm{ECSA_{Pd/PANI}}$ (85 m^2/g) > $\mathrm{ECSA_{Pd/PEDOT}}$ (20 m^2/g). Chronoamperometry (CA) measurements demonstrate that the higher stability compared with the commercial Pd/C catalysts, which suggest the significant advantages of polymer support over carbon composites as shown in Figure 6.4b. The results showed that the maximum stable peak current density (forward peak current) for Pd/PPy, Pd/PEDOT, and Pd/PANI catalysts are 12.96, 4.05, and 7.05 mA/cm^2, respectively. Hence the specific catalytic activities of the catalysts follow the order Pd/PPy > Pd/PANI > Pd/PEDOT, which consistent with the relative order of ECSA as calculated, i.e. $\mathrm{ECSA_{Pd/PPy}} > \mathrm{ECSA_{Pd/PANI}} > \mathrm{ECSA_{Pd/PEDOT}}$. The author proposed that the increased number of catalytic active sites with high ECSA may enhance ion accessibility of Pd/PPy, which results in the significant improvement of its catalytic performance.

In general, the polymer nanofibers having porous structure and anisotropic morphology are expected to improve mass transfer rate and efficient diffusion paths for intercalation of the electroactive species, which may noticeably lower the onset potential of the forward anodic peak, positively shift the onset potential of the backward scan peak, and consequently enhance the electroactivity and durability of the Pd/PPy. It was shown that the presence of polymer nanostructures as a support

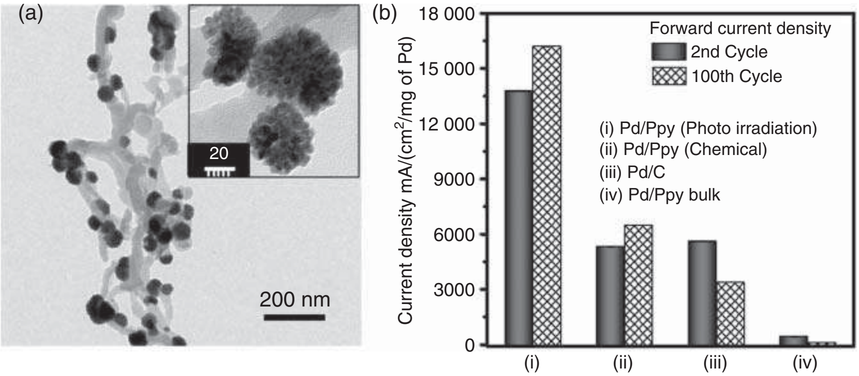

Figure 6.5 (a) Transmission electron micrograph of Pd/PPy nanohybrid. (b) Comparative values of mass activity of Pd/PPy (i, photo irradiation), Pd/PPy (ii, chemical oxidation), Pd/C (iii, commercial), and Pd/PPy (iv, bulk) electrodes for ethanol oxidation in alkaline medium. Source: Reproduced from Ref. [51] with permission from Elsevier, 2018.

could remarkably improve the stability of Pd nanoparticles for EOR, which is crucial for large scale application. Moreover, significantly enhanced catalytic activity for the electrochemical oxidation of ethanol has been obtained by using branched Pd nanostructures decorated conducting PPy polymer nanofibers by Ghosh et al. [51]. Figure 6.5a showed that the branched Pd nanocrystals have an average outer size of 50 nm on PPy nanofibers. It can be clearly seen that the as prepared Pd nanostructures composed of self-assembly of small Pd nanoparticles as shown inset of Figure 6.5a. Polymer supported electrocatalysts demonstrated superior ethanol oxidation activity compared with commercial carbon supported catalysts Pd/C in terms of current density. Figure 6.5b indicates that the current density for ethanol oxidation using of Pd/PPy via photoreduction synthesis electrode was 2.7 times higher than that of commercial Pd/C, which strongly support significant role of PPy nanofibers in the Pd catalysts. It is noted that Pd/PPy (photo reduction) showed highest current density, which is 3.5 and 5.2 times higher than that of Pd/PPy (chemical reduction) and Pd/PPy (bulk polymer), respectively, as shown in Figure 6.5b. This also suggests the advantage of clean method using light for the reduction of metal nanoparticles without using any strong reducing agent.

Pandey and Lakshminarayanan [27] also developed a multistep process for the electrochemical deposition of Pd NPs on PEDOT film, which displays electrochemical activity towards ethanol and methanol. Su et al. [52] developed a facile procedure for Pd supported on Polyamide 6 Nanofibers, which can be used as freestanding electrocatalytic electrodes for a series of alcohol oxidation such as methanol, ethanol, and isopropanol without using any conductive support. Choi et al. [53] observed that PPy hollow spherical nanocapsules can be used as an efficient support matrix to load PtRu NPs through γ-radiation and used as a catalyst. Unfortunately, the application of pure Pt catalyst is limited by its relative scarcity and high cost. Alloying Pt with a low-cost metal (M = Pd, Ni, Ag, Fe, Sn, etc.) has been an efficient strategy for decreasing Pt utilization and improving catalytic activity [54–56]. In this context, few reports are available in the literature regarding the CP supported multimetallic electrocatalyst specifically for the electrooxidation of alcohol. For example, the PANI supported Pt-Ru and Pt-Sn binary catalyst for the electrochemical oxidation of methanol and ethanol has been reported by Hable and Wrighton [57]. Li and coworkers [58] reported PPy functionalized PtPd/PPy/PtPd three-layered nanotube arrays (TNTAs) for the electrooxidation of liquid fuel (methanol, ethanol, and formic acid). They found that the use of PtPd/PPy/PtPd TNTAs showed $\sim$6.5 times higher specific electroactivity with excellent cycle stability than that of the Pt/C catalysts. The authors proposed that the enhanced catalytic activity and improved stability may associated with the hollow, array sandwich-like structures of PtPd/Ppy/PtPd electrocatalysts, which allow rapid transport of electroactive species and high surface area. Moreover, electron transfer from PPy polymer to the metal Pt and Pd atoms due to electron delocalization among the π-conjugated ligands of PPy with Pt 4f orbitals and Pd 3d orbitals may contribute to enhance the catalytic activity. Similarly, Wang et al. [59] showed shape effects and synergistic effects of Pd-PANI composites for the oxidation of small organic molecules for direct alcohol fuel cells. The as prepared hybrid Pd/PANI/Pd sandwich-structured nanotube array (SNTA) displayed significantly improved electrocatalytic activity and durability compared with Pd NTAs and commercial Pd/C catalysts due to electron delocalization between Pd d orbitals and PANI π-conjugated ligands and in electron transfer from Pd to PANI. Additionally, the unique SNTAs provide fast transport and short diffusion paths for electroactive species and high utilization rate of catalysts. Further, Gajendran and Saraswathi [60] optimized the experimental parameters to obtained electrocatalytic performance of POPD-Pt–Ru nanocomposite for methanol oxidation. The onset potential for the oxidation of methanol is found to be effectively reduced by 220 mV for the (PoPD)-Pt–Ru (1 : 1) nanocomposite and also shows a value of 4.2 for the ratio of forward to reverse peak current that is relatively a high value compared to PoPD-Pt electrode for methanol oxidation. Rajathi et al. [61] fabricated a nanostructured Pt/Cu bimetallic on PEDOT with a relatively low Pt loading of $5.48 \times 10^{-6}/\text{cm}^2$, which can be used as a cost-effective alternative anode catalyst for direct methanol fuel cells. Ghosh et al. [62] developed a green and surfactant free strategy to deposit bimetallic PtPd NPs and trimetallic PtPdAu NPs on PPy nanofibers by radiolytic method. By changing the initial concentration of the starting precursors, PtPd NPs with different composition such as $Pt_{66}Pd_{34}$/PPy, $Pt_{49}Pd_{51}$/PPy, and $Pt_{25}Pd_{75}$/PPy can be produced on PPy nanofibers. Figure 6.6a shows $Pt_{66}Pd_{34}$ NPs are uniformly deposited on PPy nanofibers and average particle size of $Pt_{66}Pd_{34}$ NPs anchored on the PPy nanofibers is found to be 3.1 nm. Initially, Pt(II) or other metal ions are selectively absorbed on the surface of polymer nanostructures due to the electrostatic interaction between Pt(II) cation and surfactant functionalized polymer nanofibers. Then, the radiolytic formation of platinum atoms is followed by association of atoms with ions and complexes, dimerization reactions that are reduced, and coalescence of these oligomers leading to Pt nanostructures [63, 64]. The monometallic clusters are formed initially, further association and reduction reactions gradually build bimetallic or trimetallic alloyed cluster. The probable formation of alloyed structure or segregation of metal in a core–shell type structure

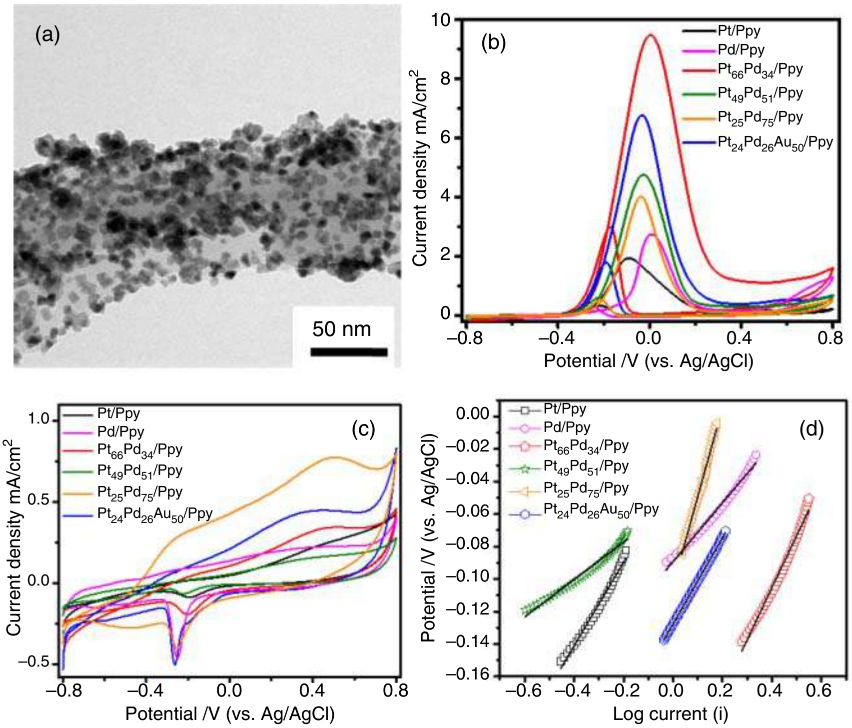

Figure 6.6 Transmission electron micrograph image of $Pt_{66}Pd_{34}$/PPy composites. (b) CV profiles for the electrocatalytic oxidation of methanol. (c) CV Profiles without methanol in 0.1 M KOH at scan rate 20 mV/s. (d) Tafel plots at a scan rate of 1 mV/s using Pt/PPy, Pd/PPy, $Pt_{66}Pd_{34}$/PPy, $Pt_{49}Pd_{51}$/PPy, $Pt_{25}Pd_{75}$/PPy, and $Pt_{24}Pd_{26}Au_{50}$/PPy as working electrodes. Source: Reproduced from Ref. [62] with permission from Royal Society of Chemistry, 2017.

depends on the kinetic competition between the irreversible release of metal ions that displaced by the excess ions of more noble metal after electron transfer as well as radiation induced reduction of both metal ions. Cyclic voltammograms shows $Pt_{66}Pd_{34}$/PPy electrocatalysts have superior catalytic activity for MOR with high current density under alkaline medium as shown in Figure 6.6b. Due to the synergetic effects between Pt and Pd, and the enhanced electronic conductivity of PPy, $Pt_{66}Pd_{34}$/PPy display markedly superior electrocatalytic activity for methanol oxidation with a lower onset potential, higher peak current density compared with Pt/C, Pd/PPy, Pt/PPy, $Pt_{49}Pd_{51}$/PPy, $Pt_{11}Pd_{89}$/PPy, and $Pt_{24}Pd_{26}Au_{50}$/PPy electrodes. From Figure 6.6c, the ECSA of the Pd electrodes have been calculated by determining the columbic charge (Q) for the reduction of palladium oxide (PdO) monolayer, whereas for Pt based catalyst, ECSA was determined by measuring the charge collected in the hydrogen adsorption/desorption region after double-layer correction ($Q_{\text{ref}} = 210\,\mu\text{C/cm}^2$) for oxidation of a single layer of hydrogen on a smooth Pt surface. The calculated ECSA of Pt/PPy, Pd/PPy, $Pt_{66}Pd_{34}$/PPy, $Pt_{51}Pd_{49}$/PPy, $Pt_{25}Pd_{75}$/PPy, and $Pt_{24}Pd_{26}Au_{50}$/PPy is 19.5, 65.5, 22.3, 19.9, 176, and 265 m^2/g, respectively. The enhanced catalytic activity may be associated with accessibility of large number of active sites with Pt—Pd heterojunctions and cooperative action of the metals in the alloy composition. Moreover, tafel plots has been considered using potentiodynamic pseudo steady state polarization at low scan rate of 1 mV/s to compare the kinetics of monometallic catalysts with bimetallic and trimetallic alloys using following Eqs. (6.5) and (6.6):

$$\eta = a + b \log i \tag{6.5}$$

$$\eta = -\frac{2.303RT}{\alpha nF} \log i_0 + \frac{2.303RT}{\alpha nF} \log i \tag{6.6}$$

where η is the over potential, a is Tafel intercept, and b is Tafel slope. i_0 is called exchange current density, α is the charge transfer coefficient, F is the Faraday constant, R is the gas constant, and T is the absolute temperature in K. The exchange current density for $Pt_{24}Pd_{26}Au_{50}$/PPy is c. 0.33 and 0.19 mA for $Pt_{66}Pd_{34}$/PPy suggests that the tri metallic alloy and conducting polymer support enhanced the catalytic performance during MOR (Figure 6.6d). It is important to highlight that this work are not only for the synthesis of high-quality Pt-based alloy nanostructures via a facile and general approach, but also for the development of polymer supported advanced nanocatalysts with remarkably enhanced electrocatalytic activity.

In continuation to Pt alloy, Pd rich trimetallic nanoalloys deposited on polymer nanofibers based electrode displayed excellent electrocatalytic effect for ethanol oxidation under alkaline medium [65]. Figure 6.7a demonstrates the PPy nanofibers with a high and uniform coverage by $Pd_{89}Pt_{11}$ NPs of the average particle size of about 5.7 nm. Figure 6.7b shows the fine $Pd_{30}Pt_{29}Au_{41}$NPs on the polymer surfaces with average particle sizes of ~8 nm. A volcano relationship has been observed for the Pd based nanohybrids having different metallic content (Figure 6.7c). The peak current density for $Pd_{30}Pt_{29}Au_{41}$/PPy exhibits significantly enhanced catalytic activity, which is ~5.5 times higher compared to Pd/C catalyst. The catalytic efficiency increase in the order of the catalysts: $Pd_{30}Pt_{29}Au_{41}$/PPy (5.5-fold) > $Pd_{54}Au_{46}$/PPy (2.4-fold) > $Pd_{89}Pt_{11}$/PPy (2.3-fold) > $Pd_{51}Pt_{49}$/PPy (1.2-fold) > Pt/PPy (1-fold) ≅ Pd/PPy (chosen as reference). It has been proposed that when Pd is combined with platinum or gold in the crystal structure, the d-band of Pd may be shifted up with larger number of active sites and as a result affects the overall electronic structure of the Pd. Additionally, the close contact between Pd NPs and polymer nanofibers may boost up the dispersity and availability of metal catalysts during catalysis. At the end of 1000 cycles, the current densities of $Pd_{54}Au_{46}$/PPy and $Pd_{30}Pt_{29}Au_{41}$/PPy still remain about 93.4% and 97% of their highest values and 53% for Pd/PPy as shown in Figure 6.7d. This suggests that $Pd_{54}Au_{46}$/PPy and $Pd_{30}Pt_{29}Au_{41}$/PPy electrocatalysts could be efficiently recycled without noticeable loss of activity.

Besides alcohol oxidation, polymer nanofibers supported catalyst may also useful in the wide range of other catalytic applications such as the ORR, hydrogen evolution, and water splitting [66–68]. For example, Gurgul and coworkers [69] showed the effect of the polymer to Pd weight ratio in palladium/polypyrrole (Pd/PPy) electrocatalysts towards ORR in 0.5 M H_2SO_4. The rotating ring disc electrode voltammetry (RRDE) and cyclic voltammetry measurements suggests that catalytic

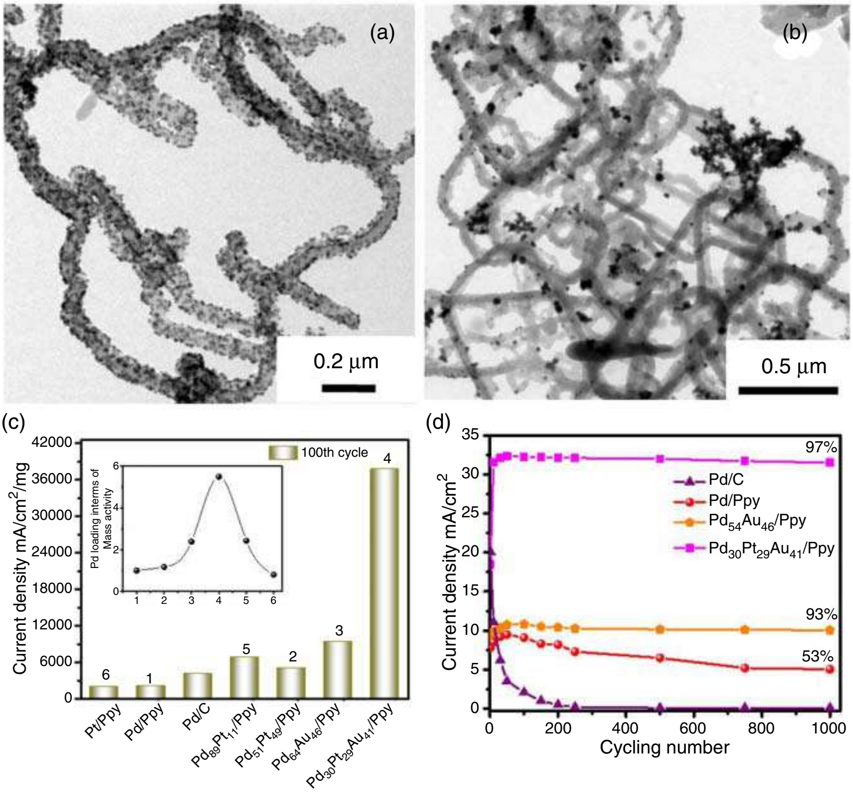

Figure 6.7 TEM images of (a) $Pd_{89}Pt_{11}$/PPy and (b) Pd_{30} $Pt_{29}Au_{41}$/PPy. (b) Mass activity of Pd/C, Pd/polymer composite electrodes for ethanol oxidation in alkaline medium. (c) Long cycling study of Pd/C, Pd/PPy, $Pd_{54}Au_{46}$/PPy, and $Pd_{30}Pt_{29}Au_{41}$/PPy electrodes in a solution of 1 M KOH and 1 M ethanol at scan rate of 50 mV/s. Source: Reproduced from Ref. [65] with permission from American Chemical Society, 2017.

performance in terms of the increased reduction current and positively shifted half-wave potential was improved when Pd content in polymer was grown from 2 to 12 wt% Pd and molecular oxygen underwent mainly a desired four-electron reduction at the optimum Pd content of 10–12 wt%. Bogdanović et al. [70] proposed gold–polyaniline (Au–PANI) nanocomposite as a new class of Pt-free oxygen reduction electrocatalyst showed excellent electrocatalytic performance towards the electrochemical ORR with high onset potential and good selectivity. It has been shown that polyaniline in the composite is in the conducting emeraldine salt form, containing high amount of Au (28.85 wt%) and the electrical conductivity of the nanocomposite was found to be fourfold higher than that of the polymer alone. Except noble metal catalysts, metal chalcogenide based catalyst, for example, V_2Se_9@Poly(3,4-ethylenedioxythiophene) nanosheet array, has been also reported as a new electrocatalyst for the hydrogen evolution reaction by Xu et al. [71]

Figure 6.8a shows a detailed process of fabrication of V_2Se_9@PEDOT NSs/NF. Initially, the V_2O_5 NSs/NF was obtained via calcining the NH_4VO_3 nanosheet arrays precursor at 300 °C for 100 minutes in muffle furnace. Then, V_2O_5 NSs/NF

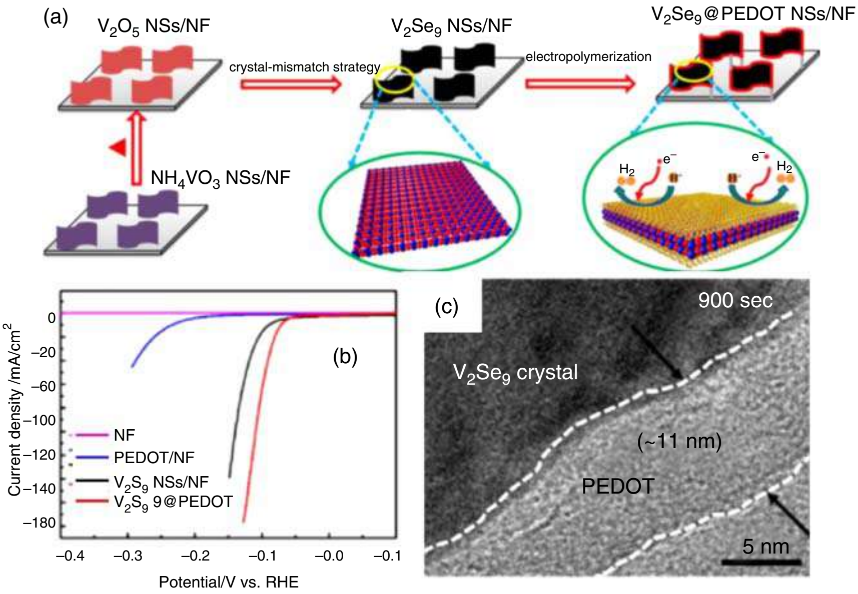

Figure 6.8 (a) Fabrication process of V_2Se_9@PEDOT NSs/NF. Linear sweep voltammetry (LSV) curves of (b) V_2Se_9@PEDOT NSs/NF, V_2Se_9 NSs/NF, PEDOT/NF, and NF (c) TEM images of V_2Se_9@ PEDOT nanosheets with deposition times of 900 seconds. Source: Reproduced from Ref. [71] with permission from American Chemical Society, 2017.

was treated with $NaBH_4$ and Se powder under N_2 flow followed by heating at 300 °C for 60 minutes in argon atmosphere to remove the excess Se. A layer of PEDOT was further deposited onto the surface of V_2Se_9 NSs/NF by potentiostatic electrodeposition technique in an aqueous medium. The V_2Se_9 nanosheet arrays exposed with the highly active (100) facet have been proposed as a new efficient catalyst for hydrogen evolution reaction (HER). The polarization curves in Figure 6.8b showed that V_2Se_9@PEDOT NSs/NF possesses near-zero onset overpotential, and with the overpotential decreasing further, the cathodic current rapidly increases, which is much better than that of NF, PEDOT/NF, and V_2Se_9 NSs/NF. Here, conductive PEDOT acting as a co-catalyst further contributed to the redistribution of charge and reduction of hydrogen the thickness of PEDOT layers could be controlled via deposition time as shown in Figure 6.8c. The results showed that when the coating thickness is 6 nm, the structure possesses the highest electrocatalytic activity. The porous PEDOT coating may lead to lower energy for adsorbing on active sites and improve the electrical conductivity of the architecture, consequently, all of the catalytically active sites are more easily accessible to electrons coming from the electrode.

6.2.2 Metal Catalysts Deposited on Modified Conducting Polymer Nanostructures

Over the years, polymer-supported metal nanoparticles have attracted a great deal of attention and polymer acts as an active support in these systems [24, 30]. However, modification of polymer enhances the performance of the composite material and enabling further tuning of its properties by the introduction of defects and/or dopants. For example, Patra and Munichandraiah [72] reported high catalytic activity of electrodeposited Pt NPs of about 5 nm on PEDOT coated carbon paper, which possess a high electrochemical activity and beneficial role of PEDOT actively contribute to speeding up the kinetics of MOR compared with Pt deposited on carbon in the absence of PEDOT polymer. Dash Munichandraiah [73] also showed electrodeposition of Pd nanodendritic on PEDOT modified carbon paper (Pd–PEDOT/C) and used as efficient electrode for the electrooxidation of a series of alcohol such as propanol, 1,2-propanediol, 1,3-propanediol, and glycerol under alkaline medium compared to Pd/C electrode. Gharibi et al. [74] synthesized Vulcan XC-72 and PANI-doped trifluoromethane sulfonic acid supports based Pt/C-PANI composites catalyst, which demonstrates significant high catalytic activity and stability towards MOR. In another report, Pt NPs distributed into a PEDOT–poly(styrene sulfonic acid) (PSS) displayed high catalytic current for methanol oxidation (2.51 mA/cm^2) in comparison with bulk Pt electrode (0.45 mA/cm^2) by Kuo et al. [75]. Ghosh et al. [76] reported an alternative strategy using poly(diphenylbutadyine) (PDPB) polymer nanofiber in combination with Nafion (an ion-exchange membrane) as support for 2D Pd nanoplates that significantly improved electrocatalytic activity of Pd nanostructures for EOR compared with Nafion supported Pd catalysts. The strong interaction between Pd nanostructures and polymer support enhanced the availability of nanostructures during catalysis and make them promising anode catalyst in DAFCs. Recently, Ye et al. [77] designed a proton (perfluorosulfonic acid, PFSA) and electron (polyaniline, PANI) conductor polymer costabilized Pt catalyst (Pt-PFSA/C@PANI) electrocatalyst to improve the long-term stability of PEMFCs. As prepared electrocatalysts display comparable ORR and significantly higher electrochemical stability than commercial porous carbon nanosphere supported Pt catalysts (Pt/C) due to the presence of PANI as protector, which inhibits carbon nanospheres from corrosion of carbon supports in harsh electrochemical conditions. Moreover, the increased metal–support interaction caused by the strong electrostatic attraction between PANI and PFSA with corresponding positive and negative charges may avoid aggregation and detachment of Pt NPs. Liu et al. [78] reported an interesting study on sequence of deposition of Pt and Ru NPs into nanofibrous network of polyaniline–PSS on electrocatalytic oxidation of methanol. It has been shown that Ru particles were deposited into interior regions in PANI–PSS–Pt–Ru film exhibits an enhanced electrocatalytic activity toward methanol oxidation with a diminished poisoning effect for CO. Moreover, platinum NPs decorated poly (aniline-co-methoxy aniline) (Ani-co-MAni)-rice straw black liquor based porous carbon (RSBLPC), (Poly(Ani-co-MAni)-RSBLPC) composite reveals a significant enhancement towards the oxidation of methanol in comparison with Pt/Poly(Ani-co-MAni) and Pt/RSBLPC catalysts, which may expected from the synergic effect of RSBLPC and conductive polymer material [79]. Furthermore, Joice et al. [80] fabricated an efficient electrocatalysts based on PANI decorated with nanocactus platinum on carbon fiber paper for toluene oxidation. A similar group also reported electrocatalytic oxidation of benzyl alcohol by using platinum decorated polythiophene modified stainless steel electrode [81]. Recently, polypyrrole-carbon (PPy-C) composites decorated with platinum NPs (Pt/PPy-C) were also investigated for borohydride oxidation reaction in alkaline medium and for hydrogen peroxide reduction reaction in acidic medium [82]. It has been shown that Pt/PPy-C electrodes are used as both anode and cathode in a direct borohydride-peroxide fuel cell, which gave the highest peak power density of $1432\,\mathrm{W/g_{Pt}}$ at current density of $2046\,\mathrm{A/g_{Pt}}$ and cell voltage of 0.70 V.

Conducting polymer functionalized with metal oxides or graphene, carbon nanotubes have been also utilized as supporting material in order to enhance the catalytic activity of metal catalysts [83, 84] In fact, platinum NPs and hydrous molybdenum oxide ($\mathrm{Pt/H_{\mathit{x}}MoO_3}$) electrodeposited onto poly(3,4-ethylenedioxythiophene)-poly(styrene sulfonic acid) (PEDOT-PSS) film demonstrated superior electrocatalytic activity of methanol oxidation with less CO poisoning. Xu et al. [85] also reported multilayered $\mathrm{Pt/CeO_2}$/PANI three-layered hollow nanorod arrays (THNRAs) and $\mathrm{ZnO/Pt/CeO_2}$/PANI hybrid hollow nanorod arrays by combining conducting polymer with metal oxides as multilayered supporting material which illustrated elevated electrocatalytic activity towards MOR. Figure 6.9a displays cyclic voltammetry (CV) profiles of $\mathrm{Pt/CeO_2}$/PANI THNRAs, Pt/PANI HNRAs, $\mathrm{Pt/CeO_2}$ HNRAs, and commercial Pt/C catalysts and the ECSA values of catalysts were calculated considering the hydrogen desorption areas after the deduction of the double layer region.

The calculated ECSA of $\mathrm{Pt/CeO_2}$/PANI THNRAs, $\mathrm{Pt/CeO_2}$ HNRAs, Pt/PANI HNRAs, and commercial Pt/C catalysts is 43.26, 10.42, 26.49, and $45.08\,\mathrm{m^2/g_{Pt}}$ respectively. The ECSA value of Pt/ $\mathrm{CeO_2}$/PANI THNRAs has been found to be about four times higher than $\mathrm{Pt/CeO_2}$ HNRAs, which may be attributed to the highly uniform dispersion of metal NPs, and the synergistic effects among NPs and polymer. The specific peak current density and I_f/I_b ratio of $\mathrm{Pt/CeO_2}$/PANI THNRAs (I_f/I_b ~0.96) is higher for the oxidation of methanol than Pt/PANI HNRAs (0.84), and commercial Pt/C (0.80) catalysts due to the synergistic effects among Pt, $\mathrm{CeO_2}$, and PANI and the special three-layered hollow nanorod arrays, as shown in Figure 6.9b. The I_f/I_b ratio suggests presence of $\mathrm{CeO_2}$ can effectively relieve the poisoning of carbonaceous species and the $\mathrm{Pt/CeO_2}$/PANI THNRAs possess higher poisoning resistance than Pt/PANI HNRAs and commercial Pt/C electrocatalysts. It has been proposed that $\mathrm{Pt/CeO_2}$/PANI THNRAs having hollow nanorod array structures can facilitate the transportation of electroactive species; and presence of conducting polymer support would enhance the structural stability (Figure 6.9c). This may provide a direct path for electron transport, and electron delocalization among PANI π-conjugated ligands, Ce 3d orbitals, and Pt 4f orbitals may alter the electronic structure and d-band center of Pt, which promote removal of surface adsorbed carbonaceous intermediates through weakening the adsorption energy of carbonaceous intermediates on the Pt surfaces. Moreover, $\mathrm{CeO_2}$ in the catalyst can well promote the dispersion of Pt and provide the labile OH species for electrooxidation of surface adsorbed carbonaceous intermediates to produce $\mathrm{CO_2}$ during methanol oxidation. Kuo et al. [86] also designed a complex system comprising by electrochemical deposition of Pt and ruthenium oxide

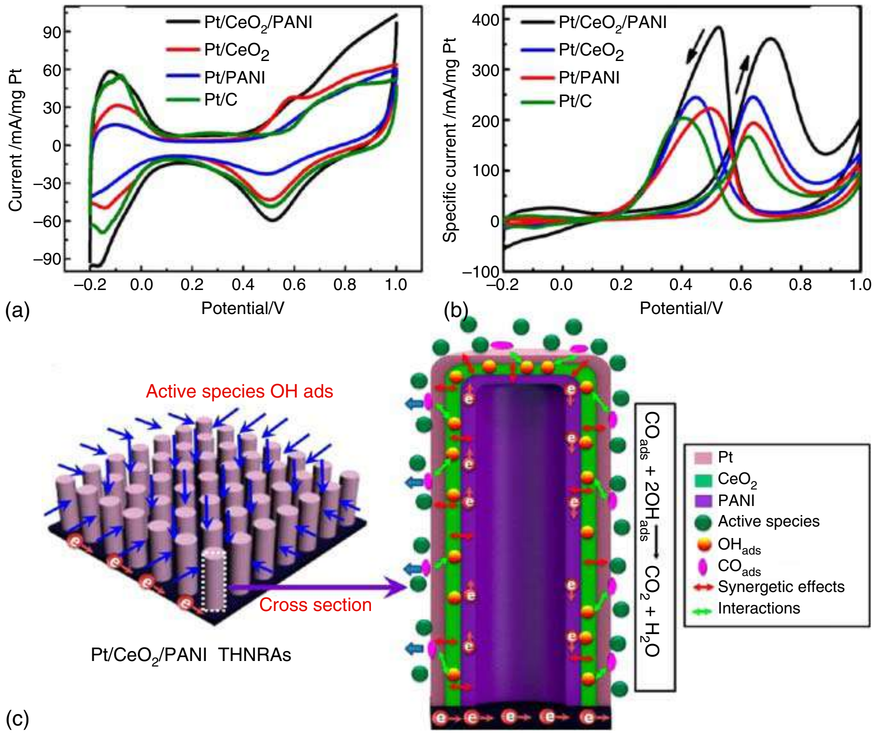

Figure 6.9 (a) Cyclic voltammograms of Pt/CeO$_2$/PANI THNRAs, Pt/PANI HNRAs, Pt/CeO$_2$ HNRAs, and commercial Pt/C catalysts in the solution of 0.5 M H_2SO_4 at 100 mV/s. (b) Cyclic voltammograms of Pt/CeO$_2$/PANI THNRAs, Pt/PANI HNRAs, Pt/CeO$_2$ HNRAs, and commercial Pt/C catalysts for methanol oxidation at 100 mV/s. (c) Schematic illustration for the advantages of Pt/CeO$_2$/PANI THNRAs. Source: Xu et al. [85]. © 2016, American Chemical Society

(RuO_2) particles on PANI-poly(acrylic acid-co-maleic acid) (PAMA) film to obtain PANI-PAMA-Pt-RuO$_2$ composite electrodes, which showed high catalytic activity and stability toward MOR.

Although, carbon nanotubes (CNTs) are excellent supports for electrocatalysts because of their large surface area, excellent electronic conductivity, and high chemical and structural stability [87, 88] but incorporation of CNT into conducting polymers can lead to produce composites support with all the advantages of the individual components, such as mechanical and optical properties, electrocatalytic activity, electrical conductivity, and charge density, and also improved properties by a synergistic effect. For instance, Wu et al. [89] electrodeposited Pt particles into PANI modified single wall CNTs, which exhibited high catalytic activity. Selvaraj and Alager [90] dispersed Pt and Pt-Ru NPs in PPy/multiwall CNTs and the obtained Pt–Ru/PPy–CNT catalysts, which reveal higher catalytic activity for MOR due to the high electrochemically accessible surface areas, high electronic conductivity contributed from CP, and easier charge transfer. The same group also developed carbon nanotubes based supporting material with *in situ* polymerization of thiophene (Th) and further Pt and Pt–Ru NPs deposited on polythiophene/CNT composites (PTh-CNTs) for ethylene glycol oxidation reaction. Conducting polymer modified carbon nanotubes provides higher electrochemical active surface area, enhanced electronic conductivity, and facile charge transfer at the interfaces. Moreover, polymer composites based supporting material permits higher dispersion of Pt–Ru NPs, which in turn improve electrocatalytic activity of Pt–Ru/PTh–CNT electrodes for ethylene glycol electrooxidation than the Pt/PTh electrodes [91]. Shi et al. [92] also prepared polyaniline wrapped carbon nanotubes (CNT–PANI) core–shell composites via interfacial polymerization and used as a support for Pt NPs with controllable loading density for methanol oxidation with lower anodic overpotential suggests high catalytic activity. In the CNT–PANI composites, PANI form a bridge between the Pt NPs and CNT walls through via platinum–nitride (Pt–N) and π–π bonding, which provided exceptional electrochemical activity for MOR.

In order to further improve the electrocatalytic activity, Prasanna and Selvaraj [93] used multifunctional carbon nanotube (amine terminated cyclophosphazene, ATCP/cyclophosphazene, CP/hexafluoroisopropylidenedianiline, HFPA-CNT) composite as support for platinum (Pt) and platinum-gold (Pt-Au) NPs electrocatalysts towards methanol electrooxidation reaction under alkaline medium. Compared with Pt/CNT and Pt/C catalysts, ATCP/CP/HFPA-CNT composite supported Pt catalysts display high anodic current density and significant CO tolerance. Wei et al. [94] reported similar trend of catalytic activity where highly dispersed Pt NPs supported on carbon nanotubes composite were modified with manganese oxide and PEDOT polymer for enhanced MOR as compared with the PEDOT–MWCNTs or MWCNTs modified Pt catalysts. Noroozifar et al. [95] provided a systematic study on the incorporation of palladium NPs and multi-walled carbon nanotubes (MWCNTs) into chitosan-coated glassy carbon (GC) electrode for electrooxidation of different alcohols (methanol, ethanol, and isopropanol). It was shown that dispersion of Pd nanoparticles on the MWCNTs significantly improved the performance of the PdNPs/chitosan composite for electrooxidation of the C1–C3 alcohols. Electrodeposition of three-dimensional Pd nanoflowers on PPy@MWCNT composites support exhibits the enhanced electrocatalytic activity where the mass activity of Pd NFs/PPy@MWCNTs (725 mA/mg) is 8.09 times higher than that of the Pd NFs catalyst (89.6 mA/mg) and long-term stability for methanol electrooxidation due to higher electrochemically surface area and electronic conductivity [96]. Recently, Wang et al. [97] deposited Pt NPs on a polyindole (PIn)-functionalized MWCNT composite (Pt/PIn-MWCNT) and used as anode materials for the MOR with higher electrocatalytic activity, and durability than the commercial Pt/C catalysts.

In addition to CNT, graphene and graphitic carbon-based conducting polymer-containing cathode or anode catalysts have also been investigated. Graphene oxides has attracted great interest because of its superior mechanical, structural, and thermal properties and also its low cost compared with other conventional carbon nanomaterials like CNT [98, 99]. Yang et al. [100] fabricated vertically orientated polyaniline-reduced graphene oxide hybrid nanosheets by

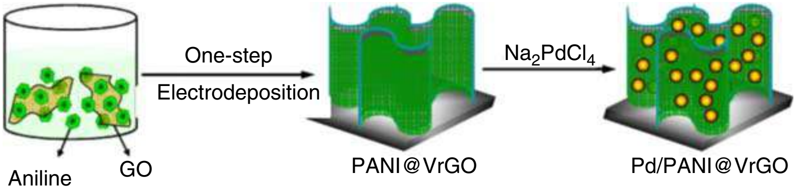

Figure 6.10 Schematic presentation of PANI@VrGO supporting materials for Pd catalysts. Source: Yang et al. [100]. © 2016, American Chemical Society.

single-step electrodeposition technique, which anchors palladium NPs through the spontaneous redox reaction between PANI and palladium salt and the as-prepared composites used as an active and stable electrocatalyst for methanol and EOR (Figure 6.10).

In another report, PEDOT functionalized graphene with palladium nanoparticles (denoted as Pd/PEDOT/rGO) showed remarkable electrocatalytic activity for ORR and stability compared with Pd/rGO and state-of-the-art Pt/C [101]. The Koutecký–Levich and Tafel analysis suggest that the proposed main path in the ORR mechanism has direct four-electron transfer process with faster transfer kinetic rate on the Pd/PEDOT/rGO. Yang et al. [102] employed graphene nanosheets-polypyrrole hybrid material as a highly active catalyst support for formic acid electrooxidation. As a conductive supporting material for the catalyst, graphitic carbon nitride (g-C_3N_4) has also emerged as a promising candidate, and many attempts have been carried out to use it as composites with conducting polymer, alternative to carbon black [103]. Ponnusamy and coworkers [104] reported a simple one-step fabrication of novel graphitic carbon nitride/polyaniline/palladium nanoparticles nanohybrid, which showed superior electrooxidation and excellent catalytic performance towards methanol oxidation compared to commercial 10% palladium loaded carbon black material and other previously reported electrode materials.

6.3 Conclusion

In summary, CPNs with excellent environmental stability, facile synthesis, and high conductivity have been considered the most promising alternative to carbon supports in fuel cells. The use of CPNs eventually affects the electrocatalytic activity of metal nanostructure catalysts with high current density and stability. A number of strategies have been summarized to improve the catalytic activity of nanostructured materials using CPNs as support. Many types of metal nanoparticles nanoalloys can be deposited on polymer via both *ex situ* method where the polymer can be dissolved in an appropriate solvent, then NPs may combined to the polymer solution and *in situ* method through polymerization in the presence of NPs or synthesis of polymer network with nanostructures. The enhanced electrocatalytic activity may be achieved due to the effective dispersion of the metal nanostructures within the CPNs and polymer support facilitating an easier access of fuel molecules to the catalytic sites. Moreover, manipulating surface of the CPN and used as supporting materials may also provide opportunity to tailor the catalytic properties of metal nanocrystals. Furthermore, the large-scale synthesis of stable, low cost, multi-metallic nanocrystals should be devoted as future efforts for fuel cell applications. In this context, more studies are needed in scale-up feasibility for the utilization of CPN in fuel cells.

References

1 Edwards, P.P., Kuznetsov, V.L., David, W.I.F., and Brandon, N.P. (2008). Hydrogen and fuel cells: towards a sustainable energy future. *Energy Policy* 36: 4356–4362.

2 Konno, N., Mizuno, S., Nakaji, H., and Ishikawa, Y. (2015). Development of compact and high performance fuel cell stack. *SAE Int. J. Altern. Powertrains* 4: 123–129.

3 Ghosh, S., Thandavarayan, M., and Basu, R.N. (2017). Recent advances in nanostructured electrocatalysts for direct alcohol fuel cells, Chapter 11. In: *Electrocatalysts for Low Temperature Fuel Cells–Fundamentals and Recent Trends* (eds. T. Maiyalagan and V.S. Saji), 347–372. Germany: Wiley-VCH VerlagGmbh & Co. KGaA.

4 Baldauf, M. and Preidel, W. (2001). Experimental results on the direct electrochemical oxidation of methanol in PEM fuel cells. *J. Appl. Electrochem.* 31: 781–786.

5 Ghosh, S., Holade, Y., Remita, H. et al. (2016). One-pot synthesis of reduced graphene oxide supported gold-based nanomaterials as robust nanocatalysts for glucose electrooxidation. *Electrochim. Acta* 212: 864–875.

6 An, L. and Chen, R. (2016). Recent progress in alkaline direct ethylene glycol fuel cells for sustainable energy production. *J. Power Sources* 329: 484–501.

7 Wee, J.H. (2007). Applications of proton exchange membrane fuel cell systems. *Renewable Sustainable Energy Rev.* 11: 1720–1738.

8 Corti, H.R. and Gonzalez, E.R. (2014). Introduction to direct alcohol fuel cells. In: *Direct Alcohol Fuel Cells* (eds. H. Corti and E. Gonzalez), 1–32. Dordrecht: Springer.

9 Gasteiger, H., Kocha, S., Sompalli, B., and Wagner, F. (2005). Activity benchmarks and requirements for Pt, Pt-alloy, and non-Pt oxygen reduction catalysts for PEMFCs. *Appl. Catal., B* 56: 9–35.

10 Zhao, X. (2011). Recent advances in catalysts for direct methanol fuel cells. *Energy Environ. Sci.* 4: 2736–2753.

11 Bianchini, C. and Shen, P.K. (2009). Palladium-based electrocatalysts for alcohol oxidation in half cells and in direct alcohol fuel cells. *Chem. Rev.* 109: 4183–4206.

12 Aricó, A.S., Antonucci, P.L., Modica, E. et al. (2002). Effect of Pt-Ru alloy composition on high-temperature methanol electro-oxidation. *Electrochim. Acta* 47: 3723–3732.

13 Ren, X., Lv, Q., Liu, L. et al. (2020). Current progress of Pt and Pt-based electrocatalysts used for fuel cells. *Sustainable Energy Fuels* 4: 15–30.

14 Rajeswari, J., Viswanathan, B., and Varadarajan, T.K. (2007). Tungsten trioxide nanorods as supports for platinum in methanol oxidation. *Mater. Chem. Phys.* 106: 168–174.

15 Xu, C., Shen, P.K., and Liu, Y. (2007). Ethanol electrooxidation on Pt/C and Pd/C catalysts promoted with oxide. *J. Power Sources* 164: 527–531.

16 Kumar, A. and Ramani, V. (2014). Strong metal–support interactions enhance the activity and durability of platinum supported on tantalum-modified titanium dioxide electrocatalysts. *ACS Catal.* 4: 1516–1525.

17 Antolini, E. (2009). Carbon supports for low-temperature fuel cell catalysts. *Appl. Catal., B* 88: 1–24.

18 Ghosh, S., Remita, H., Kar, P. et al. (2015). Facile synthesis of Pd nanostructures in hexagonal mesophases as a promising electrocatalyst for ethanol oxidation. *J. Mater. Chem. A* 3: 9517–9527.

19 Debe, M.K. (2012). Electrocatalyst approaches and challenges for automotive fuel cells. *Nature* 486: 43–51.

20 Kongkanand, A. and Mathias, M.F. (2016). The priority and challenge of high-power performance of low-platinum proton-exchange membrane fuel cells. *J. Phys. Chem. Lett.* 7: 1127–1137.

21 Xie, C., Niu, Z., Kim, D. et al. (2020). Surface and interface control in nanoparticle catalysis. *Chem. Rev.* 120: 1184–1249.

22 Ghosh, S., Natalie, K.A., Ramos, L. et al. (2015). Conducting polymer nanostructures for photocatalysis under visible light. *Nat. Mater.* 14: 505–511.

23 Shi, Y., Peng, L., Ding, Y. et al. (2015). Nanostructured conductive polymers for advanced energy storage. *Chem. Soc. Rev.* 44: 6684–6696.

24 Ghosh, S., Thandavarayan, M., and Basu, R.N. (2016). Nanostructured conducting polymers for energy applications: towards a sustainable platform. *Nanoscale* 8: 6921–6947.

25 Dutta, K., Das, S., Rana, D., and Kundu, P.P. (2015). Enhancements of catalyst distribution and functioning upon utilization of conducting polymers as supporting matrices in DMFCs: a review. *Polym. Rev.* 55: 1–56.

26 Vercelli, B., Zotti, G., and Berlin, A. (2009). Mono- and multilayers of platinum nanoparticles and poly(3,4-ethylenedioxythiophene) as nanostructures for methanol electrooxidation. *J. Phys. Chem. C* 113: 3525–3529.

27 Pandey, R.T.K. and Lakshminarayanan, V. (2010). Enhanced electrocatalytic activity of Pd-dispersed 3,4-polyethylenedioxythiophene film in hydrogen evolution and ethanol electro-oxidation reactions. *J. Phys. Chem. C* 114: 8507–8514.

28 Kost, K.M., Bartak, D.E., Kazee, B., and Kuwana, T. (1988). Electrodeposition of platinum microparticles into polyaniline films with electrocatalytic applications. *Anal. Chem.* 60: 2379–2384.

29 Dutta, K., Das, S., Rana, D., and Kundu, P.P. (2014). A review on aromatic conducting polymer based catalysts supporting martrices for application in microbial fuel cells. *Polym. Rev.* 54: 401–435.

30 Xu, P., Han, X., Zhang, B. et al. (2014). Multifunctional polymer–metal nanocomposites via direct chemical reduction by conjugated polymers. *Chem. Soc. Rev.* 43: 1349–1360.

31 Ghosh, S., Mullick, A.K., and Basu, R.N. (2018). Enhanced photocatalytic activity and photoresponse of poly(3,4-ethylenedioxythiophene) nanofibers decorated with gold nanoparticle under visible light. *Sol. Energy* 159: 548–560.

32 Iqbal, S. and Ahmad, S. (2018). Recent development in hybrid conducting polymers: synthesis, applications and future prospects. *J. Ind. Eng. Chem.* 60: 53–84.

33 Das, S., Dutta, K., and Kundu, P.P. (2015). Nickel nanocatalyst supported on sulfonated polyaniline: potentials toward methanol oxidation and as anode materials of DMFCs. *J. Mater. Chem. A* 3: 11349–11357.

34 Qi, Z., Shan, J., and Pickup, P. (2002). Conducting polymer-supported fuel cell catalysts. *ACS Symp. Ser.* 832: 166–183.

35 Mallick, K., Witcomb, M.J., Dinsmore, A., and Scurrell, M.S. (2005). Fabrication of a metal nanoparticles and polymer nanofibers composite material by an in situ chemical synthetic route. *Langmuir* 21: 7964–7967.

36 Gangopadhyay, R. and De, A. (2000). Conducting polymer nanocomposites: a brief overview. *Chem. Mater.* 12: 608–622.

37 Chen, S., Wei, Z., Qi, X.Q. et al. (2012). Nanostructured polyaniline-decorated Pt/C@PANI core–shell catalyst with enhanced durability and activity. *J. Am. Chem. Soc.* 134: 13252–13255.

38 Yuan, X., Ding, X.L., Wang, C.-Y., and Ma, Z.F. (2013). Use of polypyrrole in catalysts for low temperature fuel cells. *Energy Environ. Sci.* 6: 1105–1124.

39 Rajesh, B., Thampi, K.R., Bonard, J.M. et al. (2004). Nanostructured conducting polyaniline tubules as catalyst support for Pt particles for possible fuel cell applications. *Electrochem. Solid-State Lett.* 7: A404–A407.

40 Jin, W., Huang, X., Cheng, H. et al. (2019). Polyaniline hollow tubes loading tiny platinum nanoparticles for boosting methanol oxidation. *Appl. Surf. Sci.* 483: 489–495.

41 Salavagione, H.J., Sanchís, C., and Morallón, E. (2007). Friendly conditions synthesis of platinum nanoparticles supported on a conducting polymer: methanol electrooxidation. *J. Phys. Chem. C* 111: 12454–12460.

42 Jiang, C. and Lin, X. (2007). Preparation of three-dimensional composite of poly(*N*-acetylaniline) nanorods/platinum nanoclusters and electrocatalytic oxidation of methanol. *J. Power Sources* 164: 49–55.

43 Kim, K., Ahn, H., and Park, M.J. (2017). Highly catalytic Pt nanoparticles grown in two-dimensional conducting polymers at the air–water interface. *ACS Appl. Mater. Interfaces* 9: 30278–30282.

44 Rajesh, B., Thampi, B., Bonard, K.R. et al. (2003). Conducting polymeric nanotubules as high performance methanol oxidation catalyst support. *Chem. Commun.*: 2022–2023.

45 Maiyalagan, T. (2008). Electrochemical synthesis, characterization and electro-oxidation of methanol on platinum nanoparticles supported poly(*o*-phenylenediamine) nanotubes. *J. Power Sources* 179: 443–450.

46 Chen, Z., Xu, L., Li, W. et al. (2006). Polyaniline nanofibre supported platinum nanoelectrocatalysts for direct methanol fuel cells. *Nanotechnology* 17: 5254–5259.

47 Guo, S., Dong, S., and Wang, E. (2009). Polyaniline/Pt hybrid nanofibers: high-efficiency nanoelectrocatalysts for electrochemical devices. *Small* 5: 1869–1876.

48 Sun, X., Zhang, N., and Huang, X. (2016). Polyaniline-coated platinum nanocube assemblies as enhanced methanol oxidation electrocatalysts. *ChemCatChem* 8: 3436–3440.

49 Ma, Y., Jiang, S., Jian, G. et al. (2009). CNx nanofibers converted from polypyrrole nanowires as platinum support for methanol oxidation. *Energy Environ. Sci.* 2: 224–229.

50 Ghosh, S., Bhandary, N., Basu, S., and Basu, R.N. (2017). One pot synthesis of Pd/polypyrrole nanofiber composites as a high performance electrocatalyst for ethanol oxidation. *Electrocatalysis* 8: 329–339.

51 Ghosh, S., Bera, S., Karmakar, N., and Basu, R.N. (2018). Enhanced electrocatalytic activity of branched Pd nanostructures decorated conducting polymer nanofibers for alkaline fuel cells. *Materials Today: Proceedings* 5: 9733–9742.

52 Su, L., Jia, W., Schempf, A. et al. (2009). Free-standing palladium/polyamide 6 nanofibers for electrooxidation of alcohols in alkaline medium. *J. Phys. Chem. C* 113: 16174–16180.

53 Choi, S.-H., Gopalan, A.I., Ryu, J.-H., and Lee, K.-P. (2010). Hollow spherical nanocapsules of poly(pyrrole) as a promising support for Pt/Ru nanoparticles based catalyst. *Mater. Chem. Phys.* 120: 18–22.

54 Ghosh, S., Bysakh, S., and Basu, R.N. (2019). Bimetallic $Pd_{96}Fe_4$ nanodendrites embedded in graphitic carbon nanosheets as highly efficient anode electrocatalysts. *Nanoscale Adv.* 1: 3929–3940.

55 Chowdhury, S.R., Ghosh, S., and Bhattachrya, S.K. (2017). Improved catalysis of Green-synthesized Pd-Ag alloy-nanoparticles for anodic oxidation of methanol in alkali. *Electrochim. Acta* 225: 310–321.

56 Chowdhury, S.R., Ghosh, S., and Bhattachrya, S.K. (2017). Enhanced and synergistic catalysis and mechanisctic study of Pd-Ni alloy nanoparticles for anodic oxidation of methanol in alkali. *Electrochim. Acta* 250: 124–134.

57 Hable, C.T. and Wrighton, M.S. (1993). Electrocatalytic oxidation of methanol and ethanol: a comparison of platinum-tin and platinum-ruthenium catalyst particles in a conducting polyaniline matrix. *Langmuir* 9: 3284–3290.

58 Xu, H., Ding, L.-X., Liang, C.-L. et al. (2013). High-performance polypyrrole functionalized PtPd electrocatalysts PtPd/PPy/PtPd three-layered nanotube arrays based on for the electrooxidation of small organic molecules. *NPG Asia Mater.* 5: e69–e72.

59 Wang, A.-L., Xu, H., Feng, J.-X. et al. (2013). Design of Pd/PANI/Pd sandwich-structured nanotube array catalysts with special shape effects and synergistic effects for ethanol electrooxidation. *J. Am. Chem. Soc.* 135: 10703–10709.

60 Gajendran, P. and Saraswathi, R. (2013). Electrocatalytic performance of poly(*o*-phenylenediamine)-Pt–Ru nanocomposite for methanol oxidation. *J. Solid State Electrochem.* 17: 2741–2747.

61 Rajathi, P.M., Sivakumar, C., and Berchmans, S. (2018). Methanol electro-oxidation by nanostructured Pt/Cu bimetallic on poly 3,4 ethylene-dioxythiophene (PEDOT). *Electrochim. Acta* 282: 163–170.

62 Ghosh, S., Bera, S., Bysakh, S., and Basu, R.N. (2017). Conducting polymer nanofiber-supported Pt alloys: unprecedented materials for methanol oxidation with enhanced electrocatalytic performance and stability. *Sustainable Energy Fuels* 1: 1148–1161.

63 Belloni, J., Mostafavi, M., Remita, H. et al. (1998). Radiation-induced synthesis of mono- and multi-metallic clusters and nanocolloids. *New J. Chem.* 22: 1239–1255.

64 Grand, J., Ferreira, S.R., de Waele, V. et al. (2018). Nanoparticle alloy formation by radiolysis. *J. Phys. Chem. C* 122: 12573–12588.

65 Ghosh, S., Bera, S., Bysakh, S., and Basu, R.N. (2017). Highly active multimetallic palladium nanoalloys embedded in conducting polymer as anode catalysts for electrooxidation of ethanol. *ACS Appl. Mater. Interfaces* 9: 33775–33790.

66 Ghosh, S., Rashmi, D., Bera, S., and Basu, R.N. (2019). Functionalized conjugated polymer with plasmonic Au nanoalloy for photocatalytic hydrogen generation under visible-NIR. *Int. J. Hydrogen Energy* 44: 13262–13272.

67 Milikić, J., Stamenović, U., Vodnik, V. et al. (2019). Gold nanorod-polyaniline composites: synthesis and evaluation as anode electrocatalysts for direct borohydride fuel cells. *Electrochim. Acta* 328: 135115–135119.

68 Kirubaharan, C.J., Kumar, G.G., Sha, C. et al. (2019). Facile fabrication of Au@polyaniline core-shell nanocomposite as efficient anodic catalyst for microbial fuel cells. *Electrochim. Acta* 328: 135136.

69 Kurbiel, M.G., Drelinkiewicz, A., Kosydar, R. et al. (2014). Palladium content effect on the electrocatalytic activity of palladium–polypyrrole nanocomposite for cathodic reduction of oxygen. *Electrocatalysis* 5: 23–40.

70 Bogdanović, U., Pašti, I., Marjanović, G.Ć. et al. (2015). Interfacial synthesis of gold–polyaniline nanocomposite and its electrocatalytic application. *ACS Appl. Mater. Interfaces* 7: 28393–30282.

71 Xu, H., Jiang, Z., Zhang, H. et al. (2017). New efficient electrocatalyst for the hydrogen evolution reaction: erecting a V2Se9@Poly(3,4-ethylenedioxythiophene) nanosheet array with a specific active facet exposed. *ACS Energy Lett.* 2: 1099–1104.

72 Patra, S. and Munichandraiah, N. (2009). Electrooxidation of methanol on Pt-modified conductive polymer PEDOT. *Langmuir* 25: 1732–1738.

73 Dash, S. and Munichandraiah, N. (2013). Electrocatalytic oxidation of C3-aliphatic alcohols on electrodeposited Pd-PEDOT nanodendrites in alkaline medium. *J. Electrochem. Soc.* 160: 197–202.

74 Gharibi, H., Kakaei, K., and Zhiani, M. (2010). Platinum nanoparticles supported by a vulcan XC-72 and PANI doped with trifluoromethane sulfonic acid substrate As a new electrocatalyst for direct methanol fuel cells. *J. Phys. Chem. C* 114: 5233–5240.

75 Kuo, C.-W., Huang, L.-M., Wen, T.-C., and Gopalan, A. (2006). Enhanced electrocatalytic performance for methanol oxidation of a novel Pt-dispersed poly(3,4-ethylenedioxythiophene)–poly(styrene sulfonic acid) electrode. *J. Power Sources* 160: 65–72.

76 Ghosh, S., Teillout, A.L., Floresyona, D. et al. (2015). Conducting polymer-supported palladium nanoplates for applications in direct alcohol oxidation. *Int. J. Hydrogen Energy* 40: 4951–4959.

77 Ye, B., Cheng, K., Li, W. et al. (2017). Polyaniline and perfluorosulfonic acid co-stabilized metal catalysts for oxygen reduction reaction. *Langmuir* 33: 5353–5361.

78 Liu, F.-J., Huang, L.-M., Wen, T.-C. et al. (2008). Effect of deposition sequence of platinum and ruthenium particles into nanofibrous network of polyaniline–poly(styrene sulfonic acid) on electrocatalytic oxidation of methanol. *Synth. Met.* 158: 603–609.

79 Vaithilingam, S. and Ramanujam, T.M. (2018). Development of rice straw black liquor based porous carbon-poly(aniline-co-methoxy aniline) as supporting for electrochemical performances of alcohol oxidations. *Ionics* 24: 3923–3935.

80 Joice, E.K., Anitha, V., Sudhakar, Y.N. et al. (2018). Poly(aniline) decorated with nanocactus platinum on carbon fiber paper and its electrocatalytic behavior toward toluene oxidation. *J. Electrochem. Soc.* 165: H399–H406.

81 Joice, E.K., Rison, S., Akshaya, K.B., and Anitha, V. (2019). Platinum decorated polythiophene modified stainless steel for electrocatalytic oxidation of benzyl alcohol. *J. Appl. Electrochem.* 49: 937–947.

82 Oliveira, R.C.P., Milikić, J., Daş, E. et al. (2018). Platinum/polypyrrole-carbon electrocatalysts for direct borohydride-peroxide fuel cells. *Appl. Catal., B* 238: 454–464.

83 Zhao, Y., Zhan, L., Tian, J. et al. (2011). Enhanced electrocatalytic oxidation of methanol on Pd/polypyrrole–graphene in alkaline medium. *Electrochim. Acta* 56: 1967–1972.

84 Kuo, C.-W., Sivakumar, C., and Wen, T.-C. (2008). Nanoparticles of $\mathrm{Pt/H}x\mathrm{MoO_3}$ electrodeposited in poly(3,4-ethylenedioxythiophene)-poly(styrene sulfonic acid) as the electrocatalyst for methanol oxidation. *J. Power Sources* 185: 807–814.

85 Xu, H., Wang, A.L., Tong, Y.X., and Li, G.R. (2016). Enhanced catalytic activity and stability of $\mathrm{Pt/CeO_2}$/PANI hybrid hollow nanorod arrays for methanol electro-oxidation. *ACS Catal.* 6: 5198–5206.

86 Kuo, C.-W., Kuo, Z.-Y., Jow, J.-J. et al. (2012). Enhanced electrocatalytic performance for methanol oxidation via insertion of ruthenium oxide particles into Pt and polyaniline-poly(acrylic acid-co-maleic acid) composite electrode. *Int. J. Electrochem. Sci.* 7: 4974–4987.

87 Planeixm, J.M., Coustel, N., Coq, B. et al. (1994). Application of carbon nanotubes as supports in heterogeneous catalysis. *J. Am. Chem. Soc.* 116: 7935–7936.

88 Yan, Y., Miao, J., Yang, Z. et al. (2015). Carbon nanotube catalysts: recent advances in synthesis, characterization and applications. *Chem. Soc. Rev.* 44: 3295–3346.

89 Wu, G., Li, L., Li, J.-H., and Xu, B.-Q. (2006). Methanol electrooxidation on Pt particles dispersed into PANI/SWNT composite films. *J. Power Sources* 155: 118–127.

90 Selvaraj, V. and Alagar, M. (2007). Pt and Pt–Ru nanoparticles decorated polypyrrole/multiwalled carbon nanotubes and their catalytic activity towards methanol oxidation. *Electrochem. Commun.* 9: 1145–1153.

91 Selvaraj, V. and Alagar, M. (2008). Ethylene glycol oxidation on Pt and Pt–Ru nanoparticle decorated polythiophene/multiwalled carbon nanotube composites for fuel cell applications. *Nanotechnology* 19: 045504.

92 Shi, L., Liang, R.-P., and Qiu, J.-D. (2012). Controllable deposition of platinum nanoparticles on polyaniline-functionalized carbon nanotubes. *J. Mater. Chem.* 22: 17196–17203.

93 Prasanna, D. and Selvaraj, V. (2016). Cyclophosphazene based conductive polymer-carbon nanotube composite as novel supporting material for methanol fuel cell applications. *J. Colloid Interface Sci.* 472: 116–125.

94 Wei, L., Fan, Y.J., Ma, J.H. et al. (2013). Highly dispersed Pt nanoparticles supported on manganese oxide-poly(3,4-ethylenedioxythiophene) carbon nanotubes composite for enhanced methanol electrooxidation. *J. Power Sources* 238: 157–164.

95 Noroozifar, M., Khorasani-Motlagh, M., Ekrami-Kakhki, M.-S., and Khaleghian-Moghadam, R. (2014). Electrochemical investigation of Pd nanoparticles and MWCNTs supported Pd nanoparticles-coated electrodes for alcohols (C1–C3) oxidation in fuel cells. *J. Appl. Electrochem.* 44: 233–243.

96 Fard, L.A., Ojani, R., and Raoof, J.B. (2016). Electrodeposition of three-dimensional Pd nanoflowers on a PPy@MWCNTs with superior electrocatalytic activity for methanol electrooxidation. *Int. J. Hydrogen Energy* 41: 17987–17994.

97 Wang, R.-X., Fan, Y.J., Wang, L. et al. (2015). Pt nanocatalysts on polyindole functionalized carbon nanotubes composite with high performance for methanol electrooxidation. *J. Power Sources* 287: 341–348.

98 Khan, A.H., Ghosh, S., Pradhan, B. et al. (2017). Two-dimensional (2D) nanomaterials towards electrochemical nanoarchitectonics in energy-related applications. *Bull. Chem. Soc. Jpn.* 90: 1–21.

99 Ghosh, S., Kar, P., Bhandary, N. et al. (2017). Reduced graphene oxide supported hierarchical flower like manganese oxide as efficient electrocatalysts toward reduction and evolution of oxygen. *Int. J. Hydrogen Energy* 42: 4111–4122.

100 Yang, L., Tang, Y., Yan, D. et al. (2016). Polyaniline-reduced graphene oxide hybrid nanosheets with nearly vertical orientation anchoring palladium nanoparticles for highly active and stable electrocatalysis. *ACS Appl. Mater. Interfaces* 8: 169–176.

101 Choe, J.E., Ahmed, M.S., and Jeon, S. (2015). 3,4-Ethylenedioxythiophene functionalized graphene with palladium nanoparticles for enhanced electrocatalytic oxygen reduction reaction. *J. Power Sources* 281: 211–218.

102 Yang, S., Shen, C., Liang, Y. et al. (2011). Graphene nanosheets-polypyrrole hybrid material as a highly active catalyst support for formic acid electro-oxidation. *Nanoscale* 3: 3277–3284.

103 Dinari, M., Momeni, M.M., and Afshari, M. (2016). Fabrication and characterization of hybrid films based on polyaniline and graphitic carbon nitride nanosheet. *J. Appl. Polym. Sci.* 133: 44059–44061.

104 Eswaran, M., Dhanusuraman, R., Tsai, P.C., and Ponnusamy, V.K. (2019). One-step preparation of graphitic carbon nitride/Polyaniline/Palladium nanoparticles based nanohybrid composite modified electrode for efficient methanol electro-oxidation. *Fuel* 251: 91–97.

7

Conjugated Polymer Nanostructures for Photocatalysis

Srabanti Ghosh

CSIR-Central Glass and Ceramic Research Institute, 196, Raja S. C. Mullick Road, Kolkata 700032, India

7.1 Introduction

Semiconductor photocatalysis has aroused an increasing interest in environmental remediation technology for water disinfection and energy conversion application [1–5]. In general, a significant number of inorganic semiconductor materials have been examined for the pollutant removal and photocatalytic water-splitting reaction, in fact most of them are oxide materials and based on the engineering of their electronic structure and heterojunctions formation and on the modification of the surface properties by noble metals or co-catalysts to achieve increased charge separation [6–10]. However, sufficiently stable and efficient visible light driven photocatalytic activity of the modified materials for practical use has not yet been realized. To utilize the solar energy more efficiently, the development of photocatalysts having a narrow band gap and wide light absorption range, efficient charge separation, photo-stable, chemically inert, reusable, and low cost is therefore important. Hence, discovery of a new material to enhance the energy conversion efficiency via manipulating the aforementioned important factors is a continuous matter of concern. Among various newly developed photocatalysts, conjugated polymer nanostructures (CPNs) with fascinating conjugated backbone consisting alternating single and double bonds along the polymer backbone (conjugated bonds), e.g. acetylene or that are composed of aromatic rings such as phenylene, naphthalene, anthracene, pyrrole, and thiophene, which are of low-cost, earth-abundant elements, have drawn broad attention as a robust, metal-free, and visible-light-active material in the fields of both environmental remediation and solar energy conversion [11–14]. The details of polymer structures and electronic properties have been described in Chapter 1. It is noted that a significant change in physicochemical properties of CP has been realized in nanoscale dimensions compared to their bulk counterpart. The CPNs show high surface area, unique optoelectronic properties, stability, flexibility and processability, high electrical conductivity, and high electrochemical activity, as compared with its macrogranular structure or self-supporting films [15–18]. For example, Ghosh et al. [19]

Conjugated Polymer Nanostructures for Energy Conversion and Storage Applications,
First Edition. Edited by Srabanti Ghosh.

reported that the electrical conductivity of the poly-(diphenylbutadiyne) (PDPB) nanostructures is 0.13 S/cm, which is several order of magnitude higher compared to the bulk polyacetylene (10^{-11} S/cm). There are many reports on morphology and size depend electric conductivity of CPNs, such as Jang et al. [20] obtained smaller size of polyaniline (PANI) nanoparticles (4 nm) with high crystallinity, which demonstrated high conductivity of 85 S/cm due to a highly compact and ordered structure of PANI chains. Wang et al. [21] showed greatly enhanced conductivity of self-assembled interconnected one-dimensional PPy nanofibers due to enhanced interchain charge transport, P3HT nanowires possessed a good crystallinity, high carrier mobility, and a favorable optical absorption spectrum developed by Friedel et al. [22], dependence of transport properties on shape of one-dimensional (1D) poly(3,4-ethylenedioxythiophene) (PEDOT) nanomaterials explored by Yoon et al. [23]. More importantly, CPNs demonstrated long red tail of an overall blue-shifted absorption spectrum, which may associated with a multitude of chain conformations and locally variable degrees of order and the size-dependent optoelectronic properties of CPN with the continuous bathochromic absorption and significantly enhanced emission behaviors originated from the smaller Frenkel excitons with the extended π-conjugation systems, whose exciton size can be tuned by both the chemical alteration of the π-conjugated molecular structures and their intermolecular interactions [24]. Hence, compared with their bulk forms, nanostructured conductive polymers exhibit improved physicochemical properties and shortened pathways for charge or mass or ion transport, good crystallinity, a high carrier mobility, and a favorable optical absorption spectrum make them ideal for applications in photocatalysis. CPNs based catalytic materials may be broadly classified into two categories, (i) nanostructures such as nanoparticles (NPs), nanowires, nanofibers, and nanotubes of pure conjugated polymers; and (ii) nanocomposites, which are mixtures of metal or metal oxide nanoparticles with CP at nanoscale. The nanostructure engineering and hybridization of polymer have received extensive attention particularly in the field of energy conversion application because of their facile synthesis, easy functionalization, attractive electronic band structure, high physicochemical stability, and photocatalytic activity [25, 26]. To promote photocatalytic efficiencies via extending the absorption of solar energy and facile charge separation, a series of metal, carbon material, inorganic semiconductor, etc. has been integrated with CP, which showed promising application in the field of catalysis [27–32]. Up to now, many excellent reviews regarding the development of conducting polymer such as polyaniline, polypyrrole, polymer film electrode, and their applications in sensing, solar cell, biomedical, etc. have been appeared [33–35]. The other reviews based on conjugated polymer nanocomposites for sensor, biomedical applications, wastewater purification, microwave absorbing materials, and modern advanced devices have been reported [36–40]. In the last few years, a considerable number of novel strategies including heterojunctions and composites have been proposed to offer polymer nanocomposites as an energy storage material in Li-ion battery and supercapacitor applications [41, 42]. Moreover, the evaluation of their effectiveness in electrocatalysis and fuel cell application has been summarized in Chapter 6. This chapter presents the latest advancements in the rational design and development of CPNs and modified or functionalized CPNs

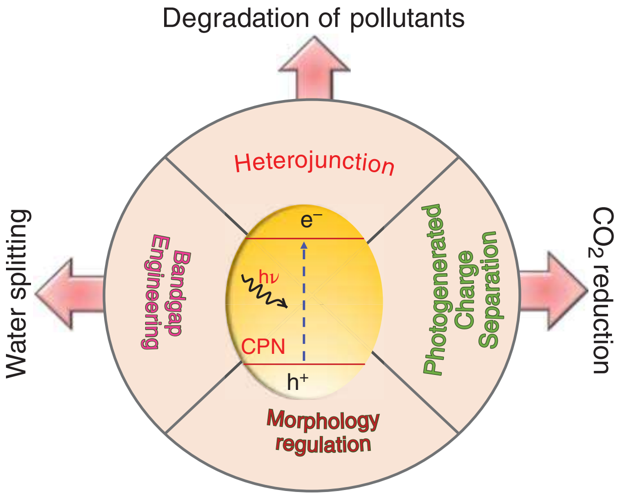

Figure 7.1 Possible application of conjugated polymers nanostructures in photocatalysis.

photocatalysts for pollutant degradation, water splitting, hydrogen production, and carbon dioxide reduction as shown in Figure 7.1. Then a series of highly efficient CPN based photocatalysts, e.g. metal/CPNs, semiconductor/CPNs, graphitic carbon nitride (g-C_3N_4)/CPNs, carbon/CPNs, and sensitizer/CPNs, are also exemplified.

7.2 Application of Conjugated Polymer Nanostructures as Photocatalysts

7.2.1 Photocatalysis for Environmental Protection and Organic Pollutant Degradation

The direct disposal of heavy metal, colored wastes such as dyes, pigments into water from various textiles, paper, plastics, tannery, and paints industries causes serious environmental pollutions, and solar light photocatalysis has been considered as the economic way for detoxification of wastewater [2, 43, 44]. Recently, carbon nanostructures have been used as photocatalysts with high carrier mobility and well-matched energy levels with inorganic semiconductor, forming an interface that enhanced charge separation [45–47]. In this context, CPNs have been considered as a promising candidate for efficient photocatalysts for organic pollutant removal under visible light because of their small band gaps, stable structures, and unique optoelectronic properties and can be produced at relatively low cost [48]. Ghosh et al. [49] reported the use of CPN as photocatalysts under visible light. The PDPB nanofibers of tunable diameter (5–25 nm) were fabricated in the oil tubes of the hexagonal mesophases followed by photo-induced radical polymerization using a chemical initiator (benzoin methyl ether, BME, 1%) via 1,4-addition reaction to form alternating ene-yne polymer chains or by γ irradiation without using free radical initiators [50] as shown in Figure 7.2a,b.

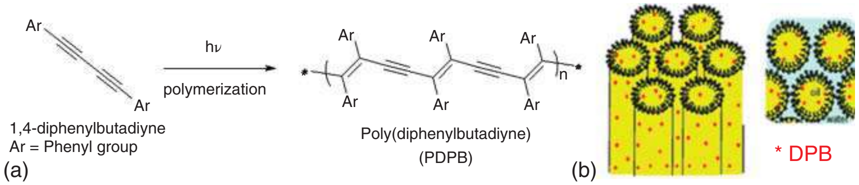

Figure 7.2 (a) Schematic representation of polymerization of diphenylbutadiyne (DPB) by UV irradiation, (b) hexagonal mesophases loaded with DPB. Source: Ghosh et al. [50]. © Royal Society of Chemistry.

Under a visible light irradiation, PDPB nanofibers demonstrated significant catalytic activity for the degradation of phenol and methyl orange as model pollutants without the assistance of sacrificial reagents or precious metal co-catalysts. It was shown that polymer nanostructures are very stable even after repeated cycling. PDPB nanofibers show a high photocatalytic activity, 75% photodegradation of MO under visible light irradiation much higher than that of plasmonic metal modified traditional oxides semiconductor, TiO_2 (19%). The authors investigated the electronic structure of polymer nanofibers and effect of scavengers for trapping photo-induced charges to explore the photocatalytic mechanism. Based on density functional theory (DFT) calculation, the calculated band gap value of the PDPB nanofibers is 1.95 eV, which was further supported with experimental study through cyclic voltammetry (CV) measurement of energy gap around 1.81 eV. The trapping experimental result indicated that the role oxidative radicals ($O_2^{\cdot -}$ superoxide radical, $^{\cdot}OH$ radicals, etc.), which can degrade and mineralize organic pollutants. The author proposed that when PDPB nanostructures illuminated with photons of energy exceeding or equal to the band gap ($E \geq 1.81$ eV or $\lambda \leq 685$ nm), excess electrons and holes are formed in the conjugated polymer chains. Further, the electrons and holes migrate to the semiconductor surface and generate highly oxidative radicals ($O_2^{\cdot -}$ superoxide radical, $^{\cdot}OH$ radicals, etc.), which can degrade and mineralize organic pollutants through the consideration of energy levels as shown in Figure 7.3.

Under visible light, electrons are injected from the CP and react with oxygen to form the oxidizing $O_2^{\cdot -}$ superoxide radical:

$$O_2 + e^- \rightarrow O_2 \cdot^- \tag{7.1}$$

According to the valence band (VB) energy level, OH^- cannot react with the holes to yield oxidative $^{\cdot}OH$; however, a small amount of $^{\cdot}OH$ radicals can be formed by the following reactions:

$$O_2 \cdot^- + H^+ \rightarrow HO_2\cdot \tag{7.2}$$

$$2\ HO_2\cdot \rightarrow H_2O_2 + O_2 \tag{7.3}$$

$$H_2O_2 + O_2 \cdot^- \rightarrow \cdot OH + O_2 + OH^- \tag{7.4}$$

$$H_2O_2 + h\nu \rightarrow 2 \cdot OH \tag{7.5}$$

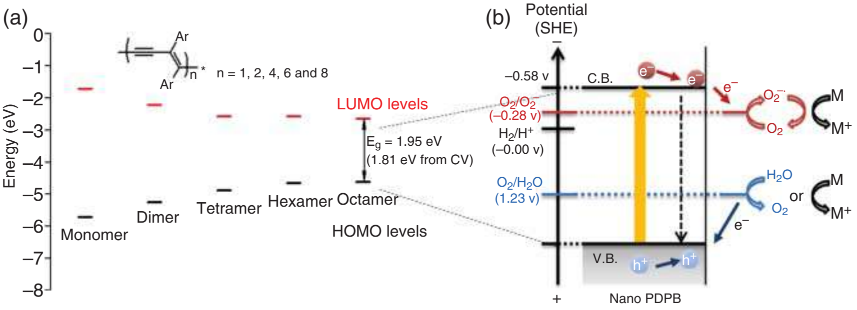

Figure 7.3 (a) Energy diagram of PDPB polymer representing the evaluated HOMO and LUMO levels by density functional theory. (b) Possible photocatalysis mechanism with charge separation in nano PDPB, where organic pollutants (noted as M), V. B. and C. B. represent the valence band and the conduction band of PDPB polymer respectively. Source: Ghosh et al. [49].

PEDOT has been regarded as another promising conjugated polymer for photocatalytic application owing to narrow band gap excellent environmental stability and high electrical conductivity [51–53]. Ghosh et al. [54] reported synthesis of PEDOT nanostructures with spindle-like or vesicle-like shapes in the hydrophobic domains of hexagonal mesophases via chemical oxidative polymerization of 3,4 ethylenedioxythiophene (EDOT) monomers using $FeCl_3$ as oxidizing agent as shown in Figure 7.4a,b. A systematic comparison of catalytic performances between polymers and modified TiO_2 for the degradation of MO under visible light is displayed in Figure 7.4c. The results indicated that the highest catalytic activity was achieved for the PEDOT nanospindles with MO photodegradation of 100% degradation after 180 minutes irradiation compared with PDPB nanofibers and metal modified P25-TiO_2. It is worth noting that PEDOT vesicles remained inactive for both phenol and MO degradation under visible light [55]. Although, both PEDOT polymer structures can absorb light in visible region, photo-induced electrons are less mobile (i.e. lower conductivity) in PEDOT vesicle structures and the recombination of charge carriers may be faster. The results showed that the conductivity of PEDOT vesicles (7×10^{-2} S/cm) is much lower in comparison with that of PEDOT nanospindles (0.4 S/cm), which support the lower photocatalytic degradation of organic molecules observed for PEDOT vesicles compared with PEDOT nanospindles. Additionally, due to larger size of vesicle PEDOT suggests presence of more defects in vesicles (sub-micron size) and bulk PEDOT favoring higher e^-–h^+ recombination. Similar results also reported previously for PDPB nanofibers having significantly high photocatalytic activity than bulk PDPB. The results showed that nanostructure and morphology of the conjugated polymer played significant role in photocatalytic activity.

The enhanced catalytic activity can be explained on the basis of band gap structure of the PEDOT nanostructures and along with the effects of scavengers for degradation of organic pollutants. Compared with PDPB or TiO_2, less energy is required to promote an electron to the conduction band for PEDOT due to low band gap (1.69 eV). Based on proposed energy diagram, under visible-light irradiation, a

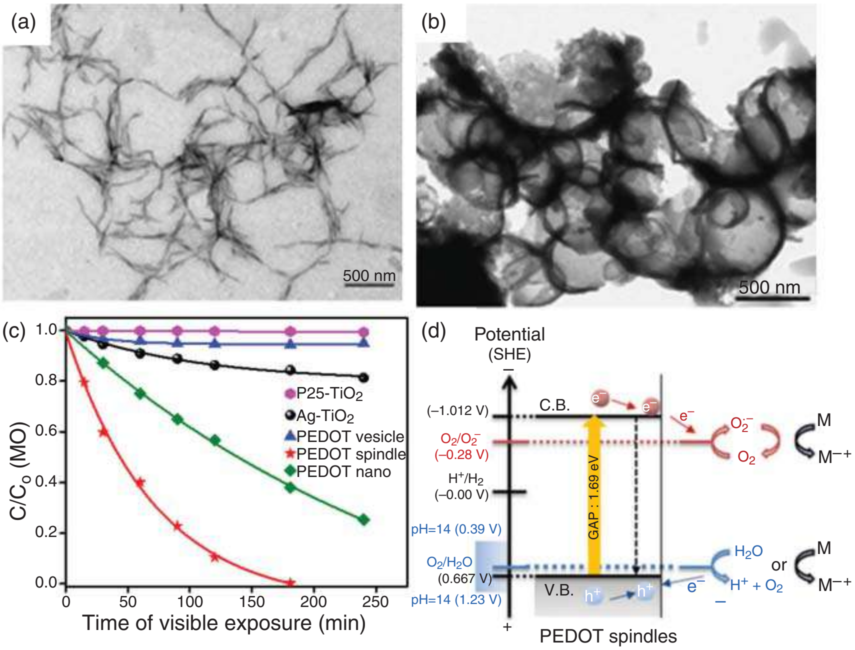

Figure 7.4 (a,b) TEM images of PEDOT synthesized in hexagonal mesophases. (c) Photocatalytic degradation of methyl orange (MO) in the presence of commercial P25 TiO$_2$ and Ag-TiO$_2$, PDPB nanofibers and the synthesized PEDOT vesicles and PEDOT nanospindles under visible light (>450 nm). (d) Photocatalysis mechanism with charge separation in PEDOT nanospindles with electron reducing oxygen and hole oxidizing water. Source: (a, b) Reproduced with permission from Ghosh et al. [55]. Copyright 2015, Nature, Springer, (c, d) Ghosh et al. [55]. Licensed Under CC BY 4.0.

photon (with energy higher that the band gap) excites an electron from the valence band (VB) to the conduction band (CB) of PEDOT nanospindles and the electrons can easily migrate to the surface of the PEDOT and react with oxygen to form oxidizing $O_2^{\cdot-}$ superoxide radical (Figure 7.4d). Moreover, the photogenerated holes on PEDOT (E_{CB}, +0.139 vs. Ag corresponding to +0.667 eV vs. SHE) cannot produce hydroxyl radicals. It is noted that the photocatalysis mechanism involves $O_2^{\cdot-}$, photo induced h$^+$, and HO$^{\cdot}$ radicals mediated degradation of organic pollutant with effective charge separation in PEDOT nanospindles. Hence, PEDOT nanostructures having a narrow band gap and excellent light absorption in visible and near infrared region demonstrate unprecedented photocatalytic activities for water treatment without the assistance of sacrificial reagents and even better than TiO$_2$ as benchmark catalyst. Further, Yuan et al. [56] compared the photocatalytic activity of PPy nanostructures prepared by two different method using hexagonal mesophases as a template via chemical oxidation with homogeneous spherical nanostructures of an average size of 40 nm and direct polymerization by using gamma radiation as shown in Figure 7.5a,b where PPy nanoballs of uniform sizes of 400 nm obtained. PPy-NS-c nanostructures were synthesized by chemical oxidation of the PPy monomer confined in the oil phase of hexagonal mesophases with FeCl$_3$ in another mesophases

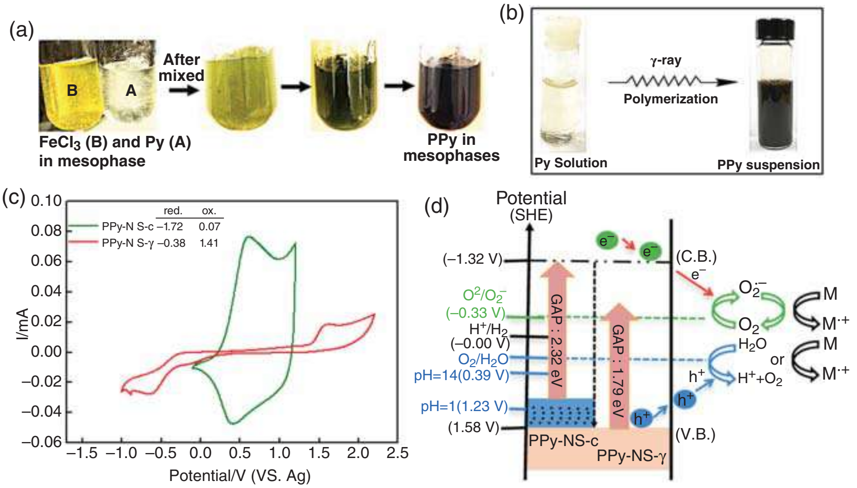

Figure 7.5 (a) Chemical oxidative synthesis process of PPy in mesophases leading to PPy-NS-c. (b) Radiolytic polymerization of PPy. (c) Cyclic Voltammetry of PPy recorded at 20 mV/s in acetonitrile and 0.1 M tetrabutylammonium perchlorate. (d) Energy ban diagram of both PPy nanostructures. Source: (a, b) Reproduced with permission from Yuan et al. [56]. Copyright 2018 Elsevier, (c, d) Yuan et al. [56].

followed by mixing, whereas radiolysis of aqueous solution is able to polymerize monomers into polymers by oxidative hydroxyl radical reaction. A further detailed discussion on radiolytic synthesis of polymer nanostructures has been included in Chapter 4. The results showed that PPy-NS-c demonstrated the best photocatalytic activity with degradation rate of phenol about 100% after 4.5 hours under UV light compared with PPy-NS-γ. To further understand the photocatalytic activity of PPy nanostructures, their electronic properties such as the energy levels of the lowest unoccupied molecular orbital (LUMO) and the highest occupied molecular orbital (HOMO) and band gap were measured by the CV. Figure 7.5c shows CV of PPy-NS-γ, and PPy-NS, the main oxidation (p-doping) process occurs at onset potentials of 0.07 V (PPy-NS-c) and 1.41 V (PPy-NS-γ), while reduction (*n*-doping) process starts at −1.72 V (PPy-NS-c) and − 0.38 V (PPy-NS-γ) and band gap was estimated to be 1.79 and 2.32 eV, respectively. The suitable potential of energy level (Figure 7.5d) and narrow band gap of PPy nanosphere make them suitable for potential application in optoelectronics and photocatalysis.

Poly(3-hexylthiophene) (P3HT) nanowires of about 30 nm diameter deposited on flat supports such as quartz and applied them as photocatalysts for degradation of phenol and Rhodamine B under visible light irradiation [57]. It is noted that the photocatalytic activity of these P3HT nanostructures is much enhanced, with highly accelerated phenol degradation kinetics when they are supported, which reveal a new perspective in photocatalytic reactors and self-cleaning surfaces. It is worth noting that conjugated polymers have high binding energy of excitons and to improve transfer efficiency of charge carriers, the construction of a heterostructure that facilitates the special charge separation through interfacial junction is an

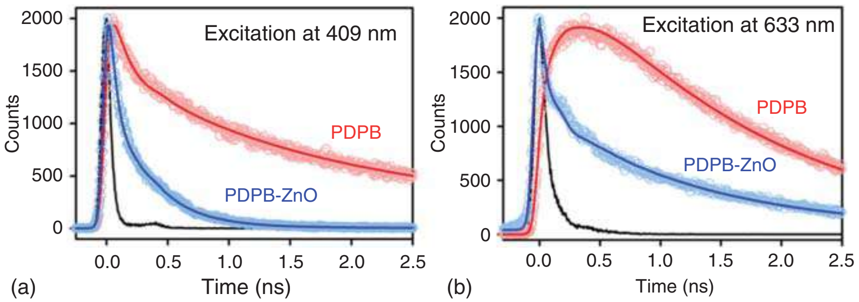

Figure 7.6 The interfacial carrier dynamics at the heterojunction of PDPB-ZnO. Fluorescence decay profiles of PDPB and PDPB-ZnO at (a) 520 nm (excitation at 409 nm) (b) 660 nm (excitation at 633 nm). Source: Sardar et al. [59]. Licensed Under CC BY 4.0.

effective method to realize high catalytic activity under visible light irradiation [58]. Recently, the combination of different CPNs with semiconductors and metal of different structure and unique properties to construct heterojunction, which can improve the charge separation, light absorption, and steadiness, offers a promising way to achieve efficient photocatalyst. Sardar et al. [59] reported an effective surface modification method to activate PDPB nanofibers through deposition of ZnO NPs and studied the ultrafast photo-induced charge separation at the semiconductor-conjugated polymer heterojunction (ZnO-PDPB) interface. It was shown that fluorescence decay curve of ZnO-PDPB deviates from single exponential to biexponential display one significant shorter lifetime 30 ps and a longer lifetime of 1.24 ns, which indicates the efficient photo-induced charge separation takes place at the nano-heterojunction where electrons are transferred from the CP nanofibers to the ZnO NPs and holes remain in the polymer (Figure 7.6a,b). The highly efficient charge separation has been corroborated with ~fivefold increase in photocatalytic degradation of methyl orange dye in comparison with pure PDPB polymer nanofibers under visible light irradiation. Author also proposed the Förster resonance energy transfer (FRET) from the donor ZnO NPs to the acceptor PDPB nanofibers. A shorter excited state lifetime of the ZnO NPs in the picosecond resolved fluorescence decay profile is observed in the presence of PDPB. From FRET calculations, the distance between the donor ZnO NPs and acceptor PDPB nanofibers is determined to be 3.4 and 3.1 nm for two different defect states of ZnO, which is consistent with the size of the ZnO NPs (radius = 2.5 nm). This further confirms the proximity between the PDPB and ZnO as well as UV light harvesting in the light harvesting nanohybrid (LHNH) via energy transfer from ZnO to PDPB nanofibers.

Following this work, few studies have been reported using PDPB nanofibers as component for synthesizing semiconductor-based composites with high catalytic activity. For example, Wang et al. [60] prepared a PDPB/SnO_2 p–n heterojunction by an *in situ* growth route that demonstrated four times higher solar-driven photodegradation rate of Rhodamine B than that of the pure SnO_2 and two times higher than that of the pure PDPB nanofibers. Formation of heterojunction between PDPB and SnO_2 may promote the transference efficiency of electrons and holes between these two components and PDPB could act as the sensitizer to enlarge the solar light absorption region of the heterojunction. Further, new polymer composites consisting of PDPB and g-C_3N_4 have been reported by Lei et al. [61]. It was shown that the presence of PDPB in composites can clearly increase the visible light absorption of the catalysts, consequently, enhanced visible-light photocatalytic activity for degradation of Rh B and phenol. A similar group also reported gold-loaded graphene oxide/PDPB (polymer poly(diphenylbutadiyne)) (Au-GO/PDPB) for synchronous photocatalytic removal of heavy metal ions and organic pollutants. The optimal loading mass of GO and Au NPs on the PDPB; the Au_1-GO_2/PDPB (2.0 wt% GO and 1.0 wt% Au) composite displayed the best photocatalytic activity for the synchronous photoreduction of hexavalent chromium (Cr(VI)) and photo-oxidation of phenol [62]. Ghosh et al. [63] also reported visible-light-induced reduction of Cr(VI) by PDPB-ZnO nanohybrids. The ZnO modified PDPB nanofiber based electrodes were fabricated by facile adsorption of ZnO NPs on PDPB nanofibers, which demonstrated enhanced photocatalytic activity compared with bare PDPB for the photoreduction of hexavalent chromium Cr(VI), which is consistent with trend obtained for organic pollutant removal. The effect of polymer loading showed that ZnO loaded with 10 wt% of PDPB displayed highest catalytic activity for Cr(VI) reduction under visible light irradiation, which was further confirmed by X-ray photoelectron spectroscopy data revealed the presence of Cr(III) on the surface of nanohybrid during photoreduction of Cr(VI). The enhanced photocatalytic activity of PDPB-ZnO could be attributed from the co-sensitization of ZnO NPs by oligomeric and polymer chain unit of PDPB nanofibers as well as due to the formation of donor-acceptor junction introduced by the n-type inorganic semiconductor (ZnO) and p-type organic semiconductor (PDPB) having higher separation and transfer efficiency of photo excited electrons. Mott–Schottky (M–S) analysis ($1/C^2$ vs. electrode potential) has been performed to determine the energy band structure including band gaps, CB, and VB positions of ZnO, PDPB, PDPB-ZnO nanohybrids. The flat band potential of a semiconductor can be obtained from Mott–Schottky plot using the Eq. (7.6):

$$\frac{1}{C^2} = \frac{2}{q\varepsilon\varepsilon_0 N_d}\left(V_{\mathrm{app}} - V_{\mathrm{FB}} - \frac{kT}{q}\right) \tag{7.6}$$

where ε is the dielectric constant of the semiconductor, ε_0 is the permittivity of the vacuum, N_{d} is the donor density, V_{app} is the applied potential, V_{FB} is the flat band potential, and kT/q is the temperature-dependent term. The intercept of linear plot at $1/C^2 = 0$ gives the flat band potential.

In Figure 7.7a, the ZnO shows a positive slope in the M–S plots with flat band potential −0.34 V (vs. Ag/AgCl), indicating n-type behavior with electrons as the majority carriers. In contrast, PDPB shows a positive slope in the M–S plots with flat band potential 1.61 V (vs. Ag/AgCl), indicating p-type behavior. However, the co-existence of positive and negative slopes with two flat band potential values (−0.88 V and 0.68 V vs. Ag/AgCl) have been observed for PDPB-ZnO NHs (10%), indicating the formation of p–n junction within the nanohybrids. The flat band

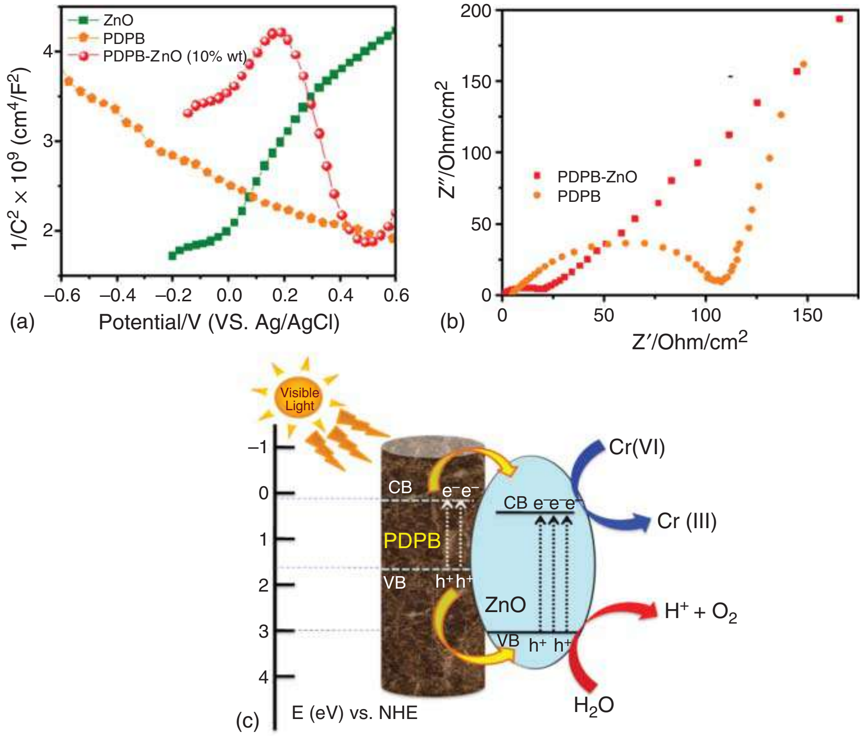

Figure 7.7 (a) Mott–Schottky plots for pure ZnO, PDPB, and PDPB-ZnO NHs (10%) in the presence of 0.1 M Na_2SO_4 electrolytes (pH 7) using an AC frequency of 1000 Hz. (b) The electrochemical impedance spectroscopy of (a) PDPB-ZnO NHs and bare PDPB in 0.1 M Na_2SO_4 aqueous solution. (c) Proposed photocatalytic process for PDPB-ZnO under visible light irradiation. Source: Ghosh et al. [63]. Copyright 2018 Elsevier.

potential of PDPB-ZnO NHs is more negative when compare to pure ZnO, suggesting the decrease in band bending, consequently facilitating the transfer of electrons. Interestingly, the calculated charge carrier concentration (N_d) from the slope of M–S plot suggests that an increase in the N_d value for PDPB-ZnO NHs (8.5×10^{19} cm^{-3}) compared with ZnO (2.5×10^{19} cm^{-3}) and PDPB (6.2×10^{19} cm^{-3}) indicates charge transfer of ZnO has been improved due to formation of heterojunction with CP, which facilitate the charge separation. Figure 7.7b showed electrochemical impedance spectroscopy (EIS) Nyquist plots of PDPB nanofibers and PDPB-ZnO NHs where the semicircle portion corresponds to the charge transfer process, with the diameter of the semicircle equivalent to the charge transfer resistance (R_{ct}). The linear portion reflects the diffusion limited processes at the electrode interface. The R_{ct} decreased from 107.7 Ω (PDPB) to 21.5 Ω (PDPB-ZnO), suggesting that the PDPB-ZnO NHs can facilitate the charge transfer. Hence, EIS measurement further confirmed that the presence of ZnO NPs in nanohybrid could significantly improve the electron transfer efficiency of CP and the photocatalytic efficiency. The visible light induced Cr(VI) reduction reaction in presence of PDPB-ZnO catalysts can be proposed by step reactions in Eqs. (7.7) and (7.8).

$$\mathrm{PDPB - ZnO + h\nu \rightarrow PDPB - ZnO\,(e^-, h^+)} \tag{7.6}$$

$$\mathrm{Cr_2O_7{}^{2-} + 14H^+ + 6e^- \rightarrow 2Cr^{3+} + 7H_2O} \tag{7.7}$$

Figure 7.7c displayed that the excited electrons from PDPB can be readily injected into the conduction band of ZnO, after migration of these charge species to the catalysts surface, the photogenerated electrons reduce Cr(VI) to Cr(III). Additionally, the effects of free radical scavengers on the reduction of Cr(VI) indicate that as an electron scavenger, O_2 may competes with Cr(VI) for the photogenerated electrons at CB of PDPB-ZnO catalysts, which will decrease the Cr(VI) reduction rate whereas presence of iso-propanol as hole scavengers enhances Cr(VI) reduction. This is due to competitive reaction of excess holes with isopropanol lower the charge recombination rate and consequently increases the Cr(VI) reduction kinetics.

In order to enhance the charge separation and increase the photocatalytic performance, recently, Ghosh et al. [64] reported that the sensitization of CPNs with plasmonic nanocrystals that can improve charge separation as well as useful to promote photocatalysis under visible light where metallic nanostructures act as the light absorber and also increases catalytic active site. The results showed that the decoration of PEDOT nanofibers with Au NPs improved the photocatalytic removal of MO and Rh B where Au/PEDOT can reduce 100% of dye molecules within 90 minutes under visible light irradiation and 60% and 80% can removed by pure PEDOT nanofibers for MO and Rh. B, respectively. The author proposed that immediately after irradiation under visible light, both in PEDOT nanofibers and Au/PEDOT NHs, exciton is generated, which is composed of holes in the highest occupied molecular orbital, (HOMO, h^+) and electrons in the lowest unoccupied molecular orbital, LUMO (LUMO, e^-) Eq. (7.8).

$$\mathrm{PEDOT + h\nu \rightarrow PEDOT\,(e^-{}_{LUMO}, h^+{}_{HOMO})} \tag{7.8}$$

However, CP follow the Frenkel type of exciton, usually having high binding energy in the order of 1 eV, consequently it is difficult to separate exciton. Whereas for Au/PEDOT, it is well accepted in the literature that Au NPs act as good electron reservoirs and improved separation between electrons and holes generated via photo-induced interfacial charge transfer [65, 66]. The photo-generated excitons are decomposed at the interface of the metal–polymer hybrid system to generate charge species (7.9).

$$\mathrm{PEDOT\,(e^-{}_{LUMO}, h^+{}_{HOMO}) + Au\,NPs \rightarrow Au\,(e^-{}_{LUMO}) + PEDOT\,(h^+{}_{HOMO})} \tag{7.9}$$

Further, the photogenerated electrons on the surface of Au NPs then react with dissolved oxygen in water to form oxidizing $O_2{}^{\cdot -}$ superoxide radical ($E^0\,(O_2/O_2\cdot{}^-) = -0.33\ V_{SHE}$). The superoxide radical anions then react with water to generate hydroperoxy radicals ($OH^{\cdot}$) (Eq. (7.10), (7.4)–(7.6)):

$$\mathrm{O_2 + Au\,NPs\,(e^-{}_{LUMO}) \rightarrow O_2\cdot{}^-} \tag{7.10}$$

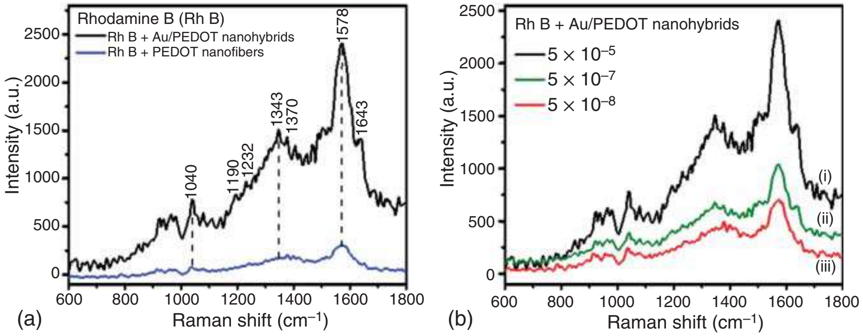

Figure 7.8 (a) Raman spectra of Rh B on the Au/PEDOT NHs and PEDOT nanofibers. Both samples were soaked in 5×10^{-5} M Rh B aqueous solution before the measurement. (b) A series of soaking concentrations of Rh B were used: 5×10^{-5} M (black line), 5×10^{-7} M (green line), 5×10^{-8} M (red line). The acquisition times were all 10 seconds. Source: Ghosh et al. [67]. Copyright 2018 Elsevier.

$$\mathrm{H_2O_2} + \mathrm{PEDOT}\,(\mathrm{h^+}_{\mathrm{HOMO}}) \rightarrow 2\,\mathrm{HO}\cdot \tag{7.11}$$

$$\mathrm{HO}\cdot + \mathrm{MO\ or\ Rh\ B} \rightarrow \mathrm{Degradation\ product} + \mathrm{CO_2} + \mathrm{H_2O} \tag{7.12}$$

Notably, Au/PEDOT nanohybrids (NHs) display high surface-enhanced Raman scattering (SERS) enhancement for simultaneous detection of dye and act as self-cleaning SERS substrate. The Au/PEDOT NHs spectra show the intense peaks of Rh B as evident from Figure 7.8a, whereas control PEDOT nanofibers illustrated relatively low SERS intensity, which may be associated with the charge transfer between PEDOT and the dye molecules. This suggests photo catalytically active Au/PEDOT NHs has been employed as an SERS substrate for the simultaneously detection and removal of dye molecules. Notably, Raman signals can be observed on Au/PEDOT NHs soaked with Rh B solution at a low concentration of 5×10^{-8} M due to enhancement effect as shown in Figure 7.8b. Calculation of enhancement factor (EF) for both probe molecules with Au/PEDOT substrate has been carried out by comparing SERS intensity with enhanced Raman intensity by following the Eq. (7.13):

$$\mathrm{EF} = \frac{I_{\mathrm{SERS}} C_{\mathrm{RS}}}{I_{\mathrm{RS}} C_{\mathrm{SERS}}} \tag{7.13}$$

where I_{SERS} and I_{RS} were the respective Raman intensities with and without Au NPs on PEDOT substrates, respectively, for the analyte concerned. C_{SERS} and C_{RS} represents concentration of the dye adsorbed on the PEDOT substrates with and without Au NPs attached to it, respectively. The EF found is 2.9×10^4 for Rh B considering the $1578\,\mathrm{cm^{-1}}$ peak in the SERS spectrum. The Raman enhancement could be attributed to the combined structures of both polymer nanofibers and the well dispersed Au NPs, which is potential for the development of highly efficient SERS substrates. In another example, Saha et al. [68] explored the catalytic activity of 2D $\mathrm{MoS_2}$-1D PANI for the degradation of organic pollutants such as methylene blue (MB) and 4-chlorophenol (4-CP). Notably, poor electronic conductivity and agglomeration between the nanosheets of 2D MoS_2 layers can be overcome by intercalating with 1D PANI and the improved photoactivity has been proposed by the transfer of photogenerated electrons from PANI to the CB of MoS_2, thus preventing the direct recombination of electrons and holes. Many studies showed that performance of photocatalysts consists of PANI with semiconductor, which can enhance the migration efficiency of charge carriers between PANI and semiconductor. For instance, PANI@CdS [69], Ag_3PO_4@PANI [70], PANI/BiOCl [71], PANI/ZnO [72], PANI/TiO_2 [73], PANI/$BiVO_4$ [74, 75], PANI/$CuCr_2O_4$ [76], etc. Further, Xu et al. [77] reported a unique polyaniline-/bismuth-rich bismuth oxyhalide composite using long-wavelength light for the degradation of ciprofloxacin (CIP) and tetracycline (TC) antibiotics. The results indicated that use of the long wavelength light ($\lambda > 550$ nm) due to the introduction of PANI helps to extend the light absorption region and thereby promoting the photocatalytic ability due to the interface interaction between PANI and $Bi_4O_5Br_2$, which contributes to the electron–hole separation. A hierarchical composite of PANI nanorods is grown on the surface of g-C_3N_4 sheets (CN-PANI), which displayed much higher photocatalytic activity than pure g-C_3N_4 and PANI for the photodegradation of MO under visible light irradiation [78]. Patra and coworkers provide a perspective on the understanding of the light harvesting processes like exciton dynamics, energy transfer, exciton generation and diffusion, and charge carrier dynamics, at the interface of polymer and nanomaterials, which is crucial for photocatalysis applications [79]. Jana et al. [80] reported that strong electronic interaction of semiconducting P3HT polymer NPs with Au NPs exhibits a bathochromic shift of absorption bands and significant photoluminescence quenching of P3HT NPs in the raspberry type organic–inorganic hybrid nanostructures of the poly-3-hexylthiophene–Au NPs, which demonstrated high photocatalytic activity under the visible light irradiation and the degradation efficiency is found to be 90.6%. They proposed that the electron transfer process happened at the interphase between P3HT polymer nanoparticles (PNPs) and Au NPs because the HOMO and LUMO positions of regiorandom P3HT are −5.5 and −3.2 eV, respectively, and the work function of Au NPs is −5.1 eV. Consequently, electrostatic attraction between opposite charged PNPs with negatively charged Au NPs may enhance the charge separation at the interface by electron transfer from PNP to Au NP, which is further supported with decay dynamics of the donor in the presence of an acceptor reveals the shortening of the decay time, and the appearance of a faster decay component confirms the electron transfer from the PNP to Au NP. Same group also showed electron transfer process from the excited state of poly[2-methoxy-5-(2-ethylhexyloxy)-1,4-phenylenevinylene] (MEH-PPV) NPs to reduce graphene oxides (r-GO) at the interface though ultrafast femtosecond up-conversion and transient absorption spectroscopy study, and an increase (2.6-fold) of photocurrent under visible light illumination obtained due to charge separation in these nanocomposites has potential for the development of efficient light-harvesting systems [81]. The results showed electron transfer from MEH-PPV PNP towards r-GO by reducing the average decay time in ultrafast fluorescence spectroscopic study. Moreover, a series of ternary heterostructures has been developed for efficient removal of organic pollutant and most of them are based on polyaniline and pyrrole conjugated polymer. Very recently, Xie and Zhang [82] reported an efficient visible light active photocatalysts based on PANI with double Z-scheme PANI/Ag_3PO_4/CNO heterojunction, which showed excellent dye degradation activity. The results showed that the apparent degradation rate for Rh B reached up to 0.2668 min^{-1}, which is approximately 1.31, 2.68, 5.28, and 17.12 times faster than those of PANI/Ag_3PO_4, Ag_3PO_4/CNO, Ag_3PO_4, and CNO, respectively. Such enhanced activity has been proposed by considering the band structures of the three semiconductors and radical scavenging experiments, which significantly accelerates the transfer of photogenerated electrons on the conduction band of Ag_3PO_4 and both PANI and *in situ* grown Ag NPs act as electron mediators, thereby improving the activity and stability of Ag_3PO_4. Bu and Chen [83] obtained PANI/Ag/Ag_3PO_4 composites, which show strong photocatalytic activity and proposed the role of polyaniline. First, PANI with branch-like structure was prepared, and subsequently Ag_3PO_4 NPs were *in situ* grown on the surface of PANI. Then the *in situ* growth of Ag_3PO_4 NPs, some metallic Ag (Ag^0), was formed on the surface of PANI, resulting in the formation of PANI/Ag/Ag_3PO_4 composite. The significant high and stable catalytic activity for Rh B degradation is reported using 20 wt% PANI/Ag/Ag_3PO_4 heterostructure, which is four times higher than that of pure Ag_3PO_4. EIS can be used to study the migration ability and the interface reaction ability of the electrons at the heterojunction electric field between PANI and Ag_3PO_4. Figure 7.9a indicates the impedance value of Ag_3PO_4 is significantly larger than that of 20 wt% PANI/Ag/Ag_3PO_4 heterostructure, illustrating that PANI can clearly promote the reaction ability of the photogenerated electrons and holes on the interface between the electrolyte and Ag_3PO_4 and increase the migration ability of the photogenerated electrons and holes in the composite. This is further supported with the flat band potential calculated from Mott–Schottky plots. Both Ag_3PO_4 and 20 wt% PANI/Ag/Ag_3PO_4 show the characteristics of the n-type semiconductor from slopes of the tangent lines of the Mott–Schottky plots as shown in Figure 7.9b and the introducing of PANI onto the surface of Ag_3PO_4 negatively shifted the flat band potential, demonstrating that an interfacial electric field is built at the interface of PANI and Ag_3PO_4. Figure 7.9c displays the shift of the electronic energy level of Ag_3PO_4 due to the presence of extensively conjugated π system of PANI, which can inhibit the recombination of photo-induced e^-–h^+ and then facilitate the fast separation of photo-generated charge carriers. Although, the Fermi levels of PANI and Ag are much more negative than 0.74 V, however due to the formation of PANI/Ag/Ag_3PO_4, the energy band of the surface layer bended downward, consequently the electrons on the surface of Ag_3PO_4 will transfer to the surface of PANI to form an electron rich layer there, and a hole rich layer will form on the surface of Ag_3PO_4 at the same time.

Similar, enhanced photocatalytic activity of PPy@Ag/g-C_3N_4 has been reported for removal of various organic pollutants in water, which may originated from π conjugated electronic structures of PPy and Ag species as the electron transfer mediator between PPy and g-C_3N_4 and that facilitated the charge carrier separation and then expending the lifetime of the carriers [84]. A one-dimensional ternary nanostructure composed of Ag_2CO_3 nanorod cores coated with an intermediate

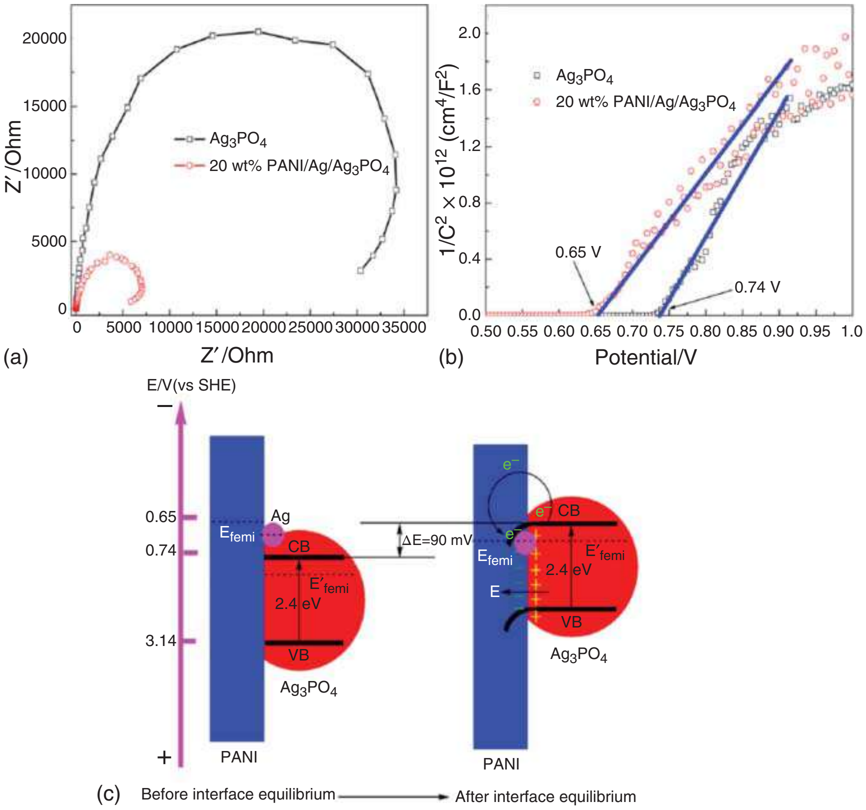

Figure 7.9 (a) EIS spectra and (b) Mott–Schottky plots of Ag_3PO_4 and PANI/Ag/Ag_3PO_4 heterostructure based photoelectrodes in 0.1 mol/l Na_2SO_4. (c) Schematic presentation of n energy levels of PANI/Ag/Ag_3PO_4. Source: Bu and Chen [83]. Copyright 2014, ACS Publications.

layer of Ag NPs and a sheath of CP PANI has been reported by Chen et al. [85]. Such composite nanorods exhibit significantly enhanced photoelectrochemical current response and photoactivity in degrading methyl orange under visible-light illumination ($\lambda > 420$ nm), which further proposed through facile charge separation via Z-scheme mechanism. Wu et al. [86] described an enhanced photocatalytic performance of a ZnO/rGO/polyaniline ternary nanocomposite for the photodegradation of methyl orange with a maximum degradation efficiency of almost 100% within 60 minutes under UV light irradiation compared with pure ZnO (15%). In such enhanced catalytic efficiency in ternary composite, rGO could reduce the recombination of electron–hole pairs, the PANI increases the absorption of light and adsorption of dyes, and the synergistic effect among ZnO, rGO, and PANI. Alternatively, another 2D based graphitic carbon nanosheets (CN-NS) based ternary heterostructure (CN-NS/PANI/ZnO) possesses excellent visible photocatalytic performance for MB and 4-CP degradation due to the synergetic effect of PANI and ZnO coupling [87]. It is worth noting that quaternary heterostructures

$BiVO_4$-GO-TiO_2-PANI demonstrated excellent photocatalytic efficiencies for methylene blue (MB) and phenol degradation under visible light irradiation after adhering the PANI to the photocatalyst [88]. Lee and Chang reviewed on recent development of conductive polymer based composite photocatalysts [89]. In Chapter 8, a detailed discussion on polymer-based nanocomposite photocatalysts is included.

7.2.2 Photocatalysis for Water Splitting and H_2 Generation

Photocatalytic hydrogen production from water splitting is a promising approach to resolve the high energy demand and environmental concerns [90], However, development of efficient photocatalysts is a major challenge to overcome the common issue such as limited light absorption, high charge recombination, and low quantum yield [1]. To overcome such limitation of photocatalysts, significant efforts have been devoted for the advancement of carbon-based photocatalysts due to their low fabrication cost, large surface area, high electronic conductivity, and tunable structures [91]. Up to now, most widely used carbon-based nanostructures including graphene, carbon nanotubes (CNTs), carbon quantum dots (CQDs), and graphitic carbon nitride (g-C_3N_4) have been used for water splitting due to their high physiochemical stability, earth abundant, and low synthesis cost [45, 92–94]. A significant advancement has been achieved for the development of polymeric g-C_3N_4 through surface modification, heterostructures or composites formation, and various review articles; book chapter covers application of g-C_3N_4 for water splitting [67, 95–97]. Since last five years, the area of conjugated polymer photocatalysts has evolved rapidly and a significant effort has been made to correlate structure–property relationship [98–103]. However, there is lack of understanding on why different polymers show very different photocatalytic activities.

Recently, poly[(9H-carbazole-2,7-diyl)-1,4-phenylene] and its derivatives, [101] covalent organic frameworks, [104–106], and porous organic polymers [107–110] have been investigated as promising photocatalyst systems. A brief summary on the recent development of various promising polymer photocatalysts for hydrogen evolution from aqueous solutions, including linear polymers, planarized polymers, triazine/heptazine polymers, and other related organic conjugated semiconductors, with a particular focus on the rational manipulation in the composition, architectures, and optical and electronic properties, has been reviewed by Dai and Liu [111]

For example, Wang et al. [112] reported 1,3-diyne-linked conjugated microporous polymer nanosheets (CMPNs) as a highly efficient photocatalysts for splitting pure water ($pH \approx 7$) into stoichiometric amounts of H_2 and O_2 under visible light. This observation further supported with first-principles calculations that revealed the photocatalytic H_2 and O_2 evolution reactions are energetically feasible for CMPNs under visible light irradiation. They prepared CPMNs by oxidative coupling of terminal alkynes such as 1,3,5-tris-(4-ethynylphenyl)-benzene (TEPB) and 1,3,5-triethynylbenzene (TEB) were tested for water splitting with apparent quantum efficiencies at 420 nm are 7.6% and 10.3%, respectively. Kong et al. [113] fabricated a self-assembled supramolecular system consisting of phosphoric acid substituted perylene diimide (P-PMPDI) nanobelts, which has been successfully developed for highly efficient photocatalytic hydrogen evolution. The results show that compared with a carboxylic substituent perylene diimide (P-CMPDI), P-PMPDI showed a superior H_2 evolution reaction rate of 11.7 mmol/(g/h) and a recorded apparent quantum yield (AQY) of 2.96% at 550 nm. In another example, Tian and coworkers [114] reported novel organic semiconducting polymer dots (Pdots) based on poly[(9,9′-dioctylfluorenyl-2,7-diyl)-co-(1,4-benzo-{2,1′,3} thiadiazole)] (PFBT) and polystyrene grafting with carboxyl-group-functionalized ethylene oxide (PS–PEG–COOH) as a photocatalyst toward visible-light-driven hydrogen generation in a completely organic solvent-free system. They proposed that the productive electron transfer quench of the excited state of Pdots by an electron donor is about 40% as well as Pdots can tolerate oxygen during catalysis, which is crucial for light-driven water splitting that further supported with an impressive initial rate constant of 8.3 mmol/(g /h) was obtained for visible-light-driven hydrogen production, which is 5-orders of magnitude higher than that of pristine PFBT polymer. The same group prepared modified polymer dots using photoactive polymer poly[(9,90-dioctylfluoreny-2,7-diyl)-co-(1,4-benzo-(2,10,3) thiadiazole)] (PFODTBT) that possess a hollow nanostructure under ultrasonication with a polymer shell mimicking the membrane of photosynthetic bacteria, integrated with photocatalytic CP and amphiphilic PEG–COOH–grafted polystyrene (PS) as shown in Figure 7.10a. [115]. It was shown that the nanostructure of Pdots was formed by self-assembled of particles with diameters 1–3 nm, having nanoscale porous polymer shell (thickness 6 nm) with a number of hydrophilic channels. The photocatalytic activity of hollow nanostructure shows 50 times enhancement of initial hydrogen evolution reaction (HER) rate as compared with solid NPs. Figure 7.10b shows the hydrogen production are 2.6, 4.6, and 18.1 mmol/(g/h) for Pdots with 90, 70, and 50 nm, respectively. The results show that a significant increase in the photocatalytic performance was achieved by the decrease in Pdots size from 90 to 50 nm, which suggests decrease in the particle size may highly increase the total surface area, consequently enhanced mass transport and light capture by light scattering in the hollow polymer structure.

Similarly, Pati et al. [116] showed that converting an organic polymer into polymer dots is an efficient way to improve the photocatalytic performance. It is noted that a highly efficient organic polymer nano-photocatalyst for light driven proton reduction has been developed with an initial rate of hydrogen evolution up to 50 mmol/(g/h). They proposed that nitrogen center of the benzothiadiazole unit plays a crucial role in the photocatalysis and that the Pdots structure holds a close to ideal geometry to enhance the photocatalysis through both experimental and theoretical study. Tseng et al. [117] reported a unique approach to prepare a series of cycloplatinated Pdots, in which the platinum complex unit is presynthesized as a comonomer and then covalently linked to a conjugated polymer backbone through Suzuki–Miyaura cross-coupling polymerization. It is noted that the hydrogen evolution rate of the cycloplatinated Pdots can be enhanced by 12 times in comparison to that of pristine Pdots under similar reaction conditions suggests cyclometallic Pdot systems appear to be alternative types of efficient photocatalysts for visible-light-driven hydrogen evolution. In another approach, Cu@PANI core–shell

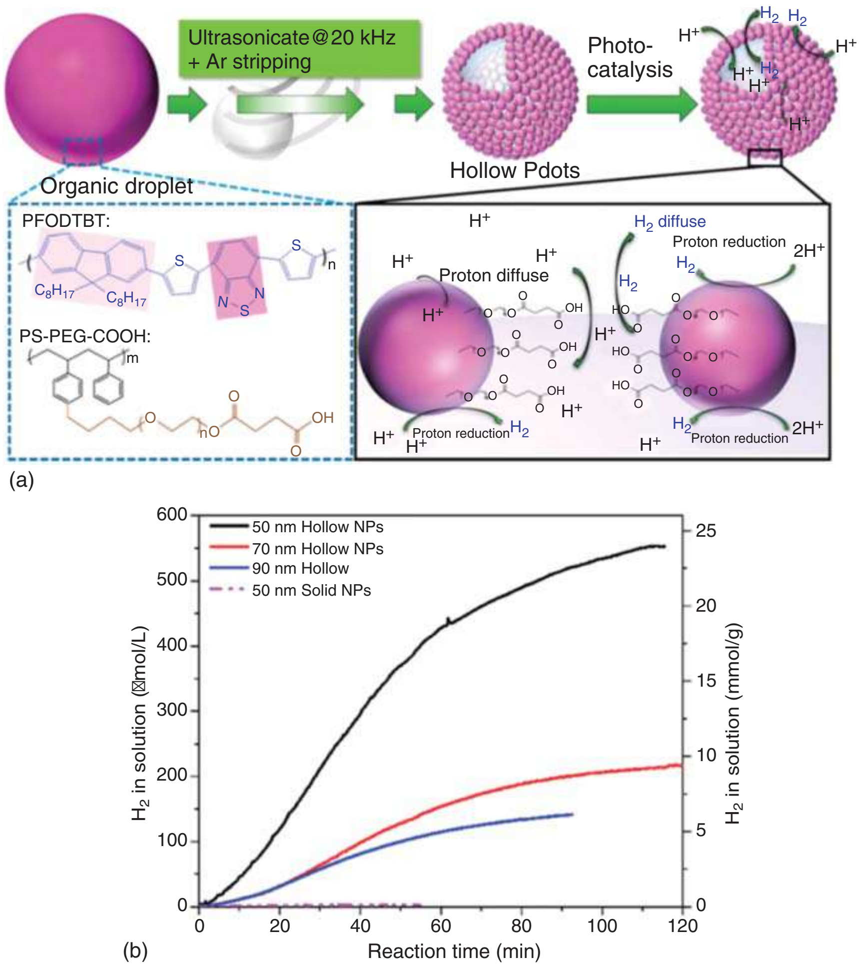

Figure 7.10 (a) Schematic of hollow Pdots prepared under ultrasonication and the resultant hollow Pdots contain hydrophilic. (b) Kinetic of hydrogen generation of hollow Pdots with sizes of 50, 70, and 90 nm and solid NPs with 50 nm. Source: Liu et al. [115]. Licensed Under CC BY 3.0.

nanospheres has been fabricated by Wang et al. [118] and measured the performance of photocatalytic hydrogen production. Figure 7.10a shows Cu@PANI2.5% exhibits the highest photocatalytic H_2 evolution rate (1.97 mmol/(g/h)), which is about two times as much as that of Cu NPs suggests the presence of PANI may improve the photocatalytic activity of Cu NPs. It is worth noting that the band gap of Cu@PANI core–shell nanospheres was lower than that of pure PANI, which may expand the spectral response and increases the electron transfer between valence and conduction bands resulting in obtaining more electron–hole pairs (Figure 7.11b). The author proposed that as the Fermi level of PANI was higher than that of Cu NPs (4.65 eV), photo-generated electrons of PANI transfer to the surface of Cu NPs, which can act as surface traps for absorbing the electrons from the CB of

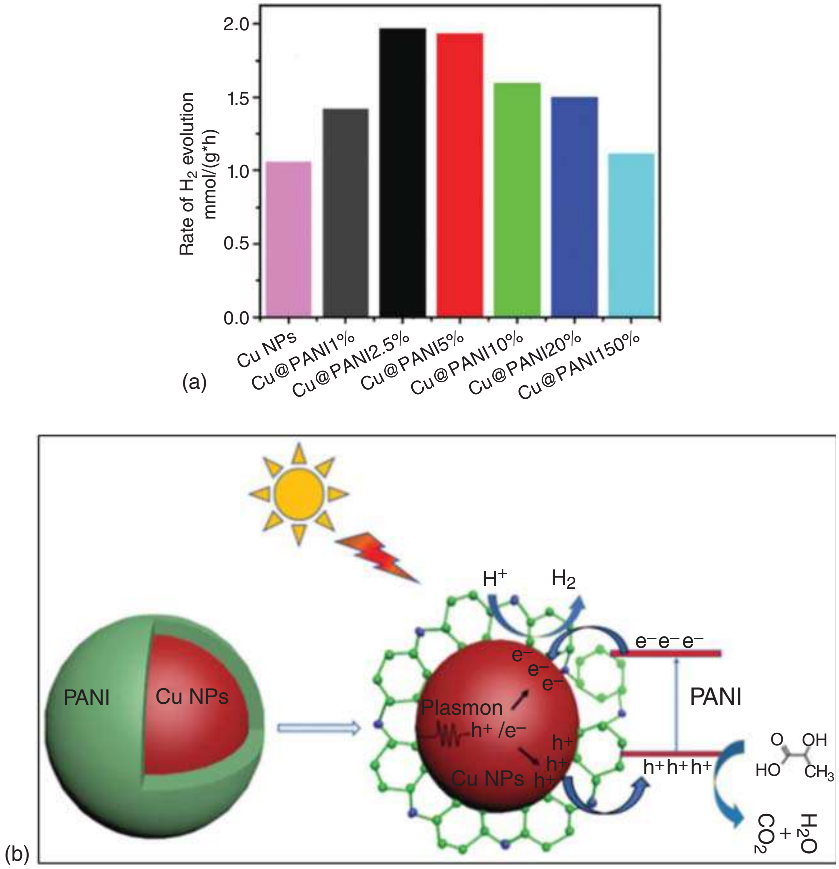

Figure 7.11 (a) Photocatalytic H_2 evolution of Cu@PANI core–shell nanospheres under solar light irradiation. (b) Photocatalytic mechanism for Cu@PANI core–shell nanospheres under irradiation. Source: Wang et al. [118].

PANI and then react with H^+ to generate H_2. On the other hand, the excited holes generated by Cu NPs may be injected into the VB of PANI and the recombination of photo-generated electron hole pairs was inhibited by the efficient transfer of the charge, therefore enhancing the photocatalytic activity of the Cu@PANI core–shell nanospheres.

Similarly, polyaniline sensitized Pt@TiO_2 exhibits high catalytic activity (61.8 μmol/(h/g)) and good stability for visible-light-driven H_2 generation (with an average AQY of 10.1%) with thioglycolic acid as an electron donor [119]. This study indicates that use of conjugated polymer to sensitize other semiconductor photocatalysts could be an efficient approach to enhance catalytic performance for H_2 generation. In another report, PPy also utilized to sensitize visible light-driven Nb-doped Ta_3N_5 catalysts for efficient overall water splitting [120]. They proposed that PPy having π-conjugated electron system may be combined with the VB and the CB of Nb doped Ta_3N_5 and acted as a sensitizer to enhance the charge transfer for migration of the generated electrons and holes to its surface and thus prevent their fast recombination, which in turn increased the electron hole separation efficiency of the modified Ta_3N_5 photocatalysts. Ghosh et al. [121] reported efficient photocatalytic H_2 generation from multimetallic nanoalloys deposited on polymer nanofibers, which may attribute to the surface plasmon resonance (SPR) effect of Au for enhanced visible light absorption and boosting the photogenerated charge separation. Notably, $Au_{50}Pt_{24}Pd_{26}$/PPy catalysts exhibit remarkable amount of H_2 generation ~40 mmol/h, which is ~5.7 times and 2.7 times higher than that of pure PPy and Au/PPy, respectively. Figure 7.12a displays H_2 generation rate after 60 minutes of visible light illumination, which follows the increasing order of $Au_{50}Pt_{24}Pd_{26}$/PPy (40 mmol/h) > $Au_{54}Pd_{46}$/PPy (31 mmol/h) > $Au_{41}Pt_{29}Pd_{30}$/PPy (26 mmol/h) > Pd/PPy (19 mmol/h) > Pt/PPy (15.2 mmol/h) > Au/PPy (15 mmol/h) > PPy (7 mmol/h).

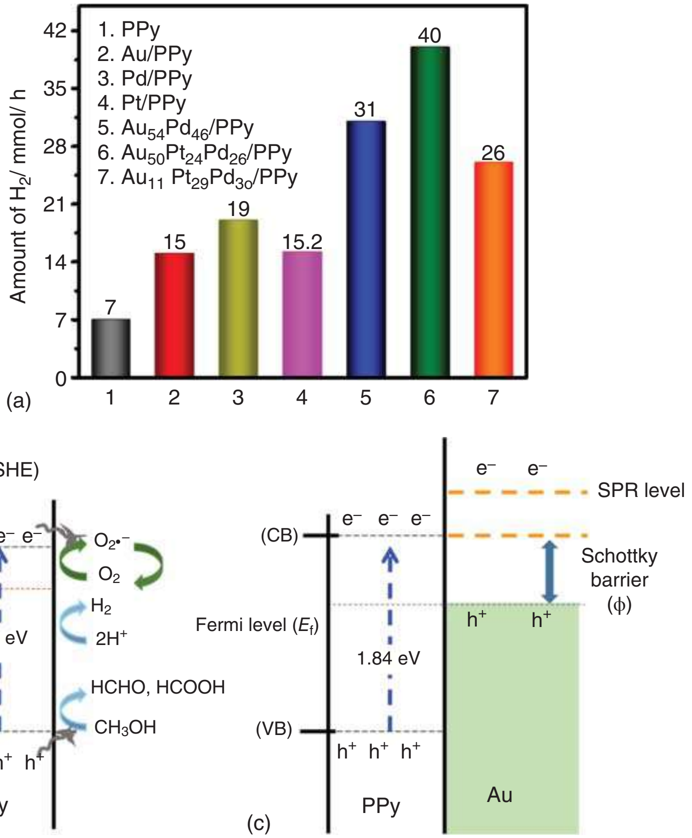

Figure 7.12 (a) Photocatalytic hydrogen generation using PPy and Au/PPy, $Au_{54}Pd_{46}$/PPy, $Au_{50}Pd_{24}Pt_{26}$/PPy as catalysts under visible light irradiation using 250 W Xe-arc lamp with UV light cutoff filter ($\lambda > 420$ nm) from an aqueous solution containing 25 vol% methanol and 0.5 mg/ml of each catalyst at pH 7. Possible mechanism involved in the photocatalytic activity of (b) PPy and (c) Au/PPy. Source: Ghosh et al. [121]. Copyright 2019 Elsevier.

The observed enhancement in photocatalytic activity for Au/PPy and $Au_{50}Pd_{24}Pt_{26}$/PPy NHs owes to the localized SPR of Au NPs, which may cause electron transfer from Au NPs to the polymer. A possible photocatalytic mechanism of PPy nanostructures has been proposed as shown in Figure 10.7b. The energy band diagram of Au/PPy interface shows the formation of Schottky barrier at the metal-polymer interface, E_f is the Fermi level, while e^-/h^+ are generated due to photo-excitation of Au NPs. Additionally, the Fermi level of the metal NPs contributes to the formation of the Schottky barrier (φ) to support the photo-induced charge separation and make the e^- shifts to a more negative potential. Upon photo-excitation, e^- injection possibly occurs from the SPR energy level of Au NPs to the conduction band (CB) of PPy, leaving a photogenerated h^+ in Au NPs, which is separated by the Schottky junction formed at the interface. Although plasmon mediated photocatalysis provides an alternative approach for visible-light driven H_2 production, the shorter lifetimes of hot e^- in Au/PPy may causes faster recombination of e^-/h^+ in plasmonic Au NP. Additionally, presence of multimetallic nanoalloy may suppress the recombination of hot electrons and holes in Au NPs, which may enhance the efficiency of plasmonic photocatalysts.

Moreover, polymer/polymer surface heterojunction catalyst has been reported for wide visible-light-driven H_2 production [122]. For example, the photocatalytic H_2 production activity of the P3HT/g-C_3N_4 catalysts containing 3 wt% P3HT shows highest AQY of 77.4% at 420 nm light irradiation in the field of g-C_3N_4-based catalyst, and wide visible/near infrared (NIR)-light-responsive ability with AQY of 59.4%, 20.2%, 3.2%, and 0.68% at 500, 600, 700, and 800 nm monochromatic light irradiation, respectively. The extremely high photoactivity is caused by the wide visible-light absorption and efficient charge transfer at the interface of P3HT/g-C_3N_4. Hayat et al. [123] reported the synthesis of conducting PPy NPs into the skeleton of inorganic semi-conductor g-C_3N_4 by loading of its small amount and tested for the evolution of hydrogen energy from water splitting and also demonstrated the photodegradation phenomena under visible light illumination ($\lambda = 420$ nm). Zang et al. [124] developed a concise construction of heterojunction based on pyrene-based polymer (PyP) and MoS_2 and extended to other transition metal sulfides (FeS_2, CoS_2, NiS_2) for photocatalytic H_2 evolution reaction. The results show at the optimized MoS_2/PyP sample exhibited a tenfold increase in comparison with pure PyP without modification. They proposed that the extended π-conjugation, high surface area, and widely exposed 2D interface highlight the importance of PyP as effective supports for stabilizing the homogeneously dispersed MoS_2, thus ensuing in an efficient photocatalytic activity. It has been also shown that effective photocorrosion inhibition and highly improved photocatalytic hydrogen production on monodisperse PANI@CdS core–shell nanospheres by Wang et al. [125].

Author proposed that the newly formed C—S and/or N—Cd bonds in PANI@CdS may prevent the reduction of the surface sulfide ions to sulfur, leading to effective photocorrosion inhibition and additionally, the photogenerated holes migrating from VB of CdS to the HOMO of PANI lead to the enhanced photocatalytic hydrogen production.

7.2.3 Conjugated Polymer Nanostructures for CO_2 Photo Reduction

With the significant rise in greenhouse gases, photoreduction of CO_2 and generation of clean and sustainable fuel such as methane or methanol becomes a hot research area [126, 127]. Various photocatalysts have been intensively used for CO_2 reduction but light harvesting and charge separation and the adsorption or activation and reduction of CO_2 on the surface of catalysts remain a big challenge, which limits the overall photoconversion efficiency and selectivity of CO_2 reduction [128]. Recently, polymeric g-C_3N_4 have been used widely for CO_2 photoreduction due to their high surface area, pore size distribution, and surface state. In 2012, Dong and Zhang [129] evaluated the photocatalytic CO_2 reduction to CO using g-C_3N_4 as a catalyst in the presence of water vapor under visible light. It is noted that the use of g-C_3N_4 for CO_2 reduction may couples organic basic functionality to photocatalytic functionality and allows for activation/adsorption and reduction of CO_2 [130–132]. A helical nanorod-like g-C_3N_4 showed significantly high catalytic activity with ~22-fold enhancement compared with traditional g-C_3N_4 nanosheets for CO_2 reduction to CO under visible light irradiation [133]. In order to improve the catalytic activity, combing the g-C_3N_4 with a ruthenium complex as light-harvesting units has been found as a promising heterogeneous system for the reduction of CO_2 into formic acid under visible-light irradiation, reported by Maeda and coworkers [134]. It was shown that replacing mesoporous g-C_3N_4 with g-C_3N_4 nanosheets as photocatalyst exhibited a good turnover number (TON) (>2000) and high CO_2 reduction selectivity (approximately 98%) for photocatalytic reduction of CO_2 to HCOOH in aqueous solution [135]. This suggests the great promise of ultrathin 2D conjugated polymer nanosheets for photocatalytic CO_2 reduction. Yang et al. [136] fabricated triazine-based conjugated microporous polymers to capture, activate, and reduce CO_2 to CO under visible light. They fabricated triazine-based CPs and electron-withdrawing (benzothiadiazole) and the optical band gap of the CMPs is engineered by electron-donating units (thiophene) on the skeleton of the triazine rings while creating organic donor–acceptor junctions to promote the charge separation. For example, three CPs were designed via coupling 2,4,6-tris(4-bromophenyl)-1,3,5-triazine (TBPT-Br) with 1,4-phenylenediboronic acid (B), 2,5-thiophenediboronic acid (Th), and 2,1,3-benzothiadiazole-,4,7-bis (boronic acid pinacol ester) (BT) as electron donor and acceptor building blocks. This coupling was done using palladium-catalyzed Suzuki cross-coupling polycondensation reaction to form the corresponding conjugated polymer networks CPs-B, CPs-Th, and CPs-BT, respectively. The scanning electron microscopy (SEM) and transmission electron microscopy (TEM) both revealed a hollow nanotubular morphology of CPs-BT with an average length of ~25 μm with an inner diameter of ~135 nm and a wall thickness of approximately 60 nm as shown in Figure 7.13a,b. The elemental mapping images of clearly shown that CPs-BT composed of C, N, and S (Figure 7.13c). The result shows with the incorporation of different electron donor or acceptor units, the efficiency of photocatalytic CO_2 reduction into CO could be enhance, giving CO formation rates of up to 18.2 μmol/h.

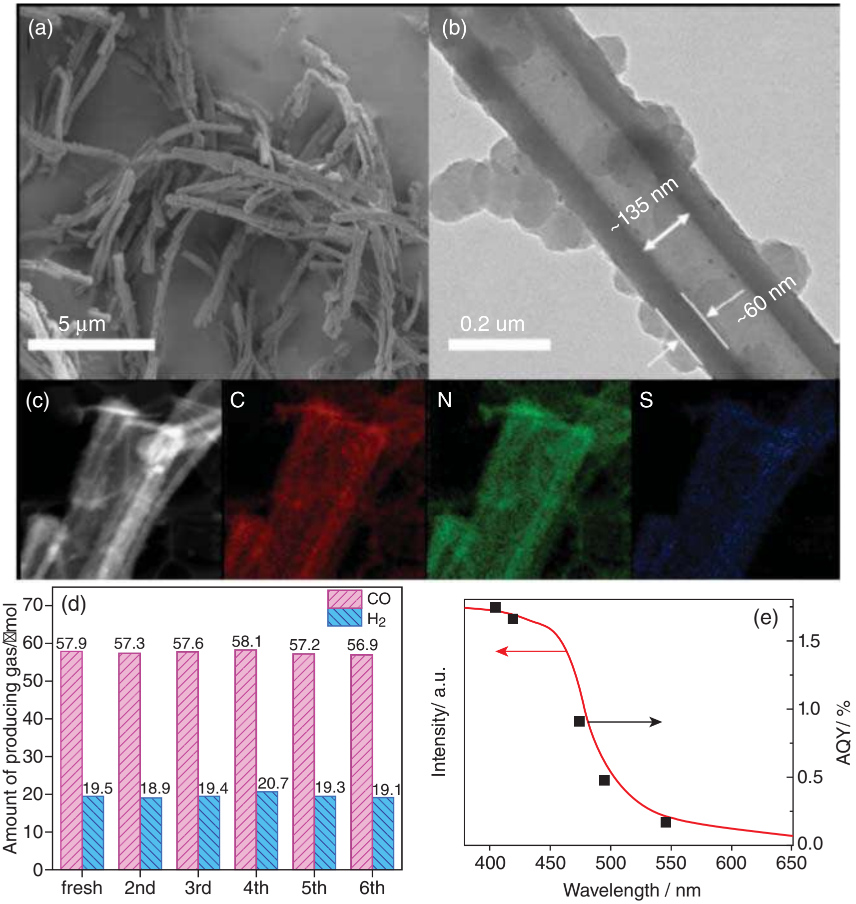

Figure 7.13 Characteristics of CPs-BT nanotube morphology. (a) SEM and (b) TEM images and (c) Element Mapping of C, N, and S. (d) Stability and reusability tests for CO_2 reduction by photocatalyst CPs-BT under visible light irradiation ($\lambda > 420$ nm). (e) Wavelength dependence of AQY for the H_2 and CO production. Source: (a–c) Reproduced with permission from Ref. Yang et al. [136]. Copyright 2018 Wiley, (d, e) Yang et al. [136].

During the recyclability experiments, more than 400 μmol of CO gas was generated, corresponding to a catalytic turnover number of ~20 for CPs-BT (Figure 7.13d). As a side product, the formation of H_2 gas was also identified with a hydrogen evolution rate of 4.1 μmol/h. Notably, a selectivity of 81.6% was achieved with a maximal AQY of 1.75% at 405 nm in a water/acetonitrile/triethanolamine reaction medium as shown in Figure 7.13e. This study provides direct evidence on a correlation between the structures of conjugated polymer photocatalysts to their photocatalytic performance in CO_2 reduction.

Hence, CPNs with the ability to modify their chemical composition, electronic structure, and surface functionality may be use for carbon photofixation and solar fuel production. It is worth noting that CPNs have been relatively less explored so far. For the development of CPNs for CO_2 photoreduction, some factors such as suitable band gaps, high surface area, CO_2 absorption, energy level alignments, and facile photogenerated charge separation are required to be taken into account with selectivity. Additionally, the external environment and operating conditions, such as catalyst quantity, solution pH, CO_2 pressure, temperature, etc., may influence the activity and selectivity of CO_2 reduction.

7.3 Conclusion

In conclusion, conjugated polymer nanostructures demonstrated superior photocatalytic activity for various photocatalytic applications, including organic dye degradation, water splitting, and CO_2 reduction. CPNs represent as a highly efficient photocatalytic materials due to intrinsic advantages of tunable band structure, absorption of visible light, facile fabrication process, earth abundant nature, and high stability. The photocatalytic activity of CPNs depends also on the size and shape of the polymer nanostructures. The use of various CPNs including PPy, PEDOT, PANI, g-C_3N_4, linear CPs, porous CPs, water-soluble conjugated polymer, and organic framework materials in photocatalytic applications is presented. CPNs showed excellent dye degradation ability under visible light, which can be used as an effective technology for environmental remediation. It is noted that photocatalytic overall water splitting has been reported by conjugated microporous polymer nanosheets. The roles of polymer structures for successful water-splitting systems are summarized. Up to now, the fundamentals of the photocatalytic process and structure–activity relationship of the polymer are not well understood. Moreover, the effect of co-catalysts on CPNs is prominent in enhanced catalysis but interaction mechanism between the polymer and co-catalysts is still not clear. It is noted that few CPNs have been used for photocatalytic CO_2 reduction and suffer from low activities. Various attempts may useful to improve the performance, such as loading co-catalysts and heterojunctions.

References

1 Tong, H., Ouyang, S., Bi, Y. et al. (2012). Nano-photocatalytic materials: possibilities and challenges. *Adv. Mater.* 24: 229–251.

2 Chen, C., Ma, W., and Zhao, J. (2010). Semiconductor-mediated photodegradation of pollutants under visible-light irradiation. *Chem. Soc. Rev.* 39: 4206–4219.

3 Low, J., Yu, J., Jaroniec, M. et al. (2017). Heterojunction photocatalysts. *Adv. Mater.* 29: 1601694.

4 Marschall, R. (2014). Semiconductor composites: strategies for enhancing charge carrier separation to improve photocatalytic activity. *Adv. Funct. Mater.* 24: 2421–2440.

5 Wang, H., Zhang, L., Chen, Z. et al. (2014). Semiconductor heterojunction photocatalysts: design, construction, and photocatalytic performances. *Chem. Soc. Rev.* 43: 5234–5244.

6 Fujishima, A. and Honda, K. (1972). Electrochemical photolysis of water at a semiconductor electrode. *Nature* 238: 37–38.

7 Kubacka, A., Garcia, M.F., and Colon, G. (2012). Advanced nanoarchitectures for solar photocatalytic applications. *Chem. Rev.* 112: 555–1614.

8 Wang, Q. and Domen, K. (2020). Particulate photocatalysts for light-driven water splitting: mechanisms, challenges, and design strategies. *Chem. Rev.* 120: 919–985.

9 Bera, S., Ghosh, S., Shyamal, S. et al. (2019). Photocatalytic hydrogen generation using gold decorated $BiFeO_3$ heterostructures as an efficient catalyst under visible light irradiation. *Sol. Energy Mater. Sol. Cells* 194: 195–206.

10 Ghosh, S. (ed.) (2018). *Visible-Light-Active Photocatalysis: Nanostructured Catalyst Design, Mechanisms, and Application*. Wiley-VCH. ISBN: 978-3-527-34293-8.

11 Yin, Z. and Zheng, Q. (2012). Controlled synthesis and energy applications of one-dimensional conducting polymer nanostructures: an overview. *Adv. Energy Mater.* 2: 179–218.

12 Zhou, Q. and Shi, G. (2016). Conducting polymer-based catalysts. *J. Am. Chem. Soc.* 138: 2868–2876.

13 Wang, Y., Vogel, A., Sachs, M. et al. (2019). Current understanding and challenges of solar-driven hydrogen generation using polymeric photocatalysts. *Nat. Energy* 4: 746–760.

14 Ghosh, S., Remita, H., and Basu, R.N. (2018). *Visible-Light-Active Photocatalysis: Nanostructured Catalyst Design, Mechanisms, and Applications*, Chapter 9 (ed. S. Ghosh), 227–252. Wiley-VCH.

15 Shi, Y., Peng, L., Ding, Y. et al. (2015). Nanostructured conductive polymers for advanced energy storage. *Chem. Soc. Rev.* 44: 6684–6696.

16 Hu, X., Chen, G., Wang, X., and Wang, H. (2015). Tuning thermoelectric performance by nanostructure evolution of a conducting polymer. *J. Mater. Chem. A* 3: 20896–20902.

17 Ramanathan, K., Bangar, M.A., Yun, M.H. et al. (2004). Individually addressable conducting polymer nanowires array. *Nano Lett.* 4: 1237–1239.

18 Pecher, J. and Mecking, S. (2010). Nanoparticles of conjugated polymers. *Chem. Rev.* 110: 6260–6279.

19 Ghosh, S., Ramos, L., Dazzi, A. et al. (2015). Conducting polymer nanofibers with controlled diameters synthesized in hexagonal mesophases. *New J. Chem.* 39: 8311–8320.

20 Jang, J., Ha, J., and Kim, S. (2007). Fabrication of polyaniline nanoparticles using microemulsion polymerization. *Macromol. Res.* 15: 154–159.

21 Wang, Y., Shi, Y., Pan, L. et al. (2015). Dopant-enabled supramolecular approach for controlled synthesis of nanostructured conductive polymer hydrogels. *Nano Lett.* 15: 7736–7741.

22 Friedel, B., McNeill, C.R., and Greenham, N.C. (2010). Influence of alkyl side-chain length on the performance of poly(3-alkylthiophene)/polyfluorene all-polymer solar cells. *Chem. Mater.* 22: 3389–3392.

23 Yoon, H., Hoon, J.-Y., and Jang, J. (2007). Charge-transport behavior in shape-controlled poly(3,4-ethylenedioxythiophene) nanomaterials: intrinsic and extrinsic factors. *Small* 3: 1774–1783.

24 Scholes, G.D. and Rumbles, G. (2006). Excitons in nanoscale systems. *Nat. Mater.* 5: 683–698.

25 Janáky, C. and Rajeshwar, K. (2015). The role of (photo)electrochemistry in the rational design ofhybrid conducting polymer/semiconductor assemblies: from fundamental concepts to practical applications. *Prog. Polym. Sci.* 43: 96–135.

26 Singh, P. and Shukla, S.K. (2020). Advances in polyaniline-based nanocomposites. *J. Mater. Sci.* 55: 1331–1365.

27 Xu, P., Han, X., Zhang, B. et al. (2014). Multifunctional polymer–metal nanocomposites via direct chemical reduction by conjugated polymers. *Chem. Soc. Rev.* 43: 1349–1353.

28 Su, Y.-W., Lin, W.-H., Hsu, Y.-J., and Wei, K.-H. (2014). Conjugated polymer/nanocrystal nanocomposites for renewable energy applications in photovoltaics and photocatalysis. *Small* 10: 4427–4442.

29 Han, J., Wang, M., Hu, Y. et al. (2017). Conducting polymer-noble metal nanoparticle hybrids: synthesis mechanism application. *Prog. Polym. Sci.* 70: 52–91.

30 Reiss, P., Couderc, E.G., De, J., and Pron, A. (2011). Conjugated polymers/semiconductor nanocrystals hybrid materials—preparation, electrical transport properties and applications. *Nanoscale* 3: 446–489.

31 Lu, X., Zhang, W., Wang, C., and Wei, Y. (2011). One-dimensional conducting polymer nanocomposites: synthesis, properties and applications. *Prog. Polym. Sci.* 36: 671–712.

32 Thirugnanasambandan, T. (2019). Polymers-metal nanocomposites. In: *Environmental Nanotechnology. Environmental Chemistry for a Sustainable World*, vol. 21 (eds. N. Dasgupta, S. Ranjan and E. Lichtfouse), 213–254. Cham: Springer.

33 Ameen, S., Akhtar, M.S., and Husain, M.M. (2010). A review on synthesis processing, chemical and conduction properties of polyaniline and its nanocomposites. *Sci. Adv. Mater.* 2: 441–462.

34 Yuan, X., Ding, X.L., Wang, C.-Y., and Ma, Z.F. (2013). Use of polypyrrole in catalysts for low temperature fuel cells. *Energy Environ. Sci.* 6: 1105–1124.

35 Shimpi, N.G., Mishra, S., and Sen, T. (2016). Synthesis and sensing applications of polyaniline nanocomposites: a review. *RSC Adv.* 6: 42196–42222.

36 Chen, J., Yu, Q., Cui, X. et al. (2019). An overview of stretchable strain sensors from conductive polymer nanocomposites. *J. Mater. Chem. C* 7: 11710–11730.

37 Rajesh, A. and T., and Kumar, D. (2009). Recent progress in the development of nano-structured conducting polymers/nanocomposites for sensor applications. *Sens. Actuators, B* 136: 275–286.

38 Baker, C.O., Huang, X., Nelson, W., and Kaner, R.B. (2017). Polyaniline nanofibers: broadening applications for conducting polymers. *Chem. Soc. Rev.* 46: 1510–1525.

39 Zhan, C., Yu, G., Lu, Y. et al. (2017). Conductive polymer nanocomposites: a critical review of modern advanced devices. *J. Mater. Chem. C* 5: 1569–1585.

40 Huang, Y., Li, J., Chen, X., and Wang, X. (2014). Applications of conjugated polymer based composites in wastewater purification. *RSC Adv.* 4: 62160–62178.

41 Sajedi-Moghaddam, A., Saievar-Iranizad, E., and Pumera, M. (2017). Two-dimensional transition metal dichalcogenide/conducting polymer composites: synthesis and applications. *Nanoscale* 9: 8052–8065.

42 Yang, J., Liu, Y., Liu, S. et al. (2017). Conducting polymer composites: material synthesis and applications in electrochemical capacitive energy storage. *Mater. Chem. Front.* 1: 251–268.

43 Hunger, K. (2003). *Industrial Dyes: Chemistry, Properties, Applications*. Weinheim: Wiley-VCH.

44 Keane, D.A., Guigan, K.G.M., Ibáñez, P.F. et al. (2014). Solar photocatalysis for water disinfection: materials and reactor design. *Catal. Sci. Technol.* 4: 1211–1226.

45 Syed, N., Huang, J., Feng, Y. et al. (2019). Carbon-based nanomaterials via heterojunction serving as photocatalyst. *Front. Chem.* 7: 713.

46 Ong, W.-J., Tan, L.-L., Ng, Y.H. et al. (2016). Graphitic carbon nitride (g-C$_3$N$_4$)-based photocatalysts for artificial photosynthesis and environmental remediation: are we a step closer to achieving sustainability? *Chem. Rev.* 116: 7159–7329.

47 Chen, D., Zhang, H., Liu, Y., and Li, J. (2013). Graphene and its derivatives for the development of solar cells, photoelectrochemical, and photocatalytic applications. *Energy Environ. Sci.* 6: 1362–1387.

48 Ghosh, S., Thandavarayan, M., and Basu, R.N. (2016). Nanostructured conducting polymers for energy applications: towards a sustainable platform. *Nanoscale* 8: 6921–6947.

49 Ghosh, S., Natalie, K.A., Ramos, L. et al. (2015). Conducting polymer nanostructures for photocatalysis under visible light. *Nat. Mater.* 14: 505–511.

50 Ghosh, S., Ramos, L., Dazzi, A. et al. (2015). Size tunable synthesis of one-dimensional conducting polymer nanostructures in hexagonal mesophases. *New J. Chem.* 39: 8311–8320.

51 Wang, X., Ishwara, T., Gong, W. et al. (2012). High-performance metal-free solar cells using stamp transfer printed vapor phase polymerized poly(3,4-ethylenedioxythiophene) top anodes. *Adv. Funct. Mater.* 22: 1454–1460.

52 Levermore, P.A., Chen, L., Wang, X. et al. (2007). Fabrication of highly conductive poly(3,4-ethylenedioxythiophene) films by vapor phase polymerization and their application in efficient organic light-emitting diodes. *Adv. Mater.* 19: 2379–2385.

53 Lattach, Y., Garnier, F., and Remita, S. (2012). Influence of chemical and structural properties of functionalized polythiophene-based layers on electrochemical sensing of atrazine. *ChemPhysChem* 13: 281–290.

54 Ghosh, S., Remita, H., Ramos, L. et al. (2014). PEDOT nanostructures synthesized in hexagonal mesophases. *New J. Chem.* 38: 1106–1115.

55 Ghosh, S., Kouame, N.A., Remita, S. et al. (2015). Visible-light active conducting polymer nanostructures with superior photocatalytic activity. *Sci. Rep.* 5: 18002–18011.

56 Yuan, X., Floresyona, D., Aubert, P.-H. et al. (2018). Photocatalytic degradation of organic pollutant with polypyrrole nanostructures under UV and visible light. *Appl. Catal., B* 242: 284–292.

57 Floresyona, D., Goubard, F., Aubert, P.-H. et al. (2017). Highly active poly(3-hexylthiophene) nanostructures for photocatalysis under solar light. *Appl. Catal., B* 209: 23–32.

58 Liras, M., Barawi, M., de la Peña O'Shea, A., and V. (2019). Hybrid materials based on conjugated polymers and inorganic semiconductors as photocatalysts: from environmental to energy applications. *Chem. Soc. Rev.* 48: 5454–5487.

59 Sardar, S., Kar, P., Remita, H. et al. (2015). Enhanced charge separation and FRET at heterojunctions between semiconductor nanoparticles and conducting polymer nanofibers for efficient solar light harvesting. *Sci. Rep.* 5: 17313–17327.

60 Wang, Y., Deng, Y., Fan, L. et al. (2017). In situ strategy to prepare PDPB/SnO_2 p–n heterojunction with a high photocatalytic activity. *RSC Adv.* 7: 24064–24069.

61 Lei, J., Liu, F., Wang, L. et al. (2017). A binary polymer composite of graphitic carbon nitride and poly(diphenylbutadiyne) with enhanced visible light photocatalytic activity. *RSC Adv.* 7: 27377–27383.

62 Liu, J., Fang, W., and Wang, Y. (2018). Gold-loaded graphene oxide/PDPB composites for the synchronous removal of Cr(VI) and phenol. *Chin. J. Catal.* 39: 8–15.

63 Ghosh, S., Remita, H., and Basu, R.N. (2018). Significantly enhanced photocatalytic reduction of Cr(VI) on ZnO-conducting polymeric nanofibers heterojunction under visible-light irradiation. *Appl. Catal., B* 239: 362–372.

64 Ghosh, S., Mallik, A.K., and Basu, R.N. (2018). Enhanced photocatalytic activity and photoresponse of poly(3,4-ethylenedioxythiophene) nanofibers decorated with gold nanoparticle under visible light. *Sol. Energy* 159: 548–560.

65 Clavero, C. (2014). Plasmon-induced hot-electron generation at nanoparticle/metal-oxide interfaces for photovoltaic and photocatalytic devices. *Nat. Photonics* 8: 95–103.

66 Wang, M., Ye, M., Locozzia, J. et al. (2016). Plasmon-mediated solar energy conversion via photocatalysis in noble metal/semiconductor composites. *Adv. Sci.* 3: 1600024 (1–14).

67 Boddu, S., Nishanthi, S.T., and Kailasam, K. (2018). Visible-light heterogeneous catalysts for photocatalytic CO_2 reduction. In: *Visible-Light-Active Photocatalysis: Nanostructured Catalyst Design, Mechanisms, and Applications*, Chapter 15 (ed. S. Ghosh), 421–446. Wiley-VCH.

68 Saha, S., Chaudhary, N., Mittal, H. et al. (2019). Inorganic–organic nanohybrid of MoS_2-PANI for advanced photocatalytic application. *Int. Nano Lett.* 9: 127–139.

69 Zhang, H. and Zhu, Y. (2010). Significant visible photoactivity and antiphotocorrosion performance of CdS photocatalysts after monolayer polyaniline hybridization. *J. Phys. Chem. C* 114: 5822–5826.

70 Wang, Q., Hui, J., Li, J. et al. (2013). Photodegradation of methyl orange with PANI-modified BiOCl photocatalyst under visible light irradiation. *Appl. Surf. Sci.* 283: 577–583.

71 Liu, L., Ding, L., Liu, Y. et al. (2017). A stable Ag_3PO_4 @PANI core@shell hybrid: enrichment photocatalytic degradation with π-π conjugation. *Appl. Catal., B* 201: 92–104.

72 Zhang, H., Zong, R., and Zhu, Y. (2009). Photocorrosion inhibition and photoactivity enhancement for zinc oxide via hybridization with monolayer polyaniline. *J. Phys. Chem. C* 113: 4605–4611.

73 Radoičić, M., Ćirić-Marjanović, G., Spasojević, V. et al. (2017). Superior photocatalytic properties of carbonized PANI/TiO_2 nanocomposites. *Appl. Catal., B* 213: 155–166.

74 Shang, M., Wang, W., Sun, S. et al. (2009). Efficient visible light-induced photocatalytic degradation of contaminant by spindle-like PANI/$BiVO_4$. *J. Phys. Chem. C* 113: 20228–20233.

75 Biswas, M.R.U.D., Cho, K.Y., Na, J.D., and Oh, W.-C. (2009). Highly electro-conductive graphene-decorated PANI-$BiVO_4$ polymer-semiconductor nanocomposite with outstanding photocatalytic performance. *Mater. Sci. Eng., B* 251: 114469.

76 Baoum, A., Amin, M.S., and Mohamed, R.M. (2019). Development of $CuCr_2O_4$ nanocomposite adopting decoration with polyaniline for acridine orange dye degradation. *Appl. Nanosci.* 59: 1–10.

77 Xu, Y., Ma, Y., Ji, H. et al. (2019). Enhanced long-wavelength light utilization with polyaniline/bismuth-rich bismuth oxyhalide composite towards photocatalytic degradation of antibiotics. *J. Colloid Interface Sci.* 537: 101–111.

78 Zhang, S., Zhao, L., Zeng, M. et al. (2014). Hierarchical nanocomposites of polyaniline nanorods arrays on graphitic carbon nitride sheets with synergistic effect for photocatalysis. *Catal. Today* 224: 114–121.

79 Jana, B., Ghosh, A., and Patra, A. (2017). Photon harvesting in conjugated polymer-based functional nanoparticles. *J. Phys. Chem. Lett.* 8: 4608–4620.

80 Jana, B., Bhattacharyya, S., and Patra, A. (2015). Conjugated polymer P3HT-Au hybrid nanostructures for enhancing photocatalytic activity. *Phys. Chem. Chem. Phys.* 17: 15392–15399.

81 Ghosh, A., Jana, B., Maiti, S. et al. (2017). Light harvesting and photocurrent generation in a conjugated polymer nanoparticle−reduced graphene oxide composite. *ChemPhysChem* 18: 1308–1316.

82 Xie, M. and Zhang, T. (2020). A novel efficient visible-light-driven double Z-scheme PANI/Ag_3PO_4/CNO heterojunction photocatalyst mediated by PANI and in situ grown AgNPs. *J. Mater. Sci.* 55: 3974–3990.

83 Bu, Y. and Chen, Z. (2014). Role of polyaniline on the photocatalytic degradation and stability performance of the polyaniline/silver/silver phosphate composite under visible light. *ACS Appl. Mater. Interfaces* 6: 17589–17598.

84 Zhu, Z., Tang, X., Ma, C. et al. (2016). Fabrication of conductive and high-dispersed Ppy@Ag/g-C_3N_4 composite photocatalysts for removing various pollutants in water. *Appl. Surf. Sci.* 387: 366–374.

85 Chen, F., Wu, Y., Ning, J. et al. (2017). Facile preparation of ternary Ag_2CO_3/Ag/PANI composite nanorods with enhanced photoactivity and stability. *J. Mater. Sci.* 52: 4521–4531.

86 Wu, H., Lin, S., Chen, C. et al. (2016). A new ZnO/rGO/polyaniline ternary nanocomposite as photocatalyst with improved photocatalytic activity. *Mater. Res. Bull.* 83: 434–441.

87 Pandiselvi, K., Fang, H., Huang, X. et al. (2016). Constructing a novel carbon nitride/polyaniline/ZnO ternary heterostructure with enhanced photocatalytic performance using exfoliated carbon nitride nanosheets as supports. *J. Hazard. Mater.* 314: 67–77.

88 Zhao, J., Biswas, Md. R. Ud. D., and Oh, W.-C. (2019). A novel $BiVO_4$-GO-TiO_2-PANI composite for upgraded photocatalytic performance under visible light and its non-toxicity. *Environ. Sci. Pollut. Res. Int.* 26: 11888–11904.

89 Lee, S. and Chang, C.-J. (2019). Recent developments about conductive polymer based composite photocatalysts. *Polymers* 11: 206.

90 Hisatomi, T., Kubota, J., and Domen, K. (2014). Recent advances in semiconductors for photocatalytic and photoelectrochemical water splitting. *Chem. Soc. Rev.* 43: 7520–7535.

91 Yi, H., Huang, D., Qin, L. et al. (2018). Selective prepared carbon nanomaterials for advanced photocatalytic application in environmental pollutant treatment and hydrogen production. *Appl. Catal., B* 239: 408–424.

92 Yang, M.-Q., Zhang, N., Pagliaro, M., and Xu, Y.-J. (2014). Artificial photosynthesis over graphene–semiconductor composites. Are we getting better? *Chem. Soc. Rev.* 43: 8240–8254.

93 Wang, X.C., Maeda, K., Thomas, A. et al. (2009). A metal-free polymeric photocatalyst for hydrogen production from water under visible light. *Nat. Mater.* 8: 76–80.

94 Vyas, V.S., Lau, V.W., and Lotsch, B.V. (2016). Soft photocatalysis: organic polymers for solar fuel production. *Chem. Mater.* 28: 5191–5204.

95 Liu, J., Liu, Y., Liu, N. et al. (2015). Water splitting. Metal-free efficient photocatalyst for stable visible water splitting via a two-electron pathway. *Science* 347: 970–974.

96 Zhang, G., Lan, Z.-A., Lin, L. et al. (2016). Overall water splitting by Pt/g-C_3N_4 photocatalysts without using sacrificial agents. *Chem. Sci.* 7: 3062–3066.

97 Zhang, M. and Wang, X. (2014). Two dimensional conjugated polymers with enhanced optical absorption and charge separation for photocatalytic hydrogen evolution. *Energy Environ. Sci.* 7: 1902–1906.

98 Sprick, R.S., Bonillo, B., Clowes, R. et al. (2016). Visible-light-driven hydrogen evolution using planarized conjugated polymer photocatalysts. *Angew. Chem. Int. Ed.* 128: 1824–1828.

99 Li, L., Lo, W.-Y., Cai, Z. et al. (2016). Donor–acceptor porous conjugated polymers for photocatalytic hydrogen production: the importance of acceptor comonomer. *Macromolecules* 49: 6903–6909.

100 Lan, Z.-A., Fang, Y., Zhang, Y., and Wang, X. (2018). Photocatalytic oxygen evolution from functional triazine-based polymers with tunable band structures. *Angew. Chem. Int. Ed.* 57: 470–474.

101 Woods, D.J., Sprick, R.S., Smith, C.L. et al. (2017). A solution-processable polymer photocatalyst for hydrogen evolution from water. *Adv. Energy Mater.* 7: 1700479–1700485.

102 Vyas, V.S. and Lotsch, B.V. (2015). Materials chemistry: organic polymers form fuel from water. *Nature* 521: 41–42.

103 Sprick, R.S., Aitchison, C.M., Berardo, E. et al. (2018). Maximising the hydrogen evolution activity in organic photocatalysts by co-polymerisation. *J. Mater. Chem. A* 6: 11994–12003.

104 Banerjee, T., Gottschling, K., Savasci, G. et al. (2018). H_2 evolution with covalent organic framework photocatalysts. *ACS Energy Lett.* 3: 400–409.

105 Jiang, X., Wang, P., and Zhao, J. (2015). 2D covalent triazine framework: a new class of organic photocatalyst for water splitting. *J. Mater. Chem. A* 3: 7750–7758.

106 Vyas, V.S., Haase, F., Stegbauer, L. et al. (2015). A tunable azine covalent organic framework platform for visible light-induced hydrogen generation. *Nat. Commun.* 6: 8508.

107 Stegbauer, L., Schwinghammer, K., and Lotsch, B.V. (2014). A hydrazone-based covalent organic framework for photocatalytic hydrogen production. *Chem. Sci.* 5: 2789–2793.

108 Wang, X., Chen, L., Chong, S.Y. et al. (2018). Sulfone-containing covalent organic frameworks for photocatalytic hydrogen evolution from water. *Nat. Chem.* 10: 1180–1189.

109 Sprick, R.S., Bonillo, B., Sachs, M. et al. (2016). Extended conjugated microporous polymers for photocatalytic hydrogen evolution from water. *Chem. Commun.* 52: 10008–10011.

110 Xiao, Z., Huang, X., Zhao, K. et al. (2019). Band structure engineering of Schiff-base microporous organic polymers for enhanced visible-light photocatalytic performance. *Small* 15: 1900244.

111 Dai, C. and Liu, B. (2020). Conjugated polymers for visible-light-driven photocatalysis. *Energy Environ. Sci.* 13: 24–52.

112 Wang, L., Wan, Y., Ding, Y. et al. (2017). Conjugated microporous polymer nanosheets for overall water splitting using visible light. *Adv. Mater.* 29: 1702428.

113 Kong, K., Zhang, S., Chu, Y. et al. (2019). A self-assembled perylene diimide nanobelt for efficient visible-light-driven photocatalytic H_2 evolution. *Chem. Commun.* 55: 8090–8093.

114 Wang, L., Fernández-Terán, R., Zhang, L. et al. (2016). Organic polymer dots as photocatalysts for visible light-driven hydrogen generation. *Angew. Chem. Int. Ed.* 55: 12306–12310.

115 Liu, A., Tai, C.-W., and Holá, K., and Tian, H. (2019). Hollow polymer dots: nature-mimicking architecture for efficient photocatalytic hydrogen evolution reaction. *J. Mater. Chem. A* 7: 4797–4803.

116 Pati, P.B., Damas, G., Tian, L. et al. (2017). An experimental and theoretical study of an efficient polymer nano-photocatalyst for hydrogen evolution. *Energy Environ. Sci.* 10: 1372–1376.

117 Tseng, P.-J., Chang, C.-L., Chan, Y.-H. et al. (2018). Design and synthesis of cycloplatinated polymer dots as photocatalysts for visible light-driven hydrogen evolution. *ACS Catal.* 8: 7766–7772.

118 Wang, T., Wu, D., Wang, Y. et al. (2018). One-step solvothermal fabrication of Cu@PANI core-shell nanospheres for hydrogen evolution. *Nanoscale* 10: 22055–22064.

119 Liu, X., Lai, H., Li, J. et al. (2019). Polyaniline sensitized Pt@TiO_2 for visible-light-driven H_2 generation. *Int. J. Hydrogen Energy* 44: 4698–4706.

120 Truc, N.T.T., Tran, D.T., Hanh, N.T., and Pham, T.-D. (2018). Novel visible light-driven Nb-doped Ta_3N_5 sensitized/protected by PPy for efficient overall water splitting. *Int. J. Hydrogen Energy* 43: 15898–15906.

121 Ghosh, S., Rashmi, D., Bera, S., and Basu, R.N. (2019). Functionalized conjugated polymer nanostructure with plasmonic Au nanoalloys for photocatalytic hydrogen generation under Vis-NIR light. *Int. J. Hydrogen Energy* 44: 13262–13272.

122 Zhang, X., Peng, B., Zhang, S., and Peng, T. (2015). Robust wide visible-light-responsive photoactivity for H_2 production over a polymer/polymer heterojunction photocatalyst: the significance of sacrificial reagent. *ACS Sustainable Chem. Eng.* 3: 1501–1509.

123 Hayat, A., Raziq, F., Khan, M.F. et al. (2019). Visible-light enhanced photocatalytic performance of polypyrrole/g-C_3N_4 composites for water splitting to evolve H_2 and pollutants degradation. *J. Photochem. Photobiol.* 379: 88–98.

124 Zang, S., Zhang, G., Lan, Z.-A. et al. (2019). Enhancement of photocatalytic H_2 evolution on pyrene-based polymer promoted by MoS_2 and visible light. *Appl. Catal., B* 251: 102–111.

125 Wang, C., Wang, L., Jin, J. et al. (2016). Probing effective photocorrosion inhibition and highly improved photocatalytic hydrogen production on monodisperse PANI@CdS core-shell nanospheres. *Appl. Catal., B* 188: 351–359.

126 White, J.L., Baruch, M.F., Pander, J.E. et al. (2015). Light-driven heterogeneous reduction of carbon dioxide: photocatalysts and photoelectrodes. *Chem. Rev.* 115: 12888–12935.

127 Chang, X., Wang, T., and Gong, J. (2016). CO_2 photo-reduction: insights into CO_2 activation and reaction on surfaces of photocatalysts. *Energy Environ. Sci.* 9: 2177–2196.

128 Li, K., An, X., Park, K.H. et al. (2014). A critical review of CO_2 photoconversion: catalysts and reactors. *Catal. Today* 224: 3–12.

129 Dong, G. and Zhang, L. (2012). Porous structure dependent photoreactivity of graphitic carbon nitride under visible light. *J. Mater. Chem.* 22: 1160–1166.

130 Niu, P., Yang, Y., Yu, J.C. et al. (2014). Switching the selectivity of the photoreduction reaction of carbon dioxide by controlling the band structure of a g-C_3N_4 photocatalyst. *Chem. Commun.* 50: 10837–10840.

131 Maeda, K., Kuriki, R., Zhang, M. et al. (2014). The effect of the pore-wall structure of carbon nitride on photocatalytic CO_2 reduction under visible light. *J. Mater. Chem. A* 2: 15146–11151.

132 Lin, J., Pan, Z., and Wang, X. (2014). Photochemical reduction of CO_2 by graphitic carbon nitride polymers. *ACS Sustainable Chem. Eng.* 2: 353–358.

133 Zheng, Y., Lin, L.H., Ye, X.J. et al. (2014). Helical graphitic carbon nitrides with photocatalytic and optical activities. *Angew. Chem. Int. Ed.* 53: 11926–11930.

134 Kuriki, R., Sekizawa, K., Ishitani, O., and Maeda, K. (2015). Visible-light-driven CO_2 reduction with carbon nitride: enhancing the activity of ruthenium catalysts. *Angew. Chem. Int. Ed.* 127: 2436–2439.

135 Kuriki, R., Yamamoto, M., Higuchi, K. et al. (2017). Robust binding between carbon nitride nanosheets and a binuclear ruthenium(II) complex enabling durable, selective CO_2 reduction under visible light in aqueous solution. *Angew. Chem. Int. Ed.* 56: 4867–4871.

136 Yang, C., Huang, W., Caire da Silva, L. et al. (2018). Functional conjugated polymers for CO_2 reduction using visible light. *Chem. Eur. J.* 24: 17454–17458.

8

Conjugated Polymer-Based Nanocomposites as Photocatalysts

Rituporn Gogoi, Sunil Dutt, and Prem F. Siril

Indian Institute of Technology Mandi, School of Basic Sciences, Mandi 175005, Himachal Pradesh, India

8.1 Introduction

The introduction of conductivity in polymers has created a subclass of polymers known as conducting polymers. Intrinsically conducting polymers essentially have extended conjugation in their polymeric backbone, which render them electrically conductive [1]. They are hence also called conjugated polymers (CPs). Like any other polymer, properties of CPs also can be tuned by forming composites including nanocomposites (NCs). While conjugated polymer nanocomposites (CPNCs) have a plethora of applications, the focus of the present chapter will be limited to the photocatalytic applications of CPNCs. Polymer composites are intricate mixtures of compounds where at least one of the components should be a polymer, as per the International Union of Pure and Applied Chemistry (IUPAC) definition [2]. The mixture should lead to synergistic improvement in properties of the constituents to be termed as a composite. A nanocomposite should contain at least a nanomaterial as one of the constituents.

CPNCs mostly contain a CP matrix in which the nanoparticles of metals, metal oxides, semiconductors, and carbon materials are embedded [3]. On the other hand, CPNCs can also be made by confining the CP nanostructures within porous materials. Such CPNCs are relatively much less explored for photocatalytic applications, when compared with the CPNC with a polymer matrix. CPs find applications in sensors, actuators, energy storage devices, adsorption of pollutants, antistatic coating, corrosion prevention, biomaterials, photocatalysis, and so on [4–6]. Formation of CPNCs essentially helps us to tune the properties of CPs to enhance their properties in the aforementioned applications. The nanoparticles render them additional functionalities such as magnetically separable adsorbents and catalysts [7, 8]. However, the nanomaterials can be used to tune the band gap and facilitate charge separation through the formation of heterojunctions of CPs for photocatalytic applications [3].

Conjugated Polymer Nanostructures for Energy Conversion and Storage Applications,
First Edition. Edited by Srabanti Ghosh.

Photocatalysis deals with the use of electromagnetic radiation to promote chemical reactions. In a broad sense, photocatalysis is the basis of existence of life on the planet earth as plants perform photosynthesis of carbohydrates by combining carbon dioxide and water in presence of sun light. Chlorophyll acts as the photocatalyst in this reaction. Solar light is a freely available source of energy. Due to the adverse consequences of global warming that is caused mainly by the rise of anthropogenic carbon dioxide emission to the atmosphere, there is renewed interest to develop visible light photocatalysis to achieve sustainable chemical reactions. Photocatalytic splitting of water to generate hydrogen, which is believed to be the next generation carbon-free fuel, is a stellar example of the importance of photocatalysis. Thus, the present chapter focuses essentially on the photocatalytic applications of CPNCs. Some general methods of their synthesis are discussed here briefly. Detailed methods can be found in many excellent reviews [9, 10]. Fundamental principles of photocatalysis are discussed briefly followed by the application of CPNCs for various photocatalytic applications. The discussion on applications is exemplary rather than exhaustive, with an objective to focus on the value of CPNCs as photocatalysts.

8.2 General Methods of Synthesis of Conjugated Polymer Nanocomposites

Over the years, a plethora of CPNCs have been reported, mostly with nanoparticles that are embedded in a CP matrix. These CPNCs have wide ranging applications. However, CPNCs having conductive or semi conductive nanomaterials as fillers in the CP matrix are mainly interesting for photocatalytic applications. Based on the nature of the filler material, CPNCs can be classified into:

i. Inorganic semiconductor (oxides, chalcogenides, and nitrides of metals) – CP nanocomposites
ii. Metal based nanocomposites of CP – metal can be plasmonic or non-plasmonic
iii. Non-metallic nanocomposites of CP

Some fundamental methods of their synthesis are briefly discussed here. CPs can be synthesized via chemical, electrochemical, and radiolytic polymerization methods [11, 12]. In the former case, the chemical oxidation of a suitable monomer by using a strong oxidant like ammonium persulfate or hydrogen peroxide leads to polymerization. These so-called bulk polymerization methods may not yield CP nanostructures. However, salts of metals (Fe, Cu, Pd, Au, Ag, and Pt) can also be used as oxidizing agents. The metal ions get reduced during the oxidative polymerization and form reduced metal and often lead to the formation of CPNCs. However, metals such as Fe and Cu get oxidized during the process and often form CPNCs containing metal oxides. This is a way of *in situ* preparation of CPNCs. However, nanomaterials such as metals, metal oxides, and carbon nanomaterials can be incorporated into a CP matrix by *ex situ* processes also. The nanomaterial is first prepared and mixed with the monomer and polymerized to yield the CPNCs *ex situ*.

Sometimes, C–H/C–C/C–N coupling of monomer units also can be used to form CPs in the presence of organometallic complexes as catalysts [13]. The monomers used for such coupling reactions can be same (homocoupling) or different (cross-coupling). In the Suzuki and Stille coupling reactions, the boronic acid and stannylated derivatives are, respectively, coupled with halogenated reactants in the presence of Pd metal-based complexes. Radical polymerization is yet another technique where polymerization is carried out by excitation of the monomer by a suitable radiation such as UV light, electron beam, or γ-rays [14, 15]. In the electrochemical polymerization method, an external electrical potential is used as a driving force for polymerization between monomer units in a three-electrode equipped electrochemical cell [16]. On application of an external voltage, the monomers in the electrolyte, undergoes oxidation followed by deposition on the electrode surface (Anode). Here the extend of polymerization can be controlled based on the parameters like solvent, duration of polymerization, and types of electrolyte and electrodes. CPNCs can be made by any of the polymerization methods using the *ex situ* approach [17].

8.3 Classification of the Approaches for the Synthesis of Conjugated Polymer Nanocomposites

The shape and size-controlled synthesis of CPNCs is a key step to achieve efficient photocatalysts. The morphology control can be achieved by two fundamental ways:

(a) Bottom up approach
(b) Top down approach

Bottom up approach can be *in situ* or *ex situ* as mentioned earlier. The nanostructured CPs and nanoparticles of the fillers can be prepared separately and finally loaded one over another [18]. Mixing of the nanoparticle of the filler material in the monomer followed by oxidation of the monomer over it can yield core–shell CPNCs [19]. *In situ* polymerization using metal salts can also yield metal or metal oxide based CP nanocomposites [20, 21]. More often, this process occurs in the case of redox polymerization techniques, where metal precursor acts as oxidizing agents for the oxidation of monomer units [22, 23]. For example, Au nanoparticles immobilized CP based nanocomposites were prepared via reduction of Au (III) precursors using 2-methoxyaniline [24], 3,4-ethylenedioxythiophene (EDOT) [25], and aniline [8]. Pd containing CPNCs as shown in Figure 8.1 were prepared via reduction of $PdCl_2$ salts in respective monomers [23, 26].

Top down method is however a more difficult approach in terms of achieving uniform and regular CPNCs. In this method, bulk composite is made first followed by its downsizing. For instance, mechanical grinding of CPNCs via ball milling approach. In the most widely used bottom up approaches, the growth of the CP particles during polymerization has to be confined to yield CPNCs. Confining the growth of the CPs can be done by using a size limiting template. However, kinetic control of the growth of the CPs to yield CPNCs can be achieved without the presence of a template as well.

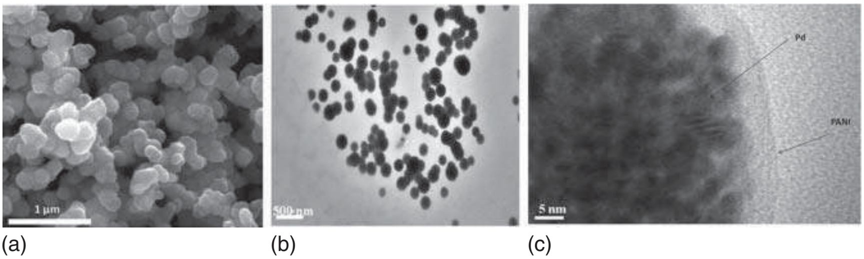

Figure 8.1 Images of Pd-polyaniline nanocomposite (a) scanning electron and (b) transmission electron microscopy images. (c) High resolution transmission electron microscopy (TEM) image showing the presence of small Pd nanoparticles that are embedded in the polyaniline matrix. Source: Adapted from Dutt et al. [23]. Copyright 2015, Royal Society of Chemistry.

8.3.1 Template Assisted Methods

Nanodimensions of CP based nanostructures can be achieved using template guided approach. In the template assisted techniques, the growth of nanostructures is confined within the pores or channels or cavity of the template to form the nanostructures with desired architecture. By using suitable templates, CPNCs having fibrillar, rod, tube, and spherical morphologies could be synthesized. The templates can be porous solids having permanent porosity such as mesoporous silica. These are called hard templates. However, self-assembled structures such as micelles and vesicles also can be used as “soft” templates [27, 28].

a. *Hard template assisted synthesis of CPNCs*: Highly controlled and well oriented nanostructures of CPNCs can be prepared with hard template assisted methods [29]. Porous solids having ordered porosity such as mesoporous silica, anodized aluminum oxide, and etched polycarbonate membranes are examples of hard templates. However, this method requires post-processing tools to remove the template. The post-processing may warrant the use of harsh conditions such as high temperature or corrosive chemicals that may be detrimental to the properties of CPNCs.
b. *Soft template assisted synthesis of CPNCs*: This technique is relatively simple, cost effective, and convenient for the fabrication of CPNCs. The size confinement of the CPNCs is achieved by using micelles or vesicles that are formed by the self-assembly of surfactants or polymers. The shape and size of the soft-templates are highly dependent on the nature of hydrophilic or hydrophobic chain of surfactants and the concentrations of the surfactants, doping agents, and oxidants. The soft templates synthesis can be *in situ* or *ex situ*. There are numerous examples of the synthesis of CP-metal nanocomposites using soft templates approach [7, 30, 31].

8.3.2 Template Free Method

Template free strategy is a very promising tool for the preparation of CPNCs. The important parameters to obtain the tuned morphologies is the consideration of non-covalent interactions like hydrogen bonding, ionic interactions, dispersibility, solubility, etc. As the technique does not require any template to their fabrication, the issues related to the post-processing can be avoided.

8.4 Fundamental Principles of Photocatalysis

Nanostructured materials have gained much attention as photocatalysts in the past few years. Conventionally used bulk semiconducting materials like TiO_2, ZnO, and recently emerged perovskites are mostly used in various solar light driven applications like environment remediation, self-cleaning surfaces, and photo redox reactions. Briefly, in a photocatalytic system, semiconducting material gets excited via absorption of light with specific energy equivalent to or more than the energy required for the transition of the electrons from valence band (VB) or highest occupied molecular orbitals (HOMOs) to the conduction band (CB) or lowest unoccupied molecular orbitals (LUMOs), i.e. E_g ($h\nu \geq E_g$). Photoexcitation ends up with excited electrons at the LUMO/CB and holes at the HOMO/VB of a semiconducting material. This process is called charge separation which leads to electron–hole pair generation. The process of such charge separation is alternatively called as carrier activation step and the electron–hole pair is also called exciton. The charge carriers may get deactivated by recombination or get transferred to another molecule, which may result in some reaction. Minimizing recombination and increasing the charge transfer are thus key strategies in photocatalytic processes. The processes occurring during a photocatalytic reaction may be summarized as follows:

(i) *Carrier activation step*: Generation of electron–hole pairs via absorption of photon with greater than or equal to the band gap of the semiconductor.
(ii) *Carrier deactivation/relaxation step*: The energetic charged species migrate to the surface of the semiconductor which may be trapped by the defect sites in bulk and/or on the surface of semiconductor material. This step is also known as charge carrier recombination step.
(iii) *Carrier transfer step*: Recombination of charge carriers releases the energy in the form of heat/light or utilized by reactants to form desired products.

The carrier deactivation or recombination may occur in the form of radiant light (photon) or non-radiant (heat). This process is also called carrier recombination step (Figure 8.2). The recombination of charge carriers is much favorable due to their highly unstable or reactive nature. If the carrier recombination can be limited, the electron and hole pairs can be utilized for many photochemical transformations including chemical oxidation, reduction, and redox reactions. For photooxidation reactions, excited hole in VB oxidize the reactant A via accepting an electron from the substrate. In case of photoreduction reactions, the excited electron in CB reduces the reactant B via donating an electron. If oxidation of reactant A and reduction of the reactant B happens in the same photocatalytic system, then the process is known as photocatalytic redox reaction.

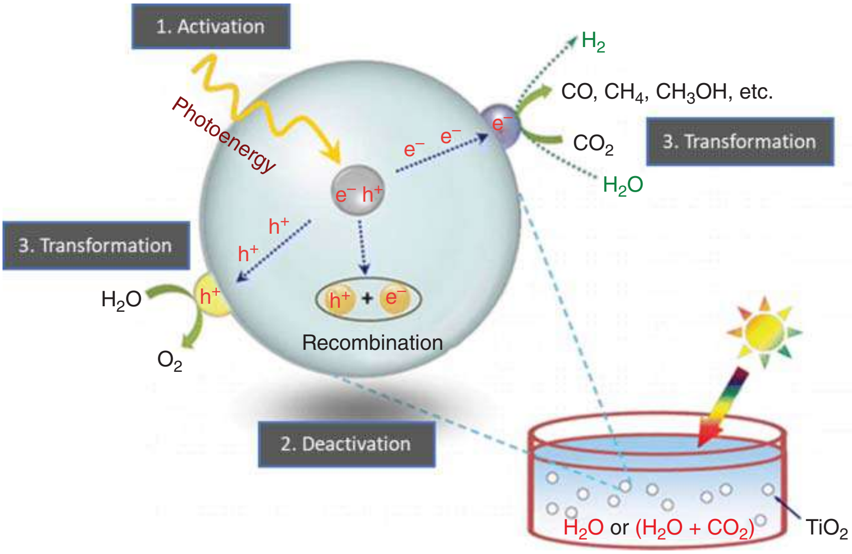

Figure 8.2 Schematic representation of photocatalytic generation of hydrogen, carbon monoxide, methane, methanol, etc. at the expense of water. Source: Ma et al. [32]. Copyright 2014, ACS Publications.

8.5 Conjugated Polymer Nanocomposites and Current Challenges in Their Photocatalysis

In a photocatalytic process, several challenges need to be addressed. Out of them, carrier recombination is one of the most important challenges. The generated excitons are more prone to recombination due to the entrapment of the carriers in the bulk and surface of the semiconducting materials. The surface recombination can be reduced by engineering the properties of the interface between the surface of semiconductors and the electrolyte/reactants. Heterojunction of CPNCs stabilizes the excited electrons and holes via transferring the excited electrons from the highly energetic CB to the materials with comparatively equal or lower energy. Holes migrates to the opposite direction to the flow of excited electrons. Heterogenization therefore ends up with stabilized electron–hole pairs by facilitating another pathway of energy dissipation. The dissipation of energy increases the lifetime of the excited carriers. Therefore, charge carriers easily get involved during the reaction conversion via photooxidation, photoreduction, and photoredox reactions, which are interfacial phenomena between photocatalytic surface and reaction medium.

Yet another challenge in photocatalysis is the range of light absorbed by the catalyst. Recently, there is renewed interest in harnessing solar light for photocatalysis for achieving sustainability. Traditional photocatalysts such as TiO_2 and ZnO are active only in the UV region. However, only 4% of the full solar spectrum falls under UV light and rest is visible light (43%) and near infrared (NIR) (53%). Therefore, photocatalysts with broad range absorption property are highly impactful for energy utilization [33]. During the past decades, a huge number of CP based photocatalytic systems were developed. Like other semiconducting material based photocatalysts, the photocatalytic performance of CPs could further be improved via heterogenization with other materials such as metals and non-metals of semiconducting materials.

Therefore, making heterojunctions of CPs to form CPNCs is a solution to both the aforementioned challenges. CPs have tunable band positions and can easily be engineered with other UV active materials to make efficient photocatalysts for various photochemical conversions under solar light. The light absorption properties can easily be tuned via changing doping level as well. Usually, doping (whether positively doped or negatively doped) facilitates the absorption of light toward higher wave length region. In addition to this, tuning the dimensions of CPs also changes the optochemical properties. Additionally, the bulk recombination can be improved by reducing the material size and dimension to minimum. In addition to this, reducing the dimensions of a materials from the bulk to nanostructure can not only increase the active sites of a photocatalysts, but also reduces the deactivation of charge carriers via controlling the bulk recombination step.

8.6 Band Structure Engineering in Conjugated Polymer Nanocomposites

Hybridization of semiconducting materials with other materials, which have aligned band structures, can reduce the recombination of electron hole pairs. In addition to this, materials with suitable band alignment can also absorb the photon with higher wavelength. CPs themselves are known to be suitable candidates for hybridization with several semiconducting materials because of their electrical and optical properties. CPs are low band gaped organic semiconducting materials that can sufficiently reduce the issues in electron hole pair recombination when it gets hybridized.

Semiconducting materials are of two types: intrinsic and extrinsic. In intrinsic semiconducting materials, the position of Fermi energy (E_F) level is exactly midway in between CB and VB. The Fermi level is defined as the energy level where probability of finding electrons is 1/2 at 0 K. The Fermi levels in extrinsic semiconducting materials varies depending upon the level of vacancies or impurities. For n-type semiconducting materials, the impurities are electron donating in nature and it is opposite in case of p-type semiconductors. Therefore, the Fermi energy level in n-type semiconducting materials exists closer to the CB and toward VB in the case of p-type semiconducting materials. CPs are intrinsic semiconductors where the conductivity can often be tuned by doping. Semiconducting materials such as CPs are often combined with metals, metal oxides, or non-metals to enhance charge separation and engineer their band structure. Such heterojunctions are essentially present in CPNCs and hence a description of their properties is given here.

For a photochemical reaction to be thermodynamically favorable, we need to know the band positions in two different interfaces:

(A) Solid–solid interfaces between the heterojunctions.
(B) Solid–liquid interface between the semiconductor (solid) and medium (liquid).

The band positions also vary with change in surface lattice periodicity, external field effect, and adsorption of donor or acceptor reactants on the semiconductor surface [34].

8.6.1 Solid–Solid (S–S) Interface

Solid–solid interface is related to the formation of heterojunction between two solid counterparts. There are two possibilities in such cases:

(1) semiconductor–semiconductor (SC–SC) and
(2) semiconductor–metal (SC–M)

A careful band structure engineering in these heterojunctions can result in highly efficient photocatalysts.

8.6.1.1 SC–SC Heterojunction

This class of heterojunction is formed between two semiconducting materials (organic or inorganic semiconductors). Depending upon the relative position of band gaps, the SC–SC heterojunctions are classified further into three types as shown in Figure 8.3:

a. *Type I (Straddling gap)*: $CB_{SC2} < CB_{SC1}$ and $VB_{SC2} > VB_{SC1}$. In this case, e^- and h^+ both are injected from SC1 to SC2. Straddling type band structure occurs when a wide band gap SC such as TiO_2 is combined with a narrow band gap material such as CPs. For example, TiO_2@Poly(*o*-phenylenediamine) core–shell nanostructures [35].
b. *Type II (Staggered gap)*: $CB_{SC2} < CB_{SC1}$ and $VB_{SC2} < VB_{SC1}$. In this case, e^- are injected from SC1 to SC2 and h^+ are injected from SC2 to SC1.
c. *Type III (Broken gap)*: $CB_{SC2} \ll CB_{SC1}$ and $VB_{SC2} \ll VB_{SC1}$. Band gaps of two heterojunctions do not overlap. In this case, e^- are injected from SC1 to SC2 and h^+ injects from SC2 to SC1.

Due to the less efficiency in separation of charges in Type I and Type III, Type II form of S–S heterojunctions is highly studied in photocatalytic applications [36]. Therefore, we will mostly discuss about staggered types of heterojunctions here. SC–SC heterojunctions can be a combination of either p–n or non p-n based heterojunctions.

p–n Junction-Based Heterojunctions

In semiconducting heterojunctions, the flow of charge carriers depends upon position of the Fermi levels, which further deals with the positions of their CBs and VBs. When two p–n type of semiconductors come in contact, electrons from the n-type SC diffuse to the p-type SC until their Fermi energy levels reach an equilibrium position. Such a diffusion of electrons occurs because of imbalanced electron and hole densities (or difference in chemical potential) in the p-type and n-type semiconductors

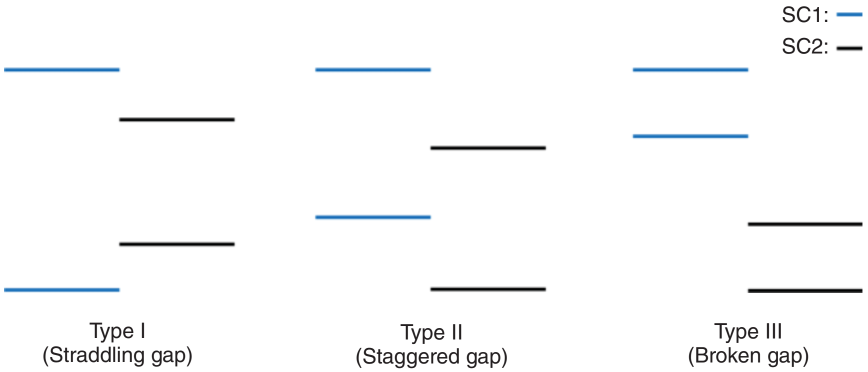

Figure 8.3 Band positions of three different types of semiconductor heterojunctions w.r.t. to SHE.

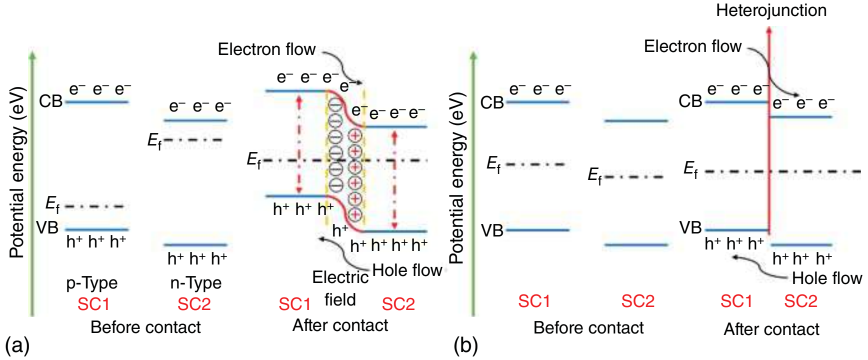

Figure 8.4 Semiconductor–semiconductor heterojunctions: (a) p–n type heterojunction and (b) non-p–n type heterojunction.

before they come into contact with each other. For example, when a p-type CP is heterogenized with a n-type CP, the process of diffusion is as shown in Figure 8.4a [37]. This creates an electrical potential difference at the interface between two SCs. When the p–n junction is exposed to light, the excited electrons flow from the CB of p-type SC to the CBs of n-type SC. On the other hand, holes migrate from n-type VB to p-type VB. Therefore, the electron hole pair recombination process is suppressed due to the in-built internal field generated at the interface of the p–n junction. In addition to this, p–n junction based heterojunctions have several other advantages like rapid and effective charge separation with better long term stability [38]. Using an appropriate wavelength of excitation, the charge transfer process of the p–n junction-based nanocomposites can also be enhanced [39].

Basically, p- or n-types of CPs are obtained via chemical or electrochemical doping processes. The n-type CPs are obtained when the polymer is synthesized with strong reducing agents like metal alkali metal vapor, $Na^+(C_{10}H_8)^-$ [40] or γ-irradiation [41]. In addition to this, atomic or molecular engineering of the monomers can also change the type of CPs. For example, carbon nitride based graphitic carbon nitrides are known as n-type CPs because of the electron rich nitrogen atoms in the polymeric matrix. Nevertheless, the n-type g-C_3N_4 can be transformed to p-type via external application of acids [42, 43].

Several p–n junction-based CPNCs are reported which are efficiently utilized in photocatalytic applications. For example, ordered ZnO nanowires/polyaniline (PANI) microrods as efficient diodes for photodetection application was reported [44]. PANI based poly-(aniline-*co*-*N*-(4-sulfophenyl)-aniline) (PAPSA)/coordination polymer nanorod (CPNR) was prepared for photocatalytic evolution of hydrogen [45]. Ghosh and coworkers [46] prepared an excellent CPNC by decorating n-type ZnO nanoparticles over p-type poly(diphenylbutadiyne) (PDPB) nanofibers. This CPNC was found to be suitable photocatalyst for methyl orange (MO) degradation reaction. The CPNC was having better photocatalytic activity than PDPB nanowires and the ZnO nanoparticles under UV–Vis light irradiation [19]. The high photocatalytic activity of PDPB-ZnO CPNC is mainly due to efficient charge transfer from the CB of PDPB to the ZnO surface. PDPB-ZnO CPNC carries 2.5 times higher photocurrent than the pure ZnO NPs. This reflects the higher charge separation and transfer efficiency of photoexcited electrons from the PDPB to ZnO NPs. So, for the degradation of MO, the photocatalytic mode of electron and hole transfer process involved through the following mechanism (Figure 8.5).

PANI based semiconductor was incorporated with inorganic p–n junctions to enhance absorbance of visible light. In this case, p-type cobalt molybdate ($CoMoO_4$) and n-type TiO_2 were coupled with PANI, which was found to be efficient visible light active photocatalysts for many photodegradation and photoreduction reactions under visible light illumination [47].

Non-p–n Based Heterojunction

In case of non-p–n junction-based heterojunctions, the flow mechanism is similar to the p–n heterojunction-based semiconductors. However, the enhanced interfacial electric field generation does not occur and hence does not provide efficient electron and hole separation as compared with the p–n junction-based semiconductor heterojunctions. This kind of heterojunction is however observed between the nanocomposites of intrinsic–intrinsic (I–I) semiconductor heterojunctions. I–I heterojunctions have their Fermi energy levels existing half-way between the CB and VB. The chemical potential for reaching electronic equilibrium is relatively lower in case of I–I junction than the p–n junction-based nanocomposites. So, I–I heterojunction-based composites are relatively less efficient in terms of photo generated charge carrier transfer than p–n junction-based heterojunctions. Nevertheless, I–I type hetero-nanocomposites are also designed by considering various semiconducting materials with matching band positions, especially to create staggered type of heterojunctions. The flow of photoexcited electrons occurs from the semiconductor with higher CB band to the other semiconductor having lower CB. However, holes move from semiconductor having lower VB to the second semiconductor having higher VB of a Type II or staggered heterojunction. This phenomenon results in accumulation of excited electrons and holes on opposite semiconductors with lower CB and higher VB positions, respectively. Thus, I–I

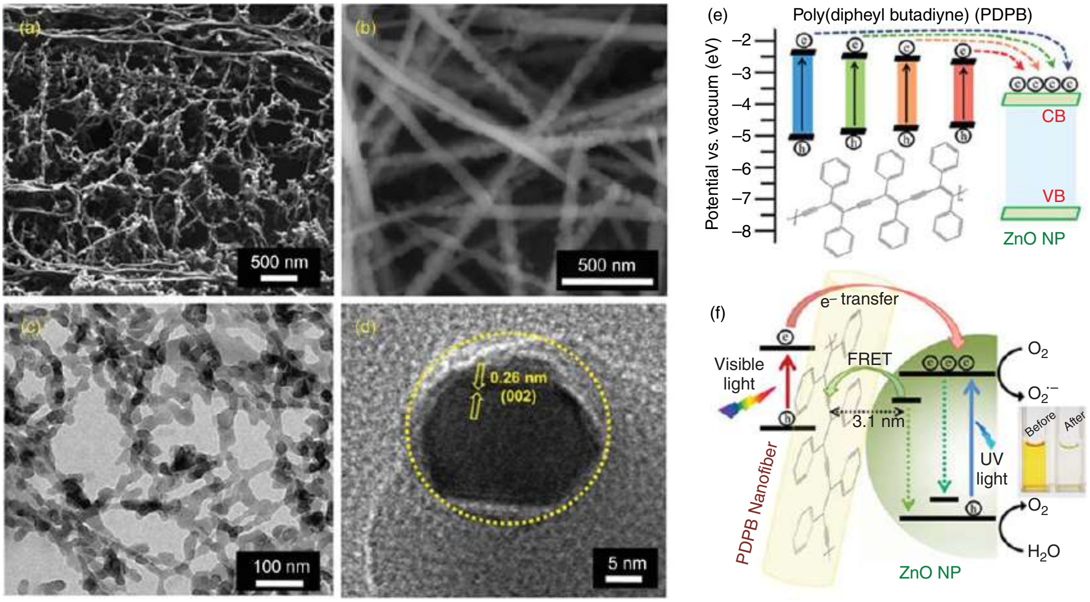

Figure 8.5 Characteristics of ZnO-PDPB nanohybrids (NH): scanning electron microscopy (SEM) images of (a) PDPB nanofibers and (b) PDPB-ZnO NH, TEM images of (c) PDPB nanofibers and (d) PDPB-ZnO NH; (e) the co-sensitization of different PDPB oligomers to ZnO NPs with molecular structure of PDPB polymer and (f) the interfacial carrier dynamics at the heterojunction showing the photocatalytic degradation of MO in aqueous solution. Source: (a–d) Adapted with permission from Sardar et al. [46]. Copyright 2015, Nature Springer, (e, f) Sardar et al. [46]. Licenced under CC BY 4.0.

type of heterojunction also generates an internal field which is responsible for good separation of electron–hole pairs under the influence of suitable light similar to p–n junction-based semiconductors. The process of charge carrier transfer mechanism is depicted in Figure 8.4b [38].

There are several I–I type heterojunctions containing CPNCs. C–C coupling reactions, like Suzuki reactions [17], Yamamoto reactions [48], Sonogashira–Hagihara reactions [49], Schiff-base reactions [50], and Ullmann coupling reaction [51], can be used for creating I–I heterojunction based CPNCs. Most of these kinds of reactions involve metal (Pd and Ni) based catalysts. which usually follow oxidative addition followed by reductive elimination mechanism. For example, modified poly-benzothiadiazole flake (BE) and its nanocomposites with black TiO_2 (BE-black TiO_2) [52]. A PANI/TiO_2 CPNC was reported to be very efficient for the degradation of dyes such as methylene blue and rhodamine B [53].

Z-Scheme Type CPNCs

Z-scheme type of photocatalysts is a special type of Type II heterojunctions where the CB and VB band positions of two semiconductors are well oriented to undergo transformations of photogenerated charge carriers. Z-scheme is a bioinspired system, mimicking the process of photosystems occurring in natural green plants [54]. The charge transfer in such type of heterojunctions is controlled by a shuttle redox mediator between two staggered semiconductors. The function of such a mediator is to endow facile transfer of excited electrons from CB of one semiconductor to VB of other semiconductor and vice versa. Thus, depending upon the type of mediator, Z-scheme based photocatalysts are differentiated into three generations (Figure 8.6).

(i) *First generation*: Traditional Z-scheme requires an acceptor for electrons and donors for holes.
(ii) *Second generation*: All-solid-state Z-scheme incorporates metal mediators as carrier transporters.
(iii) *Third generation*: Direct Z-scheme is of most appealing Z-scheme as it does not need any charge transferring agents for efficient charge transfer [55].

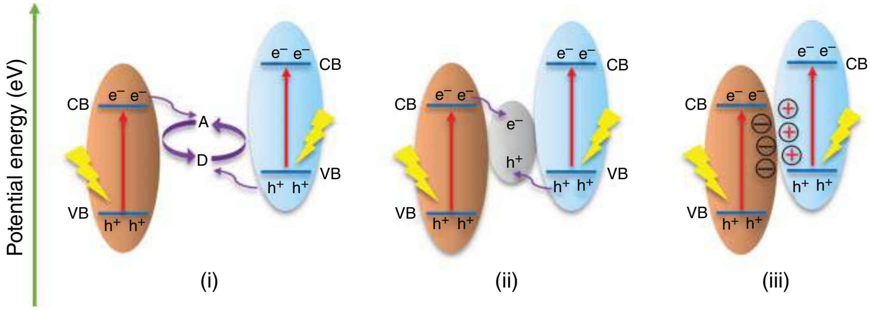

Figure 8.6 Three generations of Z-scheme photocatalysts: (i) traditional Z-scheme, (ii) all-solid-state Z-scheme, and (iii) direct Z-scheme.

Liu and Cai [56] reported a Z-scheme photocatalysts based on Ag mediated polypyrrole and BiOBr heterojunction (BiOBr-Ag-PPY). A Nyquist plot of the Z-scheme photocatalyst is compared with the pure BiOBr, BiOBr-PPY, and BiOBr-Ag suggesting the lowest resistance offered by BiOBr-Ag-PPY photocatalyst validating maximum charge transfer ability than the ordinary Type II heterojunctions.

The specialty about Z-scheme is its potential for oxidation and reduction during a chemical transformation. For a photoreduction reaction, the CB position should be highly negative than the reactant while for the photooxidation process VB should be highly positive than the corresponding reactant to be oxidized. Z-scheme provides maximized VB and CB positions of Type II heterojunctions. For better understanding, we can consider the example of TiO_2 and graphitic carbon nitride (g-C_3N_4) heterojunction. TiO_2 and g-C_3N_4 are state-of-the-art photocatalysts among metallic and non-metallic SCs, respectively. g-C_3N_4 has higher reduction potential (CB; −1.12 eV) than TiO_2 (CB; −0.3 eV) and TiO_2 has higher oxidation potential (VB; +2.9 eV) than g-C_3N_4 (VB; +1.57 eV) [57]. Thus, using a suitable mediator with energy levels matching with CB of one semiconductor and VB of other semiconducting material, one can easily synthesize an excellent photocatalyst. Therefore, Z-scheme heterostructures can easily oxidize and reduce reactants [57].

8.6.1.2 Semiconductor–Metal (SC–M) Heterojunction

The semiconducting (SC) materials form heterojunctions with non-plasmonic (SC–Mn) and plasmonic metals (SC–Mp). For SC–Mn heterojunctions with $E_{F,S} > E_{F,m}$, i.e. for heterojunction of Mn with n-type semiconductor, the E_f of both materials reaches equilibrium position via the injection of electrons from the n-type SC to the metal. This endows a band bending in the upward direction with depletion of electrons at the surface of the semiconductor generating potential difference at the interface. On the other hand, accumulation of electrons in the semiconductor occurs, when the condition is inversed. During the process, there is a deformation of band structures at the junction forming an energy barrier. This barrier is commonly known as the Schottky barrier (Figure 8.7). Mathematically, Schottky barrier (φ_B) is represented as:

$$\varphi_B = \varphi_m - \chi_s \tag{8.1}$$

where φ_m and χ_s are the work function (energy required to bring an electron to the vacuum) and electron affinity (tendency to accept electrons) of respectively for metal and the semiconductors. The Schottky barrier acts as an electron trap from where transferred electrons never flow back and leading to enhanced life span of the excited electrons. Usually, metals have lower E_F levels than n-type semiconductors. Therefore, continuous irradiation of light never ends up with discontinuity in the flow of excitons [58]. Pd nanoparticles immobilized conjugated microporous polymers (CMPs), poly(benzoxadiazole) (B-BO_3) was proved to be an efficient heterogeneous photocatalyst for the Suzuki coupling reaction between aryl iodide and phenyl boronic acid under the influence of visible light [59]. The CPNC (Pd@B-BO_3) contains 3% of Pd nanoparticles of sizes ranging from 5 to 10 nm.

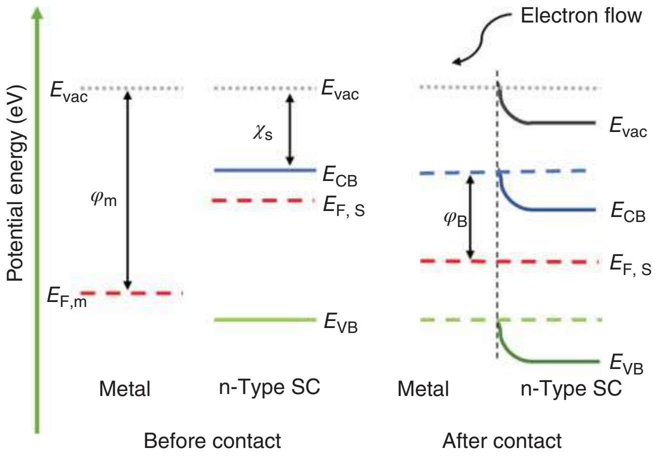

Figure 8.7 Schottky junction formation at the metal–semiconductor interface.

However, if the metal incorporated to the p-type semiconducting materials is plasmonic in nature, like Au, Ag, Cu, etc., the flow of electrons occurs toward p-type semiconducting material. Like semiconducting materials, plasmonic materials can also absorb solar light due to the loosely bound electrons on the surface (plasmons). Under the influence of light, excitation of plasmons from plasmonic energy levels can take place leading to the release of highly energetic electrons known as "hot electrons." This is known as surface plasmon resonance (SPR) effect. Therefore, integration of plasmonic metals with CPs is being utilized for the stabilization of electron hole pairs. A directional change in the flow of electron and hole pairs occurs in plasmonic material-based nanocomposites depending upon the type of semiconductors.

For n-type semiconductors, the formation of Schottky barrier based on the difference in work functions of the plasmonic material and the n-type semiconductor occurs. After application of an external light, the excited hot electrons flow from plasmonic materials to n-type semiconductor. On the other hand, holes are injected from the plasmonic materials to p-type semiconductors. In Figure 8.8, both conditions are

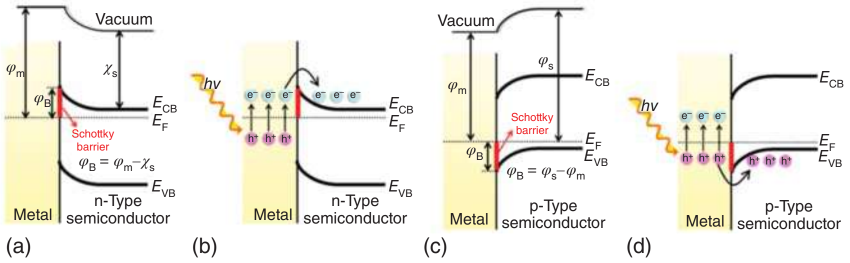

Figure 8.8 Hot electron injection process in plasmonic metal-based heterojunctions: (a) metal-n-type semiconductors, (b) insertion of hot electrons to n-type semiconductor, (c) metal-p-type semiconductors, and (d) insertion of holes from plasmonic metals to p-type semiconductor. Source: Zhang et al. [60]. Copyright 2018, Elsevier.

represented. The flow direction of the electrons via SPR effect is opposite to that of the Schottky barrier effect. However, the Schottky effect plays more significant effect on photoinduced enhancement of catalysis [58]. Although metal/semiconductor heterojunctions show good efficiency in most of the photocatalytic applications, it has less impact on sustainable development. This is mainly because plasmonic metals are rarely available natural sources and are therefore highly costly.

Plasmonic metal-CP nanocomposites are reported as photocatalysts for several photocatalytic conversions. S. Ghosh et al. [61] have reported Au nanoparticle immobilized poly(3,4-ethylenedioxythiophene) (PEDOT) NC (Au/PEDOT), which could be a good example in this case. The CPNC was synthesized via surfactant mediated one pot oxidative polymerisation method. It was studied for sensing and degradation of MO dye under visible light irradiation. Owing to the plasmonic nature of Au along with the semiconducting nature of CPs, such nanocomposite can absorb visible light. The CPNC was found to be an efficient material for surface enhanced raman scattering (SERS) and degradation of MO and rhodamine-B (RhB) dyes.

The photocatalytic activity of the Au/PEDOT CPNC was compared with PEDOT nanofibers, Au/TiO_2 and TiO_2 in both UV and visible light. The activity of Au/PEDOT heterojunction showed much better degradation efficiency both in UV and visible light than the other nanostructures. Although the trend of degradation in these nanomaterials is same for both of MO and RhB, in fact, much rapid degradation was observed in case of UV irradiation than visible light (Figure 8.9). The CPNC could act as an effective photocatalyst as the Au NPs act as good electron reservoir that improve abstraction of photoexcited electrons generated in the PEDOT nanofibers during the photo-illumination process. A schematic diagram showing the mechanism of Au enhanced energy transfer and degradation of organic pollutants (Figure 8.9).

Au nanowires were used for the modification of spontaneous emission spectrum, polarization direction, and emission lifetime of single monolithically coupled poly(3-hexylthiophene), P3HT [62]. Zhang and coworkers [59] reported a good example explaining Schottky effect between Pd nanoparticles and CMPs. Here, Pd incorporated conjugated microporous poly(benzoxadiazole) network (B-BO_3) for the Schottky effect enhanced photocatalysis under visible light. For the same application, Li et al. [63] showed the Mott–Schottky effect of Pd and g-C_3N_4 heterogenized nanocomposites is an interesting photocatalyst at room temperature.

8.6.2 Solid–Liquid Interface

For heterogeneous photocatalytic systems such as CPNCs, the solid–liquid interface properties are also important. Solid–liquid interface is concerned with the CPNC (solid) and reactants in the solvent (liquid) interface. Although, the effect is highly pronounced in photoelectrochemical processes, the mechanism is same for photocatalysis of other mediums also. The space charge layer generated between solid semiconductor and the medium containing reactants also follows the same mechanism as the solid–solid interface (Figure 8.10) [64].

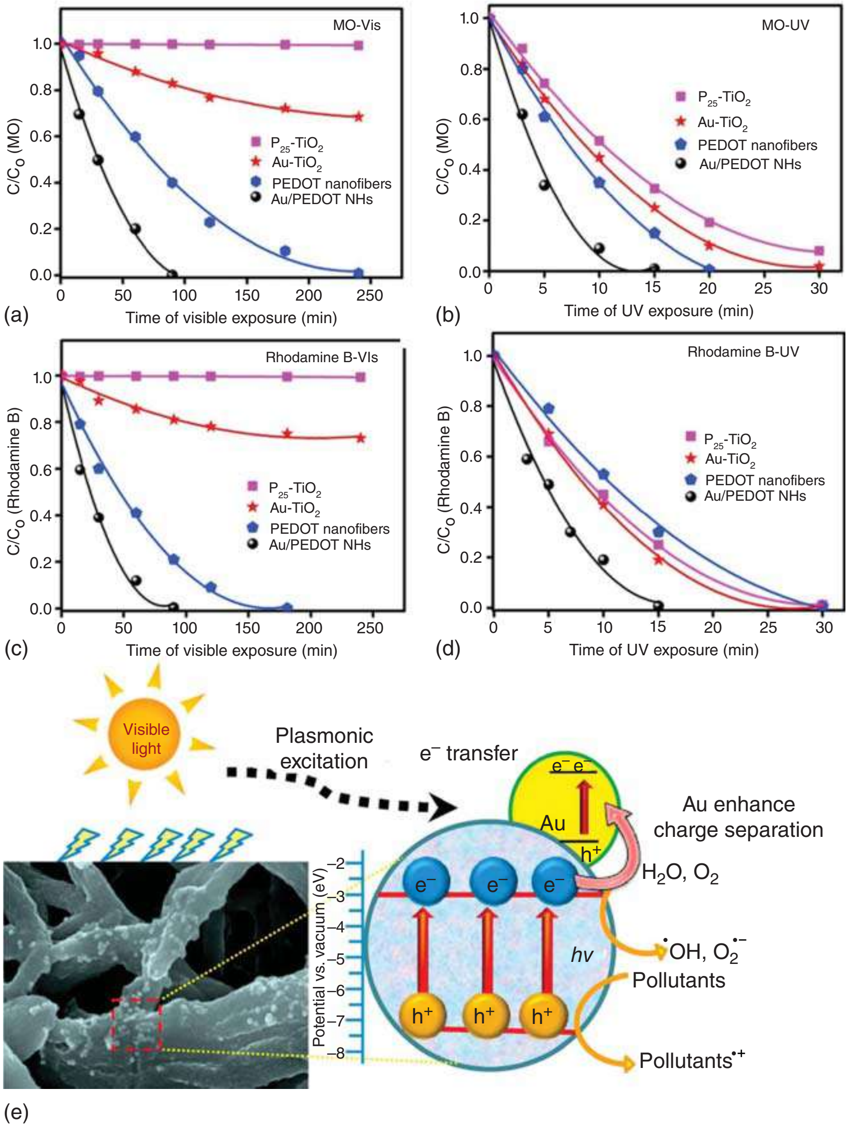

Figure 8.9 Comparative photocatalytic activity of PEDOT nanofibers, Au/PEDOT NHs, TiO_2, and Au-TiO_2: (a) photodegradation of methyl orange (MO) visible light (>450 nm) and (b) UV light, photodegradation of RhB (c) under visible and (d) UV light, and (e) plausible mechanism of photocatalytic degradation for Au/PEDOT nanohybrids under visible light. Source: (e) Adapted with permission from Ghosh et al. [61]. Copyright 2018, Elsevier.

From the thermodynamic point of view, these processes are well explained in the literature. Photocatalysts with suitable band positions, i.e. for a photoreduction process the CB/LUMO minima of the photocatalyst, should be more negative or more cathodic than standard reduction potential of the reactants (P_{red}). Similarly, VB/HOMO maxima should be more positive or more anodic than the standard

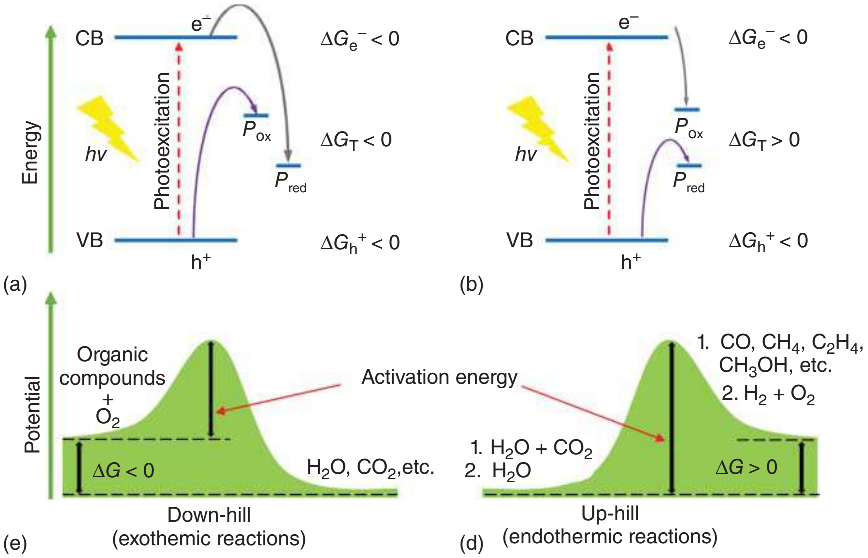

Figure 8.10 Gibbs free energy change in semiconducting photocatalysts at solid–liquid interface: (a, b) electronic structure and potential barrier of (c) exergonic photodegradation of down-hill reactions (degradation of organic dyes, drugs, etc.) and (d) endergonic photocatalytic conversion of some up-hill reactions (e.g. evolution of H_2 and O_2 from H_2O, reduction of CO_2 to CO, CH_4, CH_3OH, etc.)

oxidation potential of the reactant to undergo photooxidation reaction (P_{ox}). For photoredox reaction, both conditions should be fulfilled by the photocatalytic system. For a reaction to be thermodynamically feasible, the overall Gibbs free energy change ($\Delta G = P_{red} - P_{ox}$) should be negative. However, thermodynamically non-feasible reactions can also be easily carried out using semiconducting materials based photocatalytic systems. On the basis of thermodynamic feasibility, the reactions are classified into two categories, uphill (energy absorbing or endergonic) and downhill reactions (energy releasing or exergonic process). Therefore, thermodynamically uphill reactions like evolution of hydrogen and oxygen from water ($\Delta G = 237$ kJ/mol), fixation of nitrogen to ammonia and oxygen ($\Delta G = 678$ kJ/mol), and even reduction of carbon dioxide to CO ($\Delta G = 237$ kJ/mol), methanol ($\Delta G = 703$ kJ/mol), and methane gas ($\Delta G = 818$ kJ/mol) can be easily done with semiconducting photocatalysts in addition to the thermodynamically downhill reactions like, photodegradation reactions [64].

8.7 Photocatalytic Applications of Conducting Polymer Nanocomposites

There are numerous photocatalytic reactions where CPNCs can be effectively used as photocatalysts. As discussed earlier, oxidation, reduction, and redox reactions can be catalyzed by CPNCs. Owing to the concerns over environmental pollution and quest for developing sustainable chemical processes, recent focus has been mostly on few very important energy and environment related applications. Some of these applications will be discussed briefly.

8.7.1 Water Remediation Using CPNCs

Industrial production of various commodities often results in significant pollution of air, water, and soil. Bio persistent organic molecules from textile, pharmaceutical, and tanning industries causes significant pollution to river bodies. Domestic usage of plastics, cloths, detergents, and pharmaceuticals also leads to the release bio persistent organic compounds to water bodies. Organic chemicals such as bisphenol A are known to have large impact on reproductive systems. Similarly, 2,4-dichlorophenol causes anemia and several nervous systems symptoms. Tetracycline hydrochloride and chlortetracycline reduce immune systems and disturbs many physiological functions [65]. Therefore, removal or denaturation of bio persistent organic compounds is an important concern.

Photo-physicochemical treatment is one of the techniques that basically uses a photocatalyst for adsorption of the organic pollutant followed by its photocatalytic decomposition. The organic pollutant can be oxidatively decomposed into innocuous compounds under the irradiation of light in presence of a catalyst. Although many of the organic compounds such as dyes can absorb light, they do not get decomposed under normal conditions [66]. A suitable photocatalyst is necessary for the effective degradation of the organic pollutants. Owing to the voluminous literature, we chose to discuss the application of CPNC based photocatalysts for water remediation, as per the classification given in Section 8.2.

8.7.1.1 Inorganic Semiconductor Based CP Nanocomposites as Photocatalysts for Water Remediation

There are several semiconducting materials that are known to be hybridized with CPs and used for photocatalytic degradation of the organic compounds. This includes metal oxide based CPNCs of TiO_2 [67], ZnO [68], and BiOX (where X = I, Br, or Cl) [69–71]. Metal chalcogenides (ZnS, MoS_2, CdS) and metal nitrides have also recently been used to modify the photocatalytic performance of CPs. Among all, TiO_2 is well known as state-of-art photocatalysts due to its excellent chemical and photostability, less toxicity, and low cost. However, its large band gap energy of 3.2 eV and high degree of electron hole pair recombination limits its visible light application. CPNCs with TiO_2 can easily be applied for the decontamination of organic pollutants as a solar light sensitive photocatalysts.

In the photocatalytic degradation of organic pollutants, several reactive species are generated in presence of suitable light, which are responsible for degradation of organic dyes. These species include hydroxyl radical ($^{\cdot}OH$), singlet oxygen ($^1O_2$), superoxide radical ($^{\cdot}O_2^-$), peroxide radical ($^{\cdot}OOH$), and photogenerated electron (e^-) and hole (h^+) pairs [72]. These reactive species are sufficiently active for the degradation organic dyes. Figure 8.11 represents a schematic diagram of photocatalytic mechanism for the degradation of organic dyes. In the presence of

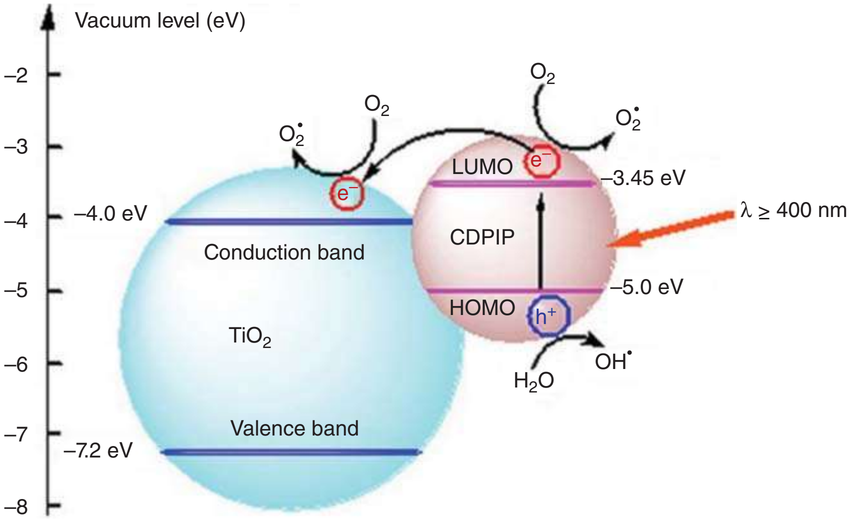

Figure 8.11 Photocatalytic mechanism of TiO_2/conjugated derivative of polyisoprene (CDPIP) based nanocomposites. Source: Luo et al. [73]. Copyright 2012, ACS Publications.

visible light, the electrons of the CP get excited from their HOMOs or VB to LUMOs or CB due to the π–π* transition. The excited electrons in LUMO (−3.45 eV) of CP get transferred to the CB of UV light active TiO_2 (−4.0 eV). These electrons are captured by dissolved oxygen in the water and forms reactive species called superoxide radical anion ($^{\cdot}O_2^-$). On the other hand, the holes generated during the photoinduced excitation process oxidize the water molecule to $^{\cdot}OH$ radicals. These radicals also can be involved in the degradation of organic pollutants [73]. There are three major advantages during the formation of CP-TiO_2 heterojunctions. Firstly, incorporation of CP renders the UV light active TiO_2 to absorb visible light. Secondly, the photodegradation capabilities are greatly enhanced in comparison with the pure counterparts. And thirdly, TiO_2 get stabilized via heterogenization with CPs.

Layered Bismuth based oxyhalides, BiOX (X = I, Br, Cl), are known to be very good semiconducting materials for photocatalytic applications due to their excellent band structures that are suitable for solar light absorption. Therefore, these materials are utilized in several important application like wastewater treatment, hydrogen evolution, indoor-gas purification, CO_2 reduction, and even in organic synthesis [74]. Because of their broad ranged absorbance and narrow band gap, these materials can be easily coupled with several carbonaceous materials for easy electrical charge transfer through the heterojunctions [75]. Therefore, BiOX are widely used for the construction of CP based nanostructures for effective photocatalysis [76]. Polypyrrole based BiOI nanocomposites [65], BiOI loaded PANI [71], PANI based BiOBr [70] and BiOCl [69] nanocomposites are known for photocatalytic degradation of organic pollutants. Fe_3O_4 based CPNCs are also known for visible light active photocatalyst for Methylene blue degradation [77].

Among the various sulfide semiconducting materials, CdS is known to be effective photocatalysts because of its tunable optical properties and the visible light activity. Its usual band gap is 2.42 eV, however can be modified by varying its morphology. In addition, with changing particles size from bulk to nanometer dimensions, the surface area can also be enhanced, which facilitates high rate of adsorption during the process of pre-photocatalysis. Furthermore, hetero-coupling with CPs, significantly improves their activity under visible light. A comparative study was done between prepared nanostructures of various CPs and their CPNCs with CdS quantum dots for degradation of MB under visible light irradiation [66]. CdS/CP NCs outperformed their individual CPs with CdS/PPy being the best performing photocatalyst.

8.7.1.2 Plasmonic Metal-Based CPNCs

Incorporation of plasmonic noble metals into CPs, can also significantly stabilize the electron hole pair of CPs due to their labile conducting electrons on the surface. These surface-active electrons are highly active for visible light absorption of different wavelengths of light depending the size and shape. Photocatalytic degradation using plasmonic metal based CPNCs is well discussed in Section 8.6.1.2. The improved photodegradation of RhB and MO is mainly because of metal-CP heterojunction formation, which induces the Frenkel type of excitons for easy charge carrier separation under visible light.

8.7.1.3 Conjugated Polymer-Conjugated Polymer-Based Nanocomposites

Graphitic carbon nitride is a widely explored CP because of its suitable band gap of 2.7 eV. Pure g-C_3N_4 has many shortcomings including fast electron hole pair recombination rate and low surface area. However, it can be prepared in a one-step method from commercially available and cheap sources like cyanamide, urea, thiourea, melamine, and dicyanamide. Mesoporous g-C_3N_4 that has pore size ranging from sub nano to macro level can greatly enhance the surface area and hence the high rate of surface adsorption. Additionally, reducing its dimensions from the bulk g-C_3N_4 to 2D nanosheets, 1D nanorods or nanowires, and 0D spherical nanodots can greatly enhance its surface area. These materials are widely explored in many applications including photocatalysis. Integration with other materials also narrow down the band gap of semiconducting CPs via blue to red shift absorbance. Heterogenization of CPs with other materials not only improves the stabilization of electron–hole pairs but also helps the chemical and physical stability of the corresponding materials. Moreover, heterogenisation improves the long-term recyclability and reusability and can be implemented industrially.

Recently, 3D hierarchical structures of CN have shown much accessible surface area, ability to prevent aggregation or restacking and easy recyclability makes them promising photocatalysts [78]. Interestingly, the reactive charge carriers of CN can be stabilized when coupled with CP nanostructures to improve photocatalytic efficiency. For instance, Jiang et al. [78] synthesized a novel polyaniline and carbon nitride nanosheet composite hydrogel (PANI/CNNS) as separation free and efficient photocatalyst for MB adsorption and *in situ* photocatalytic oxidation. The reason for the enhanced photocatalytic activity was the larger surface area and good and long-time interfacial charge separation than the pure CNNS. In another report, PANI nanorods grown on g-C_3N_4 via dilute polymerization technique under −20 °C were used for degradation of methylene blue and MO [79]. Under visible light irradiation, the photocatalytic degradation efficiency of g-C_3N_4 can be greatly enhanced with increasing PANI content in the nanocomposites.

8.7.2 Hydrogen Generation Application

Energy crisis and environmental concerns are among the most important global challenges to the whole humanity. Owing to the non-renewable nature and the release of CO_2 gas, fossil fuels need to be replaced with alternative fuels. Hydrogen gas has the potential to be a green, renewable, and sustainable alternative. However, the present methods of commercial production of hydrogen such as steam reforming lead to the release of CO_2. Photocatalytic water splitting has to be developed for realizing the sustainable hydrogen fuel dream. Utilization of natural sun light as an energy source for production of solar fuels can greatly resolve many of the energy related issues. This is because, the energy release by the sun is nearly twelve thousand times higher than the current energy demand, i.e. $\sim 3 \times 10^{24}$ J/yr. Most commonly, hydrogen, methane, and methanol are utilized as solar fuels. However, hydrogen has gained much attention because, burning of fossil fuels ultimately causes global warming simply because of CO_2 produced as by-product. In the photocatalytic hydrogen evolution reaction (PHER) from water involves three major steps:

1. Photoexcitation of electrons that lead to the formation of highly reactive electrons (LUMO) and holes (HOMO).
2. The generated carrier charges may recombine or migrate to the surface of the photocatalysts.
3. Adsorption of water molecules on the catalyst's surface.
4. Oxidation of adsorbed water molecules via holes forming oxygen and reduction by excited electrons to molecular hydrogen.
5. Lastly, desorption of the adsorbed oxygen and hydrogen.

For a photocatalyst with suitable band alignments or redox potentials, i.e. HOMO (VB) and LUMO (CB), positions are essential for the photocatalytic water splitting to produce hydrogen gas. Basically, the LUMO or CB of the photocatalysts must be more negative than the reduction potential of H^+/H_2 (0.00 V) and the oxidation potential of the HOMO or VB should be more positive than oxidation potential of O_2/H_2O (1.23 V) wrt the normal hydrogen electrode (NHE) [80]. Only band alignment is not sufficient enough for a good photocatalyst. The fast recombination step as mentioned in the second step earlier is one of the major concerns. The fast recombination step (surface or bulk) usually takes nanosecond time scale while the surface reaction occurs normally in microsecond time scale [81]. As the surface recombination step is the most important part of heterogeneous photocatalysts, first strategy should be the design of the heterojunction to enhance the stability of the charge carriers.

In 1972, the discovery of the photoelectrochemical set up established by Akira Fujishima and Kenichi Honda showed a revolutionary work for development of photocatalysts for hydrogen evolution reaction (HER) reaction from water [82]. Presence of TiO_2 electrode as UV light initiator produced molecular oxygen, while platinum black facilitated hydrogen evolution in their electrochemical cell. Since then, various photocatalysts were developed for HER reaction, mostly based on metal oxides (e.g. TiO_2, $BiVO_4$, Ag_3PO_4, Fe_2O_3, WO_3, and Cu_2O) [83], metal sulfides (e.g. CdS, CuS, Ag_2S, ZnS, and MoS_2) [84], metal phosphides (e.g. Ni_2P and InP) [83] and very rarely metal nitrides (InN, InGaN) [85] and Ta_3N_5 [86]. CPs are low band gap semi conducting materials and hence can be very promising candidates for hydrogen gas generation via splitting of water under visible light.

Linear poly(*p*-phenylene) (PPP), which was discovered by Yanagida and coworkers [87] in 1985, was the first CP based photocatalyst for water splitting. Later in 1990, PPP-Ru nanocomposite was used for visible light PHER. Depending on irradiation wavelength, the PHER rate could be enhanced from 3 to 20 times than the unloaded PPP. Unfortunately, there are only very few reports where the PHER rate could be further enhanced using linear CP-based materials.

Nevertheless, a number of CPNCs were applied as photocatalysts for HER. A nanocomposite of TiO_2 (size 4.5 nm) with granules of polypyrrole (200–300 nm) using 1 wt% Pt as co-catalysts was reported [88]. CdS immobilized linear PANI nanocomposite was found to be efficient for PHER under the visible light without using any co-catalysts. The evolution efficiency was 7.7 times higher than the pure CdS highlighting the enhanced PHER due to PANI loading [89]. It was showed that the stability of the excitons can be enhanced by planarizing linear CPs. Here, binding linear PPP chains via methylene bridges or other linkage functionalities like fluorene, carbazole, dibenzo[*b*,*d*]thiophene, and dibenzo-[*b*,*d*]thiophene sulfone can reduce the torsional angles of phenylene rings via hindering axial rotation that actually decrease the coulomb binding energy facilitating dissociation of excitons [90]. Therefore, 2D organic semiconducting materials like carbon nitrides (C_3N_4), CMPs, metal organic frameworks (MOFs), etc. are known to be excellent photocatalysts over 1D materials.

As a desired candidate for PHER, donor–acceptor (D-A) CP-based hybrid is also known. Chen et al. [91] reported TiO_2 nanoparticles of size 20 nm anchored on two D-A CPs as an interesting CPNC for PHER. A significant correlation was observed between the interfacial charge transfer and PHER. The CP with end functionalized carboxylic acid was found to have two times higher activity than the non-functionalized CPNCs. This may be due to the ester linkage formed via carboxyl functionalized D-A polymer and surface hydroxyl functionality of TiO_2. This ester linkage at the interface facilitates easy electron transfer from D-A CPs to the CB of TiO_2 via electron withdrawing nature of carboxylic acid.

The PHER can further be enhanced as we move from binary nanocomposites of CPs to multicomponent CPNCs. In a case reported by Ghosh et al., a significant change in PHER was observed as the number of heterointerfaces increases in CPNC. The nanohybrid composites were prepared using γ-irradiation on nano-polypyrrole (PPY) in the corresponding metal salt solution without using any reducing agents.

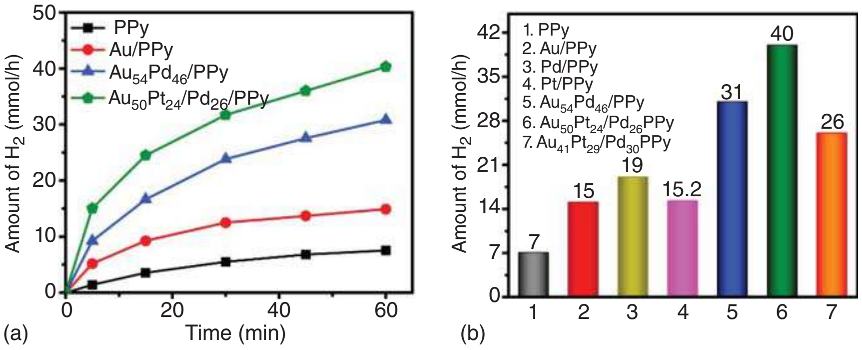

Figure 8.12 (a, b) A comparative study on PHE using pure PPY with it's binary, ternary, and quaternary CPNCs as photocatalyst under visible light irradiation ($\lambda > 420$ nm). Source: Ghosh et al. [92]. Copyright 2019, Elsevier.

In fact, quaternary CPNCs carrying Au, Pt, Pd, and PPY ($Au_{50}Pt_{24}Pd_{26}$/PPY) have shown highest PHE under visible light (>420 nm). In an hour, the quaternary CPNC can generate around 40 mmol/h hydrogen. On other hand, ternary CPNC ($Au_{54}Pd_{46}$/PPY), binary CPNC (Au/PPY), and even pure PPY produce less quantity of hydrogen as compared with the quaternary CPNC as shown in Figure 8.12. Almost 5.5 times increase in charge carrier concentration was also observed in case of quaternary $Au_{50}Pt_{24}Pd_{26}$/PPY than the pure PPY nanowires. The plot also shows a correlation with the photocurrent under on and off experiment which is six times higher than the pure PPY [92].

8.7.3 Other Applications of CP Nanocomposites

CPNCs are also known for photocatalytic CO_2 reduction, NO removal, decomposition of gaseous acetone, and performing many useful photoredox reactions. PPy-Ag-TiO_2 nanofibers (shell formed by post polymerization) exhibited remarkable photocatalytic performance for the decomposition of gaseous acetone under illumination using visible light as a source of energy. Under the visible light illumination, the excited electron migrated from HOMO of PPY to LUMO of TiO_2, which finally intensifies the electron density in the Fermi energy levels of Ag [93]. Polymeric g-C_3N_4 coupled with $NaNbO_3$ nanowires composites was found to have enhanced photocatalytic reduction of CO_2 into renewable fuels [94]. In addition to this, removal of NO even up to ppb level is also known using g-C_3N_4/g-C_3N_4 based metal-free heterojunction CPNCs in a continuous flow reactor. The mesoporous g-C_3N_4 CPNCs was prepared via *in situ* thermal treatment of urea and thiourea where the individual g-C_3N_4 have different band gaps, i.e. 2.45 eV for thiourea and 2.73 eV for urea-based g-C_3N_4 [95]. Therefore, this example could be a good approach for the development of metal free CPNCs for several potential applications in the future.

8.8 Conclusion

CPs are narrow band semiconductors. Effective band structure engineering of CPs can be achieved by using other metals and semiconductors. Such heterojunctions in CP nanocomposites are attractive for visible light absorption and to prevent charge carrier recombination. The efficacy of the CPNCs as photocatalysts is highly reliant on the solid–solid and the liquid–solid interfaces. Out of the various semiconductor–semiconductor heterojunctions possible, the p–n type of CPNCs is the superior. Better charge transfer efficiency in p–n type heterojunctions is due to the internal electric field enhanced due to high electronic potential difference at the interface. Metals with plasmonic nature, basically the noble metals, also can be utilized to extend the absorbance range and enhance the charge separation of the CPNCs. This is because of the possibility to generate hot electrons and can enhance the photocatalytic activity of the CPNC. In addition, CPs with porous nature are highly admirable materials for their enlarged surface areas. The property of excellent light absorption cum high surface area of the such porous CPs can definitely boost up the electron–hole pair transfer in the nanocomposite. CPNCs of such materials also show potential over the state-of-art graphitic carbon nitride from many different directions. Although, CPNCs are mostly used as photocatalysts for environment remediation, more beneficial applications in hydrogen generation and biofuel production are gaining attention.

References

1 Chandrasekhar, P. (1999). Basics of conducting polymers (CPs). In: *Conducting Polymers, Fundamentals and Applications*, 3–22. Boston, MA: Springer US.

2 Work, W.J., Horie, K., Hess, M., and Stepto, R.F.T. (2004). Definitions of terms related to polymer blends, composites, and multiphase polymeric materials (IUPAC Recommendations 2004). *Pure Appl. Chem.* 76 (11): 1985–2007.

3 Liras, M., Barawi, M., and de la Peña O'Shea, V.A. (2019). Hybrid materials based on conjugated polymers and inorganic semiconductors as photocatalysts: from environmental to energy applications. *Chem. Soc. Rev.* 48 (22): 5454–5487.

4 Rajesh, Ahuja, T., and Kumar, D. (2009). Recent progress in the development of nano-structured conducting polymers/nanocomposites for sensor applications. *Sens. Actuators, B* 136 (1): 275–286.

5 Dutt, S. and Siril, P.F. (2014). Morphology controlled synthesis of polyaniline nanostructures using swollen liquid crystal templates. *J. Appl. Polym. Sci.* 131 (18): 40800–40808.

6 Dutt, S. and Felix, P. (2014). A novel approach for the synthesis of polyaniline nanostructures using swollen liquid crystal templates. *Mater. Lett.* 124: 50–53.

7 Dutt, S., Vats, T., and Siril, P.F. (2018). Synthesis of polyaniline-magnetite nanocomposites using swollen liquid crystal templates for magnetically separable dye adsorbent applications. *New J. Chem.* 42 (8): 5709–5719.

8 Dutt, S., Siril, P.F., Sharma, V., and Periasamy, S. (2015). Gold core – polyaniline shell composite nanowires as a substrate for surface enhanced Raman scattering and catalyst for dye reduction. *New J. Chem.* 39 (2): 902–908.

9 Hatchett, D.W. and Josowicz, M. (2008). Composites of intrinsically conducting polymers as sensing nanomaterials. *Chem. Rev.* 108 (2): 746–769.

10 Gangopadhyay, R. and De, A. (2000). Conducting polymer nanocomposites: a brief overview. *Chem. Mater.* 12 (3): 608–622.

11 Pan, L., Qiu, H., Dou, C. et al. (2010). Conducting polymer nanostructures: template synthesis and applications in energy storage. *Int. J. Mol. Sci.* 11 (7): 2636–2657.

12 Long, Y.-Z., Li, M.-M., Gu, C. et al. (2011). Recent advances in synthesis, physical properties and applications of conducting polymer nanotubes and nanofibers. *Prog. Polym. Sci.* 36 (10): 1415–1442.

13 Xu, Y., Jin, S., Xu, H. et al. (2013). Conjugated microporous polymers: design, synthesis and application. *Chem. Soc. Rev.* 42 (20): 8012.

14 Bahry, T., Cui, Z., Deniset-Besseau, A. et al. (2018). An alternative radiolytic route for synthesizing conducting polymers in an organic solvent. *New J. Chem.* 42 (11): 8704–8716.

15 Cui, Z., Bahry, T., Dazzi, A. et al. (2019). Conducting polymers synthesized by γ-radiolysis in very acidic aqueous medium. *Radiat. Phys. Chem.* 159: 47–56.

16 Scherer, M.R.J. (2013). Electropolymerization of conjugated polymers. In: *Double-Gyroid-Structured Functional Materials*. Springer Theses (Recognizing Outstanding Ph.D. Research), 135–156. Springer, Heidelberg. https://doi.org/10.1007/978-3-319-00354-2_7.

17 Zhan, C., Yu, G., Lu, Y. et al. (2017). Conductive polymer nanocomposites: a critical review of modern advanced devices. *J. Mater. Chem. C* 5 (7): 1569–1585.

18 Huang, J., Virji, S., Weiller, B.H., and Kaner, R.B. (2004). Nanostructured polyaniline sensors. *Chem. Eur. J.* 10 (6): 1314–1319.

19 Wang, D., Zhang, J., Luo, Q. et al. (2009). Characterization and photocatalytic activity of poly(3-hexylthiophene)-modified TiO_2 for degradation of methyl orange under visible light. *J. Hazard. Mater.* 169 (1–3): 546–550.

20 Xu, J., Hu, J., Quan, B., and Wei, Z. (2009). Decorating polypyrrole nanotubes with Au nanoparticles by an in situ reduction process. *Macromol. Rapid Commun.* 30 (11): 936–940.

21 Zhang, X. and Manohar, S.K. (2005). Narrow pore-diameter polypyrrole nanotubes. *J. Am. Chem. Soc.* 127 (41): 14156–14157.

22 Li, X., Li, Y., Tan, Y. et al. (2004). Self-assembly of gold nanoparticles prepared with 3,4-ethylenedioxythiophene as reductant. *J. Phys. Chem. B* 108 (17): 5192–5199.

23 Dutt, S., Kumar, R., and Siril, P.F. (2015). Green synthesis of a palladium–polyaniline nanocomposite for green Suzuki–Miyaura coupling reactions. *RSC Adv.* 5 (43): 33786–33791.

24 Dai, X., Tan, Y., and Xu, J. (2002). Formation of gold nanoparticles in the presence of *o*-anisidine and the dependence of the structure of poly(*o*-anisidine) on synthetic conditions. *Langmuir* 18 (23): 9010–9016.

25 Kumar, S.S., Kumar, C.S., Mathiyarasu, J., and Phani, K.L. (2007). Stabilized gold nanoparticles by reduction using 3,4-ethylenedioxythiophene-polystyrenesulfonate in aqueous solutions: nanocomposite formation, stability, and application in catalysis. *Langmuir* 23 (6): 3401–3408.

26 Fang, Y., Phillips, B.M., Askar, K. et al. (2013). Scalable bottom-up fabrication of colloidal photonic crystals and periodic plasmonic nanostructures. *J. Mater. Chem. C* 1 (38): 6031.

27 Ghosh, S., Kouamé, N.A., Ramos, L. et al. (2015). Conducting polymer nanostructures for photocatalysis under visible light. *Nat. Mater.* 14 (March): 505–511.

28 Dutt, S., Siril, P.F., and Remita, S. (2017). Swollen liquid crystals (SLCs): a versatile template for the synthesis of nano structured materials. *RSC Adv.* 7 (10): 5733–5750.

29 de Abreu Rosa, A.C., Correa, C.M., Faez, R. et al. (2018). Direct synthesis of SILVER nanoparticles and polyaniline into the MESOPORES of SBA-15. *J. Polym. Res.* 25 (8): 182.

30 Dutt, S. and Siril, P.F. (2015). Controlling the morphology of polyaniline–platinum nanocomposites using swollen liquid crystal templates. *Synth. Met.* 209: 82–90.

31 Ghosh, S.K., Deguchi, S., Mukai, S., and Tsujii, K. (2007). Supercritical ethanol – a fascinating dispersion medium for silica nanoparticles. *J. Phys. Chem. B* 111 (28): 8169–8174.

32 Ma, Y., Wang, X., Jia, Y. et al. (2014). Titanium dioxide-based nanomaterials for photocatalytic fuel generations. *Chem. Rev.* 114 (19): 9987–10043.

33 Kumar, S., Kumar, A., Kumar, A., and Krishnan, V. (2019). Nanoscale zinc oxide based heterojunctions as visible light active photocatalysts for hydrogen energy and environmental remediation. *Catal. Rev.* 62 (3): 1–60.

34 Zhang, Z. and Yates, J.T. (2012). Band bending in semiconductors: chemical and physical consequences at surfaces and interfaces. *Chem. Rev.* 112 (10): 5520–5551.

35 Muthirulan, P., Nirmala Devi, C.K., and Sundaram, M.M. (2013). Facile synthesis of novel hierarchical TiO$_2$@poly(*o*-phenylenediamine) core–shell structures with enhanced photocatalytic performance under solar light. *J. Environ. Chem. Eng.* 1 (3): 620–627.

36 Dasgupta, U., Bera, A., and Pal, A.J. (2017). Band diagram of heterojunction solar cells through scanning tunneling spectroscopy. *ACS Energy Lett.* 2 (3): 582–591.

37 Yang, S., Jiang, C., and Wei, S.-H. (2016). Metal compound semiconductors functionalized by polymers and their photosensitive properties. *Appl. Phys. Rev.* 3 (4): 041306.

38 Liu, S., Han, C., Tang, Z.-R., and Xu, Y.-J. (2016). Heterostructured semiconductor nanowire arrays for artificial photosynthesis. *Mater. Horiz.* 3 (4): 270–282.

39 Wang, S., Wang, F., Su, Z. et al. (2019). Controllable fabrication of heterogeneous p-TiO$_2$ QDs@g-C$_3$N$_4$ p-n junction for efficient photocatalysis. *Catalysts* 9 (5): 439.

40 Li, Y. (2015). Conducting polymers. In: *Organic Optoelectronic Materials. Lecture Notes in Chemistry*, vol. 91 (ed. Y. Li), 23–50. Cham: Springer. https://doi.org/10.1007/978-3-319-16862-3_2.

41 Cui, Z., Coletta, C., Rebois, R. et al. (2016). Radiation-induced reduction–polymerization route for the synthesis of PEDOT conducting polymers. *Radiat. Phys. Chem.* 119: 157–166.

42 Luo, J., Dong, G., Zhu, Y. et al. (2017). Switching of semiconducting behavior from n-type to p-type induced high photocatalytic NO removal activity in g-C_3N_4. *Appl. Catal., B* 214: 46–56.

43 Safaei, J., Mohamed, N.A., Noh, M.F.M. et al. (2018). Facile fabrication of graphitic carbon nitride, (g-C_3N_4) thin film. *J. Alloys Compd.* 769: 130–135.

44 Tang, Q., Lin, L., Zhao, X. et al. (2012). p–n Heterojunction on ordered ZnO nanowires/polyaniline microrods double array. *Langmuir* 28 (8): 3972–3978.

45 Jia, Y., Mei, M., Xu, X., and Wang, L. (2016). The coating of conducting copolymer on coordination polymer nanorod: a visible light active p-n heterojunction photocatalyst for H_2 production. *Solid State Sci.* 56: 45–53.

46 Sardar, S., Kar, P., Remita, H. et al. (2015). Enhanced charge separation and FRET at heterojunctions between semiconductor nanoparticles and conducting polymer nanofibers for efficient solar light harvesting. *Sci. Rep.* 5 (1): 17313.

47 Feizpoor, S., Habibi-Yangjeh, A., Yubuta, K., and Vadivel, S. (2019). Fabrication of TiO_2/$CoMoO_4$/PANI nanocomposites with enhanced photocatalytic performances for removal of organic and inorganic pollutants under visible light. *Mater. Chem. Phys.* 224: 10–21.

48 Yuan, K., Guo-Wang, P., Hu, T. et al. (2015). Nanofibrous and graphene-templated conjugated microporous polymer materials for flexible chemosensors and supercapacitors. *Chem. Mater.* 27 (21): 7403–7411.

49 Yang, X., Xiang, Y., Wang, X. et al. (2018). Pyrene-based conjugated polymer/Bi_2MoO_6 Z-scheme hybrids: facile construction and sustainable enhanced photocatalytic performance in ciprofloxacin and Cr(VI) removal under visible light irradiation. *Catalysts* 8 (5): 185.

50 Thote, J., Aiyappa, H.B., Deshpande, A. et al. (2014). A covalent organic framework-cadmium sulfide hybrid as a prototype photocatalyst for visible-light-driven hydrogen production. *Chem. Eur. J.* 20 (48): 15961–15965.

51 Lipton-Duffin, J.A., Miwa, J.A., Kondratenko, M. et al. (2010). Step-by-step growth of epitaxially aligned polythiophene by surface-confined reaction. *Proc. Natl. Acad. Sci. U.S.A.* 107 (25): 11200–11204.

52 Zhang, X., Xiao, J., Peng, C. et al. (2019). Enhanced photocatalytic hydrogen production over conjugated polymer/black TiO_2 hybrid: the impact of constructing active defect states. *Appl. Surf. Sci.* 465: 288–296.

53 Zhang, H., Zong, R., Zhao, J., and Zhu, Y. (2008). Dramatic visible photocatalytic degradation performances due to synergetic effect of TiO_2 with PANI. *Environ. Sci. Technol.* 42 (10): 3803–3807.

54 Wang, Z., Li, C., and Domen, K. (2019). Recent developments in heterogeneous photocatalysts for solar-driven overall water splitting. *Chem. Soc. Rev.* 48 (7): 2109–2125.

55 Xu, Q., Zhang, L., Yu, J. et al. (2018). Direct Z-scheme photocatalysts: principles, synthesis, and applications. *Mater. Today* 21 (10): 1042–1063.

56 Liu, X. and Cai, L. (2018). Novel indirect Z-scheme photocatalyst of Ag nanoparticles and polymer polypyrrole co-modified BiOBr for photocatalytic decomposition of organic pollutants. *Appl. Surf. Sci.* 445: 242–254.

57 Javadzadeh, Y. and Hamedeyazdan, S. (2014). Floating drug delivery systems for eradication of helicobacter pylori in treatment of peptic ulcer disease. In: *Trends in Helicobacter pylori Infection* (ed. B.M. Roesler). IntechOpen, DOI: 10.5772/57353.

58 Khan, M.R., Chuan, T.W., Yousuf, A. et al. (2015). Schottky barrier and surface plasmonic resonance phenomena towards the photocatalytic reaction: study of their mechanisms to enhance photocatalytic activity. *Catal. Sci. Technol.* 5 (5): 2522–2531.

59 Wang, Z.J., Ghasimi, S., Landfester, K., and Zhang, K.A.I. (2015). Photocatalytic Suzuki coupling reaction using conjugated microporous polymer with immobilized palladium nanoparticles under visible light. *Chem. Mater.* 27 (6): 1921–1924.

60 Zhang, N., Han, C., Fu, X., and Xu, Y.-J. (2018). Function-oriented engineering of metal-based nanohybrids for photoredox catalysis: exerting plasmonic effect and beyond. *Chem* 4 (8): 1832–1861.

61 Ghosh, S., Mallik, A.K., and Basu, R.N. (2018). Enhanced photocatalytic activity and photoresponse of poly(3,4-ethylenedioxythiophene) nanofibers decorated with gold nanoparticle under visible light. *Sol. Energy* 159: 548–560.

62 O'Carroll, D.M., Hofmann, C.E., and Atwater, H.A. (2010). Conjugated polymer/metal nanowire heterostructure plasmonic antennas. *Adv. Mater.* 22 (11): 1223–1227.

63 Li, X.-H., Baar, M., Blechert, S., and Antonietti, M. (2013). Facilitating room-temperature Suzuki coupling reaction with light: Mott–Schottky photocatalyst for C–C-coupling. *Sci. Rep.* 3 (1): 1743.

64 Yang, M.-Q., Gao, M., Hong, M., and Ho, G.W. (2018). Visible-to-NIR photon harvesting: progressive engineering of catalysts for solar-powered environmental purification and fuel production. *Adv. Mater.* 30 (47): 1802894.

65 Xu, J., Hu, Y., Zeng, C. et al. (2017). Polypyrrole decorated BiOI nanosheets: efficient photocatalytic activity for treating diverse contaminants and the critical role of bifunctional polypyrrole. *J. Colloid Interface Sci.* 505: 719–727.

66 Hiragond, C.B., Khanna, P.K., and More, P.V. (2018). Probing the real-time photocatalytic activity of CdS QDs sensitized conducting polymers: featured PTh, PPy and PANI. *Vacuum* 155: 159–168.

67 Xu, S., Zhu, Y., Jiang, L., and Dan, Y. (2010). Visible light induced photocatalytic degradation of methyl orange by polythiophene/TiO_2 composite particles. *Water Air Soil Pollut.* 213 (1–4): 151–159.

68 Gilja, V., Vrban, I., Mandić, V. et al. (2018). Preparation of a PANI/ZnO composite for efficient photocatalytic degradation of acid blue. *Polymers (Basel)* 10 (9): 940.

69 Wang, Q., Hui, J., Li, J. et al. (2013). Photodegradation of methyl orange with PANI-modified BiOCl photocatalyst under visible light irradiation. *Appl. Surf. Sci.* 283: 577–583.

70 Hao, X., Gong, J., Ren, L. et al. (2017). Preparation of polyaniline modified BiOBr with enhanced photocatalytic activities. *Funct. Mater. Lett.* 10 (04): 1750040.

71 Yan, C., Zhang, Z., Wang, W. et al. (2018). Synthesis and characterization of polyaniline-modified BiOI: a visible-light-response photocatalyst. *J. Mater. Sci. - Mater. Electron.* 29 (21): 18343–18351.

72 Gao, B., Iftekhar, S., Srivastava, V. et al. (2018). Insights into the generation of reactive oxygen species (ROS) over polythiophene/$ZnIn_2S_4$ based on different modification processing. *Catal. Sci. Technol.* 8 (8): 2186–2194.

73 Luo, Q., Bao, L., Wang, D. et al. (2012). Preparation and strongly enhanced visible light photocatalytic activity of TiO_2 nanoparticles modified by conjugated derivatives of polyisoprene. *J. Phys. Chem. C* 116 (49): 25806–25815.

74 Long, Y., Han, Q., Yang, Z. et al. (2018). A novel solvent-free strategy for the synthesis of bismuth oxyhalides. *J. Mater. Chem. A* 6 (27): 13005–13011.

75 Zhang, X., Ai, Z., Jia, F., and Zhang, L. (2008). Generalized one-pot synthesis, characterization, and photocatalytic activity of hierarchical BiOX (X = Cl, Br, I) nanoplate microspheres. *J. Phys. Chem. C* 112 (3): 747–753.

76 Li, J., Yu, Y., and Zhang, L. (2014). Bismuth oxyhalide nanomaterials: layered structures meet photocatalysis. *Nanoscale* 6 (15): 8473–8488.

77 Zhang, X., Wu, J., Meng, G. et al. (2016). One-step synthesis of novel PANI–Fe_3O_4@ZnO core–shell microspheres: an efficient photocatalyst under visible light irradiation. *Appl. Surf. Sci.* 366: 486–493.

78 Jiang, W., Luo, W., Zong, R. et al. (2016). Polyaniline/carbon nitride nanosheets composite hydrogel: a separation-free and high-efficient photocatalyst with 3D hierarchical structure. *Small* 12 (32): 4370–4378.

79 Zhang, S., Zhao, L., Zeng, M. et al. (2014). Hierarchical nanocomposites of polyaniline nanorods arrays on graphitic carbon nitride sheets with synergistic effect for photocatalysis. *Catal. Today* 224: 114–121.

80 Cao, S., Piao, L., and Chen, X. (2020). Emerging photocatalysts for hydrogen evolution. *Trends Chem.* 2 (1): 57–70.

81 Ozawa, K., Emori, M., Yamamoto, S. et al. (2014). Electron–hole recombination time at TiO_2 single-crystal surfaces: influence of surface band bending. *J. Phys. Chem. Lett.* 5 (11): 1953–1957.

82 Fujishima, A. and Honda, K. (1972). Electrochemical photolysis of water at a semiconductor electrode. *Nature* 238 (5358): 37–38.

83 Li, X., Yu, J., Low, J. et al. (2015). Engineering heterogeneous semiconductors for solar water splitting. *J. Mater. Chem. A* 3 (6): 2485–2534.

84 Lee, S.L. and Chang, C.-J. (2019). Recent progress on metal sulfide composite nanomaterials for photocatalytic hydrogen production. *Catalysts* 9 (5): 457.

85 Kibria, M.G., Chowdhury, F.A., Zhao, S. et al. (2015). Visible light-driven efficient overall water splitting using p-type metal-nitride nanowire arrays. *Nat. Commun.* 6 (1): 6797.

86 Hitoki, G., Ishikawa, A., Takata, T. et al. (2002). Ta_3N_5 as a novel visible light-driven photocatalyst ($\lambda < 600$ nm). *Chem. Lett.* 31 (7): 736–737.

87 Yanagida, S., Kabumoto, A., Mizumoto, K. et al. (1985) Poly(P-phenylene)-catalysed photoreduction of water to hydrogen. *J. Chem. Soc. - Ser. Chem. Commun.*, 8: 474–475.

88 Dimitrijevic, N.M., Tepavcevic, S., Liu, Y. et al. (2013). Nanostructured TiO_2/polypyrrole for visible light photocatalysis. *J. Phys. Chem. C* 117: 15540–15544.

89 He, K., Li, M., and Guo, L. (2012). Preparation and photocatalytic activity of PANI-CdS composites for hydrogen evolution. *Int. J. Hydrogen Energy* 37 (1): 755–759.

90 Sprick, R.S., Bonillo, B., Clowes, R. et al. (2016). Visible-light-driven hydrogen evolution using planarized conjugated polymer photocatalysts. *Angew. Chem. Int. Ed.* 55 (5): 1792–1796.

91 Chen, B., Wang, X., Dong, W. et al. (2019). Enhanced light-driven hydrogen-production activity induced by accelerated interfacial charge transfer in donor–acceptor conjugated polymers/TiO_2 hybrid. *Chem. Eur. J.* 25 (13) https://doi.org/10.1002/chem.201805740.

92 Ghosh, S., Rashmi, D., Bera, S., and Basu, R.N. (2019). Functionalized conjugated polymer with plasmonic Au nanoalloy for photocatalytic hydrogen generation under visible-NIR. *Int. J. Hydrogen Energy* 44 (26): 13262–13272.

93 Yang, Y., Wen, J., Wei, J. et al. (2013). Polypyrrole-decorated Ag-TiO 2 nanofibers exhibiting enhanced photocatalytic activity under visible-light illumination. *ACS Appl. Mater. Interfaces* 5 (13): 6201–6207.

94 Shi, H., Chen, G., Zhang, C., and Zou, Z. (2014). Polymeric g-C_3N_4 coupled with $NaNbO_3$ nanowires toward enhanced photocatalytic reduction of CO_2 into renewable fuel. *ACS Catal.* 4 (10): 3637–3643.

95 Dong, F., Zhao, Z., Xiong, T. et al. (2013). In situ construction of g-C_3N_4/g-C_3N_4 metal-free heterojunction for enhanced visible-light photocatalysis. *ACS Appl. Mater. Interfaces* 5 (21): 11392–11401.

9

Nanostructured Conjugated Polymer for Solar Cell Applications

Emilie Dauzon[1], Guillaume Noirbent[2], Cedric Vancaeyzeele[1],
Thanh-Tuan Bui[1], Frederic Dumur[2], and Fabrice Goubard[1]

[1] CY Cergy Paris Université, LPPI, 95000, Cergy, France
[2] Aix Marseille Univ, CNRS, ICR UMR 7273, F-13397, Marseille, France

9.1 Introduction

Polymer-based solar cells have attracted a great deal of attention using conjugated polymers, which have potential advantages over inorganic materials and have the potential to be efficient, inexpensive, and solution processable. Nanostructured conjugated polymers with tunable optoelectronic properties can be achieved and applied in different energy-related devices including solar cells, rechargeable lithium batteries, thermoelectric generators, and photocatalytic systems [1, 2].

Conjugated polymer nanostructured surface will be described in this chapter in the context of organic photovoltaics (OPVs). Indeed, it constitutes a fundamental point to obtain an appreciable photovoltaic efficiency based on a fragile balance between nanostructured surface on a very fine scale (nanometer) allowing a significant separation of charges and on a larger scale (hundreds of nanometers) to increase charge transport by reducing the recombination rate. After short explanation of the energy conversion processes and parameters implemented in the OPV application, we will detail the state of the art and main scientific orientations used in the case of chemical and physical strategy for developing the nanostructure of the active layer.

OPV cells are used to convert light energy into electrical energy through the absorption of incident light by a photoactive layer between two electrodes. During the last 30 years, this type of solar cell has become a hot subject and can exhibit a high efficiency of over 17.3% [3]. The photovoltaic system lies in semiconductors materials. The active layer of OPV is composed of organic semiconductor materials, typically a combination of semiconductors – a donor (D) and an acceptor (A). When light reaches a photovoltaic cell, several physical mechanisms occur, leading to the production of electrical charges. Four steps describe the photovoltaic process, as shown in Figure 9.1: (1) absorption of photons and creation of exciton, (2) diffusion of excitons to the A/D interface, (3) dissociation of excitons, and (4) transport and extraction of carriers to the electrodes.

Conjugated Polymer Nanostructures for Energy Conversion and Storage Applications,
First Edition. Edited by Srabanti Ghosh.

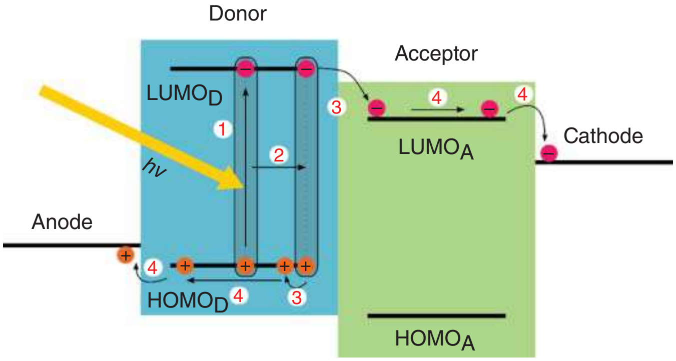

Figure 9.1 Mechanisms involved in organic photovoltaics for the conversion of the light into electricity.

At each stage of this process, several limitations, of course, tend to reduce conversion efficiencies. In the following parts, the mechanisms will be briefly described for each step.

(i) Absorption of light and creation of exciton
When a photon reaches the active layer of the photovoltaic cell, a photon can be absorbed by this layer and can produce an electron–hole pair, also called an exciton. The transition of an electron from the HOMO level induces the exciton formation. This requires the energy of the absorbed photon excels minimal energy corresponding to the HOMO–LUMO gap. The exciton formation depends on the band gap, but as well as the thickness and the absorption coefficient to maximize photon collection. Because of the high absorption coefficient, most organic semiconductors do not require more than a few hundred nanometers thin films to absorb most of the light and obtain important photovoltaic characteristics [4]. Electron–hole pair is electrically neutral, but strong Coulomb interactions link them. When the two charges are localized on the same molecule, the exciton is the Frenkel type with high binding energy ($E_b > 0.1$ eV) [5]. *A contrario*, if the two charges are delocalized on several monomer units, the exciton is then called the Mott–Wannier ($E_b < 0.01$ eV) [6]. In the case of organic materials, these excitons are most often the Frenkel type, because of the tremendous binding energy between the two charges (unlike the excitons of inorganic materials).

(ii) Diffusion of excitons
In comparison with inorganic semiconductors, most organic semiconductors have a lower dielectric constant, which induces a strong Coulombic interaction between the electron and the hole. The thermal energy at room temperature ($E_T = 0.025$ eV at 25 °C) is not sufficient to dissociate the charges. The probability of recombination in organic materials is, therefore, significant. For effective charge generation, the excitons have to diffuse to the D/A interface and dissociate before their recombination [7]. This ability to reach a dissociation site is characterized by the exciton diffusion length L and the exciton lifetime τ

($L = (D{\cdot}\tau)^{1/2}$, where D is the diffusion coefficient) [8]. The distance between the point of creation of the exciton and its site of dissociation (the interface of the materials) must not exceed diffusion length.

(iii) Dissociation of excitons

The dissociation process and generation of free charge carriers occur at the D/A interface. The necessary condition for the separation of the exciton resides at the energy band levels of the two materials. The energy difference between the LUMO of the donor (LUMO_D) and the LUMO of the acceptor (LUMO_A) must be smaller than the Coulombic attraction of the electron–hole pair of the exciton. At the interface, the migration of electron from the LUMO_D to the LUMO_A becomes an energetically favorable mechanism due to the difference in energy levels, which provides the driving force for the excitons separation [9–11]. If the difference between these two levels is not at least 0.3 eV [9], dissociation is unlikely.

On the other hand, beyond this value, the separation of the exciton takes place and forms charge-transfer states, also named CT states. In this state, the electron and hole are still Coulombically bound. These CT states can either decay to the ground state or lead to a charge-separated state (CS state). In the CS states, carriers corresponding to unbound electron–hole pairs can transfer freely in the active layer [8, 11].

(iv) Transport and extraction of carriers to the electrodes

Once the exciton dissociated, the charges must be collected at the electrodes in a shorter time than their lifetime. Transport of the charge carriers to the electrodes is provided by the electron donor for the holes and by the electron acceptor for the electrons. The driving forces for transporting charges carriers are the drift and diffusion currents. When the donor and acceptor are brought into contact between two electrodes, a potential internal gradient causes the charges to move along this gradient, i.e. drift current. When an external field is applied, the drift current is mainly the driving force of transportation. Once the dissociation occurred, the concentration of electrons and holes is generally higher at the heterojunction. The charges will then diffuse along this accumulated charge concentration gradient to form a diffusion current in the opposite direction of the drift current [12]. Several parameters influence transport efficiency toward the electrode, such as carrier mobility depending among others, on domains purity, molecular packing organization, and connectivity. The holes mobility in the donor material and the electrons' mobility in the acceptor material must be as high as possible to ensure the transport of the charge carriers at best. A more significant molecular organization is often a factor of excellent mobility, but the impurities and discontinuous pathways can also influence the efficiency of charge transport values in a negative way [10, 13, 14]. The work-functions of the electrodes mainly guide the collection process. Nevertheless, the extraction is a bit more complicated and can also depend on interfaces and compatibility with the organic layer and the electrode [8].

9.2 Architectures of Organic Cells

9.2.1 Schottky Cell

The first OPV cell was published in 1982 by Weinberger et al. [15]. It was made from a polyacetylene layer inserted between two metal electrodes. This configuration is called the Schottky junction. The photocurrent is due to the dissociation of the excitons at the organic/metal-semiconductor interfaces. The nature of the electrodes strongly influences photovoltaic properties. Different polymers have been tested since Weinberger's work, but the power conversion efficiency (PCE) remains low (<1%) [16–21]. This monolayer structure requires high mobility materials with high optical absorption and really thin film to achieve high efficiency. Because the Schottky-type solar cell has a simple structure with an ultrathin monolayer, a high power density up to 2.5 MW/kg, and easy to scale up to make it still attracting in the solar research field [21].

9.2.2 Bilayer Structure

Tang contributed to a significant advance in the OPV field by publishing the first solar cell composed of two superimposed organic materials: copper phthalocyanine and a tetracarboxylic perylene derivative [22]. This breakthrough led to an energy conversion efficiency (ECE) record of 1%. A bilayer of pure donor/acceptor materials, also called p–n heterojunction, was used as the active layer (Figure 9.2a). The dissociation of the exciton is done at the heterojunction between the two semiconductors, thanks to the electric field present. This type of structure was intensively studied from the early 1990s. A next breakthrough was the incorporation of C_{60} into organic solar cells. In addition to having a high electronic affinity, the C_{60} has high electron mobility, making it an ideal candidate as an electron-accepting material. The Nobel team of Heeger and Sariciftci worked C_{60} and poly[2-methoxy-5-(2′-ethylhexyloxy)-*p*-phenylenevinylene] (MEH-PPV) and showed an increase of photo-current and the existence of a high-speed charge

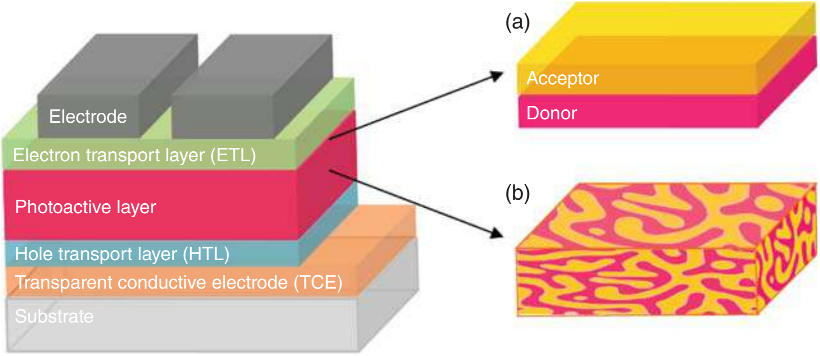

Figure 9.2 Structure of an organic solar cell (a) bi-layer heterojunction type and (b) bulk heterojunction type. The donor is represented in pink and acceptor in yellow.

transfer [23, 24]. Moriata et al. [25] made the same observation with poly(3-alkylthiophene) (P3AT) and C_{60}. However, the main disadvantage of C_{60} is its solubility in solvents. In 1995, Hummelen et al. improved its solubility by synthesizing fullerene derivatives [26].

Ideally, the active layer of these cells should be as thin as the exciton diffusion length to avoid recombination losses. In return, these cells will suffer because of the low absorption of the incident light. Even in the case of the thick film, better absorption, only at the interface between the D/A materials, allows splitting the excitons. Hence, excitons can be generated far from the interface, and many recombination can take place limiting considerably, charges extraction at bilayer configuration [27, 28].

9.2.3 Bulk Heterojunctions

To overcome this recombination problem, a new solar cell configuration has been introduced by Yu et al. by mixing MEH-PPV and [6,6]-phenyl-C_{61}-butyric acid methyl ester commonly named $PC_{61}BM$ or PCBM, a fullerene derivative [29]. This initiative was the first bulk heterojunction (BHJ) solar cell with a record photovoltaic conversion efficiency of 2.9%. Unlike a bilayer-type cell, BHJ solar cell has a more extensive interface between the two materials of the photoactive layer (Figure 9.2b). Consequently, a typical diffusion length of excitons becomes similar to the domain size of the donor and acceptor [30]. This configuration remains today the most used, and fullerene derivatives are now a standard in organic solar cells [31].

Organic solar cells have theoretically, a maximum PCE up to 20% [32], leading them behind the conventional inorganic photovoltaic device. Nevertheless, they certainly offer many advantages over silicon devices. Organic films are lightweight, soft, have excellent compatibility with plastics substrates, flexible, low-cost, ease of processing, and structurally tunable. They are typically solution based, which allow processes that offer benefits like printing large area and ease of upscaling lab-process, e.g. spin-coating, to industrially fabrication (printing, spray coating, evaporation, roll-to-roll) [33]. In comparison, silicon devices are problematic to apply to large-area electronics.

9.3 Chemical Strategy for Developing the Nanostructure of the Active Layer

9.3.1 Block Copolymers

Certainly, in terms of nanostructured surface, the most representative polymeric materials are block copolymers (BCPs): various nanoscale structures can be generate from the microphase separation via a particular molecular self-assembly mechanism [34–36]. Chemically different polymer blocks are covalently linked to each other and promote a large screening of different nanostructures as ordered dense nanodomains of spheres, cylinders, or lamellae with percolation way in sub −100 nm scale well adapted to photovoltaic application. Moreover, spontaneous microphase can be generated but also external stimuli can help to obtain the requested nanostructure such as heat [36–38] and pressure [39–41]. As thermodynamically stable phases, BCP self-assembled structures can also be generated during polymer synthesis [42–44] and can be exploited as main partner (donor, acceptor, or single donor acceptor component) in the active layer [45] or as additives (rod-coil component) involving the structured domains [46]. Besides, they can be utilized for 3D nanopatterning technology, which exploits flexible, stretchable, and nonplanar substrate geometry [47–49]. Finally, a challenge with BCPs is that small density differences between most constituent polymers make microstructure characterization through conventional methods difficult.

Firstly, in traditional OPV configuration, we can emphasize the interest by inserting a BCP layer as extraction electron-layer (EEL) between the transparent electrode and the active layer. As known, the hydrophilic and hydrophobic properties of a BCP play a major role in solution-based processing, for which its overall solubility can be controlled by changing the respective blocks in the composition. Moreover, with low-temperature solution processability and superior flexibility compared with inorganic material like TiO_2 or ZnO, organic electron-transporting materials BCPs are promising materials in OPV application. Various polythiophene-/polyfluorene-based conjugated polymers with side-chain groups containing polar moieties, such as amines, phosphates, and alkoxy groups, have been exploited [48–51]. Chen and coworkers [52] have elaborated a series of poly(*n*-butyl acrylate) (poly(*n*BA)) and poly(NVTri) blocks with poly(NVTri) as water-/alcohol-soluble moieties owing to its polar nature, and poly(*n*BA) to enrich the hydrophobic property and to enable the better compatibility with the adjacent organic BHJ layers (Figure 9.3). Results are promising with decent PCE of 8.03% (with PBDBT:ITIC as active layer) and above all, more than 80% of its initial performance was retained after being heated at 60 °C or exposed under continuous illumination for 1000 hours, greatly surpassing the lifetime of the control device and the reference device using a common PFN EEL. The results revealed the merit of using crosslinked BCPs in improving the long-term stability of OPVs.

The first works were more particularly intended to develop donor based PCB in order to involve nanostructuration with acceptor molecules in active layer. Elaboration of regioregular poly(3-hexylthiophene) (rr-P3HT) was the subject of much studies [53–56]. Yokozawa and coworkers [57] and McCullough and coworkers [58–60] have developed the controlled polymerization of rr-P3HT by Grignard metathesis (GRIM) polymerization separately. Moreover with poly(3-hexylthiophene)-*block*-poly(3-(2-ethylhexyl)thiophene) [61], poly(butylthiophene)-*block*-poly(octylthiophene) [62], and poly(4-vinyltriphenylamine)-*block*-poly(3-hexylthiophene)-*block*-poly(4-vinyltriphenylamine) [63] nanomorphology with well-defined polymer structures ($M_w/M_n \sim 1.1$–1.3) exhibit clear lamellar phase separation with PCBM well adapted for OPV application increasing PCE values (2.37%) and long term performance.

Since a couple of years, BCPs composed of both donor and acceptor segments (D–A BCPs) have been of interest, because of their potential applications as full

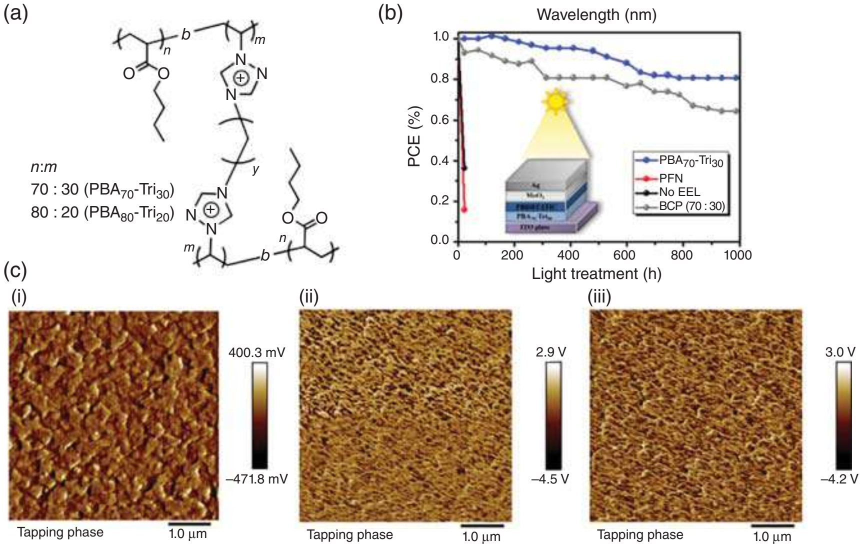

Figure 9.3 (a) Chemical formula of the cross-linked BCPs (poly(*n*BA)-*b*-poly(NVTri)); (b) photo stability of studied devices based on the PBDBT:ITIC BHJ system; (c) phase images of AFM analyses for ITO (left), ITO/PBA70-Tri30 (middle), and ITO/PBA70-Tri30 heating 80 °C for 10 minutes (right). Source: (a, b) Huang et al. [52]. Copyright 2018, ACS Publications, (c) Adopted with permission Huang et al. [52]. Copyright 2018, Nature Springer.

acceptor–donor materials instead of using well-known fullerene derivatives in OPVs [64–68]. Effectively, until 2010, fullerene derivative such as PCBM was the conventional acceptor material for OPVs mainly because of its high electron mobility (c. 0.002 $cm^2/(V\,s)$). Unfortunately, many drawbacks limit its use in OPVs: (i) negligible light absorption in the visible-near-IR regions; (ii) low compatibility with donor polymeric materials; (iii) very sensitive to oxidation limiting long term performance; and (iv) high cost for synthesis and purification. The investigation of non-fullerene acceptor materials that can potentially replace PCBM in OPVs has proven essential in order to increase both photovoltaic performances and its stability. Moreover, non-fullerene materials with tunable HOMO–LUMO allow a large screening of possibilities of D–A block structure with expected high open-circuit voltages. Although D–A BCP characteristics, like electron-transporting properties derived from acceptor blocks, broad light absorption, and nanomorphology derived from the D–A block structure, can be considered to be ideal for use as OPV acceptor materials, the number of D–A BCPs is still limited, because of mainly their synthetic difficulties. Ideally in such a system, the donor and acceptor units will self-assemble into domains in the order of the size of the individual components, therefore to achieve 10 nm domains, the materials must necessarily be polymeric. Recent work on molecular donor–acceptor materials produced promising PCEs. However, the loss of charge carriers to recombination within the overly small domains is another difficulty to overcome, which could be detrimental for the performance of the device. The optimal morphology is obtained when the materials obtain complete phase separation into well-defined domains. Although BCPs with flexible backbones can adopt a variety of morphologies depending on the composition, fully conjugated BCPs are more rigid and so tend to adopt lamellar morphologies [69]. If properly oriented perpendicular to the electrode substrate, these lamellae could provide excellent charge percolation pathways, ideal for OPV function. The application of this envisioned morphology in an OPV is depicted in Figure 9.4. The highest performing example of this strategy to date achieved a PCE of 3.1% employing BCP with poly(3-hexylthiophene) (P3HT) as the donor material and poly(2,7-(9′,9′-dioctylfluorene)-alt-5,5-(4′,7′-di-2-thienyl-2′,1′,3′-benzothiadiazole) (PFTBT) as the acceptor material (R = H) [70]. The authors observed phase separation into 9 nm domains in this system (Figure 9.4c), which may have contributed to the high performance. On the contrary, no phase separation was observed with P3HT-*b*-PFT6BT (R = C_6H_{13}). The lack of phase separation is attributed to the incorporation of solubilizing alkyl side chains on the PFTBT acceptor materials,

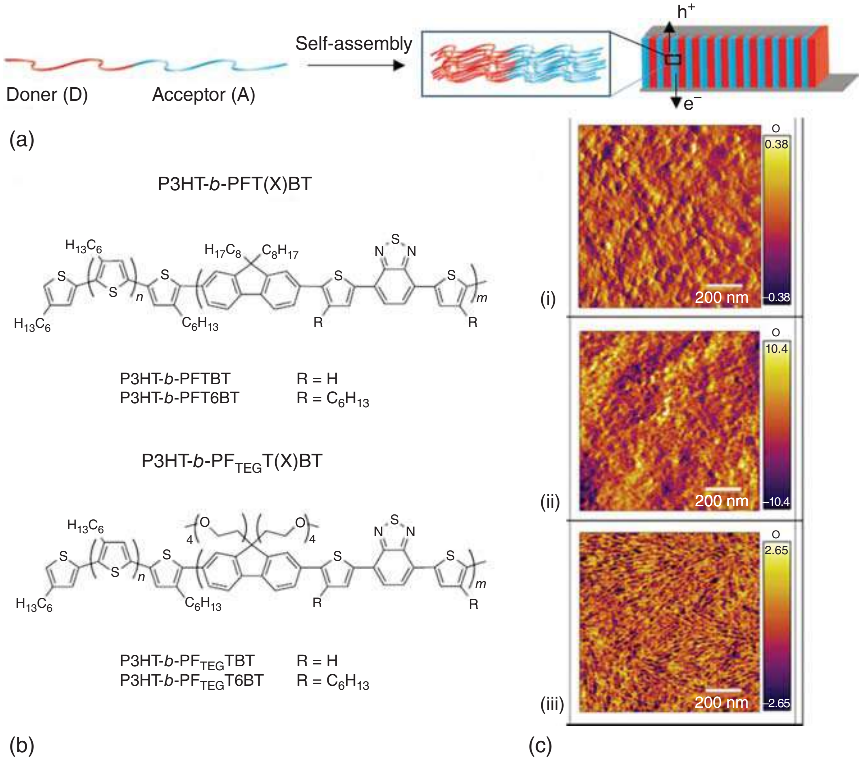

Figure 9.4 (a) Schematic of proposed block copolymer self-assembly into lamellar active layer morphology; (b) structures of P3HT-*b*-PFT(X)BT and P3HT-*b*-PF_{TEG}T(X)BT block copolymers amphiphilic analogs; (c) tapping mode AFM of annealed films of (top) PF_{TEG}T6BT/P3HTblend, (middle) PF_{TEG}T6BT/P3HT/P3HT-*b*-PF_{TEG}T6BT blend, and (bottom) P3HT-*b*-PF_{TEG}T6BT deposited from 2% BrAni in xylene before and after annealing. Source: (a, b) Mitchell et al. [69], (c) Adopted with permission Mitchell et al. [69]. Copyright 2017, ACS.

and hypothesized that additional alkyl chains led to an increased miscibility of the donor and acceptor. The poor morphologies led to a drastic decrease in OPV performance.

Another possibility is to introduce a synthetic strategy for step-growth BCPs employing 1,2-bis(trialkylstannyl)ethene as one monomer, which, in addition to offering improved backbone planarity, directly yields a vinylene-terminated macromonomer suitable for the Heck–Mizoroki coupling [71]. A representative BCP based on a diketopyrrolopyrrole (DPP) copolymer coded pBDTTDPP as the donor block and a perylenediimide (PDI) copolymer coded as pPDIV as the acceptor block has been elaborated as pPDIV-*b*-pBDTTDPP-*b*-pPDIV as single-component BHJ OPV. Devices achieved a PCE of 1.51% after thermal stress at 150 °C compared with 0.02% for a control device consisting of a comparable blend of pBDTTDPP and pPDIV. The difference in performance is ascribed to the morphological stability of the BHJ when using the BCP. However, in another study with a fully conjugated D–A block copolymer (CDABP) [72], performance as single component polymer solar cell (SC-PSC) showed the maximum PCE of 5.28%. This latter value can be attributed to its fine internal/surface morphology and high crystallinity of the CDABP film. In addition, transient absorption experiments on the CDABP films showed that charge carrier generation is faster and the lifetime of the generated charge carriers is longer in the annealed film than in the as-cast film.

9.3.2 Polymer Nanowires

π-Conjugated polymer nanowires (PNWs) have been extensively used to produce highly crystalline π-conjugated polymer active layers [73]. The formation of PNWs results in an increase in the charge transport and crystallinity as well as a decrease in the band gap, compared with the bulk material [72, 73]. As nanowires exhibit anisotropic light interactions and charge transport, it is possible to exploit this anisotropy to amplify charge properties by aligning PNW along a given axis [74–76]. PNWs are commonly formed by self-assembly in solution where a poor solvent for the polymer is used. Typically, the polymer is dissolved in the hot solvent. One the polymer is completely dissolved; the solution is left to cool down undisturbedly. The polymer chains will readily self-assemble into PNWs resulting in a solution of nanowires that can be directly used to cast thin film in device making. PNWs have typical dimension of several nanometer tall, around 20 nm wide and up to several micrometer in length, which could be controlled by the side-chain length, solvent choice, and solvent temperature [77–79]. The crystallinity and, therefore, electronic properties of the PNWs could effectively be controlled by the aging time (the time that the solution is left to self-assemble). For instance, by optimizing the aging time, the charge mobility can be increased by 3 orders of magnitude, which could be attributed to improving long-range order and increasing in intermolecular interactions, or H-type aggregation [80, 81]. Figure 9.5 shows an example of an atomic force microscopy (AFM) image of P3HT PNWs spin-casted films.

In addition to optimize the aging time, it is common to seed nanowire growth to quickly produce nanowires with even higher crystallinity. While aging time method

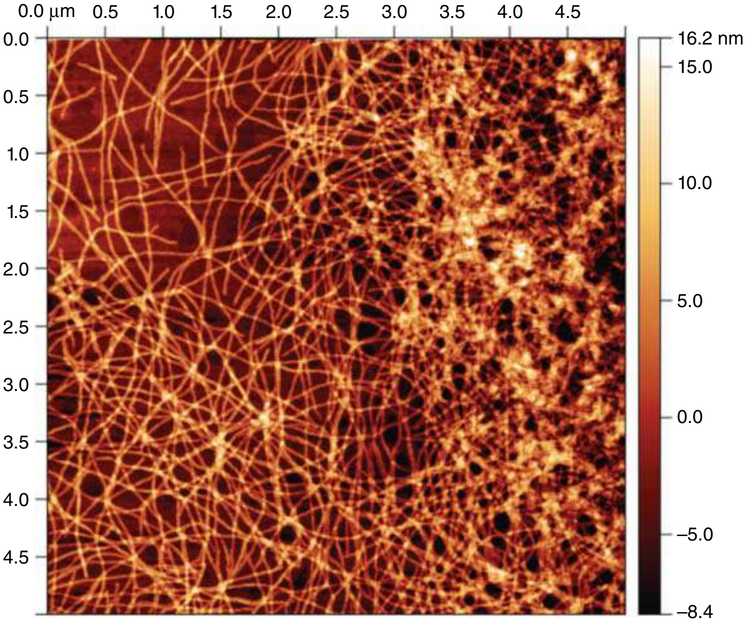

Figure 9.5 AFM image of P3HT nanowires. Source: Adopted with permission Kim et al. [82]. Copyright 2005, Wiley.

rely on amorphous aggregates to initiate crystallization, the seeded growth approach builds PNWs from a highly crystalline aggregate, which helps coordinate growth through the nanowire giving high crystalline quality. Tatum and Luscombe [73] have recently discussed in detail the different ways to form and align PNWs in their review paper. Evidently, such high degrees of long-range order of PNWs are particularly attractive for photovoltaic applications where charge transport through the conjugated materials is crucial.

As mentioned earlier, P3AT and especially P3HT are one of the most popular photovoltaic polymers. P3HT PNWs can be readily excessive by different preparation methods such as solvent vapor-induced nanowire formation [82], etc. Jenekhe and coworkers [83] prepared OPV from poly(3-butylthiophene) PNWs as donor and fullerene derivatives ($PC_{61}BM$ and $PC_{71}BM$) as acceptors. The filed effect charge mobility of the PNWs/acceptor have been 1–2 order of magnitude higher than that of the corresponding polymer/acceptor blends. The fullerene/poly(3-butylthiophene)-nanowire nanocomposites exhibit an electrically bicontinuous morphology leading to an approved photovoltaic performance. The efficiency reached 2.2% in PNW systems compared with 1.0% in corresponding bulk polymer/$PC_{61}BM$ device and even reached 3.0% in case of $PCB_{71}M$. This amelioration is due to an increase in photocurrent and V_{OC} of the optimized device and the photovoltaic performance strongly correlate with PNWs/fullerene BHJ nanostructure [83]. Optimizing the thermal annealing they obtained a poly(3-butylthiophene)-PBWs/$PCB_{71}M$ solar cell with an efficiency of 3.35% ($V_{OC} = 0.66\,V$, $J_{SC} = 8.12\,mA/cm^2$, and $FF = 0.63$). Luscombe and coworkers

[84] also demonstrated how the vertical morphology of BHJ OPV with an active layer consisting of P3HT-PNWs and $PC_{61}BM$ can be beneficially influenced the global device performance. Common OPV device fabrication routes employ an annealing step to influence active layer morphology. However, this process can create an unfavorable phase migration where P3HT is driven toward the top of the active layer. By introducing the P3HT-PNWs in the active layer, they observed an increase in relative fullerene concentration at the top of the active layer. Cho and coworkers [85] fabricated P3HT-PNWs/$PC_{61}BM$ OPV in a marginal solvent without posttreatments and optimized the morphology and photovoltaic properties via aging time of the P3HT precursor solution. The optimal light absorption and charge transport balance was found at 60 hours aging time. Applying optimized annealing conditions P3HT-PNWs/$PC_{61}BM$ OPV could be obtained with 3.94% efficiency. When combined with indene-C_{60} bisadduct as acceptor material, Cho and coworkers [85] obtained a significant device enhancement reaching 5.42%. It is interesting to note that the photocurrent did not decrease significantly up to a thickness of 600 nm, resulting in a non-negligible PCE of 3.75%. This finding could open the way to fabricate thick OPV device. Rice et al. [84] also studied PNWs/$PC_{71}BM$ based OPV using diblock copolymer semiconductors, poly(3-butylthiophene)-*block*-poly(3-octylthiophene), of different block compositions. While PNWs have similar width (13–16 nm), the average aspect ratio length/width was tuned in the range of 50–260 and the device efficiency of the cells increased, increasing the aspect ratio, reaching 3.4% at the highest average aspect ratio of 260. The SCLC hole mobility measurement of the blend PNWs/$PC_{71}BM$ was invariant with aspect ratio reflecting the parallel orientation of the PNWs to the substrate. The authors thus explained the enhancement of photovoltaic efficiency with increasing aspect ratio of PNWs in terms of increased exciton and charge photogeneration and collection. Seferos and coworkers [86] doped P3HT PNWs with various amount of selenophene, resulting in a copolymer PNWs networks. Selenophene doping increases optical absorption far beyond what can be achieved by simply blending two materials (Figure 9.6a,b). PNWs solar cells using selenophene-doped P3HT outperform native P3HT PNWs and corresponding ternary blend solar cells, reaching an overall maximum performance of >4% PCE ($J_{SC} = 11.47\ \text{mA/cm}^2$, $V_{OC} = 0.55\ \text{V}$, FF = 0.64, PCE = 4.1%) (Figure 9.6c,d). Comparison and morphologies active layer surface demonstrate a better nanostructuration with P3HT-stat-P37S-nanowire (80 : 20): $PC_{71}BM$ (Figure 9.6e,f).

In the continuity of their work, Cho and coworkers used donor–acceptor conjugated thiophene polymers (named P4TNTz-2F) to prepare PNWs for inverted BHJ OPV (Figure 9.7) [87].

The chemical structure of P4TNTz-2F is given in Figure 9.7a. A notable high PCE of 10.62% was obtained with a single junction inverted cell with a 350 nm thick active layer containing highly crystalline PNWs based on P4TNTz-2F (Figure 9.7c) employing DIO as solvent additive. P4TNTz-2F possesses a deep-lying HOMO level (−5.46 eV) and a low-band gap (1.59 eV) derived from absorption spectra (Figure 9.7b) as well as a planar/rigid backbone. The thick active layer in the P4TNTz-2F:$PC_{71}BM$-based OPV, which can be easily made at a mild blending

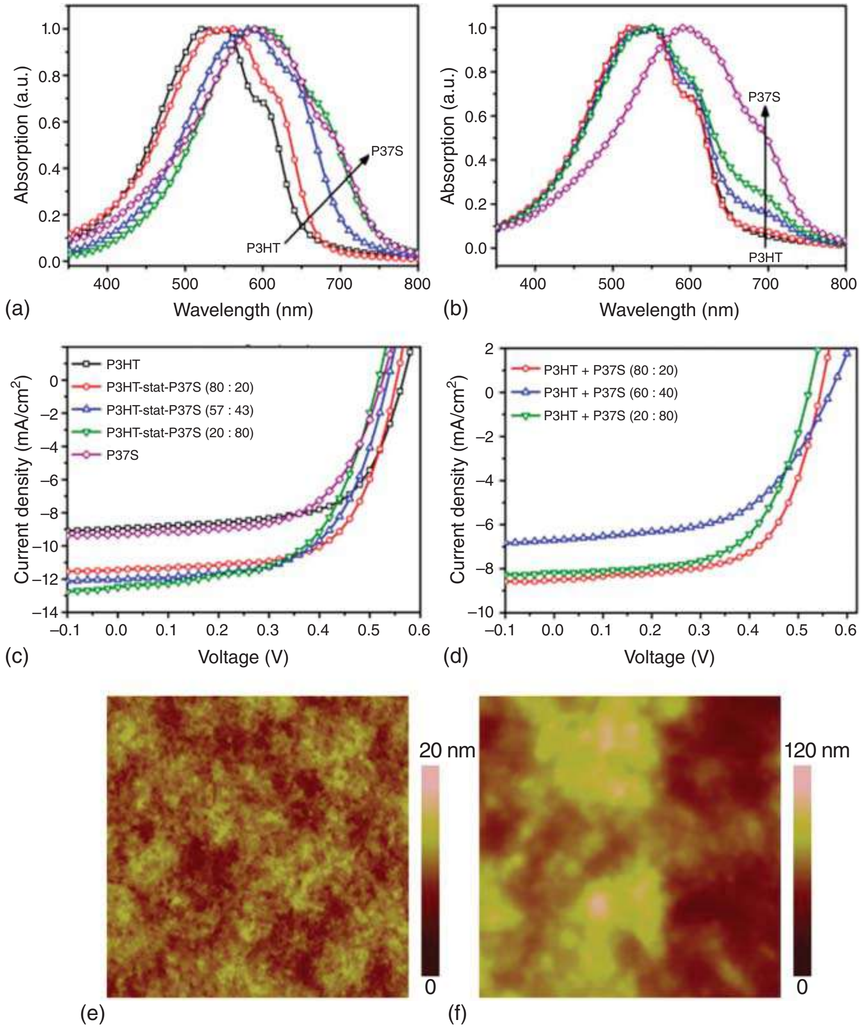

Figure 9.6 Thin film absorption spectra of (a) polymer nanowires composed of P3HT, P37S, and statistical polymer and (b) P3HT, P37S, and blend polymers with the same unit ratio of corresponding statistical copolymers (black square, P3HT; red circle, unit ratio of 80 : 20; blue up-triangle, unit ratio of 60 : 40; olive down-triangle, unit ratio of 20 : 80; purple diamond, P37S). (a–d) Photovoltaic performances of polymer nanowire solar cells composed of statistical copolymers and blend polymers mixed with PC$_{71}$BM; (c, d) corresponding J–V curves; (e) height P3HT-*stat*-P37S-nanowire (80 : 20): PC$_{71}$BM images from tapping-mode (2 μm × 2 μm); (f) (P3HT + P37S)-nanowire (80 : 20):PC$_{71}$BM. Source: (a–d) Yan et al. [86]. Copyright 2014, ACS Publications, (e, f) Adopted with permission Yan et al. [86]. Copyright 2014, ACS.

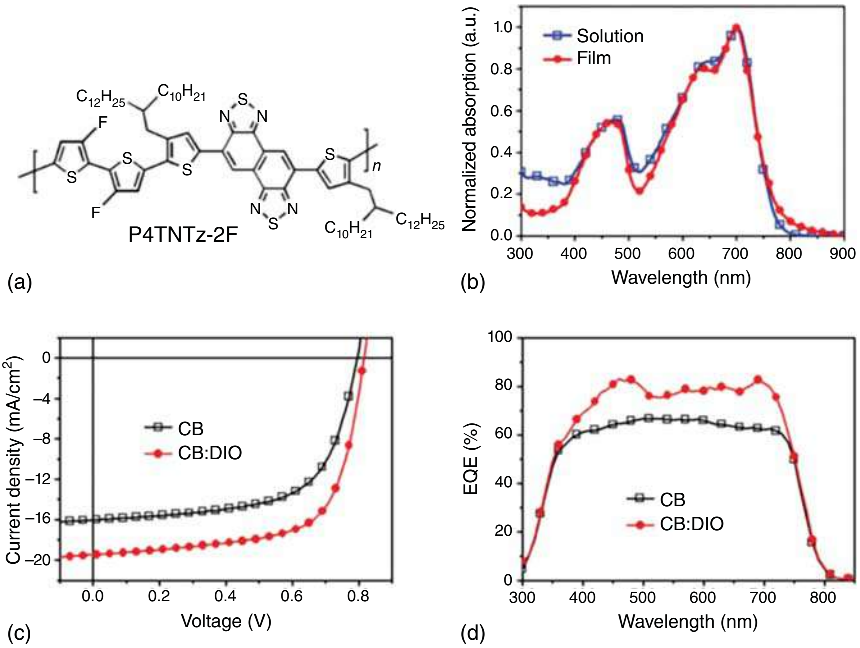

Figure 9.7 (a) Molecular structure of P4TNTz-2F. (b) UV–vis absorption spectra of P4TNTz-2F (M-MW) in CB solution and as a thin film. (c) *J*–*V* curves and (d) EQE spectra of the optimized P4TNTz-2F (M-MW):$PC_{71}BM$ PSCs prepared from CB and CB:DIO. Source: Lee et al. [87]. Copyright 2017, RSC.

temperature (c. 70 °C), absorbs strongly in the full visible spectral domain and contributing to a high $J_{SC} = 19.45\,\text{mA/cm}^2$. The high device efficiency is attributed to the continuous polymer network with narrow PNWs (c. 6 nm in width and several hundred nanometers in length) in the thick film blended with $PC_{71}BM$ facilitating charge separation ($Q_{PL} = 98\%$) and hole transport ($\mu_h = 8.31 \times 10^{-3}\,\text{cm}^2/(\text{V s})$). All of these results demonstrate the great promise of PNWs in preparation of effective and stable active layer in OPV.

9.3.3 Polymer Nanoparticles (PNPs)

9.3.3.1 Synthesis of PNPs via Precipitation Methods

While most of the formulation of nanoparticles (NPs) dispersions rely on the miniemulsion method (see Section 9.4) [88], the precipitation technique is a quick and simple synthetic way to produce semiconducting polymer nanoparticles (PNPs) via the injection of a solution of polymers (or mixture of materials) into a second solvent of poor solubility [89, 90]. Especially, the synthesis does not use surfactant and does not require heating in the NPs synthesis phase and thus could easily be scaled up for the large-scale synthesis of PNPs. It is known that synthesized dispersions have lower stability and exhibit a compositional change upon standing due to preferential precipitation of particles of differing composition.

However, this precipitation approach could be included into an active solution deposition procedure in which PNPs being generated as and when required. Due to its excellent optoelectronic properties, rr-P3HT has been one of the most studied semiconducting polymer for organic and hybrid electronics. Polythiophene P3HT and fullerene derivatives are certainly the most popular donor/acceptor couple OPV materials [91]. Using the miniemulsion method, OPV with a regular device architecture from stabilized P3HT and indene-C_{60} bisadduct ICBA NPs yielding a PCE of 2.5% has been made [92]. It is noteworthy to mention that the stabilizers in the emulsion approach remain in the active layer after deposition and may hamper the BHJ formation, thus badly affect the global device performance and its life-time. For instance, it has been reported that the BHJ morphology and the dependence of the photovoltaic performance on the thermal device treatment are very different for stabilized and non-stabilized P3HT:PCBM nanoparticulate OPV [93]. To overcome the limitations imposed by utilizing surfactant stabilized PNPs, Gärtner et al. synthesized and investigated non-stabilized PNPs based on P3HT:ICBA donor–acceptor combination using a surfactant-free precipitation method [94]. The P3HT:ICBA PNPs dispersions were formulated by precipitating P3HT:ICBA (1.0 : 0.8 by weight) from chloroform solution in non-solvent EtOH or MeOH without any stabilizer. MeOH enabled higher P3HT:ICBA concentrations due to better dispersion stability compared to EtOH. The hydrodynamic diameter of the almost mono-disperse P3HT:ICBA PNPs in EtOH was determined to 125 ± 31 nm, while the corresponding diameter of the P3HT:ICBA NPs in MeOH was determined to 160 ± 31 nm. Both P3HT:ICBA dispersions are stable for a couple of days not exhibiting any visible particle sedimentation. The absorption spectra of the non-stabilized P3HT:ICBA NPs in both EtOH and MeOH are compared with that of P3HT:ICBA mixture in dichlorobenzene (DCB) solution, which featured a peak at 450 nm that is commonly related to the absorption of disordered, amorphous P3HT. In the PNPs dispersions, the P3HT absorption is red shifted accompanied by distinct vibronic features (c. 610, 560, and 510 nm) indicating an enhanced inter-chain interaction in semicrystalline P3HT domains and hence leading to smaller band gaps. This led to conclusion that semi-crystalline P3HT domains have already formed inside the NPs during particle synthesis. The AFM images of the as-cast P3HT:ICBA layers deposited from MeOH dispersion as shown a typical roughness $R_q \approx 40$ nm with NPs being clearly distinguishable. Thermal annealing gave smoother surface and the NPs being less distinguishable. In addition, these thermal annealing hardly affects the optical properties of P3HT:ICBA thin film.

The performance of the corresponding solar cells with inverted device architecture of configuration Glass/ITO/ZnO/BHJ PNP active layer/MoO_3/Al has been examined. With increasing annealing temperature, all photovoltaic parameters of the device (J_{SC}, V_{OC}, FF, and PCE) simultaneously were enhanced. In particular, J_{SC} improves more than 10-fold from 0.8 mA/cm^2 in the as-cast device to 9.0 mA/cm^2 in the solar cell that comprises the active layer that was annealed at 200 °C and consequently of overall PCE yielding up to 4.1% with good reproducibility (Figure 9.8). This improvement of J_{SC} is attributed to the physical changes of the active layer by reducing and suppressing the voids between NPs upon annealing, the concomitant

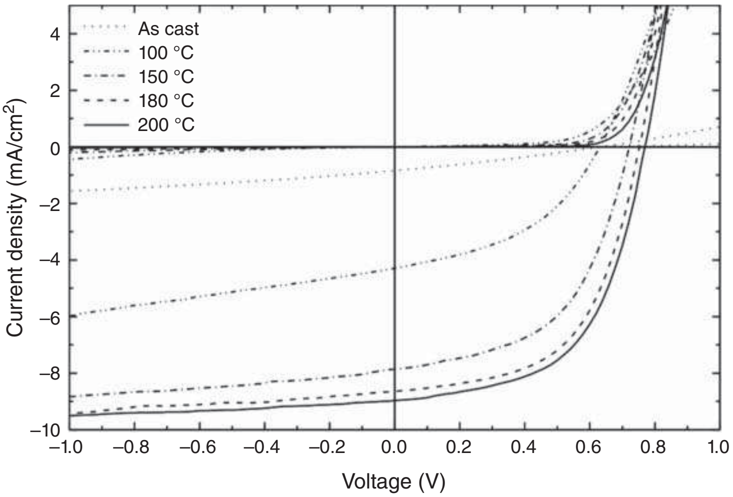

Figure 9.8 Typical *J*–*V* curves of P3HT:ICBA PNP OPV for different annealing temperatures. Source: Gärtner et al. [94]. © 2014, Wiley Online Library.

volume shrinkage and finally the better film homogeneity. Consequently, this led to more intimate connection of the NPs, which leads to better charge carrier transport toward the electrodes and to less failure due to device shunting. In contrast, the as-cast samples with distinguishable PNPs domains promote recombination of charges.

The P3HT:ICBA NPs made by precipitation method is thus a typical example of making the OPV photo-active layers from alcohol in order to pave the way to a low-cost and fully eco-friendly, large-scale fabrication of OPV, where non-toxic fabrication processes are important in order to avoid costly safety measures, and may well be adapted for other organic optoelectronic devices.

9.3.4 Polymer Nanofiber (PNF)

Polymer nanofibers (PNF) have attracted much interest as one-dimensional functional units in various research fields with their unique advantages. PNFs have many strong points to contribute in ameliorate OPVs performance such as huge surface-to-volume ratio, large exciton diffusion length, easy morphology control, and high charge carrier mobility. The precision control of nanofiber orientation in π-conjugated polymer thin films has been demonstrated to importantly impact on charge transport property [95]. P3AT PNF have been the most investigated polymer family within the OPV field. For instance, the π–π stacked P3HT chains can exhibit both H- and J-aggregate behavior that opens up new possibilities for controlling electronic coupling through noncovalent stacking interactions [96]. Otherwise ultrahigh charge mobility (average mobility above 3.1 cm^2/(V s)) can also be achieved by controlled orientation of the polymer crystallites enabling the most efficient and fastest charge transport along the chain backbones and across multiple chains. PNF incorporated in OPVs can be prepared by different methods such as

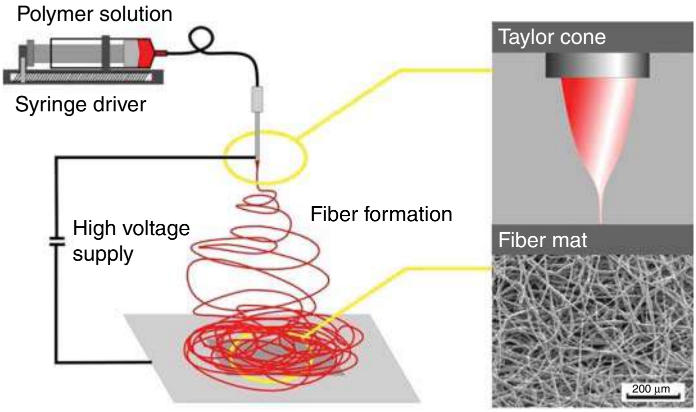

Figure 9.9 Schematic diagram of a typical electrospinning setup. Source: Courtesy of Oxolutia. https://www.oxolutia.com/wp-content/uploads/2014/09/electrospinning-1.jpg.

AAO-template assisted [97], nanoimprint lithography [98], physical vapor deposition [99], electrospinning [100], self-assembly [101], etc. Among these methods of nanofiber fabrication, electrospinning and self-assembly have been in the spotlights because of its simplicity and versatility [102]. The schematic presentation of the electrospinning technique is showed in Figure 9.9 and the detailed description of this technique can be found in relevant literature [103–105].

Electrospinning formation of PNF can give new research possibilities in OPVs with its ability to easily fabricate multicomponent ultrathin PNFs from a variety of materials. However, the use of electrospun PNFs in OPV has been challenged because the active layer is typically composed of polymer donor/small molecular acceptor blend solutions (for example: P3HT and fullerene derivatives), which cannot provide sufficient chain entanglement for continuous fiber formation in electrospinning process due to their low molecular weight and rigid chemical structure. Coaxial electrospinning technique has been employed to fabricate solar cloth made of P3HT and PCBM blend nanofibers [106]. To render the P3HT/PCBM blend solutions electrospun, polyvinylpyrrolidone (PVP) was introduced in the blend as the shell to form core–shell PNFs containing P3HT/PCBM blend inside as the core. PVP was then washed by soaking in EtOH affording to P3HT/PCBM PNF having diameters of $0.94 \pm 0.18\,\mu$m. However, the photovoltaic cloth delivered very poor photovoltaic output with J_{SC} of 3.2×10^{-6} mA/cm^2, $V_{OC} = 0.12$ V, FF = 0.22, and overall PCE = 8.7×10^{-6}%. This unsatisfied result could be mainly explained by the porous nature of formed PNF, which significantly decrease the volume and total interfacial area of P3HT/PCBM BHJ when compared with those of thin film. This cause a significant drop in exciton generation and separation. Other reason can be a poor contact between PNFs and electrodes lowering charge extraction to electrodes. Bedford et al. [107] significantly optimized similar OPV system by co-electrospun P3HT/PCBM blend with polycaprolactone (PCL) as an electrospinnable sheath material. PCL subsequently was washed away by cyclopentanone to make pure P3HT/PCBM PNF with diameter of 120 ± 30 nm (Figure 9.10a–d).

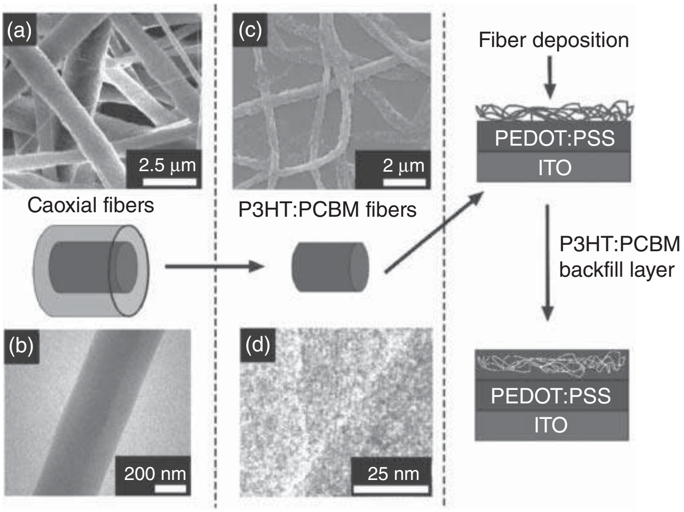

Figure 9.10 A schematic depicting P3HT:PCBM fiber generation from the coaxial fibers and the subsequent deposition of nanofibers within the active layer of the BHJ–OPV device, along with (a) SEM micrograph; (b) TEM micrograph of P3HT:PCBM (core)–PCL (sheath) fibers (2.5 μm and 200 nm scale bars, respectively); (c) an SEM micrograph of P3HT:PCBM nanofibers after removal of the PCL sheath (2 μm scale bar); and (d) a high-resolution TEM micrograph of the P3HT:PCBM fibers after removal of the sheath PCL (25 nm scale bar). Source: Adopted with permission Bedford et al. [107] Copyright 2012, Wiley.

The P3HT:PCBM PNF-incorporated OPVs had greatly improved PCE (4.0%), which was even surpassed that of thin film P3HT:PCBM OPVs with same structure (3.2%). This amelioration could be reasoned by the presence of spin-coated P3HT/PCBM backfill layer on the top of PNF layer, increasing the active volume and D/A interfacial area. The charge extraction was also improved by adding depositing PEDOT:PSS as hole transporting layer. Furthermore, the optimized optical absorption caused by the increased in-plane alignment of P3HT chains during electrospinning process significantly contributes to the overall device performance and overcome that of thin film devices without the incorporation of P3HT/PCBM PNF sub-layer.

P3HT PNF have also widely prepared from solution for studying in OPV. A simple and scalable film fabrication technique that allows reproducible control of thickness, and morphological homogeneity at the nanoscale, is highly desired for large areas industrial production. For this purpose, many researches have been dedicated in the controlled preparation of PNF. For instance, Kaner and coworkers [108] have reported a quick synthetic route in order to form monolayer of conducting PNFs such as polyaniline, polythiophene, and P3HT based on a thermodynamically driven solution-based process leading to the growth of transparent thin films of interfacially adsorbed nanofibers. Vandewal et al. [109] have investigated the influence on CT state energy and V_{OC} of PNF P3AT:PCBM solar cells by varying polymer crystallinity in the nanofiber. P3AT PNF were prepared by slow cooling of P3AT solution in non-solvent [110]. Bertho et al. [111] controlled the morphology of nanofiber-P3HT:PCBM blends for BHJ OPV by heating the deposition solution. By changing the solution temperature, the fiber content in the casting solution was controlled and they obtained an optimized device efficiency of 3.2%, which was showed to be strongly correlated with the morphology of the active layer. Many other works have also been done in order to control and investigate the influence of P3HT nanofiber growth on the photovoltaic performance of P3HT PNF based solar cells. Lam and coworkers [112] used a mixed-solvent approach for controlling P3HT PNF growth. They explored the effect of different poor solvents in driving P3HT chain self-assembly into nanofibers and also the effect of a small amount of good solvent in such a poor solvent system in controlling the nanofiber morphology. They successfully optimized the OPV devices based on the blend of P3HT PNF and PCBM by improving J_{SC} when anisole was used compared with *p*-xylene. They also found that the presence of a small amount of good solvent such as chlorobenzene (CB) in anisole resulted in a higher degree of crystallinity and thinner PNF compared with purely anisole system. The optimized anisole/CB system resulted in an improved efficiency of 2.3%; a relative improvement of more than 50% compared with the pure anisole system, due to improved crystallinity. Zang and coworkers [113] demonstrated the direct achievement of a thermally stable active layer morphology by creating a network of densely distributed crystalline conjugated PNFs. They constructed densely distributed P3HT PNF in the pristine composite films with PCBM from solution without any post treatments. Consequently, a PCE of 3.37% is readily achieved with optimized condition.

Qin and coworkers [114] precisely constructed stable and controllable conjugated polymer/fullerene nanostructures by building in noncovalent interactions between PNF and fullerene derivatives affording to supramolecular polymer/fullerene composite nanofiber in solution (Figure 9.11).

The authors studied a conjugated BCP having P3HT backbone selectively functionalized with polar isoorotic acid moieties, as the building block. Self-assembly of the polymer in mixed solvents leads to well-defined PNFs decorated with isoorotic acid groups on the periphery, onto which PCBM molecules are subsequently attached noncovalently. When applied in OPV, the novel composite PNFs lead to not only much improved thermal stability and better defined and controllable morphology, but also superior performance compared with conventional BHJ devices.

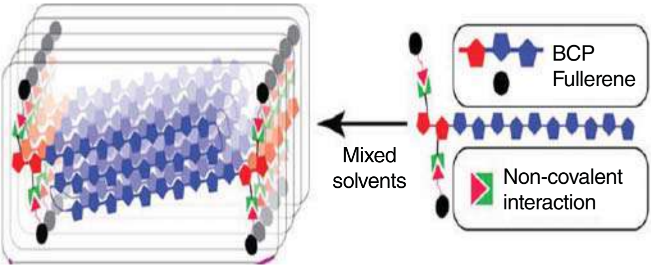

Figure 9.11 Noncovalent interaction approach developed by Qin and coworkers. Source: Li et al. [114]. Copyright 2014, ACS Publications.

Sum and coworkers [115] also found that external electric field treatment improve the charge transport of these devices. Under external electric field treatment of the active layer, the random polymer chains between the PNFs were aligned perpendicular to the electrode, improving mobility (37.5% improvement) and device efficiency (22.7% improvement). Recently, Kim and coworkers [116] have utilized an interdigitated bilayer of an alkoxynaphthalene-based PNF/fullerene to develop the sequential solution deposition (SqD) process of fabrication of OPV. The procedure is illustrated in Figure 9.12. Dense PNFs with diameters of 30–50 nm have been obtained when spin-coating a polymer solution incorporated with 1-chloronaphthalene (1-CN). Subsequently, the fullerene top layer is deposited onto the PNF bottom layer to form a BHJ through the interdiffusion of fullerene. Compared with a plane polymer bottom layer, the preformed PNFs bottom layer provide effective interdiffusion of $PC_{71}BM$ by facilitating the fast swelling of the $PC_{71}BM$ solvent into the polymer bottom layer. The SqD processed OPV utilizing a PNF/fullerene bilayer exhibits higher photocurrent density and superior solar cell performance compared with the control device utilizing a plane polymer layer/fullerene bilayer. Combined characterizations of optical, morphological, and *J*–*V* properties on the photoactive layers reveal that improved ordering of the polymer chain with proper direction and increased BHJ area are the main contributors to the superior photovoltaic performance. These results suggest an efficient interdigitated BHJ morphology that can be realized by a sequentially deposited, preformed nanofiber/fullerene bilayer without a thermal annealing process.

One of the elegant strategies to address the instability issues of the morphology of the OPV active layer is the development of single-component OPVs consisting of based on ambivalent materials containing electron donor and acceptor units capable to ensure the basic functions of light absorption, exciton dissociation, and charge transport. This research direction has been received a lot of attention and

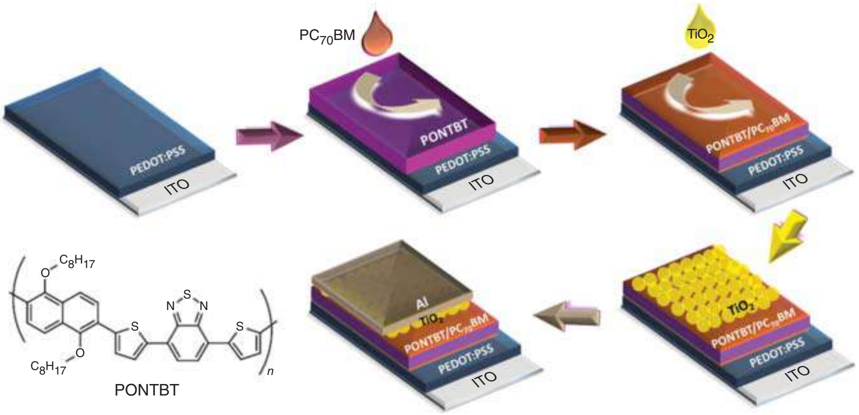

Figure 9.12 Chemical structure of the PONTBT polymer and schematic illustration for the fabrication of the SqD processed OPV. Source: Xie et al. [116]. Copyright 2016, ACS Publications.

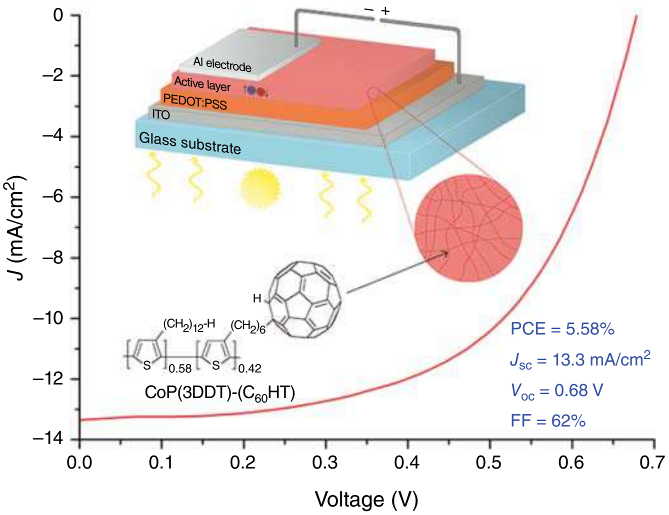

Figure 9.13 Copolymer structure, device architecture, and *J*–*V* characteristics of single component OPV. Source: Pierini et al. [118]. © 2017, ACS Publications.

significant advances have been reported [117]. Recently, Pierini et al. [118] took advantage of PNF materials to develop single-component OPV based on electrospun fullerene-grafted polythiophene nanofibers.

The chemical structure and associated device architecture (ITO/PEDOT:PSS/Active layer: CoP(3DDT)-C_{60}HT/Al) are given in Figure 9.13. The P3AT chains were chemically tailored in order to reduce the side effects of charge recombination and enabled to synthesize a copolymer with high solubility, molecular weight, regioregularity, and fullerene content. The correlations of the active layer hierarchical structure given by the inclusion of electrospun nanofibers and the solar cell photovoltaic properties were examined. The photovoltaic efficiency can be strongly increased by optimizing the supramolecular and nanoscale structure of the active layer, while achieving the highest reported efficiency value (PCE = 5.58% with J_{SC} = 13.3 mA/cm^2, V_{OC} = 0.68 V, FF = 0.62, Figure 9.13). The enhanced performance may be attributed to well-packed and properly oriented polymer chains.

9.4 Physical Strategies for Fabricating Polymer Nanostructures

9.4.1 Template Methods

In the last decade impressive results have been achieved for BHJ OPVs, such as PCEs exceeding the 16% benchmark [119] and outdoor lifetimes of OPV measured up to 10 000 hours [120]. As the roll-to-roll printing process is the intended technique for high-throughput manufacturing of OPVs, so-called solar inks need to be produced.

However, they are often based on harmful chlorinated solvents such as chloroform, CB, or DCB. Some efforts were drawn from the OPV's community to switch to less harmful solvents like toluene, *o*-xylene, mesitylene, or mixtures thereof [121]. A much more sustainable development would come with inks based on green solvents such as ethanol or even water.

In that purpose, MacEdo et al. [122] prepared thin films of poly(2,2′-bithiophene) (PBT) by electrochemical deposition on PEDOT:PSS modified indium tin oxide (ITO) substrates. Ultrasonic emulsification of aqueous perchloric acid and 2,2′-bithiophene monomer is an effective method to disperse this water insoluble monomer in micro droplets that improved the contact with the electrode (Figure 9.14a). An electron transfer takes place between the electrode and the droplets of the monomer resulting in the formation of homogeneous films with a higher degree of organization. The thickness of PBT was adjusted by the control of the potential applied and the charge achieved during the deposition (Figure 9.14b). PBT films were also probed by AFM. The PBT layer polymerized directly on ITO (Figure 9.14c) showed an irregular morphology presenting plate like structures with root mean square (RMS) roughness (R_{rms}) of 3.5 nm. Whereas the PBT layer polymerized on PEDOT:PSS modified ITO shows homogeneous morphology (Figure 9.14d), composed of particles with 55 ± 5 nm of diameter, with R_{rms} of around 2.9. AFM images indicate effective covering with PBT.

The short circuit current (J_{SC}) of photovoltaic devices is related to the amount of absorbed light and the charge collected by the electrodes. In polymer:fullerene solar cells, the reduction of J_{SC} have been attribute to leakage of electrons back to the anode electrode [123]. The anode buffer layer is a strategic procedure to avoid the leaking of electrons to the ITO electrode and improvement of the anode electrode efficiency in collecting and extracting positive carriers. The buffer layer must be a film that is transparent, is insoluble in organic solvents, and displays good mechanical and transport properties [124]. The electrodeposited PBT films were applied in two distinct functionalities: as active layer in bilayer solar cells and, in order to increase the J_{SC} parameter, as buffer layer inserted between the bottom electrode and the active layer polymer: PCBM in BHJ solar cells (Figure 9.14e).

The thin films solar cells based on PBT polymer as bilayer result in a PCE of $\eta = 0.3\%$. The PBT films, used as buffer layer in BHJ solar cells influenced positively the open circuit voltage and increased about 1.6 times the short circuit current, increasing the efficiency from 1.3% up to 2.9%, due its higher ionization potential of PBT buffer (5.2 eV). It improved the charge collection, reducing the withdraw of electrons into the PEDOT:PSS layer.

Caricato et al. [125] and then Ge et al. [126] have developed emulsion-based resonant infrared matrix-assisted pulsed laser evaporation (RIR-MAPLE) for the deposition of conjugated polymer films for photovoltaic applications (Figure 9.15). MAPLE has been developed for the deposition of polymer thin films. A laser (IR in this case) is used to ablate the target polymer that flushes onto the substrate to form the polymer thin film. When a solvent is incorporated as a matrix in the polymer target, it is vaporized by absorbing most of the laser energy and subsequently pumped away in vacuum, leaving the polymer deposited in a dry state on the substrate. So, the

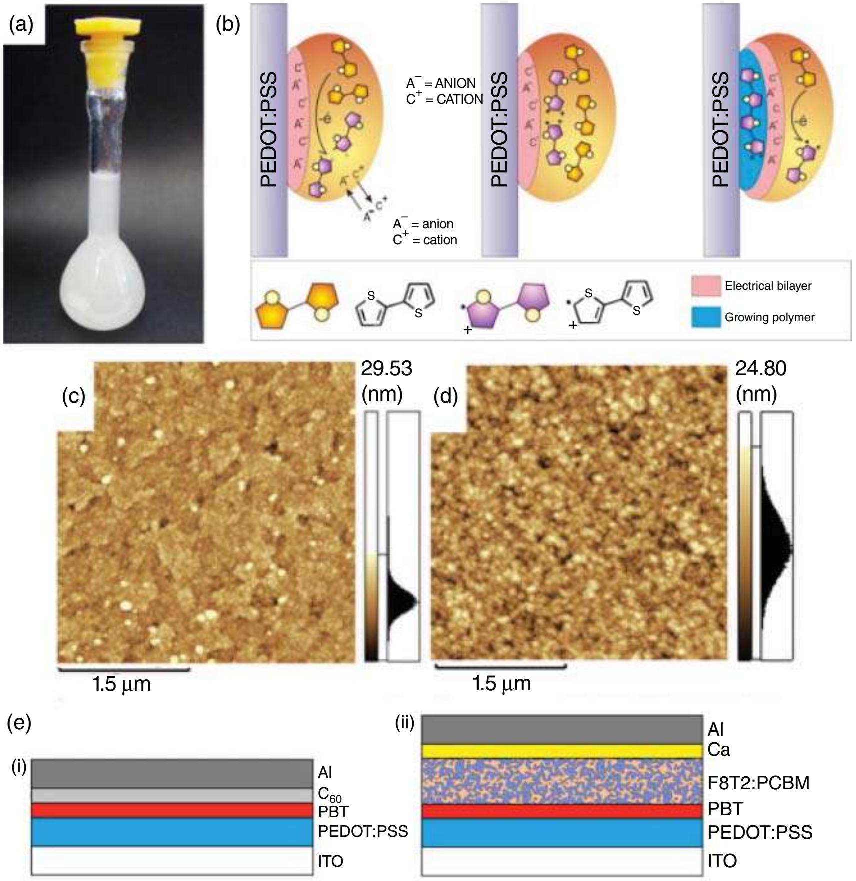

Figure 9.14 (a) Image of the emulsion containing micelles of 2,2′-bithiophene monomer achieved after ultrasonic stirring and (b) schematic representation of the electropolymerization of 2,2′-bithiophene onto PEDOT:PSS. Height AFM images of (c) ITO/PBT and (d) ITO/PEDOT:PSS/PBT, respectively. (e) Schematic representation of bilayer (left) and bulk heterojunction (right) devices indicating the localization of the PBT layer. Source: (b, e) Macedo et al. [122]. Copyright 2013, Elsevier, (a, c, d) Macedo et al. [122]. Copyright 2016, Elsevier.

photochemical degradation of the target polymer resulting from laser irradiation is minimized. Emulsion-based RIR-MAPLE vaporation (RIR-MAPLE) was developed [127, 128] with the capability to form polymer films without photochemical or structural degradation [129].

Conjugated polymers are dissolved or confined within the organic solvent droplets to form polymer clusters. Ekrt et al. [130] proposed in a comprehensive study the hypothesis that during RIR-MAPLE deposition, polymer film formation occurs by the direct transfer of these polymer clusters from the target to the substrate with sizes of the polymer clusters defined by the emulsion droplet size. The impact of this film formation mechanism is that the size of polymer clusters and the packing

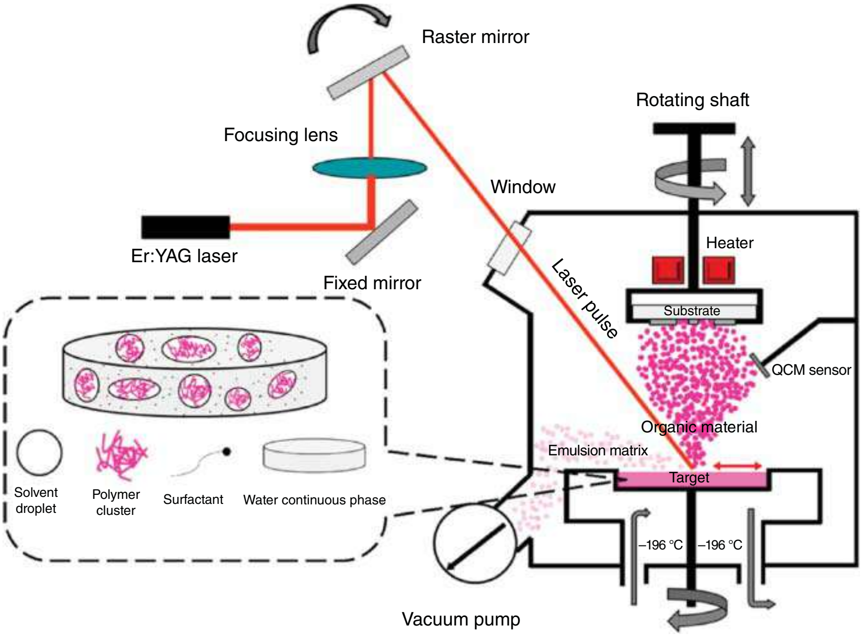

Figure 9.15 Schematic diagram of emulsion-based RIR-MAPLE system: an infrared Er:YAG laser pulse enters a vacuum chamber through the optical system. The laser ablates a solid frozen emulsion target with the guest organic materials (polymers) dispersed inside. The generated organic materials plume is deposited onto the substrate, whereas the emulsion host matrix is vaporized by the laser energy and pumped away. The composition and morphology of the frozen emulsion target are also shown in the zoomed figure, in which the organic solvent is dispersed as droplets in the continuous water phase. The hydrophobic polymer only dissolves into the organic solvent and tends to aggregate into clusters that are confined inside the organic solvent droplets.

between these clusters determine the surface roughness and internal morphology of the polymer film. MAPLE deposition results usually in polymer films with poor surface quality, very rough due to the presence of nanostructures. While rough films have high specific surface area beneficial for enhancing the sensitivity in detection applications, such films usually have poor electrical performance because the surface roughness increases the contact resistance to metal electrodes. The polymer film formation in RIR-MAPLE process depends on the state of dispersion of the polymer in the emulsion. The target oil-in-water emulsion that is frozen for RIR-MAPLE deposition is composed of the organic liquid phase, with conjugated polymer dissolved in primary solvent, dispersed as droplets in the continuous water phase. During deposition, the water ice continuous phase of the emulsion absorbs the laser energy, sublimes, and is pumped away, leaving the polymer to be randomly deposited on the substrate as discrete packets of the polymer clusters (Figure 9.16a). Even if the size of the polymer cluster is determined by the solvent droplet size in the emulsion, they have different shapes and sizes. Therefore, the stacked clusters are not likely to exhibit close packing. Accordingly, the film surface will be inherently rough, with surface features corresponding to the cluster size and voids created inside the film.

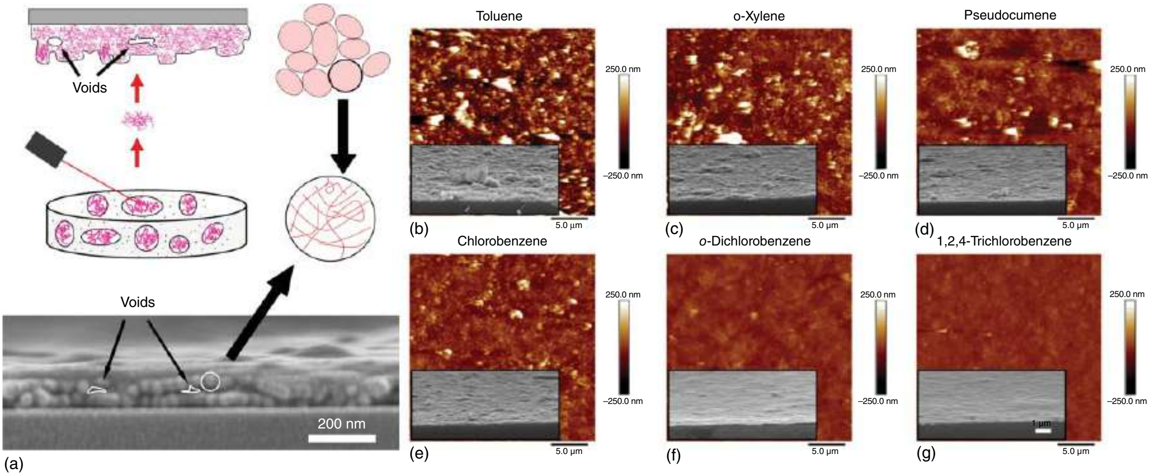

Figure 9.16 (a) Schematic illustrations of the film formation mechanism and the two scales of order present for polymer packing in films deposited by emulsion-based RIR-MAPLE. The surface roughness and internal voids of the illustrated film are highlighted by blackline. A cross-sectional SEM image of an RIR-MAPLE deposited polymer film (PCPDTBT deposited from *o*-dichlorobenzene) shows the presence of polymer clusters and voids highlighted by white line. AFM images of P3HT films deposited from chlorinated aromatic solvents: (b) toluene, (c) *o*-xylene, (d) pseudocumene (1,2,4-trimethylbenzene), and alkyl aromatic solvents: (e) chlorobenzene, (f) *o*-dichlorobenzene, (g) 1,2,4-trichlorobenzene. The inset images are the corresponding cross-sectional SEM images for the same films. Source: (a) Ge et al. [126]. Copyright 2016, ACS Publications, (b–g) Adopted with permission Ge et al. [126]. Copyright 2016, ACS.

Figure 9.16b–g shows the AFM height images of P3HT films deposited from different primary solvents by Kim et al. These AFM height images reveal a general trend; when the solvent solubility-in-water and vapor pressure decreases the film becomes smoother. From the SEM images, micrometer size polymer clusters are scattered on the rough films. Solvents used in emulsion-based RIR-MAPLE have a significant impact on the surface roughness of deposited polymer films and so affect the performance of BHJ Organic Solar Cells. The authors observed an increasing current density for smoother films and attributed it to an enhanced photon to electron conversion across the entire P3HT absorption spectrum due to the improved collection of free charge carriers. This ingenious emulsion-based RIR-MAPLE strategy still needs some improvements; i.e. the best performing P3HT:PCBM organic solar cells (OSCs) display a PCE of $\eta = 3.27\%$ using trichlorobenzene, which is lower than that reported with OSCs device prepared by spin-casting (5.0%) [131].

9.4.1.1 Miniemulsion

Smart strategy to ecofriendly built up BHJ OCVs active layer from water based chemistry relies in the synthesis of organic semiconductor nanoparticles (NP) via the miniemulsion process. By definition, miniemulsion allows the generation of small, homogeneous, and stable droplets of monomer or polymer precursors, which are then transformed by polymer reactions to the final polymer latexes, keeping their particular identity without serious exchange kinetics being involved [132, 133]. An ideal polymerization of miniemulsions can therefore be described that each monomer nanodroplet polymerizes independently from all others, i.e. the monomer droplets before the polymerization and polymer particles after the polymerization have about the same size and are composed in a similar manner. An original strategy of this mini-emulsion applied to BHJ layer was introduced in 2002 by Landfester et al. [88]. The miniemulsion process allows fairly good control over the particle size, giving a handle to externally influence the domain size of the BHJ. The authors produced nanoparticles from a semiconducting polymer (Figure 9.17a) in aqueous phase via the miniemulsion process. As mentioned earlier, polymer dispersions can be obtained from a miniemulsion where the monomeric droplets are polymerized to give polymer particles, but another possibility is the formation of latexes from the droplets of the preformed polymer dissolved in a good organic solvent. After evaporation of the solvent, a polymer dispersion is obtained (Figure 9.17b).

Layers of conjugated semiconducting polymers can be deposited by spin-coating from aqueous dispersions prepared by miniemulsion with controlled particle sizes ranging from 70 to 250 nm (Figure 9.17c). Layers of particles exhibit a particulate structure, revealing the shape of individual PNPs. Annealing above polymer T_g results in coalescing of the particles to larger domains.

Later, this group proposed two approaches to blend polymers and control the dimensions of phase separation in thin polymer blend layers thanks to PNPs prepared by the miniemulsion [134]. Still, a solution of the polymer in an organic solvent is mixed with water containing an appropriate surfactant: i.e. a miniemulsion is formed on stirring and ultrasonication. Then, the solvent is evaporated, resulting in solid PNPs dispersed in water (Figure 9.18a). The upper limit for the

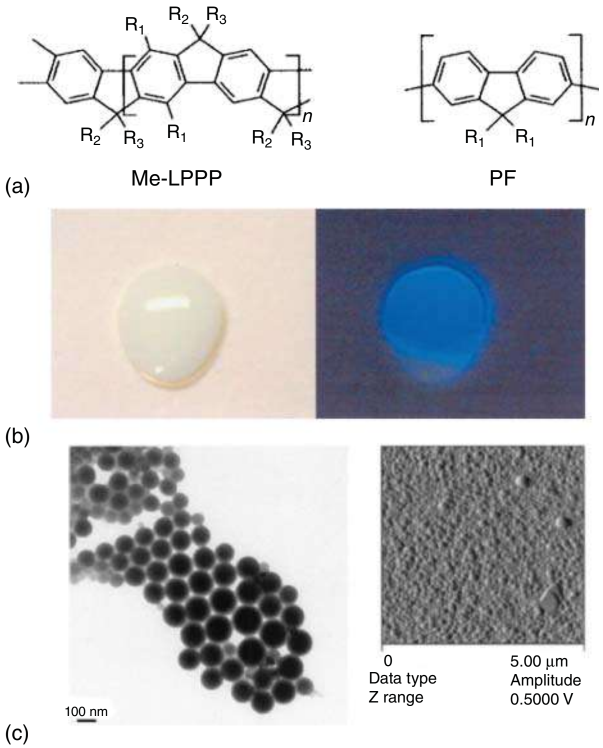

Figure 9.17 (a) Chemical structure of Me-LPPP ladder poly(*p*-phenylene) ($-R_1$: hexyl, $-R_2$: methyl, $-R_3$: decylphenyl) and PF polyfluorene ($-R_1$: 2-ethyl-hexyl). (b) Photographs of a droplet of a dispersion of polyfluorene nanospheres, in white light (left) or under UV lamp (right, $\lambda = 365$ nm). (c) TEM image of Me-LPPP particles (left) and AFM image (right) of a film formed by spin-coating from Me-LPPP dispersion. Source: (a) Landfester et al. [88]. Copyright2002, Wiley Online Library, (b, c) Adopted with permission Landfester et al. [88]. Copyright 2002, Wiley.

extent of phase separation is determined by the size of the individual nanoparticles (tens of nanometers). In the first approach, solid layers of phase separated polymer blend are prepared from an aqueous dispersion containing nanoparticles of two polymers. In the second approach, both polymers are already contained in each individual nanoparticle (Figure 9.18b). At first, the authors applied these two strategies on conjugated polymers, the fluorescent of which is indicative of any significant changes of the polymers' electronic properties during layer processing. Accordingly, they could probe the morphology of the phase-separated structures using energy-transfer experiments. Dispersions were prepared from poly(*p*-phenylene)-type ladder polymer, m-LPPP, (T_g 300–350 °C), and a derivative of polyfluorene, PF11112, with T_g close to room temperature (Figure 9.18c).

For the first approach, the dispersions of the single-component nanoparticles were homogeneously mixed and spin-coated onto substrates. The resulting film consists of closely packed spheres, with some of the particles of the low-T_g PF11112 already coalesced during the deposition process. After annealing, the PF11112

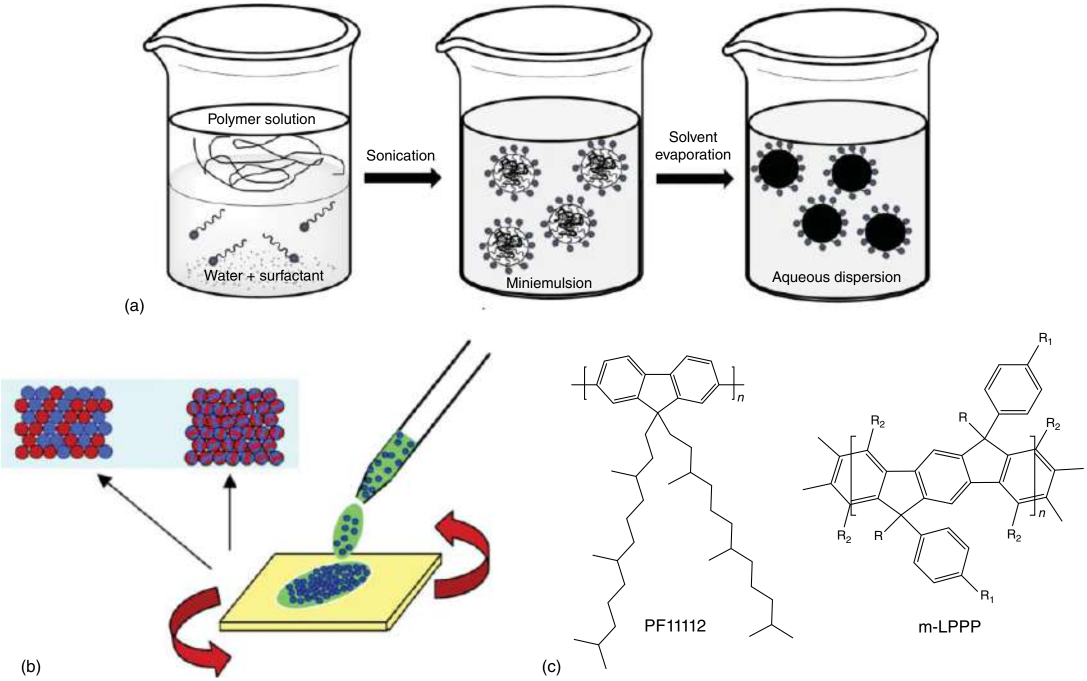

Figure 9.18 (a) Preparation of a dispersion of solid polymer nanoparticles in water. (b) Strategies to prepare binary polymer blends using polymer nanospheres. Phase-separated structures at the nanometer scale can be prepared either by coating a layer from a dispersion containing nanoparticles of two different polymers, or by using dispersions that contain both polymers in each individual nanoparticle. Chemical structure of (c) poly(9,9-bis(3,7,11-trimethyldodecyl)fluorene-2,7-diyl) (PF11112) and the ladder-type poly(*p*-phenylene) (m-LPPP).The substituents on m-LPPP are: R = methyl; R_1 = decyl, and R_2 = hexyl. Source: Kietzke et al. [134]. Copyright 2004, ACS Publications.

particles appear to have coalesced to form the continuous phase, while the high-T_g m-LPPP spheres appear to be uniformly embedded within the PF11112 layer. The absorption spectra indicate that the polymers did not degrade on annealing. Then, samples were excited at 380 nm, with a maximum absorption of PF11112 and not the m-LPPP. The fluorescence spectra show that the emission is dominated by the m-LPPP emission peaks at 463 and 492 nm, indicating significant energy transfer from PF11112 to m-LPPP already in the as-prepared layer. Annealing at 200 °C induces morphological change probed by the rate of energy transfer, strongly dependent on the distance between donor and acceptor [135, 136]. The PF11112 emission, with the main peak at 422 nm, is completely quenched, whereas the m-LPPP emission has gained in intensity due to energy transfer from the soft PF11112 phase. At this stage, the PF11112 phase homogeneously surrounds the individual m-LPPP particles. In the second approach, the resulting nanoparticle dispersion contains a blend of both polymers inside each individual nanoparticle. In the TEM image, these particles have a spherical shape, with only a small variation in size. The two polymers are not homogeneously mixed within the nanospheres. The phase separation inside the particles occurs at the stage of solvent evaporation, with the domain size controlled mainly by the diameter of the particles.

The authors applied this concept for controlling nanophase morphology of the active layer composed of the hole-accepting polymer PFB and the electron acceptor F8BT (Figure 9.19a) [137]. They prepared nanoparticles from a mixture of PBT and F8BT using either xylene or chloroform as the solvent in the miniemulsion process. Solar cells were fabricated by spin-coating the aqueous dispersion onto glass covered with a transparent ITO electrode. The external quantum efficiency (EQE) of these devices are comparable (Figure 9.19b), with a peak value of about 1.7%. The solar-cell properties are entirely controlled by the size of the two-component particle, with almost no effect of the choice of organic solvent. The phase separation in these layers is indeed determined by the particle diameter.

The efficiencies of their solar cells are good but still below the efficiencies reported for layers deposited from chloroform. For comparison, single-layer solar cells using PFB/F8BT (1 : 1) blend layers spin-coated from xylene yielded to EQE between 0.25% and 1.5% and those cells prepared from chloroform up to 4% [138, 139]. Further developments were carried with the second approached and the highest quantum efficiency finally reached 4% for nanoparticles with a weight ratio PFB:F8BT of 1 : 2 [134]. This indicates that a slightly larger amount of F8BT is necessary in the blend particles to obtain optimum conditions for exciton dissociation and charge extraction.

The performance of an OPV based on a blend of hole/electron accepting polymer as the active material depends on the length scale of the phase separation. To give more insight of the local morphology that could display such an active layer, Landfester and coworkers probed a model layer composed of a mixture of PS (polystyrene) or MEH-PPV (poly[2-methoxy-5-(2-ethylhexyloxy)-1,4-phenylenevinylene]) nanoparticles synthesized by miniemulsion by scanning near field optical microscopy (SNOM) [140].

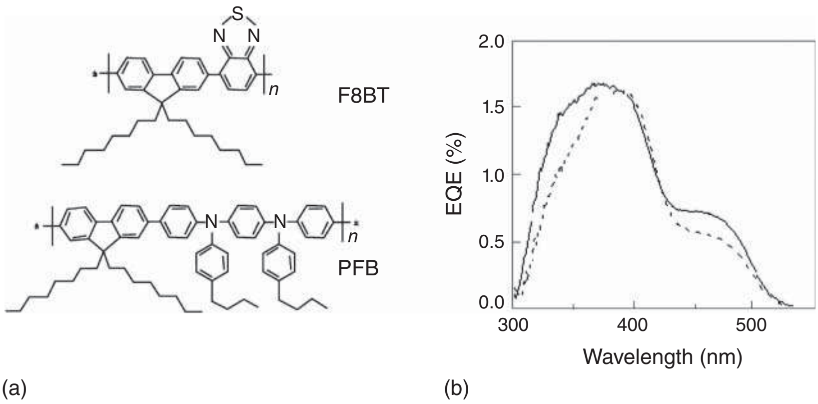

Figure 9.19 (a) Chemical structure of the electron-accepting polymer poly(9,9-dioctylfluorene-*co*-benzothiadiazole (F8BT) and the hole−acceptor poly(9,9-dioctylfluorene-*co*-*N*,*N*-bis(4-butylphenyl)-*N*,*N*-diphenyl-1,4-phenylenediamine) (PFB). (b) Spectrum of the external quantum efficiency (EQE) of single-layer solar cells fabricated from F8BT/PFB (1 : 1 weight ratio) blend particles, which were prepared using either xylene (solid line) or chloroform (dashed line) in the miniemulsion process. Source: Based on Donley et al. [137] Copyright 2005, ACS Publications.

Active layers deposited from miniemulsion need to be annealed to give interesting performance to the OPV. It is no longer possible to distinguish between the different particles using AFM topography images, the surfaces are smooth, whereas the SNOM image shows a clear nanostructured composition, since only MEH-PPV will absorb a considerable amount of light (Figure 9.20c–f). This analysis confirmed that the nanoparticle approach allows the preparation of nanostructured layers of statistically distributed particles down to the nanometer scale.

Holmes and coworkers [92] examined in detail the phase separation inside nanoparticle when composed of mixture of a blend of hole/electron accepting compounds. Indeed, they used P3HT:ICBA nanoparticles as model. These particles display core–shell morphology with the core enriched with ICBA (Figure 9.21a–c). The STXM (scanning transmission X-ray microscopy) compositional maps on the as-spun particles exhibit an ICBA core fractional composition of 0.41 ± 0.05, which is close to the 1 : 1 P3HT:ICBA solution composition, and a thin shell region that is depleted in ICBA (0.23 ± 0.05) (Figure 9.21j). The drying step at 110 °C for four minutes does not alter greatly the core–shell structure (Figure 9.21d–f). The ICBA shell fractional composition increases to 0.34 ± 0.05, while the core composition remains largely unchanged (0.44 ± 0.05).

Upon annealing, the particle shell and core compositions become effectively the same with an average composition of 0.32 ± 0.05 (Figure 9.21j). During particle formation P3HT migrates into the particle shell region resulting in the observed reduction in ICBA fraction (Figure 9.21g–i). Upon annealing of the P3HT:ICBA particles, there is continued movement of ICBA from core to shell and then diffusion from

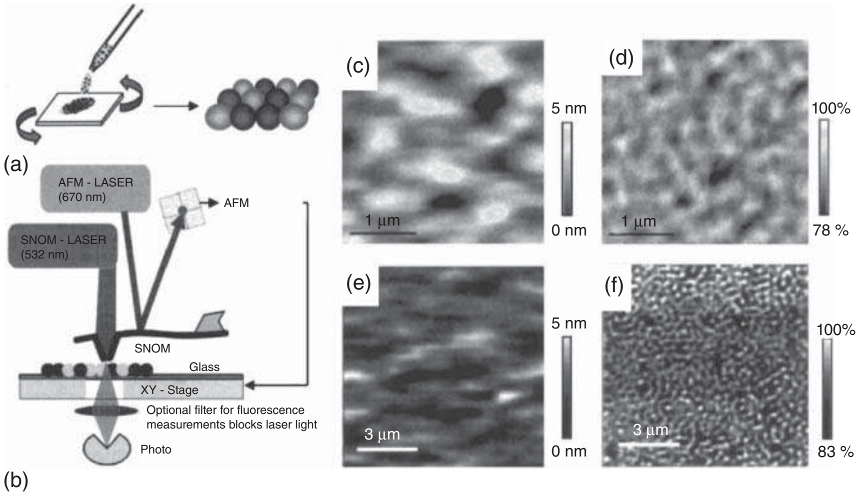

Figure 9.20 (a) Active layer deposition by spin-coating of hole/electron accepting polymer nanoparticles synthesized by miniemulsion. (b) Schematic drawing of the SNOM/AFM setup used for transmission and fluorescence measurements. (c–f) AFM height (left) and simultaneously measured SNOM transmission (right) of a mixture of PS and MEH-PPV particles. Source: (a, b) Kietzke et al. [140] Copyright 2005, Elsevier, (c–f) Adopted with permission Kietzke et al. [140]. Copyright 2005, Elsevier.

shell to outside the particle. Consequently, the P3HT and ICBA become homogenously blended (Figure 9.21k,l). These OPV devices, fabricated from water-dispersed P3HT:indene-C_{60} bisadduct (ICBA) blend nanoparticles, exhibit PCEs of up to 2.5%.

Holmes et al. [141, 142] took advantage from this conclusion for the fabrication of P3HT:phenyl C_{61} butyric acid methyl ester (PCBM) nanoparticle OPVs with varied donor–acceptor ratios from1 : 0.5 to 1 : 2. Using similar characterization procedure, they observed that the PCBM component in the nanoparticle shell phase increases from a concentration that is below the percolation limit to one that is close to the optimal weight fraction for charge transport. This increase in PCBM proportion induced an increase in PCBM photocurrent. The initial core–shell structure of these nanoparticles allows increasing the PCBM loading and directly harvest more PCBM photocurrent, in comparison with BHJ devices where an increase in PCBM loading often leads to a degradation of bulk film morphology such that exciton dissociation and charge transport are no longer efficient.

A judicious choice of particle size and a nanoparticle shell blend composition allow efficient exciton dissociation and efficient extraction of the resultant charges. Nanoparticle based OPVs offer a wise approach for controlling device morphology with performant active layer structure.

In the continuation of nanoparticle based active layer OPVs fabrication, Holmes's group exchange the semi-crystalline P3HT by the poly[2,3-bis-(3-octyloxyphenyl) quinoxaline-5,8-diyl-alt-thiophene-2,5-diyl] (TQ1) that has a particularly high T_g and amorphous nature more desirable properties for OPV fabrication and operation (Figure 9.22) [143]. They optimized TQ1:$PC_{71}BM$ (phenyl C_{71} butyric acid methyl ester) NP-OPV device performance by the application of annealing treatments and

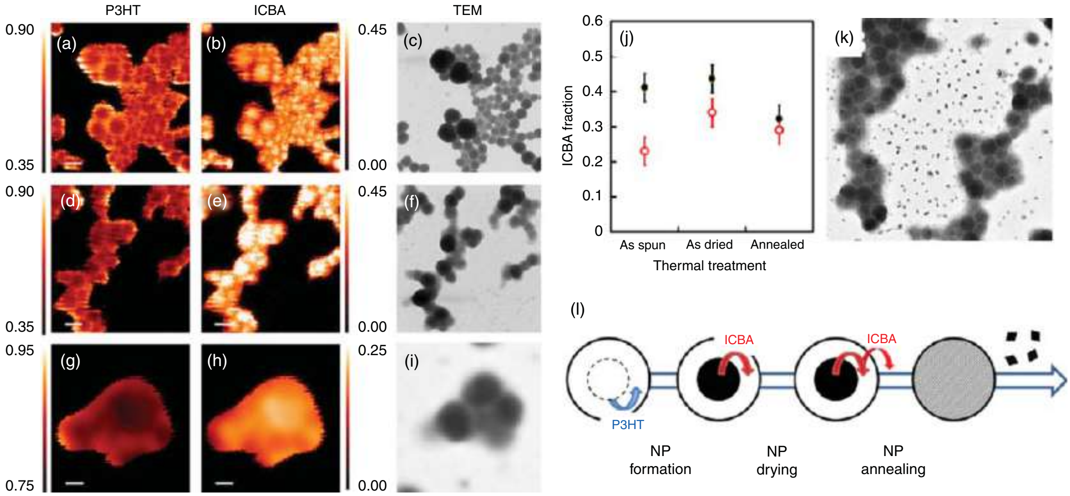

Figure 9.21 2 μm × 2 μm P3HT and ICBA STXM compositional maps for: as-spun (a, b), as-dried (d, e) NP films. 1 μm × 1 μm P3HT and ICBA STXM compositional maps for an annealed (g, h) NP film. Corresponding TEM images for the as-spun (c), as-dried (f), and annealed (i) NP films. (j) ICBA fraction of the core and shell domains as a function of thermal treatment for NP films. The closed black circles and open red circles represent the NP ICBA core and shell fractional compositions, respectively. 2 μm × 2 μm TEM image (k) of an annealed NP film clearly showing presence of small crystallites in the interstitial regions between NP domains. Schematic model (l) of NP evolution during thermal treatment. Source: (a–i, k) Adopted with permission Ulum et al. [92]. Copyright 2013, Elsevier, (l) Ulum et al. [92].

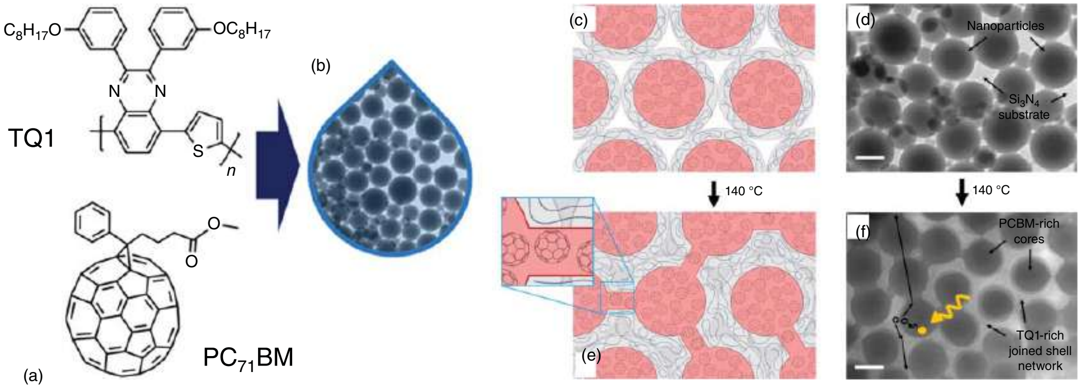

Figure 9.22 (a) TQ1 and $PC_{71}BM$ formula. (b) Schematic deposition of the blended miniemulsion based nanoparticles as the active layer of the OPV. (c) Schematic of TQ1:$PC_{71}BM$ NP film as cast and (d) TEM of the spin-coated film. (e) Schematic of TQ1:$PC_{71}BM$ NP film following mild thermal annealing showing movement of materials and (f) TEM of the NP film following this thermal treatment. Scale bars are 100 nm. In schematics (c) and (e) the $PC_{71}BM$-rich NP cores are colored red-brown, and the TQ1-rich NP shells and joined shell regions are colored gray. Source: (a, b–e) Holmes et al. [143], (d, f) Adopted with permission Holmes et al. [143], Copyright 2016, Elsevier.

reported and an in-depth study of the effect of these treatments on nanoparticle film morphology.

During the annealing the morphological evolution in nanoparticle films for OPV active layers indicate $PC_{71}BM$ nano-pathway formation between dispersed $PC_{71}BM$-rich nanoparticle cores, which have the benefit of making the bulk film more conducive to charge percolation and extraction (Figure 9.22c–f). Such annealing treatments local changes in the polymer conformation in addition to limited fullerene aggregation, resulting in a more optimized morphology for OPV performance. Thus, TQ1 has been successfully applied to NP-OPVs giving a best PCE of 2.54%.

D’Olieslaeger et al. [144] has presented a different particle formulation procedure by miniemulsion using the high boiling solvent, *o*-dichlorobenzene (*o*-DCB), to obtain water-based blended PCDTBT (poly[9-(1′-octylnonyl)-9*H*-carbazole-2,7-diyl]-2,5-thiophenediyl-2,1,3-benzothiadiazole-4,7-diyl-2,5-thiophene-diyl): PC_{71} BM nanoparticles (Figure 9.23a). The solvent was added in the particles to limit the PCDTBT–$PC_{71}BM$ phase separation during the nanoparticles formation. During the particles formation the solvent was evaporated at 60 °C and water was added to compensate the evaporation. In Figure 9.23b–j, spectroscopy imaging confirms very small compositional remixing in the blend NPs, in the size range of about 5 nm, indicating fine mixing at the molecular level.

The authors have fabricated PCDTBT:$PC_{71}BM$ OPV devices with an active layer deposited by spin-coating from the NP dispersion and annealed at 180 °C for four minutes. The morphology of the nanoparticles on the TEM grid is very similar to the structure in the functional active after annealing, which indicates that annealing is required to induce fusion of the particles but does not cause further coarsening or phase separation (Figure 9.23k,l). The PCE reached a 1.9% for the best device. Then, D’Olieslaeger et al. [145] achieved, using the same strategy, a PCE of 3.8% utilizing poly[(5,6-dihydro-5-octyl-4,6-dioxo-4*H*-thieno[3,4-*c*]pyrrole-1,3-diyl)[4,8-bis[(2-ethylhexyl)oxy]benzo[1,2-*b*:4,5-*b*′]dithiophene-2,6-diyl]] (PBDTTPD):PCBM instead of PCDTBT.

Using the miniemulsion method described by Landfester’s group, the surfactant remains in the active layer after deposition and may impede the bulk-heterojunction formation, the device performance, and the solar cell life-time. Part of the surfactant content may be reduced, by extensive dialysis steps of the miniemulsion. For example, Darwis et al. [146] reported that the bulk-heterojunction morphology and the dependence of the PCE on the thermal device treatment are very different for stabilized and non-stabilized P3HT:[6,6]-phenyl C_{61}-butyric acid methyl ester ($PC_{61}BM$) nanoparticulate devices. To overcome the limitations imposed by the surfactant, Gärtner et al. [94] synthesize non-stabilized P3HT:ICBA (mixture ratio 1 : 0.8) nanoparticles using a surfactant free precipitation method and examine the performance of the OPV. Omitting any stabilizers that may affect the bulk-heterojunction formation, they prepared stable dispersion of 10 mg/ml nanoparticle in the non-solvent methanol. The AFM images in Figure 9.24a–e show that the casted layer has a typical root-mean-square roughness $R_q = 40$ nm, the nanoparticles are clearly distinguishable. After annealing for 10 minutes

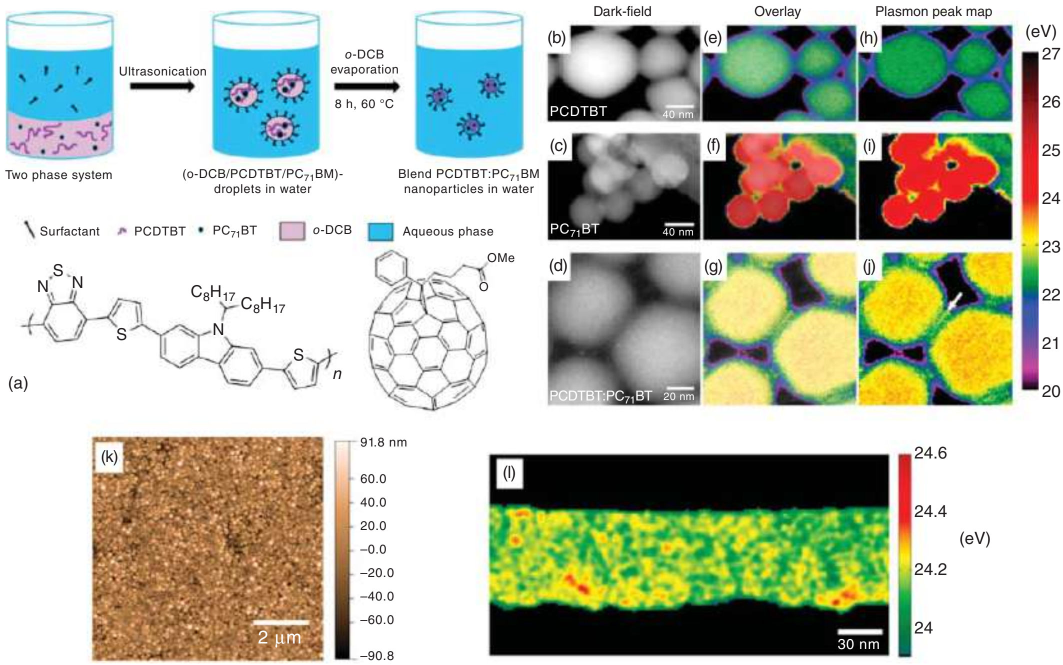

Figure 9.23 (a) (Top) Schematic illustration of the PCDTBT:PC$_{71}$BM blend NP synthesis; (bottom) chemical structures of PCDTBT (Left) and PC$_{71}$BM (Right). Spectroscopic imaging of different NPs. STEM dark-field images from (b) NP 1–0%PC$_{71}$BM, (c) NP 8–100%PC$_{71}$BM, and blend particles (d) NP 7–75%PC$_{71}$BM. Overlays of dark-field images with plasmon peak maps (e–g) and plasmon peak maps. And plasmon peak maps (h–j) created from Lorentzian fits to spatially resolved plasmon peaks (2 nm step size for pure particles and 1.3 nm step size for blend). The white arrow in (j) points to a small spatial feature, where also mixed PCDTBT and PC$_{71}$BM are found between joining particles. (k) AFM image of spin-coated NPs and (l) plasmon peak map of the active layer of a PCDTBT:PC$_{71}$BM (1 : 4)NP OPV device. Source: (a) D'Olieslaeger et al. [144], (b–l) Adopted with permission D'Olieslaeger et al. [144]. Copyright 2017, Elsevier.

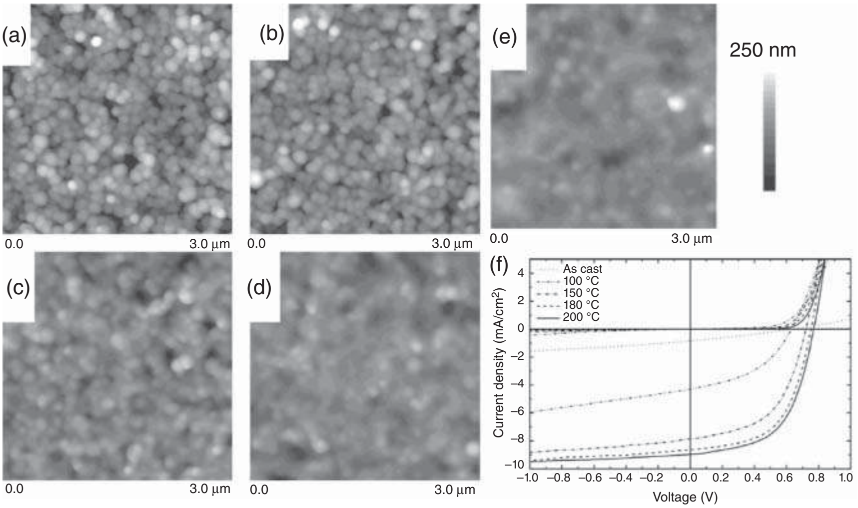

Figure 9.24 3 × 3 µm^2 AFM images of the P3HT:ICBA nanoparticle active layers spin coated from a 10 mg/ml dispersion in methanol: (a) As-cast photo-active layer. (b) Photo-active layer annealed for 10 minutes at 100 °C, (c) 150 °C, (d) 180 °C, and (e) 200 °C. The corresponding root mean square roughness R_q is (a) 43 nm, (b) 46 nm, (c) 30 nm, (d) 24 nm, and (e) 23 nm, respectively. (f) Typical J–V curves of nanoparticulate solar cells for different annealing temperatures. Source: (a–e) Adopted with permission Gärtner et al. [94] Copyright 2014, Wiley, (f) Gärtner et al. [94].

at 150 °C, the surface became smoother and the nanoparticles less discernable $R_q = 30$ nm. Further reduction of the surface roughness was achieved by increasing the annealing temperature to 180 °C and 200 °C yielding $R_q = 20$ nm.

Increasing annealing temperature up to 200 °C enhances the solar cell's PCE yielding up to 4.1% (Figure 9.24f). Although photo-generated excitons are dissociated within the nanoparticles, free charges are captured in the nanoparticles. Since the free charges cannot migrate to the electrodes, they recombine. Upon annealing, the authors assumed that a more intimate contact between the nanoparticles facilitates charge carrier transport and extraction from the active layer effectively suppressing the bimolecular recombination.

Colberts et al. [147] studied the sodium dodecyl sulfate (SDS) concentration in the NP dispersion used for preparing the photovoltaic layers. They investigated OPV devices based on poly[[2,5-bis(2-hexyldecyl)-2,3,5,6-tetrahydro-3,6-dioxopyrrolo[3,4-*c*]pyrrole-1,4-diyl](3‴,4′-dihexyl[2,2′:5′,2″:5″,2‴:5‴,2⁗-quinquethiophene]-5,5⁗-diyl)] (PDPP5T) and [60]PCBM or [70]PCBM processed from aqueous nanoparticle in miniemulsion. Cryo-TEM suggested that the NPs possess a core–shell-like morphology with PDPP5T dominating in the shell of the particle and PCBM in the center. The size of the blend nanoparticles is controlled by the surfactant (SDS) concentration at the start of the process. This concentration is also important in the film forming process of the photovoltaic layers. A too high SDS concentration causes de-wetting, while a too low concentration results in aggregation of the NPs. Both give rise to shorted devices and limit the reproducibility of the device performance. By controlling the amount of free and surface-bound SDS on the NP, solar cells can be made reproducibly. Thus, optimized NP cells based on PDPP5T with [60]PCBM and [70]PCBM gave a PCEs of 2.0% and 2.4%, respectively. The PCEs of the PDPP5T:PCBM NP solar cells still fall short compared with BHJ solar cells because of non-optimized morphology with more pronounced bimolecular recombination and limited optimal thickness of the photoactive layer to a range where a too small fraction of light is absorbed.

Similarly, Xie et al. [148] processed PDPP5T-2 and PC$_{71}$BM are into mixed polymer: fullerene nanoparticles, allowing the formation of BHJ composites with different domain sizes. Mild thermal annealing was still required to melt the nanospheres and enable the formation of interconnected pathways within mixed phases. The authors estimated that reducing the domain size favors charge collection but does decrease trapping in NP film. The optimized solar cell processed by ultra-small NPs delivered a PCE of about 3.4%.

Further research was proposed by Subianto et al. [149] who fabricated Aqueous dispersions by the miniemulsion process of P3HT:PCBM nanoparticles (NPs) using a thiophene-based surfactant 2-(3-thienyl)ethyloxybutylsulfonate sodium salt (TEBS, Figure 9.25a).

The use of TEBS resulted in a stable colloidal dispersion of P3HT:PCBM NPs free of passive surfactant that may impede the bulk-heterojunction formation and so the device performance (Figure 9.25b). SEM images of TEBS- and SDS-stabilized NPs give similar particle size distribution with a main peak observed around 70–85 nm, a large number of smaller particles (30–40 nm) and some larger aggregates (Figure 9.25d). DLS analysis of both dispersions showed average particle sizes around 200 and 150 nm for TEBS- and SDS-stabilized NPs, respectively (Figure 9.25e). The internal structure and electrochemical performances of TEBS stabilized P3HT:PCBM NPs were compared with that of SDS-stabilized core–shell (PCBM-P3HT) NPs at same surfactant concentration. Neutron scattering revealed a homogeneous distribution of small demixed P3HT and PCBM domains in the internal structure of TEBS-stabilized P3HT:PCBM NPs, reminiscent of cast film (Figure 9.25f). Moreover, electron microscopy images displayed diffused NP surface/interface upon drying (without annealing). So, the thiophene-containing TEBS may improve compatibility and film-forming properties of fabricated P3HT:PCBM NPs, and consequently be more suited for conventional film processing methods for organic solar cell applications. The authors did not report any OPV performance using this promising active layer.

9.4.1.2 Microemulsion

The last 20 years development on the preparation of optimized active layer of OPV from nanoparticles (NP) via the miniemulsion has led to interesting conclusions. It allows increasing the fullerene proportion and directly harvest more fullerene photocurrent, in comparison with BHJ devices for which an increase in fullerene loading often leads to a degradation of bulk film morphology. The phase separation into core–shell structure induced during nanoparticles preparation, due to the difference

Figure 9.25 (a) Chemical structure of P3HT, PCBM, TEBS, and SDS, SEM micrograph of (b) TEBS-stabilized and (c) SDS-stabilized P3HT:PCBM (1 : 1) NP dispersions. Particle size distribution from (d) SEM and (e) dynamic light scattering. (f) Proposed schematic of the internal structure of TEBS- and SDS-stabilized P3HT:PCBM (1 : 1) NP dispersions based on neutron scattering data. Source: (a, d–f) Subianto et al. [149]. Copyright 2018, ACS Publications, (b, c) Adopted with permission Subianto et al. [149]. Copyright 2018, ACS.

of polarity of the active compounds, has to be limited for optimizing the PCE performance. The distance between donor and acceptor has to be strongly limited; they must be intimately intertwined all together while promoting charge extraction and good electron transfer to the electrode.

Soft templating of the active layer by bicontinuous microemulsion could meet these needs [150]. The preparation of microemulsion is a tricky but efficient method to produce a soft template for the synthesis of structured materials such as ion conducting membrane [151–153], nanofiltration membrane [154], or encapsulating materials for drug delivery [155, 156]. Similarly, the optimal morphology of an organic solar cell may be characterized by cocontinuous, interpenetrating donor and acceptor domains with nanoscale dimensions and high interfacial areas. In doing so, Ganesan's group presented a theoretical analysis of the ternary phase behavior to demonstrate that it may be possible to produce bicontinuous microemulsion morphologies from conjugated polymer/fullerene blends [157–160].

Using coarse-grained simulations, they identified the blend compositions composed of poly(thieno[3,4-*b*]-thiophene-*co*-benzodithiophene) (PTB7, Figure 9.26a), PTB7-*b*-polynaphthalene diimide (PTB7-*b*-PNDI, Figure 9.26b) and phenyl-C_{61}-butyric acid methyl ester (PCBM) that would be most likely to result in donor/acceptor morphologies resembling the bicontinuous microemulsion [161]. Experimentally, they determined these compositions with TEM (Figure 9.26c–f) and grazing-incidence X-ray scattering measurements (Figure 9.26g). The darker color regions are composed of PTB7 and PCBM intermixed, while the white ones are rich in PNDI (poor in PCBM). The bicontinuous-like morphology was obtained experimentally and described earlier for the case of $\varphi_{\text{PTB7-}b\text{-PNDI}} = 0.65$. It is a promising OPV active layer because it is characterized by cocontinuous and thermally stable donor and acceptor domains of roughly 100–300 nm in size. Thus, the authors also demonstrate that all-conjugated BCP additives could be used as compatibilizers to produce thermally stable, co-continuous donor/acceptor. The authors did not report yet any OPV performance using this promising strategy.

9.4.2 Porous Inorganic Materials

The use of porous inorganic materials in order to create polymer nanostructures is an interesting alternative to the well-established electropolymerization of polymers. By creating nanostructured polymers with inorganic materials, the active area between the electron donor and acceptor can be drastically increased, directly impacting the photon-to-electron conversion of the resulting device. Technically, nanostructuration of a conjugated polymer can be obtained by first elaborating a well-defined nanostructure of the electron acceptor. This strategy was notably applied while using TiO_2 arranged in periodic hexagonal hole arrays [162]. If a porous nanostructure containing small holes in the corner of an hexagonal structure could be obtained as illustrated in Figure 9.27, it can be considered as a template method used to nanostructure the polymer. Besides comparing the performance of the equivalent device comprising an active layer made of a conjugated polymer, i.e. poly[2-methoxy-5-(2′-ethyl-hexyloxy)-1,4-phenylenevinylene] (MEH-PPV)

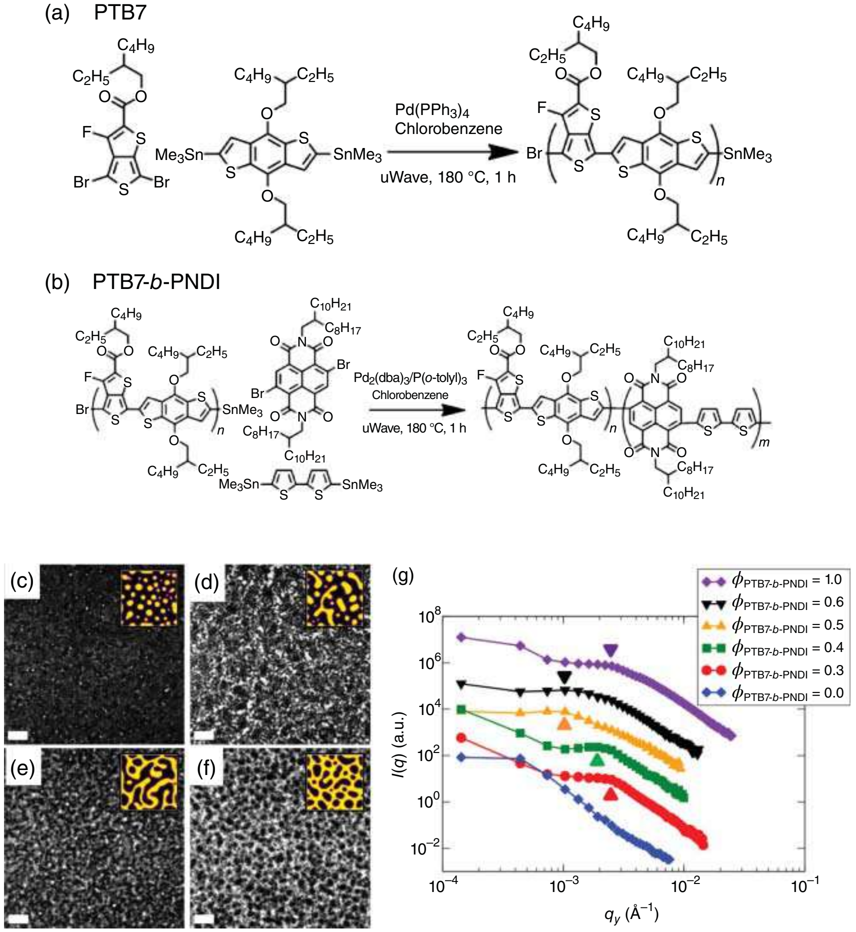

Figure 9.26 (a) Chemical formula of poly(thieno[3,4-*b*]-thiophene-*co*-benzodithiophene) (PTB7) and (b) PTB7-*b*-polynaphthalene diimide (PTB7-*b*-PNDI). Cross-sectional TEM images of thermally annealed thin films with $\varphi_{\text{PTB7}}/(\varphi_{\text{PTB7}} + \varphi_{\text{PCBM}}) = 0.65$: (c) $\varphi_{\text{PTB7-}b\text{-PNDI}} = 0.3$, (d) $\varphi_{\text{PTB7-}b\text{-PNDI}} = 0.4$, (e) $\varphi_{\text{PTB7-}b\text{-PNDI}} = 0.5$, (f) $\varphi_{\text{PTB7-}b\text{-PNDI}} = 0.6$. The scale bar is 1 μm. The insets show the volumetric density of PNDI resulting from SCMF simulations to match the experiments. (g) GISAXS profiles of thermally annealed thin films. In all cases, $\varphi_{\text{PTB7}}/(\varphi_{\text{PTB7}} + \varphi_{\text{PCBM}}) = 0.65$ and $\varphi_{\text{PTB7-}b\text{-PNDI}} = 1.0 - \varphi_{\text{PTB7}} - \varphi_{\text{PCBM}}$. Source: (a, b, g) Kipp et al. [161], (c–f) Adopted with permission Kipp et al. [161]. Copyright 2015, ACS.

incorporating a randomly distributed layer of TiO_2 nanoparticles, an enhancement of 0.21% of the PCE was observed for cells fabricated with the nanostructured titanium dioxide (TiO_2) layer.

However, the contact between the electron donor and the electron acceptor can be further improved, by reaching a better nanostructuration of the electron-accepting moiety. To get this result, several key requirements aiming at optimizing the photon-to-electron conversion in solar cells have first to be mentioned. Notably, solar cells based on bilayer heterojunctions are considered to be better devices

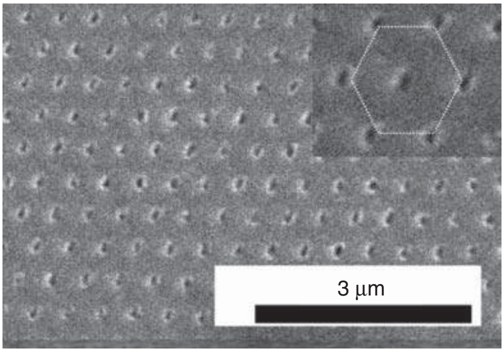

Figure 9.27 Nanostructured layer of TiO_2 onto which the electron donating MEH-PPV acting as a light absorber has been spin-coated. Source: Adopted with permission Kim et al. [162], Copyright 2007, Elsevier.

than those made of a unique material comprising both the electron-donating and electron-accepting moieties. Indeed, for bilayered devices, a large donor–acceptor interface can be created, improving excitons generation and diffusion, and finally charge separation. This concept is not new and was proposed as soon as 1987 by Tang and VanSlyke [163]. When BHJ solar cells are considered, inherent disorder within the active layer often results in poor device efficiencies due to excitons recombination. In this context, control of the morphology at the nanoscale level has to be obtained and several strategies consisting in nanostructuring the absorbing polymers have been developed [164]. Notably, to improve the donor acceptor interaction, the size of the nanostructure has to be directly related to the diffusion length of excitons, which is around 5 to 10 nm for polymer-based solar cells. Ideally, size of the nanostructures should be in this order of magnitude.

Porous inorganic materials offer a unique opportunity to nanostructure polymer materials. From a technical point of view, the polymer is introduced in the pores by infiltration or by spin-coating. In the case of specific metals such as titanium, the metal surface used to polymers nanostructured can be kept, acting as an electron acceptor for the device. In this case, device fabrication is greatly facilitated and modification of the polymer structure due to the removal of the inorganic material is avoided [165]. Highly nanostructured polymers are actively researched to optimize the polymer/electrode interface. Besides, one drawback of this approach is that the nanostructured electrode can be completely filled by the polymer. In this field, an interesting work was reported in 2003 by Coakley et al. [166]. By using a BCP as a structure-directing agent for controlling the distribution of the pores as well as their sizes, titanium films with a regular distribution of pores could be obtained. By playing with the temperature used during spin-casting (100–200 °C), infiltration of P3HT inside the titanium film could be efficiently controlled and 33% of the total volume of pores could be filled at 200 °C, thickness of the mesoporous film being of 180 nm (see Figure 9.28).

To determine the temperature dependence of infiltration, measurements of optical density were notably carried out. At 200 °C, a thickness for the polymer layer of approximately 60 nm was determined, corresponding to 1/3 of the total thickness of the mesoporous film. Following this initial work, Coakley and McGehee evaluated these infiltrated $P3HT^-$ titanium layers in devices [167]. Interestingly,

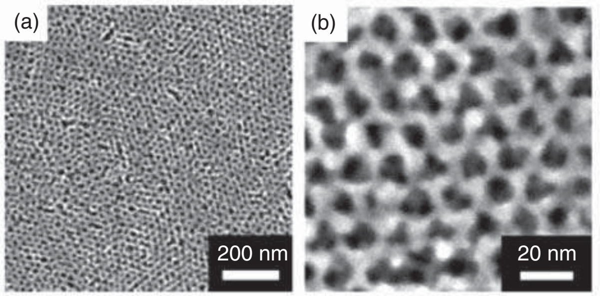

Figure 9.28 (a, b) High resolution scanning electron microscopy (HRSEM) images of the titanium layer at different magnifications. Source: Adopted with permission Coakley et al. [166]. Copyright 2003, Wiley.

the pore sizes were close to 10 nm, corresponding to the exciton diffusion length for numerous conjugated polymers. Besides, the photon-to-electron conversion remained low, peaking at 1.5% for a monochromatic light at 514 nm. To support the lower PCE, variation of the amount of polymer inside the mesoporous film revealed the low performance to be directly related to the low hole-transport ability of the conjugated polymer. In 2005, Chui and coworkers increased the number of pores as well as their sizes by using another structure-directing agent polystyrene-*block*-polyethylene oxide (PS-*b*-PEO) diblock copolymer instead of poly(ethylene oxide)–poly(propylene oxide)–poly(ethylene oxide) triblock copolymer for Coakley and coworkers [168, 169]. As interesting feature, the pore size of the mesoporous layer could be controlled by the amount of Ti precursor. Notably, a decrease of the pore size with the concentration of the titanium precursor was evidenced and pores of ~23 nm were obtained with a precursor concentration of 35%. While evaluating the benefits of this nanostructuration on the device efficiency, a PCE of 0.29% under AM 1.5 solar illumination was determined for devices with the following structure ITO/TiO_2/MEH-PPV/Au device comprising a poly(2-methoxy-5-(20-ethyl-hexyloxy)-phenylene vinylene) (MEH-PPV) layer of 40 nm. Another strategy to produce a nanotemplate with a regular structure consists in using 2D surface relief gratings (SRGs) [162]. In this case, polymer films made of well-organized titanium pores were used as a template for MEH-PPV, which was spin-coated on top of it. Here again, a poor improvement compared with a flat layer of TiO_2 was obtained. Indeed, if a PCE of 0.05% was obtained for a flat surface of TiO_2, this value increased up to 0.21% for the nanoporous layer.

9.4.3 Electropolymerization

Control of the morphology of the active layer is a critical issue for solar cells and to perfectly control the nanostructuration, electropolymerization was examined as a possible approach. However, it proved to be a difficult way to design solar cells with remarkable electron-to-photon conversion. One of the main issues of electropolymerization is the roughness of the electropolymerized layer, which grows upwards from the electrode surface, adversely affecting the electron-to-photon conversion

[170]. One of the main advantages of electropolymerization is that there is no need for polymer processing subsequently to the polymer generation. Parallel to this, considering that only the monomer will be manipulated, the solubility of the final polymer is not an issue to elaborate solar cells and the introduction of solubilizing side chains is not needed. To end, the thickness as well as the oxidation state of the polymer can be carefully controlled. Despite these different advantages, electropolymerization has only been scarcely used to prepare components of the PSC. Most of the semiconducting polymers can be prepared electrochemically and polymers such as poly(carbazole), poly(thiophene), and poly(triphenylamine) were electrogenerated. Among electro-generated polymers, poly(thiophenes) were undoubtedly the most widely studied. This polymer is characterized by a remarkable thermal and chemical stability under air [171] and good electronic properties [172–174]. However, the chemical synthesis of polythiophene suffers from adverse alpha-beta couplings between thiophene units, resulting in conjugated polymers exhibiting a poor regioregularity and thus poor electronic properties. To address this issue, the substitution of the thiophene ring at the 3 and/or 4-positions by various groups was examined as an effective way to block these two positions. However, the steric hindrance generated between adjacent groups can negatively impact the π-conjugation of poly(thiophene) and enforce a rotation of the consecutive thiophene units, introducing a distortion in the polymer backbone. To overcome these problems and to introduce enough space between functionalized thiophene units, the polymerization of terthiophenes instead of thiophenes was examined [175–178]. In fact, four parameters govern the polymer band gap, namely, the regioregularity of the polymer, the chain length, the intermolecular interactions between polymer chains. and the substituent effects. However, the efficiency of solar cells is also governed by other parameters such as the molar extinction coefficients of the photosensitizer as well as the electron-transfer rate.

9.4.3.1 Poly(thiophenes)

Numerous solar cells based on electrogenerated poly(terthiophenes) as photosensitizers have been developed over the years. Among substituents, carboxylic group proved to be the best anchoring group, by facilitating the adsorption of the polymer onto the TiO_2 layer through the formation of C-O-Ti bonds. Parallel to this, the electron transfer from the polymer to the TiO_2 layer is improved by the proximity with the electrode. Beyond the simple adsorption of the polymer onto the TiO_2 layer, the peripheral carboxylic group also acts as an electron acceptor, whereas poly(terthiophene) acts as an electron donor. Due to the limited exciton diffusion length, the proximity of the charge generation and collection is of crucial importance. Interestingly, introduction of a phenyl ring in T1 [179] between the terthiophene unit and the carboxylic group enabled to greatly improve the maximum ECE, relative to that determined with T2 [177] (see Figure 9.29). An enhancement of the ECE from 2.32% for T2 to 3.97% for T1 was observed under an AM 1.5 solar simulated light irradiation of 100 mW/cm^2 and a simple device structure TiO_2/poly(thiophene)/electrode. To support the lower efficiency of T2-based solar cells, a wider band gap for poly(T2) relative to poly(T1) was determined

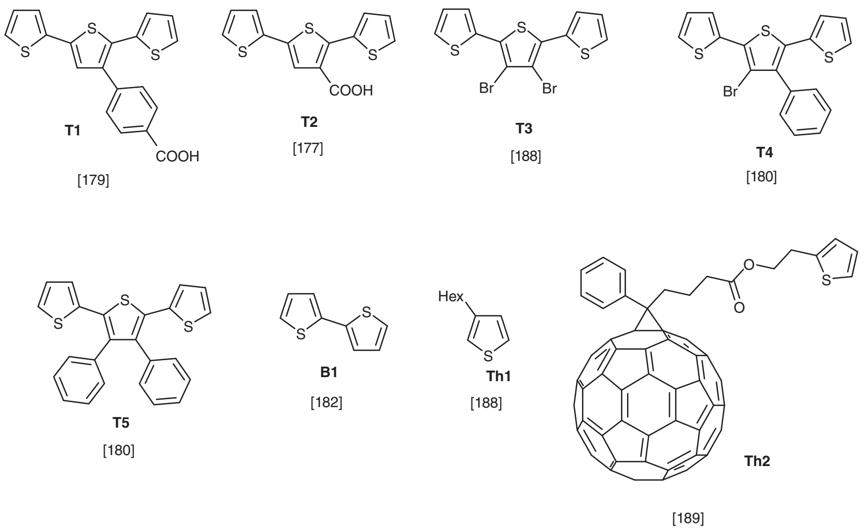

Figure 9.29 Chemical structures of thiophene-based monomers used for electropolymerization.

(2.10 eV vs. 1.98 eV for poly(T1)). While optimizing the electropolymerization conditions, a monomer concentration of 4 mM, an electropolymerization carried out by running six cycles between 0.0 to 1.4–1.6 V vs. Ag/AgCl at a scan rate of 100 mV/s proved to be the best conditions. Using these conditions, a polymer layer of 12.5 nm was determined for poly(T2). Conversely, for poly(T1), a polymer layer composed of particles with a diameter of 73.2 nm and a RMS surface roughness of 1.75 nm for the polymer layer was found.

Electropolymerized poly(terthiophenes) were also used as electron donors in combination with 3,4,9,10-perylene-tetracarboxylic-dianhydride (PTCDA) as the acceptor. Prior to the elaboration of the solar cells, the ability of T3 [180], T4, or T5 [181] to be electropolymerized was examined by cyclic voltammetry. In these works done by Bernède and coworkers, the use of anhydrous conditions for electro-polymerization was determined as being the key parameter to get reproducible results. By applying a voltage lower than 1.5 V, long electrolysis time was found for T3-T5, whereas an over-oxidation of the polymer film was observed upon applying a voltage higher than 1.5 V. Using these conditions, namely, by applying a constant voltage around 1.5 V, a smooth and uniform polymer layer composed of granules of similar sizes was found for T3. While elaborating the electron-donating layer by sweeping between −0.20 V and 1.40 V, 20 cycles were determined as being necessary to observe the expected photovoltaic effect. Despite the remarkable quality of the polymer film, ECE of the following solar cells glass/ZnO (180 nm)/poly(T3)/PTCDA (200 nm)/LiF (<15 nm)/Al remained low, peaking at 0.006% under an AM 1.5 solar simulated light irradiation of 100 mW/cm^2. By attempting to replace the bromine atoms of T3 by phenyl rings in T4 and T5, no photovoltaic effects were found for the T4- and T5-based devices fabricated in the same conditions than those used for T3. On the opposite, the resulting devices behaved as electroluminescent diodes, exhibiting a turn-on voltage higher than 8 V.

If low performances were obtained with terthiophenes, bithiophenes were also investigated. In this field, a fully electropolymerized device was reported in 2011, in which the hole-transport layer, i.e. poly(3,4-ethylenedioxythiophene) (PEDOT), the semi-conducting layer made of PBT, and the electron-accepting layer composed of electrodeposited fullerenes, were successively generated on top of an ITO electrode [182]. In this study, 2,2′-bithiophene was selected instead of thiophene due to its lower electropolymerization potential (0.7 V vs. SHE relative to the unsubstituted thiophene in acetonitrile), thus avoiding the formation of side products, crosslinkage between polymer chains and the formation of short chains [183]. From a technical point of view, by adding boron trifluoride diethyl etherate in the solution of 2,2′-bithiophene B1, a consecutive polymerization of PEDOT and PBT could be obtained, the electropolymerization of PBT being obtained by scanning up to 0.9 V contrarily to 1.1 V for PEDOT. Finally, electrodeposition of C_{60} was obtained by using an epoxide derivative and by applying a negative potential. Indeed, previous works on the electrodeposition of unsubstituted C_{60} have revealed the amount of deposited fullerenes to be negligible when the fullerene is not substituted with epoxides [184–187]. Examination of the morphology of the different layers revealed the hole transport layer (HTL) to exhibit a brush-like architecture with nanofibers of 50 nm diameter. A roughness of ±15 nm was determined for the PEDOT layer. On the opposite, electropolymerization of PBT produced nanoparticles of polymer, with particle size ranging from 50 to 200 nm. Due to the polydispersity of the particles, the roughness increased up to ±50 nm. Finally, a smooth layer was found for the fullerene layer but an unequal deposition on top of the PBT layer was also evidenced by AFM measurements. Fabrication of the PSCs revealed the best results to be obtained for devices comprising a PBT layer obtained after 15 cycles. An overall efficiency of 0.031%, a fill factor of 31%, and a low open circuit voltage V_{OC} of 0.18 V were determined. While comparing with devices fabricated by spin-coating the fullerene layer, a major improvement of the performance was observed, the ECE increasing up to 0.37%, associated with a significant increase of the V_{OC} to 0.47 V. Therefore, it could be concluded that the roughness of the fullerene layer and the poor quality of the layer was the main factor affecting the efficiency of the electrochemically prepared solar cells.

More promising results were obtained with thiophene derivatives. From a morphology point of view, an ideal structure for the active layer is a bicontinuous network of electron donors and acceptors with a nanofibrillar structure for the semiconducting polymer to offer a large surface area to improve the contact between both partners. Ideally, to favor charge collection, the nanostructure is organized perpendicular to the electrode surface. In 2008, Ratcliff et al. prepared a bilayer solar cell where C_{60} was evaporated on top of an electropolymerized layer of 3-hexylthiophene Th1 [188]. As specificity, the textured P3HT film could be obtained using a pulsed-potential-step electrodeposition method. The nucleation of P3HT microclusters in the third dimension allowed to create nanorods standing perpendicular to the electrode surface. As a result of this nanostructuration, an ECE of 1% and a short-circuit current of 3 mA/cm^2 were determined. By covalently linking C_{60} to thiophene (Th2), copolymers made of 3-octylthiophene and Th2 could be electrochemically prepared, exhibiting a double cable structure [189]. Considering that 3-octylthiophene and Th2 can only be polymerized by applying opposite potentials, the step-potential bias method was used, consisting in applying a negative bias for the predetermined duration to polymerize Th2 and by applying a positive bias to copolymerize 3-octylthiophene for the predetermined duration. By alternating the positive and the negative bias, a copolymer poly(3-octylthiophene/Th2) could be prepared. By AFM analyses, annealing of the copolymerized layer for one hour does not modify the morphology, maintaining a regular distribution of fullerenes over the entire surface and preventing fullerene migration. Besides these appealing features, device performances proved to be highly sensitive to the purity of the system. An open circuit voltage of 0.66 V, a short-circuit current of 52 μA/cm^2, and an ECE of 0.0068% under an AM 1.5 100 mW/cm^2 were determined. To support the low conversion efficiency, a fast exciton recombination due to an inappropriate organization of the BHJ was evoked. Parallel to this, low amounts of contaminants were determined as adversely affecting the electron-to-photon conversion, making electro-polymerization a difficult approach to design highly efficient solar cells. Better results were obtained while codepositing thiophene and the unsubstituted C_{60} [184]. In this last case, despite the low fullerene content, an ECE of 0.3% and a V_{OC} of 0.805 V and a fill factor of 38% were determined under standard irradiation conditions. While examining the morphology of the poly(thiophene)/C_{60} films, layers composed of grains with sizes of a few tens of nanometers were imaged by SEM. A fast degradation of the devices within one hour was also demonstrated under light exposure, the BF_4^- counter-ion of the support electrolyte detected as trace amount in the electrogenerated polymer, decomposing as HF and BF_3, and de-doping the semiconducting polymer. A higher fullerene content could be obtained while codepositing 2,2′-bithiophene B1, and C_{60} in the presence of small amounts of C_{60}-epoxide [190]. Compared with the former study, a similar morphology was found for the BHJ, consisting of particles with sizes of a few tens of nanometers. By electrochemistry, the thickness of the active layer as well as the composition could be finely tuned. Compared with the composition obtained by cycling between −1.20 V and + 1.20 V, by cycling at a more negative potential than −1.20 V, the fullerene content within the active layer could be increased, whereas the active layer could be enriched by cycling at a potential higher than +1.20 V. While fabricating a bilayer device ITO/PEDOT/poly(thiophene)-C_{60}/Al, the photoresponse of solar cells was low, a J_{SC} of 0.30 mA/cm^2, a V_{OC} of 0.81 V, and an ECE of 0.3% being determined. Electrochemistry is also an efficient method to deposit a polymer layer on complex architecture and thiophene was notably polymerized on top of a nanostructured ZnO layer [191]. Considering that the exciton diffusion length is lower than 10 nm, electropolymerization of poly(thiophene) onto nanorods spaced of 20 nm was examined. It was determined that polythiophene was covalently linked to the ZnO nanorods by mean of Zn—S bond and the thiophene cycle was standing perpendicular to the ZnO surface. However, a low fill factor was found for the corresponding cells, electropolymerization of polythiophene furnishing regiorandom polymers, with numerous structural defects resulting from crosslinking between chains, and α-β connection between thiophene units. Consequently, the poor packing of the polymer chains, the low conjugation length, and the low carrier mobility furnished solar cells of low efficacy.

9.4.3.2 Poly(carbazole)

Currently, the dominant technology of photovoltaics cells is dominated by the well-known P3HT/PCBM combination to elaborate the active layer. Besides, alternatives can be found to thiophene for light harvesting and carbazole is one of those. The first report mentioned the electropolymerization of carbazole was reported in 2011 [192]. To get a good penetration of the monomer inside the porous silicon, pores with an average diameter of 100 nm were used. Poly(carbazole) could be electrogenerated by cycling between 0 and + 1.5 V and the entire volume of pores was polymerized after seven to eight cycles. Cross-section SEM images of porous silicon after electropolymerization revealed the nanostructure not to be altered by the electropolymerization process and the nanotubes to be entirely filled by the polymer, until the bottom part of the nanotubes. Under illumination, a moderate photovoltaic affect was found, the PCE ranging between 0.2 and 0.5%, a V_{OC} of 280 mV and a J_{SC} of 3.2 mA/cm^2. To produce a porous semiconducting polymer, a three-dimensional monomer can be used, as exemplified with a tetraphenylmethane substituted by four peripheral carbazoles TPTCz (Figure 9.30) [193]. Polycarbazole could be formed by sweeping between −0.8 V and +0.97 V and a smooth film integrating micropores of 1 nm diameter regularly dispersed over the entire film was shown by high-resolution transmission electron microscopy. A perfect control of the polymer thickness could be obtained, this latter evolving linearly with the scans number. An electrochemical doping of the polymer could also be obtained while using perchlorate as the anion for the support electrolyte. Doping of polycarbazole could be finely controlled by mean of the applied oxidation potential as well as the duration. A doping level as high as 62% could be obtained, by immobilizing perchlorate anions in the micropores. While using polycarbazole as a doped interlayer in a PSC, ECE of the following device ITO/PEDOT:PSS (30 nm)/doped poly(TPTCz) (≈10 nm)/PCDTBT:PC$_{71}$BM (90 nm)/LiF (0.5 nm)/Al, was determined as peaking at 7.56%, significantly enhanced relative to PEDOT:PSS-only devices (5.68%). A simultaneous enhancement of the three parameter V_{OC}, J_{SC}, and FF was obtained upon introduction of the interlayer. This trends was confirmed by the same authors with another device structure, i.e. ITO/PEDOT:PSS (30 nm)/doped poly(TPTCz) (10 nm)/PTB7:PC$_{71}$BM (100 nm)/LiF (0.5 nm)/Al [194]. Here again, by introducing the doped poly(TPTCz) interlayer, ECE of PSCs could be increased from 7.07 to 8.42%, compared with the performances obtained for the PEDOT:PSS-only devices. To improve the hole-extraction process at the cathode, the carbazole-based triphenylethylene polymer poly(TPCz) could provide a similar enhancement of ECE than that observed with TPTCz [195].

By means of the twisted structure of TPCz, electropolymerization of this monomer resulted in a porous and smooth polymer layer comprising pores of 1 nm diameter. Upon introduction of the poly(TPCz) interlayer in the PSC ITO/PEDOT:PSS

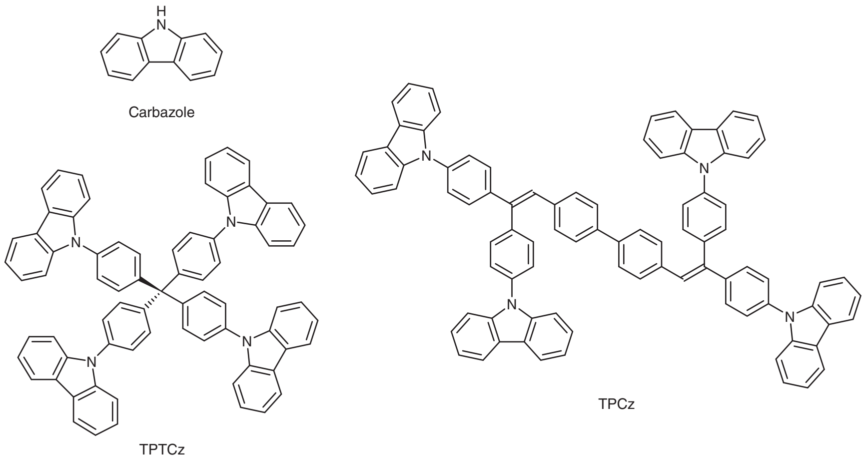

Figure 9.30 Chemical structures of carbazole-based monomers used for electropolymerization.

Figure 9.31 Chemical structures of the triphenylamine-based monomer used for electropolymerization.

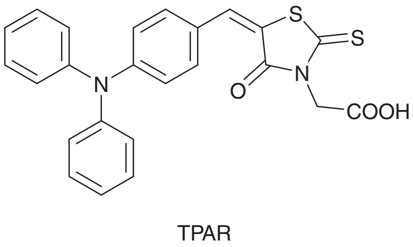

(40 nm)/poly(TPCz) (10 nm)/PTB7:PC$_{71}$BM (100 nm)/Ca (20 nm)/Al, ECE and FF of devices could be improved from 7.38% and 68% to 8.32% and 71% respectively.

9.4.3.3 Poly(triphenylamine)

To maintain the morphology of the active layer as well as the nanostructuration of the active layer during device operation, polymerization of the dye is an efficient technique that was applied to TPAR (Figure 9.31) [196]. In this field, triphenylamine is a candidate of choice for electropolymerization due to its similarity with aniline. Indeed, aniline has been extensively studied as an electropolymerizable group for the electrochemical generation of polyaniline. Considering the similarity of structure, the possibility to electropolymerize TPAR was ensured.

Upon polymerization of TPAR, a blue-shift of the absorption spectrum was found for poly(TPAR) relative to TPAR and can be assigned to an extension of the conjugation. While examining the incident photon-to-current conversion efficiency (IPCE) of poly(TPAR) and TPAR-based devices, a lower IPCE was found for the polymer-based device (4.57% vs. 3.04% for TPAR-based devices) and this counter-performance was assigned to the blue-shift of the absorption, reducing the absorption properties in the 470–510 nm range. If no real morphological characterizations of the electropolymerized layer on top of the nanoporous TiO$_2$

electrode were carried out, a completely different organization of the dyes within the active layer was demonstrated. Notably, for the free dyes, the formation of J-type aggregates on the TiO_2 surface was demonstrated, what was not detected for the polymer layer.

9.5 Conclusion

A short overview of different strategies employed to finely tune the nanostructure of the active layer of an all-organic photovoltaic cell has been given in this chapter. Either through a chemical or a physical method, smart structures have been produced, sometimes with mixing of compounds in proportion inaccessible by simple blending. In the field of solar cells, yield efficiency is very legitimate for the final justice of the peace. At the same time, we have attempted to show that strategies of on-demand structuration of an active layer, developed usually on poorly efficient model chemical compounds, are noteworthy as they could boost the yield for future solar cell improvements.

References

1 Chen, J.T. and Hsu, C.S. (2011). Conjugated polymer nanostructures for organic solar cell applications. *Polym. Chem.* 2: 2707–2722.

2 Xie, J., Zhao, C.E., Lin, Z.Q. et al. (2016). Nanostructured conjugated polymers for energy-related applications beyond solar cells. *Chem. Asian J.* 11 (10): 1489–1511.

3 Meng, L., Zhang, Y., Wan, X. et al. (2018). Organic and solution-processed tandem solar cells with 17.3% efficiency. *Science* 361 (6407): 1094–1098.

4 Xu, T. and Yu, L. (2014). How to design low bandgap polymers for highly efficient organic solar cells. *Biochem. Pharmacol.* 17 (1): 11–15.

5 Gélinas, S., Paré-Labrosse, O., Brosseau, C.-N. et al. (2011). The binding energy of charge-transfer excitons localized at polymeric semiconductor heterojunctions. *J. Phys. Chem. C* 115 (14): 7114–7119.

6 Wannier, G.H. (1937). The structure of electronic excitation levels in insulating crystals. *Phys. Rev.* 52 (3): 191–197.

7 Bartesaghi, D., del Carmen Pérez, I., Kniepert, J. et al. (2015). Competition between recombination and extraction of free charges determines the fill factor of organic solar cells. *Nat. Commun.* 6 (1): 7083.

8 Brédas, J.-L., Norton, J.E., Cornil, J., and Coropceanu, V. (2009). Molecular understanding of organic solar cells: the challenges. *Acc. Chem. Res.* 42 (11): 1691–1699.

9 Scharber, M.C., Mühlbacher, D., Koppe, M. et al. (2006). Design rules for donors in bulk-heterojunction solar cells – towards 10 % energy-conversion efficiency. *Adv. Mater.* 18 (6): 789–794.

10 Brédas, J.-L., Beljonne, D., Coropceanu, V., and Cornil, J. (2004). Charge-transfer and energy-transfer processes in π-conjugated oligomers and polymers: a molecular picture. *Chem. Rev.* 104 (11): 4971–5004.

11 Vandewal, K., Albrecht, S., Hoke, E.T. et al. (2013). Efficient charge generation by relaxed charge-transfer states at organic interfaces. *Nat. Mater.* 13: 63–68.

12 Barker, J.A., Ramsdale, C.M., and Greenham, N.C. (2003). Modeling the current-voltage characteristics of bilayer polymer photovoltaic devices. *Phys. Rev. B* 67 (7): 075205.

13 Fichou, D. (2000). Structural order in conjugated oligothiophenes and its implications on opto-electronic devices. *J. Mater. Chem.* 10 (3): 571–588.

14 Kuik, M., Koster, L.J.A., Wetzelaer, G.A.H., and Blom, P.W.M. (2011). Trap-assisted recombination in disordered organic semiconductors. *Phys. Rev. Lett.* 107 (25): 256805.

15 Weinberger, B.R., Akhtar, M., and Gau, S.C. (1982). Polyacetylene photovoltaic devices. *Synth. Met.* 4 (3): 187–197.

16 Akama, T., Okita, W., Nagai, R. et al. (2017). Schottky solar cell using few-layered transition metal dichalcogenides toward large-scale fabrication of semitransparent and flexible power generator. *Sci. Rep.* 7 (1): 11967.

17 Glenis, S., Horowitz, G., Tourillon, G., and Garnier, F. (1984). Electrochemically grown polythiophene and poly(3-methylthiophene) organic photovoltaic cells. *Thin Solid Films* 111 (2): 93–103.

18 Glenis, S., Tourillon, G., and Garnier, F. (1986). Influence of the doping on the photovoltaic properties of thin films of poly-3-methylthiophene. *Thin Solid Films* 139 (3): 221–231.

19 Hosokai, T., Aoyama, T., Kobayashi, T. et al. (2010). Photovoltaic properties of bisazomethine dye thin films. *Chem. Phys. Lett.* 487 (1–3): 77–80.

20 Gustafsson, G., Inganäs, O., Sundberg, M., and Svensson, C. (1991). Rectifying metal/poly(3-hexylthiophene) contacts. *Synth. Met.* 41 (1–2): 499–502.

21 Bernardi, M., Palummo, M., and Grossman, J.C. (2013). Extraordinary sunlight absorption and one nanometer thick photovoltaics using two-dimensional monolayer materials. *Nano Lett.* 13 (8): 3664–3670.

22 Tang, C.W. (1986). Two-layer organic photovoltaic cell. *Appl. Phys. Lett.* 48 (2): 183.

23 Sariciftci, N.S., Smilowitz, L., Heeger, A.J., and Wudl, F. (1992). Photoinduced electron transfer from a conducting polymer to buckminsterfullerene. *Science* 258 (5087): 1474–1476.

24 Sariciftci, N.S., Braun, D., Zhang, C. et al. (1993). Semiconducting polymer-buckminsterfullerene heterojunctions: diodes, photodiodes, and photovoltaic cells. *Appl. Phys. Lett.* 62 (6): 585–587.

25 Morita, S., Zakhidov, A.A., and Yoshino, K. (1993). Wavelength dependence of junction characteristics of poly(3-alkylthiophene)/C_{60} layer. *Jpn. J. Appl. Phys.* 32: L873–L874.

26 Hummelen, J.C., Knight, B.W., Lepeq, F. et al. (1995). Preparation and characterization of fulleroid and methanofullerene derivatives. *J. Org. Chem.* 60 (3): 532–538.

27 Wang, Z., Hong, Z., Zhuang, T. et al. (2015). High fill factor and thermal stability of bilayer organic photovoltaic cells with an inverted structure. *Appl. Phys. Lett.* 106 (5): 053305.

28 Kodali, H.K. and Ganapathysubramanian, B. (2013). Sensitivity analysis of current generation in organic solar cells – comparing bilayer, sawtooth, and bulk heterojunction morphologies. *Sol. Energy Mater. Sol. Cells* 111: 66–73.

29 Yu, G., Gao, J., Hummelen, J.C. et al. (1995). Polymer photovoltaic cells: enhanced efficiencies via a network of internal donor-acceptor heterojunctions. *Science* 270 (5243): 1789.

30 Mayer, A.C., Scully, S.R., Hardin, B.E. et al. (2007). Polymer-based solar cells. *Mater. Today* 10 (11): 28–33.

31 He, Y. and Li, Y. (2011). Fullerene derivative acceptors for high performance polymer solar cells. *Phys. Chem. Chem. Phys.* 13 (6): 1970–1983.

32 Koster, L.J.A., Shaheen, S.E., and Hummelen, J.C. (2012). Pathways to a new efficiency regime for organic solar cells. *Adv. Energy Mater.* 2 (10): 1246–1253.

33 Forrest, S.R. (2004). The path to ubiquitous and low-cost organic electronic appliances on plastic. *Nature* 428 (6986): 911–918.

34 Ohta, T. and Kawasaki, K. (1986). Equilibrium morphology of block copolymer melts. *Macromolecules* 19 (10): 2621–2632.

35 Bates, F. (1990). Block copolymer thermodynamics: theory and experiment. *Annu. Rev. Phys. Chem.* 41: 525–557.

36 Amundson, K., Helfand, E., Davis, D.D. et al. (1991). Effect of an electric field on block copolymer microstructure. *Macromolecules* 24 (24): 6546–6548.

37 Jeon, H.U., Jin, H.M., Kim, J.Y. et al. (2017). Electric field directed self-assembly of block copolymers for rapid formation of large-area complex nanopatterns. *Mol. Syst. Des. Eng.* 2: 560–566.

38 Thurn-Albrecht, T., Schotter, J., Kastle, G.A. et al. (2000). Ultrahigh-density nanowire arrays grown in self-assembled diblock copolymer templates. *Science* 290 (5499): 2126–2129.

39 Fredrickson, G.H. (1994). Steady shear alignment of block copolymers near the isotropic–lamellar transition. *J. Rheol. (N.Y.)* 38 (4): 1045.

40 Winey, K.I., Patel, S.S., Larson, R.G., and Watanabe, H. (1993). Interdependence of shear deformations and block copolymer morphology. *Macromolecules* 26 (10): 2542–2549.

41 Patel, S.S., Larson, R.G., Winey, K.I., and Watanabe, H. (1995). Shear orientation and rheology of a lamellar polystyrene–polyisoprene block copolymer. *Macromolecules* 28 (12): 4313–4318.

42 Thomas, E.L., Alward, D.B., Kinning, D.J. et al. (1986). Ordered bicontinuous double-diamond structure of star block copolymers: a new equilibrium microdomain morphology. *Macromolecules* 19 (8): 2197–2202.

43 Ulrich, R., Du Chesne, A., Templin, M., and Wiesner, U. (1999). Nano-objects with controlled shape, size, and composition from block copolymer mesophases. *Adv. Mater.* 11 (2): 141–146.

44 Zhao, D., Feng, J., Huo, Q. et al. (1998). Triblock copolymer syntheses of mesoporous silica with periodic 50 to 300 angstrom pores. *Science* 279 (5350): 548–552.

45 Mitchell, V.D. and Jones, D.J. (2018). Advances toward the effective use of block copolymers as organic photovoltaic active layers. *Polym. Chem.* 9: 795–814.

46 Goubard, F. and Wantz, G. (2014). Ternary blends for polymer bulk heterojunction solar cells. *Polym. Int.* 63 (8): 1362–1367.

47 Onses, M.S., Song, C., Williamson, L. et al. (2013). Hierarchical patterns of three-dimensional block-copolymer films formed by electrohydrodynamic jet printing and self-assembly. *Nat. Nanotechnol.* 8: 667–675.

48 Ross, C.A., Berggren, K.K., Cheng, J.Y. et al. (2014). Three-dimensional nanofabrication by block copolymer self-assembly. *Adv. Mater.* 25 (26): 4386–4396.

49 KG, A.T., Gotrik, K.W., Hannon, A.F. et al. (2012). Templating three-dimensional self-assembled structures in bilayer block copolymer films. *Science* 336 (6086): 1294–1298.

50 Jin, S.H., Kim, D.H., Jun, G.H. et al. (2013). Tuning the photoluminescence of graphene quantum dots through the charge transfer effect of functional groups. *ACS Nano* 7 (2): 1239–1245.

51 He, Z., Zhong, C., Su, S. et al. (2012). Enhanced power-conversion efficiency in polymer solar cells using an inverted device structure. *Nat. Photonics* 6: 591–595.

52 Huang, K.T., Shih, C.C., Liu, H.Y. et al. (2018). Alcohol-soluble cross-linked poly(nBA)$_n$-*b*-poly(NVTri)$_m$ block copolymer and its applications in organic photovoltaic cells for improved stability. *ACS Appl. Mater. Interfaces* 10 (51): 44741–44750.

53 Osaka, I. and Mccullough, R.D. (2008). Advances in molecular design and synthesis of regioregular polythiophenes. *Acc. Chem. Res.* 41 (9): 1202–1214.

54 Boudouris, B.W., Frisbie, C.D., and Hillmyer, M.A. (2008). Nanoporous poly(3-alkylthiophene) thin films generated from block copolymer templates. *Macromolecules* 41 (1): 67–75.

55 Boudouris, B.W., Molins, F., Blank, D.A. et al. (2009). Synthesis, optical properties, and microstructure of a fullerene-terminated poly(3-hexylthiophene). *Macromolecules* 42 (12): 4118–4126.

56 Ohshimizu, K. and Ueda, M. (2008). Well-controlled synthesis of block copolythiophenes. *Macromolecules* 41 (14): 5289–5294.

57 Miyakoshi, R., Yokoyama, A., and Yokozawa, T. (2005). Catalyst-transfer polycondensation. Mechanism of Ni-catalyzed chain-growth polymerization leading to well-defined poly(3-hexylthiophene). *J. Am. Chem. Soc.* 127 (49): 17542–17547.

58 Iovu, M.C., Sheina, E.E., Gil, R.R., and McCullough, R.D. (2005). Experimental evidence for the quasi-"living" nature of the Grignard metathesis method for the synthesis of regioregular poly(S-alkylthiophenes). *Macromolecules* 38 (21): 8649–8656.

59 Loewe, R.S., Khersonsky, S.M., and McCullough, R.D. (1999). A simple method to prepare head-to-tail coupled, regioregular poly(3-alkylthiophenes) using Grignard metathesis. *Adv. Mater.* 11 (3): 250–252.

60 Loewe, R.S., Ewbank, P.C., Liu, J. et al. (2001). Regioregular, head-to-tail coupled poly(3-alkylthiophenes) made easy by the GRIM method: investigation of the reaction and the origin of regioselectivity. *Macromolecules* 34 (13): 4324–4333.

61 Zhang, Y., Tajima, K., and Hashimoto, K. (2009). Nanostructure formation in poly(3-hexylthiophene-*block*-3-(2-ethylhexyl)thiophene)s. *Macromolecules* 42 (18): 7008–7015.

62 Wu, P.-T., Ren, G., Kim, F.S. et al. (2010). Poly(3-hexylthiophene)-*b*-poly(3-cyclohexylthiophene): synthesis, microphase separation, thin film transistors, and photovoltaic applications. *J. Polym. Sci., Part A: Polym. Chem.* 48 (3): 614–626.

63 Higashihara, T. and Ueda, M. (2009). Living anionic polymerization of 4-vinyltriphenylamine for synthesis of novel block copolymers containing low-polydisperse poly(4-vinyltriphenylamine) and regioregular poly(3-hexylthiophene) segments. *Macromolecules* 42 (22): 8794–8800.

64 Robb, M.J., Ku, S.-Y., and Hawker, C.J. (2013). 25th anniversary article: no assembly required: recent advances in fully conjugated block copolymers. *Adv. Mater.* 25 (40): 5686–5700.

65 Wang, J. and Higashihara, T. (2013). Synthesis of all-conjugated donor-acceptor block copolymers and their application in all-polymer solar cells. *Polym. Chem.* 4: 5518–5526.

66 Scherf, U., Gutacker, A., and Koenen, N. (2008). All-conjugated block copolymers. *Acc. Chem. Res.* 41 (9): 1086–1097.

67 Yassar, A., Miozzo, L., Gironda, R., and Horowitz, G. (2013). Rod-coil and all-conjugated block copolymers for photovoltaic applications. *Prog. Polym. Sci.* 38 (5): 791–844.

68 Guo, X., Baumgarten, M., and Müllen, K. (2013). Designing π-conjugated polymers for organic electronics. *Prog. Polym. Sci.* 38 (12): 1832–1908.

69 Mitchell, V.D., Gann, E., Huettner, S. et al. (2017). Morphological and device evaluation of an amphiphilic block copolymer for organic photovoltaic applications. *Macromolecules* 50 (13): 4942–4951.

70 Guo, C., Lin, Y.-H., Witman, M.D. et al. (2013). Conjugated block copolymer photovoltaics with near 3% efficiency through microphase separation. *Nano Lett.* 13 (6): 2957–2963.

71 Rahmanudin, A., Yao, L., Sekar, A. et al. (2019). Fully conjugated donor–acceptor block copolymers for organic photovoltaics via heck–Mizoroki coupling. *ACS Macro Lett.* 8 (2): 134–139.

72 Park, C.G., Park, S.H., Kim, Y. et al. (2019). Facile one-pot polymerization of a fully conjugated donor-acceptor block copolymer and its application in efficient single component polymer solar cells. *J. Mater. Chem. A* 7: 21280–21289.

73 Tatum, W.K. and Luscombe, C.K. (2018). π-Conjugated polymer nanowires: advances and perspectives toward effective commercial implementation. *Polym. J.* 50 (8): 659–669.

74 Mazzio, K.A., Rice, A.H., Durban, M.M., and Luscombe, C.K. (2015). Effect of regioregularity on charge transport and structural and excitonic coherence in poly(3-hexylthiophene) nanowires. *J. Phys. Chem. C* 119 (27): 14911–14918.

75 Lu, G., Chen, J., Xu, W. et al. (2014). Aligned polythiophene and its blend film by direct-writing for anisotropic charge transport. *Adv. Funct. Mater.* 24 (31): 4959–4968.

76 Chang, M., Su, Z., and Egap, E. (2016). Alignment and charge transport of one-dimensional conjugated polymer nanowires in insulating polymer blends. *Macromolecules* 49 (24): 9449–9456.

77 Ihn, K.J., Moulton, J., and Smith, P. (1993). Whiskers of poly(3-alkylthiophene)s. *J. Polym. Sci., Part B: Polym. Phys.* 31 (6): 735–742.

78 Mårdalen, J., Samuelsen, E.J., and Pedersen, A. (1993). The nucleation process and the crystalline structure of poly(3-alkylthiophenes) precipitated from marginal solvents. *Synth. Met.* 55 (1): 378–383.

79 Liu, J., Arif, M., Zou, J. et al. (2009). Controlling poly(3-hexylthiophene) crystal dimension: nanowhiskers and nanoribbons. *Macromolecules* 42 (24): 9390–9393.

80 Spano, F.C. and Silva, C. (2014). H- and J-aggregate behavior in polymeric semiconductors. *Annu. Rev. Phys. Chem.* 65 (1): 477–500.

81 Kleinhenz, N., Rosu, C., Chatterjee, S. et al. (2015). Liquid crystalline poly(3-hexylthiophene) solutions revisited: role of time-dependent self-assembly. *Chem. Mater.* 27 (7): 2687–2694.

82 Kim, D.H., Park, Y.D., Jang, Y. et al. (2005). Solvent vapor-induced nanowire formation in poly(3-hexylthiophene) thin films. *Macromol. Rapid Commun.* 26 (10): 834–839.

83 Xin, H., Reid, O.G., Ren, G. et al. (2010). Polymer nanowire/fullerene bulk heterojunction solar cells: how nanostructure determines photovoltaic properties. *ACS Nano* 4 (4): 1861–1872.

84 Rice, A.H., Giridharagopal, R., Zheng, S.X. et al. (2011). Controlling vertical morphology within the active layer of organic photovoltaics using poly(3-hexylthiophene) nanowires and phenyl-C_{61}-butyric acid methyl ester. *ACS Nano* 5 (4): 3132–3140.

85 Kim, J.-H., Kim, M., Jinnai, H. et al. (2014). Organic solar cells based on three-dimensionally percolated polythiophene nanowires with enhanced charge transport. *ACS Appl. Mater. Interfaces* 6 (8): 5640–5650.

86 Yan, H., Hollinger, J., Bridges, C.R. et al. (2014). Doping poly(3-hexylthiophene) nanowires with selenophene increases the performance of polymer-nanowire solar cells. *Chem. Mater.* 26 (15): 4605–4611.

87 Lee, J., Sin, D.H., Moon, B. et al. (2017). Highly crystalline low-bandgap polymer nanowires towards high-performance thick-film organic solar cells exceeding 10% power conversion efficiency. *Energy Environ. Sci.* 10 (1): 247–257.

88 Landfester, K., Montenegro, R., Scherf, U. et al. (2002). Semiconducting polymer nanospheres in aqueous dispersion prepared by a miniemulsion process. *Adv. Mater.* 14 (9): 651–655.

89 Shimizu, H., Yamada, M., Wada, R., and Okabe, M. (2008). Preparation and characterization of water self-dispersible poly(3-hexylthiophene) particles. *Polym. J.* 40 (1): 33–36.

90 Millstone, J.E., Kavulak, D.F.J., Woo, C.H. et al. (2010). Synthesis, properties, and electronic applications of size-controlled poly(3-hexylthiophene) nanoparticles. *Langmuir* 26 (16): 13056–13061.

91 Dang, M.T., Hirsch, L., and Wantz, G. (2011). P3HT:PCBM, best seller in polymer photovoltaic research. *Adv. Mater.* 23 (31): 3597–3602.

92 Ulum, S., Holmes, N., Barr, M. et al. (2013). The role of miscibility in polymer: fullerene nanoparticulate organic photovoltaic devices. *Nano Energy* 2 (5): 897–905.

93 Darwis, D., Holmes, N., Elkington, D. et al. (2014). Surfactant-free nanoparticulate organic photovoltaics. *Sol. Energy Mater. Sol. Cells* 121: 99–107.

94 Gärtner, S., Christmann, M., Sankaran, S. et al. (2014). Eco-friendly fabrication of 4% efficient organic solar cells from surfactant-free P3HT:ICBA nanoparticle dispersions. *Adv. Mater.* 26 (38): 6653–6657.

95 Chu, P.H., Kleinhenz, N., Persson, N. et al. (2016). Toward precision control of nanofiber orientation in conjugated polymer thin films: impact on charge transport. *Chem. Mater.* 28 (24): 9099–9109.

96 Niles, E.T., Roehling, J.D., Yamagata, H. et al. (2012). J-aggregate behavior in poly-3-hexylthiophene nanofibers. *J. Phys. Chem. Lett.* 3 (2): 259–263.

97 Nguyen, T.-Q., Wu, J., Doan, V. et al. (2000). Control of energy transfer in oriented conjugated polymer-mesoporous silica composites. *Science* 288 (5466): 652–656.

98 Ding, B., Wang, M., Wang, X. et al. (2010). Electrospun nanomaterials for ultrasensitive sensors. *Mater. Today* 13 (11): 16–27.

99 Jo, S.B., Lee, W.H., Qiu, L., and Cho, K. (2012). Polymer blends with semiconducting nanowires for organic electronics. *J. Mater. Chem.* 22 (10): 4244–4260.

100 Li, W.J., Laurencin, C.T., Caterson, E.J. et al. (2002). Electrospun nanofibrous structure: a novel scaffold for tissue engineering. *J. Biomed. Mater. Res.* 60 (4): 613–621.

101 Wu, S., Tai, Q., and Yan, F. (2010). Hybrid photovoltaic devices based on poly(3-hexylthiophene) and ordered electrospun ZnO nanofibers. *J. Phys. Chem. C* 114 (13): 6197–6200.

102 Cho, H., Min, S.-Y., and Lee, T.-W. (2013). Electrospun organic nanofiber electronics and photonics. *Macromol. Mater. Eng.* 298 (5): 475–486.

103 Teo, W.E. and Ramakrishna, S. (2006). A review on electrospinning design and nanofibre assemblies. *Nanotechnology* 17 (14): R89–R106.

104 Greiner, A. and Wendorff, J.H. (2007). Electrospinning: a fascinating method for the preparation of ultrathin fibers. *Angew. Chem. Int. Ed.* 46 (30): 5670–5703.

105 Li, D. and Xia, Y. (2004). Electrospinning of nanofibers: reinventing the wheel? *Adv. Mater.* 16 (14): 1151–1170.

106 Sundarrajan, S., Murugan, R., Nair, A.S., and Ramakrishna, S. (2010). Fabrication of P3HT/PCBM solar cloth by electrospinning technique. *Mater. Lett.* 64 (21): 2369–2372.

107 Bedford, N.M., Dickerson, M.B., Drummy, L.F. et al. (2012). Nanofiber-based bulk-heterojunction organic solar cells using coaxial electrospinning. *Adv. Energy Mater.* 2 (9): 1136–1144.

108 D'Arcy, J.M., Tran, H.D., Tung, V.C. et al. (2010). Versatile solution for growing thin films of conducting polymers. *Proc. Natl. Acad. Sci. U.S.A.* 107 (46): 19673–19678.

109 Vandewal, K., Oosterbaan, W.D., Bertho, S. et al. (2009). Varying polymer crystallinity in nanofiber poly(3-alkylthiophene): PCBM solar cells: influence on charge-transfer state energy and open-circuit voltage. *Appl. Phys. Lett.* 95 (12): 123303.

110 Oosterbaan, W.D., Vrindts, V., Berson, S. et al. (2009). Efficient formation, isolation and characterization of poly(3-alkylthiophene) nanofibres: probing order as a function of side-chain length. *J. Mater. Chem.* 19 (30): 5424–5435.

111 Bertho, S., Oosterbaan, W.D., Vrindts, V. et al. (2009). Controlling the morphology of nanofiber-P3HT:PCBM blends for organic bulk heterojunction solar cells. *Org. Electron.* 10 (7): 1248–1251.

112 Sun, S., Salim, T., Wong, L.H. et al. (2011). A new insight into controlling poly(3-hexylthiophene) nanofiber growth through a mixed-solvent approach for organic photovoltaics applications. *J. Mater. Chem.* 21 (2): 377–386.

113 Li, L., Jacobs, D.L., Che, Y. et al. (2013). Poly(3-hexylthiophene) nanofiber networks for enhancing the morphology stability of polymer solar cells. *Org. Electron.* 14 (5): 1383–1390.

114 Li, F., Yager, K.G., Dawson, N.M. et al. (2014). Stable and controllable polymer/fullerene composite nanofibers through cooperative noncovalent interactions for organic photovoltaics. *Chem. Mater.* 26 (12): 3747–3756.

115 Solanki, A., Wu, B., Salim, T. et al. (2014). Performance improvements in polymer nanofiber/fullerene solar cells with external electric field treatment. *J. Phys. Chem. C* 118 (21): 11285–11291.

116 Xie, L., Lee, J.S., Jang, Y. et al. (2016). Organic photovoltaics utilizing a polymer nanofiber/fullerene interdigitated bilayer prepared by sequential solution deposition. *J. Phys. Chem. C* 120 (24): 12933–12940.

117 Roncali, J. and Grosu, I. (2019). The dawn of single material organic solar cells. *Adv. Sci.* 6 (1): 1801026.

118 Pierini, F., Lanzi, M., Nakielski, P. et al. (2017). Single-material organic solar cells based on electrospun fullerene-grafted polythiophene nanofibers. *Macromolecules* 50 (13): 4972–4981.

119 Cui, Y., Yao, H., Zhang, J. et al. (2019). Over 16% efficiency organic photovoltaic cells enabled by a chlorinated acceptor with increased open-circuit voltages. *Nat. Commun.* 10 (1): 1–8.

120 Zhang, Y., Samuel, I.D.W., Wang, T., and Lidzey, D.G. (2018). Current status of outdoor lifetime testing of organic photovoltaics. *Adv. Sci.* 5 (8): 1800434.

121 Zhang, S., Ye, L., Zhang, H., and Hou, J. (2016). Green-solvent-processable organic solar cells. *Mater. Today* 19 (9): 533–543.

122 MacEdo, A.G., Silva, D.C., Yamamoto, N.A.D. et al. (2013). Bilayer and bulk heterojunction solar cells with functional poly(2,2′-bithiophene) films electrochemically deposited from aqueous emulsion. *Synth. Met.* 170 (1): 63–68.

123 Blom, P.W.M., Mihailetchi, V.D., Koster, L.J.A., and Markov, D.E. (2007). Device physics of polymer: fullerene bulk heterojunction solar cells. *Adv. Mater.* 19 (12): 1551–1566.

124 Po, R., Carbonera, C., Bernardi, A., and Camaioni, N. (2011). The role of buffer layers in polymer solar cells. *Energy Environ. Sci.* 4 (2): 285–310.

125 Caricato, A.P., Cesaria, M., Gigli, G. et al. (2012). Poly-(3-hexylthiophene)/[6,6]-phenyl-C_{61}-butyric-acid-methyl-ester bilayer deposition by matrix-assisted pulsed laser evaporation for organic photovoltaic applications. *Appl. Phys. Lett.* 100 (7): 073306.

126 Ge, W., Li, N.K., McCormick, R.D. et al. (2016). Emulsion-based RIR-MAPLE deposition of conjugated polymers: primary solvent effect and its implications on organic solar cell performance. *ACS Appl. Mater. Interfaces* 8 (30): 19494–19506.

127 Pate, R. and Stiff-Roberts, A.D. (2009). The impact of laser-target absorption depth on the surface and internal morphology of matrix-assisted pulsed laser evaporated conjugated polymer thin films. *Chem. Phys. Lett.* 477 (4–6): 406–410.

128 Pate, R., McCormick, R., Chen, L. et al. (2011). RIR-MAPLE deposition of conjugated polymers for application to optoelectronic devices. *Appl. Phys. A: Mater. Sci. Process.* 105 (3): 555–563.

129 McCormick, R.D., Lenhardt, J., and Stiff-Roberts, A.D. (2012). Effects of emulsion-based resonant infrared matrix assisted pulsed laser evaporation (RIR-MAPLE) on the molecular weight of polymers. *Polymers (Basel)* 4 (1): 341–354.

130 Ekrt, O., Vyslouzil, F., Kopecky, D. et al. (2006). Thin organic layers prepared by MAPLE for gas sensor application. *Conference on Optoelectronic and Microelectronic Materials and Devices. Proceedings COMMAD*, Volume 495, pp. 268–271.

131 Kim, J.Y., Kim, S.H., Lee, H.H. et al. (2006). New architecture for high-efficiency polymer photovoltaic cells using solution-based titanium oxide as an optical spacer. *Adv. Mater.* 18 (5): 572–576.

132 Landfester, K., Bechthold, N., Förster, S., and Antonietti, M. (1999). Evidence for the preservation of the particle identity in miniemulsion polymerization. *Macromol. Rapid Commun.* 20 (2): 81–84.

133 Landfester, K. (2001). Polyreactions in miniemulsions. *Macromol. Rapid Commun.* 22 (12): 896–936.

134 Kietzke, T., Neher, D., Kumke, M. et al. (2004). A nanoparticle approach to control the phase separation in polyfluorene photovoltaic devices. *Macromolecules* 37 (13): 4882–4890.

135 Zhao, Y., Lévesque, J., Roberge, P.C., and Prud'homme, R.E. (1989). A study of polymer blends by nonradiative energy transfer fluorescence spectroscopy. *J. Polym. Sci., Part B: Polym. Phys.* 27 (10): 1955–1970.

136 Tomba, J.P., Ye, X., Li, F. et al. (2008). Polymer blend latex films: miscibility and polymer diffusion studied by energy transfer. *Polymer (Guildf.)* 49 (8): 2055–2064.

137 Donley, C.L., Zaumseil, J., Andreasen, J.W. et al. (2005). Effects of packing structure on the optoelectronic and charge transport properties in poly(9,9-di-n-octylfluorene-alt-benzothiadiazole). *J. Am. Chem. Soc.* 127 (37): 12890–12899.

138 Halls, J.J.M., Arias, A.C., MacKenzie, J.D. et al. (2000). Photodiodes based on polyfluorene composites: influence of morphology. *Adv. Mater.* 12 (7): 498–502.

139 Arias, A.C., MacKenzie, J.D., Stevenson, R. et al. (2001). Photovoltaic performance and morphology of polyfluorene blends: a combined microscopic and photovoltaic investigation. *Macromolecules* 34 (17): 6005–6013.

140 Kietzke, T., Stiller, B., Landfester, K. et al. (2005). Probing the local optical properties of layers prepared from polymer nanoparticles. *Synth. Met.* 152 (1–3): 101–104.

141 Holmes, N.P., Nicolaidis, N., Feron, K. et al. (2015). Probing the origin of photocurrent in nanoparticulate organic photovoltaics. *Sol. Energy Mater. Sol. Cells* 140: 412–421.

142 Dam, H.F., Holmes, N.P., Andersen, T.R. et al. (2015). The effect of mesomorphology upon the performance of nanoparticulate organic photovoltaic devices. *Sol. Energy Mater. Sol. Cells* 138: 102–108.

143 Holmes, N.P., Marks, M., Kumar, P. et al. (2016). Nano-pathways: bridging the divide between water-processable nanoparticulate and bulk heterojunction organic photovoltaics. *Nano Energy* 19: 495–510.

144 D'Olieslaeger, L., Pfannmöller, M., Fron, E. et al. (2017). Tuning of PCDTBT:PC71BM blend nanoparticles for eco-friendly processing of polymer solar cells. *Sol. Energy Mater. Sol. Cells* 159: 179–188.

145 D'Olieslaeger, L., Pirotte, G., Cardinaletti, I. et al. (2017). Eco-friendly fabrication of PBDTTPD:PC71BM solar cells reaching a PCE of 3.8% using water-based nanoparticle dispersions. *Org. Electron.* 42: 42–46.

146 Darwis, D., Holmes, N., Elkington, D. et al. (2014). Solar energy materials & solar cells surfactant-free nanoparticulate organic photovoltaics. *Sol. Energy Mater. Sol. Cells* 121: 99–107.

147 Colberts, F.J.M., Wienk, M.M., and Janssen, R.A.J. (2017). Aqueous nanoparticle polymer solar cells: effects of surfactant concentration and processing on device performance. *ACS Appl. Mater. Interfaces* 9 (15): 13380–13389.

148 Xie, C., Classen, A., Späth, A. et al. (2018). Overcoming microstructural limitations in water processed organic solar cells by engineering customized nanoparticulate inks. *Adv. Energy Mater.* 8 (13): 1–10.

149 Subianto, S., Balu, R., De Campo, L. et al. (2018). Sulfonated thiophene derivative stabilized aqueous poly(3-hexylthiophene):phenyl-C_{61}-butyric acid methyl ester nanoparticle dispersion for organic solar cell applications. *ACS Appl. Mater. Interfaces* 10 (50): 44116–44125.

150 Sager, C. (2007). Microemulsion templating. In: *Nanostructured Soft Matter: Experiments, Theory, Simulation and Perspectives* (ed. V. Zvelindovsky), 3–44.

151 Chew, C.H., Gan, L.M., Ong, L.H. et al. (1997). Bicontinuous structures of polymerized microemulsions: ^{1}H NMR self-diffusion and conductivity studies. *Langmuir* 13 (11): 2917–2921.

152 Bourcier, S., Vancaeyzeele, C., Vidal, F., and Fichet, O. (2013). Microemulsion as the template for synthesis of interpenetrating polymer networks with predefined structure. *Polymer* 54 (17): 4436–4445.

153 Noirjean, C., Vancaeyzeele, C., Bourcier, S. et al. (2016). Nanostructure changes upon polymerization of aqueous and organic phases in organized mixtures. *Langmuir* 32 (39): 10104–10112.

154 Liu, J., Teo, W.K., Chew, C.H., and Gan, L.M. (2000). Nanofiltration membranes prepared by direct microemulsion copolymerization using poly(ethylene oxide) macromonomer as a polymerizable surfactant. *J. Appl. Polym. Sci.* 77 (12): 2785–2794.

155 Vancaeyzeele, C., Olivier, F., Petroffe, G. et al. (2017). Nanostructured thermal responsive materials synthesized by soft templating. *ACS Appl. Mater. Interfaces* 9 (14): 12706–12718.

156 Bombonnel, C., Vancaeyzeele, C., Guérin, G., and Vidal, F. (2020). Fabrication of bicontinuous double networks as thermal and pH stimuli responsive drug carriers for on-demand release. *Mater. Sci. Eng., C* 109: 110495.

157 Kipp, D., Wodo, O., Ganapathysubramanian, B., and Ganesan, V. (2015). Achieving bicontinuous microemulsion like morphologies in organic photovoltaics. *ACS Macro Lett.* 4 (2): 266–270.

158 Kipp, D., Verduzco, R., and Ganesan, V. (2016). Design of bicontinuous donor/acceptor morphologies for use as organic solar cell active layers. *J. Polym. Sci. Part B: Polym. Phys.* 54 (9): 884–895.

159 Kipp, D. and Ganesan, V. (2016). Exploiting the combined influence of morphology and energy cascades in ternary blend organic solar cells based on block copolymer additives. *Macromolecules* 49 (14): 5137–5144.

160 Kipp, D., Wodo, O., Ganapathysubramanian, B., and Ganesan, V. (2017). Utilizing morphological correlators for device performance to optimize ternary blend organic solar cells based on block copolymer additives. *Sol. Energy Mater. Sol. Cells* 161: 206–218.

161 Kipp, D., Mok, J., Strzalka, J. et al. (2015). Rational design of thermally stable, bicontinuous donor/acceptor morphologies with conjugated block copolymer additives. *ACS Macro Lett.* 4 (9): 867–871.

162 Kim, S.S., Jo, J., Chun, C. et al. (2007). Hybrid solar cells with ordered TiO_2 nanostructures and MEH-PPV. *J. Photochem. Photobiol., A* 188: 364–370.

163 Tang, C.W. and VanSlyke, S.A. (1987). Organic electroluminescent diodes. *Appl. Phys. Lett.* 51: 913–915.

164 Slota, J.E., He, X., and Huck, W.T.S. (2010). Controlling nanoscale morphology in polymer photovoltaic devices. *Nano Today* 5: 231–242.

165 He, X., Gao, F., Tu, G. et al. (2011). Formation of well-ordered heterojunctions in polymer:PCBM photovoltaic devices. *Adv. Funct. Mater.* 21: 139–146.

166 Coakley, K.M., Liu, Y., McGehee, M.D. et al. (2003). Infiltrating semiconducting polymers into self-assembled mesoporous titania films for photovoltaic applications. *Adv. Funct. Mater.* 13: 301–306.

167 Coakley, K.M. and McGehee, M.D. (2003). Photovoltaic cells made from conjugated polymers infiltrated into mesoporous titania. *Appl. Phys. Lett.* 83: 3380–3382.

168 Oey, C.C., Djurišić, A.B., Wang, H. et al. (2006). Polymer-TiO_2 solar cells: TiO_2 interconnected network for improved cell performance. *Nanotechnology* 17: 706–713.

169 Wang, H., Oey, C.C., Djurišić, A.B. et al. (2005). Titania bicontinuous network structures for solar cell applications. *Appl. Phys. Lett.* 87: 023507.

170 Nicolas, M. (2008). Fabrication of superhydrophobic surfaces by electropolymerization of thiophene and pyrrole derivatives. *J. Adhes. Sci. Technol.* 22: 365–377.

171 McCullough, R.D. (1998). The chemistry of conducting polythiophenes. *Adv. Mater.* 10: 93–116.

172 Andersson, M.R., Thomas, O., Mammo, W. et al. (1999). Substituted polythiophenes designed for optoelectronic devices and conductors. *J. Mater. Chem.* 9: 1933–1940.

173 Li, G., Shrotriya, V., Huang, J. et al. (2005). High-efficiency solution processable polymer photovoltaic cells by self-organization of polymer blends. *Nat. Mater.* 4: 864–868.

174 Tyler McQuade, D., Pullen, A.E., and Swager, T.M. (2000). Conjugated polymer-based chemical sensors. *Chem. Rev.* 100: 2537–2574.

175 Lee, T.Y. and Shim, Y.B. (2001). Direct DNA hybridization detection based on the oligonucleotide-functionalized conductive polymer. *Anal. Chem.* 73: 5629–5632.

176 Seol, H., Kang, D.M., Shin, S.C., and Shim, Y.-B. (2006). Electrochemical synthesis and characterization of poly[3′-(4-formyl-3-hydroxyphenyl)-5,2′:5′,2″-terthiophene] film. *Synth. Met.* 156 (1): 65–69.

177 Yoon, J.H., Kim, D.M., Yoon, S.S. et al. (2011). Comparison of solar cell performance of conducting polymer dyes with different functional groups. *J. Power Sources* 196 (20): 8874–8880.

178 Koh, W.C.A., Chandra, P., Kim, D.M., and Shim, Y.B. (2011). Electropolymerized self-assembled layer on gold nanoparticles: detection of inducible nitric oxide synthase in neuronal cell culture. *Anal. Chem.* 83: 6177–6183.

179 Kim, D.M., Yoon, J.H., Won, M.S., and Shim, Y.B. (2012). Electrochemical characterization of newly synthesized polyterthiophene benzoate and its applications to an electrochromic device and a photovoltaic cell. *Electrochim. Acta* 67: 201–207.

180 Vélez, J.H., Díaz, F.R., Del Valle, M.A. et al. (2008). Synthesis of 3′,4′-disubstituted terthiophenes – characterization and electropolymerization. II. S′-bromo-4′-thienyl- 2,2′:5′,2′-terthiophene and 3′,4′-diphenyl-2, 2′:5′,2′-terthiophene in photovoltaic displays. *J. Appl. Polym. Sci.* 109: 1722–1729.

181 Vélez, J.H., Díaz, F., Del Valle, M.A. et al. (2006). Synthesis of 3′,4′-disubstituted terthiophenes. Characterization and electropolymerization. I. 3′,4′-dibromo-2, 2′;5′,2″-terthiophene in photovoltaic display. *J. Appl. Polym. Sci.* 102: 5314–5321.

182 Nasybulin, E., Feinstein, J., Cox, M. et al. (2011). Electrochemically prepared polymer solar cell by three-layer deposition of poly(3,4-ethylenedioxythiophene)/poly(2,2′-bithiophene)/fullerene (PEDOT/PBT/C_{60}). *Polymer (Guildf.)* 52: 3627–3632.

183 Waltman, R.J., Bargon, J., and Diaz, A.F. (1983). Electrochemical studies of some conducting polythiophene films. *J. Phys. Chem.* 87 (8): 1459–1463.

184 Fan, B., Wang, P., Wang, L., and Shi, G. (2006). Polythiophene/fullerene bulk heterojunction solar cell fabricated via electrochemical co-deposition. *Sol. Energy Mater. Sol. Cells* 90 (20): 3547–3556.

185 Fedurco, M., Costa, D.A., Balch, A.L., and Fawcett, W.R. (1995). Electrochemical synthesis of a redox-active polymer based on buckminsterfullerene epoxide. *Angew. Chem. Int. Ed. Engl.* 34: 194–196.

186 Krinichnaya, E.P., Moravsky, A.P., Efimov, O. et al. (2005). Mechanistic studies of the electrochemical polymerization of C_{60} in the presence of dioxygen or $C_{60}O$. *J. Mater. Chem.* 15: 1468–1476.

187 Winkler, K., Costa, D.A., Balch, A.L., and Fawcett, W.R. (1995). Study of fullerene epoxide electroreduction and electropolymerization processes. *J. Phys. Chem.* 99: 17431–17436.

188 Ratcliff, E.L., Jenkins, J.L., Nebesny, K., and Armstrong, N.R. (2008). Electrodeposited, “textured” poly(3-hexyl-thiophene) (e-P3HT) films for photovoltaic applications. *Chem. Mater.* 20: 5796–5806.

189 Kim, S.Y., Lee, K.H., Chin, B.D., and Yu, J.W. (2009). Network structure organic photovoltaic devices prepared by electrochemical copolymerization. *Sol. Energy Mater. Sol. Cells* 93: 129–135.

190 Nasybulin, E., Cox, M., Kymissis, I., and Levon, K. (2012). Electrochemical codeposition of poly(thieno[3,2-b]thiophene) and fullerene: an approach to a bulk heterojunction organic photovoltaic device. *Synth. Met.* 162 (1–2): 10–17.

191 Feng, W., Wan, A.S., and Garfunkel, E. (2013). Interfacial bonding and morphological control of electropolymerized polythiophene films on ZnO. *J. Phys. Chem. C* 117: 9852–9863.

192 Nahor, A., Berger, O., Bardavid, Y. et al. (2011). Hybrid structures of porous silicon and conjugated polymers for photovoltaic applications. *Phys. Status Solidi* 8 (6): 1908–1912.

193 Gu, C., Chen, Y., Zhang, Z. et al. (2013). Electrochemical route to fabricate film-like conjugated microporous polymers and application for organic electronics. *Adv. Mater.* 25: 3443–3448.

194 Gu, C., Chen, Y., Zhang, Z. et al. (2014). Achieving high efficiency of PTB7-based polymer solar cells via integrated optimization of both anode and cathode interlayers. *Adv. Energy Mater.* 4: 1301771.

195 Liu, C., Luo, H., Shi, G. et al. (2017). Electrochemical route to fabricate porous organic polymers film and its application for polymer solar cells. *Dyes Pigm.* 142: 132–138.

196 Yang, C.H., Chen, H.L., Chen, C.P. et al. (2009). Electrochemical polymerization effects of triphenylamine-based dye on TiO_2 photoelectrodes in dye-sensitized solar cells. *J. Electroanal. Chem.* 631: 43–51.

Part III

Conjugated Polymer Nanostructures for Energy Storage

10

Conjugated Polymer Nanostructures for Electrochemical Capacitor and Lithium-Ion Battery Applications

Thanh-Hai Le[1] *and Hyeonseok Yoon*[1,2]

[1] Chonnam National University, Graduate School, Department of Polymer Engineering, 77 Yongbong-ro, Gwangju 61186, South Korea
[2] Chonnam National University, School of Polymer Science and Engineering, 77 Yongbong-ro, Gwangju 61186, South Korea

10.1 Introduction

In recent years, renewable energies from solar, hydropower, wind, and geothermal power have brought significant benefits to daily life and have provided solutions to help solve current environmental issues [1, 2]. These clean and safe energies have led global researchers to seek advanced renewable energy storage devices (ESDs). Meanwhile, energy storage through electrochemical means using electrochemical capacitors (ECs) and lithium-ion batteries (LIBs) has been widely studied, and these devices play a significant role in providing power for small portable and other miscellaneous devices in modern society, such as laptops, smartphones, digital cameras, electric vehicles, military field electronics, and sensors. In order to meet the power requirements of advanced electronic devices, the properties of current ESDs should be improved further with regard to energy density, power density, safety, cyclic stability, and cost. Among these aspects, the energy density and power density are critical factors because the improved electronic devices require fast charging, high power supply, and high energy for their long-time performance with reliance upon a single storage/power cell. Researchers have attempted to develop materials to enhance energy density while maintaining high power density to achieve high performance and maintain the stability of ESDs. In particular, inorganic materials such as Co_3O_4, MnO_2, NiO, Fe_3O_4, RuO_2, and Li–Mn–PO_4 have been studied as the best candidates for ESDs because of their high theoretical capacitance based on their multiple reduction/oxidation states. However, their low cyclic stability, conductivity, and high cost prevent them from being widely used in practical applications.

Because of the inherent advantages of polymers, such as chemical diversity, environmental stability, light weight, and flexibility, conjugated polymers with narrow band gaps possess beneficial properties such as high conductivity and efficient redox properties, which make it possible to use conjugated polymers as materials for ESDs. The electrical conductivity of conjugated polymers with narrow

Conjugated Polymer Nanostructures for Energy Conversion and Storage Applications,
First Edition. Edited by Srabanti Ghosh.

band gaps, such as polypyrrole (PPy), polyaniline (PANI), and polythiophene, can achieve metallic conductivities via appropriate doping. In spite of this, the use of conjugated polymers in commercial ESDs has been prohibited because of various inherent limitations. However, when bulk conjugated polymers are converted into nanostructures, the nanodimensionality features can improve their inherent limitations and offer some advantages, including quantized electronic energy levels, enlarged surface-to-volume ratio, and more efficient mass transport into and out of the polymer [3–5]. In addition, the hybridization of conjugated polymer nanostructures (CPNs) with inorganic or nanocarbon species has been found to improve their major characteristics, such as conductivity, mechanical properties, long-term stability, and solubility, which make them possible strong candidates for use in ESDs. CPNs are favorable to form better conductive bridges and can act as a buffer to partially accommodate the volumetric changes during charge storage process. Consequently, the nanostructure design of conjugated polymers may rapidly enhance the cyclic stability and performance of ESDs, because the resulting electrodes undergo small absolute volume changes, and thus can overcome pulverization. This chapter will discuss the fundamentals of CPNs and their composites regarding their use in ECs and LIBs. The key issues for achieving optimized performances of these ESDs, such as through fabricating nanostructured electrodes and tailoring the microstructures of conjugated polymer composites, are described and concisely discussed, and recent research conducted in this area is discussed.

10.2 Terminology and Differences Between ECs and LIBs

The conjugated polymer-based ECs and conjugated polymer-based LIBs have similar device components and follow similar mechanisms for their operation, as both store charge through a redox reaction. The main differences between ECs and LIBs are their performances in terms of power density and energy density. **Energy density** is used to describe how much energy is stored in an ESD, and it can be expressed in two different ways: volumetric energy density and gravimetric energy density. The **gravimetric energy density** of an electrode specifies the total energy storage relative to the electrode's weight (Wh/kg), while the volumetric energy density of an electrode is the amount of energy stored per unit volume (Wh/m^3) [6]. Similarly, **power density** indicates the energy release per unit volume (**volumetric power density** – W/m^3) or unit weight (**gravimetric** power density – W/kg).

Conventional capacitors store charge through non-Faradaic phenomena (electric double layer capacitor, EDLC), which can provide very high power rates but suffer from low energy density [7]. LIBs, on the other hand, can store high quantities of energy but have low power density, which is limited by their redox reaction. Conjugated polymer-based ECs or Faradaic capacitors have intermediate power and energy delivery capabilities, lying between EDLCs and LIBs (Figure 10.1). Some researchers have suggested the name **pseudocapacitor** [9] for the Faradaic capacitor class as the transition boundary between conventional capacitors and LIBs. The charge storage of pseudocapacitors is achieved by a redox reaction

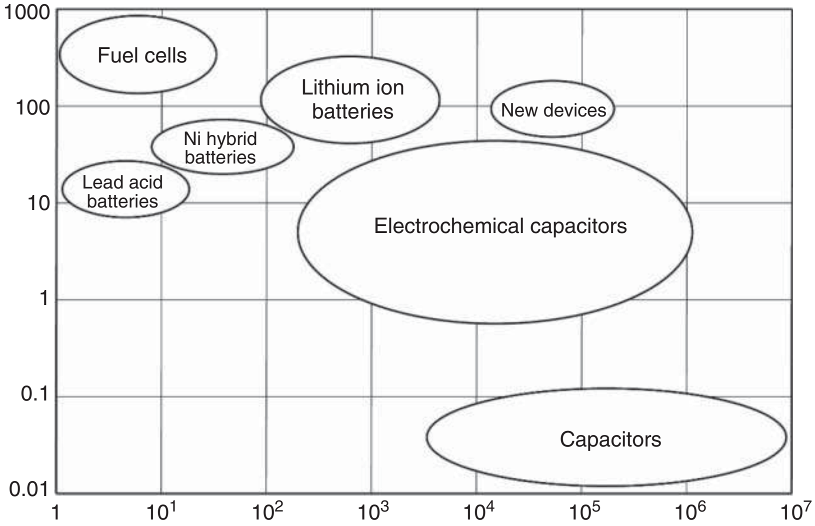

Figure 10.1 Energy density and power density of various ESDs. Source: Modified from Zhao et al. [8].

and a small non-Faradaic contribution occurring at the interface between an electrolyte and the electrode material. Compared with non-Faradaic charge storage mechanism, the charge/discharge process in Faradaic ESDs is relatively slow and can damage the microstructure of active materials inside the device over time. As a result, they lose the capability to maintain a constant energy level throughout the required storage time owing to inherent material degradation. Aside from energy and power densities, the **capacitance** is an additional value used to represent the performance of all classes of capacitors, while **capacity** is largely used for LIBs in the modern research community.

The **coulombic efficiency** is expressed as the amount of the output charge of the device to the input charge available at each charge and discharge cycle. In other words, a higher coulombic efficiency indicates a better cycle life for ESDs. The coulombic efficiency of LIBs is normally better than 98%, while ECs have a lower value than LIBs. Similarly, many researchers have frequently presented discharge capacitance/capacity at an individual **current density** value, which is defined as the flow rate of the electric charge per unit mass or area of an active material. **Charge retention** (capacitance or capacity retention) is the fully stored charge available from a device under specified conditions of discharge or storage time as compared with the first discharge cycle, which affects the lifespan of ECs and LIBs. Moreover, the loss of charge in these devices during storage time is referred to as the **self-discharge**, which is counted in percent loss per day, month, or year. Researchers continuously attempt to improve these properties. Over two decades, remarkable progress has been made in the development of ECs and LIBs as power supplies for modern and advanced devices. The advantages and disadvantages of ECs and LIBs are summarized in Table 10.1.

Table 10.1 Advantages and disadvantages of ECs and LIBs.

	Advantages	**Disadvantages**
ECs	The device voltage is not limited by chemical reaction and is determined by the applied circuit	Linear discharge voltage limits their use in some applications
	High power density	Power can be exhausted in a short period owing to low power density
	Simple charging method and much faster than LIBs	
	Long term stability with more than 500 000 charge/discharge cycles	High self-discharge; can be 20% of the rated capacity over 12 h
	Are never overcharged and have long life-spans (up to 20 yr)	
LIBs	Very high energy density	Low power density and slow charge process
	Low self-discharge compared to ECs and other batteries (1% or 2% per month)	Protection required to prevent overcharging or excessive discharging
	LIBs require a simple charging method, and charge time is improved as time goes by	Aging issue after 500–1000 charge–discharge cycles, after which their capacity declines
		High production costs because of rare metal and expensive onboard computer circuitry requirements

10.3 CPNs for ECs

10.3.1 Fundamentals of ECs

Over the past few decades, ESDs (such as ECs, fuel cells, and secondary batteries) have received much attention in fundamental studies and several device models have been commercialized. Among them, ECs have been considered as promising devices for electricity applications ranging from conventional portable electronics to electric vehicles, and even smart grid systems, because of their strong potential for high voltage and power density, long-term life span, and very fast charge rate. Historically, the first/basic concept of ECs was identified by Helmholtz in 1853, who stored an electric charge at the interface between two layers of solid/electrolyte materials. The first EC device, called a low voltage electrolytic capacitor or EDLC [10] using high specific area porous carbon material, was constructed by Becker at the General Electric Company in 1957, and was used in a commercial application in 1971. The electric energy storage mechanism of ECs can be based on Faradaic or non-Faradaic processes at the electrode/electrolyte interface. Figure 10.2 presents two EC models consisting of symmetric and asymmetric structures, fabricated by depositing materials on the anode and cathode electrodes. In general, an EC consists of two electrodes

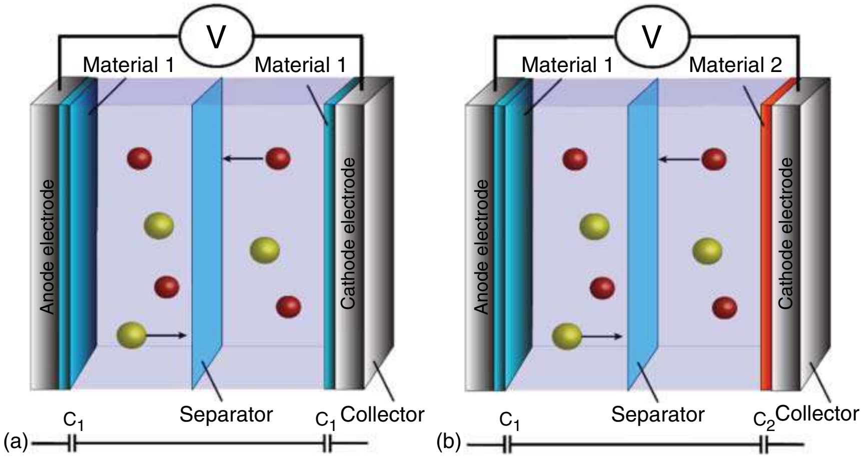

Figure 10.2 Schematic representations of (a) symmetric and (b) asymmetric ECs.

separated by a membrane separator, which are electrically connected by a conductive electrolyte. The electrode materials are crucial factors that determine the storage performance of ECs. The separator is a passive component used to prevent direct physical contact and to facilitate ion transfer between two electrodes. While the electrolyte's primary role is to act as a medium for the energy storage process, it can also enhance the energy density by increasing the cell voltage.

Three characteristic quantities: specific capacitance, energy density, and power density, are always associated with the performance of ECs. Both **cyclic voltammetry** (CV) and **galvanostatic charge/discharge** (GCD) measurement are methods frequently used for calculating such values and evaluating the electrochemical processes within a device. The **capacitance** of a **cell** (F), measured from CV data, can be calculated from Eq. (10.1), and can be applied to both two- and three-electrode cell configurations.

$$C_{\text{cell}} = \frac{\int_i^f i\text{d}V}{2s(V_\text{f} - V_\text{i})} \tag{10.1}$$

For a three-electrode cell, the active material is deposited on one electrode, where the capacitance of the cell or device (C_{cell}) is equal to the capacitance of the electrode ($C_{\text{electrode}}$). Therefore, the specific capacitance of a single-electrode material (C_s, F/g) is also the specific capacitance of the cell, and can be expressed as

$$C_\text{s} = \frac{C_{\text{electrode}}}{m} = \frac{C_{\text{cell}}}{m} \tag{10.2}$$

In the case of a **symmetrical two-electrode cell**, where $2C_{\text{cell}} = C_{\text{electrode}}$, the specific capacity of a single-electrode material is given as

$$C_\text{s} = \frac{C_{\text{electrode}}}{m} = 4\frac{C_{\text{cell}}}{m} \tag{10.3}$$

where $\int_i^f i\text{d}V$ is the integrated area under the CV curve, s is the potential sweep rate, m (g) is the total mass of the active electrode material, and V_i and V_f are the initial and final potentials of the forward scan, respectively. In the expressions given in Eqs. (10.1) and (10.3), the factor 2 indicates the forward and backward scans, while the factor 4 is added to substitute for the capacitance and mass of the individual electrode. In practice, CV is commonly used to study electrochemical processes, while GCD with a two-electrode configuration is the accepted technique to determine the capacitance/specific capacitance in the industry, because it produces more accurate values that are closer to those measured in practical applications. Moreover, the three-electrode configuration in GCD is not preferred for evaluating the performance of an EC owing to the unreliable values it produces. Here, **the capacitance of the cell** (F) and the **specific capacitance of single-electrode** materials in a **symmetrical two-electrode cell** are calculated based on the GCD curves using the following equations.

$$C_{\text{cell}} = \frac{i\Delta t}{\Delta V} \tag{10.4}$$

$$C_{\text{s}} = 4\frac{i\Delta t}{m\Delta V} \tag{10.5}$$

From the capacitance of the cell (F) and specific capacitance of the single-electrode (F/g), the energy density (E, Wh/kg), and power density (P, W/kg) of **the device** can be calculated according to Eqs. (10.6) and (10.7).

$$E = \frac{C_{\text{cell}}\Delta V^2}{2m \times 3.6} = \frac{C_{\text{s}}\Delta V^2}{8 \times 3.6} \tag{10.6}$$

$$P = \frac{1000 \times E}{\Delta t} \tag{10.7}$$

Here, i (A), Δt (s), and ΔV (V) are the discharge/applied current, the discharge time, and the working potential window, respectively, and m (g) is the total mass of the active material in both electrodes.

Note that if the two-electrode cell is asymmetrical, the specific capacitance of an individual electrode can be determined from a three-electrode system or a two-electrode cell in which one of the electrodes has a known specific capacitance. If both electrode materials are unknown, a symmetrical cell from one of the two materials can first be built, and then the specific capacitance of each electrode material can be determined subsequently. It is acceptable to report only the specific capacitance of the cell without specifying the specific capacitance of each electrode material. However, the specific capacitance of individual electrodes is needed to finally calculate the cell energy and power densities. To make the design more likely to be accepted, it is better to compare the cell energy capacity with those reported in the literature for cells made from similar or different materials. Lastly, some authors refer to the performance of ECs by the areal (or geometric) capacitance and volumetric capacitance, which are presented in (F/cm^2) and (F/cm^3).

Overall, ECs possess high power density and the potential to complement and even replace conventional batteries when high power delivery is highly demanded. However, their energy density is still lower compared with batteries. Numerous models and materials have been used to improve the energy density while attempting to maintain the power density. Based on available electrode materials and their charge

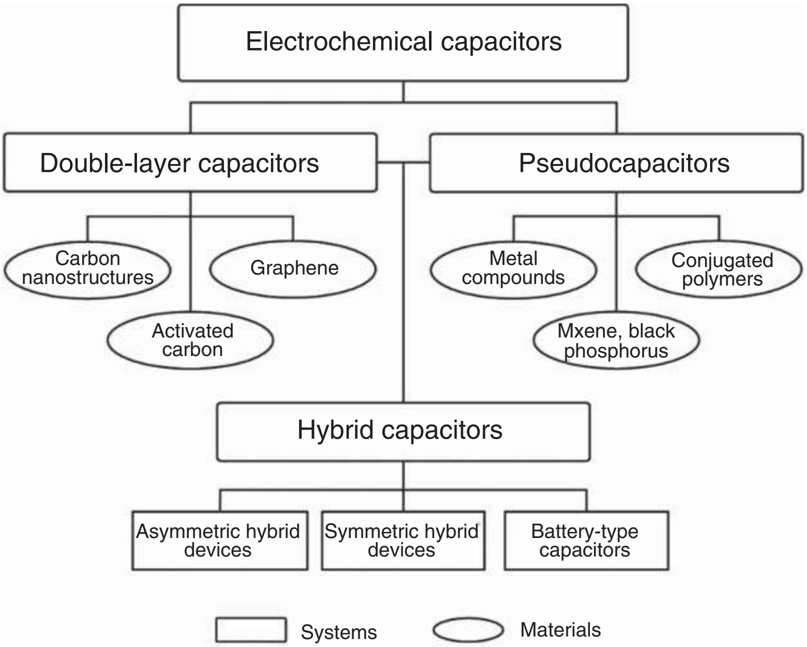

Figure 10.3 Classification of ECs based on the charge storage mechanism and active electrode material.

storage mechanism, current ECs can be divided into three device types: EDLCs, pseudocapacitors, and hybrid capacitors (Figure 10.3).

More specifically, **EDLC**s store charge based on non-Faradaic phenomena by using reversible ion adsorption–desorption over large-surface area electrode materials. Carbon materials such as carbon nanotubes (CNTs), carbon nanofibers (CNFs), graphene, porous carbon, activated carbon (AC), and carbon aerogels are the most widely studied and available commercial EDLC materials owing to their good conductivity, tunable microstructural characteristics, and outstanding chemical stability [11, 12]. The remarkable electrochemical performance of developed electrode materials is summarized in Table 10.2. EDLCs offer good cyclic stability and high power at the expense of low energy density. With the assistance of advanced spectroscopy and simulation software, gaining a deeper understanding of the chemical and physical processes of energy storage mechanisms has become a hot topic regarding enhancing the performance of EDLCs. By contrast, the charge storage mechanism of **pseudocapacitors** is provided by reversible Faradaic redox reactions. CPNs and transition metal oxide nanoclusters are candidate materials to develop high-performance pseudocapacitors. In order to improve the performance of pseudocapacitors, three parameters must be considered: (i) large surface area for a fast redox reaction, (ii) doping to increase the conductivity level, and (iii) a wide potential window. To combine the advantages of existing different types of ECs, hybrid forms of EDLCs and pseudocapacitors have been actively researched and developed, namely, **hybrid capacitors**. The charge storage mechanisms in this

Table 10.2 Material development and electrochemical performance of EDLCs.

Material	Configuration	Electrolyte	Potential window (V)	Current density/ scan rate	Specific capacitance (F/g)	References
N-doped carbon nanosheets	Two	$EMIMBF_4$ a)	3.5	2.0 A/g	222–242	[13]
N-doped carbon nanowhiskers	Two	6 M KOH	1.0	5 mV/s	210	[14]
Mesoporous carbons	Two	$NaClO_4$	3.0	2.5 A/g	66–78	[15]
Carbonaceous gels	Two	1 M H_2SO_4	0.8	0.1–10 A/g	99–600	[16]
Mesophase carbon	Two	1 M H_2SO_4	0.8	0.1–5.0 A/g	150–206	[17]
Hyper-crosslinked carbon	Three	1 M H_2SO_4	3.5	0.1–1000 mV/s	195–270	[18]
Halogen-nanoporous carbon	Three	6 M KOH	1.0	0.5–40 A/g	110–313	[19]
N-doped nanoporous carbon	Three	6 M KOH	1.0	1.0–10 A/g	175–250	[20]
N-doped carbon nanospheres	Three	6 M KOH	1.0	0.5–40 A/g	62–194	[21]

a) 1-Ethyl-3-methylimidazolium tetrafluoroborate.

type of EC take advantage of both the non-Faradaic phenomenon of EDLCs and the reversible Faradaic redox reactions of pseudocapacitors, and thus exhibit some improvement in energy density and power density. Hybrid systems aim to achieve retaining the cyclic stability of the electrode performance, which is the limiting issue for successful applications of ECs especially with high energy density.

A variety of materials such as conjugated polymers, transition metal compounds (metal oxides, sulfides, nitrides, and carbides), black phosphorous, and MXene have emerged in the research community as excellent electrode materials for advanced capacitors. Among them, pseudocapacitors or hybrid capacitors based on CPNs offer low cost, high specific energy and power, high conductivity, light weight, and enhanced flexibility over other materials [3–5, 22].

10.3.2 Pseudocapacitive CPNs in ECs

10.3.2.1 Conventional Heterocyclic CPNs

Conjugated polymers offer unique electrical and optical properties, which originate from their inherent molecular structure and external doping agents [22]. Pristine conjugated polymers have conjugated single and double bonds along the backbone and the overlap of adjacent p_z-orbitals in the chain of double bonds (π-bonds), and thus the polymer has very low conductivity (10^{-4}–10^{-9} S/cm). An external exciting factor called "doping" can help the polymer to achieve very high conductivities, up to 10^5 S/cm in certain cases, by inserting dopant species in the carbon chains of conjugated polymers. The role of the dopant is to extract an electron from the highest occupied molecular orbital (HOMO) of the valence band (p-type doping, oxidation) or add an electron to the lowest unoccupied molecular orbital (LUMO) of the conduction band (n-type doping, reduction). Therefore, doped conjugated polymers can be applied as storage charge materials in ECs. In general, the charging process involves the insertion of dopant ions from an electrolyte to the polymer backbone, corresponding to the oxidation reaction of n-type doping or the reduction reaction of p-type doping, while the chemical reaction of discharge is a reduction reaction process for n-type doping or an oxidation reaction for p-type doping polymers. The charge/discharge process of the n-type and p-type polymers can be depicted as follows.

$$\mathrm{CP} + n\mathrm{SO_4^{2-}} \leftrightarrows \mathrm{CP}^{2n+}(\mathrm{SO_4^{2-}})_n + 2n \tag{10.8}$$

$$\mathrm{CP} + \mathrm{Li}^+ \leftrightarrows \mathrm{CP}^{n-}(\mathrm{Li}^+)_n + n\mathrm{e} \tag{10.9}$$

Owing to specific characteristics of conjugated polymers, ECs based on fully active conjugated polymers can be constructed in three configuration types: (i) a symmetric capacitor using a 50% p-doped conjugated polymer for both electrodes, (ii) an asymmetric capacitor based on two p-doped conjugated polymers in which one is more than 50% doped for the anode and another is less than 50% doped as the cathode, and (iii) a symmetric/asymmetric capacitor with a neutral state existing in both p- and n-type doped conjugated polymers acting as the anode and cathode.

The comparison among different conjugated polymers for Type I (PPy/PPy), Type II (PPy/pMeT) ,[1] and Type III (pDTT/pDTT) [2] was investigated by Arbizzani et al. [23]. The configuration of the Type III exhibits higher performance in terms of energy and power densities than those achieved by the Type I and II configurations owing to the higher doping level and discharge voltage. A similar result was reported for TMATFMS[3]-doped poly(3-(4-fluorophenyl)thiophene) (PFPT), with a high energy density of 39 Wh/kg and power density of 3500 W/kg [24], with cell voltage exceeding 3.0 V. To obtain higher energy density and power density, a porous 3-(4-cyanophenyl)thiophene (PCNPT) film was developed, where exploring the polymer backbone with respect to the electrolyte was the means considered to enhance capacitor performance [25]. The growth and cycling of electrolytes are the key factors affecting the morphologies and electrochemical performance of a cell. The capacitor device exhibited high energy and power densities of 53.0 Wh/kg and 4600 W/kg, respectively, as compared with PFPT film (44.3 Wh/kg and 4200 W/kg) at the same discharge rate of 10 mA/cm^2. In other words, the high surface area enables fast kinetics and good electrochemical stability, resulting in enhanced energy density and power density of the device. Many poly(*p*-phenylene), polythiophene, and their derivatives have been used as fully active Type II EC materials, and their electrochemical performances are summarized in Table 10.3.

---

[1] Poly(3-methylthiophene).

[2] Poly(dithieno[3,4-*b*,3′,4′-*d*]thiophene).

[3] Tetramethylammonium trifluoromethanesulfonate.

Table 10.3 Performance of ECs based on Type II configuration.

Conjugated polymer	**Electrolyte**	**Voltage**	**Energy density (W/kg)**	**Power density (W/kg)**	**Current density (mA/cm^2)**	**References**
PMSPT[a]	$Me_4NCF_3SO_3$	2.9	44.3	4200	10	[25]
MPFPT[b]	Et_4NBF_4	2.8	40.0	2600	10	[25]
pMeT[c]	Et_4NBF_4	2.7	13	1400	5	[26]
PCDT[d]	Et_4NBF_4	2.0	6	1000	2	[27]
PTMTPA[e]	Et_4NBF_4	2.0	8.6	1600	0.2	[28]

a) 3-(4-Methylsulfonylphenyl)thiophene.
b) 3-(3,4-Difluorophenyl)thiophene.
c) Poly(3-methylthiophene).
d) Poly(cyclopenta[2,1-*b*,3,4-*b*′]dithiophen-4-one).
e) Poly-(*E*)-*R*-[(2-thienyl)methylene]-2-thiopheneacetonitrile.

Conjugated polymers such as PANI, PPy, and poly(3,4-ethyelenedioxythiophene) (PEDOT) represent the possibility of fabricating flexible electrodes as well as achieving a suitable theoretical capacitance to produce ECs. However, their poor cyclic stability and low practical capacitance are the main issues preventing them from industrial applications [24, 27, 28]. These issues can be overcome by improving the morphology of the nanostructured materials based on new hybridization and fabrication methods [3–5]. EC devices using these CPNs can achieve enhanced power density and energy density, along with greater cyclic stability. For example, Park et al. [29] have reported a clear correlation between the specific capacitance and morphology of PANI nanostructures based on symmetric construction. Anisotropic growth of PANI was performed in an aqueous solution, where the morphology could evolve from nanospheres to nanorods and nanofibers by increasing the steric stabilizer or surfactant (Figure 10.4). Interestingly, the specific capacitance was found to increase in the order of nanospheres < nanorods < nanofibers, based on both two- and three-electrode GCD measurements. PANI nanofibers possess a higher aspect ratio, which is considered to be a factor that facilitates faster electrode kinetics and low internal resistance, resulting in higher capacitance. For similar EC constructions, the effect of the morphology on the performance of the EC was further confirmed by Chen et al. [30] for PANI nanospheres, nanofibers, and nanotubes synthesized using MnO_2 templates. Among these nanostructures, PANI nanotubes exhibited broader redox peaks than nanospheres and nanofibers because of their higher specific area. The nanotubes exhibited a maximum specific capacitance of 764 F/g at a current density of 10 A/g in a redox active (H_2SO_4–hydroquinone [HQ]) electrolyte, which is as high as 57% above other morphologies. In addition, PANI nanotubes exhibited great cyclic stability and retained 65% of the first cycle specific capacitance. A variety of morphologies, such as spheres, sole-like plates, roses, cloud-like, rhombic plates, layered flowers, columns, blocks, and dendrites have been developed for PANI in the presence of different surfactants such as sodium

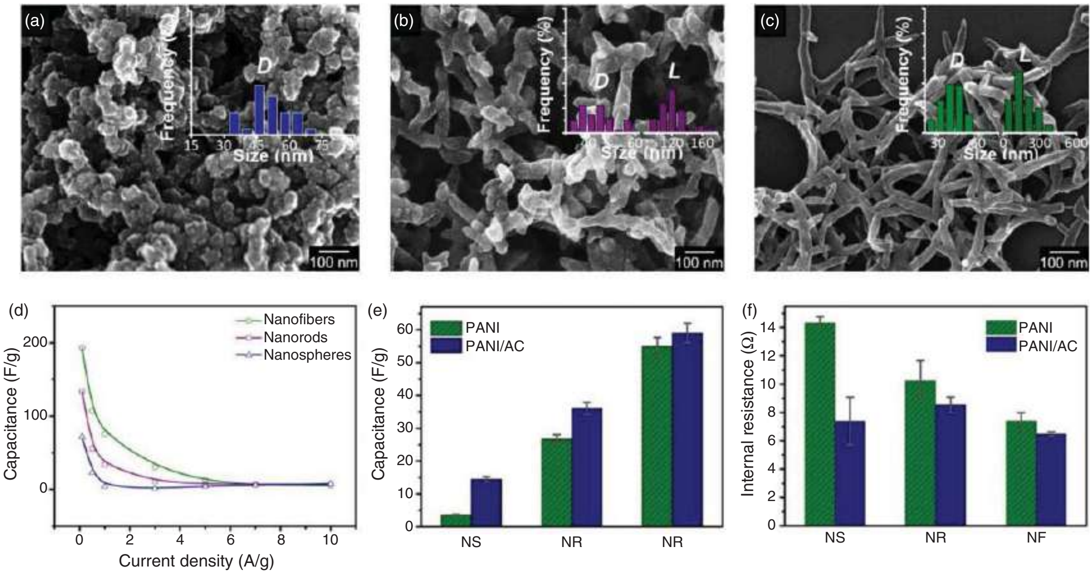

Figure 10.4 Field emission scanning electron microscopes (FE-SEM) images of PANI (a) nanospheres, (b) nanorods, and (c) nanofibers with their size distribution inset (*D* – diameter; *L* – length), prepared with the aid of a stabilizer in aqueous solution. (d) Measured specific capacitances of nanospheres, nanorods, and nanofibers from a three-electrode configuration at different current densities. Comparison of galvanostatic discharge capacitance (e) and internal resistance (f) of activated carbon and different PANI nanostructure nanocomposites at a current density of 0.1 A/g. Source: (a–c) Adapted with permission from Park et al. [29]. Copyright 2012, American Chemical Society.

dodecyl sulfonate, cetyltrimethylammonium chloride, cetyltrimethylammonium bromide, polyethylene glycol, polyvinylpyrrolidone, sodium dodecylbenzenesulfonate, and sodium lauryl sodium, respectively [31]. Among them, layered flowers achieve the highest specific area, which permits fast diffusion and accelerates the reaction between the electrolyte and active materials, resulting in the highest cell-specific capacitance of 272 F/g at a low current density of 1.0 A/g. Although conjugated polymer nanospheres have high surface-to-volume ratios, their large core and interparticle pore volume can cause a decrease in the density of the electrode material. Precise packing using different sizes of conjugated polymer nanospheres may increase the electrode density, prevent nanosphere aggregation, and therefore enhance the specific capacitance of the EC. The effect of binary nanosphere mixtures on the performance of EC electrodes was examined by Lee et al. [32] based on 20, 60, and 100 nm PPy nanospheres (Figure 10.5). The kinetics of energy storage can result from (i) ion transport from the electrolyte to the nanospheres, (ii) nanosphere to nanosphere interactions, and (iii) electron transfer from nanospheres to the current collector. According to experiments and numerical simulations, it was found that the mixtures comprising 20 and 100 nm nanospheres offered denser and more efficient packing, and led to better specific capacity and coulombic efficiency based on a three-electrode configuration. The dense packing of the nanospheres could facilitate ion transport pathways through the reduced sphere–sphere space and the enlarged surface area for better charge storage. Another approach is to enlarge the surface-to-volume ratios by using hollow conjugated polymer nanospheres. With the increase of surface area, the specific capacitance of hollow nanospheres was two times higher than filled nanospheres, and reached 326 F/g at a current density of at 0.1 A/g [33]. Therefore, physical factors such as porosity, aspect ratio or morphology, and surface area of CPNs can be used to design the enhanced performance of electrodes.

However, the optimized materials in these reports were focused on enhancing the specific capacitance rather than the durability of the device. Fabrication of conjugated polymers in hydrogel networks may be an excellent means for fabricating high performance, durable, flexible ECs because it theoretically provides a large surface area, the material is soft, and high electrolyte permeability is feasible. Shi et al. [34] fabricated a hierarchic 3D porous PPy hydrogel constructed through interconnected nanospheres by an interfacial polymerization method for flexible symmetric and asymmetric ECs. The hydrogel electrode exhibited a high specific capacitance of 380 F/g at a current density of 0.2 A/g in a PVA-H_2SO_4 solid electrolyte, with good mechanical properties. In addition, over 80% of the initial discharge cycle specific capacitance was maintained, indicating that the 3D porous PPy hydrogel provides good electrochemical stability to the EC. Finally, the connectivity and permeability of hydrogel networks not only provide good mechanical as well as cyclic stability, but also enable the fast ion and electron transport necessary for high performance, stable ECs. PEDOT:polystyrenesulfonate (PSS) hydrogel fibers have displayed a specific capacitance as high as 202 F/cm^3 at a current density of 0.54 A/cm^3 with nearly zero reduction of the capacitance after 10 000 cycles, even under curvature conditions [35]. With a well-defined hydrogel network, it is possible to fabricate a

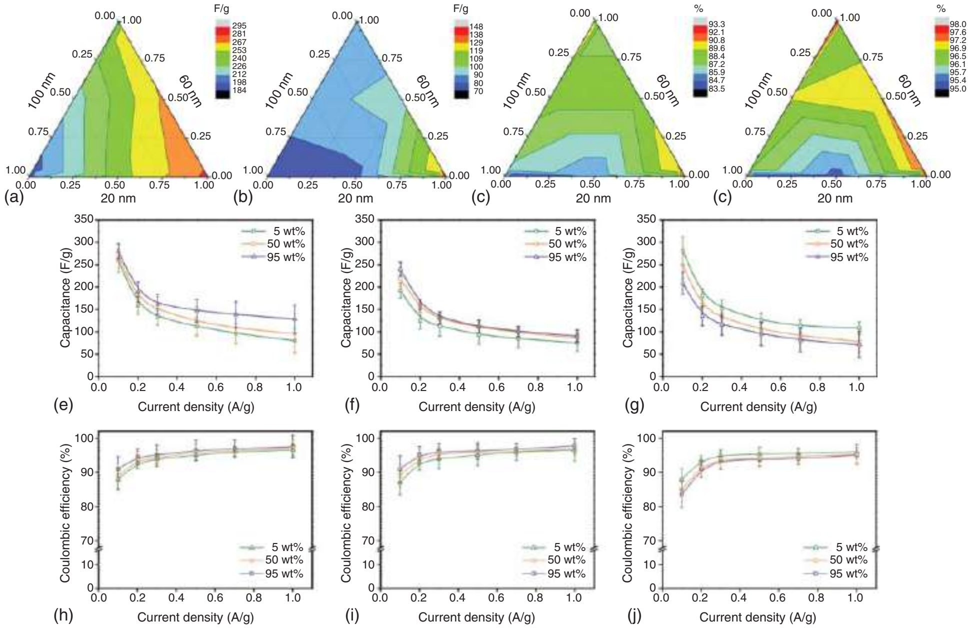

Figure 10.5 Ternary diagrams for the PPy nanospheres of three different diameters (20, 60, and 100 nm) showing the distribution of (a, b) specific capacitance and (c, d) coulombic efficiency as a function of the mixed weight fraction measured at a (a, c) 0.1 A/g and (b, d) 1.0 A/g. Plots of (e–g) specific capacitance and (h–j) coulombic efficiency of the binary nanosphere mixture electrodes at different current densities with the two different-diameter nanosphere species: (e, h) 20/60, (f, i) 60/100, and (g, j) 100/20. Source: Adapted with permission from Lee et al. [32]. Copyright 2016, Royal Society of Chemistry.

device with good cyclic stability and higher specific capacitance. Zhou et al. [36] recently reported that PANI hydrogel can increase the performance of an EC in terms of specific capacitance and cyclic stability. *In situ* polymerization using a template may be the best approach, as it allows generating a high aspect ratio of the hydrogel-based PANI nanofibers. The PANI hydrogel-based asymmetric EC achieved a very high specific capacitance of up to 636 F/g at a current density of 2.0 A/g and 626 F/g at 25.0 A/g with 83% retention after 10 000 cycles. However, traditional conjugated polymers such as PANI, PPy, polythiophene, and their derivatives are less durable and sometimes have lower specific capacitance because of their large volumetric swelling and shrinkage after a number of charge–discharge cycles, which lead to mechanical deterioration of the linear polymer structure and to a rapid decay in capacitance. Generally, their capacitances are significantly weakened after more than 1000 charge/discharge cycles [36].

10.3.2.2 Microporous Conjugated Polymers

Significant interest toward the enhancement of EC performance lies in the synthesis of new CPNs. Since first reported in 2005 [37], microporous conjugated polymers[4] (MCPs) have received much attention related to storage, catalysis, and energy storage applications. In this context, an MCP is formed through the strong covalent connections (bonds) of small π-conjugated molecule building blocks with three or more functionalities, forming 3D polymer networks with a microporous structure. Their classes can range from amorphous classic hyper-crosslinked polymers and intrinsic microporosity polymers to crystalline covalent-organic frameworks (COFs). Well-designed MCPs are believed to possess some remarkable advantages owing to combining the π-systems of conventional conjugated polymers (with distinct micropore properties) with redox-active sites and large surface area, thus facilitating the interface kinetics and reversible reactions needed to enhance the performance of ECs. An outstanding performance of MCPs involving symmetric ECs was reported by Jiang and coworkers [38]. Upon integrating the advantages of inherent pores and the π-conjugated system, aza-fused MCPs (synthesized from 1,2,4,5-benzenetetramine and triquinoyl hydrate) with large surface area (546 m^2/g) achieved a highly stable specific capacitance of 398 F/g at a current density of 5 A/g and 378 F/g at 10 A/g with excellent life cycle during the charge and discharge tests, resulting in a stable and rapid power supply. DeBlase et al. [39] reported that electrodes with 2D redox-active COF synthesized from the polymerization of 2,6-diaminoanthraquinone and 1,3,5-triformylphloroglucinol (DAAQ-TFP COF) display higher capacitance than electrodes using DAAQ monomer and *p*-diaminobenzene (DAB)-TFP at the same current density of 0.1 A/g in an acidic solution (Figure 10.6d–f). The structure of these MCPs is introduced in Figure 10.6a. The high specific capacitance is achieved through the large redox-active sites of DAAQ and TFP monomers, uniform pore size, and the highest specific surface area of COF (1800 m^2/g), which approaches the theoretical value of the framework

---

[4] Some researchers also refer to them as conjugated microporous polymers.

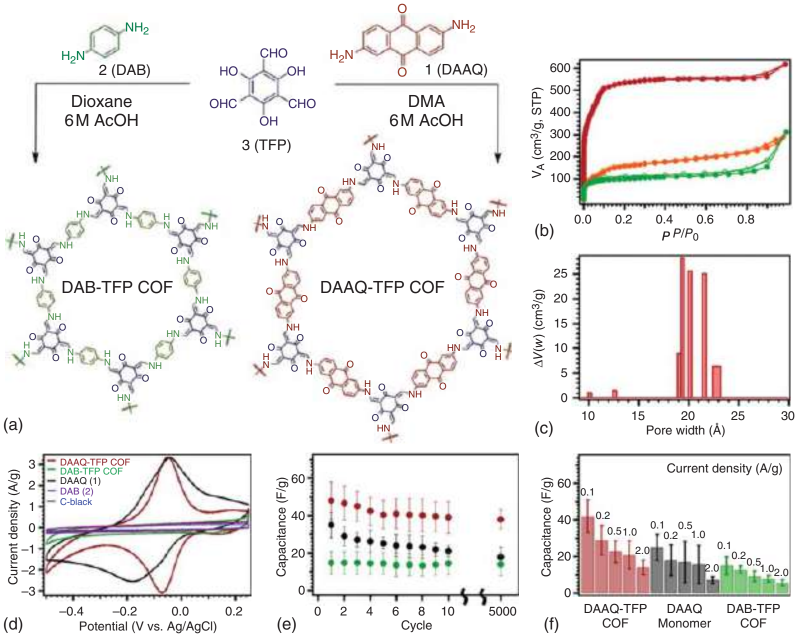

Figure 10.6 Synthesis procedure and chemical structure of (a) DAB- and DAAQ-TFP COFs; (b) nitrogen adsorption/desorption behaviors of DAAQ-TFP COF (red), dioxane (orange), and DAB-TFP (green); (c) pore size distribution of DAAQ-TFP COF. The comparison of (d) cyclic voltammograms, (e) average discharge capacitance vs. cycling at a current density of 0.1 A/g, and (f) average discharge capacitance at different current densities between DAAQ-TFP COF (red), DAB-TFP COF (green), and their monomers (gray). The error bar is normalized to 1 (std. dev.). Source: Adapted with permission from DeBlase et al. [39]. Copyright 2013, American Chemical Society.

(2340 m^2/g) (Figure 10.6b,c). The presence of heteroatom-rich elements such as nitrogen and oxygen on MCPs can increase the capacitance of ECs by enriching the negative charge on the polymer backbone as well as by enhancing the charge mobility of the MCPs for rapid intrachain charge transport and reversible redox reactions. The crucial role of a high uniform surface area/porous structure and high nitrogen content for the redox reaction (rather than oxygen) have been confirmed by Li et al. in a study of redox-active MCPs derived from π-conjugated and nitrogen-rich triazatruxene building blocks and a terephthalaldehyde (TPAL) (TAT-MCP-2) linker, as compared with a pyromellitic dianhydride (PMDA) linker (TAT-MCP-1) [40]. In these MCPs, nitrogen atom exists as ternary nitrogen, quaternary nitrogen, and oxidized nitrogen, which appear in the range from 400.1 to 402.8 eV under X-ray photoelectron spectroscopy (XPS). Both quaternary nitrogen and oxidized nitrogen peaks disappeared after the reduction process with CV scanning from 0.0 to −2.0 V. This indicates that the high N content provides the main contribution to the redox reaction mechanisms of MCP-based ECs. Owing to the larger surface area/porous structure and higher N content, a TAT-MCP-2 electrode can produce a specific capacitance of 183 F/g (three-electrode cell), which is higher than that of TAT-MCP-1 (141 F/g) at a current density of 1.0 A/g, and has the highest specific capacitance per unit surface area (>160 μF/cm^2) reported to date. In particular, TAT-MCP-2 exhibits an excellent reversible charge/discharge process at a very high current density of 10 A/g with an efficiency of 95% after 10 000 cycles, thus strongly supporting the possible use of nitrogen-rich MCPs as electrodes for high power, stable ECs.

Although controlling the morphology and size of CPNs can improve the performance of ECs, their less-than theoretical values and poor cyclic stability are still present in CPN-based ECs owing to intrinsic limits. Successful modified or hybridized CPNs with heterogeneous materials can improve the mechanical stability and conductivity, and therefore can enhance the performance and durability of ECs. In this approach, conjugated polymer nanocomposites have received much attention and extensive studies have been conducted regarding advanced ESDs recently.

10.3.3 Conjugated Polymer Nanocomposites

Owing to their outstanding theoretical capacitance, mild synthetic condition, tunable conductivity, and cost effectiveness, CPNs have received attention as potential pseudocapacitive materials [3, 5, 22, 41]. However, unfortunately, the dimensional stability of conjugated polymers at the nanoscale becomes seriously lowered. Hence, they may suffer from poor cyclic stability because of large volumetric changes that occur in the insertion/de-insertion process during charge/discharge cycles. In addition, their electrical conductivities are much lower in their undoped state, caused by large electrode polarization and poor rate capability. Therefore, single component CPNs are too unstable to be used in EC applications. Many researchers have thus used CPNs in the form of a composite, which can achieve enhanced performance compared with pristine CPNs and bulk conjugated polymers. A conjugated polymer can be coupled with other functional materials in the nanometer regime, such as transition metals and carbon species, to improve their electrochemical performance. The low conductivity of conjugated polymers in undoped form can be overcome through the use of metallic compounds. In contrast, conjugated polymers can afford microstructural deformation, prevent corrosion and metal ion leaching, and, in the presence of metal oxides, provide electrical pathway. For instance, a heterojunction of a $NiCo_2O_4$ core and PANI shell ($NiCo_2O_4$@PANI) can render a high specific capacitance while maintaining good cyclic stability [42]. The core–shell structure was simply fabricated by coating PANI onto highly porous $NiCo_2O_4$ nanorod arrays grown on carbon cloth through a hydrothermal process and electrodeposition technique **(**Figure 10.7). $NiCo_2O_4$ nanorod arrays offered fast electron transport and high surface area. On the other hand, the PANI shell provided high stability and activity in the acidic solution, which protected the $NiCo_2O_4$ from dissolution in an acidic environment. Thereby, the $NiCo_2O_4$@PANI composite electrode showed a high specific capacitance of 901 F/g at a current density of 1 A/g in H_2SO_4 solution, as well as excellent cyclic stability at a high current density of 10 A/g with 91% capacitance retention after 3000 discharge cycles. It was reported that 3D CoO@PPy hybrid nanowire arrays on a nickel foam electrode [43] delivered a high specific capacitance (up to 2223 F/g) at a current density of 1 mA/cm, and exhibited high

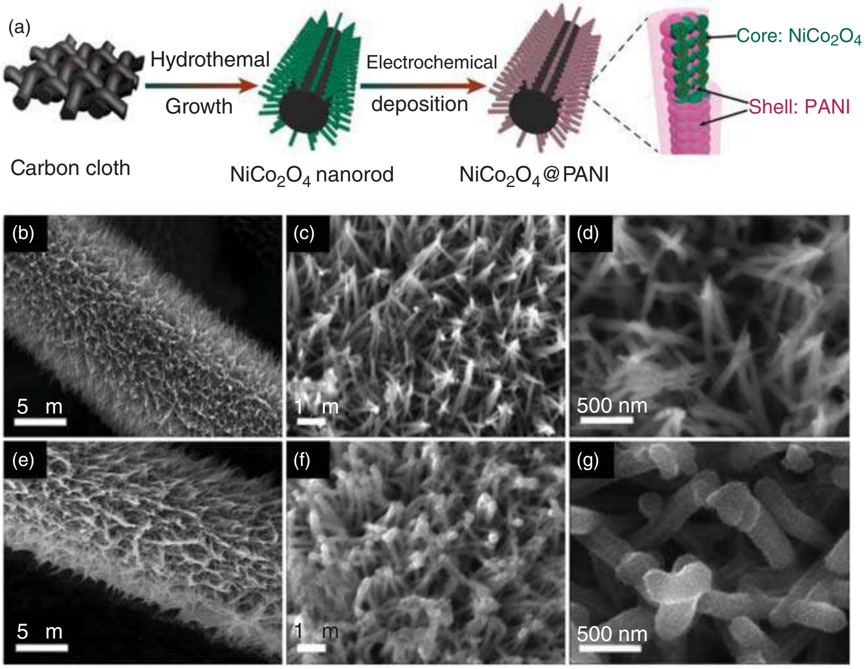

Figure 10.7 (a) Scheme of synthetic fabrication procedure for $NiCo_2O_4$@PANI nanorod arrays. (b–d) FE-SEM images of $NiCo_2O_4$ nanorod arrays coated with carbon fibers and (e–g) after conformal growth of PANI shell. Adapted with permission from Jabeen et al. [42]. Copyright 2016, American Chemical Society.

power capability and capacitance retention of 91.5% after 2000 cycles. In addition, an asymmetric EC made from CoO@PPy (cathode) and AC film (anode) exhibited a high energy density of 43.5 Wh/kg, and high power density of ~5500 W/kg. This excellent performance was achieved because of the high electrochemical activity and large surface area of both CoO and PPy nanostructures along with the high electrical conductivity of PPy, which facilitated the redox reaction and electron transport in the hybrid material. Moreover, the presence of the PPy shell could better protect the CoO nanowires, and therefore significantly improved the cyclic stability of the electrode material. To reduce the "dead volume" of an active material, a hollow structure can be used to reinforce the capacity of the EC. PANI coated h-MoO$_3$ hollow nanorods minimized the high strain generated from large volume changes in charge/discharge cycles and delivered a maximum specific capacitance of 270 F/g, which is two times higher than the h-MoO$_3$ (126 F/g) and PANI (180 F/g) individual capacitances, with enhanced cyclic stability [44]. Regarding an asymmetric EC, the loading weight ratio of anode/cathode materials affects the overall capacitive behavior of the device [45]. In the case of MnO$_2$–mPNTs(+)/RGO[5](−) EC, a 1 : 1 sample exhibited the highest performance in terms of cell capacitance, while increasing or decreasing the ratio led to lower capacitance and coulombic efficiency. Moreover, further optimization of the cell system and electrode material are believed possible for the successful development of high performance ECs based on MnO$_2$–mPNTs.

Regarding recent progress of materials development, metal-organic framework (MOF) hybridized CPNs have emerged as a promising active material for ECs [46]. Taking advantage of the high conductivity of the doped polymer and the high surface area and porosity of the COF, a composite consisting of a zeolitic imidazolate framework and conductive PPy nanotubes (ZIF−PPy) exhibited a specific capacitance five times higher (597.6 F/g) than a ZIF electrode (99.2 F/g) at a current density of 0.5 A/g, as well as improved capacitance retention. With the growth of the EC research community, various metal compounds such as α-Fe$_2$O$_3$, MnO$_2$, WO$_3$, MoS$_2$, Ce, CuO, and Bi$_2$O$_3$ have been used to hybridize CPNs for EC devices, and their greater capacitances have been reported (Table 10.4).

Not only metal compounds, but also the combinations of carbon materials and conjugated polymers at the nanoscale are of interest in the development of high-performance ECs. Commonly, the Faradaic redox process makes the nanostructured conjugated polymer and metal compound less stable than carbon-based electric double-layer (EDL) capacitors [7, 22, 57–59]. Carbon materials, on the other hand, store charge through electrical double layers (non-Faradaic reactions), which allows enhancing the cycle life to more than 500 000 cycles. Hybrids of carbon materials and conjugated polymers have been developed to enhance chemical stability and to overcome the low conductivity of conjugated polymers in the undoped state. The π–π stacking and electrostatic interactions are the main binding forces in the hybrid structure. Carbon materials are able to not only provide a high-conductivity supporting substrate, but also supply efficient diffusion paths for ions or small molecules in the hybrid electrode. Typically, nanostructured carbon materials have

---

[5] mPNTs/RGO: Multidimensional PEDOT nanotubes/reduced graphene oxide.

Table 10.4 Performances of ECs based on conjugated polymer/inorganic material nanocomposite electrodes.

Material	Configuration	Electrolyte	Potential window (V)	Current density/ scan rate	Specific capacitance (F/g)	References
PANI/α-Fe_2O_3	Three	1 M H_2SO_4	1.0	2.0 mV/s	974	[47]
PANI/MnO_2 nanotubes	Two	1 M H_2SO_4	0.7	2.0 A/g	626	[48]
Ag/PEDOT/MnO_2	Two	0.5 M Na_2SO_4	1.0	10 mV/s	838	[49]
MoS_2/PEDOT	Three	2 M HCl	1.6	5.0 mV/s	452	[50]
MoS_2/PANI nanotube	Two	1 M H_2SO_4	0.7	0.5 A/g	552	[51]
PEDOT/WO_3	Three	0.5 M H_2SO_4	1.0	200 mV/s	324	[52]
CeO_2/PANI	Two	1 M HCl	0.8	2.0 A/g	1452	[53]
Eu_2O_3/PPy/CuO	Two	1 M H_2SO_4	1.0	1.0 A/g	320	[54]
Co_3O_4@PPy nanowires	Three	2 M KOH	0.6	5 mA/cm^2	2122	[55]
PANI/γ-Al_2O_3	Two	0.5 M H_2SO_4	1.0	1.0 A/g	292	[56]

a useful porous structure and large surface area, which can be decorated by conjugated polymers to form a nanostructured composite with enhanced performance for EC applications. Enhanced capacitance and cyclic stability have been observed in the nanocomposites of conjugated polymers with carbon materials, such as graphene, CNTs, CNFs, and ACs. In an asymmetric electrode configuration system, AC/PEDOT:PSS nanocomposites yielded an enhanced capacitance of EC cells over that of PEDOT:PSS or ACs only [60, 61]. CNT/CNF-hybridized conjugated polymer nanocomposites can be simply obtained by *in situ* polymerization [62, 63] or solution blending methods [64, 65]. Niu et al. [66] fabricated a thin and flexible single-walled carbon nanotube (SWCNT)/PANI film by *in situ* electrochemical polymerization using a reticulate-architecture SWCNT film, which acts as the skeleton, and PANI layers, which act as the skin. The flexible nanocomposite electrode material with a unique "skeleton/skin" structure achieved much higher conductivity compared with the SWCNT/PANI composite films reported so far, and delivered a high energy and power density of 31 Wh/kg and 62.5 kW/kg, respectively. PANI-coated freestanding CNFs fabricated through a one-step vapor deposition polymerization technique were reported by Jang et al. [67]. Here, the thickness of the PANI was controlled through the initiator/monomer ratio, reaction pressure, and polymerization temperature. A 20 nm-thick PANI coated CNF nanocomposite displayed an improved EC performance with a maximum value of 264 F/g. However, pristine CNFs have less dispersion in the liquid phase, which causes aggregation during the subsequent polymerization of conjugated polymers, thereby resulting in unsatisfactory capacitance of the device. In order to overcome this drawback, efficient routes to the surface-modification of CNFs have been reported as necessary to fabricate viable ECs [68]. As reported, functionalized CNFs induce better mechanical properties, high surface area, and high compatibility with conjugated polymers, as compared with pristine CNFs. Therefore, these nanocomposite electrodes achieved a high specific capacitance of 557 F/g and 86% capacity retention after 2000 charge/discharge cycles at 0.3 A/g [69]. In contrast, carbon-coated conjugated polymer showed exceptionally high capacitance retentions of 95% for PANI and 85% for PPy after 10 000 cycles [69], which are the best values reported thus far for polymer-based EC electrodes in an aqueous electrolyte.

With successful commercialization in recent years, two-dimensional graphene materials such as graphite, graphene oxide (GO), and reduced graphene oxide (RGO), have attracted much interest toward their development in electrochemical ECs. Hybridization of two-dimensional carbon materials and conjugated polymers can be accomplished by physical or chemical methods. A simple physical method to fabricate graphene/PANI nanohybrids for flexible EC has been introduced by Choi et al. [70]. In this case, conductive PANI was physically intercalated into two graphene sheets without causing serious damage to the sp^2 hybridized carbon structure using sonication (Figure 10.8a). The graphene sheets exfoliated by PANI showed good colloidal stability. Without the assistance of the PANI, the graphene

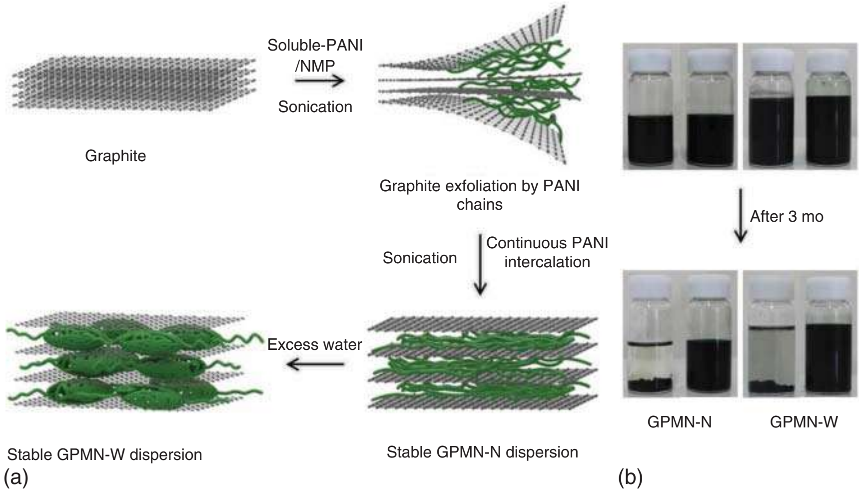

Figure 10.8 (a) Schematic illustration of the formation of graphene-PANI multilayered structures (GPMNs) by direct physical exfoliation of graphite with PANI (soluble-PANI); (b) Photographs showing the long-term colloidal stability of the GPMN dispersion solution in the absence (left) and the presence (right) of PANI. GPMNs exhibited outstanding colloidal stability in both NMP and water. The GPMNs dispersed in NMP and water were named GPMN-N and GPMN-W, respectively. Source: Reprinted with permission from Choi et al. [70]. Copyright 2015, John Wiley & Sons, Inc.

sheets would restack and aggregate after a short period of time (Figure 10.8b). Finally, the graphene/PANI nanohybrids showed twice-improved specific capacitance and 80% capacitance retention after 5000 cycles. Graphene with excellent dimensional stability generated a charge-transfer complex with PANI and helped to reduce the structural degradation of the PANI due to large volume changes under charge/discharge cycles. It was observed that the intercalated PANI morphology was highly dependent on dispersion media. The morphology of the PANI transformed fibrillar clusters to larger granular clusters between graphene sheets when *N*-methyl-2-pyrrolidone (NMP) was replaced by water. The graphene/PANI nanohybrids in water provides a better porous structure, resulting in diverse electrochemical properties and enhanced performance of ECs. Graphene, in the form of GO or RGO having functional groups such as carboxyl, epoxides, or hydroxyl groups on edges and planes, is a candidate for application in ECs because of its excellent electrical and electrochemical performances. RGO-sheet-wrapped PANI nanowire on a nitrogen-doped carbon fiber cloth (NCFC) offered greater chemical, mechanical, and physical properties [71]. The RGO/PANI/NCFC nanocomposite electrode provided superior conductivity and high surface area, which could deliver a high specific capacitance of 1145 F/g with high capacitance retention of over 94% after 5000 cycles. These studies demonstrate that the carbon materials were very effective in preserving the microstructures of conjugated polymers during charge/discharge cycling, thereby resulting in excellent capacitance retention rates. Consequently, different carbon materials have been used to hybridize various conjugated polymers, such as CNF/GO/PANI, PPy/RGO and PANI/RGO bilayers, PANI/graphene nanosheets, and PANI or PPy/carbonaceous films as well as their ternary nanocomposites. Their electrochemical performances are summarized in Table 10.5. The challenge is to improve the stable distribution of conjugated polymers in the skeleton material and combine the advantages of carbon materials to improve the specific capacitance and cycle performance. In addition, developing new hybrid types and improving fabrication technologies represent future directions for conjugated polymer/carbon nanocomposite electrode research.

10.4 CPNs for LIBs

10.4.1 Fundamentals of LIBs

LIBs can operate at voltages between 3.0 and 4.5 V with a specific energy ranging from 100 to 265 Wh/kg, and currently dominate world markets. In general, a common LIB consists of six components, including a cathode (electron acceptor) made from lithium metal oxide, an anode (electron donor) formed by layered graphite material, a separator commonly made from a polymer to prevent direct physical contact between two electrodes, an electrolyte containing a lithium salt in an organic solvent to transport electrons and ions inside the cell, a binder, and current collectors embedded on both electrodes. Figure 10.9 shows the structure of and the reactions in a typical $LiMO_2$ battery. In the charging process, the movement of Li^+ ions (positive charges) and electrons between anode and cathode through the separator can

Table 10.5 Electrochemical performances of conjugated polymer/carbon material composites for ECs.

Material	Configuration	Electrolyte	Potential window (V)	Current density/ scan rate	Specific capacitance (F/g)	References
PANI/few-layer graphene (FLG)-coated ACFs[a]	Three	1 M H_2SO_4	0.8	0.1 A/g	400	[72]
CNT/PPy film	Two	PVA–H_3PO_4	0.9	5.0 mV/s	331.4	[73]
PEDOT/carbon fiber	Two	PVA–H_2SO_4	1.0	0.5 A/g	181	[74]
PEDOT/CFC[b]	Two	1 M H_2SO_4	0.8	5.0 mV/s	203	[75]
PANI/RGO	Three	1 M H_2SO_4	0.8	10 mV/s	300–535	[76]
PPy/carbon cloth	Two	5.0 M LiCl	1.2	1.0 A/g	699	[77]
PEDOT/GO	Three	0.1 M KCl	1.2	100 mV/s	115	[78]
RGO/$MnFe_2O_4$/PPy	Two	1 M H_2SO_4	1.0	5.0 mV/s	232	[79]
MnO_2/GO/PEDOT	Three	0.5 M Na_2SO_4	1.0	10 mV/s	841	[80]

a) Polyaniline and few-layer graphene coated active carbon fibers.
b) Carbon fiber cloth.

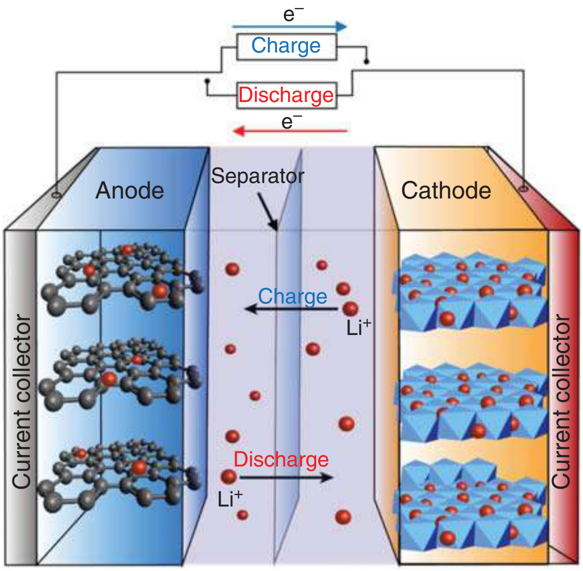

Figure 10.9 Working principles of typical LIBs.

Table 10.6 Chemical reactions during charge/discharge cycles of a $LiMO_2$ battery.

	Charge	Discharge
Cathode	$LiMO_2 \rightarrow Li_{1-x}MO_2 + xLi^+ + xe^-$	$Li_{1-x}MO_2 + xLi^+ + xe^- \rightarrow LiMO_2$
Anode	$xLi^+ + xe^- + xC_6 \rightarrow xLiC_6$	$xLiC_6 \rightarrow xLi^+ + xe^- + xC_6$
Overall reaction	$LiMO_2 + C_6 \leftrightarrow Li_{1-x}MO_2 + Li_xC_6 + xe^-$	$Li_{1-x}MO_2 + Li_xC_6 + xe^- \rightarrow LiMO_2 + C_6$

be summarized in three steps: (i) Li^+ ions generated from the cathode pass through the electrode and electrolyte, (ii) the ions move into the electrolyte and cross the separator, and (iii) positive charge is intercalated to the structure of the anode material, allowing electrons to flow from the anode to the cathode [10]. The reverse reaction will occur during the discharging process. The detailed electrochemical reactions at the electrodes of LIBs during charge/discharge are described in Table 10.6.

The process of charging and discharging has been defined as a cycle in a battery. After the first intercalation of lithium-ion to anode material, successive delithiation will be never achieved 100% after the first discharge-state owing to the inherent structure of the anode material. Although LIBs possess high energy and voltage, they have a low rate of capacity decay when the battery is stored over its lifetime. The decreased capacity is due to an internal chemical reaction of the battery, even without any direct connection between the electrodes. Capacity losses can be classified by two types: reversible or irreversible. The reversible loss is known as self-discharge, and such capacity loss will be refilled in the next cycle of charge, whereas irreversible capacity loss is called capacity fade, in which a portion of the capacity will be lost forever owing to permanent internal damage. To date, manufacturers have commercialized seven types of LIBs with various forms, as shown in Table 10.7, and their price has decreased year by year. Lithium nickel cobalt aluminum oxide has the best performance, and further improving the lifespan of LIBs will open a larger, more inexpensive battery market.

10.4.2 Conjugated Polymer Nanostructures for LIBs

In rechargeable LIBs, lithium ions are moved freely by the electrolyte from the cathode to the anode as electrons flow through an external circuit from the anode to the cathode, producing power during discharge. During recharge, ions and electrons are driven in the reverse direction by an external voltage, storing electrical energy as chemical energy in the battery. During the charge/discharge process, anode materials undergo a large volume change (up to 400%), which causes great strain in the material and thus leads to cracking and crumbling in the structures of the active materials. This results in poor reversible capacity and irreversible capacity loss after the first cycle [81, 82]. There have been many reports on the role of conjugated polymers as active or/and supporting electrode materials, such as improving electrical

Table 10.7 Performances of various commercial LIBs.

Type of battery	Voltage (nominal) (V)	Specific energy (Wh/kg)	Specific power (W/kg)	Cost per kWh (USS)	Self-discharge (per month) (%)	Cycle life
Lithium manganese oxide	3.0–4.2 (3.7)	100–150	250–400	~\$400	5	300–700
Lithium cobalt oxide	3.0–4.2 (3.6)	140–200	100–1000	~\$400	1–5	500–1000
Lithium iron phosphate	2.5–3.65 (3.2)	90–160	245–430	~\$580	<1	1000–2000
Lithium nickel manganese cobalt oxide	3.0–4.2 (3.6)	140–220	500–3000	~\$420	1	1000–2000
Lithium nickel cobalt aluminum oxide	3.0–4.2 (3.6)	200–260	1500–1900	~\$350	2–10	>1000
Lithium titanate	$1.8–28.5 \times 10^{-1}$ (2.4)	30–110	3000–5100	\$1005	2–10	3000–7000
Lithium ion polymer	3.0–4.2 (3.6)	100–265	—	—	10–50	300–500

conductivity, decreasing polarization, and promoting electrolyte permeation. CPNs have also been properly combined with inorganic redox oxides as electrodes, producing systems suitable for electrochemical lithium intercalation with improved performance [83].

10.4.2.1 Conjugated Polymers as Fully Active Electrode Materials for LIBs

The potential use of conjugated polymers for LIBs arises from the electrochemical doping/de-doping properties of polymers, wherein active anode material is obtained by the insertion of a counter-anion into the polymer chain (p-type doping), whereas the cathode material is constructed from the migration of counter-cations into the polymer chain (n-type doping). This particular electrochemical doping/de-doping of conjugated polymer is reversible and is analogous to the charge/discharge process of a typical galvanic cell, which forms the basic concept for developing conjugated polymers suitable for rechargeable batteries.

Novel LIBs can be fabricated by utilizing the undoped or doped forms of a conjugated polymers as an active material for anode/cathode development, and numerous electrochemical doping/dedoping cycles can be applied as charge/discharge processes. The stored energies of conjugated polymers depend on the doping level applied during the charging process. With the growth of ESDs, a wide variety of

Table 10.8 Conventional classifications of conjugated polymer-based LIBs.

LIB system	Anode	Cathode
Type I	Inorganic materials	Low-level p-doped conjugated polymer
	Inorganic materials	Undoped (p-type) conjugated polymer
Type II	Low-level n-doped conjugated polymer	Inorganic materials
	Undoped (n-type) conjugated polymer	Inorganic materials
Type III	Low-level n-doped conjugated polymer	Low-level p-doped conjugated polymer
	n-Undoped conjugated polymer	p-Undoped conjugated polymer

LIB systems using conjugated polymers have been constructed and can be classified into three types (Table 10.8).

Herein, the charging mechanism of a LIB system involves the electrochemical doping of anions into a conjugated polymer cathode (Type I), cations into a conjugated polymer anode (Type II), or anions and cations into conjugated polymer cathodes and anodes (Type III), while the discharging mechanism is the de-insertion of such ions from the electrodes to produce electricity.

As an example of a cathode electrode, the electrochemical reaction of a fully charged/discharged BF_4^-doped PANI based on a cathode electrode and Li(Al–Li) as an anode can be represented as follows:

$$\text{Anode: Li(Al} - \text{Li)} \leftrightarrows (\text{Al} - \text{Li}) + \text{Li}^+ + \text{e} \tag{10.10}$$

$$\text{Cathode: } [\text{PANI}^m(\text{BF}_4^-)_y]_n + n\text{e} \leftrightarrows [\text{PANI}^m(\text{BF}_4^-)_{m-1}]_n + n\text{BF}_4^- \tag{10.11}$$

where m is the doping level and n is the number of repeat units. The cell works well in both aqueous and nonaqueous electrolytes with a nominal voltage ranging from 3.0 to 4.0 V. When the conjugated polymer uses an anode (cation doping is used to store the energy), it can exhibit a stable nominal voltage at 3.5 V. For an instant, the full chemical reaction of charge storage involving polyacetylene is:

$$\text{Anode: } [(\text{CH})^{-y}\text{Li}_m^+]_n \leftrightarrows m(\text{CH})_n + nm\text{Li}^+ + nm\text{e} \tag{10.12}$$

$$\text{Cathode: TiS}_2 + \text{Li}^+ + \text{e} \leftrightarrows \text{Li}^+(\text{TiS}_2)^- \tag{10.13}$$

Along with PANI and polyacetylene, PPy, polythiophene, and polyphenylene have also been extensively studied for use in LIBs [84–86]. Pioneering studies have proven that the electrochemical performance of conjugated polymers can be improved by increasing the surface area through design of special nanostructures, as confirmed by a comparison between PANI nanotubes and bulk powder. For example, ClO_4^--doped PANI nanotubes exhibited 1.4 times higher performance

Table 10.9 Energy densities of CPNs acting as fully active electrode material for LIBs.

Conjugated polymers	**Dopant**	**Energy density (Wh/kg)**	**Open circuit voltage (V)**	**Current density (mA/cm^2)**	**Coulombic efficiency (%)**	**References**
Polyacetylene	$LiClO_4$	270	3.7	1.0	76.6	[87]
Polyacetylene	$LiClO_4$	250	3.5	—	>95	[88]
Polyacetylene[a]	$LiClO_4$	270	3.4	—	82	[89]
PANI[a]	$LiClO_4$	340	3.6	0.4	98	[90]
PANI[a]	$LiClO_4$	100	4.0	—	100	[91]
PANI	$LiClO_4$	350	3.6	0.5	100	[66]
P_3MT[b]	$LiBF_4$	326	3.3	0.05	96	[92]
PPy	$LiClO_4$	60	3.6	—	—	[93]
PPy	PF_4^-	85	3.9	1.0	92	[94]
PPy	$LiBF_4$	135	2.7	0.1	91	[95]

a) Polymer used as both anode and cathode materials.
b) Poly(3-methylthiophene).

than commercial doped PANI powder. The performances of conjugated polymers as active electrode materials for one or both of the electrodes in LIB studies are summarized in Table 10.9. Although the use of conjugated polymers in LIBs was intensively studied in the 1980s–1990s, it gradually disappeared in later years. Several critical issues exist regarding the use of conjugated polymers as electrodes for LIBs that have prevented their commercialization. Some conjugate polymers, such as polyacetylene, show poor stability in the presence of moisture and oxygen. Spontaneous de-doping of conjugated polymers occurring in electrolytes leads to a decrease in the lifespan of charged batteries. The short shelf life of batteries can be clearly observed through the discharge of a polyacetylene/lithium-ion cell delayed for 16 hours at different constant currents [96]. Increasing the doping level could overcome the poor conductivity of conjugated polymers in their de-doped state to improve the capacity, energy density, and efficiency of batteries. However, the coulombic efficiency dramatically decreased by up to 35% in the case of polyacetylene when increased doping levels were attempted [96]. Recent research has focused more on the use of CPNs as conductive additives, binders, or electrolytes for LIBs to increase the capacity and cyclic stability of the devices. Some researchers have focused on developing novel heterocyclic CPNs to enhance the performance of LIBs.

10.4.2.2 Conjugated Polymers as Protective/Network Layers for LIBs

Although possessing many advantages, problems associated with the utilization of conjugated polymers stem from intractability, conductivity, diffusion, and stability issues. Intrinsically low capacity and cycling stability of conjugated polymers are often considered to be the main issues hindering their use in LIBs. These problems have been addressed by nanoscale combinations of conjugated polymers with redox active inorganic species or carbon materials. The concept behind designing a composite electrode is to immerse redox active materials into a polymer matrix through covalent bonds, ionic bonds, or physical interactions. By adopting this concept, conducing polymer hybrid carbonaceous materials have been developed as electrode material for LIBs, in which carbonaceous materials store charge through non-Faradaic reactions and possess high cycling stability. They can help to maintain conductivity in a nanocomposite when the polymer has been reduced to a non-conductive state. The CNT/PEDOT combination obtained from the "free-standing" method achieved a high discharge capacity of 1050 mAh/g in the first cycle and a stable discharge capacity of 265 mAh/g after 50 cycles (current density of 0.1 mA/cm^2) when used as an anode. A PPy/RGO nanohybrid can deliver a high stable capacity of 200 mAh/g at a high current density of 800 mA/g, which is three times higher than a PPy-based electrode. These hybrid materials may be viable candidates for flexible LIBs. However, the number of high performance conjugated polymer/carbon nanocomposites is low. The research community considers that hybrid conjugated polymers combined with inorganic materials can better enhance the storage performance of a battery.

Conjugated polymers have been used to coat inorganic compounds (Table 10.10), where such combinations are intended to decrease the resistance between the active materials and the current collector. The flexibility of a conjugated polymer can provide good electrical connectivity and protect active inorganic materials from volume expansions, while the capacitance is mainly contributed by the active inorganic materials. This should improve the capacitance and the cyclic and thermal stability of a cell. For example, a major drawback associated with the use of lithium

Table 10.10 Electrochemical performances of conjugated polymer/inorganic nanocomposite based LIBs.

Materials	Electrode	Capacity (mAh/g)	Cycle number	Current density (mA/g)	Coulombic efficiency (%)	References
$NiCo_2O_4$@PPy	Anode	600	100	400	99	[86]
CuO–PPy	Anode	613	45	100	94	[97]
Fe_3O_4@PANI	Anode	1090	50	100	98	[98]
MnO_2@PEDOT	Anode	628	850	1000	95	[99]
LiNi0.8Co0.1Mn0.1O2@PANI	Cathode	151.0	110	1480	88	[100]
$LiNi_{0.5}Mn_{1.5}O_4$@PEDOT	Cathode	123	103	148	97	[101]
MnO_2@PPy	Anode	620	300	30	—	[102]
$Li_{1.2}Ni_{0.2}Mn_{0.6}O_2$–PEDOT	Cathode	147	100	148	77	[103]
MoS_2–PANI	Anode	1207	100	200	89	[104]

iron phosphate as cathode material is its poor capacity owing to its low electrical conductivity and density. It is necessary to use a material that can improve the conductivity and density of $LiFePO_4$; hence, a conjugated polymer can be a suitable candidate. Lepage et al. [105] reported that PEDOT-coated $LiFePO_4$ could provide a capacity similar to the theoretical capacity of $LiFePO_4$ (170 mAh/g). PEDOT plays the role of a conductive additive that facilitates fast electronic transfer between the particles associated with ion diffusion by increasing the surface area and porosity, resulting in the enhanced capacity of the composite electrode. Yang et al. [106] used a PEDOT-encapsulated ordered carbon mesoporous (CMK-3)/sulfur composite to improve the poor stability of the Li–S battery. The well-known rapid capacity fading of the Li–S battery is caused by the large volumetric expansion of sulfur (∼80%) during cycling and the dissolution of intermediate lithium polysulfide into the electrolyte. PEDOT served as an effective encapsulation shell and prevented the dissolution of the active electrode material during cycling (Figure 10.10). With the assistance of conjugated polymer, the discharge capacity of the sulfur electrode was 10% higher than that of the bare counterpart, and the capacity retention increased from ∼60%/100 cycles to ∼85%/100 cycles (Figure 10.10c–e). Following this direction, a PEDOT-coated sulfur nanoparticles-based cathode showed excellent cyclic stability, with initial discharge capacity of 1117 mAh/g and stable capacity of 930 mAh/g after 50 cycles, which is mainly at the low end of the bare sulfur electrode [107]. Furthermore, conjugated polymers may replace conventional insulator binders and conductive additive components, which present problems in future ultrahigh-capacity batteries (such as low conductivity and low or no connectivity due to substantial volume changes during electrochemical processes). A three-dimensional nanostructured PPy gel framework can play a role as both binder material and 3D conductive network, ensuring electron transport to the entire electrode while preventing aggregation of Fe_3O_4 nanoparticles [108]. As a result, a PPy/Fe_3O_4 hydrogel anode electrode achieved the best rate performance and highest specific capacity with good retention after charge/discharge cycling when compared with bare Fe_3O_4 nanoparticles (NPs) and a carbon/Fe_3O_4 hybrid. Based on the same strategy, PEDOT:PSS/silicon nanoparticles composites were developed and were able to store 3685 mAh/g (with current density of 500 mA/g) at the first charge cycle with 75% capacity retention, corresponding to 1950 mAh/g after 100 cycles [109].

Although conjugated polymer-based nanocomposites have garnered a great deal of attention as electrode materials, the role of conjugated polymers is minor (e.g. a conducting additive or network), which is to facilitate ion and electron transport. Recently, novel organic materials with high energy density and good cycling stability have been discovered by different groups, and these studies may lead to the development of ultra-LIBs using fully active polymer electrodes in the near future.

10.4.2.3 Heterocyclic Conjugated Polymer Nanostructures and Their Composites for LIBs

In order to overcome the limitations of conventional conjugated polymers in terms of capacity and power density, growing numbers of researchers have been seeking better-conjugated polymers to enhance the performance of LIBs. In 2012, the Sun

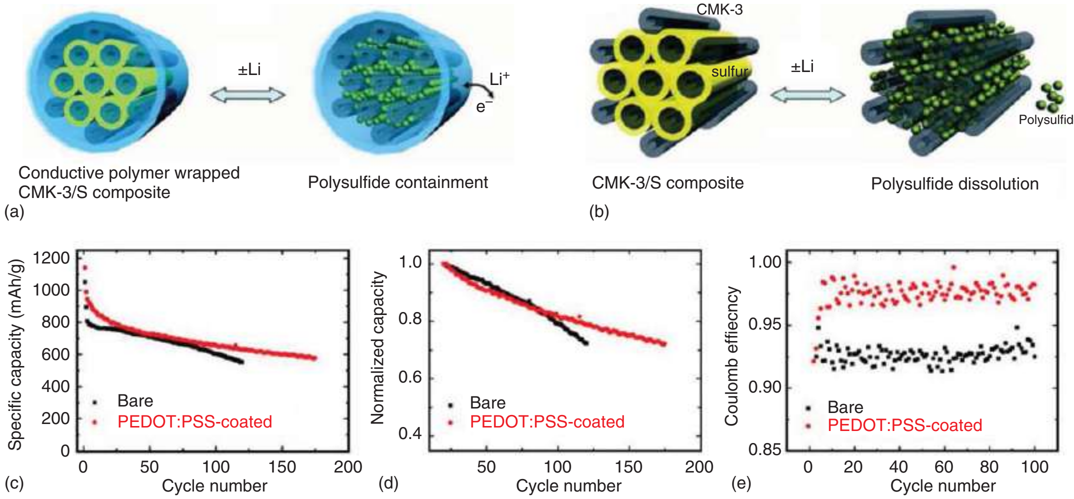

Figure 10.10 (a) Scheme of charge storage mechanisms for PEDOT:PSS-coated CMK-3/sulfur composite and (b) bare CMK-3/S particles. Comparison of specific capacitance (c, d) and coulomb efficiency (e) of bare particles and polymer-coated particles after charge/discharge cycles. Source: Adapted with permission from Yang et al. [106]. Copyright 2011, American Chemical Society.

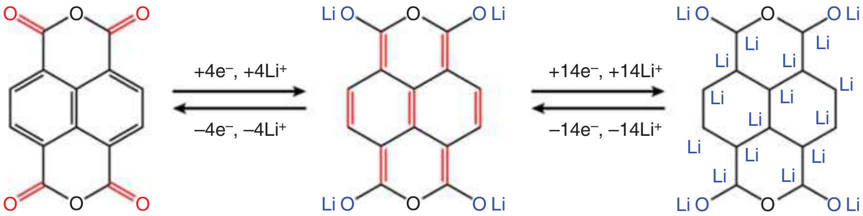

Figure 10.11 Charge storage mechanisms of small molecules containing heteroatom-based LIBs. Source: Based on Luo et al. [111].

group [110] first introduced a unique charge storage mechanism consisting of small conjugated organic materials as the anode material for LIBs by the insertion of Li^+ into unsaturated carbon atoms and atoms with lone pairs of electrons (oxygen and nitrogen) (Figure 10.11). In a particular study, the electrochemical reaction of small molecule 1,4,5,8-naphthalenetetracarboxylic dianhydride (NTCDA) via discharge revealed that each NTCDA can adopt 18 Li^+ ions, corresponding to a high capacity of 1800 mAh/g. Similar behavior was also observed in sodium ion batteries for 3,4,9,10-perylene-tetracarboxylicacid-dianhydride (PTCDA) [111]. The presence of anhydride, carbonyl, or carboxyl groups in conjugate systems can lower the free energy of the lithiation process compared with unsubstituted aromatic compounds [112, 113]. However, the high discharge capacity only occurs at the initial discharge cycle, and the small molecules exhibit poor cyclic stability due to dissolution problems. Taking advantage of these discoveries, a novel organic material named "heterocyclic CPNs" (also known as conjugated ladder polymers) may be the ideal candidates for LIBs to overcome the low conductivity and dissolution problems. Unlike conventional conjugated polymers and small conjugated organic materials, conjugated ladder polymers (CLPs) have a large π-conjugated structure, rich nitrogen, and oxygen heteroatoms, and multi-ring aromatics, which are believed to facilitate redox reactions, fast intrachain charge transport, and reduce any torsional defects. Therefore, nanostructured CLP electrode-based LIBs can exhibit high specific capacity, high-energy density, and cyclic stability.

Poly(benzobisimidazobenzophenanthroline) (BBL) was used earlier to investigate the performance of CLPs in LIBs. BBL nanoparticles were simply prepared by a precipitation method to obtain diameters of approximately 30 and 70 nm. Owing to a multi-aromatic system with large π-conjugated structure and numerous nitrogen and oxygen heteroatoms, the BBL nanoparticles can absorb 44.7 Li^+ ions per unit and therefore exhibit a high initial reversible capacity of 1592 and 1785 mAh/g at room temperature (RT) and 50 °C, respectively, when used as an anode in LIBs [114]. However, the discharge capacity gradually decreased and only achieved 38% and 66% in the next cycle, respectively. The low cyclic stability of BBL may be caused by the poor linking between two large polymer chains during the polymerization. In another study, nanoparticles of polyazaacene (poly(1,6-dihydropyrazino [2,3*g*]quinoxaline-2,3,8-triyl-7-(2*H*)-ylidene-7,8-dimethylidene) (PQL) containing rich numbers of nitrogen atoms was investigated as anode material for LIBs [115]. The prepared PQL nanoparticles with diameter of 40–60 nm improved the electrical conductivity (2.1×10^{-3} S/cm) compared with pristine material (1×10^{-5} S/cm) based on the four-point measurement method. PQL nanoparticles can accept 13.6 Li^+ ions per unit and can achieve a discharge capacity of 1550 mAh/g at a current density of 100 mA/g after 100 cycles. In the search for better stability of CLPs, polydopamine (PDA) nanospheres used as both electrode and binder exhibited excellent electrochemical performance, including a high specific capacity of 1818 mAh/g and excellent cycling stability (1414 mAh/g after 580 cycles with a capacity retention of 93% under 500 mA/g) for LIB applications [116]. The controllable partial oxidization is believed to be the key to balancing the proportion of redox-active carbonyl groups, thus guaranteeing long-term cycling and high capacity of the battery. These studies reveal that CLPs can be excellent materials for commercial polymer-based LIBs in the near future.

Along with CLPs, MCPs (sub-class: COFs) have gained much attention as electrode materials for LIBs over the past few years. In these conjugated polymers, covalent bonds connect atoms to form molecules and further link these molecules to giant covalent structures, which make such polymers valuable for suppressing the dissolution of current organic materials. In addition, the introduction of functionalities (redox-active sites) and π-conjugated backbones into a microporous material allows for improved contact area with the electrolyte, more surface sites available for reversible reactions with Li^+, and shorter Li^+ diffusion pathways, leading to enhanced charge/discharge kinetics and capacity. The use of MCPs in LIBs was first reported by Xu et al. [117] for hexaazatrinaphthalene (HATN) MCP. The charge storage mechanism of a HATN-MCP based cathode electrode and its porous structure are shown in Figure 10.12a. The triquinoxalinylene unit serves as a redox-active component in the lithiation and delithiation process. The electrode stability is enhanced by the covalent network and ion transport is facilitated by the open meso-channels, resulting in a stable capacity of 65–100 mAh/g for a current density of 500–200 mAh/g after 50 cycles. At a high current density of 350 mA/g, Bai et al. [119] reported that N_2-COF (synthesized from 1,3,5-triformylbenzene (TFB) with benzidine and the triazine core amine 4,4′,4″-((1,3,5-triazine-2,4,6-triyl)trianiline)) used as a cathode could generate a high discharge capacity of 600 mAh/g after 500 cycles with 82% capacity retention after the first cycle. Several MCPs, such as PDCzBT, OPTPA, SPTPA, YPTPA, TThPP, and PAT have been designed for anode and cathode electrode applications in LIBs [120, 121]. Remarkably, the PAT[6]-based anode [118] exhibited high reversible capacities of 1770 mAh/g at 200 mA/g and 760 mAh/g at 1 A/g after 400 cycles and maintained a coulombic efficiency of nearly 100% during cycling (Figure 10.12b–e).

Numerous efforts have been made to synthesize new MCPs for LIBs recently, and their electrochemical performances are summarized in Table 10.11. From the performance comparison, it can be seen that MCP-based electrodes could be promising candidates to achieve high-performance organic-based rechargeable batteries. However, MCP-based LIBs have not been commercialized to date. How to

---

[6] Polyanthraquinone-triazine.

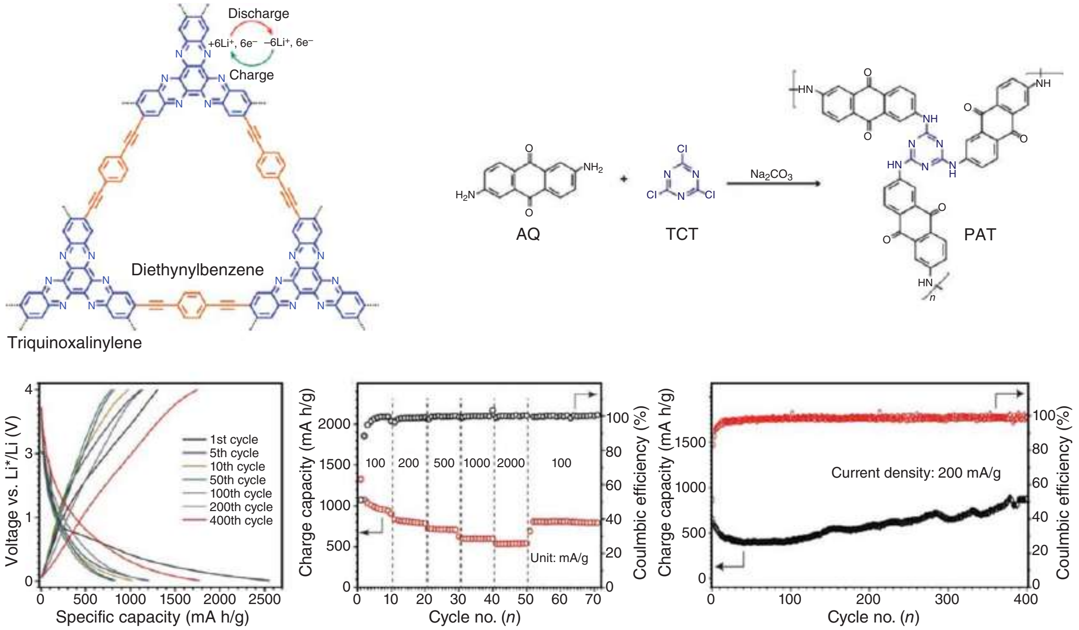

Figure 10.12 (a) Molecular structure and charge storage mechanism of HATN MCP; (b) synthesis procedure of PAT-based CPN, (c) GCD profile at a current density of 200 mA/g, (d) discharge capacity at different current densities, and (e) long-term stability of PAT MCP at a current density of 200 mA/g. Source: Adapted with permission from Kang et al. [118]. Copyright 2018, American Chemical Society.

Table 10.11 Electrochemical performances of a variety of MCP-based LIBs.

MCPs	Electrode	Capacity (mAh/g)	Cycle number	Current density (mA/g)	Coulombic efficiency (%)	References
HATN	Cathode	100	50	200	100	[117]
YPTPA[a)]	Cathode	93	500	2000	95	[120]
Tp-DANT-COF[b)]	Cathode	~79	200	200	95	[122]
PDCzBT[c)]	—	312	400	200	98	[121]
Polyporphyrin	Anode	381	200	1000	99	[123]
Bicarbazole-COF	Anode	236	400	100	99	[124]
P33DT	Anode	663	1000	500	80	[125]
PAT	Anode	1770	200	400	99	[118]

a) Homocoupled polymer from the reaction of N^4,N^4,$N^{4\prime}$,$N^{4\prime}$-tetrakis(4-bromophenyl)biphenyl-4,4′-diamine under Ni(cod)$_2$ and 2,2′-bipyridyl in dimethylformamide (DMF).

b) Synthesized from reaction of 1,3,5-triformylphloroglucinol (TP) and 2,7-diaminobenzo[*lmn*][3,8]phenanthroline-1,3,6,8(2*H*,7*H*)-tetraone.

c) Polymer 4,7-dicarbazyl-[2,1,3]-benzothiadiazole.

achieve both high capacitance and long cycling performance continues to be a major bottleneck in using COFs as the electrode materials in LIBs because of structural defects, low energy level matching, and insufficient device optimization during the charge/discharge process. From this viewpoint, further research into new 2D COFs and gaining ideas and insights from other better-performing materials is highly encouraged.

10.5 Conclusion

A wide range of conjugated polymers has been used to fabricate polymer-based ESDs such as ECs and LIBs. Conjugated polymer offer many advantages to ECs and LIBs, because they are flexible, have high solubility, high electrical conductivity, free-volume, and are environmentally stable. Many conjugated polymers have been used as anode material, and a few conjugated polymers may be applied as cathode materials. The major disadvantages of conjugated polymers when used in ECs and LIBs are poor cycle life, low conductivity in the undoped state, and sensitivity. Although conjugated polymer-based ECs and LIBs are in demand for today's portable electronics, they lack commercial success because of their low stability, high cost, and relatively low power and energy density. By converting bulk conjugated polymers into nanostructures and hybridizing them with other materials, the new nanocomposite or hybrid materials should open new opportunities for high-performance ECs and LIBs. At the same time, exploiting new conjugated polymers and improving current fabrication technologies are also future directions for the successful application of CPN-based electrodes. Thus, further research involving CPNs and their composites should offer great potential opportunities for the construction of the next-generation ESDs over existing ECs and LIBs.

References

1 Bull, S.R. (2001). Renewable energy today and tomorrow. *Proc. IEEE* 89: 1216–1226.

2 Panwar, N.L., Kaushik, S.C., and Kothari, S. (2011). Role of renewable energy sources in environmental protection: a review. *Renewable Sustainable Energy Rev.* 15: 1513–1524.

3 Nguyen, D.N. and Yoon, H. (2016). Recent advances in nanostructured conducting polymers: from synthesis to practical applications. *Polymers* 8: 118.

4 Shi, Y., Peng, L., Ding, Y. et al. (2015). Nanostructured conductive polymers for advanced energy storage. *Chem. Soc. Rev.* 44: 6684–6696.

5 Ghosh, S., Maiyalagan, T., and Basu, R.N. (2016). Nanostructured conducting polymers for energy applications: towards a sustainable platform. *Nanoscale* 8: 6921–6947.

6 Simpson, C. (2011). *Characteristics of Rechargeable Batteries*. Dallas: Texas Instruments Inc.

7 Choi, H. and Yoon, H. (2015). Nanostructured electrode materials for electrochemical capacitor applications. *Nanomaterials (Basel)* 5: 906–936.

8 Zhao, X., Sánchez, B.M., Dobson, P.J., and Grant, P.S. (2011). The role of nanomaterials in redox-based supercapacitors for next generation energy storage devices. *Nanoscale* 3: 839–855.

9 Conway, B.E., Birss, V., and Wojtowicz, J. (1997). The role and utilization of pseudocapacitance for energy storage by supercapacitors. *J. Power Sources* 66: 1–14.

10 Becker, H.I. (1957). Low voltage electrolytic capacitor. US2800616A, filed 14 April 1954.

11 Deschamps, M., Gilbert, E., Azais, P. et al. (2013). Exploring electrolyte organization in supercapacitor electrodes with solid-state NMR. *Nat. Mater.* 12: 351.

12 Griffin, J.M., Forse, A.C., Tsai, W.-Y. et al. (2015). In situ NMR and electrochemical quartz crystal microbalance techniques reveal the structure of the electrical double layer in supercapacitors. *Nat. Mater.* 14: 812.

13 Hou, J., Cao, C., Idrees, F., and Ma, X. (2015). Hierarchical porous nitrogen-doped carbon nanosheets derived from silk for ultrahigh-capacity battery anodes and supercapacitors. *ACS Nano* 9: 2556–2564.

14 Zhang, J., Zhang, X., Zhou, Y. et al. (2014). Nitrogen-doped hierarchical porous carbon nanowhisker ensembles on carbon nanofiber for high-performance supercapacitors. *ACS Sustainable Chem. Eng.* 2: 1525–1533.

15 Phan, T.N., Gong, M.K., Thangavel, R. et al. (2019). Enhanced electrochemical performance for EDLC using ordered mesoporous carbons (CMK-3 and

CMK-8): role of mesopores and mesopore structures. *J. Alloys Compd.* 780: 90–97.

16 Kim, Y., Kim, S., Noh, S. et al. (2018). Single-walled carbon nanotube-mediated physical gelation of binary polymer blends: an efficient route to versatile porous carbon electrode materials. *Chem. Eng. Sci.* 353: 849–857.

17 Kong, H.J., Kim, S., Le, T.-H. et al. (2017). Nanostructured mesophase electrode materials: modulating charge-storage behavior by thermal treatment. *Nanoscale* 9: 17450–17458.

18 Lee, J.-S.M., Briggs, M.E., Hu, C.-C., and Cooper, A.I. (2018). Controlling electric double-layer capacitance and pseudocapacitance in heteroatom-doped carbons derived from hypercrosslinked microporous polymers. *Nano Energy* 46: 277–289.

19 Chen, X.Y., Cheng, L.X., Deng, X. et al. (2014). Generalized conversion of halogen-containing plastic waste into nanoporous carbon by a template carbonization method. *Ind. Eng. Chem. Res.* 53: 6990–6997.

20 Cho, K.T., Lee, S.B., and Lee, J.W. (2014). Facile synthesis of highly electrocapacitive nitrogen-doped graphitic porous carbons. *J. Phys. Chem. C* 118: 9357–9367.

21 Chen, X.Y., Chen, C., Zhang, Z.J., and Xie, D.H. (2013). Nitrogen-doped porous carbon spheres derived from polyacrylamide. *Ind. Eng. Chem. Res.* 52: 12025–12031.

22 Le, T.-H., Kim, Y., and Yoon, H. (2017). Electrical and electrochemical properties of conducting polymers. *Polymers* 9: 150.

23 Arbizzani, C., Mastragostino, M., and Meneghello, L. (1996). Polymer-based redox supercapacitors: a comparative study. *Electrochim. Acta* 41: 21–26.

24 Rudge, A., Davey, J., Raistrick, I. et al. (1994). Conducting polymers as active materials in electrochemical capacitors. *J. Power Sources* 47: 89–107.

25 Ferraris, J.P., Eissa, M.M., Brotherston, I.D., and Loveday, D.C. (1998). Performance evaluation of poly 3-(phenylthiophene) derivatives as active materials for electrochemical capacitor applications. *Chem. Mater.* 10: 3528–3535.

26 Mastragostino, M., Arbizzani, C., Paraventi, R., and Zanelli, A. (2000). Polymer selection and cell design for electric-vehicle supercapacitors. *J. Electrochem. Soc.* 147: 407–412.

27 Fusalba, F., El Mehdi, N., Breau, L., and Bélanger, D. (1999). Physicochemical and electrochemical characterization of polycyclopenta[2,1-*b*;3,4-*b*′]dithiophen-4-one as an active electrode for electrochemical supercapacitors. *Chem. Mater.* 11: 2743–2753.

28 Fusalba, F., Ho, H.A., Breau, L., and Bélanger, D. (2000). Poly(cyano-substituted diheteroareneethylene) as active electrode material for electrochemical supercapacitors. *Chem. Mater.* 12: 2581–2589.

29 Park, H.-W., Kim, T., Huh, J. et al. (2012). Anisotropic growth control of polyaniline nanostructures and their morphology-dependent electrochemical characteristics. *ACS Nano* 6: 7624–7633.

30 Chen, W., Rakhi, R.B., and Alshareef, H.N. (2013). Morphology-dependent enhancement of the pseudocapacitance of template-guided tunable polyaniline nanostructures. *J. Phys. Chem. C* 117: 15009–15019.

31 Ma, Y., Hou, C., Zhang, H. et al. (2017). Morphology-dependent electrochemical supercapacitors in multi-dimensional polyaniline nanostructures. *J. Mater. Chem. A* 5: 14041–14052.

32 Lee, Y., Noh, S., Kim, M.-S. et al. (2016). The effect of nanoparticle packing on capacitive electrode performance. *Nanoscale* 8: 11940–11948.

33 Ahn, K.-J., Lee, Y., Choi, H. et al. (2015). Surfactant-templated synthesis of polypyrrole nanocages as redox mediators for efficient energy storage. *Sci. Rep.* 5: 14097.

34 Shi, Y., Pan, L., Liu, B. et al. (2014). Nanostructured conductive polypyrrole hydrogels as high-performance, flexible supercapacitor electrodes. *J. Mater. Chem. A* 2: 6086–6091.

35 Yao, B., Wang, H., Zhou, Q. et al. (2017). Ultrahigh-conductivity polymer hydrogels with arbitrary structures. *Adv. Mater.* 29: 1700974.

36 Zhou, K., He, Y., Xu, Q. et al. (2018). A hydrogel of ultrathin pure polyaniline nanofibers: oxidant-templating preparation and supercapacitor application. *ACS Nano* 12: 5888–5894.

37 Côté, A.P., Benin, A.I., Ockwig, N.W. et al. (2005). Porous, crystalline, covalent organic frameworks. *Science* 310: 1166–1170.

38 Kou, Y., Xu, Y., Guo, Z., and Jiang, D. (2011). Supercapacitive energy storage and electric power supply using an aza-fused π-conjugated microporous framework. *Angew. Chem. Int. Ed.* 50: 8753–8757.

39 DeBlase, C.R., Silberstein, K.E., Truong, T.-T. et al. (2013). β-Ketoenamine-linked covalent organic frameworks capable of pseudocapacitive energy storage. *J. Am. Chem. Soc.* 135: 16821–16824.

40 Li, X.-C., Zhang, Y., Wang, C.-Y. et al. (2017). Redox-active triazatruxene-based conjugated microporous polymers for high-performance supercapacitors. *Chem. Sci.* 8: 2959–2965.

41 Han, Y. and Dai, L. (2019). Conducting polymers for flexible supercapacitors. *Macromol. Chem. Phys.* 220: 1800355.

42 Jabeen, N., Xia, Q., Yang, M., and Xia, H. (2016). Unique core–shell nanorod arrays with polyaniline deposited into mesoporous $NiCo_2O_4$ support for high-performance supercapacitor electrodes. *ACS Appl. Mater. Interfaces* 8: 6093–6100.

43 Zhou, C., Zhang, Y., Li, Y., and Liu, J. (2013). Construction of high-capacitance 3D CoO@polypyrrole nanowire array electrode for aqueous asymmetric supercapacitor. *Nano Lett.* 13: 2078–2085.

44 Kumar, V. and Lee, P.S. (2015). Redox active polyaniline-h-MoO_3 hollow nanorods for improved pseudocapacitive performance. *J. Phys. Chem. C* 119: 9041–9049.

45 Lee, J.E., Park, S.J., Kwon, O.S. et al. (2014). Systematic investigation on charge storage behaviour of multidimensional poly(3,4-ethylenedioxythiophene) nanostructures. *RSC Adv.* 4: 37529–37535.

46 Xu, X., Tang, J., Qian, H. et al. (2017). Three-dimensional networked metal-organic frameworks with conductive polypyrrole tubes for flexible supercapacitors. *ACS Appl. Mater. Interfaces* 9: 38737–38744.

47 Prasanna, B.P., Avadhani, D.N., Raghu, M.S., and Yogesh, K.K. (2017). Synthesis of polyaniline/α-Fe_2O_3 nanocomposite electrode material for supercapacitor applications. *Mater. Today Commun.* 12: 72–78.

48 Jaidev, Jafri, R.I., Mishra, A.K., and Ramaprabhu, S. (2011). Polyaniline–MnO_2 nanotube hybrid nanocomposite as supercapacitor electrode material in acidic electrolyte. *J. Mater. Chem.* 21: 17601–17605.

49 Patil, D.S., Pawar, S.A., and Shin, J.C. (2018). Silver decorated PEDOT:PSS wrapped MnO_2 nanowires for electrochemical supercapacitor applications. *J. Ind. Eng. Chem.* 62: 166–175.

50 Alamro, T. and Ram, M.K. (2017). Polyethylenedioxythiophene and molybdenum disulfide nanocomposite electrodes for supercapacitor applications. *Electrochim. Acta* 235: 623–631.

51 Ren, L., Zhang, G., Yan, Z. et al. (2015). Three-dimensional tubular MOS_2/PANI hybrid electrode for high rate performance supercapacitor. *ACS Appl. Mater. Interfaces* 7: 28294–28302.

52 Zhuzhelskii, D.V., Tolstopjatova, E.G., Eliseeva, S.N. et al. (2019). Electrochemical properties of PEDOT/WO_3 composite films for high performance supercapacitor application. *Electrochim. Acta* 299: 182–190.

53 Nallappan, M. and Gopalan, M. (2018). Fabrication of CeO_2/PANI composites for high energy density supercapacitors. *Mater. Res. Bull.* 106: 357–364.

54 Majumder, M., Choudhary, R.B., Thakur, A.K., and Karbhal, I. (2017). Impact of rare-earth metal oxide (Eu_2O_3) on the electrochemical properties of a polypyrrole/CuO polymeric composite for supercapacitor applications. *RSC Adv.* 7: 20037–20048.

55 Guo, D., Zhang, M., Chen, Z., and Liu, X. (2017). Hierarchical Co_3O_4@PPy core-shell composite nanowires for supercapacitors with enhanced electrochemical performance. *Mater. Res. Bull.* 96: 463–470.

56 Arjomandi, J., Lee, J.Y., Movafagh, R. et al. (2018). Polyaniline/aluminum and iron oxide nanocomposites supercapacitor electrodes with high specific capacitance and surface area. *J. Electroanal. Chem.* 810: 100–108.

57 Li, Q., Horn, M., Wang, Y. et al. (2019). A review of supercapacitors based on graphene and redox-active organic materials. *Materials (Basel)* 12: 703.

58 Borenstein, A., Hanna, O., Attias, R. et al. (2017). Carbon-based composite materials for supercapacitor electrodes: a review. *J. Mater. Chem. A* 5: 12653–12672.

59 Bryan, A.M., Santino, L.M., Lu, Y. et al. (2016). Conducting polymers for pseudocapacitive energy storage. *Chem. Mater.* 28: 5989–5998.

60 Sonia, T.S., Mini, P.A., Nandhini, R. et al. (2013). Composite supercapacitor electrodes made of activated carbon/PEDOT:PSS and activated carbon/doped PEDOT. *Bull. Mater. Sci.* 36: 547–551.

61 Selvakumar, M. and Krishna Bhat, D. (2008). Activated carbon-polyethylenedioxythiophene composite electrodes for symmetrical supercapacitors. *J. Appl. Polym. Sci.* 107: 2165–2170.

62 Sidhu, N.K. and Rastogi, A.C. (2016). Electrochemical performance of supercapacitors based on carbon nanofoam composite and microporous poly(3,4-ethylenedioxythiophene) thin film asymmetric electrodes. *Mater. Chem. Phys.* 176: 75–86.

63 Tufani, A. and Ince, G.O. (2015). Permeability of small molecules through vapor deposited polymer membranes. *J. Appl. Polym. Sci.* 132: 42453.

64 Huang, Y., Kormakov, S., He, X. et al. (2019). Conductive polymer composites from renewable resources: an overview of preparation, properties, and applications. *Polymers* 11: 187.

65 Yan, X.-b., Han, Z.-j., Yang, Y., and Tay, B.-k. (2007). Fabrication of carbon nanotube−polyaniline composites via electrostatic adsorption in aqueous colloids. *J. Phys. Chem. C* 111: 4125–4131.

66 Niu, Z., Luan, P., Shao, Q. et al. (2012). A "skeleton/skin" strategy for preparing ultrathin free-standing single-walled carbon nanotube/polyaniline films for high performance supercapacitor electrodes. *Energy Environ. Sci.* 5: 8726–8733.

67 Jang, J., Bae, J., Choi, M., and Yoon, S.-H. (2005). Fabrication and characterization of polyaniline coated carbon nanofiber for supercapacitor. *Carbon* 43: 2730–2736.

68 Du, X., Liu, H.-Y., Cai, G. et al. (2012). Use of facile mechanochemical method to functionalize carbon nanofibers with nanostructured polyaniline and their electrochemical capacitance. *Nanoscale Res. Lett.* 7: 111.

69 Kotal, M., Thakur, A.K., and Bhowmick, A.K. (2013). Polyaniline–carbon nanofiber composite by a chemical grafting approach and its supercapacitor application. *ACS Appl. Mater. Interfaces* 5: 8374–8386.

70 Choi, H., Ahn, K.-J., Lee, Y. et al. (2015). Free-standing, multilayered graphene/polyaniline-glue/graphene nanostructures for flexible, solid-state electrochemical capacitor application. *Adv. Mater. Interfaces* 2: 1500117.

71 Yu, P., Li, Y., Zhao, X. et al. (2014). Graphene-wrapped polyaniline nanowire arrays on nitrogen-doped carbon fabric as novel flexible hybrid electrode materials for high-performance supercapacitor. *Langmuir* 30: 5306–5313.

72 Chu, H.-J., Lee, C.-Y., and Tai, N.-H. (2016). Three-dimensional porous polyaniline/graphene-coated activated carbon fiber electrodes for supercapacitors. *RSC Adv.* 6: 111465–111471.

73 Zhou, Y., Hu, X., Shang, Y. et al. (2016). Highly flexible all-solid-state supercapacitors based on carbon nanotube/polypyrrole composite films and fibers. *RSC Adv.* 6: 62062–62070.

74 Anothumakkool, B., Torris, A.T.A., Bhange, S.N. et al. (2014). Electrodeposited polyethylenedioxythiophene with infiltrated gel electrolyte interface: a close contest of an all-solid-state supercapacitor with its liquid-state counterpart. *Nanoscale* 6: 5944–5952.

75 Rajesh, M., Raj, C.J., Manikandan, R. et al. (2017). A high performance PEDOT/PEDOT symmetric supercapacitor by facile in-situ hydrothermal polymerization of PEDOT nanostructures on flexible carbon fibre cloth electrodes. *Mater. Today Energy* 6: 96–104.

76 Gupta, S. and Price, C. (2016). Investigating graphene/conducting polymer hybrid layered composites as pseudocapacitors: interplay of heterogeneous electron transfer, electric double layers and mechanical stability. *Composites, Part B* 105: 46–59.

77 Huang, Z.-H., Song, Y., Xu, X.-X., and Liu, X.-X. (2015). Ordered polypyrrole nanowire arrays grown on a carbon cloth substrate for a high-performance pseudocapacitor electrode. *ACS Appl. Mater. Interfaces* 7: 25506–25513.

78 Nabilah Azman, N.H., Lim, H.N., and Sulaiman, Y. (2016). Effect of electropolymerization potential on the preparation of PEDOT/graphene oxide hybrid material for supercapacitor application. *Electrochim. Acta* 188: 785–792.

79 Ishaq, S., Moussa, M., Kanwal, F. et al. (2019). Facile synthesis of ternary graphene nanocomposites with doped metal oxide and conductive polymers as electrode materials for high performance supercapacitors. *Sci. Rep.* 9: 5974.

80 Patil, D.S., Pawar, S.A., Shin, J.C., and Kim, H.J. (2018). MnO_2-graphene oxide-PEDOT:PSS nanocomposite for an electrochemical supercapacitor. *J. Korean Phys. Soc.* 72: 952–958.

81 Boukamp, B.A., Lesh, G.C., and Huggins, R.A. (1981). All-solid lithium electrodes with mixed-conductor matrix. *J. Electrochem. Soc.* 128: 725–729.

82 McDowell, M.T., Woo Lee, S., Wang, C., and Cui, Y. (2012). The effect of metallic coatings and crystallinity on the volume expansion of silicon during electrochemical lithiation/delithiation. *Nano Energy* 1: 401–410.

83 Novák, P., Müller, K., Santhanam, K.S.V., and Haas, O. (1997). Electrochemically active polymers for rechargeable batteries. *Chem. Rev.* 97: 207–282.

84 Sengodu, P. and Deshmukh, A.D. (2015). Conducting polymers and their inorganic composites for advanced Li-ion batteries: a review. *RSC Adv.* 5: 42109–42130.

85 Long, B., Qiao, Z., Zhang, J. et al. (2019). Polypyrrole-encapsulated amorphous Bi_2S_3 hollow sphere for long life sodium ion batteries and lithium–sulfur batteries. *J. Mater. Chem. A* 7: 11370–11378.

86 Luo, Y., Guo, R., Li, T. et al. (2019). Conductive polypyrrole coated hollow $NiCo_2O_4$ microspheres as anode material with improved pseudocapacitive contribution and enhanced conductivity for lithium-ion batteries. *ChemElectroChem* 6: 690–699.

87 Shinozaki, K., Tomizuka, Y., and Nojiri, A. (1984). Performance of lithium/polyacetylene cell. *Jpn. J. Appl. Phys.* 23: L892–L894.

88 Chien, J.C.W. and Schlenoff, J.B. (1984). Limiting battery performance parameters for polyacetylene. *Nature* 311: 362–363.

89 Nagatomo, T., Ichikawa, C., and Omoto, O. (1987). All-plastic batteries with polyacetylene electrodes. *J. Electrochem. Soc.* 134: 305–308.

90 Taguchi, S. and Tanaka, T. (1987). Fibrous polyaniline as positive active material in lithium secondary batteries. *J. Power Sources* 20: 249–252.

91 Morita, M., Miyazaki, S., Ishikawa, M. et al. (1995). Layered polyaniline composites with cation-exchanging properties for positive electrodes of rechargeable lithium batteries. *J. Electrochem. Soc.* 142: L3–L5.

92 Nagatomo, T. and Omoto, O. (1988). Poly(3-methylthiophene): a stable cathode-active material for secondary batteries. *J. Electrochem. Soc.* 135: 2124–2128.

93 Bittihn, R., Ely, G., Woeffler, F. et al. (1987). Polypyrrole as an electrode material for secondary lithium cells. *Makromol. Chem. Macromol. Symp.* 8: 51–59.

94 Naoi, K., Sakai, H., Ogano, S., and Osaka, T. (1987). Application of electrochemically formed polypyrrole in lithium secondary batteries: analysis of anion diffusion process. *J. Power Sources* 20: 237–242.

95 Yamamoto, T., Zama, M., Hishinuma, M., and Yamamoto, A. (1987). Lithium secondary cells using LiX (X = ClO_4, BF_4) as electrolyte and poly(2,5-pyrrolylene) and poly(2,5-thienylene) as materials for positive electrodes. *J. Appl. Electrochem.* 17: 607–612.

96 Maxfield, M., Mu, S.L., and MacDiarmid, A.G. (1985). Energy density, power density, and polarization studies of the partially oxidized ("p-doped") polyacetylene cathode. *J. Electrochem. Soc.* 132: 838–841.

97 Yin, Z., Fan, W., Ding, Y. et al. (2015). Shell structure control of PPy-modified CuO composite nanoleaves for lithium batteries with improved cyclic performance. *ACS Sustainable Chem. Eng.* 3: 507–517.

98 Wang, X., Liu, Y., Han, H. et al. (2017). Polyaniline coated Fe_3O_4 hollow nanospheres as anode materials for lithium ion batteries. *Sustainable Energy Fuels* 1: 915–922.

99 Chen, X., Cao, Z., Xing, L. et al. (2017). Improved Li-storage performance with PEDOT-decorated MnO_2 nanoboxes. *Nanoscale* 9: 18467–18473.

100 Cao, Y., Qi, X., Hu, K. et al. (2018). Conductive polymers encapsulation to enhance electrochemical performance of Ni-rich cathode materials for Li-ion batteries. *ACS Appl. Mater. Interfaces* 10: 18270–18280.

101 Kwon, Y., Lee, Y., Kim, S.-O. et al. (2018). Conducting polymer coating on a high-voltage cathode based on soft chemistry approach toward improving battery performance. *ACS Appl. Mater. Interfaces* 10: 29457–29466.

102 Feng, L., Zhang, Y., Wang, R. et al. (2017). Preparation of PPy-coated MnO_2 hybrid micromaterials and their improved cyclic performance as anode for lithium-ion batteries. *Nanoscale Res. Lett.* 12: 518.

103 Wu, F., Liu, J., Li, L. et al. (2016). Surface modification of Li-rich cathode materials for lithium-ion batteries with a PEDOT:PSS conducting polymer. *ACS Appl. Mater. Interfaces* 8: 23095–23104.

104 Wang, H., Jiang, H., Hu, Y. et al. (2017). 2D MoS_2/polyaniline heterostructures with enlarged interlayer spacing for superior lithium and sodium storage. *J. Mater. Chem. A* 5: 5383–5389.

105 Lepage, D., Michot, C., Liang, G. et al. (2011). A soft chemistry approach to coating of $LiFePO_4$ with a conducting polymer. *Angew. Chem. Int. Ed.* 50: 6884–6887.

106 Yang, Y., Yu, G., Cha, J.J. et al. (2011). Improving the performance of lithium–sulfur batteries by conductive polymer coating. *ACS Nano* 5: 9187–9193.

107 Chen, H., Dong, W., Ge, J. et al. (2013). Ultrafine sulfur nanoparticles in conducting polymer shell as cathode materials for high performance lithium/sulfur batteries. *Sci. Rep.* 3: 1910–1910.

108 Shi, Y., Zhang, J., Bruck, A.M. et al. (2017). A tunable 3D nanostructured conductive gel framework electrode for high-performance lithium ion batteries. *Adv. Mater.* 29: 1603922.

109 Higgins, T.M., Park, S.-H., King, P.J. et al. (2016). A commercial conducting polymer as both binder and conductive additive for silicon nanoparticle-based lithium-ion battery negative electrodes. *ACS Nano* 10: 3702–3713.

110 Han, X., Qing, G., Sun, J., and Sun, T. (2012). How many lithium ions can be inserted onto fused C_6 aromatic ring systems? *Angew. Chem. Int. Ed.* 51: 5147–5151.

111 Luo, W., Allen, M., Raju, V., and Ji, X. (2014). An organic pigment as a high-performance cathode for sodium-ion batteries. *Adv. Energy Mater.* 4: 1400554.

112 Peng, C., Ning, G.-H., Su, J. et al. (2017). Reversible multi-electron redox chemistry of π-conjugated N-containing heteroaromatic molecule-based organic cathodes. *Nat. Energy* 2: 17074.

113 Renault, S., Oltean, V.A., Araujo, C.M. et al. (2016). Superlithiation of organic electrode materials: the case of dilithium benzenedipropiolate. *Chem. Mater.* 28: 1920–1926.

114 Wu, J., Rui, X., Wang, C. et al. (2015). Nanostructured conjugated ladder polymers for stable and fast lithium storage anodes with high-capacity. *Adv. Energy Mater.* 5: 1402189.

115 Wu, J., Rui, X., Long, G. et al. (2015). Pushing up lithium storage through nanostructured polyazaacene analogues as anode. *Angew. Chem. Int. Ed.* 127: 7462–7466.

116 Sun, T., Li, Z.-j., Wang, H.-g. et al. (2016). A biodegradable polydopamine-derived electrode material for high-capacity and long-life lithium-ion and sodium-ion batteries. *Angew. Chem. Int. Ed.* 55: 10662–10666.

117 Xu, F., Chen, X., Tang, Z. et al. (2014). Redox-active conjugated microporous polymers: a new organic platform for highly efficient energy storage. *Chem. Commun.* 50: 4788–4790.

118 Kang, H., Liu, H., Li, C. et al. (2018). Polyanthraquinone-triazine – a promising anode material for high-energy lithium-ion batteries. *ACS Appl. Mater. Interfaces* 10: 37023–37030.

119 Bai, L., Gao, Q., and Zhao, Y. (2016). Two fully conjugated covalent organic frameworks as anode materials for lithium ion batteries. *J. Mater. Chem. A* 4: 14106–14110.

120 Zhang, C., Yang, X., Ren, W. et al. (2016). Microporous organic polymer-based lithium ion batteries with improved rate performance and energy density. *J. Power Sources* 317: 49–56.

121 Zhang, S., Huang, W., Hu, P. et al. (2015). Conjugated microporous polymers with excellent electrochemical performance for lithium and sodium storage. *J. Mater. Chem. A* 3: 1896–1901.

122 Yang, D.-H., Yao, Z.-Q., Wu, D. et al. (2016). Structure-modulated crystalline covalent organic frameworks as high-rate cathodes for Li-ion batteries. *J. Mater. Chem. A* 4: 18621–18627.

123 Yang, H., Zhang, S., Han, L. et al. (2016). High conductive two-dimensional covalent organic framework for lithium storage with large capacity. *ACS Appl. Mater. Interfaces* 8: 5366–5375.

124 Feng, S., Xu, H., Zhang, C. et al. (2017). Bicarbazole-based redox-active covalent organic frameworks for ultrahigh-performance energy storage. *Chem. Commun.* 53: 11334–11337.

125 Zhang, C., He, Y., Mu, P. et al. (2018). Toward high performance thiophene-containing conjugated microporous polymer anodes for lithium-ion batteries through structure design. *Adv. Funct. Mater.* 28: 1705432.

11

Conjugated Polymer Based Nanocomposites as Electrode Materials

Saptarshi Dhibar, Puspendu Das, Sanjoy Mondal, Utpal Rana, and Sudip Malik

Indian Association for the Cultivation of Science, School of Applied and Interdisciplinary Sciences, 2A & 2B
Raja S. C. Mullick Road, Kolkata, Jadavpur 700032, India

11.1 Introduction

Since 1976, the discovery of polyacetylene masterminded by Heeger, MacDiarmid, and Shirakawa created an important breakthrough in the class of π-conjugated materials known as conducting organic polymers [1]. In this class of polymer, conjugations arising from the alternating C–C single as well as double the π-electron are successfully delocalized along polymer backbone, leading to unique physical and chemical properties. Conjugated polymers (CPs) have become a fascinating area of research due to their very unique characteristic of being organic materials with electrical conductivity. Typical examples of CPs are polyacetylene, polypyrrole (PPy), polythiophene (PTh), polyaniline (PANI), polyfuorene, polycarbazole, so on [2–4]. Nowadays these CPs (Figure 11.1) have attracted more research interests in various application oriented field, and numerous research works have already been done. Several works are still going on the optimization of processing parameters as well as the fabrication of devices based on this CPs. In the year 2000, the Noble Prize in Chemistry was awarded for the great work on conducting polymers. Presently, it is essential to develop an alternative renewable energy source in modern society because of the rising demand for energy storage as the rapid consumption of fossil fuel and global warming problems. Therefore, energy storage turns into a massive challenge to the major world power and scientific societies. Generally, in nature most of the sources of renewable energies are irregular and for this reason it is urgently necessitated the development of alternative energy storage technologies. Rechargeable batteries have outstanding energy performance, however, owing to their low power performances, it limits their utilizations in various power demanding applications. Alternatively, electrochemical capacitors (called as ultracapacitors or supercapacitors) are playing a significant role in different energy storage technologies because of their superior electrochemical behaviors, like long cycle life, higher power density than batteries, as well as moderate energy density. In the current chapter, we are mainly focused to the utilization of CPs or

Conjugated Polymer Nanostructures for Energy Conversion and Storage Applications,
First Edition. Edited by Srabanti Ghosh.

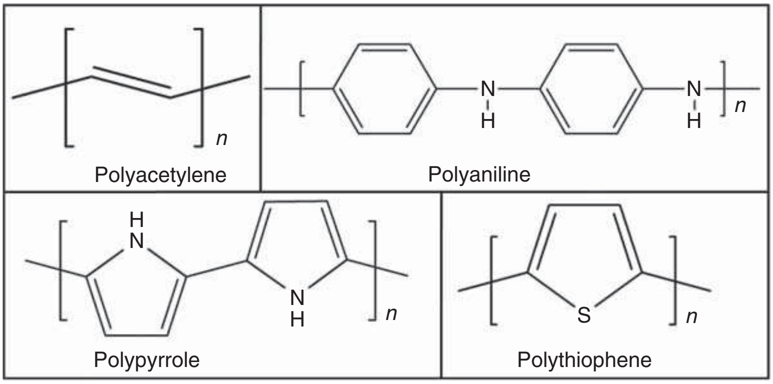

Figure 11.1 Different chemical structures of conjugated polymers.

its composites as electrode material for electrochemical capacitors, which are now frontier research areas in the field of material science.

11.1.1 Polypyrrole

PPy is the most studied CP because of their high electrical conductivities, enhanced thermal stabilities, outstanding chemical stabilities, easy synthesis procedure, and also cost effectiveness. Due to the superior property, PPy is used as gas sensors, biosensors, anti-electrostatic coating, microactuators, electrochromic windows, functional membranes, and radar absorbing materials. [5] On the other hand, PPy and their other different nano-architectures showed the unique electrical as well as electrochemical properties that make them promising candidate for the development of various types of electronic devices [6, 7].

PPy has the resonance structures which appear in the aromatic or quinoid forms. The CPs is only conducting when it is in oxidized form and in the neutral state these polymers are behaving like insulators. The charge associated with the oxidized state is usually delocalized over numerous pyrrole unites and can create a radical cation, i.e. polaron or a dication, i.e. bipolaron. Generally, the physical form of PPy is powder resulting from chemical polymerization whereas an insoluble film was obtained resulting from electro-polymerization. Over the past few years, PPy has been used as the major component for the development of electrode materials for supercapacitor.

11.1.2 Polyaniline

PANI is a conjugated polymer of the semi-flexible polymer family. It is discovered in the early of 1980s as “aniline black” by oxidation of aniline [8–10]. Its conducting nature arises from the delocalization of π-electron throughout the conjugated polymer chain, which is enhanced to the great extent by mixing with the external chemicals (doping) [11, 12]. In general, conductivity is the transfer of electron from valence band higher occupied molecular orbital (HOMO) to conduction band lower unoccupied molecular orbaital (LUMO). Doping generates several intermediate electronic states in between valence and conduction band, as a result the electron moves easily from the one state to another state and higher conducting state achieve [13, 14]. In general, PANI chain exists in three states based on their oxidation forms; each state has different colors, stabilities, and conductivities. They are known as leucoemeraldine, emeraldine, and pernigraniline. A fully reduced (only benzenoid) form is known as leucoemeraldine, partially reduced and partially oxidized as emeraldine and fully oxidized as pernigraniline state [15, 16]. The conductivity of emeraldine state is easily changed by doping and de-doping procedure. Doping by acid enhances conductivity several times and de-doping by base reduces it reversibly [17]. Among three forms emeraldine is significantly useful due to the stability and conducting nature. Versatile conductivity and high stability make this polymer potential useful in various electronic devices like chemical sensors, light emitting diodes, organic field effect transistors, electromagnetic interference shielding, antistatic materials, sensing materials, and secondary batteries [18–21].

There are several methods that have employed for the synthesis of PANI such as chemical synthesis, electrochemical synthesis, vapor-phase deposition (VDP) technique, enzyme catalyzed polymerization, and mechano-chemical method. However, the most common and popular methods for the synthesis of PANI are chemical and electrochemical procedures. The uncommon methods such as enzyme-catalyzed polymerization, photo-chemical, and mechano-chemical polymerization method are also employed in some instances. In the case of chemical synthesis procedure monomer is oxidized by oxidants (such as $FeCl_3$, ammonium persulfate $(NH_4)_2S_2O_8$, $KMnO_4$, $HAuCl_4$, etc.) is utilized at low temperature. A schematic representation for the synthesis of PANI via chemical synthesis technique is illustrated in Figure 11.2.

In the case of electrochemical polymerization techniques, monomer is oxidized by applying a potential voltage and it allows for the oxidation of monomer, followed by polymerization and finally electrodeposited onto the substrate.

11.1.3 Polythiophene

Polythiophene (PTh) or poly(3-alkylthiophene) (P3AT) is an important class of organic polymer owing to the high environmental stability, easy structural modification, and solution processability. Thiophene based polymers (PThs or P3ATs) become more demanding in researcher mind for device applications, particularly the field of photovoltaics or solar cells [22–24]. The band gaps as well as the optical properties of the thiophene based films are significantly tuned by changing the morphology as well as the geometry of the oligomer chains.

The optical absorption for PTh from π–π^* transitions lies in the visible region as shown schematically in Figure 11.3. However, after removed an electron from PTh chain forms a polaron, i.e. a positive charge PTh chains. In this condition, two polaron states, specifically P1 and P2, take place in the mid-gap area among the π–π^* bands. The induction of P1 and P2 states effects in new optical transitions in the infrared region related to the two new states. This behavior guides to optical

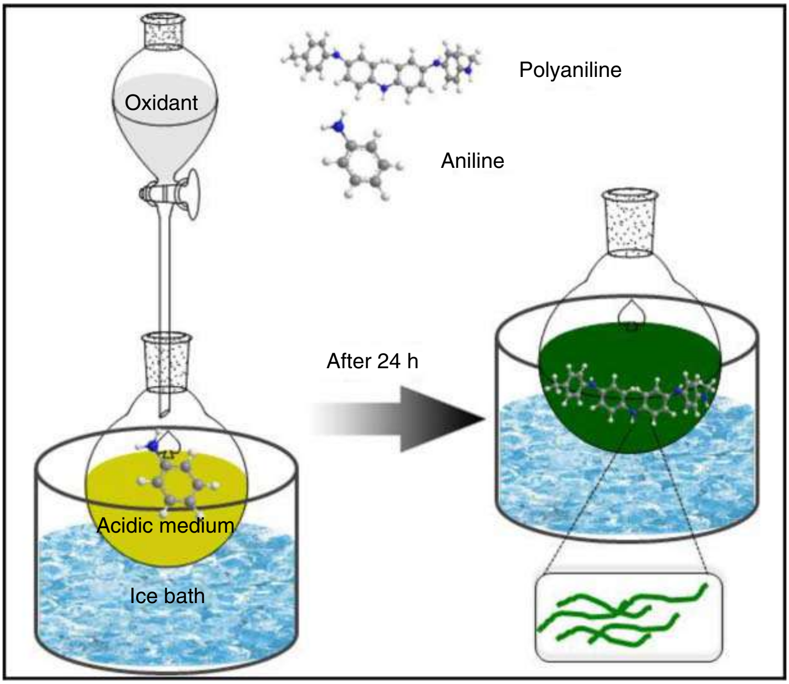

Figure 11.2 Schematic representation of the synthesis of PANI via chemical synthesis procedure.

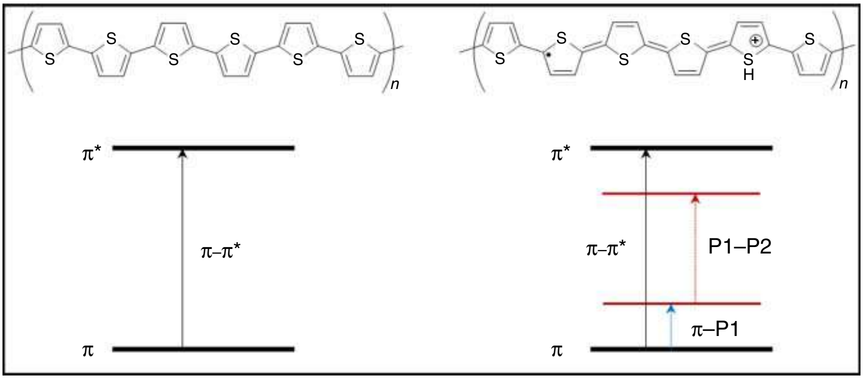

Figure 11.3 Schematic diagram of polythiophene chain undoped and doped with corresponding energy diagrams for π–π* transitions. Source: Koyama et al. [25]. Copyright 2014, ACS Publications.

transparency in the visible spectral region [26], which can also be demonstrated by analyzing the absorption spectra of the pristine as well as doped the polythiophene.

PTh and its derivatives are synthesized by the help of electro-polymerization techniques as well as via oxidative polymerization techniques. In electro-polymerization techniques, a solution containing PTh or its derivatives and an electrolyte make a conductive PTh or its derivatives film on the anode. As the polymer does not require being purified as well as isolated, that's why, electro-polymerization technique is suitable option. Though, it may generate polymers having undesirable alpha-beta linkages and varying degrees of regioregularity. Initially, the oxidation of PTh monomer develops a radical cation, which then pairs with another monomer of PTh to generate a dimer of radical cation.

11.2 Conducting Polymer Based Electrode Materials

Over the last few years, various CPs and their nanostructures along with their derivatives have been considered as the supercapacitor electrode materials [27]. Supercapacitor also known as ultracapacitor is a kind of capacitor that can store a huge volume of energy as compared with electrolytic capacitors. It is most preferred as compared with batteries because of its fast charging as well as fast delivery of charge. Depending on their charge storage mechanisms, supercapacitors are divided into two types; one is the electrochemical double layer capacitor (EDLC) that is generally based on carbonaceous materials having high surface area like, graphene, graphene oxide, and carbon nanotubes (CNTs). It utilizes capacitance occurring from the charge separation taken place at the electrode/electrolyte interface. Another one is the pseudocapacitor that is mainly generated from transition metal oxides or sulfides and conjugated polymers. The pseudocapacitance behavior is arising from the redox reaction (Faradaic process) occurred at the electrode surface. As the reversible electrochemical doping–de-doping is possible for the CPs, these are lucrative for the electrode materials of pseudocapacitor. The pseudocapacitor materials generally store the large amount of capacitance per gram as compared with EDLC materials. CPs show pseudocapacitor behavior via doping and de-doping process of the polymer backbone and it affects in the intercalation and de-intercalation of electrolyte ions inside the CP electrode to sustain the charge neutrality [28]. This charge storage mechanism permits CPs (mainly, PPy and PANI) to achieve better capacitance properties as compared with metal oxides (also acts as a pseudocapacitor materials) [29]. CPs are considered as the most important component for the fabrication of supercapacitors because of their low cost, easy synthesis procedure, very high electrical conductivity, and environmental stability [30–32]. Apart from that, their good mechanical properties allow supercapacitors of flexible, light weight, and stretchable that utilize many novel technologies like roll-up displays, wearable electronics, along with in bio-implantable devices [33, 34]. Due to these enormous advantages, researchers are interested for the development of conducting polymer based electrode materials. Though, the cyclic stability of CPs (pseudocapacitor materials) is low as compared with EDLC materials due to the repeated ion exchanges in the polymer matrix during the electrochemical cycles that take place to change the structural conformation of the CPs. On the other hand, the EDLC materials show the superior cyclic stability. Therefore, to develop advanced electrode materials, researchers are fabricated the hybrid type of materials (combination of pseudocapacitor materials along with EDLC materials), which can exhibit outstanding specific capacitance as well as superior cyclic stability [35]. Onwards, the discussion will proceed mainly with (i) nano-architectures of CPs (nanoparticles, nanofibers, nanowires, and nanotubes, etc.), (ii) CP based electrode materials, and (iii) CP based nanocomposites (mainly with CNT and Graphene) as electrode materials. Graphene (Gr) is considered as an attractive electrode material for electrochemical energy storage device because of its higher electrical conductivity as well as superior accessible surface area [36]. Until now, many researchers have tried to develop on Gr-CPs based hybrid nanocomposites for the electrode materials.

Generally, by evaluating the cyclic voltammetry data, the capacitive effect can be characterized with the help of following equation [37]:

$$i = av^{b} \tag{11.1}$$

where i represents the current in Ampere (A), v is the scan rate (mV/s), and a and b are variable parameters. By the slop of the plot of log (i) vs. log (v), the b-values are calculated. It is well known that when the b value is 0.5 it specifies diffusion controlled faradaic intercalation process and shows a battery behavior, where the current is proportional to the square root of the scan rate, according to following equation [37]:

$$i = nFAC * D^{1/2}v^{1/2}\,(\alpha nF/RT)^{1/2}\,\pi^{1/2}\,\chi(bt) \tag{11.2}$$

In which n stands for number of electrons necessitate in the reaction, F represents the Faraday constant, A stands for the surface area of the electrode material, C^* signifies the surface concentration, D represents the chemical diffusion coefficient, α symbolized for transfer coefficient, and R, T, and (bt) represent the molar gas constant, temperature, and normalized current, respectively.

Calculation of specific capacitance value is the key component of any electrode materials. Therefore, various types of equations have been used for the calculation of specific capacitance by different electrochemical techniques such as galvanostatic charge-discharge (GCD), cyclic voltammetry (CV), and electrochemical impedance spectroscopy (EIS). From the cyclic voltammogram, specific capacitance can be calculated from the following equation:

$$c = \frac{\int_{V_1}^{V_2} i(V)\mathrm{d}V}{(V_2 - V_1)vm} \tag{11.3}$$

where the numerator part of the Eq. (11.3) indicates the total charge under the CV curve, V_2 and V_1 represent the upper and lower voltage limits, respectively, v is the scan rate, and m denotes mass deposited on the electrode.

The specific capacitance also calculated from the GCD profile by the help of subsequent equations:

$$c = \frac{i \times t}{\Delta V \times m} \tag{11.4}$$

In which i/m signifies the current density (A/g), ΔV is the potential window, and t stands for the discharge time in seconds.

$$c = \frac{c}{m} = \frac{1}{2\pi f Z''} \tag{11.5}$$

Here, f represents the frequency and Z'' indicates the imaginary impedance.

For any electrode materials, energy density and power density are the two major components. Energy density is simply calculated by the following equation:

$$\text{Energy Density } (E) = \tfrac{1}{2}\, CV^2 \tag{11.6}$$

In which C is the specific capacitance and V is the operating voltage. On the other hand, power density is also calculated with the help of the following equation:

$$\text{Power Density } (P) = E/t \tag{11.7}$$

where E represents the energy density and t stands for the discharge time acquired from GCD plots.

11.2.1 Polypyrrole

11.2.1.1 Different Nano-Architectures of Polypyrrole

Various types of nano-architectures of PPy such as nanoparticles, nanofibers, nanowires, nanotubes, etc. have been investigated by several researchers for different applications. Jeon et al. [38] fabricated the PPy nanoparticles having diameter of ~85 nm and it was utilized for highly efficient counter electrode for dye-sensitized solar cells. Wen et al. [39] developed PPy nanoparticles at room temperature with the average diameter as small as 86.8 nm for the application in electrically conductive adhesives for improving conductivity. Improved electrical conductivities of the PPy nanoparticles were reported by the Liu et al. [40] through a simple alcohol-assisted microemulsion polymerization. Similarly, Li et al. [41] developed the PPy nanoparticles that are well-applicable for nanocomposite and nanocarbon precursor produced by necessarily unstirred oxidative polymerization of pyrrole in acidic aqueous medium at 0 °C without any template as shown in Figure 11.4a. On the other hand, Chronakis et al. [45] fabricated the PPy nanofibers having diameter in the range of 70–300 nm through electrospinning process and their electrical as well as morphological properties were checked. The one-step bulk chemical synthetic approach of PPy nanofibers by seeding method was reported by Zhang and Manohar [46]. Further, Goel et al. [47] synthesized the PPy nanofibers having average diameter of 75–180 nm in the presence of different dopants using a simple interfacial oxidative polymerization technique. A superhydrophilic PPy nanofiber network (Figure 11.4b) was synthesized electrochemically in an aqueous solution by using buffer solution in the absence of templates was discussed by Zang et al. [42]. Al-Mashat et al. [43] fabricated the PPy nanowires (Figure 11.4c) that were effectively deposited on the interdigitated transducers via template-free electropolymerization for hydrogen gas sensing. While Nam et al. [48] successfully produced the PPy nanowires by cathodic electropolymerization from an aqueous solution without templates and chemical additives. They also proposed the reaction mechanism of the synthesis of PPy nanowires under a cathodic potential. Like other nanoarchitectures, PPy nanotubes were also prepared by different groups using various synthetic techniques. Sapurina et al. [44] prepared PPy nanotubes (Figure 11.4d) by the oxidative polymerization of pyrrole in presence of methyl

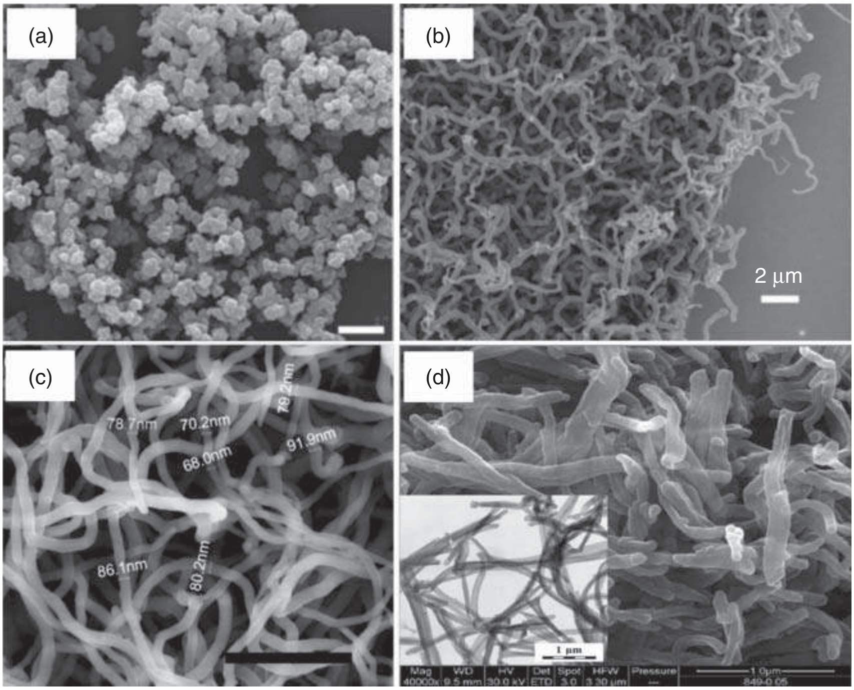

Figure 11.4 Different nanoarchitectures of polypyrrole: FESEM image of (a) PPy nanoparticles synthesizes in 0.5 M HCl. Source: Adapted with permission from Ref. [41]. Copyright 2010, American Chemical Society. (b) PPy nanofiber network. Source: Adapted with permission from Ref. [42]. Copyright 2008, American Chemical Society. (c) electrodeposited PPy nanowires. Source: Adapted with permission from Ref. [43]. Copyright 2012, American Chemical Society., and (d) PPy nanotubes and HRTEM image of PPy nanotubes (inset). Source: Adapted with permission from Ref. [44]. Copyright 2017, Elsevier B.V.

orange and those nanotubes achieved the highest bulk conductivity of 40–50 S/cm. Alternatively, using the same procedure, Kopecký et al. [49] synthesized the PPy nanotubes and measured the conductivity of 91.6 S/cm. Further, Jang and Yoon [50] reported the PPy nanotubes via chemical oxidation polymerization technique in sodium bis(2-ethylhexyl) sulfosuccinate reverse (water-in-oil) emulsions. The different forms of PPy nanoarchitectures are summarized in Figure 11.4.

11.2.1.2 Polypyrrole Nanostructures as Electrode Materials

PPy have been regarded as the most promising pseudocapacitive electrode materials due to their unique characteristics. PPy based electrode materials demonstrate a set of advantages, like easy synthesis, good conductivity, flexibility, and relatively cheap. It is well known that nanostructured PPy as well as other conducting polymers are the essential ingredients for the electrode material of supercapacitor owing to their high surface areas along with short diffusion path lengths to ions that improve the electrochemical behavior. A lot of researchers have studied the electrochemical performances of PPy and different forms of PPy individually as the superior supercapacitor electrode materials. Sahoo et al. synthesized the PPy nanofibers through a facile chemical route using sodium alginate as template and used as the supercapacitor electrode materials [51]. They studied the electrochemical characteristic by three electrode system using two different aqueous electrolytes having specific capacitance of 284 F/g at a scan rate of 10 mV/s as well as maintained their 76% specific capacitance after 600 cycles in 1 M potassium chloride (KCl) electrolyte. Further, PPy nanowires with 120 nm of width were fabricated under a mild condition where $FeCl_3$ is used as oxidant reported by Zhao et al. [52]. Electrochemical studies with the help of conventional three electrode system in 1 M sodium sulphate (Na_2SO_4) electrolyte produced the specific capacitance of 420 F/g of at 1.5 A/g current density with excellent cyclic stability having a retention of 97.9% initial capacitance after 8000 consecutive charge discharge cycles. Alternatively, Huang et al. [53] fabricated the PPy nanowire arrays grown on a carbon cloth substrate for high performance pseudocapacitor electrode using three electrode systems in 5 M lithium chloride (LiCl) aqueous electrolyte. Schematic representation of PPy nanowires growth on carbon cloth is depicted in Figure 11.5A. Observed value of specific capacitance was 699 F/g at 1 A/g with superior rate capability and it showed the enhanced energy density of 164.07 Wh/kg at a power density of 650 W/kg owing to the radial growth of PPy nanowires on carbon cloth. The GCD profiles of PPy nanowires at different current densities as well as specific capacitance values at various current densities are depicted in Figure 11.5A(a,b). The calculated energy density and power density values of the PPy nanowires are shown in Ragone plot (Figure 11.5B(c)), together with values of other one dimensionally aligned pseudocapacitive materials nanostructure arrays for comparison. Additionally, the cyclic stability of PPy nanowires was studied by a prolonged GCD analysis at 50 A/g for 5000 cycles, depicted in Figure 11.5B(d) and the PPy nanowires retained only 63% of specific capacitance after 5000 cycles (Inset: profiles of the 1st and 5000th GCD cycles). On the other hand, PPy synthesized via pulsed polymerization techniques exhibited the specific capacitance of 400 F/g as well as the energy density of 250 Wh/kg [54]. The as synthesized polypyrrole retained its 90% of specific capacitance after 10 000 charge/discharge cycles at a current density of 5 mA/cm^2. The polypyrrole nanorods deposited on cotton fabrics were also studied for the electrode materials for supercapacitor [55]. PPy nanorods coated fabrics showed the specific capacitance of 325 F/g and energy density of 24.7 Wh/kg at a current density of 0.6 mA/cm^2 with moderate retention value (63%) of specific capacitance after 500 cycles. Therefore, pristine PPy as well as the different forms of PPy individually produced excellent specific capacitance behavior. It was also noticed that polypyrrole chains in its doped states were also utilized as the electrode materials for supercapacitor [56–59].

11.2.1.3 Graphene and CNT Based Polypyrrole Nanocomposites

The conducting polymer show the higher specific capacitance and better energy densities than EDLCs. But the cyclic stability of the conjugated polymer is very less and it restricts the application potential of such materials. On the other hand, the EDLCs

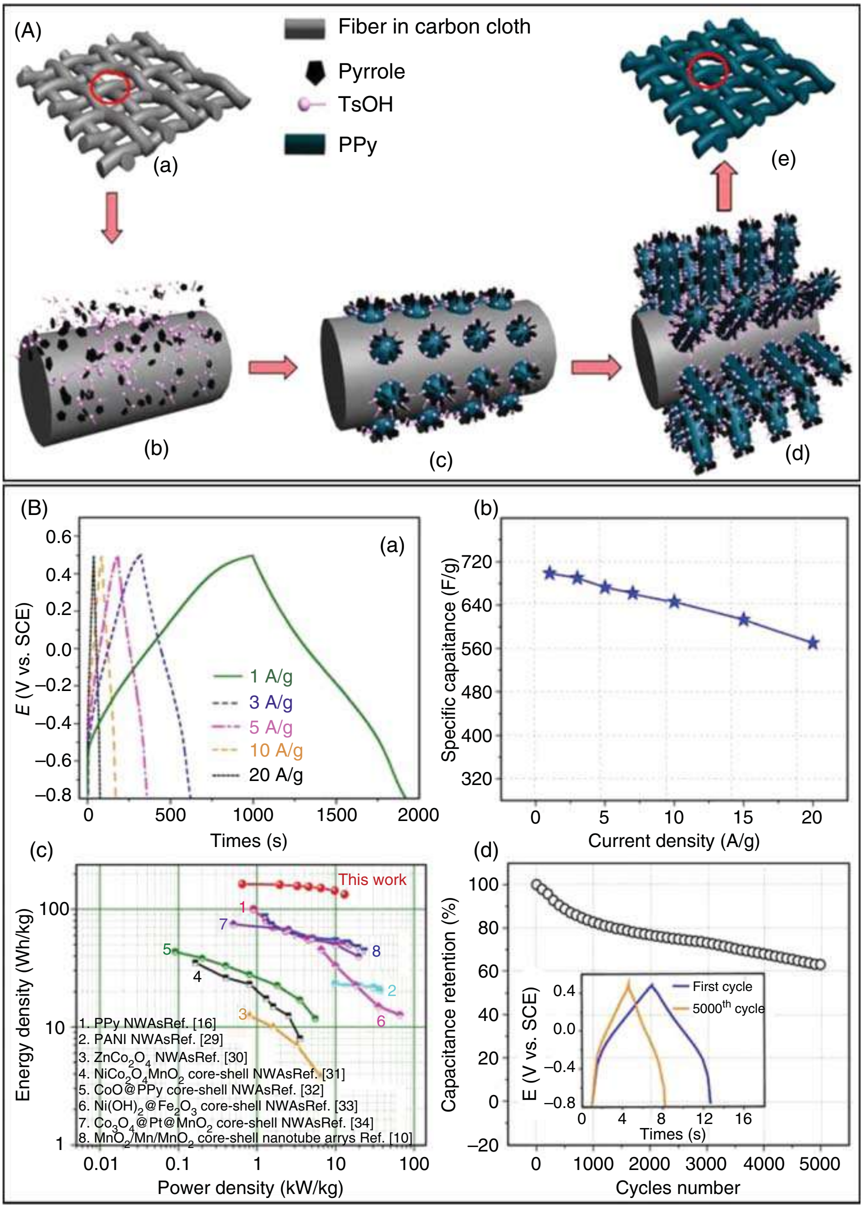

Figure 11.5 (A) Schematic representation of PPy nanowires growth on carbon cloth: (a) carbon cloth, (b) absorption of pyrrole and TsOH on the surface of the carbon fiber in carbon cloth, (c) nucleation of PPy on the surface of a carbon fiber, (d) PPy nanowires on the surface of a carbon fiber, (e) carbon cloth with PPy nanowires. (B) (a) Galvanostatic charge-discharge profiles of PPy nanowires at different current densities, (b) Specific capacitance of PPy nanowires measured at different current densities, (c) Ragone plots of PPy nanowires, together with those of other one-dimensionally aligned pseudocapacitive material nanostructure arrays for comparison, (d) Cyclic stabilities of PPy nanowires, (Inset: Profiles of the 1st and 5000th galvanostatic charge-discharge cycles). Source: Huang et al. [53]. Copyright 2015, ACS Publications.

demonstrate less specific capacitance and energy density than pseudocapacitor but they have the superior cyclic stability. Therefore, researchers are concentrated on the development of the hybrid types of electrode materials where both the EDLC and pseudocapacitor materials are present. Formation of such hybrid electrode materials can reach the higher value of specific capacitance, better energy density, and power density and superior cyclic stability. The CNTs, both the multi-walled carbon nanotubes (MWCNTs) as well as single-walled carbon nanotubes (SWCNTs), have been regarded as the electrode materials because of their superior electrical conductivity and high accessible surface area. Various research articles are available on PPy and CNT based nanocomposites for the supercapacitors electrode materials.

It was reported that the incorporation of MWCNTs in the PPy or PPy nanoarchitectures enhanced the electrochemical behavior as well as other properties. Chen et al. [60] fabricated the PPy/functionalized-MWCNTs (PPy/FM) nanocomposite by CV onto the modifies stainless steel mesh (MS), which was modified by functionalized multiwall carbon nanotube (FM) before use and studied as the electrode materials for supercapacitor. The electrochemical performance was investigated by three electrode set-up in 1 M nitric acid (HNO_3) electrolyte and obtained 1296 F/g of specific capacitance at 5 mA/cm^2 current density and also maintained their 88.1% specific capacitance after 1000 charge–discharge cycles. It was seen from their CV curve that all the curves were close to the rectangular shape but there were different degrees of distortion because of the occurrence of electrode internal resistance, polarization as well as the redox behavior deriving from doping/dedoping process of the PPy. It was also observed that the CV curves of composites exhibited a hybrid electrode performance, which possessed the pseudocapacitance behavior from PPy in addition the electrochemical double layer capacitance from MWCNTs (Figure 11.6a). The CV integrated area of the PPy/FM was much higher than that of pure PPy, mainly MS-PPy/FM showed a higher specific capacitance. It was mainly due to the interconnected tubular structure formed in MS-PPy/FM composites that enhanced the surface area and facilitates the diffusion of ions. It was seen from the GCD analysis that all the curves were not an ideal straight line but bent seriously, that was caused by the faradic reaction (Figure 11.6b). Those electrochemical impedance spectra in the form of Nyquist plots have been shown in Figure 11.6c. The AC impedance spectra of the electrode materials were mostly composed of a semicircle in the higher frequency region and tilted straight line in the low frequency region. It was observed that the PPy, SS-PPy/FM, and MS-PPy/FM showed the charge transfer resistances of 3.1, 1.7, and 1.0 Ω, respectively. The lower charge transfer resistance of MS-PPy/FM indicated the higher specific capacitance. The FM covered on the surface of stainless steel (SS) acted as supporting and indicating template in the growth of PPy and also ensured good electronic conduction in the electrode. As a result, the electrochemical behaviors of MS-PPy/FM were better than SS-PPy/FM and PPy.

Dhibar et al. [61] synthesized the copper chloride doped PPy/MWCNTs nanocomposite via *in situ* polymerization technique where ammonium persulfate utilized as the oxidant and employed as the supercapacitor electrode materials. From their morphological study, it has been proved that the MWCNTs surfaces were homogeneously coated by copper (II) chloride ($CuCl_2$) doped PPy (Figure 11.7a)

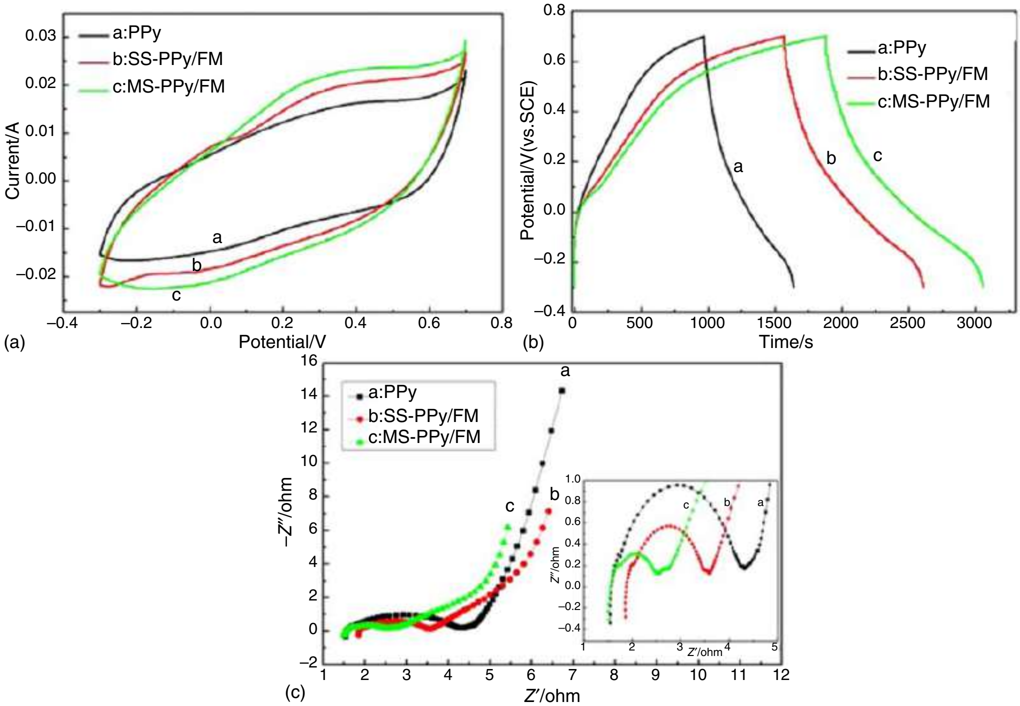

Figure 11.6 Electrochemical characterization of PPy/FM composites. (a) CV, (b) GCD, (c) EIS are compared the electrochemical properties of PPy, SS-PPy/FM, and MS-Py/FM composites. Source: Chen et al. [60]. Copyright 2017, Elsevier.

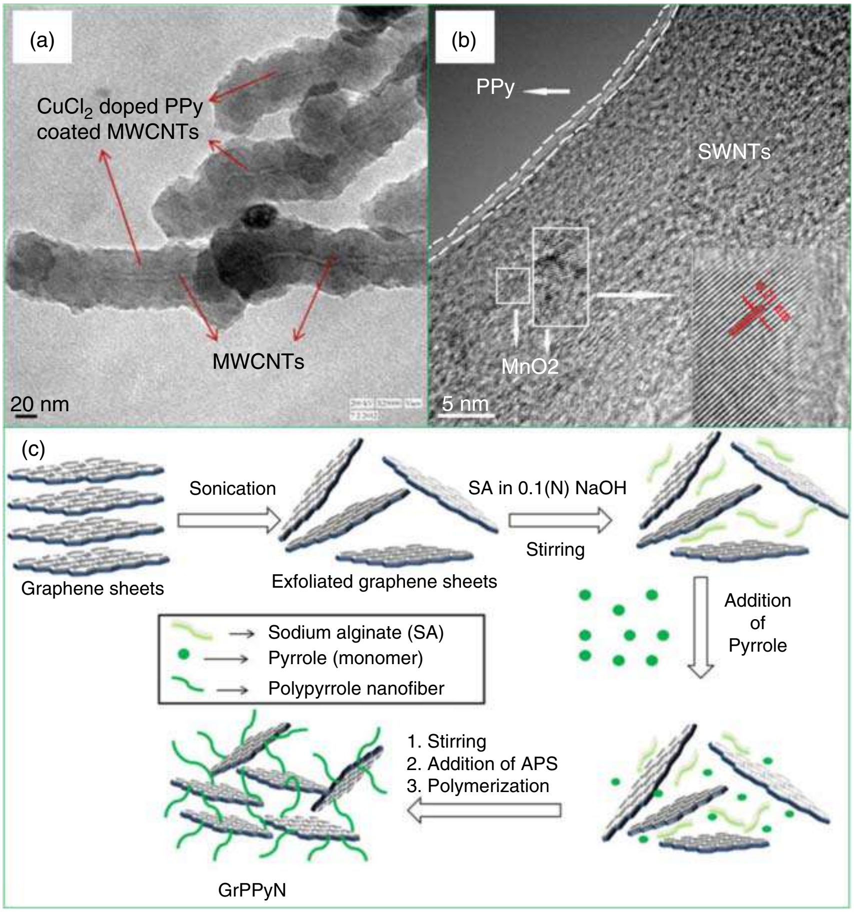

Figure 11.7 (a) HRTEM images of $CuCl_2$ doped PPy coated MWCNTs. Source: Adopted with permission from Dhibar et al. [61]. Copyright 2013, Wiley, Periodicals, Inc., (b) HRTEM images of PPy coated SWCNTs@MnO_2. Source: Adapted with permission from Liang et al. [62]. Copyright 2014, Elsevier B.V., and (c) schematic representation for the synthesis of Gr-PPy nanofibers nanocomposites. Source: Sahoo et al. [63]. Copyright 2013, Elsevier.

and observed the 312 F/g of specific capacitance at 10 mV/s scan rate. It was also reported that the nanocomposite exhibited 110.93 Wh/kg of energy density at 10 mV/s scan rate, 4479.75 W/kg of power density at a scan rate of 200 mV/s, and retained their 90% of specific capacitance after 1000 consecutive cycles, respectively. Further, Zhu et al. [64] developed the PPy-MWCNTs nanocomposites by chemical polymerization techniques for electrochemical supercapacitors using the neutral 0.5 M Na_2SO_4 aqueous electrolyte and achieved the specific capacitance of 2.430–4.798 F/cm^2 in the scan range of 2–100 mV/s having active mass loading of 10 mg/cm^2. The composite film of PPy and functionalized MWCNTs were fabricated through electropolymerization technique, and it was used as an electrode material for supercapacitors, reported by Sun et al. [65]. The nanocomposite reached 240 F/g of specific capacitance at a 10 mV/s of scan rate and also maintained 93.49% of its original capacitance after 1000 cycles. On the other hand, Shi and Zhitomirsky [66] fabricated the PPy nanofiber-MWCNTs nanocomposites by chemical polymerization method for supercapacitor electrode materials. The electrochemical characteristics were performed by three electrode method in 0.5 M Na_2SO_4 aqueous electrolyte and small value of specific capacitance (4.62 F/cm) was achieved at a material loading of 30 mg/cm^2.

Similar to MWCNTs, SWCNTs also have been used as the supercapacitor electrode materials and various researchers have incorporated SWCNTs in the PPy matrices to improve the electrochemical performance. An et al. [67] fabricated the SWCNTs-PPy nanocomposite by *in situ* chemical polymerization technique and examined for supercapacitor electrode materials. From the morphological analysis they confirmed that the SWCNTs were uniformly coated with PPy with the low specific capacitance of 265 F/g for the nanocomposite. Alternatively, de Oliveira et al. [68] prepared the composite based on TiO_2/SWCNTs complex during polymerization of hollow nanotubes of PPy for hybrid supercapacitors and obtained the specific capacitance of 282 F/g, specific energy in order of 1 Wh/kg and retained 63.9% capacitance after 1000 charge/discharge cycles. Further, Oh et al. [69] reported the SWCNTs and doped PPy highly porous sheets by filtration of SWCNTs-PPy methanol dispersion for supercapacitor applications and exhibited 131 F/g of specific capacitance at a scan rate of 10 mV/s. Alternatively, Liang et al. [62] developed the SWCNTs@MnO_2/PPy film by *in situ* synthesis technique as a supercapacitor electrode without binder to achieve high capacitance. They performed the electrochemical characterizations using a standard symmetric 2032 coin cell in 1 M Na_2SO_4 aqueous electrolyte and obtained 351 F/g of the specific capacitance based on total weight of the electrodes, 39.7 Wh/kg of energy density, 10 kW/kg of power density, and loss only 5.6% of specific capacitance after 10 000 cycles (Figure 11.7b). Hence, the addition of small amount of CNTs (both MWCNTs as well as SWCNTs) into the PPy matrix enhanced the specific capacitance, energy density, power density, and cyclic stabilities of that particular nanocomposite.

Addition of small amount of Gr into the PPy matrix or in any PPy nanoarchitectures has significant effect on the electrochemical behaviors. Biswas and Drzal [70] developed the nanoarchitecture of Gr nanosheets and PPy nanowires by chemical polymerization process for high performance supercapacitor electrodes and exhibited the specific capacitance of 165 F/g and also retained their 92% specific capacitance after 1000 charge discharge cycles. Further, Chang et al. [71] electrochemically synthesized the Gr/PPy nanocomposite for the electrode materials for supercapacitors to have the highest specific capacitance value of 424 F/g. The fabrication of Gr-PPy nanofibers nanocomposite (Figure 11.7c) by simple, inexpensive *in situ* polymerization methods for the supercapacitor electrode materials was reported by Sahoo et al. [63]. From the morphological characteristics, it was observed the random arrangement of PPy nanofibers over the Gr sheets and the development of such typical morphology helped to achieve the better specific capacitance of the nanocomposites that exhibited the 466 F/g of specific capacitance at a scan rate of 10 mV/s, 165.7 Wh/kg of energy density at a scan rate of 10 mV/s and also retained their 85% specific capacitance after 600 consecutive cycles, respectively. Alternatively, Bose et al. [72] synthesized the Gr-PPy nanocomposite through *in situ* polymerization method as a supercapacitor electrode material and achieved the specific capacitance of 267 F/g at 100 mV/s scan rate, energy density of 94.93 Wh/kg, power density of 3797.2 W/kg, and maintained their 90% of capacitance after 500 cycles. A similar type of Gr-PPy nanocomposite was synthesized by Zhang et al. for supercapacitors [73]. It provided specific capacitance of 482 F/g at a current density of 0.5 A/g and maintained their 95% of specific capacitance after 1000 cycles. Later on, highly compression-tolerant 3D porous Gr-PPy foam prepared by hydrothermal process for the electrode materials for supercapacitor was reported by Zhao et al. [74]. The electrochemical performances were executed in two electrode system in 3 M sodium chloride ($NaClO_4$) aqueous electrolyte and the specific capacitance was achieved the value of 350 F/g at 1.5 A/g current density. It was also mentioned that no change was observed in the CVs of the compressed supercapacitors having a 50% applied strain (Figure 11.8). Further, Dhibar and Das [75] prepared the silver nanoparticles decorated Gr-PPy nanocomposite via *in situ* polymerization technique and investigated as the supercapacitor electrode materials. The morphological analysis revealed that the Gr surfaces were homogeneously coated by PPy and in the coated Gr sheets there was the occurrence of Ag nanoparticles having 15–20 nm in diameter and developed a unique

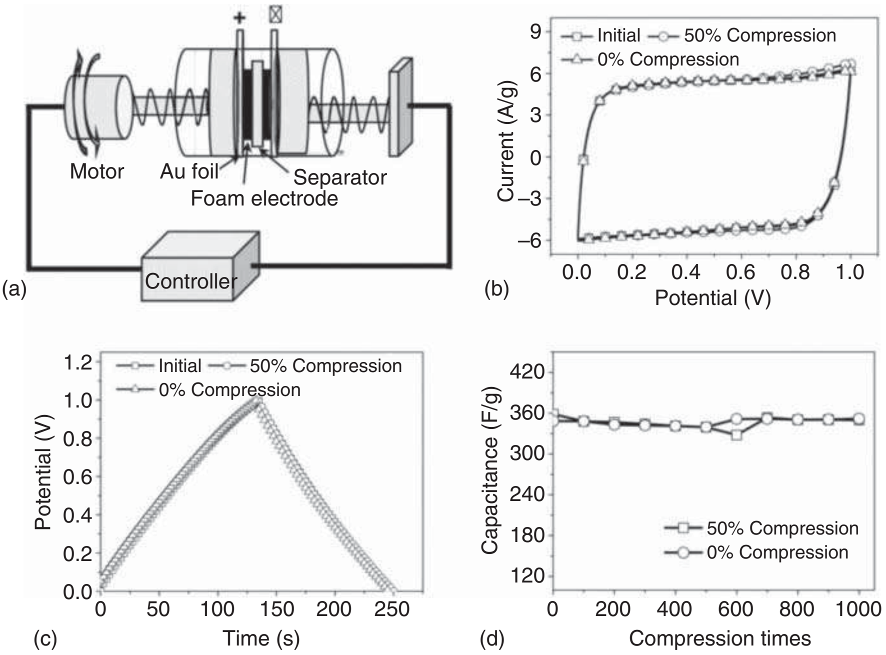

Figure 11.8 (a) Schematic illustration of Gr-PPy based supercapacitor devices. (b) CVs of the compressible supercapacitor cells based on Gr-PPy foam electrodes under 0% and 50% compression for one cycle. The scan rate is 30 mV/s. (c) The corresponding galvanostatic charge–discharge curves at a current of 1.5 A/g under 0% and 50% compression. (d) The specific capacitances at different compression states for 1000 cycles. Source: Zhao et al. [74]. Copyright 2013, Wiley Online Library.

morphology, which assisted to improve the electrochemical characteristics of the nanocomposite (specific capacitance of 472 F/g at a 0.5 A/g current density) with the energy density of 41.95 Wh/kg at 0.5 A/g, the power density of 1548.94 W/kg at 3 A/g, and retained 95% of specific capacitance after consecutive 1000 charge discharge cycles, respectively. Electrochemical characteristics of some of the PPy based electrode materials are summarized in Table 11.1.

11.2.2 Polyaniline

11.2.2.1 Different Nano-Architectures of Polyaniline

Synthesis of PANI nanostructure has received significant attention in nanoscience and nanotechnology because of their novel properties with better performances. The most striking feature of nanostructure is that the control of regularity and order in PANI nanostructure leads to remarkable enhancements in the electronic and photonic properties [76–82]. PANI nanofibers have received lot of attention, because of its unique properties and promising applications in nanomaterials and nanodevices as compared with bulk PANI [76].

PANI nanostructure could be prepared by template polymerization methods (hard or soft) [83–87]. Hard template method was a process in which the monomer units were organized by a preorganized porous template. It was a stepwise process, it included cores gaining, shell covering, and finally removing the core material by calcinations or solvent etching [83, 84]. However, the removal of the template was often tedious and affected the hollow structures. On the other hand, soft template method or template free method was relatively easier as it was based a self-assembly method. In the process, nanostructures were formed without any template or external structure directing agents. It was a simple, effective, and inexpensive process as it was without template removing process [85–87]. In the method the size and shape of the PANI nanostructure were solely depend on the reaction conditions, such as monomer concentration, dopant structure, molar ratio of aniline to oxidant, or sometimes oxidizing agent. Generally, the lower concentration of aniline helped nanotube formation, while the higher concentration was granular morphology. Moreover, the effect of dopant acid played crucial role for PANI morphology [88, 89]. Among different conducting polymers nanostructures, nanotube was the most interesting objects. Nanotubes were produced in the oxidation of aniline by making soft template that was started at low acidity, $\mathrm{pH} > 3.5$ and terminated at high acidity, $\mathrm{pH} < 2.5$. The low acidity produced sufficient amount of oligomers at the beginning of polymerization and it played the essential role for generating the nanotube. Later, high acidity ($\mathrm{pH} > 3.5$) formed PANI and took an important role in the subsequent growth of PANI nanotubes. The pH of the medium (2.5–3.5) had tremendous influences on the formation of PANI nanotube, as a result, weak acids were necessary to the medium [90–92]. In any case, the pH was the decisive factor in the formation of nanotubes, while the chemical nature of the acid was of secondary importance. Utilizing weak acidity of organic acid, series of nanostructure formation were governed by soft-template. However, the dimensions and the structure of

Table 11.1 Electrochemical properties of PPy based electrode materials.

Electrode materials	Measurement type and electrolyte	Working electrode	Specific capacitance	Energy density	Power density	Cyclic stability (%)	References
PPy nanofiber	3-electrode system; 1 M KCl	Glassy carbon electrode	284 F/g	—	—	76	[51]
PPy nanowire	3-electrode system; 1 M Na_2SO_4	Ni foam (1 cm^2)	420 F/g	—	—	97.9	[52]
PPy nanowire	3-electrode system; 5 M LiCl	PPy coated carbon cloth	699 F/g	164.07 Wh/kg	0.65 kW/kg	92.4	[53]
PPy film	3-electrode system; 0.5 M H_2SO_4	Polished graphite plate	400 F/g	250 Wh/kg	—	90	[54]
PPy nanorods deposited in cotton fabrics	3-electrode system; 2 M NaCl	(1 × 3 cm^2)	325 F/g	24.7 Wh/kg	—	63	[55]
Phosphomolybdic acid doped PPy	3-electrode system; 1 M H_2SO_4	Graphite current collector	400 F/g	—	—	—	[56]
Nafion doped PPy	3-electrode system; 3 M KCl	Gold coated polyvinylidene fluoride (PVDF) (1 × 1 cm^2)	450 F/g	—	—	70	[57]
1,4-Benzoquinone doped PPy	3-electrode system; 0.1 M $HClO_4$	1 × 1 cm stainless steel	550 F/g	—	—	—	[58]

Table 11.1 (Continued)

Electrode materials	Measurement type and electrolyte	Working electrode	Specific capacitance	Energy density	Power density	Cyclic stability (%)	References
Thermal acid doped PPy	3-electrode system; 1 M H_2SO_4	1 × 1 cm	73.3 mF/cm	0.081 mWh/cm^3	25 mW/cm^3	85.3	[59]
PPy/functionalized MWCNTs	3-electrode system; 1 M HNO_3	Stainless steel mesh	1296 F/g	—	—	88.1	[60]
$CuCl_2$ doped PPy/MWCNTs	3-electrode system; 1 M KCl	Glassy carbon electrode	312 F/g	110.93 Wh/kg	4479.75 W/kg	90	[61]
PPy-MWCNTs	3-electrode system; 0.5 M Na_2SO_4	1 cm^2 active surface	2.430–4.798 F/cm^2	—	—	—	[64]
PPy-MWCNTs	2-electrode system; 2 M KCl	1 × 1 cm tantalum substrate	240 F/g	—	—	93.49	[65]
PPy nanofibers-MWCNTs	3-electrode system; 0.5 M Na_2SO_4	—	4.62 F/cm	—	—	104.2	[66]
PPy/SWCNTs	3-electrode system; 7.5 M KOH	Ni foam	265 F/g	—	—	—	[67]
PPy/SWCNTs decorated with TiO_2 nanoparticles	2-electrode system; 2 M KCl	—	282 F/g	1 Wh/kg	—	63.9	[68]
PPy/SWCNTs	3-electrode system; 1 M KOH	Thin platinum wire	131 F/g	—	—	—	[69]

Table 11.1 (Continued)

Electrode materials	Measurement type and electrolyte	Working electrode	Specific capacitance	Energy density	Power density	Cyclic stability (%)	References
SWCNTs@MnO_2/PPy	2-electrode system; 2 M Na_2SO_4	—	351 F/g	39.7 Wh/kg	10 kW/kg	84.4	[62]
Gr/PPy	2-electrode system; 1 M NaCl	—	165 F/g	—	—	92	[70]
Gr/PPy	3-electrode system; 1 M H_2SO_4	25 mm diameter gold working electrode	424 F/g	—	—	—	[71]
Gr/PPy nanofibers	3-electrode system; 1 M KCl	Glassy carbon electrode	466 F/g	165.7 Wh/kg	—	85	[63]
Gr/PPy	3-electrode system; 2 M H_2SO_4	Glassy carbon electrode	267 F/g	94.93 Wh/kg	3797.2 W/kg	90	[72]
Gr/PPy	3-electrode system; 1 M H_2SO_4	Titanium plate with 1 cm^2 area	482 F/g	—	12.7 kW/kg	95	[73]
Gr/PPy foam	2-electrode system; 3 M $NaClO_4$	—	350 F/g	—	—	—	[74]
Ag nanoparticles decorated Gr/PPy	2-electrode system; 1 M KCl	Glassy carbon electrode	472 F/g	41.95 Wh/kg	1548.94 W/kg	95	[75]

the nanotubes were solely depending on the individual acid, especially when those acids formed the organized structures with aniline and served as templates.

The synthesis of soft-templated PANI nanotubes by weak organic acids was extensively studied by Wan and coworkers [93] and Malik and coworkers [94–97]. Aromatic dopant acids with different core sizes, number of functionality, isomeric dopant with same functionality, water soluble acid, graphene oxide, graphene quantum dot, etc. were used as a dopant. The effect of organic dopants in soft-template nanostructure formation was discussed briefly in next section.

11.2.2.2 Effect of Dopant Size in Nanostructure

Dopant acid played a main role in the soft-template method. Wan and coworkers also studied the PANI synthesis using aliphatic dicarboxylic acid dopants with different numbers (n) of $-CH_2-$ groups ($n = 0–4$) for soft-template method. They found nanofibers in all dopants, where the diameter of the fibers increased with number of $-CH_2-$ groups in the dicarboxylic acids. It was varied 80–170 nm with varied n from 0 to 4 [98]. Different core size dopants were used by Malik and coworkers [94, 97] to investigate the dopant effect on soft-template synthesized PANI nanostructure. Three different size cores, i.e. benzene, naphthalene, and perylene with four –COOH groups at symmetrical position, were used. Interestingly, in all cases high aspect ratio nanofibers were obtained and the diameter was low for benzene and high for perylene dopant. The reason was explained by the formation of vesicle like structure of the symmetrical dopant, which acted as a soft template for the formation of 1D-nanofiber. Representative field-emission scanning electron microscopy (FESEM) image of benzene tetra-carboxylic acid doped PANI nanotubes are showing in Figure 11.9.

11.2.2.3 Polyaniline Nanostructures as Electrode Materials

PANI based electrochemical capacitors or ultracapacitors are more attractive now-a-days due to their unique features, such as redox behavior and relatively high surface area. It is an ideal candidate for high power requirements systems [99–105].

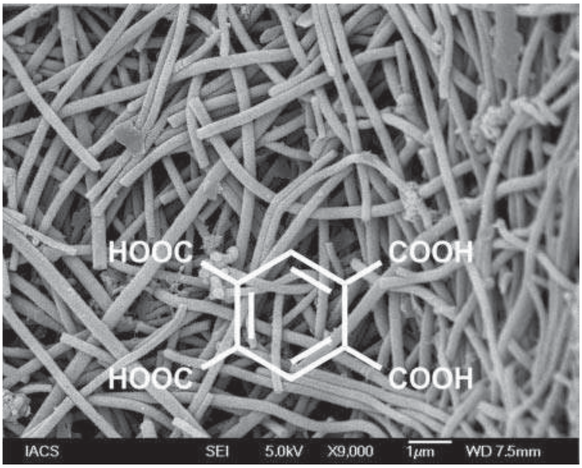

Figure 11.9 FESEM image of benzene tetracarboxylic acid doped polyaniline nanotube. Source: Adopted with permission from Rana et al. [97]. Copyright 2011, the Royal Society of Chemistry.

PANI is known as good pseudocapacitance material because of multiple and stable redox state, environmental stability, and low cost.

It was studied that PANI nanotubes were developed via a one-step *in situ* chemical polymerization techniques by MnO_2 nanotubes as sacrificial templates and utilized as supercapacitor electrode materials [106] and those PANI nanotubes achieved the specific capacitance of 528 F/g at 1 A/g current density using 1 M sulphuric acid (H_2SO_4) electrolyte in two-electrode system. In another study, by template method, PANI nanofibers were synthesized for the electrode materials for supercapacitor and that fiber revealed the specific capacitance of 428 F/g and also maintained 83% of initial capacity at a current density of 5 mA/cm^2 [107]. Similarly, PANI nanofibers with controllable wall thickness were fabricated through *in situ* polymerization techniques utilizing electrospun poly(amic acid) fiber membrane as a template as electrode materials, exhibiting the specific capacitance of 601 F/g at 1 A/g and retaining 62% of capacitance after 500 cycles [108]. In another study, PANI nanowire arrays were made and analyzed as the electrode materials with the relatively high specific capacitance of 950 F/g and it retained 88% of the original capacitance after 500 cycles, some of their electrochemical characteristics are depicted in Figure 11.10 [109]. The outstanding electrochemical behaviors come from their novel morphology of aligned PANI nanowire arrays. It is known that the pseudocapacitance of PANI is coming from the redox reaction relating counter-ion influx and outflux from the polymer chains. The advantage of vertically aligned nanowires is that it helps the ion diffusion from a bulky solution to the surface of PANI nanowires. The counter ions hereby can attain or depart the surface of PANI nanowires fast, even at very high charge–discharge rate. Alternatively, PANI nanowires having 50 nm in diameter may reduce the charge transport distance in the PANI materials. Therefore, the counter ions effortlessly penetrate the inner layer of the PANI, which makes almost full utilization of the electrode materials. Optimized ionic diffusion path as well as narrow diameter may diminish the ionic diffuse resistance along with charge transfer resistance, and for this reason, the supercapacitor provides a very high specific capacitance even at a large current density [109]. Ultrathin pure PANI nanofibers were fabricated via *in situ* polymerization approach to PANI hydrogels, with vanadium pentoxide hydrate nanowires as both sacrifice template as well as oxidant [110]. During the polymerization, a network comprised of ultrathin PANI nanofiber was generated, and the large aspect ratio of these nanofibers allowed the formation of hydrogels at a low solid content of 1.03 wt%. Those hydrogels were utilized as electrode material and displayed a high specific capacitance of 636 F/g, also retained their 83% of specific capacitance after 10 000 charge–discharge cycles. In another work, PANI nanofibers produced by electrospinning technique showed specific capacitance of 267 F/g higher than chemically synthesized PANI power (208 F/g) as well as achieved better cyclic stability and retained 86% of specific capacitance after 1000 charge discharge cycles [111]. PANI nanofibers obtained by interfacial polymerization techniques exhibited the specific capacitance of 548 F/g, specific energy of 36 Wh/kg, and specific power of 127 W/kg, respectively [103]. Different PANI nanostructures prepared through

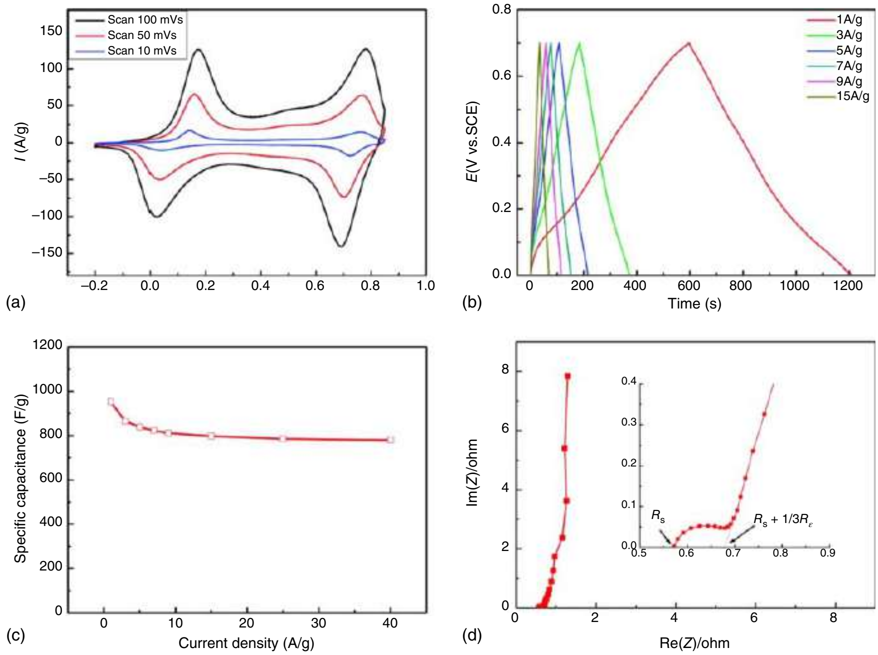

Figure 11.10 Electrochemical capacitance behavior of PANI nanowire arrays in $HClO_4$ aqueous solution: (a) cyclic voltammetry at different scan rate; (b) typical galvanostatic charge–discharge curves at several current densities; (c) specific capacitance in different current densities; (d) Nyquist plots at a frequency range from 20 kHz to 1 Hz. (the inset is an enlarged curve of the high frequency region). Source: Wang et al. [109]. Copyright 2010, ACS Publications.

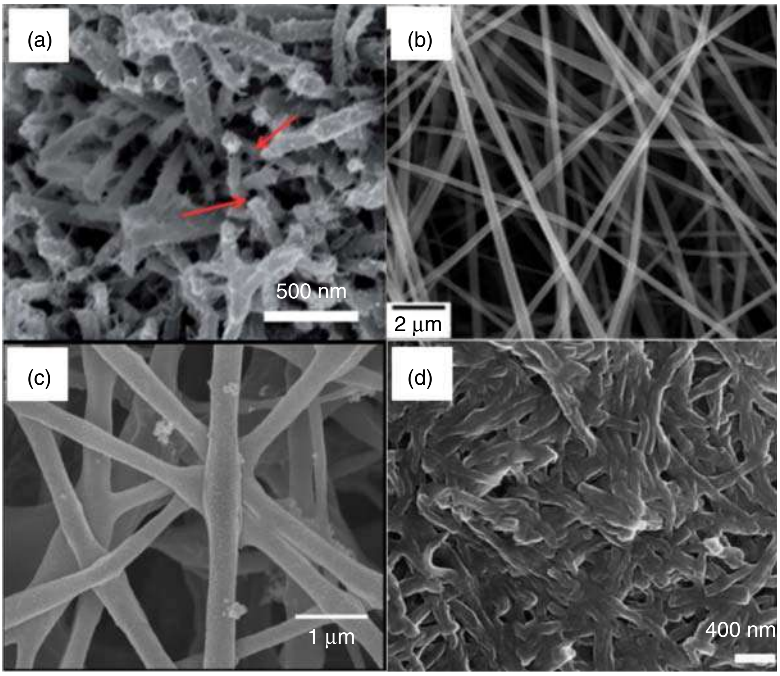

Figure 11.11 (a) PANI nanotubes synthesized via MnO_2 nanotubes as sacrificial templates. Source: Adopted with permission from Chen et al. [106]. Copyright 2013, the Royal Society of Chemistry., (b) hollow PANI nanofibers are fabricated via electrospun poly(amic acid) fiber membrane as a template. Source: Adapted with permission from Miao et al. [108]. Copyright 2013, American Chemical Society., (c) PANI nanofibers are fabricated by electrospinning. Source: Adopted with permission from Chaudhari et al. [111]. Copyright 2012, Wiley Periodicals, Inc., and (d) PANI nanofibers were developed by interfacial polymerization techniques. Source: Adopted with permission from Chaudhari et al. [103]. Copyright 2012, Wiley Periodicals, Inc.

various synthetic techniques for the electrode materials for supercapacitor are presented in Figure 11.11.

11.2.2.4 Graphene and CNT Based Polyaniline Nanocomposites

Like other CPs, PANI based nanocomposites were also the excellent component for the electrode materials for supercapacitors. The incorporation of carbonaceous materials (used as EDLC materials) into the conducting PANI matrices (used as pseudocapacitor) developed a hybrid type of materials and expected to show superior electrochemical behavior.

The PANI nanofibers incorporated MWCNTs composite were synthesized through *in situ* polymerization technique as the electrode materials for supercapacitor [112]. It was observed that the incorporation of MWCNTs in to the PANI nanofibers enhanced the specific capacitance from 554 to 606 F/g, performed in two electrode method using 1 M H_2SO_4 electrolyte. In another study, PANI/CNT composites with core–shell structure were developed for supercapacitor electrode materials, showing specific capacitance of 560 F/g with 66% PANI content, and it retained

71% of specific capacitance after 700 cycles [113]. Layer-by-layer assembled PANI nanofibers/MWCNTs composite through rapid aqueous phase polymerization of aniline were fabricated for electrochemical capacitor [114]. Those materials stored high volumetric capacitance of $\sim 238 \pm 32\,\mathrm{F/cm^3}$ and high volumetric capacity of $\sim 210\,\mathrm{mAh/cm^3}$. Similarly, flexible CNT/PANI paper-like films were studied for supercapacitor electrode [115]. This flexible electrode showed the specific capacitance of 424 F/g and also retained their 90.3% of specific capacitance after 1000 charge discharge cycles.

Like MWCNTs, SWCNTs and PANI based composites have also been used as the electrode materials for supercapacitors. The PANI/SWCNT composite prepared by electrochemical polymerization techniques was studied as the electrode materials with the observed value of specific capacitance of 485 F/g, specific energy of 228 Wh/kg, specific power of 2250 W/kg, and it also retained their 73% of capacitance after 1500 cycles [116]. It was also reported that the “skeleton/skin” strategy for the preparation of free standing, thin as well as flexible PANI/SWCNT hybrid films by the *in situ* electrochemical polymerization method by directly grown SWCNT films with continuous reticulate structure as template used for the electrode materials that produced the specific capacitance of 236 F/g, energy density of 131 Wh/kg, and power density of 62.5 kW/kg, respectively [117].

Similar to CNTs, incorporation of graphene (Gr) into the PANI matrices enhanced the electrochemical properties. It was reported that the Gr nanosheet/PANI composite prepared by *in situ* polymerization techniques was studied as the electrode materials for supercapacitor [118]. The as prepared composite produced the highest specific capacitance of 1046 F/g at 1 mV/s scan rate in a 6 M potassium hydroxide (KOH) electrolyte with the help of 3-electrode system. The specific capacitance of the composite was much higher as compared with pure PANI (115 F/g) and the composite reach the energy density of 39 Wh/kg at a power density of 70 kW/kg. Similarly, Gr/PANI nanofibers nanocomposite was also studied as the electrode materials for supercapacitors that achieved the specific capacitance of 480 F/g at a current density of 0.1 A/g using 3-electrode system in 2 M H_2SO_4 as electrolyte [119]. In another study, a Gr/PANI nanofiber (G-PNF_{30}) (Figure 11.12a) was prepared by vacuum filtration the mixed dispersions of both components, as the electrode materials for flexible supercapacitors [120]. Figure 11.12c illustrates the CV curve of the G-$PANI_{30}$ film and compares it with the chemically converted graphene (CCG) and PANI-nanofiber film having same weight. The two pairs of redox waves observed in both CV curves of G-$PANI_{30}$ and PANI-nanofiber films are assigned to the redox peak of PANI, corresponding to its leucoemeraldine/emeraldine and emeraldine/pernigraniline structural conversions, respectively. Both the CV curves have large rectangular areas, signifying these two supercapacitor have large double-layer capacitances. It was noticed that the CV curve of CCG film shows a much smaller rectangular area, only because of its compact morphology and the absence of electroactive PANI component. The supercapacitor based on CCG films showed a triangular shape charge/discharge curve (Figure 11.12d), signifying its capacitance is mostly attributed to EDLC capacitance. Although, the discharging curve of the supercapacitor fabricated from G-PNF_{30} films exhibits two voltage stages. The former stage having a short discharging duration is associated to EDLC capacitance, on the other hand, the latter stage having much higher discharging duration is ascribed with the combination of both EDLC and faradic capacitances of PANI-nanofiber component. It was also noticed that the discharge curve of PANI-nanofiber supercapacitor is similar to that of the G-PANI$_{30}$ films. The symmetric supercapacitor device using G-PANI$_{30}$ films exhibited a high specific capacitance of 210 F/g at a 0.3 A/g current density in 2-electrode system and also maintained about 94% of capacitance after 800 charge/discharge cycles. Surfactant stabilized Gr/PANI nanofiber composite was prepared via *in situ* polymerization of aniline in the presence of tetrabutylammonium hydroxide and sodium dodecyl benzenesulfonate stabilized Gr under acidic condition for the fabrication of electrode and their morphology was depicted in Figure 11.12b [122]. The as prepared composite exhibited the specific capacitance of 526 F/g at a current density of 0.2 A/g with good cyclic stability and the composite showed the better specific capacitance as compared with pure PANI. It was also reported that the amide group-connected Gr/PANI nanofiber hybrid prepared as the electrode materials showed the specific capacitance of 579.8 F/g at 0.3 A/g and also retained their 96% of specific capacitance after only 200 charge/discharge cycles [123]. Similarly, another group reported the electrode materials of Gr nanosheets/PANI nanofiber composites synthesized by *in situ* polymerization of aniline in perchloric acid ($HClO_4$) solution [121]. The remarkable enhancement of specific capacitance of 1130 F/g at a scan rate of 5 mV/s was observed for the nanocomposite, which was much better than pure PANI (402 F/g) as well as pure Gr nanosheets (270 F/g) and also retained 87% of their specific capacitance after 1000 charge/discharge cycles. In another study, Gr-wrapped PANI nanofiber as electrode materials was prepared by assembly of negatively charged graphene oxide (GO) with positively charged aqueous dispersible PANI nanofibers in an aqueous dispersion [124]. The electrochemical performance was carried out by 3-electrode system in 1 M $Et_4N^+{\cdot}BF_4^-$/polycarbonate (PC) electrolyte and exhibited an initial specific capacitance of 236 F/g, energy density of 19.5 Wh/kg, power density of 738.95 W/kg, and maintained their 73.7% of capacitance after 1000 charge/discharge cycles. Therefore, from all the reported studies, it was observed that the incorporation of Gr in the PANI as well as in different PANI nanostructures the electrochemical properties enormously improved. Different morphologies of Gr/PANI nanofibers composites are represented in Figure 11.12.

Malik and coworkers [95, 96, 105] reported on graphene oxide, graphene quantum dot and Fe_3O_4-graphene doped PANI nanostructures as electrode materials using by *in situ* soft-template method. Interestingly, it was observed the formation of nanotube like PANI where 2D graphene oxide sheet transformed to 1D nanotubes. Surprisingly, the specific capacitance value of nanotubes was ~637 F/g at a current density of 1 A/g because of high surface area and porosity of nanotube structure. Further, the surface area of the nanostructure was enhanced by the incorporation of graphene quantum dots (GQDs) from graphene oxide and same was used for PANI nanotube preparation. Interestingly, synthesized GQD doped PANI nanotubes exhibited an excellent specific capacitance value of 1044 F/g at a current density of 1 A/g, which

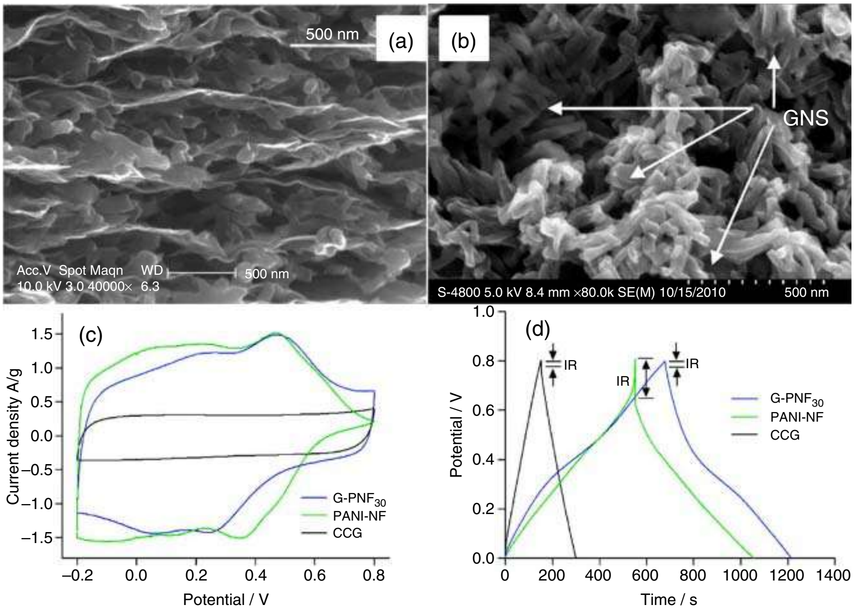

Figure 11.12 FESEM images of (a) Gr/PANI (G-PNF$_{30}$) nanofiber composite films. Source: Adapted with permission from Wu et al. [120]. Copyright 2010, American Chemical Society. (b) Gr nanosheets/PANI nanofibers composite. Source: Adapted with permission from Li et al. [121]. Copyright 2011, Elsevier B.V. (c) Cyclic voltammograms, and (d) GCD curves of Gr/PANI nanofiber composite. Source: (c, d) Wu et al. [120]. Copyright year, 2010, ACS Publications.

was the highest literature value till date for PANI nanocomposite [95]. In their next approach, a ternary composite was synthesized based on one EDLC (graphene oxide) and two pseudo capacitance materials (Fe_3O_4 and PANI). The same they used for binder-free, semiflexible, thin, all-solid-state supercapacitor device fabrication. In all solid-state devices, specific capacitance was 283.4 F/g at a current density of 1.0 A/g and showed 47.7 Wh/kg of energy density at a 550 W/kg of power density and after 5000 cycles the composite showed excellent life stability that was 78% retention of the electrochemical property (Figure 11.13d–f) [105]. Different morphology of graphene oxide based PANI composites are represented in Figure 11.13a–c. Electrochemical characteristics of some of the PANI based electrode materials are summarized in Table 11.2.

11.2.3 Polythiophene

Among the different conjugated polymers, polythiophenes (PThs) and its derivatives were much interested due to its excellent environmental stability, bulk synthesis, high electrical conductivity, etc. [125]. The main reasons of PTh to utilize as electrode materials for electrochemical supercapacitors were high stability of oxidized form and its excellent electrical conductivity with interesting electrochemical behavior.

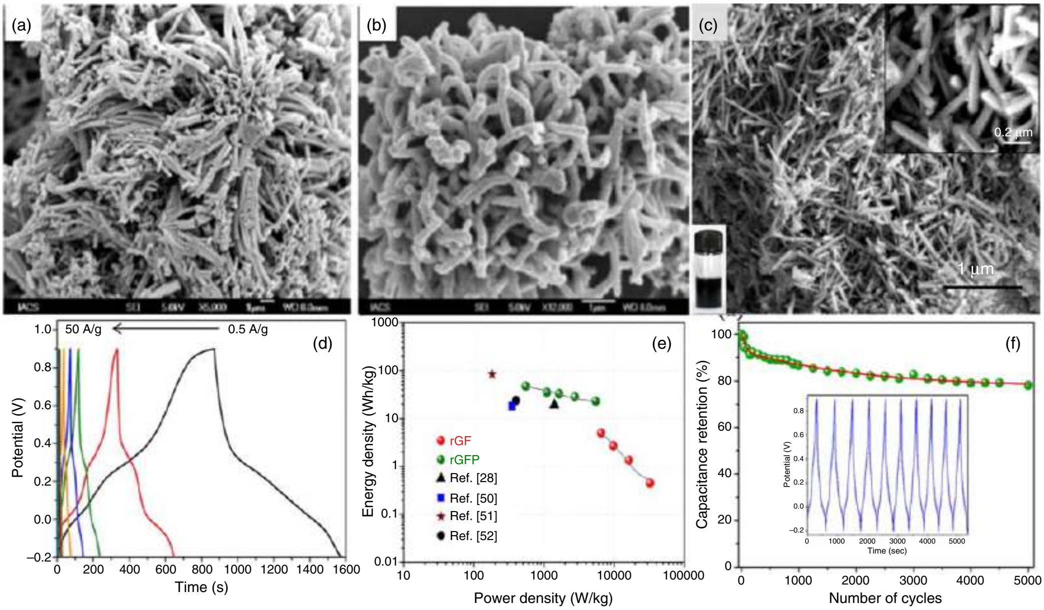

Figure 11.13 SEM images of (a) Graphene oxide doped PANI composite (25 wt%). Source: Adapted with permission from Rana and Malik [95]. Copyright, 2012, The Royal Society of Chemistry. (b) Graphene quantum dot doped PANI (10 wt%). Source: (b) Adapted with permission from Mondal et al. [105]. Copyright, 2017, American Chemical Society, (c) rGO/Fe_3O_4/PANI composite, electrochemical behavior of rGO/Fe_3O_4/PANI based flexible electrode. Source: Adapted with permission from Mondal et al. [105]. Copyright, 2017, American Chemical Society, (d) GCD measurement at different current densities, (e) Ragone plot, and (f) cyclic stability study up to 5000 cycles. Source: (d–f) Mondal et al. [105]. Copyright, 2017, ACS Publications.

Table 11.2 Electrochemical properties of PANI based electrode materials.

Electrode materials	Measurement type and electrolyte	Working electrode	Specific capacitance	Energy density	Power density	Cyclic stability (%)	References
PANI nanotubes	2-electrode system; 1 M H_2SO_4	Graphitized carbon paper	528 F/g	84 Wh/kg$_{(Cell)}$	182 kW/kg$_{(Cell)}$	—	[106]
PANI nanofibers	3-electrode system; 1 M H_2SO_4	Graphite electrode	428 F/g	—	—	83	[107]
PANI nanofibers	3-electrode system; 1 M H_2SO_4	—	601 F/g	80.2 Wh/kg	57.7 kW/kg	62	[108]
PANI Nanowire	3-electrode system; 1 M $HClO_4$	Au plate	950 F/g	130 Wh/kg	700 W/kg	78	[109]
PANI nanofibers	3-electrode system; 1 M H_2SO_4	Glass carbon electrode	636 F/g	—	—	83	[110]
PANI nanofibers	3-electrode system; 1 M H_2SO_4	Graphite substrate	267 F/g	—	—	86	[111]
PANI nanofibers	3-electrode system; 1 M H_2SO_4	Stainless steel mesh	548 F/g	36 Wh/kg	127 W/kg	75	[103]
MWCNT/PANI	2-electrode system; 1 M H_2SO_4	Ti foil	606 F/g	—	—	64	[112]
MWCNT/PANI	3-electrode system; 0.1 M H_2SO_4	Nickel mash	560 F/g	—	—	71	[113]

Table 11.2 (Continued)

Electrode materials	Measurement type and electrolyte	Working electrode	Specific capacitance	Energy density	Power density	Cyclic stability (%)	References
PANI nanofiber/MWCNTs	3-electrode system; 3 M NaCl	Indium tin oxide (ITO) coated glass	238 ± 32 F/cm^3	—	—	96	[114]
MWCNT/PANI	2-electrode system; 1 M H_2SO_4	Coin cell	424 F/g	—	—	89.4	[115]
PANI/SWCNT	3-electrode system; 1 M H_2SO_4	Stainless steel sheet	485 F/g	2250 W/kg	228 Wh/kg	94	[116]
SWCNT/PANI	2-electrode system; 1 M nonaqueous $LiClO_4$	Polyethylene terephthalate (PET) substrates	236 F/g	131 Wh/kg	62.5 kW/kg	85	[117]
Gr nanosheet/PANI	3-electrode system; 6 M KOH	Ni foam	1046 F/g	39 Wh/kg	70 kW/kg	—	[118]
Gr/PANI nanofiber	3-electrode system; 2 M H_2SO_4	Glassy carbon electrode	480 F/g	—	—	—	[119]
Gr/PANI nanofiber	2-electrode system; 1 M H_2SO_4	Platinum foil	210 F/g	—	—	94	[120]
Gr/PANI nanofiber	3-electrode system; 2 M H_2SO_4	Glassy carbon electrode	526 F/g	—	—	—	[122]
Gr quantum dot/PANI nanofiber	3-electrode system; 0.5 M H_2SO_4	Glassy carbon electrode	1044 F/g	—	—	80.1	[93]
Amide group connected Gr/PANI nanofiber	3-electrode system; 2 M H_2SO_4	Glassy carbon electrode	579.8 F/g	—	—	96	[123]
Gr nanosheets/PANI nanofiber	3-electrode system; 1 M H_2SO_4	Glassy carbon electrode	1130 F/g	—	—	87	[121]
Gr-wrapped PANI nanofiber	3-electrode system; 1 M $Et_4N^+{\cdot}BF_4^-$/PC	1 × 1 cm Nickel foam	236 F/g	19.5 Wh/kg	738.95 W/kg	73.7	[124]

11.2.3.1 Different Nano-Architectures of Polythiophene

Various PTh nano-architectures such as nanotubes, nanowires, and nanofibers were developed via different synthetic procedure for diverse applications. Park et al. synthesized the π-conjugated PTh and poly (3-methylthiophene) nanotubes and nanowires using nanoporous anodic aluminum oxide template through electrochemical polymerization method [126]. From the morphological analysis, it was observed the formation of nanotubes with diameters of 100–200 nm, wall thickness of 5–10 nm, and length of the nanotubes was up to ~40 μm. Similarly, another group also prepared PTh nanotubes (Figure 11.14a,b) via electrochemical polymerization of the monomer in the pores of porous anodic alumina template having diameter of 100 nm and length up to several micrometers for sensing riboflavin application [127]. PTh nanotubes coated with nanometer scale Cu, Ni, or Co metal were prepared using a sequential electrochemical synthesis method based on an aluminium oxide (Al_2O_3) nanoporous template, shown in Figure 11.14c,d [128]. It was examined from the morphological characterization that the total outer diameter and length of the hybrid nanotubes were about 200 nm and 10–30 μm, respectively, and the thickness of the PTh nanotubes was of 5–10 nm along with the thickness of the Cu, Ni, and Co metal nanotubes are 5–10 nm. Apart from that, Merlo and Frisbie reported on the electrical characterization of field effect transistors based on regioregular poly (3-hexylthiophene) nanofibers fabricated using nanostencil shadow masks [129]. Some of the nano-architectures are shown in Figure 11.14.

11.2.3.2 Polythiophene Nanostructures as Electrode Materials

It was observed that the different PTh nano-architectures as well as their derivatives itself were utilized as the electrode materials for supercapacitors. Gnanakan et al. prepared the organic acid doped electronically conducing polymer nanomaterial, PTh-tartaric acid nanoparticles, by cationic surfactant-assisted dilute polymerization technique, used for the supercapacitor electrode materials [130]. As prepared electrode materials showed the specific capacitance of 156 F/g, energy density of 14 Wh/kg, power density of 522 W/kg, and maintained their 97% of specific capacitance after 1000 charge/discharge cycles. In addition, Simon and coworkers synthesized PTh by poly-condensation of 2,5-dibromothiophene in tetrahydrofuran (THF), in the presence of magnesium, and catalyzed by $NiCl_2$ (diphenylphosphino) and used as active materials in supercapacitor electrode that showed the specific capacitance of 260 F/g with better cyclic stability, 500 cycles without loss of capacity [125]. Ambade et al. reported the preparation of PTh infiltrated into TiO_2 nanotubes (titanium dioxide nanotube [TNTs]) by a controlled electro-polymerization route [131]. Prepared composite materials showed good electrochemical performance with specific capacitance ~640 F/g. The resulting PTh–TNTs also exhibited considerable 62% loss in electrochemical behavior after 1100 repeated charge /discharge cycles. The power density and energy density of PTh–TNTs calculated were ~2100 W/kg and 237 Wh/kg, respectively (Figure 11.15).

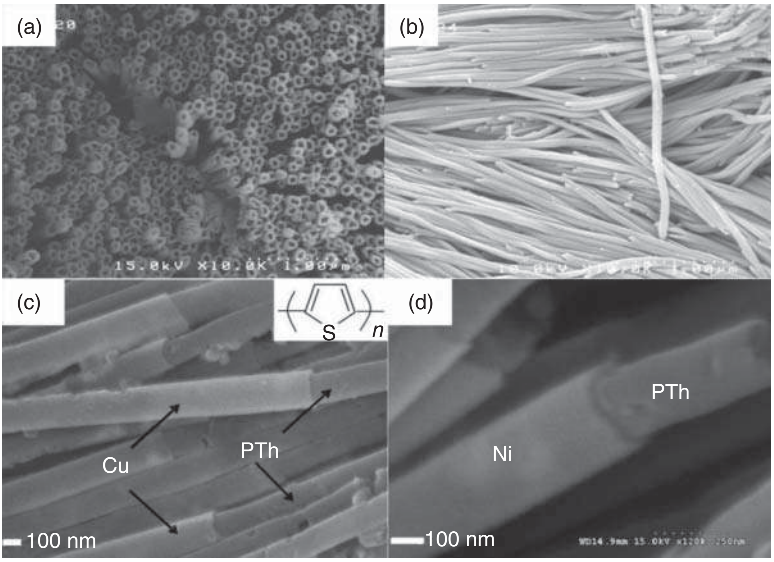

Figure 11.14 (a) SEM images of PTh nanotubes. Source: Adapted with permission from Hajian et al. [127]. Copyright, 2014, Elsevier B.V.; (b) SEM images of PTh nanotubes released from the template. Source: Adapted with permission from Hajian et al. [127]. Copyright, 2014, Elsevier B.V.; (c) SEM image of the bundle of hybrid PTh/Cu nanotubes after removal of the Al_2O_3 template. Source: Adopted with permission from Joo et al. [128]. Copyright, 2013, Wiley-VCH Verlag GmbH & Co. KGaA, Weinheim. and (d) SEM image of a bundle of hybrid PTh/Ni nanotubes after removal of the Al_2O_3 template. Source: Adopted with permission from Joo et al. [128]. Copyright, 2013, Wiley-VCH Verlag GmbH & Co. KGaA, Weinheim.

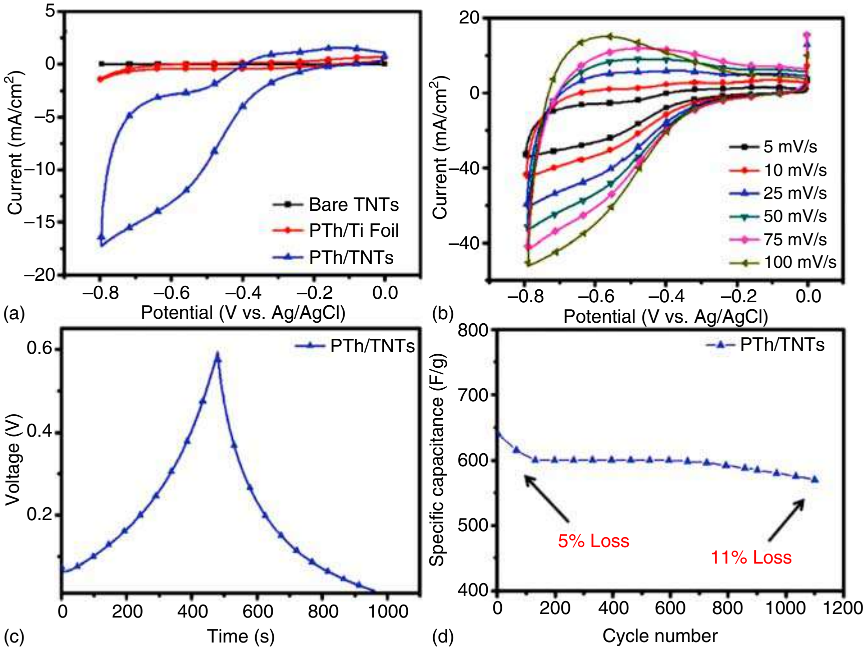

Figure 11.15 (a) Cyclic voltammogram of TNTs, PTh-Ti, and PTh–TNTs at scan rate of 5 mV/s in 1 M H_2SO_4, (b) CV of PTh–TNTs at various scan rates, (c) galvanostatic charge and discharge study at current density of 2 A/g of PTh–TNTs, and (d) cycle stability. Source: Ambade et al. [131]. Copyright 2013, The Royal Society of Chemistry.

In another study, PTh nanofibers were synthesized by anionic surfactant assisted dilute polymerization method using $FeCl_3$ as oxidant for the asymmetric supercapacitor electrode materials [132]. The asymmetric supercapacitor was assembled using PTh nanofiber as the cathode and carbonaceous PTh nanofiber as the anode in 6 M KOH electrolyte and obtained the specific capacitance of 252 F/g at 5 mV/s, specific energy of 54.6 Wh/kg, specific power of 1.7 kW/kg, and retained 93% of specific capacitance after 2000 charge/discharge cycles, respectively.

11.2.3.3 Graphene and CNT Based Polythiophene Nanocomposites

Various research groups also studied the CNT and Gr based PTh as well as its derivatives for the electrode materials for supercapacitor. It was reported that a hybrid composite consisted of poly(3-methyl-thiophene), activated carbon, and gel polymer electrolyte was fabricated for the supercapacitor electrode materials that produced the specific capacitance of 18.54 F/g, energy density of 10.2 Wh/kg, and power density of 96.2 W/kg, respectively [133]. Though, those values of specific capacitances were very less as compared to other hybrid electrode materials with PPy or PANI. In another study, hybrid supercapacitor based on poly(4-fluorophenyl-3-thiophene) and activated carbon was developed [134]. The hybrid supercapacitor exhibited the specific capacitance of 130 F/g, maximum energy density of 48 Wh/kg, and maximum power density of 9 kW/kg. Similarly, poly(3-methylthiophene)/Gr nanocomposite was synthesized via *in situ* polymerization methods and studied as the supercapacitors vn electrode materials [135]. The prepared nanocomposite exhibited the specific capacitance of 240 F/g, which was much higher as compared with pure PTh derivatives and also attended superior cyclic stability as compared with the same. The ternary nanocomposites based on poly(3-methylthiiophene), SWCNTs, and Gr were prepared by *in situ* polymerization technique using $FeCl_3$ as oxidant and were investigated as the potential electrode materials that revealed the specific capacitance of 551 F/g at 0.5 A/g, good energy density of 48.97 Wh/kg, power density of 1579.35 W/kg, as well as maintained 93% of the specific capacitance after 1000 charge/discharge cycles [136]. It was also observed that the ternary nanocomposite exhibited superior electrochemical properties as compared with pure PTh derivatives, indicating the incorporation of carbonaceous material to enhance the electrochemical characteristic of the nanocomposite. In another study, zinc ion doped poly(3-methylthiophene)/MWCNTs composite prepared by *in situ* polymerization technique and studied as the supercapacitor electrode materials [137]. As mentioned nanocomposites showed relatively low specific capacitance of 235 F/g and retained 92% of specific capacitance after 500 charge/discharge cycles. Later on, Fu et al. electropolymerized PTh onto MWCNTs modified glassy carbon electrode in ionic liquid bminPF6 solution for electrode materials [138]. The specific capacitance was 110 F/g and the composite also retained 90% of the initial capacitance after 1000 charge/discharge cycles.

Further, Alabadi et al. [139] reported that GO-PTh derivative hybrid nanosheet was prepared by a facile *in situ* polymerization method. Prepared nanosheet exhibited the energy storage performance with maximum specific capacitance 296 F/g at a current density of 0.3 A/g, in 2 M KOH electrolyte medium by three electrode

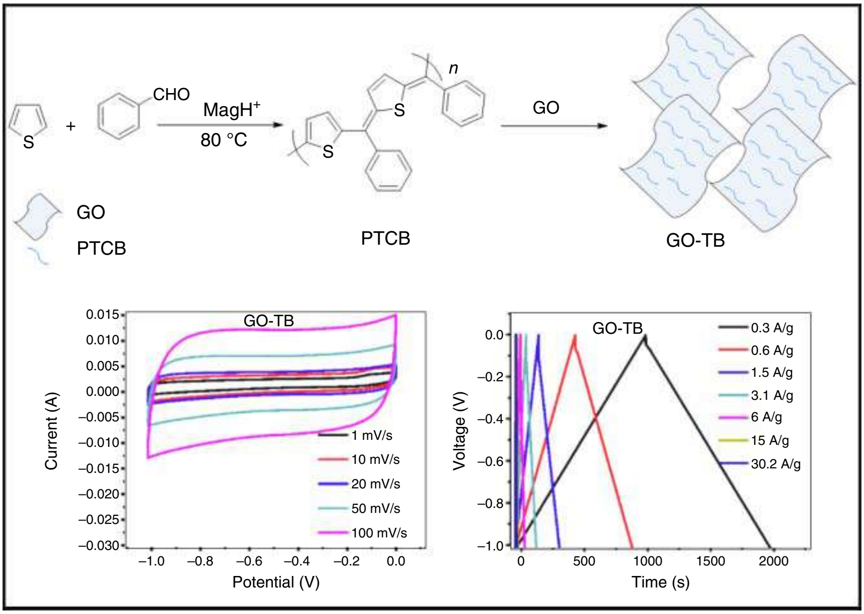

Figure 11.16 (a) Synthesis scheme for graphene-thiophene nanosheet, (b) CV of prepared nanosheet with different scan rate, (c) galvanostatic charge/discharge of prepared nanosheet. Source: Alabadi et al. [139]. Copyright 2016, Elsevier B.V.

systems. Importantly, nanosheet showing almost 92% of the long-term stability was also retained after 4000 charge/discharge repeating cycles. Furthermore, prepared nanosheet exhibited larger energy density (up to 148 Wh/kg at a power density of 41.6 W/kg). Therefore, it was concluded that Gr as well as CNT based PTh or their derivatives showed excellent capacitance behavior as compared to pure PTh or their derivatives (Figure 11.16). Electrochemical characteristics of some of the PTh and its derivatives based electrode materials are summarized in Table 11.3.

11.3 Summary

For the development of the supercapacitor electrode materials, the conjugated polymers have taken major part due to the easy synthesis procedure, low cost, high electrical conductivity, flexibility, and high capacitive behavior. Though the pure conjugated polymers mainly PPy, PANI, and PTh create a lot of problems, mainly owing to the lower energy density as well as power density with poor cyclic stabilities. To improve the electrochemical properties of conducting polymer based supercapacitors, a key requirement is to control the microstructure as well as surface morphology by modifying the polymerization technique, oxidation level, dopants content, and crystallinity. On the other hand, because of the enhanced contact surface area and improved charge storage ability, the nanostructures of conjugated polymer (itself) based supercapacitors exhibit excellent capacitance properties and also

Table 11.3 Electrochemical properties of PTh and its derivatives based electrode materials.

Electrode materials	Measurement type and electrolyte	Working electrode	Specific capacitance (F/g)	Energy density	Power density	Cyclic stability (%)	References
PTh nanoparticles	2-electrode system; 1 M $LiPF_6$	—	156	14 Wh/kg	522 W/kg	97	[130]
PTh	2-electrode system; 1 M $NEt^+{}_4$, $CF_3SO_3^-$ in acetonitrile	—	260	—	—	100%	[125]
PTh infiltrated into TiO_2 nanotubes	3-electreode system; —	Ti foil	640	237 Wh/kg	2100 W/kg	89	[131]
PTh nanofibers	2-electreode system; 6 M KOH	Coin cell	252	54.6 W/kg	1.7 kW/kg	93	[132]
Poly(3-methylthiophene)/activated carbon	3-electreode system; Et_4NBF_4/PC-EC	—	18.54	10.2 Wh/kg	96.2 W/kg	68.50	[133]
Poly(4-fluorophenyl-3-thiophene)/ activated carbon	3-electreode system; $Nt_4CF_3SO_3$/PC-EC	—	130	48 Wh/kg	9 kW/kg	—	[134]
Gr/poly(3-methylthiophene)	3-electrode system; 1 M KCl	Glassy carbon electrode	240	—	—	—	[135]
Gr/SWCNTs/poly (3-methylthiophene)	3-electrode system; 1 M KCl	Glassy carbon electrode	551	48.97 Wh/kg	1579.35 W/kg	93	[136]
Zn^{2+} doped poly(3-methylthiophene)/MWCNTs	3-electrode system; 1 M KCl	Platinum foil	235	—	—	92	[137]
PTh/MWCNTs	3-electrode system; bminPF6 ionic liquid	Glassy carbon electrode	110	—	—	90	[138]
GO/PTh	3-electrode system; 2 M KOH	—	296	148 Wh/kg	41.6 W/kg	92	[139]

provide comparatively high energy and power densities as compared with inorganic counterparts. The poor cyclic stability of the conjugated polymer is mainly because of the serious structural pulverization and counter-ion drain effect during charging and discharging. In order to further improve the electrochemical performance, EDLC materials such as CNTs and graphene are incorporated into the matrix of conjugated polymer based hybrid nanocomposite. Generally, the EDLC materials exhibit superior cyclic stability. Therefore, the combination of both pseudocapacitor materials and EDLC materials for the fabrication of hybrid nanocomposites reveals the superior electrochemical behavior having better capacitance properties and superior cyclic stability, which can serve the purpose fruitfully.

To improve the performances of conducting polymer based electrode materials for the energy storage devices, some salient aspects should be kept in mind:

(i) The electrode materials containing pseudocapacitive materials (conducting polymers, metal oxides or hydroxides) and carbonaceous materials (mainly graphene and CNTs) are promising materials for exhibiting high capacitance values along with high energy and power density. Future explore is needed on the details of the nanohybrid structures and the control of the interfacial interaction among pseudocapacitive materials with carbonaceous materials in order to enhance the overall Faradaic processes across interface.
(ii) Apart from 1D (CNTs), 2D (graphene) structures along with conducting polymer based materials; more research interests have to be paid to further investigating the tunable 3D graphene networks having interconnected porous structure for large internal surface area.
(iii) Self-powered hybrid structure or multifunctional components will be of significant research attentions for the development of future energy storage devices. The combination of electronic devices like Li-ion batteries, solar cells, nano generator, and electrochromic devices with the flexible supercapacitors or the electrode materials will open a new avenue in future energy storage systems.
(iv) Lastly, to accomplish commercialization of supercapacitors electrode materials, production cost is a significant issue in the arena of cyclic economy. Therefore, additional technological advances in cost effective manufacturing process of supercapacitor electrode materials as well as devices will be highly desirable.

The present chapter will encourage present and next generation researchers to come with novel ideas combined with technologies to the application of future energy storage.

Acknowledgment

Dr. S. Dhibar would like to thank Council of Scientific & Industrial Research (CSIR), Human Resource Development Group, New Delhi, India, for the CSIR Research Associate Fellowship [File No. 09/080(1105)/2019-EMR-I]. Mr. P. Das is thankful to DST INSPIRE, India for the fellowship. Dr. Malik acknowledges CSIR, New Delhi (project no. 01(2875)/17/EMR-II) for the financial support.

References

1 Chiang, C.K., Fincher, C.R., Park, Y.W. et al. (1977). Electrical conductivity in doped polyacetylene. *Phys. Rev. Lett.* 39: 1098–1101.

2 Kumar, M.R. and Freund, M.S. (2013). *Self-Doped Polymers* (eds. K. Mullen, T. Masuda and J.R. Reynolds). London: Royal Society of Chemistry.

3 Freund, M.S. and Deore, B.A. (2007). *Self-Doped Conducting Polymers*. Chichester, West Sussex, England: Wiley.

4 Skotheim, T.A. (1986). *In Handbook of Conducting Polymers*. New York: Marcel Dekker Incorporated.

5 Das, T.K. and Prusty, S. (2012). Review on conducting polymers and their applications. *Polym.-Plast. Technol. Eng.* 51: 1487–1500.

6 Agobi, A.U., Louis, H., Magu, T.O., and Dass, P.M. (2019). A review on conducting polymers-based composite for energy storage application. *J. Chem. Rev.* 1: 19–34.

7 Huang, Y., Li, H., Wang, Z. et al. (2016). Nanostructured polypyrrole as a flexible electrode materials of supercapacitor. *Nano Energy* 22: 422–438.

8 MacDiarmid, A.G. (2001). Nobel lecture: "synthetic metals": a novel role for organic polymers. *Rev. Mod. Phys.* 73: 701–712.

9 Kang, E.T. and Neoh, K.L. (1998). Polyaniline: a polymer with many interesting intrinsic redox states. *Prog. Polym. Sci.* 23: 277–324.

10 Gospodinova, N. and Terlemezyan, L. (1998). Conducting polymers prepared by oxidative polymerization: polyaniline. *Prog. Polym. Sci.* 23: 1443–1484.

11 Shirakawa, H. (2001). Nobel lecture: the discovery of polyacetylene film – the dawning of an era of conducting polymers. *Rev. Mod. Phys.* 73: 713–718.

12 Malinauskas, A. (2001). Chemical deposition of conducting polymers. *Polymer* 42: 3957–3972.

13 Battacharya, A. and De, A. (1999). Conducting polymers in solution–progress toward processibility. *J. Macromol. Sci., Rev. Macromol. Chem. Phys.* 39: 17–56.

14 Mort, J., Pfister, G., and Grammatica, S. (1976). Charge transport and photogeneration in molecularly doped polymers. *Solid State Commun.* 18: 693696.

15 Ram, M.H., Sunaresan, N.S., and Malhotra, B.D. (1994). Performance of electrochromic cells of polyaniline in polymeric electrolytes. *J. Mater. Sci. Lett.* 13: 1490–1493.

16 Trivedi, D.C. and Dhawan, S.K. (1993). Shielding of electromagnetic interference using polyaniline. *Synth. Met.* 59: 267–272.

17 Greeham, N.C., Moratti, S.C., Bradley, D.D.C. et al. (1993). Efficient light-emitting diodes based on polymers with high electron affinities. *Nature* 365: 628–630.

18 Tourillon, G. and Garnier, F. (1982). New electrochemically generated organic conducting polymers. *J. Electroanal. Chem.* 135: 173–178.

19 Burgmayer, P. and Murray, R.W. (1983). Faster ion gate membranes. *J. Electroanal. Chem.* 147: 339–344.

20 Malhotra, B.D., Kumar, N., and Chandra, S. (1986). Recent studies of heterocyclic and aromatic conducting polymers. *Prog. Polym. Sci.* 12: 179–218.

21 Yang, C., Wei, H., Guan, L. et al. (2015). Polymer nanocomposites for energy storage, energy saving, and anticorrosion. *J. Mater. Chem.* 3: 14929–14941.

22 Ho, H.-A., Najari, A., and Leclerc, M. (2008). Optical detection of DNA and proteins with cationic polythiophenes. *Acc. Chem. Res.* 41: 168–178.

23 Bernier, S., Garreau, S., Béra-Abérem, M. et al. (2002). A versatile approach to affinitychromic polythiophenes. *J. Am. Chem. Soc.* 124: 12463–12468.

24 Ramírez-Solís, A., Kirtman, B., Bernal-Jáquez, R., and Zicovich-Wilson, M. (2009). Periodic density functional theory studies of Li-doped polythiophene: dependence of electronic and structural properties on dopant concentration. *J. Chem. Phys.* 130: 164904.

25 Koyama, T., Nakamura, A., and Kishida, H. (2014). Microscopic mobility of polarons in chemically doped polythiophenes measured by employing photoluminescence spectroscopy. *ACS Photonics* 1: 655–661.

26 Zhou, W., Hernández-Burgos, K., Burkhardt, S.E. et al. (2013). Synthesis and electrochemical and computational analysis of two new families of thiophene-carbonyl molecules. *J. Phys. Chem. C* 117: 6022–6032.

27 Yang, J., Liu, Y., Liu, S. et al. (2017). Conducting polymer composite: metal synthesis and applications in electrochemical capacitive energy storage. *Mater. Chem. Front.* 1: 251–268.

28 Zhang, Y., Feng, H., Wu, X. et al. (2009). Progress of electrochemical capacitor electrode materials: a review. *Int. J. Hydrogen Energy* 34: 4889–4899.

29 Peng, Y.Y., Akuzum, B., Kurra, N. et al. (2016). All-MXene (2D titanium carbide) solid-state microsupercapacitors for on-chip energy storage. *Energy Environ. Sci.* 9: 2847–2854.

30 Saravanan, C., Shekhar, R.C., and Palaniappan, S. (2016). Synthesis of polypyrrole using benzoyl peroxide as a novel oxidizing agent. *Macromol. Chem. Phys.* 207: 342–348.

31 Hu, W., Chen, S., Yang, Z. et al. (2011). Flexible electrically conductive nanocomposite membrane based on bacterial cellulose and polyaniline. *J. Phys. Chem. B* 115: 8453–8457.

32 Yang, C. and Li, D. (2015). Flexible and foldable supercapacitor electrodes from the porous 3D network of cellulose nanofibers, carbon nanotubes and polyaniline. *Mater. Lett.* 155: 78–81.

33 Choi, C., Kim, S.H., Sim, H.J. et al. (2015). Stretchable, weavable coiled carbon nanotube/MnO_2/polymer fiber solid-state supercapacitors. *Sci. Rep.* 5: 9387.

34 Wang, L., Wu, Q., Zhang, Z. et al. (2016). Elastic and wearable ring-type supercapacitors. *J. Mater. Chem. A* 4: 3217–3222.

35 Shao, Y., El-Kady, M.F., Wang, L.J. et al. (2015). Graphene based materials for flexible supercapacitors. *Chem. Soc. Rev.* 44: 3639–3665.

36 Ke, Q. and Wang, J. (2016). Graphene-based materials for supercapacitor electrode – a review. *J. Materiomics* 7: 37–54.

37 Wang, F., Wu, X., Yuan, X. et al. (2017). Latest advances in supercapacitors: from new electrode materials to novel device designs. *Chem. Soc. Rev.* 46: 6816–6854.

38 Jeon, S.S., Kim, C., Ko, J., and Im, S.S. (2011). Spherical polypyrrole nanoparticles as a highly efficient counter electrode for dye-sensitized solar cells. *J. Mater. Chem.* 21: 8146.

39 Wen, J., Tian, Y., Mei, Z. et al. (2017). Synthesis of polypyrrole nanoparticles and their applications in electrically conductive adhesives for improving conductivity. *RSC Adv.* 7: 53219–53225.

40 Liu, Y., Chu, Y., and Yang, L. (2006). Adjusting the inner-structure of polypyrrole nanoparticles through microemulsion polymerization. *Mater. Chem. Phys.* 98: 304–308.

41 Li, X.G., Li, A., Huang, M.R. et al. (2010). Efficient and scalable synthesis of pure polypyrrole nanoparticles applicable for advanced nanocomposites and carbon nanoparticles. *J. Phys. Chem. C* 114: 19244–19255.

42 Zang, J., Li, C.M., Bao, S.J. et al. (2008). Template-free electrochemical synthesis of superhydrophilic polypyrrole nanofiber network. *Macromolecules* 41: 7053–7057.

43 Al-Mashat, L., Debiemme-Chouvy, C., Borensztajn, S., and Wlodarski, W. (2012). Electropolymerized polypyrrole nanowires for hydrogen gas sensing. *J. Phys. Chem. C* 116: 13388–13394.

44 Sapurina, I., Li, Y., Alekseeva, E. et al. (2017). Polypyrrole nanotubes: the tuning of morphology and conductivity. *Polymer* 113: 247–258.

45 Chronakis, I.S., Grapenson, S., and Jakob, A. (2006). Conductive polypyrrole nanofibers via electrospinning: electrical and morphological properties. *Polymer* 47: 1597–1603.

46 Zhang, X. and Manohar, S.K. (2004). Bulk synthesis of polypyrrole nanofibers by a seeding approach. *J. Am. Chem. Soc.* 126: 12714–12715.

47 Goela, S., Mazumdara, N.A., and Gupta, A. (2010). Synthesis and characterization of polypyrrole nanofibers with different dopants. *Polym. Adv. Technol.* 21: 205–210.

48 Nam, D.H., Kim, M.J., Lim, S.J. et al. (2013). Single-step synthesis of polypyrrole nanowires by cathodic electropolymerization. *Journal of Materials Chemistry A* 1: 8061–8068.

49 Kopecký, D., Varga, M., Prokeš, J. et al. (2017). Optimization routes for high electrical conductivity of polypyrrole nanotubes prepared in presence of methyl orange. *Synth. Met.* 230: 89–96.

50 Jang, J. and Yoon, H. (2005). Formation mechanism of conducting polypyrrole nanotubes in reverse micelle systems. *Langmuir* 21: 11484–11489.

51 Sahoo, S., Dhibar, S., and Das, C.K. (2012). Facile synthesis of polypyrrole nanofiber and its enhanced electrochemical performances in different electrolytes. *eXPRESS Polymer Lett.* 6: 965–974.

52 Zhao, J., Wu, J., Li, B. et al. (2016). Facile synthesis of polypyrrole nanowires for high-performance supercapacitor electrode materials. *Prog. Nat. Sci.: Mater. Int.* 26: 237–242.

53 Huang, Z.H., Song, Y., Xu, X.X., and Lie, X.X. (2015). Ordered polypyrrole nanowire arrays grown on a carbon cloth substrate for a high-performance pseudocapacitor electrode. *ACS Appl. Mater. Interfaces* 7: 25506–25513.

54 Sharma, R.K., Rastogi, A.C., and Desu, S.B. (2008). Pulse polymerized polypyrrole electrodes for high energy density electrochemical supercapacitor. *Electrochem. Commun.* 10: 268–272.

55 Xu, J., Wang, D., Fan, L. et al. (2015). Fabric electrodes coated with polypyrrole nanorods for flexible supercapacitor application prepared via a reactive self-degraded template. *Org. Electron.* 26: 292–299.

56 Cao, A., Chen, Z., Wang, Y. et al. (2019). Redox-active doped polypyrrole microspheres induced by phosphomolybdic acid as supercapacitor electrode materials. *Synth. Met.* 252: 135–141.

57 Kwon, J.S., Kim, B.C., Wallace, G.G. et al. (2010). Nafion-doped polypyrrole as a supercapacitor electrode in ionic liquid. *Mol. Cryst. Liq. Cryst.* 520: 262–266.

58 Arcila-Velez, M.R. and Roberts, M.E. (2014). Redox solute doped polypyrrole for high-charge capacity polymer electrodes. *Chem. Mater.* 26: 1601–1607.

59 Yang, Z. and Chen, Z. (2019). Thermally doped polypyrrole nanotubes with sulfuric acid for flexible all-solid-state supercapacitors. *Nanotechnology* 30: 245402.

60 Chen, Y., Li, J., Tan, L. et al. (2017). Electrodeposition of polypyrrole/functionalized - multiwalled carbon nanotubes composite and its application in supercapacitors. *Electrochim. Acta* 258: 43–50.

61 Dhibar, S., Sahoo, S., and Das, C.K. (2013). Fabrication of transition-metal-doped polypyrrole/multiwalled carbon nanotubes nanocomposites for supercapacitor applications. *J. Appl. Polym. Sci.* 130: 554–562.

62 Liang, K., Gu, T., Cao, Z. et al. (2014). In situ synthesis of SWNTs@MnO_2/polypyrrole hybrid film as binder-free supercapacitor electrode. *Nano Energy* 9: 245–251.

63 Sahoo, S., Dhibar, S., Hatui, G. et al. (2013). Graphene/polypyrrole nanofiber nanocomposite as electrode material for electrochemical supercapacitor. *Polymer* 54: 1033–1042.

64 Zhu, Y., Shi, K., and Zhitomirsky, I. (2014). Anionic dopant–dispersants for synthesis of polypyrrole coated carbon nanotubes and fabrication of supercapacitor electrodes with high active mass loading. *J. Mater. Chem. A* 2: 14666–14673.

65 Sun, X., Xu, Y., and Wang, J. (2012). Electropolymerized composite film of polypyrrole and functionalized multi-walled carbon nanotubes: effect of functionalization time on capacitive performance. *J. Solid State Electrochem.* 16: 1781–1789.

66 Shi, K. and Zhitomirsky, I. (2013). Polypyrrole nanofiber–carbon nanotube electrodes for supercapacitors with high mass loading obtained using an organic dye as a co-dispersant. *J. Mater. Chem. A* 1: 11614–11622.

67 An, K.H., Jeon, K.K., and Heo, J.K. (2002). High-capacitance supercapacitor using a nanocomposite electrode of single-walled carbon nanotube and polypyrrole. *J. Electrochem. Soc.* 149: A1058–A1062.

68 de Oliveira, A.H. and de Oliveira, H.P. (2014). Carbon nanotube/polypyrrole nanofibers core-shell composites decorated with titanium dioxide nanoparticles for supercapacitor electrodes. *J. Power Sources* 268: 45–49.

69 Oh, J., Kozlov, M.E., Kim, B.G. et al. (2008). Preparation and electrochemical characterization of porous SWNT–PPy nanocomposite sheets for supercapacitor applications. *Synth. Met.* 158: 638–641.

70 Biswas, S. and Drzal, L.T. (2010). Multilayered nanoarchitecture of graphene nanosheets and polypyrrole nanowires for high performance supercapacitor electrodes. *Chem. Mater.* 22: 5667–5671.

71 Chang, H.H., Chang, C.K., Tsai, Y.C., and Liao, C.S. (2012). Electrochemically synthesized graphene/polypyrrole composites and their use in supercapacitor. *Carbon* 50: 2331–2336.

72 Bose, S., Kim, N.H., Kuila, T. et al. (2011). Electrochemical performance of a graphene–polypyrrole nanocomposite as a supercapacitor electrode. *Nanotechnology* 22: 295202.

73 Zhang, D., Zhang, X., Chen, Y. et al. (2011). Enhanced capacitance and rate capability of graphene/polypyrrole composite as electrode material for supercapacitors. *J. Power Sources* 196: 5990–5996.

74 Zhao, Y., Liu, J., Hu, Y. et al. (2013). Highly compression-tolerant supercapacitor based on polypyrrole-mediated graphene foam electrodes. *Adv. Mater.* 25: 591–595.

75 Dhibar, S. and Das, C.K. (2017). Silver nanoparticles decorated polypyrrole/graphene nanocomposite: a potential candidate for next-generation supercapacitor electrode material. *J. Appl. Polym. Sci.* 134: 44724.

76 Chiou, N.R. and Epstein, A.J. (2005). Polyaniline nanofibers prepared by dilute polymerization. *Adv. Mater.* 17: 1679–1683.

77 Wu, J., Tang, Q., Li, Q., and Lin, J. (2008). Self-assembly growth of oriented polyaniline arrays: a morphology and structure study. *Polymer* 49: 5262–5267.

78 Xia, H., Narayanan, J., Cheng, D. et al. (2005). Formation of ordered arrays of oriented polyaniline nanoparticle nanorods. *J. Phys. Chem. B* 109: 12677–12684.

79 Wang, Y., Tran, H.D., and Kaner, R.B. (2009). Template-free growth of aligned bundles of conducting polymer nanowires. *J. Phys. Chem. C* 113: 10346–10349.

80 Han, J., Song, G.P., and Guo, R. (2007). Nanostructure-based leaf-like polyaniline in the presence of an amphiphilic triblock copolymer. *Adv. Mater.* 19: 2993–2999.

81 Lu, X., Mao, H., Chao, D. et al. (2006). Fabrication of polyaniline nanostructures under ultrasonic irradiation: from nanotubes to nanofibers. *Macromol. Chem. Phys.* 207: 2142–2152.

82 Huang, J. (2006). Syntheses and applications of conducting polymer polyaniline nanofibers. *Pure Appl. Chem.* 78: 15–27.

83 Zhang, Z.M., Deng, J.Y., and Wan, M.X. (2009). Highly crystalline and thin polyaniline nanofibers oxidized by ferric chloride. *Mater. Chem. Phys.* 115: 275–279.

84 Jang, J., Bae, J., and Lee, K. (2005). Synthesis and characterization of polyaniline nanorods as curing agent and nanofiller for epoxy matrix composite. *Polymer* 46: 3677–3684.

85 Li, J., Zhu, L.H., Luo, W. et al. (2007). Correlation between one-directional helical growth of polyaniline and its optical activity. *J. Phys. Chem. C* 111: 8383–8388.

86 Du, X.S., Zhou, C.F., and Mai, Y.W. (2008). Facile synthesis of hierarchical polyaniline nanostructures with dendritic nanofibers as scaffolds. *J. Phys. Chem. C* 112: 19836–19840.

87 Guo, S.J., Dong, S.X., and Wang, E.R. (2007). Gram-scale, low-cost, rapid fabrication of high-quality width-controlled one-dimensional conducting polymer nanobelts. *Chem. Mater.* 19: 4621–4623.

88 Laslau, C., Zujovic, Z.D., and Sejdic, J.T. (2009). Polyaniline "nanotube" self-assembly: the stage of granular agglomeration on nanorod templates. *Macromol. Rapid Commun.* 30: 1663–1668.

89 Huang, Y.F. and Lin, C.W. (2009). Exploration of the formation mechanisms of polyaniline nanotubes and nanofibers through a template-free method. *Synth. Met.* 159: 1824–1830.

90 Zhang, L., Peng, H., Hsu, C.F. et al. (2007). Self-assembled polyaniline nanotubes grown from a polymeric acid solution. *Nanotechnology* 18: 115607.

91 Zhang, Z., Wang, L., Deng, J., and Wan, M. (2002). Self-assembled nanostructures of polyaniline doped with poly(3-thiopheneacetic acid). *React. Funct. Polym.* 68: 1081–1087.

92 Konyushenko, E.N., Stejskal, J., and Sedenkova, I. (2006). Polyaniline nanotubes: conditions of formation. *Polym. Int.* 55: 31–39.

93 Huang, K. and Wan, M.X. (2002). Self-assembled polyaniline nanostructures with photoisomerization function. *Chem. Mater.* 14: 3486–3490.

94 Rana, U., Mondal, S., Sannigrahi, J. et al. (2014). Aromatic bi-, tri- and tetracarboxylic acid doped polyaniline nanotubes: effect on morphologies and electrical transport properties. *J. Materi. Chem. C* 2: 3382–3389.

95 Rana, U. and Malik, S. (2012). Graphene oxide/polyaniline nanostructures: transformation of 2D sheet to 1D nanotube and in situ reduction. *Chem. Commun.* 48: 10862–10864.

96 Mondal, S., Rana, U., and Malik, S. (2015). Graphene quantum dot-doped polyaniline nanofiber as high performance supercapacitor electrode materials. *Chem. Commun.* 51: 12365–12368.

97 Rana, U., Chakrabarti, K., and Malik, S. (2011). In situ preparation of fluorescent polyaniline nanotubes doped with perylenetetracarboxylic acids. *J. Mater. Chem.* 21: 11098–11100.

98 Zhang, Z., Wan, M., and Wei, Y. (2006). Highly crystalline polyaniline nanostructures doped with dicarboxylic acids. *Adv. Funct. Mater.* 16: 1100–1104.

99 Winter, M. and Brodd, R.J. (2004). What are batteries, fuel cells, and supercapacitors? *Chem. Rev.* 104: 4245–4270.

100 El-Kady, M.F. and Kaner, R.B. (2013). Scalable fabrication of high-power graphene micro-supercapacitors for flexible and on-chip energy storage. *Nat. Commun.* 4: 1475.

101 Wang, G., Zhang, L., and Zhang, J. (2012). A review of electrode materials for electrochemical supercapacitors. *Chem. Soc. Rev.* 41: 797–828.

102 Eftekhari, A., Li, L., and Yang, Y. (2017). Polyaniline supercapacitors. *J. Power Sources* 347: 86–107.

103 Guan, H., Fan, L., Zhang, H., and Qu, X. (2010). Polyaniline nanofibers obtained by interfacial polymerization for high-rate supercapacitors. *Electrochim. Acta* 56: 964–968.

104 Gupta, V. and Miura, N. (2005). Electrochemically deposited polyaniline nanowire's network. *Electrochem. Solid-State Lett.* 8: A630–A632.

105 Mondal, S., Rana, U., and Malik, S. (2017). Reduced graphene oxide/Fe_3O_4/polyaniline nanostructures as electrode materials for an all-solid-state hybrid supercapacitor. *J. Phys. Chem. C* 121: 7573–7583.

106 Chen, W., Rakhi, R.B., and Alshareef, H.N. (2013). Facile synthesis of polyaniline nanotubes using reactive oxide templates for high energy density pseudocapacitors. *J. Mater. Chem. A* 1: 3315–3324.

107 Mi, H., Zhang, X., Yang, S. et al. (2008). Polyaniline nanofibers as the electrode material for supercapacitors. *Mater. Chem. Phys.* 112: 127–131.

108 Miao, Y.-E., Fan, W., Chen, D., and Liu, T. (2013). High-performance supercapacitors based on hollow polyaniline nanofibers by electrospinning. *ACS Appl. Mater. Interfaces* 5: 4423–4428.

109 Wang, K., Huang, J., and Wei, Z. (2010). Conducting polyaniline nanowire arrays for high performance supercapacitors. *J. Phys. Chem. C* 114: 8062–8067.

110 Zhou, K., He, Y., Xu, Q. et al. (2018). A hydrogel of ultrathin pure polyaniline nanofibers: oxidant-templating preparation and supercapacitor application. *ACS Nano* 12: 5888–5894.

111 Chaudhari, S., Sharma, Y., Archana, P.S. et al. (2013). Electrospun polyaniline nanofibers web electrodes for supercapacitors. *J. Appl. Polym. Sci.* 129: 1660–1668.

112 Sivakkumar, S.R., Kim, W.J., Choi, J.-A. et al. (2007). Electrochemical performance of polyaniline nanofibres and polyaniline/multi-walled carbon nanotube composite as an electrodematerial for aqueous redox supercapacitors. *J. Power Sources* 171: 1062–1068.

113 Zhou, Y., Qin, Z.Y., Li, L. et al. (2010). Polyaniline/multi-walled carbon nanotube composites with core–shell structures as supercapacitor electrode materials. *Electrochim. Acta* 55: 3904–3908.

114 Hyder, M.N., Lee, S.W., Cebeci, F.C. et al. (2011). Layer-by-layer assembled polyaniline nanofiber/multiwall carbon nanotube thin film electrodes for high-power and high-energy storage applications. *ACS Nano* 5: 8552–8561.

115 Meng, C., Liu, C., and Fan, S. (2009). Flexible carbon nanotube/polyaniline paper-like films and their enhanced electrochemical properties. *Electrochem. Commun.* 11: 186–189.

116 Gupta, V. and Miura, N. (2006). Polyaniline/single-wall carbon nanotube (PANI/SWCNT) composites forhigh performance supercapacitors. *Electrochim. Acta* 52: 1721–1726.

117 Niu, Z., Luan, P., Shao, Q. et al. (2012). A "skeleton/skin" strategy for preparing ultrathin free-standing single-walledcarbon nanotube/polyaniline films for high performance supercapacitor electrodes. *Energy Environ. Sci.* 5: 8726–8733.

118 Yan, J., Wei, T., Shao, B. et al. (2010). Preparation of a graphene nanosheet/polyaniline composite with high specific capacitance. *Carbon* 48: 487–493.

119 Zhang, K., Zhang, L.L., Zhao, X.S., and Wu, J. (2010). Graphene/polyaniline nanofiber composites as supercapacitor electrodes. *Chem. Mater.* 22: 1392–1401.

120 Wu, Q., Xu, Y., Yao, Z. et al. (2010). Supercapacitors based on flexible graphene/polyaniline nanofiber composite films. *ACS Nano* 4: 1963–1970.

121 Li, J., Xie, H., Li, Y. et al. (2011). Electrochemical properties of graphene nanosheets/polyaniline nanofibers composites as electrode for supercapacitors. *J. Power Sources* 196: 10775–10781.

122 Mao, L., Zhang, K., Chan, H.S.O., and Wu, J. (2012). Surfactant-stabilized graphene/polyaniline nanofiber composites for high performance supercapacitor electrode. *J. Mater. Chem.* 22: 80–85.

123 Jianhua, L., Junwei, A., Yecheng, Z. et al. (2012). Preparation of an amide group-connected graphene-polyaniline nanofiber hybrid and its application in supercapacitors. *ACS Appl. Mater. Interfaces* 4: 2870–2876.

124 Zhou, S., Zhang, H., and Zhao, Q. (2013). Graphene-wrapped polyaniline nanofibers as electrode materials for organic supercapacitors. *Carbon* 52: 440–450.

125 Laforgue, A., Simon, P., Sarrazin, C., and Fauvarque, J.-F. (1999). Polythiophene-based supercapacitors. *J. Power Sources* 80: 142–148.

126 Park, D.H., Kim, B.H., Jang, M.K. et al. (2005). Synthesis and characterization of polythiophene and poly(3-methylthiophene) nanotubes and nanowires. *Synth. Met.* 153: 341–344.

127 Hajian, A., Rafati, A.A., Afraz, A., and Najafi, M. (2014). Electrosynthesis of high-density polythiophene nanotube arrays and their application for sensing of riboflavin. *J. Mol. Liq.* 199: 150–155.

128 Joo, J., Park, D.H., Jeong, M.-Y. et al. (2007). Bright light emission of a single polythiophene nanotube strand with a nanometer-scale metal coating. *Adv. Mater.* 19: 2824–2829.

129 Merlo, J.A. and Frisbie, C.D. (2004). Field effect transport and trapping in regioregular polythiophene nanofibers. *J. Phys. Chem. B* 108: 19169–19179.

130 Gnanakan, S.R.P., Murugananthem, N., and Subramani, A. (2011). Organic acid doped Polythiophene nanoparticles as electrode material for redox supercapacitors. *Polym. Adv. Technol.* 22: 788–793.

131 Ambade, R.B., Ambade, S.B., Shrestha, N.K. et al. (2013). Polythiophene infiltrated TiO_2 nanotubes as high-performance supercapacitor electrodes. *Chem. Commun.* 49: 2308–2310.

132 Balakrishnan, K., Kumar, M., and Subramania, A. (2014). Synthesis of polythiophene and its carbonaceous nanofibers as electrode materials for asymmetric supercapacitors. *Adv. Mater. Res.* 938: 151–157.

133 Sivaraman, P., Thakur, A., Kushwaha, R.K. et al. (2006). Poly(3-methyl thiophene)-activated carbon hybrid supercapacitor based on gel polymer electrolyte. *Electrochem. Solid-State Lett.* 9: A435–A438.

134 Laforgue, A., Simon, P., Fauvarque, J.F. et al. (2001). Hybrid supercapacitors based on activated carbons and conducting polymers. *J. Electrochem. Soc.* 148: A1130–A1134.

135 Bhattacharya, P. and Das, C.K. (2012). Poly(3-methylthiophene)/graphene composite: in-situ synthesis and its electrochemical characterization. *J. Nanosci. Nanotechnol.* 12: 7173–7180.

136 Dhibar, S., Bhattacharya, P., Ghosh, D. et al. (2014). Graphene-single-walled carbon nanotubes-poly(3-methylthiophene) ternary nanocomposite for supercapacitor electrode materials. *Ind. Eng. Chem. Res.* 53: 13030–13045.

137 Karthikeyan, G., Sahoo, S., Nayak, G.C., and Das, C.K. (2012). Investigations on doping of poly(3-methyl-thiophene) composites for supercapacitor applications. *Macromol. Res.* 20: 351–357.

138 Fu, C., Zhou, H., Liu, R. et al. (2012). Supercapacitor based on electropolymerized polythiophene and multi-walled carbon nanotubes composites. *Mater. Chem. Phys.* 132: 596–600.

139 Alabadi, A., Razzaque, S., Dong, Z. et al. (2016). Graphene oxide-polythiophene derivative hybrid nanosheet for enhancing performance of supercapacitor. *J. Power Sources* 306: 241–247.

12

Conducting Polymers Nanowires with Carbon Nanotubes or Graphene-Based Nanocomposites for Supercapacitors Applications

Thuan Nguyen Pham Truong, Philippe Banet, and Pierre-Henri Aubert

CY Cergy Paris Université, Laboratoire de Physicochimie des Polymères et des Interfaces, 5 Mail Gay Lussac,
Site de Neuville, Cergy Pontoise Cedex 95000, France

12.1 Introduction on Electrochemical Storage Using Electronic Conducting Polymers (ECP)

Massive development in portable electronic with accessible price to public implies a starvation in power for our modern society. Hence, fossil fuels are not enough and sustainable for supplying the increasing need in energy. Accordingly, seeking for high-performing technologies to recuperate and reuse energy from renewable sources becomes a major task nowadays. Recent renovations in recuperation of energy have attracted a wide attention from scientific community, resulting to a variety of technologies, e.g. photovoltaic cell, wind turbine, and tide energy generators [1–6]. However, the energy storage appears to be more problematic because of complicated issues, such as difficulty in achieving short-term charging for imminent use, low rate capability, stability, and high self-discharge rate. In this context, supercapacitors have been developed in responding to these requirements [7–9]. Unlike battery where the charge storage involves Faradaic processes, i.e. electron transfer, coupled with slow intercalation of ions, supercapacitors function based on the motion of ions under an electric field or on the fast electron transfer reactions. Accordingly, two main processes that contribute to the phenomenon are either electrostatic interaction within the Helmholtz's layer (electrical double layer capacitance) and/or fast faradaic charge – transfer reactions/rapid mass transport (pseudo-supercapacitance). In both cases, the generation of ion channel inside the active material's layer plays a crucial role in the performance, thus the importance of the porosity of the solid materials. From this point of view, pure electrical conducting polymers display severe drawbacks in charge storage with moderately low capacitance. This problem is firstly issued from densely packed polymer chains within the matrix that limit the diffusion of ions. Thus, accessible layer is in general about 10 of nanometer of thickness. Consequently, deeper active materials cause wasted mass, resulting to a dramatic decrease in gravimetric capacitance. Secondly, as the conducting polymers store charge by means of pseudocapacitive

Conjugated Polymer Nanostructures for Energy Conversion and Storage Applications,
First Edition. Edited by Srabanti Ghosh.

phenomenon, the high ionic resistance (slow ion diffusion in/out of the electronic conducting polymer [ECP] film) lowers significantly the rate capability of the supercapacitor. As a consequence, the optimization of ECP based supercapacitor consists to increase the accessible surface of the conducting polymer. Accordingly, ECPs need to be combined with other materials, affording composites in which the ECPs is thinly coated onto the second materials to reduce the ion diffusion length. Also the ECPs present large volume change during their redox process, which causes loss of capacitance upon charging/discharging. The nanostructuration by use of templating material such as porous carbons (raw, nanotubes, graphene sheets…) is a convenient way to reduce this negative effect. The host materials have to possess certain conditions to be able to form high-performing composites. Indeed, they need to be highly porous, exhibit significant specific area, and could provide sufficient electrical conductivity to the system. Among a large variety of candidates, carbon-related materials, including activated carbon (AC), carbon nanotubes (CNTs), and graphene (G), appear as best candidate in meeting these challenges due to their outstanding characteristics in electrochemical storage applications [10–14]. Thus, composites made from a combination of ECPs and aforementioned materials will be described and recent advancements in employing theses composites in supercapacitor's field will be further highlighted.

12.1.1 Electronic Conducting Polymers (ECP)

ECPs, since their discovery in the late 1970s [15], have aroused great interest worldwide till nowadays [16, 17]. ECPs, known as synthetic metal, are generally composed of an alternating single and double bonded backbone and/or of p-orbital atoms, leading to a continuous network of delocalized π-bonds (Scheme 12.1, [16]. Hence, the resulted structure is mainly responsible for their metallic–like or semiconducting behaviors, yielded from an electronic conductivities between 10^{-15} and 10^{5} S/cm [18]. This broad change in conductivity is the result of a doping process on the backbone by electron removal (positive doping, *p*-doping) or addition (negative doping, *n*-doping) and depends in particular on the doping level of the polymer, that is to say on the number of charges created per volume unit. This process refers to a redox reaction, which changes the polymer properties such as conductivity, volume, and visible light absorption leading to a very broad palette of applications such as organic electronics, sensors/actuators, electrochromic windows, and electrochemical storage [8, 19–22].

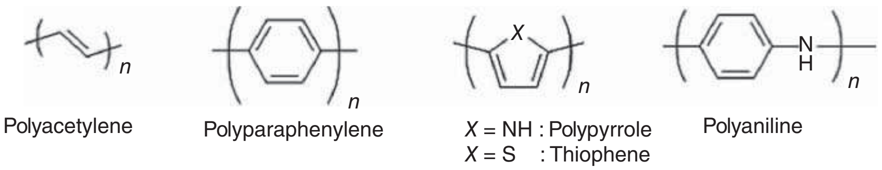

Scheme 12.1 General structures of some typical ECP.

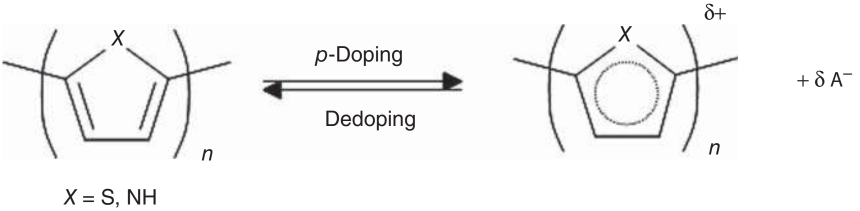

Scheme 12.2 p-Doping of ECP. δ is the doping level of the polymer ($0 < \delta < 1$) and A^- a counter-anion.

These redox processes can be realized either by chemical, photochemical, or electrochemical reactions [23]. Among these approaches, electrochemistry is inherently beneficial for electrochemical storage applications. However, due to the instability of *n*-doped ECPs in particular with the presence of oxygen and water, *p*-doped ECPs are decently exploited as positive electrode materials for electrochemical storage devices, such as batteries or pseudo-supercapacitors. Indeed, upon the *p*-doping, positive charges are created on the polymer backbone with a doping level between 0.3 and 0.5 per monomer units according to the type of ECP, and are stabilized by counter anion A^- (Scheme 12.2). It is worth noting that the generated positive charge is either in the form of a radical-cation (RC, also called polaron) or dication (DC, bipolaron) according to the doping level and the nature of the polymer.

Since most of the common p-type ECPs behave as an electron donor with a large conjugated system, it opens the doors for coupling with a π-conjugated electron acceptor materials, e.g. CNTs, graphene, etc., leading to the formation of composites by means of π-stacking and electrostatic interactions [24]. Thus, this chapter highlights the possibilities of combination between common ECPs and carbon–related materials (activated carbon, CNTs, and graphene) to generate a synergetic effect in boosting the cycling performances of the resulted composites. As aforementioned, the formation of high-performing materials depends strongly on how the polymeric chains are stacked onto the carbon networks. From this standpoint, a great understanding on the polymerization mechanism as well as the influence of synthetic conditions to the morphology and physical chemical properties of ECPs remains challenging and requires further investigations.

12.1.2 Synthesis of ECPs

From the synthetic standpoint, ECPs can be synthesized chemically or electrochemically; the oxidative chemical polymerization is the most commonly used method for the synthesis of ECP by its simplicity and its efficiency (>80% Yield), either in bulk solution or by vapor phase polymerization (VPP) (Scheme 12.3). The polymerization begins with the formation of unstable radical cations (RCs) by means of chemical oxidation of parent monomers. Imminently, as-formed radicals react with the nearest one, through RC–RC mechanism, leading to the formation of dimers. Sequentially, the reaction conducts to the formation of oligomer (∼dozen of repeating units) followed by generation of long-chain polymer [25]. The commonly used

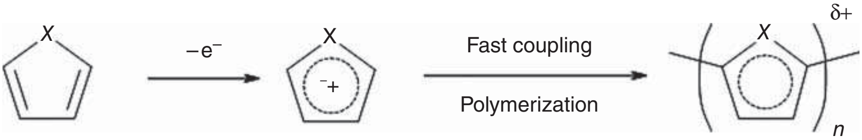

Scheme 12.3 Oxidative polymerization reaction of an heterocycle (X = NH, S, O, Se) leading to intrinsically doped ECP.

oxidants for oxidative chemical polymerization are iron III chloride [25, 26], tosylate (Ts) [27, 28] and ammonium persulfate (APS) [29, 30].

Electrochemical synthesis is also another common way to directly obtain the polymer coated on any conducting substrate such as porous carbon, CNTs, or more recently graphene. The method is very straightforward since it can be carried out in various electrolytes, ranging from aqueous and organic electrolytes to ionic liquid. In a common setup, three-electrode cell is used and is composed of a working electrode (WE) on which the oxidation reaction takes place (and therefore the polymer is deposited), a reference electrode (RE) to control the potential of the working electrode and a counter-electrode (CE) to balance the charge. Since the oxidation could be electrochemically controlled, the polymer can be prepared by different electrochemical methods (galvanostatic, potentiostatic, or potentiodynamic). Similar to chemical polymerization, the electrochemical polymerization is initiated by the electrooxidation of the monomers at the vicinity of the surface of the working electrode, affording to the formation of cationic radicals within the diffusion layer, the generated species self-reacts into dimer via RC–RC mechanism. Subsequently, oligomeric species then precipitate onto the surface due to the insolubility of long-chained ECPs, resulting to a significant increase of the electrochemical active surface area. Accordingly, the reaction's kinetics is also expanded, leading to a rapid formation of an ECP layer. As the reaction is completely governed by the quantity of injected charges, this method enables to obtain thin/thick and conducting films on the working electrode [31]. Consequently, the polymer is obtained in its doped state (Scheme 12.3) in which the counter-anions are eventually issued from the oxidant species (halide, tosylate, sulfate, etc.), or from the supporting electrolyte.

12.1.3 Electrochemical Storage Properties of ECPs

From electrochemical standpoint, the reversible doping/dedoping of ECP paves the way for electrochemical energy storage and fabrication of high-performing electrodes and devices [22, 32]. The capacitance C (farad, F) is defined as the following:

$$C = Q/U \tag{12.1a}$$

where Q is the total charge (coulomb, C) recorded during the de-doping process by cyclic voltammetry (CV) or galvanostatic charge/discharge experiments, and U is the window potential (volt, V) of the dedoping process. If we sweep the potential, Eq. (12.1a) could be rewritten as follows:

$$\mathrm{d}Q/\mathrm{d}t = C \cdot \mathrm{d}V/\mathrm{d}t \tag{12.1b}$$

Note that, although numerous studies on ECP utilize the slope of the discharge curve from galvanostatic charge/discharge experiments to determine Q, as it is done for electrical double-layer capacitor (EDLC) systems, this method is not suitable. Indeed, due to pseudocapacitive phenomena (Faradaic capacitance), typical galvanostatic charge/discharge plots of ECP present a non-linear shape contrary to EDLCs ones. A better accuracy is obtained when doing the integration of the curve. Recently, Beguin and coworkers [33] clearly highlighted and found a difference in specific capacitance and energy of c. 20% between the two methods, i.e. the first method over-estimates the performance of resulted supercapacitor about 20%, which can induce a deflection in the field. From capacitance, energy and power are defined according to Eqs. (12.2) and (12.3):

$$E = ½\, C \cdot \Delta U \tag{12.2}$$

$$P = E/t \tag{12.3}$$

where ΔU is either the window potential of discharge of the electrode (if C is the capacitance of the electrode) or the supercapacitor (if C refers to the capacitance of the supercapacitor).

In the field of electrochemical storage with ECPs, it is more usual to define a specific capacitance C_m said as the capacitance per mass of repetition unit in the main chain. Indeed, C_m is maximized for low weight monomers, the most common being pyrrole (Py, $M_\mathrm{w} = 67.09$ g/mol), thiophene (Th, $M_\mathrm{w} = 84.14$ g/mol), 3-methyl thiophene (3MT, $M_\mathrm{w} = 97.18$ g/mol), ethylenedioxythiophene (EDOT, $M_\mathrm{w} = 142.18$ g/mol), and aniline (ANI, $M_\mathrm{w} = 93.13$ g/mol, [34]. Table 12.1 gives some specific capacitance for the most usual ECPs.

12.1.4 Morphology and Nanostructuration of ECP

In literature, there are strong discrepancies for ECPs between the theoretical and experimental values of specific capacitance [35]. To reach the theoretical value, all active site on ECP have to be electrochemically accessible, i.e. solvent/electrolyte must reach to all the polymer chains. In fact, the main difference relies on the

Table 12.1 Properties of different conducting polymers (ECP) with their theoretical specific capacitance, δ is the doping level.

ECP	*M* (g/mol)	δ	U(V)	Cth (F/g)
PANI	93	0.50	0.7	750
PPY	67	0.33	0.8	620
PT	84	0.33	0.8	485
PEDOT	142	0.33	1.2	210

Source: Lota et al. [34]. Copyright 2004, Elsevier.

morphology/structure of the ECP that depends on many factors such as the type of synthesis (chemical, electrochemical), electrochemical parameters such as current density, potential, nature of solvent and counter-ions, and thickness of the polymer layer. All these factors will strongly affect the storage properties of the polymer. A porous morphology is a key parameter to achieve good storage performances of an ECP. To increase the porosity – hence the specific surface – of an ECP, several methods are used.

The first one consists in creating porosity during the synthesis process. In electrochemical polymerization process, the most relevant way is to use pulsed techniques by applying short pulse (from ms to s) of current or potential followed by a resting time and until the desired amount of polymer is deposited. Pulsed techniques applied to electropolymerization began to be studied in the late 1980s by Otero and De Larreta [36]. The study is focused in the influence of different polypyrrole (PPY) deposition techniques on the morphology and adhesion of the polymer. They showed that the PPY films synthesized by pulsed chronopotentiometry (CPp) were more adherent and had a brighter appearance than the films prepared by conventional chronopotentiometry. Sharma et al. [37] used pulsed polymerization technique to prepare PPY in acidic media. In their study "*on* pulse" time plays an important role, especially to control chain size and chain defects, whereas "*off* pulse" time contributes mainly in the structuration of the polymer (conjugation and orientation). The capacitance of the PPY films varies from 225 F/g for current "long" pulses of 50 ms to more than 400 F/g for PPY films made with short pulses of 5 ms (Figure 12.1). An unexpectedly high energy density of 250 Wh/kg in acidic electrolyte was obtained from pulsed polymerized PPY. However, the less quantity of deposited polymer (0.02 mg corresponding to a polymerization charge of 70 mC) does not allow to affirm that this trend remains valid for a larger scale, which is necessary for the production of supercapacitors. Mitchell and coworkers [38, 39] have also studied pulsed chronoamperometry in an aqueous electrolyte to synthetize PPY. They investigated the influence of pulse time on the growth rate, surface state, and molecular anisotropy. They have demonstrated that very short pulse times ($t_p < 1$ seconds) allow the growth of PPY with a high rate of alignment of the pyrrole patterns, leading to the formation of a smoother film and a better electrical conductivity than for a deposit with constant potential. Such performances are obtained due to the generation of numerous nucleation sites. Zhang et al. [40] developed PPY-based supercapacitors by a CPp ($t_{ON}/t_{OFF} = 10/100$ ms) and by classic chronoamperometry in sodium *p*-toluene sulfonate on stainless steel. For the two deposition methods, they obtain conical structures with, however, smaller cones for the pulsed method increasing the specific surface. Interestingly the specific capacitances obtained were 403 and 251 F/g in H_2SO_4 for the pulsed and non-pulsed method, respectively.

The effect of the pulsed method on the morphology of the polymer has been shown by other authors for polyaniline (PANI) or poly(3,4-ethylenedioxythiophene) (PEDOT). Indeed, PANI films were electrodeposited by Zhou et al. [41] in H_2SO_4 by pulsed chronopotentiometry method ($t_{ON}/t_{OFF} = 50/50$ ms) and by conventional chronopotentiometry method on stainless steel substrates. PANI films obtained

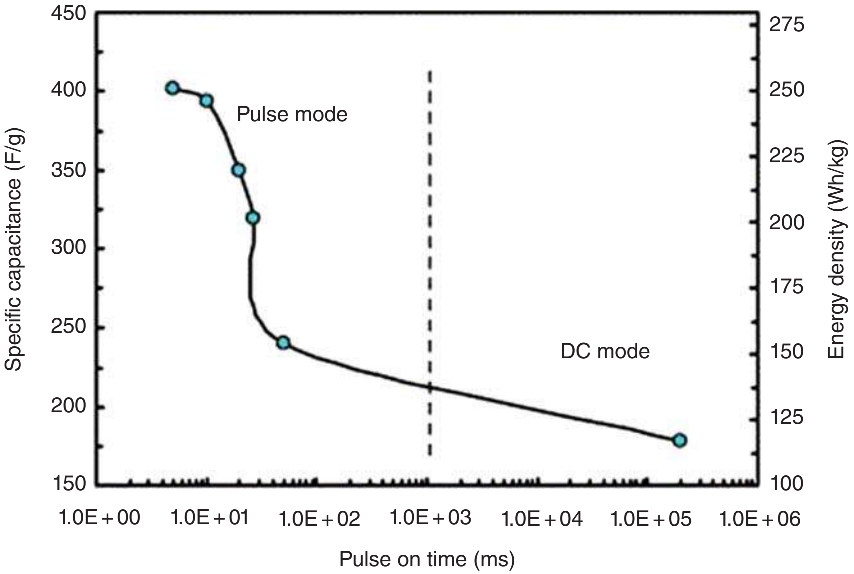

Figure 12.1 Specific capacitance and energy density of PPY prepared by pulsed chronoamperometry. Mass of PPY = 0.02 mg. Source: Sharma et al. [37] with permission from Elsevier, 2008.

by pulsed method have a stringy morphology, while those obtained by classic method form a film made of compact nodules. SEM picture clearly highlights the worthwhile role of pulsed electrochemical methods to increase the specific area of the PANI films. Furthermore, Pandey and Rastogi [42] prepared PEDOT-based supercapacitors on graphite electrodes. Again, non-pulsed (i.e. classic) and pulsed chronopotentiometric methods were compared. Here, the electrolyte is an organic medium with 0.1 M of $LiClO_4$ in acetonitrile and cauliflower structures are obtained, appearing more compact for the non-pulsed method and presenting a specific capacitance of only 100 F/g while 126 F/g were measured in case of the PEDOT prepared by the pulsed method.

A second route to enhance the specific area, the specific capacitance of ECP, is to produce fibrillar polymeric architectures. As example, Laforgue et al. [43, 44] have used electrospinning technology to prepare nanofibers of PEDOT by VPP process. They first produce a sacrificial polyvinylpyrrolidone (PVP) mat by electrospinning, the latter containing $Fe(Ts)_3$ oxidant, then coat the PEDOT through the VPP process. The fibers (average diameter ~350 nm) are fused at every intersection of the mat, ensuring a superior dimensional stability (Figure 12.2). After removal of PVP, the PEDOT nanofibers exhibit a very high conductivity of 60 S/cm, and authors have evaluated their electrochemical properties like a capacity of 30 mAh/g at 5 mV/s and a capacity retention over 90% up to 100 mV/s.

Also Zhao et al. [45] used VPP to vertically hierarchize PEDOT on surface of carbon cloth (CC). Uniform layers of high-aspect-ratio PEDOT nanofibers have been optimized and electrochemical properties of PEDOT@CC have been measured.

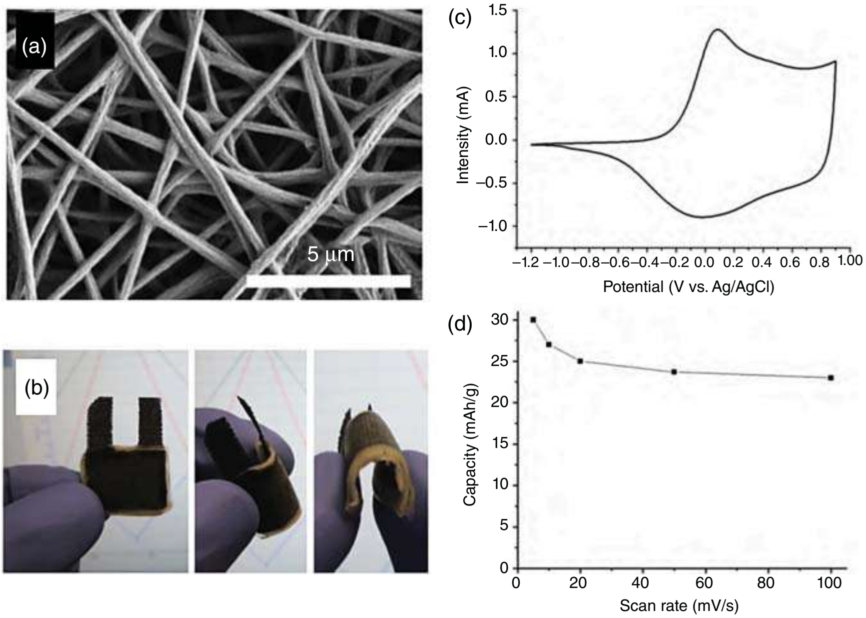

Figure 12.2 (a) SEM micrographs of the PEDOT nanofibers mat. (b) Photographs of a 3 cm^2 all-textile flexible supercapacitor; (c) Electrochemical properties of the PEDOT nanofiber mats in an organic electrolyte (NBu_4PF_6 0.1 M in acetonitrile); cyclic voltammogram at 5 mV/s; (d) electrode capacity as a function of the scan rate. Source: (a, b) Reproduced from Laforgue [44] with permission from Elsevier, 2011, (c, d) Laforgue [44]. 2011, Elsevier.

The hybrid electrode has a specific areal capacitance of 201 mF/cm^2 at 1 mA/cm^2 and a good cycling stability of 92.4% after 1000 cycles. The free-standing electrodes have been assembled into a symmetrical configuration to fabricate supercapacitor with $E_{m\_max} = 4.0$ Wh/kg and $P_{m\_max} = 4.2$ kW/kg. D'Arcy et al. [46] have obtained very original PEDOT nanostructures (Figure 12.3) with enhanced surface areas by VPP process (using $FeCl_3$ oxidant with EDOT vapors) showing needles-likes PEDOT nanostructures (Figure 12.3a–c) supported by Energy-dispersive X-ray spectroscopy (EDX) and X-ray diffraction (XRD) analysis (Figure 12.3d–f). They showed that energy storage properties of a symmetric supercapacitor were much superior compared with conventional supercapacitor made of PEDOT:PSS electrodes (C_m = 70 F/g vs. 24 F/g, respectively) with specific maximum energy and power of 2.4 Wh/g and 3.55 kW/kg, respectively. Also, the capacitance retention has been evaluated at 92% at 10 000 cycles.

These studies prove that the use of ECP in nanodimension is a convenient way to increase the energy storage properties of bulk ECP. Finally, Dubal et al. [47] were able to modify the nanostructure of PPY only by playing with scan rate during electropolymerization of PY monomer in potassium nitrate in aqueous medium. They obtained different shapes of PPY: nanobelts at 50 mV/s, nanobricks at 100 mF/s, and nanosheets at 200 mV/s.

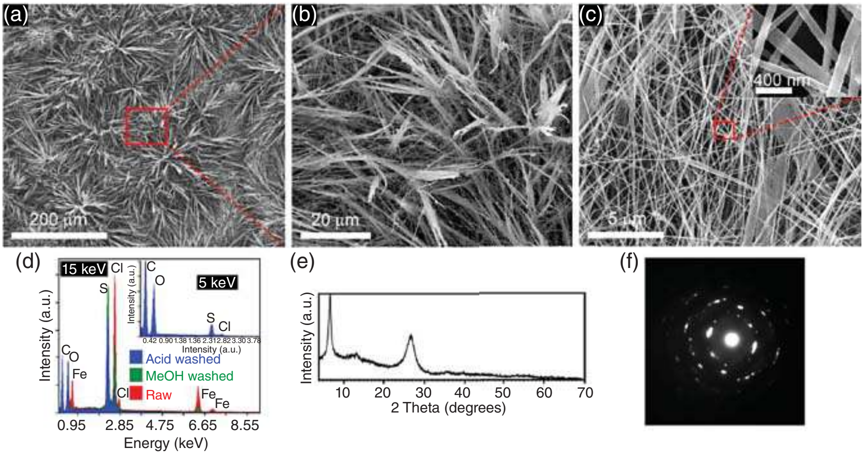

Figure 12.3 Structural analysis of evaporative vapor-phase polymerization (EVPP)-PEDOT. (a,b) Close-up sequence of SEM images demonstrates a high packing density of both vertically directed high aspect ratio nanoribbons and nanofibers. (c and inset) Top view SEM image shows nanofibers entangled with nanoribbons that possess a diameter of up to 200 nm. (d) Energy-dispersive X-ray spectroscopy demonstrates that iron is present in EVPP-PEDOT after the methanol wash (green); however, this metal is undetectable after washing with acid (blue). (e) X-ray powder diffraction of an EVPP-PEDOT shows an intense (100) peak due to preferential orientation of polymer chains on a gold substrate. (f) Electron diffraction confirms that EVPP-PEDOT is a polycrystalline material. Source: (a–c, f) Reproduced from D'Arcy et al. [46] with permission from American Chemical Society, 2014, (d, e) D'Arcy et al. [46]. 2014, ACS Publications.

The third way to increase the specific surface of an ECP consists in the elaboration of the nanostructuration during the synthetic steps. As a typical example, Ju et al. [48] have prepared micro/nanotubes of PANI by chemical and electrochemical oxidative polymerization of aniline within the pores of particle track-etched membranes. Hollow tubules are formed because PANI initially deposits on the surface of the pore walls. However, this route is not sufficient to afford good specific surface for energy storage given that the accessibility of the redox active site has to be as efficient as possible. The most common way to achieve efficient accessibility is to bring the ECP's morphology as closed as possible of the nanometer scale. For this purpose, mixing highly porous or nanostructured carbon-based materials with ECP is a straightforward approach and the formation of ECP nanostructures could be tailored during the polymerization process. In the subsections 12.2–12.4, three kinds of carbon-based nanocomposites containing ECP will be presented: porous (or activated) carbons (AC), CNT, and graphene (G) based nanomaterials.

12.2 Porous Carbon-Based Nanocomposites

Porous or activated carbons are the most common used active materials in EDLC supercapacitors due to their very large specific surface area as well as their low cost fabrication [49, 50]. AC are obtained from a rich-containing carbon organic precursors (coconut, bamboo, sugar cane, etc.) [49] by thermal treatments under an inert atmosphere and followed by activation leading to the formation of the porosity of the material. The specific surface area is ranged between 1000 and 3500 m^2/g, depending on the precursor and the activation method. Owing a theoretical specific capacitance around 10–20 μF/cm^2, specific gravimetric capacitance values between 100 and 200 F/g are obtained in Et_4NBF_4/ACN and H_2SO_4, respectively [51, 52] along with reachable volumetric capacitance of 60 F/cm^3 [49]. These materials can be used for EDLCs with ionic liquid as electrolyte, resulting to an energy and a power density of 31 Wh/kg and 8.6 W/kg, respectively. Furthermore, due to a large electrochemical window of ionic liquid, an operating voltage of 3.4 V was reached. Accompanying with the mentioned cycling performances, a strong stability was also observed with a slight degradation after 40 000 cycles [53].

12.2.1 Polypyrrole/Porous Carbon Nanocomposites

PPY is a good ECP candidate to be combined to AC to prepare nanocomposites, given its high theoretical capacitance of 620 F/g. One of the first PPY/AC composite was prepared in 1995 by Wampler et al. [54] by chemical polymerization of pyrrole in an aqueous dispersion of carbon black. Varying the carbon content of these composites from ∼5% to ∼85% (by weight), they measured the specific surface and density and compared with corresponding mixtures of carbon black and PPY as well as the effect on the electronic conductivity of the composite. With values of specific surface ranging from 14 m^2/g (5% carbon) to 110 m^2/g (85% carbon), this work opened the route to interesting family of nanocomposites to be used for electrochemical storage, not only with PPY but also all the ECP family. Especially, chemical synthesis of ECP@AC are mainly reported in literature. Madden and coworkers [55] published formerly an interesting study on the PPY/porous carbon. Controlling thickness of ECP at nm scale is a key parameter to maintain good power performances of supercapacitors. Polymer-based supercapacitors discharge times tend to be on the order of seconds, as opposed to the milli- or microseconds of conventional capacitors, so that the overall power density is still at least an order of magnitude lower. Authors have prepared PPY/porous carbon composites showing diffusion time constants of 33 ms in 158 nm thick PPY films with volumetric capacitances of 107 F/cm^3 in the composite. Increasing the PPY content into the composite increases the gravimetric capacitance up to 60 F/g, but at the expense, a non-desired increase of the charging time constant was observed. Park et al. [56] have used mini emulsion polymerization to prepare size-controllable PPY/activated carbon composites. The size of the PPY, controlled by the surfactant concentration (SDS), allows to prepare nanoparticles of PPY@C of 388 nm (diameter) and playing with SDS, down to 110 nm. The prepared PPY@C composites exhibit very interesting specific pseudo capacitances of 125 F/g@0.5 A in concentrated KOH. This value has been compared with that of pristine porous carbon (42 F/g) under similar conditions.

12.2.2 Polyaniline/Porous Carbon Nanocomposites

Chen et al. [57, 58] have deposited PANI of porous carbon electrodes ($SSA_{BET} \sim 1800$ m^2/g BET) by CV between −0.2 and 0.8 V (vs. Ag/AgCl) in 1 M H_2SO_4. The successful deposition into pores was ensured by a very slow scan rate (0.3 mV/s) over three cycles only. SEM pictures of non-coated and PANI-coated electrodes did not show obvious differences in morphology (Figure 12.4A,B); however, CV and electrochemical impedance spectroscopy (EIS) have been investigated to confirm the significant contribution of pseudocapacitance from PANI (Figure 12.4C). Finally, a symmetrical capacitor was prepared in 1 M H_2SO_4 and was evaluated at 0.5 mA constant current charge–discharge within 0 and 0.6 V potential window (Figure 12.4D). The PANI-deposited electrode exhibits high specific capacitance of 180 F/g, in comparison with a value of 92 F/g for the bare-carbon electrode.

Bleda-Martinez et al. [59] showed for the first time the importance of synthetic procedure into developing PANI/AC electrodes. Activated carbon/PANI composite electrodes have been developed using different preparation methods of these

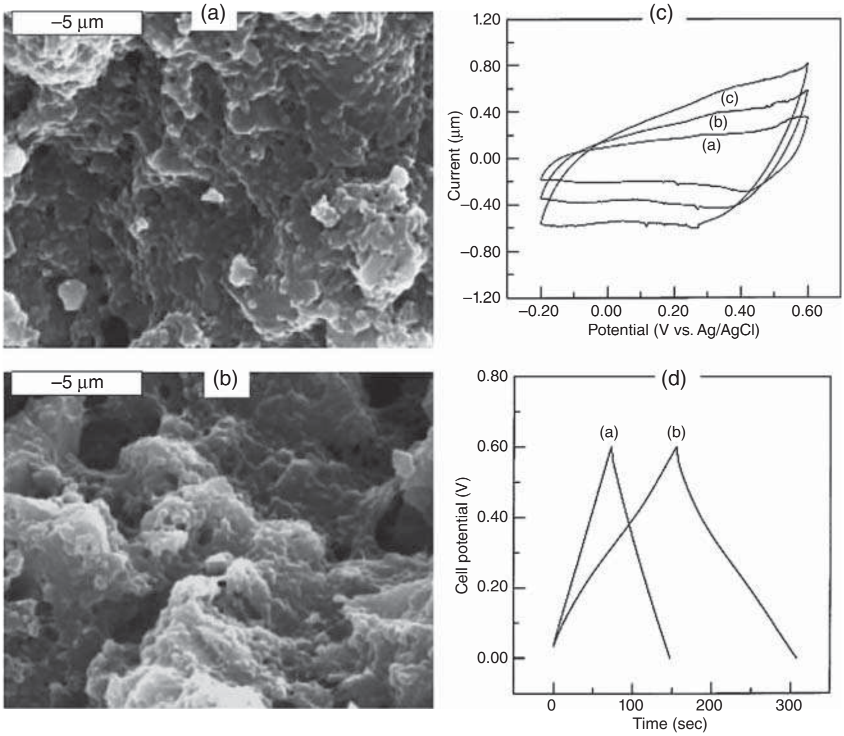

Figure 12.4 (a, b) SEM pictures of porous carbon (a) and PANI-coated porous carbon electrodes (b). (c) CV of PANI-coated porous carbon electrodes electrode in 1 M H_2SO_4 at different sweep rates: (a) 0.3; (b) 0.6; and (c) 1.0 mV/s. (d) Charge–discharge curves at 0.5 mA current of capacitors equipped with (a) porous carbon and (b) PANI-coated porous carbon electrodes. Source: (a, b) Reproduced from Chen et al. [57, 58] with permission from Elsevier, 2003, (c, d) Chen et al. [57, 58]. © 2003, Elsevier.

composites. The first method used consisted of mechanical mixing PANI with the activated carbon. In this case, PANI and AC materials do not display significant synergetic effect, i.e. the performance of the composite electrode can be considered as a simple addition of the two components. On the other hand, the second method deals with chemical polymerization of aniline monomer inside the carbon. The results suggest that the PANI coating depends strongly on the surface chemistry. Authors showed that in this case, aniline reacts with oxygen groups at carbon surface, thus removing their positive effect on capacitance with a concomitant important change in the carbon porosity. In this way, the chemical polymerization of aniline over a carbon material containing surface oxygen groups does not improve the values of the capacitance unless the activated carbon has been preliminary annealed. PANI/porous carbon composites are more effective as capacitors if the two components are mixed directly or polymerized over a carbon material with a low content of surface oxygen. Remarkably, small addition only (6 wt%) of PANI can produce an increase in capacitance of about 20% compared with the pristine activated carbon, from 125 F/g (pristine carbon) to 148 F/g (PANI/AC composite).

A more recent study was published by Yang et al. [60] on PANI-modified renewable biocarbon using static low-temperature *in situ* polymerization. Here the biomass-based porous biocarbon was derived from watermelon rind pyrolyzed at 700 °C in the presence of KOH. In the composites, the bio-carbon serves as a three-dimensional supporting skeleton for the growth of PANI, providing a large accessible surface area. A composite obtained with a carbon/PANI (mass ratio of 20 : 80) exhibits an exceptional specific capacitance of 520 F/g at a current density of 1 A/g and very good capacitance retention upon increasing current density. Furthermore, a high cycling stability of 5000 cycles with a capacitance retention rate of 71.2% was also obtained. Finally, an asymmetric supercapacitor using the PANI/biomass porous carbon as a positive electrode has been assembled with classical activated carbon as negative electrode. The moderate operating cell voltage of 1.4 V was obtained and a high energy density of 29.3 Wh/kg was measured from charge/discharge experiments. Therefore, the composite is suggested to be a promising candidate for electrochemical supercapacitor. Wang et al. [61] improved again the performances of the PANI/AC electrode with capacitance as high as 587 F/g using electrochemical deposition by CV with a scanning rate of 5 mV/s in a solution containing 0.5 M H_2SO_4 and 0.2 M aniline. Their study concluded that PANI was conformally deposited onto porous activated carbon, hence forming an interlinked porous network.

12.2.3 Polyethylenedioxythiophene/Porous Carbon Nanocomposites

Han et al. [62] prepared PEDOT@AC by chemical polymerization of EDOT on carbonized biowaste from bamboo shoot shells. The best capacitance of the obtained composites is determined at 302.5 F/g at current density of 0.5 A/g and the electrode has excellent capacitance retention of 87% after 10 000 cycles at 5 A/g in 1 M H_2SO_4 electrolyte. A supercapacitor was prepared with PEDOT@AC at both positive and negative electrodes. The energy density reaches 30 Wh/kg at power density of (only)

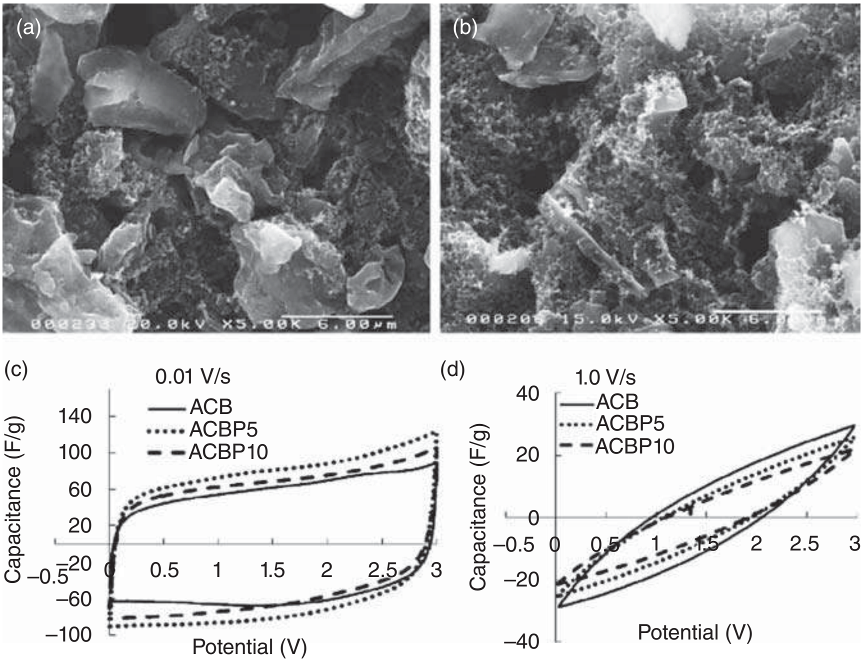

Figure 12.5 SEM micrographs of (a) porous carbon and (b) PEDOT@porous carbon electrodes. (c,d) Cyclic voltammograms of asymmetric supercapacitors cells with porous carbon (solid line), 5 wt% PEDOT composite (dotted line) and 10 wt% PEDOT composite (dashed line)1 M TEABF$_4$–PC electrolyte at two extreme sweep rates: (c) 0.01, (d) 1.0 V/s. Source: Reproduced from Lei et al. [63] with permission from Elsevier, 2011.

0.5 kW/kg in 1 M 1-butyl-3-methylimidazolium hexafluoro-phosphate (EMIMPF$_6$) in acetonitrile electrolyte. PEDOT@C can also simply be obtained by mixture of commercial solution of PEDOT:PSS in carbon [63]. The PEDOT layer is conformably formed onto the porous carbon (Figure 12.5a,b). As a result, measured capacitances of 130 F/g for 5 wt% PEDOT content (Figure 12.5c) demonstrated the facility to produce ECP@porous carbon composite electrodes for supercapacitors via a simple route. However, these electrodes suffer from drastic loss of capacitance retention at high scan rate (Figure 12.5d) due to the difficult diffusion of ions into the porous channels. However, good performances in term of specific energy and power were measured at 180 Wh/kg and 10 kW/kg respectively. Finally, VPP can also be used to prepare PEDOT@AC composite electrodes [64].

12.3 CNT-Based Nanocomposites

Since their discovery and the confirmation of their structures [65–67], CNTs have been particularly studied in recent years for various applications in energy storage. They can be in the form of a single- or multi-walled (SWCNTs, MWCNTs, respectively). CNTs can be obtained either in the form of entangled network [14, 68, 69] or aligned array [70–75]. The effect of alignment was highlighted by Zhang et al. [76] on electrochemical storage properties. Authors explain that the straight pathway of ions into the CNT network is assisted when the CNT are aligned compared with entangled. Also, intrinsic capacitances of vertically aligned carbon nanotube (VACNT) are better than entangled CNTs (25 F/g instead of 14 F/g, respectively).

12.3.1 ECP with Entangled CNT Composites

One of the most studied composites in supercapacitor is the combination of ECP and CNT. In 1999, first precursor works have been reported on the elaboration of ECP with entangled CNT Yoshino et al. [77] showing enhanced photophysical properties of CNT coated by ECP. PPY is one of the main ECP combined with CNTs for the preparation of composites [78–86]. Fan et al. [86] developed the first nanocomposite PPY on CNT (diameter of <100 nm) electrode by *in situ* polymerization. Interestingly, as-formed composite showed an increase in the electronic conductivity from 3 to 16 S/cm. At the early 2003, the first studies on ECP/CNT composites for electrochemical storage were described [87] using PPY as ECP. Consequently, this work opened the route to a very broad family of nanocomposites, resulting from a combination of a variety of ECP and CNT (single-walled, multiwalled). Among different studies on PPY@CNT, PPY/SWCNT electrodes prepared by Zhou et al. [83] were able to reach a specific capacitance of 350 F/g@0.4 A/g and retaining up to 200 F/g at a very high rate of discharge of 30 A/g. Even though these materials exhibit a high power density (P_m = 4.8 kW/kg), the specific energy reported (0.9 Wh/kg) is still too low for materials based on conducting polymers since their specific energy can reach some tens of Wh/kg. [88]

Both oxidative chemical and electrochemical routes are used for the development of composite. However, electropolymerization method stands out in particular. Indeed, this method allows a better control and to some extent, a conformal deposition. The first ECP electrodeposition on CNT was an electropolymerization of aniline on MWCNT by CV and by chronopotentiometry, which were carried out by Downs et al. [89]. One interesting synthetic route published by Hughes et al. [84] is the simultaneous deposition of PPY with CNTs by oxidizing the monomers in the presence of negatively charged multiwalled carbon nanotubes (MWCNTs). By combining PPY with 0.4 wt% of MWCNTs, a specific capacitance of 190 F/g (by mass of PPY) and a surface capacitance of 2100 mF/cm^2 were obtained. This surface capacitance is much higher than that of pure PPY and could be explained by a more open and porous structure generated by the architecture of MWCNTs. Chen et al. [82] have shown that pure PPY reaches a capacitance plateau with increasing film thickness (at 10 C/cm^2), indicating a limited access to the interior of the film. By combining the PPY with CNTs, a linear relationship between capacitance and the charge deposited, for the same film thickness, has also been observed. This suggests that CNTs allows a more open structure and limit the thickness of deposited PPY and leads to a greater accessibility of ions in the material. Similar studies lead to general comparable conclusions [80].

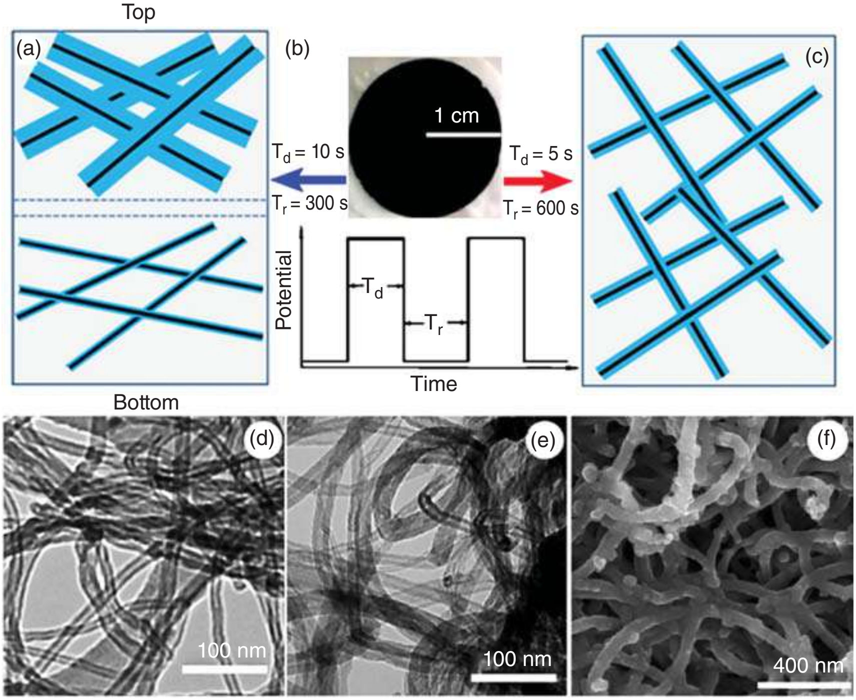

Figure 12.6 (a) and (c) Schematic of the PPY coating on MWCNTs under $T_d = 10$ seconds, $T_r = 300$ seconds and $T_d = 5$ seconds, $T_r = 600$ seconds, respectively. (b) An optical image of MWCNT membrane with the diameter of 20 mm on a filtration membrane and an illustration of the electropotential waveform for pulsed PPY electrodeposition. (d) TEM image of the pure MWCNTs. (e) TEM image of the MWCNTs after a total of 70 seconds PPY deposition with repeated pulses of $T_d = 5$ seconds and $T_r = 600$ seconds. (f) SEM image of the top surface of the MWCNT membrane after PPY deposition for 70 seconds under $T_d = 5$ seconds and $T_r = 600$ seconds. Source: (a–f) Reproduced from Fang et al. [91] with permission from Elsevier, 2010.

The pulsed electrodeposition, previously mentioned for the synthesis of ECP, is also very convenient to synthesize ECPs on CNTs [90–94]. Fang et al. [91] prepared PPY/MWNCT electrodes by pulsed chronoamperometry in aqueous solution (1 M KCl) using different deposition and resting times (T_d and T_r, respectively, see Figure 12.6A). The author proposed that the pulsed method allows to achieve homogeneous deposition of ECPs on nanostructured electrodes as well as to increase the loading amount of electrochemically active material. Consequently, this approach leads to the generation of composite having a larger active surface. In addition, the shortest pulse times allow depositing more homogeneously throughout the depth of the MWCNT compared with the longest times (Figure 12.6B,C). This statement was then confirmed by SEM pictures (Figure 12.6D–F). Indeed, the pores remain accessible to the electrolyte and lead to very good specific capacitances for the PPY of 427 F/g (in 1 M $NaSO_4$) and around 800 F/g for the PANI (in H_2SO_4 at 1 M).

12.3.2 ECP with Vertically Aligned CNT Composites

In 2001, Chen et al. [95] performed the first electropolymerization of PPY on VACNTs and first introduced the concept of conformal electrodeposition, which was used in further studies [96–98]. The polymerization was carried out by CV in classical electrolyte (0.1 M $LiClO_4$ in water) (Figure 12.7A) and remarkably, the charge/discharge was at least 23 times greater compared with coating on a platinum (Pt) or titanium (Ti) electrode, as a clue of a conformal deposition, hence shown on SEM and TEM pictures (Figure 12.7B).

Ghaffari et al. [99] have prepared PEDOT conformally coated on aligned carbon nanotubes electrodes (PEDOT/A-CNTs) and investigated symmetrical supercapacitor. Their study compared different PEDOT/CNT configurations, i.e. to those of non-coated CNTs as well as those of PEDOT randomly coated on entangled CNTs (Figure 12.8a). The electrochemical performances of their electrodes have been evaluated by CV, revealed that the PEDOT conformally coated on A-CNTs and with high volume fraction (5%) have a specific volumetric capacitance of 84.0 F/cm^3, much higher compared with the non-coated and low volume fraction ones (1%), these latter having only 3.9 F/cm^3 (Figure 12.8b,c). Moreover, they evidenced through impedance measurements that ionic transport (insertion/de-insertion processes) in the PEDOT coating layers was not limited in the A-CNT configuration compared to entangled configuration. Specific energy and power densities of 11.8 Wh/l and 34.0 kW/l, respectively, were obtained for these nano-tailored electrodes, with high capacitance retention compared with those of PEDOT coated on entangled CNTs.

Fang et al. [100] have prepared PPY on A-CNTs arrays on metal foil electrodes by electrochemical process. They confirmed the conformal deposition of PPY onto the

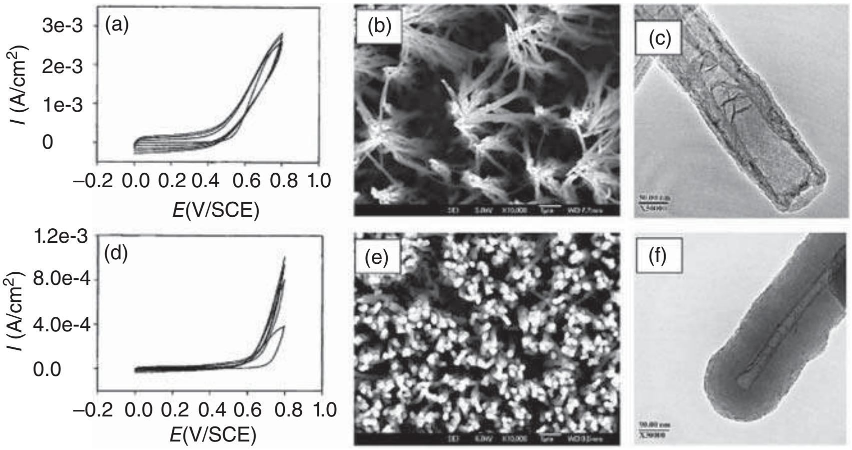

Figure 12.7 Potentiodynamic polymerization (4 cycles at 5 mV/s) of PPY on (a) VACNT and (d) Pt planar electrode in 0.1 M $LiClO_4$ aqueous solution containing 17 mM of Py. SEM (b–e) and TEM (c–f) pictures of PPY coatings at different charges (b,c) 86 mC/cm^2 and (e,f) 1306 mC/cm^2. Source: Reproduced from Chen et al. [95] with permission from Elsevier, 2001.

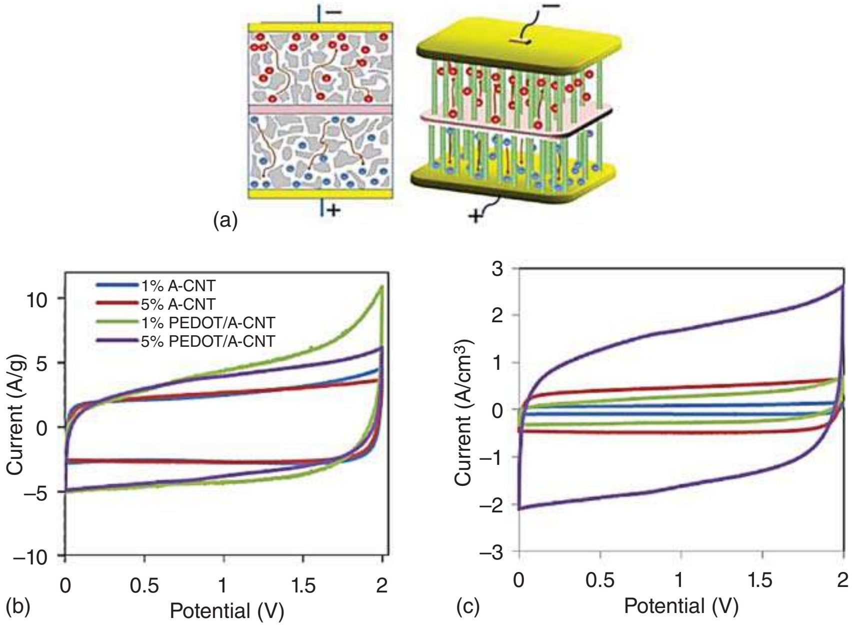

Figure 12.8 (a) Schematic comparison of the tortuous ion transport paths in nanoporous electrodes formed, for example, from activated carbons (left), and parallel ion pathways in the A-CNTs. Cyclic voltammetry curves for the pure A-CNT and PEDOT/A-CNT electrodes at 100 mV/s scan rate: (b) Gravimetric and (c) volumetric current density as a function of applied voltage. Source: Ghaffari et al. [99]. 2013, Elsevier.

CNTs arrays by TEM. As-prepared PPY/A-CNTs electrode with PPY nanostructures exalts the storage properties as shown on Figure 12.9a compared with pristine PPY and A CNTs. The specific capacitance of nanocomposites is estimated at 505 F/g (mass of PPY + A-CNTs). The nanocomposite retains high specific capacitance of $C_m \sim 300$ F/g at 20 A/g compared with pristine PPY ($C_m \sim 100$ F/g at 6 A/g), cf. Figure 12.9b,c. Assembled in symmetric supercapacitor configuration, the specific capacitances of the PPY/A-CNTs electrode materials can reach 456 F/g (vs. mass of nanocomposite) and retain its capacitance of c. 280 F/g at 10 A/g (Figure 12.9c–e). Also PANI/A-CNTs electrodes and supercapacitors were also prepared with similar approach reported by Chen and coworker [101] and obtained specific capacitances of about $C_m = 1100$ F/g.

In 2014, Aubert and coworkers [102] published a similar study than that of Fang et al. but varying many parameters such as the nature of ECP (poly(3-methylthiophene) (P3MT) instead of PPY, the choice of method (pulsed galvanostatic instead of potentiostatic), the nature of electrolyte (pure ionic liquids such as EMITFSI and PYR13TFSI instead of aqueous-based ones) as well as the nature of VACNT (~100 μm vs. ~10 μm), c. CNTs elaborated by Mayne-L'Hermite and coworkers [73, 75] on Si wafer substrate. In this case, the conformal P3MT deposition onto VACNT is even more complicated to obtain since the electrolyte is very viscous (~40 cP for ionic liquids). However, by a fine tuning of t_{ON}:t_{OFF}

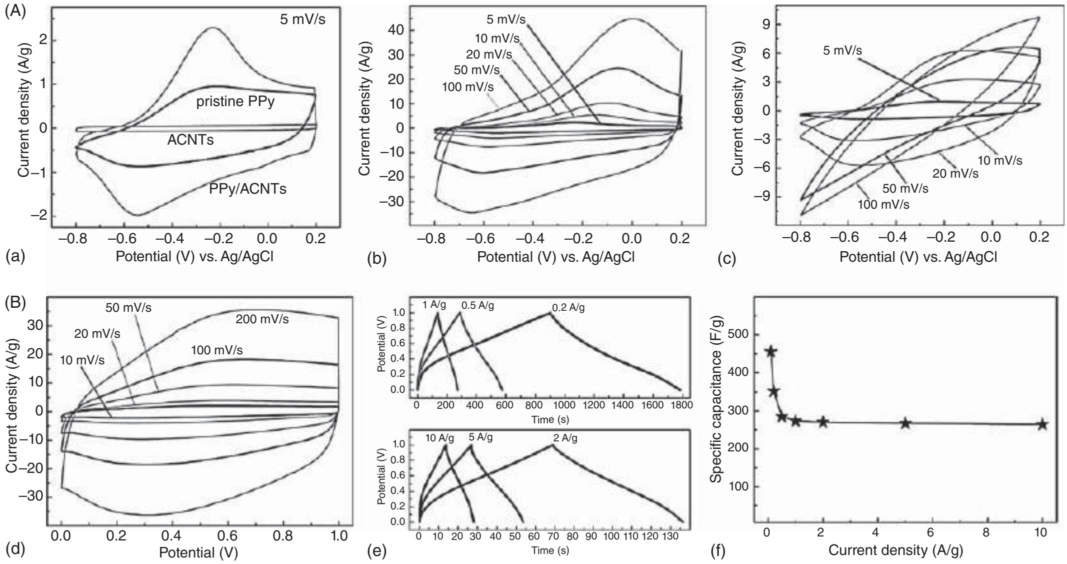

Figure 12.9 (A) CV curves of PPY/ACNTs, pristine PPY and ACNTs at a scan rate of 5 mV/s (a); CV curves at different scan rates of PPY/ACNTs (b); and pristine PPY (c); (B) Electrochemical performance of the symmetrical supercapacitor based on PPY/ACNTs: CV curves at different scan rates (d); GCD curves at different current densities (e); specific capacitances vs. different current densities (f). Source: Fang et al. [100]. 2017, Elsevier.

conformability was obtained on all the 100 μm thickness of VACNT carpet (see Figure 12.10a–d,f) compared with a conventional galvanostatic electrosynthesis (Figure 12.10e). Also, the control of P3MT can be obtained easily by the number of sequences and very thin P3MT layers were coated on the CNTs, i.e. from 9 to 30 nm. A specific capacitance of 180 F/g was obtained at a P3MT loading of 85% in the nanocomposite. Comparison with entangled nanocomposites shows an increase of 30% of capacitance similarly as a previous study of Zhang et al. [76] on pristine MWCNT (entangled and aligned) electrodes. However, due to the nature of the substrate, no supercapacitors were made to date in this configuration. The replacement of Si wafer to Aluminum substrate as current collector has been challenging [71, 103] since the VACNT growth temperature need to be decreased down to 650 °C. Very recently, Mayne-L'Hermite and coworkers [104] manage to elaborate MWCNT/Al electrodes changing carbon source (acetylene instead of toluene) and were able to produce very dense VACNT on Al substrate (10^{11} CNT/cm^2), which is two magnitude order more than for VACNT/Si. This trend is due to the characteristics of the CNTs (diameter 5–20 nm instead of 40–80 nm in the case of VACNT/Si). Hence the specific capacitance of these electrodes is ~50 F/g in EMITFSI/ACN electrolyte (instead of 4 F/g for pristine VACNT/Si). Similarly, P3MT was deposited onto these new electrodes and, meanwhile specific capacitance is relatively similar (~180 F/g), the stability of the electrode was show to be excellent (>20 000 cycles) [105].

PTh/CNTs composites have been earlier studied by Lota et al. [34] A very interesting tendency on cyclability was found since the polymer could be reversibly charge/discharged up to 20 000 times without any degradation. This increase of stability is explained by the mesoporous structure of the CNTs, which supports the polymer and allows the material to adapt to the change in volume. Then the polymeric structure does not need to contract and swell as much as for the polymer alone as it is the case for PPY/MWCNTs that exhibit greater retention of capacitance of 89% after 10 000 cycles. [106] The volume variation during charge/discharge of the ECP is often the cause of their low cyclability, hence the use of CNTs therefore helps to avoid this drawback. Finally, in 2014, Zhou et al. [107] obtained very high energy and power density of 170 Wh/kg and 270 kW/kg, respectively, from supercapacitors made from conformally coated PEDOT on vertically aligned MWCNT. These results were obtained by the fabrication of hybrid supercapacitors consisting of a positive electrode using the nanocomposite and a negative electrode of VACNTs, which allow charge the supercapacitor up to 4 V by using ionic liquid. The content of PEDOT coated on the MWCNTs was not too high but sufficient to increase significantly the energy compared with neat MWCNTs but keeping very good performances in term of power: at 0.5 A/g, the volumetric capacitance and energy are 40 F/cm^3 and 80 Wh/l, while at 5 A/g these values remain still high, i.e. 30 F/cm^3 and 50 Wh/l respectively.

Also PANI/MWCNT electrodes were elaborated in order to prepared flexible supercapacitor electrodes Benson et al. [92] in an aqueous electrolyte (H_2SO_4 at 1 M). Authors showed also the importance of the applied current during a pulsed chronopotentiometry where the weakest current density (2 mA/cm^2) allows a

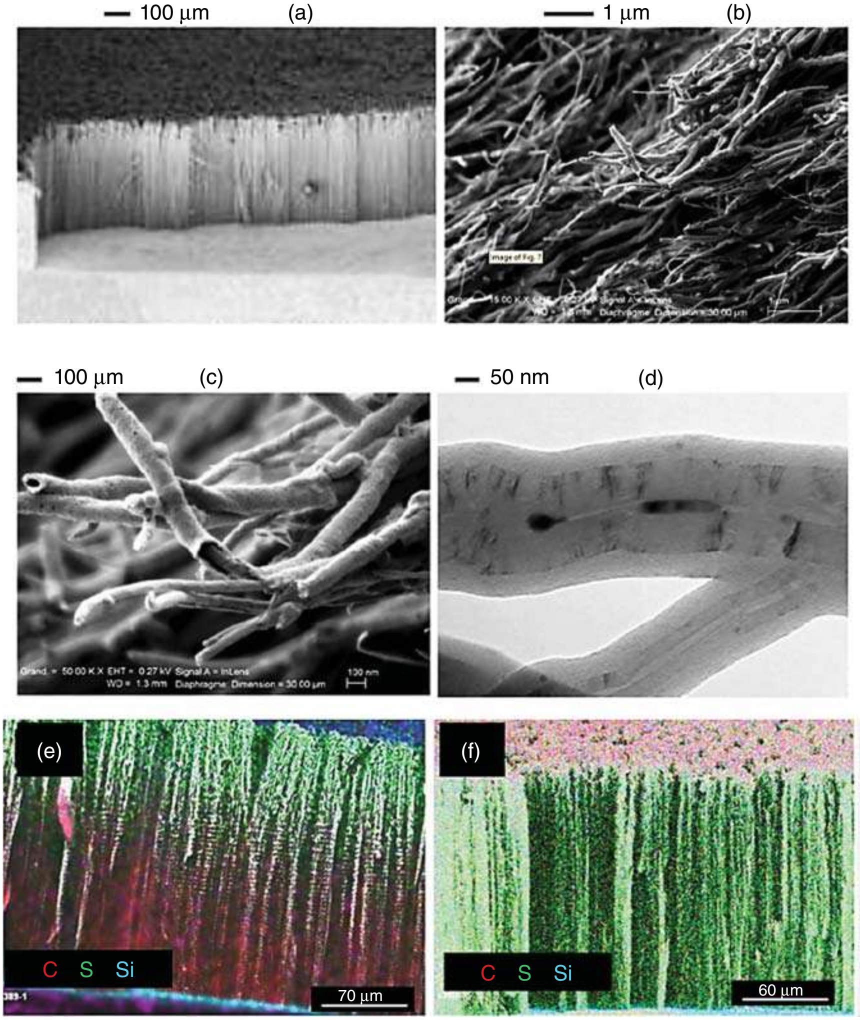

Figure 12.10 SEM and scanning electron microscope with field emission gun (SEM-FEG) pictures of the nanocomposite obtained by pulsed galvanostatic polymerization (conditions: 100 sequences applying a current density of 4 mA/cm^2 (tpolym.45 seconds, tOCP300 s) in pure EMITFSI and 0.2 M 3MT. (a) Cross-section of the nanocomposite. (b) Magnification at the center of the carpet. The alignment of CNT is partially lost due to the cleavage procedure. (v) Magnification on individual VACNTs exhibiting the polymer sheath around each CNT. (d) TEM picture showing the homogeneous nanometric polymer layer present around each CNT. (e) EDX mapping of S element (from P3MT) for a non-pulsed galvanostatic method, and (f) pulsed method. Source: Reproduced from Lagoutte et al. [102] with permission from Elsevier, 2014.

more homogeneous deposition within the MWCNT leading to higher specific capacitances, 250 F/g against 200 F/g for a deposition at higher current densities, i.e. 16 mA/cm^2. Also, one possibility to structure the ECP is the approach used by Lin et al. [108] in which they developed horizontally aligned MWCNTs for electrode having thicknesses of 250 μm. These MWCNTs then serve as a substrate for the electropolymerization of aniline or pyrrole with an electrolyte gel of H_3PO_4–PVA forming a self-supporting material. Capacitances of 230 to 200 F/g were measured as a function of the folding angle of the supercapacitor, from 0 to 180°, respectively, for the MWCNT/PANI.

12.4 Graphene-Based Nanocomposites

Since the first introduction by A. Geim and K. Novoselov at the University of Manchester in 2004 as the first synthetized 2D material with single atom thick, graphene has widely been investigated in both fundamental and applications [109]. Accordingly, graphene is composed of single carbon planar sheet with sp^2-hybridized structure. Briefly, what makes graphene so relevant compared with other family of materials? It is worth noting that this 2D configuration generates very intriguing behaviors, such as high specific surface area (2630 m^2/g), high thermal/electrical conductivity, impressive mechanical/chemical resistance, and extraordinary flexibility and transparency [110]. These excellent properties make graphene and related materials befitting to a wide spectrum of applications, ranging from transistors, sensors, all of energy storage and conversion devices, artificial skin/muscles [111, 112]. For electronic devices, the electron mobility is determined at 2.10^5 cm^2/(V/s) at electron density of 2.10^{11} cm^{-2} as a result of massless Dirac fermion within the graphene sheet, leading to extremely high electrical conductivity of the layer [113]. In terms of charge storage via formation of electrical double layer, theoretical specific capacitance of single layer graphene is calculated at 21 μF/cm^2, leading to a value of 550 F/g when the totality of the surface is used [114]. However, due to the interactions by π–π stacking and van der Waal forces, graphene sheets tend to aggregate and the electrochemical accessible surface is massively decreased, resulting to a limitation of diffusion of ions. Thus, the actual performance of pristine graphene is far lower than the theoretical values. To prevent or at least minimize the restacking phenomenon and to generate space for ions to diffuse, other material(s) need to be coupled with graphene (e.g. CNTs, polymers, nanoparticles, etc.) affording a hybrid system. Very recently, the apparition of 3D – graphene foam could be a complementary approach to resolve this problem [115–117]. Among these options, the use of polymer as spacer is certainly considered as promising to generate fluid ions channels and more importantly, to introduce supplementary functionalities to graphene. As aforementioned about the contribution of electrochemical conducting polymers (ECP) to the exaltation of storage performance of CNTs, they could also be availed themselves of their interesting properties in enhancing cycling performance of the resulted supercapacitors. Thus, the limits in the graphene/ECP related materials are being pushed much further than a simple coating of the polymer on the graphene substrate. Indeed, the microstructuration alongside with molecular engineering remained challenging for development of highly performant (micro)-supercapacitors. However, within this chapter, we do not have intention to get insight the synthesis of graphene. Consequently, we will only focus on describing the preparation and the use of ECP/G related materials for supercapacitors by highlighting recent important advancements in the field.

12.4.1 Polymer/Graphene Composites

Since the era of graphene begun in 2004, scientific community has very excited to couple graphene with other polymers, resulting to a massive number of reports in the last decade. Accordingly, numerous publications have been devoted to the preparation of polymer/graphene composites. Typically, graphene/polyurethane, [118] epoxy, [119] polystyrene (PS), [120–123] poly(vinylidene fluoride) (PVDF), [124] polycarbonate (PC), [125], etc. [126] were widely investigated. The synthesis and preparation of the reported composites vary from one group to another, ranging from a simple mixture of graphene and polymer to more complicated technique. For example, Stankovich et al. [120] reported a three-step procedure for achieving homogeneously dispersed graphene in PS matrix. The graphite oxide was treated with phenyl isocyanate in dimethylformamide for 24 hours followed by ultrasonic exfoliation, resulting to a stable dispersion of isocyanate functionalized graphene oxide (GO). Later, the PS was added to the mixture, affording to a homogeneous mixture of PS/GO, which went along with chemical reduction by using hydrazine to afford PS/rGO. Consequently, the resulted material exhibited a strong electrical conductivity (0.1 S/m) with a percolation threshold of 0.1 vol% at ambient temperature electrical conductivity. Within this context of exploring the possibility of generation of new composites, electrochemical conducting polymers started to get in touch with graphene, resulting to the creation of new type of composite. Indeed, the presence of conducting polymer allowed to strengthen the electronic conductivity of the graphene substrate as well as to provide additional conductivity and flexibility from the matrix. The very first publication on the functionalization of graphene using a conducting polymer (i.e. polystyrene sulfonate doped PEDOT) was reported in 2008 by Hong et al. [127]. Since then, numerous studies have been dedicated to the development of this family of material for a wide range of applications, including (bio)sensors [128, 129], supercapacitors, batteries [130], and electrocatalysis [131–133]. Even though there are different conducting polymers that have been used to functionalized graphene surface, three types of composites described in the previous part remained the most important ones. From specific capacitance standpoint, ECP exhibits interesting values, i.e. theoretical specific capacitance is 750, 620, 485, 210 F/g for PANI, PPY, PTh (PEDOT), respectively [34, 134].

12.4.2 Polyaniline/Graphene

Freestanding PANI coated graphene paper (GPCP) was fabricated by *in situ* electro-polymerization (AEP) of aniline by using a graphene “paper” [135]. The whole procedure as well as the final product is presented in Figure 12.11. Indeed, the graphene paper (namely, G-paper) was prepared by filtration of graphene suspension, resulting to the formation of flexible graphene electrode. Afterwards, the PANI was deposited onto G-paper by electrochemical polymerization by means of anodic polarization in aniline solution by using three-electrode setup (G-paper as WE, Pt plate as CE and SCE as RE). The as-prepared GPCP exhibited a stronger mechanical tensile of 12.6 MPa (vs. 8.8 MPa of pristine G-paper), resulting from the enhanced interconnection between graphene sheets in presence of PANI. However, the specific surface area is dramatically decreased, which was independently observed by BET (94 m^2/g for GP vs. 39 m^2/g for GPCP-900 s) and CV (6 and 3 A/g for pristine and modified graphene at −0.1 V@20 mV/s, respectively). It could be explained by the over-filling of conducting polymer to the voids of the graphene network. Nevertheless, the presence of PANI leads to an enhancement of the capacitance, resulted from the redox capacitance from the electrochemical doping of PANI. As cycling performance, the specific capacitance is found to be 233 F/g and 135 F/cm^3 as gravimetric and volumetric capacitances, respectively. Consequently,

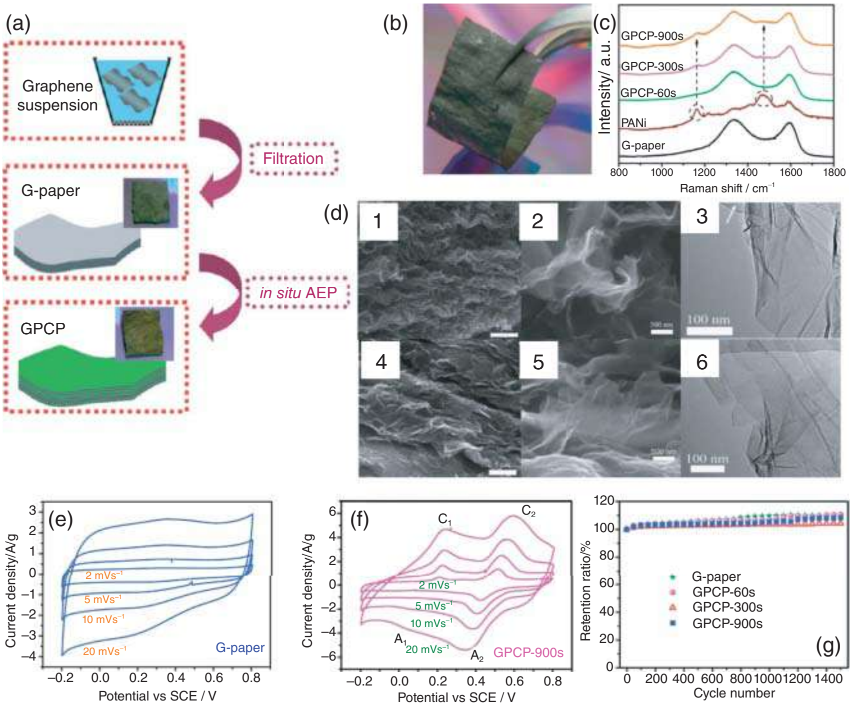

Figure 12.11 (a) Schematic procedure for preparation of PANI/G-paper; (b) Photography and (c) Raman spectra of PANI/G-paper substrates; SEM images of (d), 1–3) G-paper and ((d), 4–6) GPCP-900 s; Cyclic voltammograms of (e) GP and (f) GPCP-900 s followed by (g) stability test of different substrates. Source: Reproduced from Wang et al. [135] with permission from American Chemical Society, 2009.

the exaltation of the specific capacitance could be expected for this system by increasing the porosity of the network, e.g. adding of CNTs.

Following a similar concept, Cong et al. [136] have reported an optimized system where controlled morphology of the conducting polymer is used. Briefly, high quality G-paper was obtained by reduction of a suspension of GO dropped onto a Teflon substrate by hydroiodic acid HI followed by solvent evaporation. Later, the conducting polymer, PANI, was deposited onto the graphene substrate by electrochemical deposition. However, higher concentration of monomer was used in a mixture of water/ethanol, resulting to formation of a nanorod-PANI layer coated graphene. As-prepared substrate exhibited a strong improvement of specific capacitance (763 F/g). The significant difference of specific capacitance from similar approaches might be resulted from a strong interaction between the graphene layers and the surrounding environment (solvent-dependent deposition). Thus, the phenomenon could be explained by several factors, either a difference in organization of graphene sheets within the paper, the concentration of monomer, and/or a greater balance of hydrophilicity at the interface G-solution in presence of co-solvent, leading to deposition of PANI with rod-like structure. Indeed, when the concentration is low, the PANI is homogeneously grown onto graphene layer. In contrary, when the concentration of monomer increases, directional formation of PANI with specific nucleation sites is observed. This mechanism could be beneficial for tuning the morphology of the conducting polymer. Jin et al. [137] electrodeposited PANI onto N-doped porous graphene (NPG) by using a concentration in monomer of 50 mM, leading to the formation of homogeneously dispersed growth of PANI at the surface of NPG. Their configuration results in a specific capacitance of 330 F/g (51.9 F/cm^3) at 1 mA/cm^2. Furthermore, an asymmetric supercapacitor resulted from the assembly of polyacrylate rubber/TBABF$_4$–MeCN in sandwich between G/PANI and G/poly(1,5-diaminoanthraquinone) conducts to a strong enhancement of the cycling performance (17.0 Wh/kg and 9.58 kW/kg as energy and power density as well as a superior stability of 88.7% capacitance retention after 10 000 cycles). In order to enhance the active area of the composite, 3D graphene hydrogel (3DGH) was used as support for electrochemical polymerization of aniline [138]. Thus, the 3DGH was generated by hydrothermal treatment (Teflon – lined stainless steel autoclave) by using a suspension of graphene oxide. The as-prepared material presented a surface area of 305 m^2/g with a specific capacitance of 230 F/g@2 A/cm^2. The latter was used as template for polymerization of aniline (50 mM Ani, 1 M H_2SO_4), affording to PANI coated 3DGH. By increasing the polymerization time, the specific capacitance reaches an optimum at 710 F/g@2 A/cm^2 for a duration of 20 minutes. Beyond this duration, the specific capacitance is significantly decreased down to 364 F/g@2 A/cm^2. Besides the aforementioned works, numerous publications have also reported the use of anodic polymerization for fabrication of G/PANI (pseudo)-supercapacitors. Typical examples are be listed by Yu et al. [139] (G electrodeposited on stainless steel fabric/PANI 603.2 F/g@10 mA/cm^2 with 92% retention after 5000 cycles), Shen et al. [140] (PANI/vertical graphene (VG)/Ti 535.7 F/g@40 A/g with 86% retention after 10 000 cycles), etc.

In complement with anodic polymerization of aniline to graphene substrate, a co-polymerization of rGO/PANI composites has also been investigated, resulting from electrochemical reduction of GO and electrochemical oxidative polymerization of aniline. Feng et al. [141] reported a one-step electrochemical synthesis of G/PANI composite film for sensing and supercapacitor applications. Briefly, a GO/Aniline suspension was prepared by mixing graphene oxide and aniline, resulting from electrostatic interaction and π–π stacking of aromatic rings. The suspension was then casted onto the electrode surface followed by polarization in aqueous solution containing 1 M of sulfuric acid. By repeatedly sweeping the potential from +1.0 V/SCE to −1.3 V/SCE, aniline monomer undergoes oxidation (anodic polarization), affording to the formation of networked PANI at the surface of GO. Meanwhile, when the potential switches to cathodic, graphene oxide is transformed into the reduced form, rGO. The resulted material exhibits a specific capacitance of 640 F/g with a retention of 90% over 1000 cycles. Zhang et al. [142] presented slightly different approach where the polymerization was performed in the aqueous suspension of GO/aniline – free aniline (2.5 M sulfuric acid). It is worth noting that the graphene oxide sheets were kept as is without further transformation to graphene. Interestingly, the PANI is well covered on the totality of the graphene oxide layers, resulting to highly active material at the electrode surface. The resulted electrode leads to a supercapacitor with specific capacitance of 1136.4 F/g, which overcomes most of PANI related materials and a retention of 89% over 1000 cycles. It is worth noting that the contain of graphene oxide within the composite is strongly influential on the cycling performance of the material. [143] Being insulator as nature of graphene oxide, the capacitance of the composite must be mainly generated from the pseudo-capacitance of the conducting polymer. However, the determined value was exceeded the theoretical value for PANI (i.e. 750 F/g), which indicates that the aforementioned PANI/GO should have either a specific assembly and GO sheets are somehow conductive [144].

In complement with electrochemical approaches, oxidative polymerization has even been more widely investigated. A suspension of surfactant stabilized GO with either tetrabutylammonium hydroxide (TBAOH) or sodium dodecylbenzene sulfonate (SDBS) was reduced to TBAOH/SDBS stabilized rGO, namely, GTR/GSR. As-prepared graphene-based suspension was mixed with different amount of aniline feedstock solutions followed by "*in situ*" polymerization. As-formed composites show nanofiber-like PANI coated graphene sheets. First of all, the presence of PANI increases strongly the conductivity of the composite by 20 times. Even though the morphology of the PANI remains similar, the increasing amount of PANI leads to a decrease in the composite's conductivity, meanwhile the specific capacitance is strongly increased [145]. The resulted specific capacitance is worth at 526 F/g@0.2 A/g. However, the cycling stability over time causes the main issue of this approach (73% after 500 cycles at 2 A/g). Later on, Sun et al. [146] reported freestanding PANI@rGO composite via "*in situ*" chemical polymerization with a specific capacitance of 701 F/g@1 A/g. Concisely, GO coated nickel foam (GO@NF) was prepared by drop-casting 0.9 ml of the suspension of GO (3.75 mg/ml) onto NF (1.5 × 1.5 cm). After successive drying steps, the GO sheets were attached to the NF followed by hydrothermal treatment using hydrazine, affording to rGO@NF. Then, the nickel foam was completely removed by dissolving in HCl solution (2 M) containing $FeCl_3$ (0.8 M). Accordingly, a 3D-freestanding structure of rGO was obtained. Subsequently, as-prepared graphene template was dipped into an acidic solution of aniline in presence of APS as initiator, resulted to a flexible PANI coated rGO. As another approach, freestanding PANI@rGO could also be prepared by chemical polymerization onto a flexible rGO@ branched polyethylenimine (rGO@bPEI) [147]. A millimeter-thick layer of bPEI was deposited onto a filter paper followed by swelling in a suspension of graphene oxide, affording to a membrane of dispersed GO/bPEI. Then, a piece of as-prepared membrane was hydrothermally treated at 190 °C for 24 hours to generate rGO/bPEI. Afterwards, PANI was deposited within the film ranging from thin film to nanoparticles of conducting polymer depending upon the concentration of aniline monomer. Thus, the change in configuration of PANI layer could result in a variation of generated specific capacitance of as-formed composite. The value of SC of PANI@rGO/bPEI is, at best, 438.8 F/g@0.5 A/g (76.5% in capacitance retention after 2000 cycles at 4 A/g) in which the specific capacitance of generated PANI nanoparticles is 763 F/g@0.5 A/g. The lower value of specific capacitance could be resulted from an additional weight of the bPEI membrane to the PANI@rGO composite. Beside aforementioned examples, several studies have also been devoted to the development of PANI coated graphene related substrate as active material for supercapacitor with higher performance and cycling durability [148–152]. Typically, dispersion of PANI@GO at molecular homogeneity of PANI coating layer was used as precursor for generation of 3D network [149]. During the reduction process, the oxygen contained functional groups are eliminated that implies a decrease in dispersibility of the reduced species, leading to self-aggregation and to formation of highly porous network of PANI@rGO. Thus, the generated composite exhibits strong enhancement in specific capacitance when compared with previous works. Furthermore, by increasing the aniline content, the specific capacitance extends as well and reaches a maximal value of 808 F/g@53.33 A/g (81.3% aniline). Indeed, the current approach could provide either a minimum quantity amount of "*dead*" material or an increase of mass transport because of the high porosity of the matrix.

Other approaches have also been devoted to fabricate supercapacitors with high performance [144, 153–156]. Zhang et al. [153] proposed two-step synthesis of PPY/PANI/graphene ternary composite. Briefly, aniline is electrodeposited onto PPY paper, leading to the formation of a double layer nanotubes (DLNTs) PPY/PANI. Later, the binary composite (120 mg) is dispersed in 10 ml of ethanol by sonication for 12 hours followed by mixing with 10 ml of GO/ethanol suspension (6 mg/ml). Later, the as-prepared mixture was transferred into a Teflon-lined stainless steel autoclave and treated at 180 °C for 12 hours. The final product was collected and washed, leading to the formation of rGO/PPY/PANI ternary composite. As-prepared composite exhibited a specific capacitance of 542 F/g@1 A/g along with a moderate energy and power density of 20.8 Wh/kg and 250 W/kg, respectively. More recently, a ternary composite of GO/PANI/PEDOT:PSS was prepared as ink for preparing flexible micro supercapacitor by means of extrusion printing (Figure 12.12) [154].

Indeed, PANI@GO was synthetized by interfacial polymerization where the graphene oxide sheets were within the aqueous phase as well as the initiator (APS) and the aniline monomer was in the organic phase [154]. During the polymerization process, the monomer formed polymeric chains followed by transferring to water phase resulted to a change in color from yellow brown to dark green solution. The as-formed product was latterly used as precursor for fabrication of PEDOT:PSS@PANI@GO by a simple mixture of desired amount of PEDOT:PSS and suspension of PANI@GO, affording to active ink of GO/PA-PE. Afterwards, the active ink was used to prepare flexible micro supercapacitor by extrusion printing. Briefly, patterned Au on PET substrate was prepared by sputtering a thin layer of Au onto PET substrate followed by directly extrusion printing of active materials (Figure 12.12e). As a result, the thickness of the active layer could vary from 4.6 to 80 μm depending upon the number of printed layers. Thus, the areal capacitance is proportionally increased with the thickness where it reaches 153.6 mF/cm^2 (volumetric capacitance of 19.2 F/cm^3) at a scan rate of 5 mV/s when the thickness is about 80 μm (20 printed layers). For further improvements, asymmetric devices were developed by using GO/PA-PE as positive electrode and rGO/PEDOT:PSS as negative electrode. Even though the areal capacitance is lowered, the resulted asymmetric flexible micro-supercapacitor (AfMSC) exhibits higher cycling performance of 4.83 mWh/cm^3 (vs. 3.36 mWh/cm^3), 25.3 W/cm^3 (vs. 9.4 Wh/cm^3) as energy and power density, respectively. Accordingly, the stability of AfMSC is approved with nearly 100% capacitance retention over 10 000 charge–discharge cycles instead of 60% of capacitance retention over the same cycling conditions by using symmetric flexible micro-supercapacitor. In short, this newly developed procedure could pave the way for further developments of energy storage systems (μSC) for micro-devices [157].

12.4.3 Polypyrrole/Graphene

Possessing a second highest theoretical specific capacitance among different conducting polymers, PPY has also been strongly coupled with graphene related materials, leading to highly active composites with enhanced cycling performance [133]. Some advantages of PPY over other conducting polymer could be listed as lower oxidation potential (easier oxidation reaction) and more water soluble and it could be prepared by low-cost procedures. Similar to PANI coated graphene materials, PPY@G related composites could also be prepared by either electrochemical polymerization or oxidative polymerization. However, due to the difference in chemical structure as well as physical chemical properties, the microstructuration and morphology of the PPY@G could be differed to the PANI based composites.

As soon as PANI@G based composites were reported as active material for supercapacitors, PPY coated graphene related materials were also investigated for the same purpose. Indeed, Liu et al. [158] reported the preparation of PPY coated sulfonated graphene (SG) as active materials for supercapacitor by means

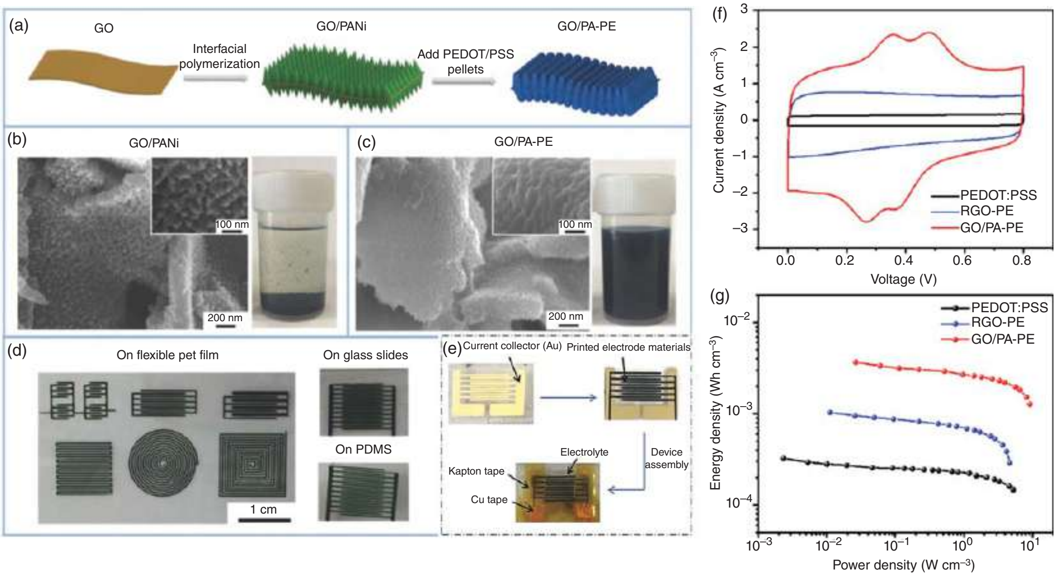

Figure 12.12 (a) Schematic illustration of the preparation of dispersible GP/PANI/PEDOT (GO/PA-PE) inks. Scanning electron microscopy (SEM) images and photographs of (b) GO/PANI and (c) GO/PANI-PEDOT:PSS composites and dispersions. (d) Digital photographs of extrusion printed GO/PANI-PEDOT:PSS patterns on various substrates. (e) Scheme for the fabrication of all-solid-state fMSCs on a flexible PET substrate, (f) CV curves at the scan rate of 50 mV/s, (g) Ragone plots showing the energy and power density of GO/PANI-PEDOT:PSS, rGO-PEDOT:PSS, and PEDOT:PSS fMSCs. Source: (a, f, g) Liu et al. [154]. 2018, Wiley Online Library, (b, c, e) Reproduced from Liu et al. [154] with permission from Wiley, 2018.

of electrochemical polymerization of pyrrole in presence of SG. From mechanistic standpoint, sulfonate groups from graphene sheets act as anionic dopant during the electrochemical formation of PPY. Accordingly, the SG sheets are embedded inside the polymer matrix, affording to the formation of composite with an enhanced conductivity from 99 S/m (pristine PPY) to over 500 S/m. Furthermore, the composite exhibits an improvement in specific capacitance (285 F/g@0.5 A/g by using 40% SG composite) of two times compared with pristine PPY (145 F/g@0.5 A/g) and five times compared with pristine SG (55 F/g@0.5 A/g). Also, the capacitive retention was determined about 92% over 800 charge–discharge cycles. The reported values are competitive with PANI-based composites in the same period. In another work, nanoparticles of PPY were generated onto graphene paper by means of pulse-electrodeposition [159]. Briefly, graphene flakes generated by Hummer's method were filtered through an 0.4 μm PC membrane, leading to formation of homogeneously distributed GFs/PC membrane. Accordingly, the as-prepared film was used as working electrode for electrochemical deposition of PPY nanoparticles. The polymerization processes by pulse-potentiometry with a short duration of 0.1 seconds per step from 0 to 1.05 V/SCE until completion of the desired time (60, 120, 360 seconds). By using this procedure, instead of formation of continuous film of PPY on the superficial side of the G membrane, nanosized particles (5–40 nm) are homogeneously generated inside the graphene layer. Consequently, the as-formed layer exhibits strong enhancement in specific capacitance (237 F/g@1 A/g) and in energy density of 32.9 Wh/kg. The increase in energy density compared with other works on ECP@G could arise from the gain in mass ratio of conducting polymer over total mass of the composite via pulsed-technique. Nevertheless, by using only graphene as support, the sheets could be stacked during filtration, leading to a decrease in ion transport during charge–discharge process. Thus, the specific capacitance would be worth lower than expected. For further optimization, adding small portion of CNT (~1% in mass) could be potentially promising to generate more space for ion channels to be established [144]. From this point of view, well-defined structuration of PPY@graphene related composites becomes major challenges for improving the cycling performance of supercapacitor. Indeed, surface chemistry of graphene has been exploited. Accordingly, Li et al. [160] reported the use of an organic molecule, 3,6-di(pyridin-2-yl)-*s*-tetrazine, for tethering the graphene sheets from self-aggregation. As a consequence, the formation of PPY was homogeneously observed during electropolymerization, leading to an improvement in cycling performance (346 F/g@0.45 A/g). However, the stability remains an issue, i.e. the trapped ions during the charging process provoke capacitance loss over cycling (60% of capacitance retention after 5000 cycles). In the other hand, for facilitating the ionic transport, aligned nanowires of PPY@rGO were prepared and reported by Chen et al. [161]. Briefly, an alumina porous membrane with a hole diameter of 220 nm was used as template for electrosynthesis of composite. Thus, the porous membrane was sputter-coated with a thin layer of gold followed by filling up the pores with PPY/GO via electropolymerization, i.e. 12 cycles of CV between 0 and 1.2 V/SCE, in a solution containing pyrrole and GO suspension. Afterwards, the as-prepared substrate is treated in 1 M of

KOH for three hours to completely remove the Al_2O_3 template, affording to fully aligned PPY@GO wires on Au substrate (Figure 12.13a–d). As an important result, the specific capacitance of as-formed composite is determined about 960 F/g over a wide range of scan rate from 10 to 100 mV/s (Figure 12.13e–f), which outperforms most of ECP@graphene composites. For short-term stability, the capacitance retention was remained constant after 100 cycles. However, long-term cycling stability was not provided. Distinctively, Zhao et al. [162] reported the elaboration of PPY@3D G foam as active material for highly compression-tolerant supercapacitor (Figure 12.14). Three-dimensional graphene foam was prepared by treating graphene oxide suspension under hydrothermal condition and in presence of pyrrole monomer. Then, the as-formed product was used as working electrode and was put under anodic polarization (0.8 V/SCE), producing 3D PPY coated graphene foam.

Interestingly, the as-prepared material exhibits a high specific surface area of 144 m^2/g, which is relatively close to pristine 3D graphene. Thus, the appearance of polymeric matrix inside the foam does not interfere to the porosity of the composite. Moreover, the presence of the coated layer improves the electrical conductivity by 2 orders of magnitude (i.e. 3000 S/m). Besides, the PPY@G foam could be compressed at different levels (up to 80% strain) without showing significant degradation. Once release, the specific surface area could recover to the initial value (Figure 12.14a–l). In terms of storage performance, the composite exhibited a specific capacitance of 350 F/g@1.5 A/g (i.e. 14 F/cm^3) in the uncompressed form and a volumetric capacitance of 28 F/cm^3 at a compressed strain of 50%. Interestingly, the specific capacitance remains constant without degradation after 1000 cycles of compression (Figure 12.14m). It should be noted that during the charge and discharge process, the adsorption and desorption of ions within the active layers cause a significant mechanical constraint to the electrode, leading to a decrease in stability over cycling. Consequently, the present approach provides an enhancement in tolerance over mechanical change during electrochemical events, resulted to an improvement of the durability of the device. From this conceptual composite, Park et al. [163] reported the use of PPY@G foam as common active material for multi-purpose, ranging from sensors (temperature and pressure) to supercapacitor, leading to a flexible wirelessly powered devices.

In parallel with electrochemical approaches, chemical polymerization plays also an important role in development of PPY@G based supercapacitors. Indeed, numerous works were reported in the literature by exploiting a variety of procedure for boosting the cycling performance of the supercapacitors [164–168]. Accordingly, a large spectrum of PPY@G based composites with different structures was prepared, such as self-assembled PPY nanowire on graphene sheets, [169] hierarchical graphene nanosheet (GNS)/PPY nanosheet composite [170], Graphene/PPY nanofibers [171], etc. In this context, PPY/bacterial cellulose (BC)/graphene paper was reported as good candidate for flexible electrodes with high performance [172]. Briefly, the PPY was polymerized to the slurry BC by means of *in situ* oxidative polymerization, leading to the formation of a slurry suspension of PPY@BC. Morphologically, the PPY is grown along the BC fibers, leading to a formation

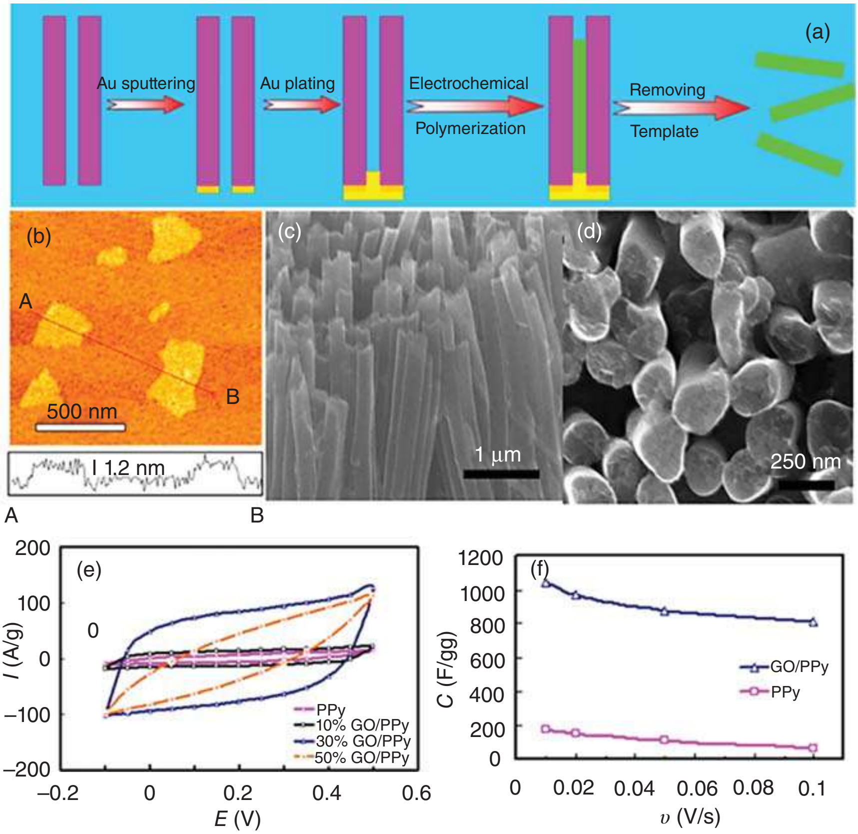

Figure 12.13 (a) Schematic illustration of graphene-containing nanowires, (b) A typical AFM image of GO sheets; scanning electron microscopy images from the (c) side view, and (d) top view of the polypyrrole/graphene oxide nanowires; (e) Cyclic voltammogram at GO/PPY nanowires with various GO contents @$v = 0.1$ V/s in aqueous solution containing 1 M of NaCl; (f) Comparison in rate capability of the GO/PPY nanowires and pure PPY nanowires. Source: (a, e, f) Chen et al. [161] © 2014 American Chemical Society, (b–d) Reproduced from Chen et al. [161] with permission from American Chemical Society, 2014.

of PPY fibered network. Then, a suspension of rGO was added into the mixture under stirring to afford self-assembled PPY@BC/rGO composite. Afterwards, the as-prepared mixture was filtered through a porous nitro cellulose membrane followed by drying process. Finally, the PPY@BC/rGO film was peeled off from the membrane and was used as freestanding electrode for supercapacitor. The latter exhibits an outperformed areal capacitance of 3.66 F/cm^2 at 1 mA/cm^2, i.e. 271 F/g and a capacitance retention of 73.5% after 8000 cycles. Similarly, Wan et al. investigated rGO/PPY@cellulose paper (RPC) as flexible electrode (sheet resistance = 1.7 Ω/sq.) for fabrication of solid-state supercapacitors [167]. Thus, the presented device displayed an areal capacitance of 0.51 F/cm^2 at 0.1 mA/cm^2 and an energy density of 1.18 mWh/cm^3. It is worth noting that the self-assembling process could be important to exploit the π–π stacking effect between pyrrole and conjugated

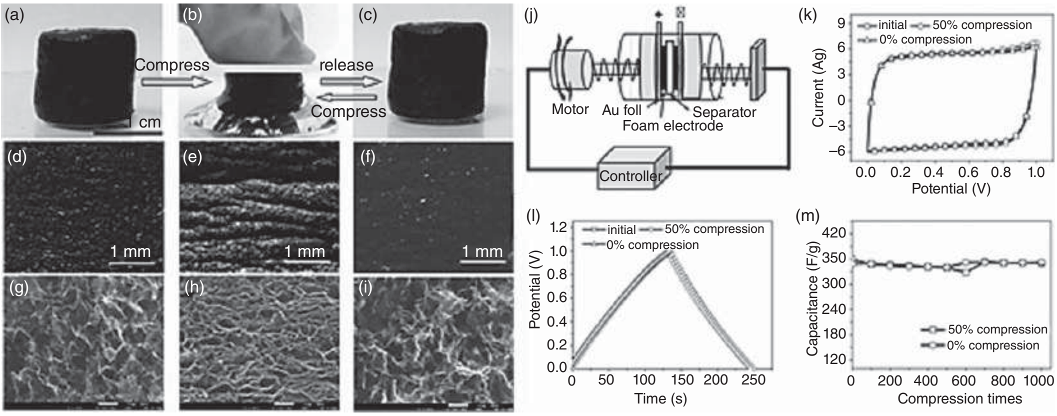

Figure 12.14 (a–c) Photographs corresponding to the compression-recovery processes of PPY-G foam; (d–f) The surface views of PPY-G foam along with (g–i) SEM images of the inner microstructures of PPY-G foam, corresponding to the unloading-loading-unloading status in (a–c), respectively. (j) Schematic representation of PPY-G based supercapacitor devices; (k) CVs of the PPY-G foam-based devices under 0% and 50% compression for one cycle ($v = 0.03$ V/s); (l) The corresponding galvanostatic charge-discharge curves at a current of 1.5 A/g under 0% and 50% compression. (m) The gravimetric capacitances at different compression states for 1000 cycles. Source: (a–i) Reproduced from Zhao et al. [162] with permission from Wiley, 2013, (j–m) Zhao et al. [162]. © 2013 John Wiley & Sons.

system of graphene in a thermodynamically stable manner, resulting to a synergetic effect from the extended aromatic regions. Besides, the interaction between PPY and graphene could also be implemented to afford highly porous composite, i.e. 3D PPY@rGO aerogel. Hence, the mixture of GO suspension and PPY nanotubes was used as a precursor for fabrication of aerogel [173]. Well-dispersed PPY@GO is gradually aggregated during chemical reduction of graphene oxide, conducting to the formation of water-insoluble PPY@rGO precipitate. After freeze-drying process, the PPY@rGO aerogel is formed as highly porous material (SSA of 17–55 m^2/g and density ranging from 0.064–0.095 g/cm^3 depending on the feeding ratio between GO and PPY). Interestingly, the composite displays excellent mechanical properties by being able to support a mass of 5000 times heavier than its own weigh. From electrochemical standpoint, a specific capacitance of 253 F/g@0.5 A/g with negligible degradation after 2000 cycles was observed.

Besides dealing with the nanostructuration of PPY as well as the composition of PPY@G related composites, surface chemistry of graphene itself is still remained scanty and is opened for further investigations. Preliminarily, nitrogen contained graphene (e.g. N-doped graphene, NH_2-functionalized graphene) was reported to facilitate the growth of PPY during polymerization process [174]. From structural standpoint, primary amine groups of NH_2-G must provide a better nucleation and growth of PPY than quaternary and pyridinic nitrogen from the N-doped graphene (NG). In contrary, the electron transfer has been proven to be more efficient with NG, [175, 176] leading to a compromise between polymer loading and electron transfer efficiency. At the same PPY loading (10% in mass), the specific capacitance of resulted NG-PPY and NH_2-G-PPY was determined at 338.8 and 230.1 F/g@0.26 A/g, indicating the important role of electrical conductivity of the graphene support to the enhancement of pseudo-supercapacitance.

Moreover, ternary composites have also attracted a wide attention from scientific community. Typically, Kalambate et al. [177] reported the use of graphene/silver nanoparticles/PPY as ternary active material. A simple mixture of rGO, silver nanoparticles (Ag NPs, diameter < 100 nm), and pyrrole monomer with appropriate mass ratios was prepared followed by chemical polymerization in presence of oxidizing agent ($FeCl_3$). The presented procedure leads to the formation of ternary material where rGO and Ag NPs are well dispersed within the polymer matrix. In presence of silver nanoparticles, the electrochemical performance of PPY@G based material is strongly exalted with a specific capacitance of 400 F/g@0.5 mA/g alongside with a capacitance retention of 92% after 1000 cycles. Nevertheless, the stripping of silver might cause important loss in performance for long-term cycling. Hence, developing ternary composites with non-electroactive metallic particles could be an alternative choice. Typically, graphene/$MnFe_2O_4$/PPY was synthetized by two-step procedure. Firstly, $MnFe_2O_4$ sub μPs (~350 nm) decorated rGO sheets were prepared by polyol process (ethylene glycol and polyethylene glycol) in presence of $MnCl_2$, $FeCl_2$, and graphene oxide sheets. Then, $MnFe_2O_4$@rGO sheets were bonded together using *in situ* polymerization in pyrrole solution, affording to PPY@$MnFe_2O_4$@rGO. Even though as-prepared composites exhibit moderately low specific capacitance of 66.1 F/g@0.5 A/g, rectangular shape CVs were barely obtained, indicating no interference of faradaic charge transfer. In the same vision, PPY@rGO@MnO_2 was prepared as high performant electrode material [178]. In brief, a graphene-based substrate was used as working electrode for electropolymerization of PPY, resulted to PPY@rGO. As-formed structure was hydrothermally treated (60 °C, 80 minutes) in presence of $KMnO_4$ (0.03 M) to generate MnO_2@PPY@rGO. The presence of PPY during the deposition of MnO_2 leads to the formation of nanoparticles ($d < 50$ nm) rather than flower-like structure ($d > 200$ nm). The growth mechanism of MnO_2 was fully described elsewhere [178]. Being as active material, the ternary composite exhibits a specific capacitance of 600 F/g@1 A/g, which outstands most of PPY based composites. The exaltation in cycling performance is mainly due to the nanoparticle structure of manganese dioxide. Indeed, small size nanoparticles could shorten the diffusion length of the ions during charge–discharge process and diminish "dead" MnO_2. In short, the performance of ternary composites depends strongly on the combination of the composition, the nature, and the morphology of metallic component.

12.4.4 Thiophene-Based Polymers/Graphene

Even though the theoretical specific capacitance of polythiophene is relatively low, it would be a massive remiss not to discuss the possible coupling of PTh and graphene for developing of supercapacitor. In the following section, recent advancements in application of polythiophene@graphene as active composite in the field of supercapacitors are presented. Since the microstructuration of the composite has significant role in achieving superior performance, different approaches have been already proposed to optimize the combination of both materials, PTh and graphene. Unlike other conducting polymers, thiophene based polymer have widely been used in their commercially available form, via a simple mixture with graphene-based materials, to generate active composites with enhanced performance. In the early stage, the most-known thiophene derivative, PEDOT:PSS was used as conductive wrapping for enhancing the storage performance of MnO_2 decorated graphene sheets (GMP) [179]. Indeed, mesoporous MnO_2 nanoparticles with flower-like structure were deposited onto graphene substrate (graphene coated polyester textiles, $R = 700\ \Omega$/sq.) by anodic polarization. Afterwards, the prepared substrate was dipped into a suspension of commercially available PEDOT:PSS (Clevios, 1 : 10 diluted PH1000 solution) and subjected to 2–3 "dip and dry" cycles. Once terminated, the polymer loading is about 0.2 mg/cm^2. As benchmark, similar procedure was applied by using a suspension of SWCNTs, resulting to G@MnO_2@SWCNTs (GMC). In presence of conductive wrapping layer, the cycling performance of GMP are strongly exalted by 1.4 times compared with GM; i.e. from 270 to 380 F/g@0.1 mA/cm^2 and by 1.2 times compared with GMC, i.e. from 320 to 380 F/g at the same current density. The enhancement in specific capacitance in GMP is related to the additional pseudo-capacitance of the PEDOT:PSS. Nevertheless, the use of SWCNTs could be more profiting over a wide voltage range due to instability of conducting polymer at high cell voltage. In terms of cycling stability, a capacitance retention of 93% and 95% over 3000 cycles was observed for GMC and GMP, respectively. The phenomenon could be explained as followed: the 3D wrapping induces an enhancement in mechanical tolerance, i.e. the MnO_2 nanoparticles are stabilized and are kept connected inside the wrapping layer without any dissolution during charge–discharge process. By owing excellent mechanical properties, PEDOT:PSS was further used to develop highly flexible all-solid-state supercapacitor by mixing with reduced graphene oxide [180]. For fabrication of the flexible electrode, a suspension of PEDOT:PSS with graphene oxide ([PEDOT:PSS + GO] = 20 mg/ml) and diethylene glycol was bar-coated onto a PVDF membrane. After drying, the film was peeled off from the support and can be further reduced to form rGO/PEDOT:PSS, which was used as freestanding electrode for fabrication of flexible supercapacitor. Even though the gravimetric capacitance of the symmetric capacitance is only 51.2 F/g at 10 mV/s, the areal capacitance is still comparable with previously reported materials, i.e. 448 mF/cm^2@10 mV/s (composite with 33% loading in rGO and with a concentration of 8.49 mg/cm^2). Importantly, the presented composite exhibits a high stability with no sign of degradation over 20 000 charge–discharge cycles and over multiple bending cycles (1000 times with various angles). Later, Liu et al. [181] reported the used of rGO/PEDOT:PSS composite for fabrication of all-solid-state micro-supercapacitor (fMSC) by means of bar coating and laser etching technique. After coating a layer of rGO/PEDOT:PSS onto Au/PET substrate, redundant part was removed from the device by laser etching, which resulted to a interdigitated supercapacitors (Figure 12.15a,b).

Interestingly, by using laser etching technique, multiple fMSCs in a desired configuration (series/parallel) could be generated. As aforementioned, supercapacitors made from a mixture of PEDOT:PSS and graphene exhibit a very strong mechanical tolerance to deformation, i.e. little change in cycling performance over bending at different levels was observed for a single fMSC(20) where 20 represents the number of striped lines of active material on a single device (Figure 12.15b). As demonstrator, a single and 12 fMSCs (6 in series +6 in parallel) systems were used to power one and 20 LEDs, respectively (Figure 12.15c). It should be noted that the capacitance is divided by the number of cells in series and the voltage is enhanced by the same factor, while the capacitance is multiplied by the number of cells in parallel. Consequently, 12 fMSCs made in this configuration result to the capacitance of a single device with an exaltation of the voltage by 6 times (6 V). In terms of charge storage performance, the fMSC(20) displays a strong stability over multiple bending cycles (Figure 12.15d–e) great capacity retention of 84% after 20 000 cycles (Figure 12.15f–g) with outstanding energy and power density of 3.05 mWh/cm^3 and 4.52 W/cm^3 (Figure 12.15h) alongside with volumetric capacitance of 14.5 F/cm^3@5 mV/s (eq. to an areal capacitance of 84.7 mF/cm^2@5 mV/s for fMSC(20) with 58 μm thickness). In another approach, hollow rGO/PEDOT:PSS fibers was prepared as fiber electrodes [182]. Briefly, a mixture of GO, PEDOT:PSS and necessary reagents was poured into glass pipes with two ends sealed followed by reduction of GO to afford rGO/PEDOT:PSS fiber. Then, the dried fibers were taken out of the pipes and resulted to highly active material for fabrication of supercapacitor, i.e. a volumetric capacitance of 143.3 F/cm^3 (areal capacitance of

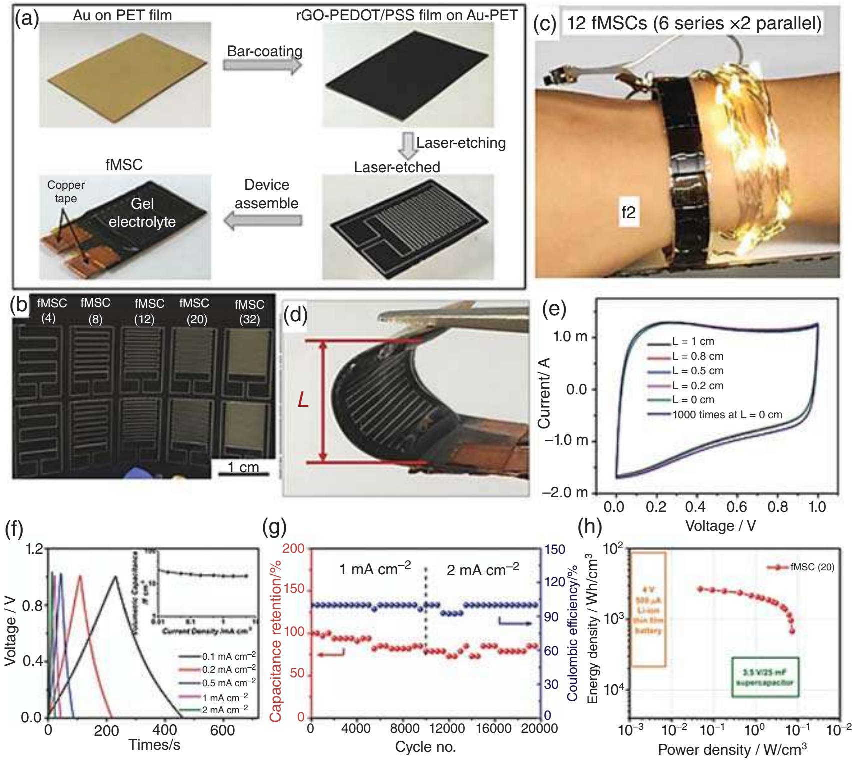

Figure 12.15 (a) Schematic representation of the fabrication procedure of all-solid-state rGO-PEDOT:PSS-based planar fMSCs on a flexible PET film using laser cutter technique; (b) Photograph of laser-etched fMSCs with different configurations on one rGO-PEDOT:PSS film; (c) Optical images of 20 LEDs powered by 12 fMSCs connected in 6 series × 2 parallel (charged to 6 V) on a long strip of flexible rGO-PEDOT/PSS film (1.5 × 18 cm); Electrochemical performance of fMSCs(20). (d) Photograph of assembled fMSC device on its bent state; (e) CVs of the fMSC device before (*L* = 1 cm) and after bending at different curvatures (*L* = 0.8, 0.5, 0.2, and 0 cm). Also shown is the CV after repeatedly bending the fMSC device from *L* = 1 to *L* = 0 for 1000 times. *v* = 50 mV/s; (f) Galvanostatic charge/discharge curves at different current densities (with inset capacitance vs. current density); (g) Capacitance retention and columbic efficiency during the 20 000 cycles; (h) Ragone plot of fMSC(20) and commercially available electrochemical devices. Source: (a–d) Reproduced from Wang et al. [151] with permission from Wiley, 2016, (e–h) Liu et al. [181]. © 2016, John Wiley & Sons.

304.5 mF/cm^2@0.1 mA/cm^2), an energy density of 27.1 μWh/cm^2 and undoubtedly a great capacitance retention of 96% over 10 000 cycles.

Far complicated than a simple mixture, *in situ* polymerization could be more appropriate to steer clear of undesired additives and to enable a great control in morphology and micro/nano-structuration. It is widely accepted that the polymerization of PEDOT follows radical–cation mechanism where several parameters could interfere to the deposited polymer film, e.g. concentration of monomer, deposition time, applied potential, solvent, and additives. Unlike aniline and pyrrole, the hydrophobic behavior of EDOT usually implies a polymerization in organic solvent, e.g. acetonitrile. Once attached to the electrode surface, PEDOT modified substrates can be further used in both aqueous and organic solvents. In this respect, electropolymerization of EDOT onto graphene@carbon cloth (G@CC) was investigated [183]. Thus, the G@CC working electrode was anodically polarized (1.2 V/Ag|Ag$^+$ at different deposition times) in MeCN solution containing EDOT monomer. Under these conditions, sphere–like particles of PEDOT with few-hundred nanometer in diameter can be successfully deposited onto graphene paper (GP). By increasing the deposition time, the densely packed PEDOT is formed and the polymer fulfilled all the voids within the GP. Hence, the specific capacitance decreases from 715 F/g@50 mV/s (three minutes of deposition) to about 200 F/g@50 mV/s (30 minutes of deposition). Parallelly, the influence of applied potential on the performance of PEDOT/GO was also investigated [184]. Indeed, there are several potentials ranging from 1 to 2 V/Ag|AgCl to ITO substrate in a solution containing 10 mM EDOT and 1.0 mg/ml of GO. At the potentials below 1.2 V, slightly wrinkled paper-like sheets of PEDOT/GO were obtained, while a pronounced wrinkled structure was observed at the beyond potentials. This change in morphology could be explained by the overoxidation of EDOT that leads to a decrease in electrical conductivity of the film, [185] thus heterogeneously deposited film. Consequently, the gravimetric capacitance is strongly reduced from 115.15 F/g ($E_{\mathrm{dep}} = 1.2\,\mathrm{V}$) to <10 F/g@0.3 A/g (2 V), resulted to a blockage of ion channels through the active film. Besides mechanistic investigations as mentioned earlier, application of electrodeposited PEDOT in fabrication of supercapacitor was lately reported [186]. Accordingly, a copolymerization method was used to deposit GO/PEDOT-CNTs ternary composite onto a CNT thin films (CNFs, thickness = 20 μm). The polymerization was carried out in a solution containing 10 mM EDOT, GO (1 mg/ml) and COOH-modified short (0.5–2 μm)/long (10–30 μm) CNTs (1 mg/ml) by using galvanostatic mode ($i_{\mathrm{dep}} = 1\,\mathrm{mA/cm^2}$, $Q_{\mathrm{tot}} = 1.8\,\mathrm{C/cm^2}$). Two types of substrates were obtained, namely, GO/PEDOT-sCNTs and GO/PEDOT-lCNTs, corresponding to short/long CNTs, respectively. lCNTs allow to generate more space for ion channels, while sCNTs enable stacking more conductive material onto the porosity of the polymer matrix, thus reducing the diffusion of ion through the film. Accordingly, the GO/PEDOT-lCNT based supercapacitor shows a superior performance with a volumetric capacitance of 2.7 F/cm^3 @42 mA/cm^3 (or an areal capacitance of 33.4 mF/cm^2@10 mV/s) and a capacitance retention of 97.5% over 5000 cycles. Even though thiophene related polymers have been widely used as active material for supercapacitor application, the number of publications about the composite of graphene and electropolymerized PEDOT is still scanty and the optimization is still in progress [187–189].

In the following part, polymerized thiophene based polymer@graphene by means of chemical polymerization has been mentioned. As a simple route for fabrication of PEDOT@rGO, a mixture of EDOT monomer and rGO suspension was prepared followed by addition of an oxidizing agent (APS) to initiate the polymerization. After the purification process, the dried PEDOT@rGO composite was used as electrode material with a specific capacitance of 104 F/g@0.5 A/g, which is far lower than PPY and PANI@rGO prepared in the same procedure

(229 and 349 F/g@0.5 A/g, respectively) [190]. Nevertheless, the PEDOT composite exhibits the strongest capacitance retention of 88% after 1000 cycles (81% for PPY@rGO and 82% for PANI@rGO) [190]. For further improvement, a thin layer of PEDOT@rGO (thickness = 3.4 nm) [191] was prepared by mixing EDOT monomer to rGO suspension followed by purification and filtration to remove excessive amount of monomer. Indeed, π–stacking effect along with electrostatic interaction induces the formation of immobilized EDOTs–rGO structure, which can be further converted in PEDOT@rGO composite by chemical polymerization by microwave-assisted method. During MW radiation, the oxygen contained groups of GO participate to oxidize EDOT and end up with their reduced form simultaneously. By possessing a particular balance between electrical double layer capacitance (i.e. rGO sheets) and Faradaic capacitance from the PEDOT layer, the resulted composite exhibits a superior energy and power density of 34 Wh/kg and 25 kW/kg, respectively. Besides, the gravimetric capacitance is about 270 F/g@1 A/g together with high capacitance retention of 93% over 10 000 cycles of charge–discharge. However, the specific capacitance is still moderate for a commercialized system. Thus, Moussa et al. [192] reported the use of a ternary composite, graphene platelets/PEDOT/MnO_2, and coated kitchen sponge as active electrode with remarkable performance. Indeed, a clean kitchen sponge was soaked into a suspension of graphene platelets (GnP) followed by 3 cycles of “dip and dry” process. Once the GnPs were homogeneously attached to the sponge, the coating layer (PEDOT) was deposited by chemical polymerization in presence of APS and $FeCl_3$. Finally, PEDOT@GnP sponge was dipped into $KMnO_4$ solution, resulted to MnO_2 decorated PEDOT@GnP. By having low electrical conductivity, the presence of MnO_2 lowers the electrical conductivity of the composite from 1032 S/cm (Pristine PEDOT@G) to 947, 583, 82 S/cm (soaking time = 5, 10, and 20 minutes, respectively). Nevertheless, by profiting the additional porosity of MnO_2, the capacitance was strongly enhanced from 257.98 F/g(PEDOT@G sponge) to 740.25 F/g@0.5 A/g (MnO_2 decorated structure). High power and energy density were also obtained about 16.27 kW/kg and 45.12 Wh/kg, respectively, with the highest energy density at 55.76 Wh/kg@4.02 kW/kg. Furthermore, the strong mechanical tolerance of PEDOT@G allows cycling at 99% capacitance retention over 1000 cycles of stretching (400% strain). For cyclability, the capacitance retention of 87.61% was obtained after 10 000 charge–discharge cycles. Unlike chemically polymerized PANI/PPY@G, reported PEDOT@G composites (exempted from few rare cases) provide relatively poor electrochemical performance [190, 193, 194].

12.5 Conclusion and Outlook

Conducting polymers are intrinsically good candidates to be used as active materials in supercapacitors for electrochemical storage as aforementioned, their pseudo-capacitance is theoretical ranged from 200 to 750 F/g. However, in practice there is a high discrepancy between these theoretical values and the experimental ones. The literatures examination detailed in this chapter clearly shows this difference is due to a partial accessibility of the active sites of the polymer and that huge improvements can be obtained when controlling the morphology of the polymer at the nanometer scale: either for pure polymer with higher porosity and/or nanostructure, or for ECP mixed with other carbon-based nanostructure like activated carbon, CNTs, graphene. As aforementioned, thanks to their large theoretical surface area and electronic properties, carbon materials have been largely used with ECP for the fabrication of pseudo-supercapacitors. Typically, it has been observed in literature that when ECP is combined to carbon materials, the cyclability is usually improved: pristine ECP offer several thousand of cycles while, when nanostructured by C-based electrodes, their electrochemical stability jumps to several tens of thousands of cycles. However, in practice, the presence of strong van der Waal interactions as well as π-stacking effect between graphitic plans (CNT, graphene sheets) still reduce massively the C|ECP interface, resulting to non-optimized covered surface by the ECP.

Among the numerous properties of these nanocomposites, they exhibit flexibility, which makes them active materials of choice for flexible supercapacitors or micro-supercapacitors necessary for powering in the field of miniaturization of electronic devices, e.g. implantable medical devices, sensor nodes, and foldable organic electronics. Indeed, powering such small devices remains very challenging in term of limited storage surface, thus a high areal (and/or volumetric) capacitance as well as high energy and power density are strongly needed.

Besides the usual utilization of conventional supercapacitors – as power supply in tandem with Li-batteries for example – one of the most challenging trend is implement energy storage devices into clothes (wearable devices) that could be able to store energy (from mechanical motion or from light through PV cells) or power IoT[1] devices monitoring body activities; these energy storage devices should be designed onto fibers (technical clothes) so that flexibility and stretchability are required; also they should afford long-term safety to the consumer (need to develop all solid-state supercapacitors with efficient encapsulation technologies), be washable (mechanical stability and encapsulation are required). As a matter as a fact, the road is still long to comply with all these requirements. More recently, Miomandre and coworkers [195] have demonstrated the possibility of continuously electrodepositing PPY on carbon fibers covered with CNTs. The ECP was deposited in order to prevent the dispersion of CNTs but this study shows that the route to prepare ECP/CNT electrodes through *roll-to-roll* process is opened, allowing to large-scale fabrication of (pseudo-)supercapacitors. In parallel, some groups have developed roll-to-roll processes to synthesize short [196] or long [197] VACNTs electrodes for supercapacitors applications and startup companies such as Nawatechnologies (Rousset, France) (www.nawatechnologies.com/) are now commercializing VACNT/Al electrodes.

Since the last decade, after the discovery of graphene and control of its synthesis, composite of ECP and graphene have been largely investigated to prepare supercapacitors. Up to date, exempted from few rare exceptions of outstanding performing materials, the development of such composites for supercapacitor application is still

---

[1] IoT: Internet of Things.

challenging such as for ECP@CNTs nanocomposites and requires further studies on the optimization of composite synthesis as well as the interactions between components. In the literature, it is largely observed that the deposition of conducting polymer, either by oxidative chemical polymerization or electrochemical approach, leads to a significant obstruction of the accessible surface of graphene networks. It could be explained by the fulfilling of ECP onto the voids between graphene sheets. In practice, the cycling performance of ECP@G-based nanocomposites widely ranged from 100 to 1100 F/g as gravimetric capacitance and they can reach relatively high energy and power densities of ∼45 Wh/kg and ∼ 50 kWh/kg, respectively, depending on the chemical structure and morphology of the materials. One could be listed is PEDOT:PSS/G produced by Sun et al. [191] exhibits an energy density of 34 Wh/kg at a power density of 25 kWh/kg. Furthermore, by tailoring the porosity of the prepared composites, superior values of areal and volumetric capacitances could be attained. From the current state of the art, pulse technique appears as a convenient way to deposit a large amount of ECP onto the graphene sheets (and CNTs) without disturbing the ion channels inside the matrix. Nevertheless, this approach has not been proved as promising method for large scale production of positive electrode because of the low loading rate. Beside cycling performance, it is worth noting that the stability and durability of such composites are also depending on their structures.

Overall, even though the ECP@carbon-based materials have exhibited great cycling performance, they are still suffering several issues. Indeed, due to the electrochemical instability at high potentials, the ECP based electrodes can only be operated at low voltage, i.e. about 1–1.5 V. However, this drawback could be overcome by assembly of a number of cells either in series and/or in parallel or by fabricating asymmetrical or hybrid supercapacitors. Besides, the stability of ECP based materials over cycling is still problematic even if, as said previously, nanostructuration leads to increase the cyclability by a factor 10, which is still not sufficient. Complementarily, even it is not commonly mentioned in most of the reported works, the self-discharge rate of supercapacitors is still one of the main drawbacks, much higher than conventional Li–ion batteries (in the range of 30–50% over a month in the best performing systems).

For future directions of ECP-based supercapacitors development, several pathways could be followed: (i) improve the performance of existing materials in parallel with seeking for novel cost-effective raw materials (biomass, abundant mineral sources); (ii) get insight the understanding of interactions between different materials in order to synthetize efficiently composites; (iii) investigation of specific interactivity of electrode materials and electrolytes; (iv) increase the cyclability of SC. For this latter, this phenomenon is explained either by the trapped charge within the layer during the cycling, (i.e. passivation of the polymer/“dead” polymer) and/or the removal of polymeric chains from the materials and/or the volume change during charge/discharge of ECP. Generally, even though PEDOT:PSS based composites have moderate specific capacitance, they have been gifted a strong stability over cycling with slight degradation over 20 000 cycles at 90% of capacitance retention. (v) explore n-doping of ECP by the development of new type of conducting polymers, (vi) optimize the interaction between conducting polymer and carbon–based templates, i.e. adhesion, morphology, etc., (vii) optimize the supercapacitor assembly (reduce serial resistance, optimization supercapacitor's topography, casing…). Alongside improved performances, the cost of as-mentioned supercapacitors needs to be reduced. As future prospects, a combination of a supercapacitor and a battery in the same devices, i.e. supercapacitor–battery hybrid, could be potentially promising for generation of high-performing system [198]. Such configuration allows to take benefit from advantageous behaviors of both components.

References

1 Bae, J., Lee, J., Kim, S. et al. (2014). Flutter-driven triboelectrification for harvesting wind energy. *Nat. Commun.* 5: 1–9.

2 Li, S., Yuan, J., and Lipson, H. (2011). Ambient wind energy harvesting using cross-flow fluttering. *J. Appl. Phys.* 109 (2): 1–4.

3 Zhang, N., Chen, J., Huang, Y. et al. (2016). A wearable all-solid photovoltaic textile. *Adv. Mater.* 28 (2): 263–269.

4 Chang, S.Y., Cheng, P., Li, G., and Yang, Y. (2018). Transparent polymer photovoltaics for solar energy harvesting and beyond. *Joule* 2 (6): 1039–1054.

5 Khaligh, A. and Onar, O.C. (2009). *Energy Harvesting: Solar, Wind, and Ocean Energy Conversion Systems*. CRC Press.

6 Rus-Casas, C., Aguilar, J.D., Rodrigo, P. et al. (2014). Classification of methods for annual energy harvesting calculations of photovoltaic generators. *Energy Convers. Manage.* 78: 527–536.

7 Gonzalez, A., Goikolea, E., Barrena, J.A., and Mysyk, R. (2016). Review on supercapacitors: technologies and materials. *Renewable Sustainable Energy Rev.* 58: 1189–1206.

8 Wang, G., Zhang, L., and Zhang, J. (2012). A review of electrode materials for electrochemical supercapacitors. *Chem. Soc. Rev.* 41 (2): 797–828.

9 Zhong, C., Deng, Y., Hu, W. et al. (2015). A review of electrolyte materials and compositions for electrochemical supercapacitors. *Chem. Soc. Rev.* 44 (21): 7484–7539.

10 Pan, H., Li, J., and Feng, Y.P. (2010). Carbon nanotubes for supercapacitor. *Nanoscale Res. Lett.* 5 (3): 654–668.

11 Futaba, D.N., Hata, K., Yamada, T. et al. (2006). Shape-engineerable and highly densely packed single-walled carbon nanotubes and their application as super-capacitor electrodes. *Nat. Mater.* 5 (12): 987–994.

12 Liu, C., Yu, Z., Neff, D. et al. (2010). Graphene-based supercapacitor with an ultrahigh energy density. *Nano Lett.* 10 (12): 4863–4868.

13 Gamby, J., Taberna, P., Simon, P. et al. (2001). Studies and characterisations of various activated carbons used for carbon/carbon supercapacitors. *J. Power Sources* 101 (1): 109–116.

14 Kaempgen, M., Chan, C.K., Ma, J. et al. (2009). Printable thin film supercapacitors using single-walled carbon nanotubes. *Nano Lett.* 9 (5): 1872–1876.

15 Chiang, C.K., Fincher, C.R., Park, Y.W. et al. (1977). Electrical conductivity in doped polyacetylene. *Phys. Rev. Lett.* 39 (17): 1098–1101.

16 Terje, S., Elsenbaumer, R., and Reynolds, J.R. (1998). *Handbook of Conducting Polymers, Second Edition, Revised and Expanded*. New York: Basel: M. Dekker, cop.

17 Qiu, Z., Hammer, B.A.G., and Müllen, K. (2019). Conjugated polymers – problems and promises. *Prog. Polym. Sci.* 100: 101179.

18 MacDiarmid, A.G. (2001). Synthetic metals: a novel role for organic polymers. *Synth. Met.* 125 (1): 11–22.

19 Jang, J. (2006). Conducting polymer Nanomaterials and their applications. In: *Emissive Materials Nanomaterials*, vol. 199, 189–260. Berlin, Heidelberg: Springer. https://doi.org/10.1007/12_075.

20 Argun, A.A., Aubert, P.H., Thompson, B.C. et al. (2004). Multicolored electrochromisin in polymers: structures and devices. *Chem. Mater.* 16 (23): 4401–4412.

21 Beaujuge, P.M. and Reynolds, J.R. (2010). Color control in pi-conjugated organic polymers for use in electrochromic devices. *Chem. Rev.* 110 (1): 268–320.

22 Snook, G.a., Kao, P., and Best, A.S. (2011). Conducting-polymer-based supercapacitor devices and electrodes. *J. Power Sources* 196 (1): 1–12.

23 Le, T.-H., Kim, Y., and Yoon, H. (2017). Electrical and electrochemical properties of conducting polymers. *Polymers (Basel)* 9 (12): 150.

24 Benny, A. and George, S. (2018). Energy: polymer supercapacitors. In: *Encyclopedia of Polymer Applications* (ed. M. Mishra), 999. CRC Press.

25 Hu, X. and Xu, L. (2000). Structure and properties of 3-alkoxy substituted polythiophene synthesized at low temperature. *Polymer (Guildf.)* 41 (26): 9147–9154.

26 Andersson, M.R., Mammo, W., Olinga, T. et al. (1999). Synthesis of regioregular phenyl substituted polythiophenes with $FeCl_3$. *Synth. Met.* 101 (1): 11–12.

27 Mattioli-Belmonte, M., Gabbanelli, F., Marcaccio, M. et al. (2005). Bio-characterisation of tosylate-doped polypyrrole films for biomedical applications. *Mater. Sci. Eng., C* 25 (1): 43–49.

28 Winther-Jensen, B., Breiby, D.W., and West, K. (2005). Base inhibited oxidative polymerization of 3,4-ethylenedioxythiophene with iron(III)tosylate. *Synth. Met.* 152 (1–3): 1–4.

29 Lee, J.Y., Kim, D.Y., and Kim, C.Y. (1995). Synthesis of soluble polypyrrole of the doped state in organic solvents. *Synth. Met.* 74 (2): 103–106.

30 Zhang, X., Zhang, J., Song, W., and Liu, Z. (2006). Controllable synthesis of conducting polypyrrole nanostructures. *J. Phys. Chem. B* 110 (3): 1158–1165.

31 Genies, E.M., Bidan, G., and Diaz, A.F. (1983). Spectroelectrochemical study of polypyrrole films. *J. Electroanal. Chem. Interfacial Electrochem.* 149 (1–2): 101–113.

32 Abdelhamid, M.E., O'Mullane, A.P., and Snook, G.A. (2015). Storing energy in plastics: a review on conducting polymers & their role in electrochemical energy storage. *RSC Adv.* 5 (15): 11611–11626.

33 Laheäär, A., Przygocki, P., Abbas, Q., and Béguin, F. (2015). Appropriate methods for evaluating the efficiency and capacitive behavior of different types of supercapacitors. *Electrochem. Commun.* 60: 21–25.

34 Lota, K., Khomenko, V., and Frackowiak, E. (2004). Capacitance properties of poly(3,4-ethylenedioxythiophene)/carbon nanotubes composites. *J. Phys. Chem. Solids* 65 (2–3): 295–301.

35 Li, H., Wang, J., Chu, Q. et al. (2009). Theoretical and experimental specific capacitance of polyaniline in sulfuric acid. *J. Power Sources* 190 (2): 578–586.

36 Otero, T.F. and De Larreta, E. (1988). Electrochemical control of the morphology, adherence, appearance and growth of polypyrrole films. *Synth. Met.* 26 (1): 79–88.

37 Sharma, R.K., Rastogi, A.C., and Desu, S.B. (2008). Pulse polymerized polypyrrole electrodes for high energy density electrochemical supercapacitor. *Electrochem. Commun.* 10 (2): 268–272.

38 Kiani, M., Bhat, N., Davis, F., and Mitchell, G. (1992). Highly anisotropic electrically conducting films based on polypyrrole. *Polymer (Guildf.)* 33 (19): 4113–4120.

39 Kiani, M.S. and Mitchell, G.R. (1992). The role of the counter-ion in the preparation of polypyrrole films with enhanced properties using a pulsed electrochemical potential. *Synth. Met.* 48 (2): 203–218.

40 Zhang, J., Kong, L.-B., Li, H. et al. (2010). Synthesis of polypyrrole film by pulse galvanostatic method and its application as supercapacitor electrode materials. *J. Mater. Sci.* 45 (7): 1947–1954.

41 Zhou, H., Chen, H., Luo, S. et al. (2005). The effect of the polyaniline morphology on the performance of polyaniline supercapacitors. *J. Solid State Electrochem.* 9 (8): 574–580.

42 Pandey, G.P. and Rastogi, A.C. (2013). Synthesis and characterization of pulsed polymerized poly(3,4-ethylenedioxythiophene) electrodes for high-performance electrochemical capacitors. *Electrochim. Acta* 87: 158–168.

43 Laforgue, A. and Robitaille, L. (2010). Production of conductive PEDOT nanofibers by the combination of electrospinning and vapor-phase polymerization. *Macromolecules* 43 (9): 4194–4200.

44 Laforgue, A. (2011). All-textile flexible supercapacitors using electrospun poly(3,4-ethylenedioxythiophene) nanofibers. *J. Power Sources* 196 (1): 559–564.

45 Zhao, X., Dong, M., Zhang, J. et al. (2016). Vapor-phase polymerization of poly(3, 4-ethylenedioxythiophene) nanofibers on carbon cloth as electrodes for flexible supercapacitors. *Nanotechnology* 27 (38): 385705.

46 D'Arcy, J.M., El-Kady, M.F., Khine, P.P. et al. (2014). Vapor-phase polymerization of nanofibrillar poly(3,4-ethylenedioxythiophene) for supercapacitors. *ACS Nano* 8 (2): 1500–1510.

47 Dubal, D.P., Lee, S.H., Kim, J.G. et al. (2012). Porous polypyrrole clusters prepared by electropolymerization for a high performance supercapacitor. *J. Mater. Chem.* 22 (7): 3044–3052.

48 Ju, Y.-W., Choi, G.-R., Jung, H.-R., and Lee, W.-J. (2008). Electrochemical properties of electrospun PAN/MWCNT carbon nanofibers electrodes coated with polypyrrole. *Electrochim. Acta* 53 (19): 5796–5803.

49 Simon, P. and Burke, A. (2008). Nanostructured carbons: double-layer capacitance and more. In: *Interface*, vol. 17 (ed. Spring), 38–43. The Electrochemical Society.

50 Zhang, L.L. and Zhao, X.S. (2009). Carbon-based materials as supercapacitor electrodes. *Chem. Soc. Rev.* 38 (9): 2520.

51 Jurewicz, K., Vix-Guterl, C., Frackowiak, E. et al. (2004). Capacitance properties of ordered porous carbon materials prepared by a templating procedure. *J. Phys. Chem. Solids* 65 (2–3, 293): 287.

52 Fernández, J.A., Morishita, T., Toyoda, M. et al. (2008). Performance of mesoporous carbons derived from poly(vinyl alcohol) in electrochemical capacitors. *J. Power Sources* 175 (1): 675–679.

53 Balducci, A., Dugas, R., Taberna, P.L. et al. (2007). High temperature carbon–carbon supercapacitor using ionic liquid as electrolyte. *J. Power Sources* 165 (2): 922–927.

54 Wampler, W.A., Rajeshwar, K., Pethe, R.G. et al. (1995). Composites of polypyrrole and carbon black: Part III. Chemical synthesis and characterization. *J. Mater. Res.* 10 (07): 1811–1822.

55 Izadi-Najafabadi, A., Tan, D.T.H., and Madden, J.D. (2005). Towards high power polypyrrole/carbon capacitors. *Synth. Met.* 152 (1–3): 129–132.

56 Park, S.J., Kim, D.W., and Lee, J.H. (2014). Electrochemical properties of size-controllable polypyrrole/porous carbon for supercapacitor electrodes. *J. Nanosci. Nanotechnol.* 14 (12): 9263–9267.

57 Chen, W.-C.C., Wen, T.-C.C., and Teng, H. (2003). Polyaniline-deposited porous carbon electrode for supercapacitor. *Electrochim. Acta* 48 (6): 641–649.

58 Chen, W.C. and Wen, T.C. (2003). Electrochemical and capacitive properties of polyaniline-implanted porous carbon electrode for supercapacitors. *J. Power Sources* 117 (1–2): 273–282.

59 Bleda-Martínez, M.J., Morallón, E., and Cazorla-Amorós, D. (2007). Polyaniline/porous carbon electrodes by chemical polymerisation: effect of carbon surface chemistry. *Electrochim. Acta* 52 (15): 4962–4968.

60 Yang, N., Lin, X.Q., Lü, Q.F. et al. (2019). Polyaniline-modified renewable biocarbon composites as an efficient hybrid electrode for supercapacitors. *Ionics (Kiel)* 25 (11): 5459–5472.

61 Wang, Q., Li, J.L., Gao, F. et al. (2008). Activated carbon coated with polyaniline as an electrode material in supercapacitors. *Xinxing Tan Cailiao/New Carbon Mater.* 23 (3): 275–280.

62 Han, J., Li, Q., Peng, C. et al. (2020). Increasing S dopant and specific surface area of N/S-codoped porous carbon by in-situ polymerization of PEDOT into biomass precursor for high performance supercapacitor. *Appl. Surf. Sci.* 502: 144191.

63 Lei, C., Wilson, P., and Lekakou, C. (2011). Effect of poly(3,4-ethylenedioxythiophene) (PEDOT) in carbon-based composite electrodes for electrochemical supercapacitors. *J. Power Sources* 196 (18): 7823–7827.

64 Tong, L., Skorenko, K.H., Faucett, A.C. et al. (2015). Vapor-phase polymerization of poly(3,4-ethylenedioxythiophene) (PEDOT) on commercial carbon coated aluminum foil as enhanced electrodes for supercapacitors. *J. Power Sources* 297: 195–201.

65 Monthioux, M. and Kuznetsov, V.L. (2006). Who should be given the credit for the discovery of carbon nanotubes? *Carbon (N.Y.)* 44 (9): 1621–1623.

66 Iijima, S. (1991). Helical microtubules of graphitic carbon. *Nature* 354 (6348): 56–58.

67 Bethune, D.S., Kiang, C.H., de Vries, M.S. et al. (1993). Cobalt-catalysed growth of carbon nanotubes with single-atomic-layer walls. *Nature* 363 (6430): 605–607.

68 Kumar, M. and Ando, Y. (2010). Chemical vapor deposition of carbon nanotubes: a review on growth mechanism and mass production. *J. Nanosci. Nanotechnol.* 10 (6): 3739–3758.

69 Kaempgen, M., Ma, J., Gruner, G. et al. (2007). Bifunctional carbon nanotube networks for supercapacitors. *Appl. Phys. Lett.* 90 (26): 264104.

70 Nessim, G.D., Seita, M., O'Brien, K.P. et al. (2009). Low temperature synthesis of vertically aligned carbon nanotubes with electrical contact to metallic substrates enabled by thermal decomposition of the carbon feedstock. *Nano Lett.* 9 (10): 3398–3405.

71 Gao, Z., Zhang, X., Zhang, K., and Yuen, M.M.F. (2015). Growth of vertically aligned carbon nanotube arrays on Al substrates through controlled diffusion of catalyst. *J. Phys. Chem. C* 119 (27): 15636–15642.

72 Jourdain, V. and Bichara, C. (2013). Current understanding of the growth of carbon nanotubes in catalytic chemical vapour deposition. *Carbon (N.Y.)* 58: 2–39.

73 Delmas, M., Pinault, M., Patel, S. et al. (2012). Growth of long and aligned multi-walled carbon nanotubes on carbon and metal substrates. *Nanotechnology* 23 (10): 105604.

74 Castro, C., Pinault, M., Coste-Leconte, S. et al. (2010). Dynamics of catalyst particle formation and multi-walled carbon nanotube growth in aerosol-assisted catalytic chemical vapor deposition. *Carbon (N.Y.)* 48 (13): 3807–3816.

75 Pinault, M., Pichot, V., Khodja, H. et al. (2005). Evidence of sequential lift in growth of aligned multiwalled carbon nanotube multilayers. *Nano Lett.* 5 (12): 2394–2398.

76 Zhang, H., Cao, G., Yang, Y., and Gu, Z. (2008). Comparison between electrochemical properties of aligned carbon nanotube array and entangled carbon nanotube electrodes. *J. Electrochem. Soc.* 155 (2): K19.

77 Yoshino, K., Kajii, H., Araki, H. et al. (1999). Electrical and optical properties of conducting polymer-fullerene and conducting polymer-carbon nanotube composites. *Fullerene Sci. Technol.* 7 (4): 695–711.

78 Mastragostino, M., Arbizzani, C., and Soavi, F. (2002). Conducting polymers as electrode materials in supercapacitors. *Solid State Ionics* 148 (3–4): 493–498.

79 Peng, C., Zhang, S., Jewell, D., and Chen, G.Z. (2008). Carbon nanotube and conducting polymer composites for supercapacitors. *Prog. Nat. Sci.* 18 (7): 777–788.

80 Hughes, M., Chen, G.Z., Shaffer, M.S.P. et al. (2004). Controlling the nanostructure of electrochemically grown nanoporous composites of carbon nanotubes and conducting polymers. *Compos. Sci. Technol.* 64 (15): 2325–2331.

81 Xiao, Q. and Zhou, X. (2003). The study of multiwalled carbon nanotube deposited with conducting polymer for supercapacitor. *Electrochim. Acta* 48 (5): 575–580.

82 Chen, G.Z., Shaffer, M.S.P., Coleby, D. et al. (2000). Carbon nanotube and polypyrrole composites: coating and doping. *Adv. Mater.* 12 (7): 522–526.

83 Zhou, C., Kumar, S., Doyle, C.D., and Tour, J.M. (2005). Functionalized single wall carbon nanotubes treated with pyrrole for electrochemical supercapacitor membranes. *Chem. Mater.* 17 (8): 1997–2002.

84 Hughes, M., Chen, G.Z., Shaffer, M.S.P. et al. (2002). Electrochemical capacitance of a nanoporous composite of carbon nanotubes and polypyrrole. *Chem. Mater.* 14 (4): 1610–1613.

85 Peng, C., Jin, J., and Chen, G.Z. (2007). A comparative study on electrochemical co-deposition and capacitance of composite films of conducting polymers and carbon nanotubes. *Electrochim. Acta* 53 (2): 525–537.

86 Fan, J.H., Wan, M.X., Zhu, D.B. et al. (1999). Synthesis, characterizations, and physical properties of carbon nanotubes coated by conducting polypyrrole. *J. Appl. Polym. Sci.* 74 (11): 2605–2610.

87 An, K.H., Jeon, K.K., Heo, J.K. et al. (2002). High-capacitance supercapacitor using a nanocomposite electrode of single-walled carbon nanotube and polypyrrole. *J. Electrochem. Soc.* 149 (8).

88 Laforgue, A., Simon, P., Fauvarque, J. et al. (2003). Activated carbon/conducting polymer hybrid supercapacitors. *J. Electrochem. Soc.* 150 (5): A645–A651.

89 Downs, C., Nugent, J., Ajayan, P.M. et al. (1999). Efficient polymerization of aniline at carbon nanotube electrodes. *Adv. Mater.* 11 (12): 1028–1031.

90 Oh, J., Kozlov, M.E., Kim, B.G. et al. (2008). Preparation and electrochemical characterization of porous SWNT-PPy nanocomposite sheets for supercapacitor applications. *Synth. Met.* 158 (15): 638–641.

91 Fang, Y., Liu, J., Yu, D.J. et al. (2010). Self-supported supercapacitor membranes: polypyrrole-coated carbon nanotube networks enabled by pulsed electrodeposition. *J. Power Sources* 195 (2): 674–679.

92 Benson, J., Kovalenko, I., Boukhalfa, S. et al. (2013). Multifunctional CNT-polymer composites for ultra-tough structural supercapacitors and desalination devices. *Adv. Mater.* 25 (45): 6625–6632.

93 Li, X. and Zhitomirsky, I. (2013). Electrodeposition of polypyrrole–carbon nanotube composites for electrochemical supercapacitors. *J. Power Sources* 221: 49–56.

94 Afzal, A., Abuilaiwi, F.A., Habib, A. et al. (2017). Polypyrrole/carbon nanotube supercapacitors: technological advances and challenges. *J. Power Sources* 352: 174–186.

95 Chen, J.H., Huang, Z.P., Wang, D.Z. et al. (2001). Electrochemical synthesis of polypyrrole films over each of well-aligned carbon nanotubes. *Synth. Met.* 125 (3): 289–294.

96 Hsia, B., Marschewski, J., Wang, S. et al. (2014). Highly flexible, all solid-state micro-supercapacitors from vertically aligned carbon nanotubes. *Nanotechnology* 25 (5): 055401.

97 Warren, R., Sammoura, F., Teh, K.S. et al. (2015). Electrochemically synthesized and vertically aligned carbon nanotube–polypyrrole nanolayers for high energy storage devices. *Sens. Actuators, A* 231: 65–73.

98 Lagoutte, S. (2010). Nanocomposites polythiophènes/nanotubes de carbone supercondensateurs en milieu liquide ionique. (PhD dissertation, Université Cergy – Pontoise, Neuville sur Oise, France). Retrieved from University's library .

99 Ghaffari, M., Kosolwattana, S., Zhou, Y. et al. (2013). Hybrid supercapacitor materials from poly(3,4-ethylenedioxythiophene) conformally coated aligned carbon nanotubes. *Electrochim. Acta* 112: 522–528.

100 Fang, Y., Jiang, X., Niu, L., and Wang, S. (2017). Constructing polypyrrole/aligned carbon nanotubes composite materials as electrodes for high-performance supercapacitors. *Mater. Lett.* 190: 232–235.

101 Huang, F. and Chen, D. (2012). Towards the upper bound of electrochemical performance of ACNT@polyaniline arrays as supercapacitors. *Energy Environ. Sci.* 5 (2): 5833–5841.

102 Lagoutte, S., Aubert, P.-H., Pinault, M. et al. (2014). Poly(3-methylthiophene)/vertically aligned multi-walled carbon nanotubes: electrochemical synthesis, characterizations and electrochemical storage properties in ionic liquids. *Electrochim. Acta* 130: 754–765.

103 Reit, R., Nguyen, J., and Ready, W.J. (2013). Growth time performance dependence of vertically aligned carbon nanotube supercapacitors grown on aluminum substrates. *Electrochim. Acta* 91: 96–100.

104 Nassoy, F., Pinault, M., Descarpentries, J. et al. (2019). Single-step synthesis of vertically aligned carbon nanotube forest on aluminium foils. *Nanomaterials* 9 (11): 1590.

105 Vignal, T., Banet, P., Pinault, M. et al. (2020). Electropolymerized poly(3-methylthiophene) onto high density vertically aligned carbon nanotubes directly grown on aluminum substrate: application to electrochemical capacitors. *Electrochim. Acta* 350: 136377.

106 Chang, Z.-H., Feng, D.-Y., Huang, Z.-H., and Liu, X.-X. (2018, 2017). Electrochemical deposition of highly loaded polypyrrole on individual carbon nanotubes in carbon nanotube film for supercapacitor. *Chem. Eng. J.* 337: 552–559.

107 Zhou, Y., Xu, H., Lachman, N. et al. (2014). Advanced asymmetric supercapacitor based on conducting polymer and aligned carbon nanotubes with controlled nanomorphology. *Nano Energy* 9: 176–185.

108 Lin, H., Li, L., Ren, J. et al. (2013). Conducting polymer composite film incorporated with aligned carbon nanotubes for transparent, flexible and efficient supercapacitor. *Sci. Rep.* 3: 1–6.

109 Geim, A.K. and Novoselov, K.S. (2007). The rise of graphene. *Nat. Mater.* 6 (3): 183–191.

110 Bonaccorso, F., Colombo, L., Yu, G. et al. (2015). Graphene, related two-dimensional crystals, and hybrid systems for energy conversion and storage. *Science* 347 (6217): 1246501.

111 Ghosh, S., Holade, Y., Remita, H. et al. (2016). One-pot synthesis of reduced graphene oxide supported gold-based nanomaterials as robust nanocatalysts for glucose electrooxidation. *Electrochim. Acta* 212: 864–875.

112 Kar, P., Sardar, S., Liu, B. et al. (2016). Facile synthesis of reduced graphene oxide–gold nanohybrid for potential use in industrial waste-water treatment. *Sci. Technol. Adv. Mater.* 17 (1): 375–386.

113 Chen, J.H., Jang, C., Xiao, S. et al. (2008). Intrinsic and extrinsic performance limits of graphene devices on SiO_2. *Nat. Nanotechnol.* 3 (4): 206–209.

114 Xia, J., Chen, F., Li, J., and Tao, N. (2009). Measurement of the quantum capacitance of graphene. *Nat. Nanotechnol.* 4 (8): 505–509.

115 Cao, X., Shi, Y., Shi, W. et al. (2011). Preparation of novel 3D graphene networks for supercapacitor applications. *Small* 7 (22): 3163–3168.

116 Liu, J., Zhang, L., Wu, H.B. et al. (2014). High-performance flexible asymmetric supercapacitors based on a new graphene foam/carbon nanotube hybrid film. *Energy Environ. Sci.* 7 (11): 3709–3719.

117 Yang, Z., Chabi, S., Xia, Y., and Zhu, Y. (2015). Preparation of 3D graphene-based architectures and their applications in supercapacitors. *Prog. Nat. Sci. Mater. Int.* 25 (6): 554–562.

118 Lee, Y.R., Raghu, A.V., Jeong, H.M., and Kim, B.K. (2009). Properties of waterborne polyurethane/functionalized graphene sheet nanocomposites prepared by an in situ method. *Macromol. Chem. Phys.* 210 (15): 1247–1254.

119 Liang, J., Wang, Y., Huang, Y. et al. (2009). Electromagnetic interference shielding of graphene/epoxy composites. *Carbon (N.Y.)* 47 (3): 922–925.

120 Stankovich, S., Dikin, D.A., Dommett, G.H.B. et al. (2006). Graphene-based composite materials. *Nature* 442 (7100): 282–286.

121 Hu, H., Wang, X., Wang, J. et al. (2010). Preparation and properties of graphene nanosheets-polystyrene nanocomposites via in situ emulsion polymerization. *Chem. Phys. Lett.* 484 (4–6): 247–253.

122 Eda, G. and Chhowalla, M. (2009). Graphene-based composite thin films for electronics. *Nano Lett.* 9 (2): 814–818.

123 Peponi, L., Tercjak, A., Verdejo, R. et al. (2009). Confinement of functionalized graphene sheets by triblock copolymers. *J. Phys. Chem. C* 113 (42): 17973–17978.

124 Erukhimovich, I. and de la Cruz, M.O. (2009). Phase equilibria and charge fractionation in polydisperse polyelectrolyte solutions. *J. Polym. Sci., Part B: Polym. Phys.* 47 (9): 888–897.

125 Kim, H. and Macosko, C.W. (2009). Processing-property relationships of polycarbonate/graphene composites. *Polymer (Guildf.)* 50 (15): 3797–3809.

126 Liang, J., Huang, Y., Zhang, L. et al. (2009). Molecular-level dispersion of graphene into poly(vinyl alcohol) and effective reinforcement of their nanocomposites. *Adv. Funct. Mater.* 19 (14): 2297–2302.

127 Hong, W., Xu, Y., Lu, G. et al. (2008). Transparent graphene/PEDOT-PSS composite films as counter electrodes of dye-sensitized solar cells. *Electrochem. Commun.* 10 (10): 1555–1558.

128 Xu, G., Jarjes, Z.A., Desprez, V. et al. (2018). Sensitive, selective, disposable electrochemical dopamine sensor based on PEDOT-modified laser scribed graphene. *Biosens. Bioelectron.* 107: 184–191.

129 Si, W., Lei, W., Zhang, Y. et al. (2012). Electrodeposition of graphene oxide doped poly(3,4-ethylenedioxythiophene) film and its electrochemical sensing of catechol and hydroquinone. *Electrochim. Acta* 85: 295–301.

130 Guo, C.X., Wang, M., Chen, T. et al. (2011). A hierarchically nanostructured composite of MnO 2/conjugated polymer/graphene for high-performance lithium ion batteries. *Adv. Energy Mater.* 1 (5): 736–741.

131 Zhang, M., Yuan, W., Yao, B. et al. (2014). Solution-processed PEDOT:PSS/graphene composites as the electrocatalyst for oxygen reduction reaction. *ACS Appl. Mater. Interfaces* 6 (5): 3587–3593.

132 Yue, R., Wang, H., Bin, D. et al. (2015). Facile one-pot synthesis of Pd-PEDOT/graphene nanocomposites with hierarchical structure and high electrocatalytic performance for ethanol oxidation. *J. Mater. Chem. A* 3 (3): 1077–1088.

133 Sun, Y. and Shi, G. (2013). Graphene/polymer composites for energy applications. *J. Polym. Sci., Part B: Polym. Phys.* 51 (4): 231–253.

134 Gao, Y. (2017). Graphene and polymer composites for supercapacitor applications: a review. *Nanoscale Res. Lett.* 12 (1): 387.

135 Wang, D., Li, F., Zhao, J. et al. (2009). Fabrication of graphene/polyaniline performance flexible electrode electropolymerization for high - composite paper via in situ anodic. *ACS Nano* 3 (7): 1745–1752.

136 Cong, H.P., Ren, X.C., Wang, P., and Yu, S.H. (2013). Flexible graphene-polyaniline composite paper for high-performance supercapacitor. *Energy Environ. Sci.* 6 (4): 1185–1191.

137 Jin, J., Mu, H., Wang, W. et al. (2019). Long-life flexible supercapacitors based on nitrogen-doped porous graphene@π-conjugated polymer film electrodes and porous quasi-solid-state polymer electrolyte. *Electrochim. Acta* 317: 250–260.

138 Gao, S., Zhang, L., Qiao, Y. et al. (2016). Electrodeposition of polyaniline on three-dimensional graphene hydrogel as a binder-free supercapacitor electrode with high power and energy densities. *RSC Adv.* 6 (64): 58854–58861.

139 Yu, J., Xie, F., Wu, Z. et al. (2018). Flexible metallic fabric supercapacitor based on graphene/polyaniline composites. *Electrochim. Acta* 259: 968–974.

140 Shen, H., Li, H., Li, M. et al. (2018). High-performance aqueous symmetric supercapacitor based on polyaniline/vertical graphene/Ti multilayer electrodes. *Electrochim. Acta* 283: 410–418.

141 Feng, X.M., Li, R.M., Ma, Y.W. et al. (2011). One-step electrochemical synthesis of graphene/polyaniline composite film and its applications. *Adv. Funct. Mater.* 21 (15): 2989–2996.

142 Zhang, Q., Li, Y., Feng, Y., and Feng, W. (2013). Electropolymerization of graphene oxide/polyaniline composite for high-performance supercapacitor. *Electrochim. Acta* 90: 95–100.

143 Zhang, K., Zhang, L.L., Zhao, X.S., and Wu, J. (2010). Graphene/polyaniline nanofiber composites as supercapacitor electrodes. *Chem. Mater.* 22 (4): 1392–1401.

144 Yan, J., Wei, T., Fan, Z. et al. (2010). Preparation of graphene nanosheet/carbon nanotube/polyaniline composite as electrode material for supercapacitors. *J. Power Sources* 195 (9): 3041–3045.

145 Mao, L., Zhang, K., On Chan, H.S., and Wu, J. (2012). Surfactant-stabilized graphene/polyaniline nanofiber composites for high performance supercapacitor electrode. *J. Mater. Chem.* 22 (1): 80–85.

146 Sun, H., She, P., Xu, K. et al. (2015). A self-standing nanocomposite foam of polyaniline@reduced graphene oxide for flexible super-capacitors. *Synth. Met.* 209: 68–73.

147 Hong, X., Zhang, B., Murphy, E. et al. (2017). Three-dimensional reduced graphene oxide/polyaniline nanocomposite film prepared by diffusion driven layer-by-layer assembly for high-performance supercapacitors. *J. Power Sources* 343: 60–66.

148 Li, P., Jin, Z., Peng, L. et al. (2018). Stretchable all-gel-state fiber-shaped supercapacitors enabled by macromolecularly interconnected 3D graphene/nanostructured conductive polymer hydrogels. *Adv. Mater.* 30 (18): 1–7.

149 Wu, J., Zhang, Q., Wang, J. et al. (2018). A self-assembly route to porous polyaniline/reduced graphene oxide composite materials with molecular-level uniformity for high-performance supercapacitors. *Energy Environ. Sci.* 11 (5): 1280–1286.

150 Meng, Q., Cai, K., Chen, Y., and Chen, L. (2017). Research progress on conducting polymer based supercapacitor electrode materials. *Nano Energy* 36: 268–285.

151 Wang, H., Yu, Z., El-Kady, M.F. et al. (2019). Graphene/oligoaniline based supercapacitors: towards conducting polymer materials with high rate charge storage. *Energy Storage Mater.* 19: 137–147.

152 Li, R., Yang, Y., Wu, D. et al. (2019). Covalent functionalization of reduced graphene oxide aerogels with polyaniline for high performance supercapacitors. *Chem. Commun.* 55 (12): 1738–1741.

153 Zhang, L., Wang, W., Cheng, J. et al. (2018). Skeleton networks of graphene wrapped double-layered polypyrrole/polyaniline nanotubes for supercapacitor applications. *J. Mater. Sci.* 53 (1): 787–798.

154 Liu, Y., Zhang, B., Xu, Q. et al. (2018). Development of graphene oxide/polyaniline inks for high performance flexible microsupercapacitors via extrusion printing. *Adv. Funct. Mater.* 28 (21): 1–12.

155 Xu, J., Wang, K., Zu, S. et al. (2010). Hierarchical nanocomposites of polyaniline nanowire arrays on graphene oxide sheets with synergistic effect for energy storage. *ACS Nano* 4 (9): 5019–5026.

156 Liu, P., Yan, J., Gao, X. et al. (2018). Construction of layer-by-layer sandwiched graphene/polyaniline nanorods/carbon nanotubes heterostructures for high performance supercapacitors. *Electrochim. Acta* 272: 77–87.

157 Wu, Z.S., Parvez, K., Li, S. et al. (2015). Alternating stacked graphene-conducting polymer compact films with ultrahigh areal and volumetric capacitances for high-energy micro-supercapacitors. *Adv. Mater.* 27 (27): 4054–4061.

158 Liu, A., Li, C., Bai, H., and Shi, G. (2010). Electrochemical deposition of polypyrrole/sulfonated graphene composite films. *J. Phys. Chem. C* 114 (51): 22783–22789.

159 Davies, A., Audette, P., Farrow, B. et al. (2011). Graphene-based flexible supercapacitors: pulse-electropolymerization of polypyrrole on free-standing graphene films. *J. Phys. Chem. C* 115 (35): 17612–17620.

160 Li, Y., Louarn, G., Aubert, P.-H. et al. (2016). Polypyrrole-modified graphene sheet nanocomposites as new efficient materials for supercapacitors. *Carbon (N.Y.)* 105: 510–520.

161 Chen, Z., Yu, D., Xiong, W. et al. (2014). Graphene-based nanowire supercapacitors. *Langmuir* 30 (12): 3567–3571.

162 Zhao, Y., Liu, J., Hu, Y. et al. (2013). Highly compression-tolerant supercapacitor based on polypyrrole-mediated graphene foam electrodes. *Adv. Mater.* 25 (4): 591–595.

163 Park, H., Kim, J.W., Hong, S.Y. et al. (2018). Microporous polypyrrole-coated graphene foam for high-performance multifunctional sensors and flexible supercapacitors. *Adv. Funct. Mater.* 28 (33): 1–11.

164 Hou, M., Xu, M., Hu, Y., and Li, B. (2019). Nanocellulose incorporated graphene/polypyrrole film with a sandwich-like architecture for preparing flexible supercapacitor electrodes. *Electrochim. Acta* 313: 245–254.

165 Yang, J., Weng, W., Liang, Y. et al. (2019). Heterogeneous graphene/polypyrrole multilayered microtube with enhanced capacitance. *Electrochim. Acta* 304: 378–385.

166 Barakzehi, M., Montazer, M., Sharif, F. et al. (2019). A textile-based wearable supercapacitor using reduced graphene oxide/polypyrrole composite. *Electrochim. Acta* 305: 187–196.

167 Wan, C., Jiao, Y., and Li, J. (2017). Flexible, highly conductive, and free-standing reduced graphene oxide/polypyrrole/cellulose hybrid papers for supercapacitor electrodes. *J. Mater. Chem. A* 5 (8): 3819–3831.

168 De Oliveira, H.P., Sydlik, S.A., and Swager, T.M. (2013). Supercapacitors from free-standing polypyrrole/graphene nanocomposites. *J. Phys. Chem. C* 117 (20): 10270–10276.

169 Biswas, S. and Drzal, L.T. (2010). Multilayered nanoarchitecture of graphene nanosheets and polypyrrole nanowires for high performance supercapacitor electrodes. *Chem. Mater.* 22 (20): 5667–5671.

170 Xu, C., Sun, J., and Gao, L. (2011). Synthesis of novel hierarchical graphene/polypyrrole nanosheet composites and their superior electrochemical performance. *J. Mater. Chem.* 21 (30): 11253–11258.

171 Sahoo, S., Dhibar, S., Hatui, G. et al. (2013). Graphene/polypyrrole nanofiber nanocomposite as electrode material for electrochemical supercapacitor. *Polymer (Guildf.)* 54 (3): 1033–1042.

172 Ma, L., Liu, R., Niu, H. et al. (2016). Freestanding conductive film based on polypyrrole/bacterial cellulose/graphene paper for flexible supercapacitor: large areal mass exhibits excellent areal capacitance. *Electrochim. Acta* 222: 429–437.

173 Ye, S. and Feng, J. (2014). Self-assembled three-dimensional hierarchical graphene/polypyrrole nanotube hybrid aerogel and its application for supercapacitors. *ACS Appl. Mater. Interfaces* 6 (12): 9671–9679.

174 Lai, L., Wang, L., Yang, H. et al. (2012). Tuning graphene surface chemistry to prepare graphene/polypyrrole supercapacitors with improved performance. *Nano Energy* 1 (5): 723–731.

175 Li, X., Wang, H., Robinson, J.T. et al. (2009). Simultaneous nitrogen doping and reduction of graphene oxide. *J. Am. Chem. Soc.* 131 (43): 15939–15944.

176 Hulicova-Jurcakova, D., Kodama, M., Shiraishi, S. et al. (2009). Nitrogen-enriched nonporous carbon electrodes with extraordinary supercapacitance. *Adv. Funct. Mater.* 19 (11): 1800–1809.

177 Kalambate, P.K., Dar, R.A., Karna, S.P., and Srivastava, A.K. (2015). High performance supercapacitor based on graphene-silver nanoparticles-polypyrrole nanocomposite coated on glassy carbon electrode. *J. Power Sources* 276: 262–270.

178 Qin, T., Liu, B., Wen, Y. et al. (2016). Freestanding flexible graphene foams@polypyrrole@MnO_2 electrodes for high-performance supercapacitors. *J. Mater. Chem. A* 4 (23): 9196–9203.

179 Yu, G., Hu, L., Liu, N. et al. (2011). Enhancing the supercapacitor performance of graphene/MnO_2 nanostructured electrodes by conductive wrapping. *Nano Lett.* 11 (10): 4438–4442.

180 Liu, Y., Weng, B., Razal, J.M. et al. (2015). High-performance flexible all-solid-state supercapacitor from large free-standing graphene-PEDOT/PSS films. *Sci. Rep.* 5: 1–11.

181 Liu, Y., Weng, B., Xu, Q. et al. (2016). Facile fabrication of flexible microsupercapacitor with high energy density. *Adv. Mater. Technol.* 1 (9): 1–10.

182 Qu, G., Cheng, J., Li, X. et al. (2016). A fiber supercapacitor with high energy density based on hollow graphene/conducting polymer fiber electrode. *Adv. Mater.* 28 (19): 3646–3652.

183 Chu, C.Y., Tsai, J.T., and Sun, C.L. (2012). Synthesis of PEDOT-modified graphene composite materials as flexible electrodes for energy storage and conversion applications. *Int. J. Hydrogen Energy* 37 (18): 13880–13886.

184 Nabilah Azman, N.H., Lim, H.N., and Sulaiman, Y. (2016). Effect of electropolymerization potential on the preparation of PEDOT/graphene oxide hybrid material for supercapacitor application. *Electrochim. Acta* 188: 785–792.

185 Du, X. and Wang, Z. (2003). Effects of polymerization potential on the properties of electrosynthesized PEDOT films. *Electrochim. Acta* 48 (12): 1713–1717.

186 Zhou, H., Zhai, H.J., and Han, G. (2016). Superior performance of highly flexible solid-state supercapacitor based on the ternary composites of graphene oxide supported poly(3,4-ethylenedioxythiophene)-carbon nanotubes. *J. Power Sources* 323: 125–133.

187 Mao, X., Yang, W., He, X. et al. (2017). The preparation and characteristic of poly (3,4-ethylenedioxythiophene)/reduced graphene oxide nanocomposite and its application for supercapacitor electrode. *Mater. Sci. Eng., B* 216: 16–22.

188 Lehtimäki, S., Suominen, M., Damlin, P. et al. (2015). Preparation of supercapacitors on flexible substrates with electrodeposited PEDOT/graphene composites. *ACS Appl. Mater. Interfaces* 7 (40): 22137–22147.

189 Miltenburg, M.B., Schon, T.B., Kynaston, E.L. et al. (2017). Electrochemical polymerization of functionalized graphene quantum dots. *Chem. Mater.* 29 (16): 6611–6615.

190 Zhang, J. and Zhao, X.S. (2012). Conducting polymers directly coated on reduced graphene oxide sheets as high-performance supercapacitor electrodes. *J. Phys. Chem. C* 116 (9): 5420–5426.

191 Sun, D., Jin, L., Chen, Y. et al. (2013). Microwave-assisted in situ synthesis of graphene/PEDOT hybrid and its application in supercapacitors. *ChemPlusChem* 78 (3): 227–234.

192 Moussa, M., Shi, G., Wu, H. et al. (2017). Development of flexible supercapacitors using an inexpensive graphene/PEDOT/MnO_2 sponge composite. *Mater. Des.* 125: 1–10.

193 Han, Y., Shen, M., Wu, Y. et al. (2013). Preparation and electrochemical performances of PEDOT/sulfonic acid-functionalized graphene composite hydrogel. *Synth. Met.* 172: 21–27.

194 Wang, W., Lei, W., Yao, T. et al. (2013). One-pot synthesis of graphene/SnO_2/PEDOT ternary electrode material for supercapacitors. *Electrochim. Acta* 108: 118–126.

195 Saba, J., Magga, Y., He, D. et al. (2013). Continuous electrodeposition of polypyrrole on carbon nanotube–carbon fiber hybrids as a protective treatment against nanotube dispersion. *Carbon (N.Y.)* 51 (41): 20–26.

196 Arcila-Velez, M.R., Zhu, J., Childress, A. et al. (2014). Roll-to-roll synthesis of vertically aligned carbon nanotube electrodes for electrical double layer capacitors. *Nano Energy* 8: 9–16.

197 Boulanger, P., Belkadi, L., Descarpentries, J. et al. (2013). Towards large scale aligned carbon nanotube composites: an industrial safe-by-design and sustainable approach. *J. Phys. Conf. Ser.* 429 (1): 012050.

198 Shah, N. and Czarkowski, D. (2018). Supercapacitors in tandem with batteries to prolong the range of UGV systems. *Electronics* 7 (1): 6.

Index

Conjugated Polymer Nanostructures for Energy Conversion and Storage Applications,
First Edition. Edited by Srabanti Ghosh.